

GENEVIÈVE CAUCHON-VOYER

**MOUVEMENTS DE MASSE EN MILIEU
CÔTIER : LE COMPLEXE DES GLISSEMENTS
DE TERRAIN DE BETSIAMITES DANS
L'ESTUAIRE DU SAINT-LAURENT, QUÉBEC,
CANADA**

Thèse présentée

à la Faculté des études supérieures et postdoctorales de l'Université Laval
dans le cadre du programme de doctorat interuniversitaire en sciences de la Terre
pour l'obtention du grade de Philosophiæ Doctor (Ph.D.)

DÉPARTEMENT DE GÉOLOGIE ET DE GÉNIE GÉOLOGIQUE
FACULTÉ DES SCIENCES ET DE GÉNIE
UNIVERSITÉ LAVAL
QUÉBEC

2011

© Geneviève Cauchon-Voyer, 2011

Résumé

Le complexe des glissements de terrain de Betsiamites, dans l'estuaire du Saint-Laurent, au pourtour du delta de la rivière Betsiamites sur la Côte-Nord, (Québec, Canada) résulte d'au moins trois épisodes de glissements de terrain. Ces mouvements de masse, d'une ampleur unique au Québec, ont causé le déplacement d'un volume total de dépôts estimé à 2000 millions de m³ (2 km³). Cette thèse contient l'analyse détaillée des éléments géologiques et géotechniques relatifs aux événements de mouvements de masse dans la région de Betsiamites. Des levés géophysiques subaériens et sous-marins intégrés aux résultats des données de forages et d'essais géotechniques *in situ* ont permis de déterminer l'architecture de la région du delta de la rivière Betsiamites et de reconstituer les principaux événements de glissements de terrain. Ainsi, la cicatrice sous-marine du complexe des glissements de terrain de Betsiamites est le résultat d'un premier mouvement de masse daté à 9250 cal BP dont le volume minimal des matériaux déplacés est estimé à 200 millions de m³. Le second événement de glissement de terrain sous-marin daté de 7250 cal BP a mobilisé un volume de dépôts estimé à 1300 millions de m³ sur une superficie de 54 km². Cette thèse démontre aussi que la portion subaérienne de la cicatrice du complexe des glissements de terrain de Betsiamites est le résultat du glissement de Colombier en 1663. Ce dernier glissement s'est déroulé en quatre phases successives dont la première a eu lieu dans le domaine sous-marin et les suivantes dans le domaine subaérien. Le séisme du 5 février 1663 a causé la première rupture dans l'environnement sous-marin qui a, par la suite, rapidement déclenché deux grandes coulées argileuses et un étalement latéral. Lors des quatre phases de rupture du glissement de Colombier, le volume des dépôts possiblement déplacés pourrait totaliser 530 millions de m³ sur une superficie de 20 km². L'événement de Colombier est l'un des plus importants glissements subaériens documentés au Canada. La présence des cicatrices sous-marines laissées par l'événement de glissement sous-marin de Betsiamites pourrait avoir agi comme facteurs de prédisposition au déclenchement des ruptures de l'événement de Colombier.

Abstract

At least three major landslide events formed the submarine and subaerial Betsiamites landslide complex localized in the vicinity of the Betsiamites river delta, on the north shore of the St. Lawrence Estuary (Québec, Canada). An estimated total volume of 2000 million m^3 (2 km^3) of deposits have been mobilized by these mass movements events, which are among the largest landslides identified in the province of Quebec. This thesis presents a detailed geological and geotechnical analysis of the mass movements events of the Betsiamites area. Linkage between offshore and onshore geophysical investigations with borehole data and *in situ* testing allows reconstruction of the architecture of the Betsiamites River delta area and leads to the identification of the main failure events. The lithostratigraphy of the Betsiamites River delta area consists of a sequence of 5 units deposited following deglaciation, the marine invasion of the Goldthwait Sea, and subsequent land emergence. The submarine scar of the Betsiamites landslide complex may have resulted from a first failure, dated at about 9250 cal BP, which mobilized a minimum volume of 200 million m^3 of deposits. A second landslide dated at 7250 cal BP mobilized a volume of 1300 million m^3 of deposits over an area of 54 km^2 . The Betsiamites submarine landslide event dated at 7250 cal BP left the largest scar yet identified on the St. Lawrence estuary seafloor. The Betsiamites submarine landslide appears to have been triggered by a strong earthquake that liquefied a sandy layer interbedded in clayey layers. Furthermore, this thesis demonstrates that the subaerial scar of the Betsiamites landslide complex is a result of the 1663 Colombier landslide event which involved four successive failure phases: one submarine and three subaerial. The February 5th 1663 earthquake triggered a submarine landslide event, which reached the shoreline, and led in a short period of time successively to two subaerial flowslides in sensitive clayey material and a subaerial lateral spread. The four failure phases mobilized a possible total volume of about 530 million m^3 of deposits over an area of 20 km^2 . The Colombier landslide event is among the largest documented historic landslides in Canada. The presence of submarine scars left by the submarine landslide event acted as predisposition factors for the development of the Colombier failure phases. The back-analysis of the Colombier landslide scar area indicates that a first submarine undrained failure (phase

1) resulting from an earthquake-induced landslide event reached the shoreline and triggered the development of flowslide (2F) and a lateral spread (3S). The subaerial flowslide 2F acted as the triggering factor for flowslide (3F). This study presents an example that flowing and spreading mechanisms occurred simultaneously in the subaerial environment.

Avant-Propos

Je tiens tout d'abord à remercier mon superviseur M. Jacques Locat pour sa disponibilité, ses nombreux conseils, son support et sa patience tout au long de ces années. Je remercie aussi M. Serge Leroueil, co-directeur, pour ses nombreux conseils et sa grande disponibilité.

Je veux par la suite remercier Guillaume St-Onge pour son implication à plusieurs niveaux dans le cadre de ce projet de doctorat ainsi que souligner la contribution importante de Denis Demers, Pascal Locat, Alexandre Lavoie, Daniel Ouellet, Denis Robitaille et Julie Therrien de la section Mouvements de terrain du Ministère des Transport du Québec (MTQ).

Je remercie tous les étudiants qui ont séjourné au laboratoire d'études sur les risques naturels (LERN) à travers ces années. Merci à Catherine Cloutier, Andrée-Anne Fortin-Rhéaume, Christiane Levesque, Ariane Locat, Pascal Locat, Pierre-Étienne Lord, Mylène Sansoucy, Julien Suret, Dominique Turmel, Sueng Won Jeong, pour nos agréables discussions et votre aide lors des divers travaux de recherche.

Je remercie Luc Boisvert, Richard Fortier et Pierre Therrien de l'Université Laval ainsi que les stagiaires Coralie Amiguet, Marie-Pier Lacroix-Beaupré, Adam Lavoie et Joannie Poupart qui ont participé à ce projet de recherche au sein du LERN. Je remercie Patrick Lajeunesse et Hubert Gagné du département de géographie de l'Université Laval, Francesco Barletta, Ursule Boyer-Villemare, Jacques Labrie et Michel Rousseau de l'Université du Québec à Rimouski et de l'Institut des Sciences de la mer, Andrée Bolduc, Calvin Campbell, Mathieu Duschene et André Pugin de la Commission Géologique du Canada, Roger Côté, André Godin and Richard Sanfaçon du Service hydrographique de l'Institut Maurice Lamontagne, Marie-Hélène Cauchon de l'Organisme des bassins versants de la Haute-Côte-Nord et finalement Bassam Ghaleb du GEOTOP UQAM-McGill.

Je remercie plusieurs techniciens, professionnels et personnel de soutien à l'Université Laval, c'est-à-dire Caroline Bédard, Jean Frenette, Christian Juneau, Marcel Langlois,

Danielle Pichette et Martin Plante, pour leur aide à plusieurs moments lors de ces travaux de recherche.

Je souligne la contribution des membres d'équipage et les participants scientifiques aux missions du F.G. Creed, Guillemot et du Coriolis II. Je remercie le Fonds québécois de recherche sur la nature et les technologies (FQRNT) pour l'octroi d'une bourse de doctorat, le Conseil de recherches en sciences naturelles et en génie du Canada (CRSNG) pour le financement de Costa-Canada et des subventions de temps navire pour les missions dans l'Estuaire du Saint-Laurent. Je remercie aussi Québec-Océan pour de l'aide financière.

Je dois finalement des remerciements spéciaux à ma famille et amis. Merci à Dominique d'avoir été inconditionnellement à mes côtés à tout moment lors de cette grande aventure. Merci à André, Hélène, Philippe et Stella pour leur support. Merci à mes amis, ceux plus proches comme ceux plus loin pour leur support, conseils et patience.

Les trois articles composant cette thèse et les deux articles présentés en annexe ont été écrits en intégralité par l'auteure de cette thèse de doctorat.

Le premier article intitulé «*Large-scale subaerial and submarine Holocene and recent mass movements in the Betsiamites area, Quebec, Canada*» est publié dans la revue *Engineering Geology*. Les co-auteurs sont Jacques Locat (U Laval), Serge Leroueil (U Laval), Guillaume St-Onge (UQAR) et Denis Demers (MTQ). Le deuxième article intitulé «*Stability and mobility of the 1663 Colombier subaerial and submarine landslide event, Quebec, Canada*» sera soumis à la *Revue canadienne de géotechnique* et les co-auteurs sont Jacques Locat (U Laval) et Serge Leroueil (U Laval). Le troisième article intitulé «*Development and potential triggering mechanisms for a large Holocene landslide in the Lower St. Lawrence Estuary*», sera présenté dans le cadre du 5^{ème} symposium international de l'IGCP *Submarine Mass Movements and Their Consequences* qui aura lieu à Kyoto en octobre 2011 et les co-auteurs sont Jacques Locat (U Laval), Guillaume St-Onge (UQAR), Serge Leroueil (U Laval) et Patrick Lajeunesse (U Laval).

Table des matières

Résumé	i
Abstract	ii
Avant-Propos	iv
Table des matières	vi
Liste des tableaux	viii
Liste des figures	ix
Liste des symboles et abréviations	xii
Liste des annexes.....	xvi
Chapitre 1 Introduction	1
1.1 Cadre général.....	1
1.2 Problématique générale	3
1.3 Problématique spécifique	8
1.4 Objectifs	11
1.5 Contenu de la thèse	13
Chapitre 2 Large-scale subaerial and submarine Holocene and recent mass movements in the Betsiamites area, Quebec, Canada	16
2.1 Abstract	16
2.2 Introduction	16
2.3 Physical setting.....	19
2.4 Data and methods	21
2.5 Surface geomorphology	24
2.6 Coastline seismostratigraphy.....	27
2.7 Lithological units.....	29
2.8 Assessment of failure surfaces and material involved in the 1663 Colombier landslide event	33
2.9 Interpretation of seismic data	36
2.10 1663 Colombier landslide failure phases	37
2.11 Interpretation of the 1663 Colombier landslide phases.....	39
2.12 Conclusions	43
2.13 Acknowledgements	44
2.14 References	45
2.15 Tables	49
2.16 Figures.....	51

Chapitre 3	Stability and mobility of the 1663 Colombier subaerial and submarine landslide event, Québec, Canada	67
3.1	Abstract.....	67
3.2	Introduction.....	67
3.3	Data and methods.....	70
3.4	Initial slope conditions prior to the 1663 event	74
3.5	Dating.....	78
3.6	1663 landslide morphologies and phases.....	78
3.7	Morphosedimentological and geotechnical models.....	82
3.8	Back-analysis and movement phases.....	85
3.9	Mobility and post-failure analysis	90
3.10	Conclusions.....	92
3.11	Acknowledgements.....	93
3.12	References.....	93
3.13	Tables.....	97
3.14	Figures	101
Chapitre 4	Development and potential triggering mechanisms for a large Holocene landslide in the Lower St. Lawrence Estuary	118
4.1	Abstract.....	118
4.2	Introduction.....	118
4.3	Data and methods.....	119
4.4	Morphology of the Betsiamites slide complex	119
4.5	Lithostratigraphy and failure surface	120
4.6	Movement development	121
4.7	Triggering mechanisms.....	121
4.8	Concluding remarks and future work	123
4.9	References.....	125
4.10	Acknowledgments	126
Chapitre 5	Synthèse, conclusions et recommandations	132
5.1	Synthèse des glissements de Betsiamites.....	132
5.2	Conclusions.....	136
5.3	Recommandations.....	138
	Bibliographie de la thèse.....	140
	Annexes	147

Liste des tableaux

Tableau 1.1	Les grands glissements historiques au Québec.....	5
Tableau 1.2.	Glissements sous-marins et subaériens au début de l'Holocène dans l'Estuaire moyen du Saint Laurent et sur la Cote-Nord et la rive-Sud, à l'est de l'embouchure du fjord du Saguenay	7
Tableau 2.1.	Radiocarbon dates on shell fragments	49
Tableau 2.2.	Summary of seismic units on the subaerial profile.....	49
Tableau 2.3.	Summary of lithostratigraphy and geotechnical properties defined on site, with boreholes and seismic correlations.	50
Tableau 3.1.	Radiocarbon dates for the subaerial landslide.	97
Tableau 3.2.	Properties of geotechnical units on the back escarpment of the 1663 flowslide 2F and lateral escarpment of flowslide 3F (borehole 46006).	98
Tableau 3.3.	Properties of geotechnical units at the foot of the lateral spread 3S (borehole 46010).....	99
Tableau 3.4.	Summary of the geotechnical and physical properties of the soil layers used in the limit equilibrium analyses	100
Tableau 5.1.	Données morphométriques des événements de glissements de terrain du complexe de Betsiamites.	136

Liste des figures

Figure 1.1.	Modèle numérique de terrain du secteur d'étude.....	15
Figure 2.1.	Study site.....	51
Figure 2.2.	Geomorphologic interpretation of the Betsiamites landslides complex area.	52
Figure 2.3.	Digital elevation model of the Colombier subaerial scar.....	53
Figure 2.4.	Beach at low tide revealing blocks of deformed clayey sediments currently eroded by marine action.....	54
Figure 2.5.	Source and depositional areas of the 7250 cal BP Betsiamites submarine landslide event.	55
Figure 2.6.	Seismostratigraphy of the Betsiamites landslide complex.....	56
Figure 2.7.	Geotechnical profile at site 46010 in the accumulation zone of the lateral spread (phase 3S) of the 1663 Colombier subaerial landslide.	57
Figure 2.8.	Geotechnical profile at site 46006 on the upper escarpment of the 1663 Colombier flowslides (phase 2F and 3F)	58
Figure 2.9.	Schematic summary of the lithostratigraphy and seismostratigraphic interpretation between boreholes 46006 and 46010.....	59
Figure 2.10.	CPTUs and topographic section along the shoreline.	60
Figure 2.11.	Sequence of 4 CPTUs carried out in the north south axis of the Colombier subaerial scar in the Central zone	61
Figure 2.12.	Sequence of 6 CPTUs carried out in the East zone of the Colombier subaerial scar.....	62
Figure 2.13.	Criteria used to identify the elevation to the failure surface on the CPTU profiles carried out in the north south axis of the subaerial scar	63
Figure 2.14.	Lithostratigraphy prior to the 1663 failure phases for the East zone and Central zone	64
Figure 2.15.	Initial topography and 1663 failure phases:.....	65
Figure 2.16.	CPTU 46002 and 46118 carried out in the East zone	66
Figure 3.1.	Map of the study area.....	101
Figure 3.2.	General view of the Betsiamites slide complex.	102
Figure 3.3.	Investigation carried out in the subaerial and submarine area of the Betsiamites slide complex.....	103
Figure 3.4.	Interpreted topography prior to the 1663 Colombier slide event.....	104
Figure 3.5.	Geotechnical properties of borehole 46006.	105
Figure 3.6.	Geotechnical properties of borehole 46010.	106

Figure 3.7.	Schematic representation of the variation the lithological and geotechnical units across the landslide area prior to the 1663 failure phases.....	107
Figure 3.8.	Well preserved tree branches exposed at low tide.....	108
Figure 3.9.	Landslide extent and failure phases of 1663 Colombier slide event.	109
Figure 3.10.	Thickness of debris and CAT-SCAN image of core COR0307-PC45 recovered offshore in debris area.....	110
Figure 3.11.	CPTUs and topographic cross-section in the subaerial flowslide 3F and 3S.....	111
Figure 3.12.	Morphology of the debris within the subaerial and submarine landslide scars.	112
Figure 3.13.	Inferred morphostratigraphy of the slope prior to failure and geomorphologic interpretations used for generating the geotechnical models.....	113
Figure 3.14.	Simplified models used for slope stability analysis with SLOPE/W.	114
Figure 3.15.	Factor of safety plotted as a function of the coefficient of horizontal acceleration for the slope of the submarine failure (Phase 1).....	115
Figure 3.16.	Thickness of debris interpreted from subaerial CPTUs and boreholes, submarine coring and subbottom profiling.....	116
Figure 3.17.	Evaluation of the yield strength using the relationship proposed by Johnson (1984)	117
Figure 4.1.	Study site and extent of the Betsiamites landslide scar.	127
Figure 4.2.	Geomorphology of the Betsiamites scar.....	128
Figure 4.3.	Seismic profile across the Betsiamites landslide scar	129
Figure 4.4.	Geotechnical profile carried out onshore along the shoreline	130
Figure 4.5.	Morphostratigraphic reconstitution of the Betsiamites landslide showing the topography prior to failure and the accumulation of debris after failure	131
Figure 5.1.	Délimitation a) du glissement sous-marin de Betsiamites daté à 7250 cal BP et b) du glissement subaérien et sous-marin de Colombier daté à 1663, qui composent le complexe de glissements de terrain de Betsiamites.....	133
Figure 5.2.	Définition des paramètres morphométriques.....	136

Liste des symboles et abréviations

	Définition française	Définition anglaise	Unité ou expression
A_s	Aire de la surface de rupture	Failure surface area	km^2
A_f	Aire totale du glissement (rupture et débris)	Total landslide area (failure + debris)	km^2
c'	Cohésion effective d'un sol	Soil cohesion	kPa
c_u	Résistance au cisaillement intacte non drainée - cône suédois	Intact undrained shear strength - Swedish cone	kPa
c_{ur}	Résistance au cisaillement remaniée non drainée - cône suédois	Remolded undrained shear strength - Swedish cone	kPa
e_f	Indice des vides final	Final void ratio	
e_o	Indice des vides initial	Initial void ratio	
FS	Coefficient de sécurité	Factor of safety	
g	Accélération gravitationnelle	Gravitational acceleration	m/s^2
H_b	Hauteur de l'escarpement arrière	Height of back escarpment	m
H_f	Épaisseur moyenne des débris	Average thickness of debris lobe	m
H_i	Épaisseur moyenne du glissement	Average landslide thickness	m
I_L	Indice de liquidité	Liquidity index	
I_p	Indice de plasticité	Plasticity index	
k	Coefficient d'accélération sismique	Coefficient of seismic acceleration	% g
L	Longueur totale du glissement	Total landslide length	m
L_r	Distance de parcours	Runout distance	m
N_{kt}	Rapport de résistance en pointe nette et de résistance au cisaillement	Ratio of net cone resistance and undrained shear strength	$(q_t - \sigma_v)/S_u$
q_c	Résistance en pointe mesurée au piézocône	Measured cone resistance	kPa

	Définition française	Définition anglaise	Unité ou expression
q_t	Résistance en pointe mesurée au piézocône, corrigée pour la pression interstitielle	Corrected cone resistance	kPa
q_T	Résistance en pointe mesurée au piézocône, nette	Net cone resistance	$q_t - \sigma_v$
R	Distance de rétrogression	Retrogression distance	m
S_r	Degré de saturation	Degree of saturation	%
S_t	Sensibilité au remaniement	Sensitivity	c_u/c_{ur}
S_u	Résistance au cisaillement intacte - scissomètre de chantier	Intact undrained shear strength - Field vane	kPa
u_{base}	Pression interstitielle au piézocône mesurée à la base du cône	Pore water pressure measured at base of cone	kPa
u_{hydro}	Pression interstitielle en condition hydrostatique	Hydrostatic pore water pressure	kPa
u_o	Pression interstitielle initiale dans le sol	Initial pore water pressure	kPa
w	Teneur en eau naturelle	Natural water content	%
w_L	Limite de liquidité	Liquid limit	%
w_P	Limite de plasticité	Plastic limit	%
α_h	Accélération sismique horizontale dans les analyses pseudostatiques	Horizontal pseudostatic seismic acceleration	% g
β_f	Angle de la surface d'écoulement	Gliding surface angle	°
β_s	Angle moyen de la surface de rupture	Average slope of failure surface	°
γ'	Poids déjaugé des débris	Buoyant unit weight of the debris flow mixture	kN/m^3
γ_T	Poids volumique humide initial	Bulk unit weight	kN/m^3
γ_w	Poids volumique de l'eau	Density of water	kN/m^3
ΔH	Hauteur totale du glissement	Landslide drop height	m

	Définition française	Définition anglaise	Unité ou expression
Δu	Surpression interstitielle	Excess pore pressure	kPa
η	Viscosité	Viscosity	Pa·s
σ'_p	Pression de préconsolidation du sol	Preconsolidation pressure	kPa
σ'_v	Contrainte effective verticale	Effective vertical stress	kPa
σ_v	Contrainte verticale totale	Total vertical stress	kPa
τ	Contrainte de cisaillement	Shear stress	kPa
τ_{ya}	Seuil d'écoulement	Apparent yield strength	kPa
ϕ'	Angle de frottement effectif d'un sol	Effective friction angle	°
AD	Ère commune, après l'an 1 du calendrier julien	Anno Domini, years in the Julian calendar	
AMS	Spectrométrie de masse par accélérateur	Accelerator mass spectrometry	
BP	Avant le présent, le présent défini à l'an 1950	Before present, present defined to year 1950	
cal	Année calendrier calibrée	Calibrated calendar year	
CAT-Scan	Tomodensitométrie ou tomographie axiale calculée par ordinateur	Computerized co-Axial Tomography	
CEC	Capacité d'échange cationique	Cation exchange capacity	$m_{eq}/100g$
CPTU	Piézocône	Cone penetration tests with pore water pressure measurement	
CSZ	Zone sismique de Charlevoix	Charlevoix Seismic Zone	
DEM	Modèle numérique d'élévation	Digital elevation model	
GLE	Méthode générale d'équilibre limite	General limit equilibrium method	
kyr	1000 ans	1000 years	
LIDAR	Balayage d'une surface par laser	Light Detection And Ranging	
LSZ	Zone sismique du Bas-Saint-Laurent (BSL)	Lower St. Lawrence Seismic Zone	

	Définition française	Définition anglaise	Unité ou expression
M	Magnitude	Magnitude	
OCR	Rapport de surconsolidation	Overconsolidation ratio	σ'_p/σ'_{vo}
PGA	Accélération de pointe au sol	Peak-ground acceleration	
PSA	Accélération sismique dans les analyses pseudostatiques	Pseudostatic seismic acceleration	
SSA	Surface spécifique	Specific surface area	m ² /g
VE	Exagération verticale	Vertical exaggeration	
V-PDB	Standard Vienna- PeeDee Belemnite	Vienna- PeeDee Belemnite standard	
XRD	Diffraction des rayons X	X-ray diffraction analyses	

Liste des annexes

Annexe A	Article “Late-Quaternary morpho-sedimentology and submarine mass movements of the Betsiamites area, Lower St. Lawrence Estuary, Quebec, Canada”	147
Annexe B	Article “Morphological and stratigraphic analysis of the Colombier landslide area, Québec”	168
Annexe C	Démarche de traitement des données de sismique réflexion avec le logiciel WinSeis	177
Annexe D	Sondages au piézocône	185
D.1	Tableau des positions des sondages au piézocône	185
D.2	Carte de localisation des sondages au piézocône	187
D.3	Résultats des sondages	188
D.4	Tableau des essais de dissipation	225
D.4.1	Exemples d’essais de dissipation	228
Annexe E	Profils de pression de préconsolidation estimés à l’aide du piézocône	230
E.1	Site 46006	230
E.2	Site 46010	231
Annexe F	Résultats de l’essai au scissomètre de chantier S46006	232
F.1	Tableau des résultats	232
F.2	Profil de l’essai au scissomètre de chantier	233
F.3	Détermination du facteur N_{kt}	234
F.4	Estimation de la valeur de résistance au cisaillement à l’aide du piézocône	235
F.4.1	Site 46006	235
F.4.2	Site 46010	236
Annexe G	Forages et échantillons prélevés	237
G.1	Localisation des forages	237
G.2	Forage F46006	237
G.3	Forage F46010	238
Annexe H	Résultats d’essais de laboratoire	239
H.1	Compilation des données géotechniques obtenues lors de l’extraction des carottes.	239
H.1.1	Tableau descriptif des analyses et essais géotechniques effectués	239
H.1.2	Compilation des essais géotechniques effectués – F46006	240
H.1.3	Compilation des essais géotechniques effectués – F46010	243
H.2	Mesures au cône suédois	250

H.2.1	Résultats des essais au cône suédois – F46006	250
H.2.2	Résultats des essais au cône suédois – F46010	252
H.2.3	Limites de consistance – F46006	253
H.2.4	Limites de consistance – F46010	254
H.3	Compressibilité (essais oedométriques)	255
H.3.1	Tableau résumé des essais	255
H.3.2	Résultats des essais oedométriques du forage F46006	256
H.3.3	Résultats des essais oedométriques du forage F46010	261
H.4	Analyses granulométriques	263
H.4.1	Distributions granulométriques - F46006	263
H.4.2	Distributions granulométriques - F46010	266
H.4.3	Distributions granulométriques de la couche d'argile marine U3	271
H.4.3.1	Forage 46006	271
H.4.3.2	Forage 46010	273
H.5	Propriétés physico-chimiques	277
H.5.1	Chromatographie ionique de l'eau interstitielle - F46006	277
H.5.2	Chromatographie ionique de l'eau interstitielle - F46010	278
H.5.3	Dosage de la calcite et de la dolomite	279
H.5.4	Surface spécifique au bleu de méthylène	279
H.5.5	Capacité d'échange cationique	279
H.6	Minéralogie	280
H.6.1	Tableau des analyses minéralogiques par diffraction des rayons X (DRX)	280
H.6.2	Spectres de diffraction-X obtenus sur les échantillons en poudre	280
H.6.3	Spectres de diffraction-X des échantillons sur lames orientées	285
H.7	Analyse microstructurale à l'aide du microscope électronique à balayage	290
H.7.1	Tableau des analyses au MEB	290
H.7.2	Grille d'analyses F46006-TM06	291
H.7.3	Grille d'analyses F46006-TM010	300
H.7.4	Grille d'analyses F46010-TM08	310
H.7.5	Grille d'analyses COR0307-BET2-42LEH	318
H.8	Données sédimentologiques obtenues lors de l'extraction des carottes	323
H.8.1	Tableau descriptif des analyses sédimentologiques effectuées	323
H.8.2	CAT-Scan et propriétés sédimentologiques - F46006	324
H.8.3	CAT-Scan, propriétés physiques et sédimentologiques - F46010	336

Annexe I	Résultats des datations au ^{14}C	363
I.1	Tableaux des résultats des datations aux forages 46006 et 46010.....	363
I.2	Photos des coquilles datées – 46006.....	365
I.3	Photos des coquilles datées - 46010	366
I.4	Tableau des résultats des datations des troncs d'arbres.....	368
Annexe J	Rapport d'analyses des isotopes stables pour le ^{13}C et ^{18}O du CaCO_3	370
J.1	Tableau des résultats.....	370
J.2	Photos des concrétions carbonatées.....	371
J.3	Corrélation régionales.....	372
Annexe K	Données de profilage de conductivité, température et de profondeur (CTD)	373

Chapitre 1 Introduction

1.1 Cadre général

Au Canada les zones côtières s'étendent sur des milliers de kilomètres et offrent un cadre propice aux activités humaines. Elles comprennent les domaines sous-marin et subaérien dont tirent profit plusieurs secteurs de l'économie par exemple, les voies navigables, les pêcheries ou encore les câbles de télécommunication déployés sur les fonds marins. Les terrains avoisinants les étendues d'eau sont souvent propices à l'agriculture ou à l'aménagement urbain, tant industriel, résidentiel que commercial. Certaines de ces zones ne sont cependant pas à l'abri de mouvements de masse qui représentent un danger important dont on doit tenir compte dans la planification des infrastructures et de l'occupation du territoire.

Plusieurs processus naturels sont actifs sur les côtes et modifient les propriétés intrinsèques à la pente et peuvent potentiellement déclencher des glissements de terrain. Certaines pentes, autant en milieu côtier qu'ailleurs sur le continent, présentent un état ou une forme montrant la présence de facteurs de prédisposition à la rupture qui, dans le cas où un mécanisme de déclenchement entrerait en action peuvent causer un glissement de terrain (Leroueil 2001). Par exemple, dans le cas du glissement côtier qui, en octobre 1979, s'est produit dans le port de Nice, ville sise à l'embouchure du fleuve Var en France (e.g., Mulder et al. 1997), il a été proposé que le fluage d'une couche d'argile sensible (Dan et al. 2007) aurait réduit la résistance de la pente et subséquemment causé la rupture. La présence d'une couche de sédiments de résistance plus faible (weak layer), ou encore d'un relief à géométrie précaire (e.g., Lefebvre et al. 1991), constituent autant de facteurs de prédisposition qui faciliteront la rupture à la suite de l'entrée en action, rapide ou lente, d'un agent aggravant ou déclenchant. Les facteurs déclenchants sont des éléments ou des forces extérieures qui provoquent directement la rupture, tandis que les facteurs aggravants modifient de façon significative les conditions de stabilité de la pente ou encore la vitesse à laquelle le processus de rupture s'effectue. Il est généralement accepté que les mouvements de masse en milieu sous-marin peuvent être causés par les tremblements de terre, l'érosion, la sédimentation forte ou rapide, la dissociation des hydrates de gaz, les glaciations, le

diapirisme, les fluctuations du niveau marin dues à l'action des vagues ou des marées (Prior et al. 1984; Locat and Lee 2002). Plusieurs de ces phénomènes sont observables en milieu côtier. Par exemple, dans le cas du glissement côtier qui s'est produit à Finneidfjord en Norvège en 1996 (Longva et al. 2003), une combinaison de facteurs aggravants et déclenchants a été répertoriée. Ce glissement, qui a causé le décès de 4 personnes, s'est développé sur la pente sous-marine de la côte et a rétrogressé au-delà de la ligne de rivage en emportant un tronçon de 250 m de route, une voiture et une maison. Le glissement aurait été déclenché à la suite de l'action d'une combinaison de facteurs climatiques et anthropiques qui auraient augmenté les pressions interstitielles dans la pente (Longva et al. 2003). De fortes pluies et un niveau élevé de la nappe phréatique avant le glissement en conjonction avec les vibrations produites par la circulation de fardiers et par le dynamitage lors des travaux de construction d'un tunnel routier à proximité auraient modifié le régime hydrogéologique de la pente. Ces augmentations de pressions interstitielles auraient donc réduit dramatiquement la résistance du sol et causé la rupture.

Finalement, il est nécessaire de réaliser que les mouvements de terrain côtiers peuvent avoir un potentiel destructeur compte tenu du fait que plusieurs activités humaines ont lieu le long des berges et des côtes. Dans une caractérisation géotechnique complète d'un glissement de terrain, il est nécessaire d'évaluer les conséquences éventuelles des mouvements de masse. Une possible conséquence majeure des mouvements sous-marin et côtier est la génération de tsunami. Par exemple, un glissement sous-marin, causé par l'effondrement subi d'un quai de bateau de croisière en réparation près de la ville de Skagway en Alaska le 3 novembre 1994, a causé une importante vague de tsunami (Campbell and Nottingham 1999; Watts et al. 2003). Cet événement s'est produit lors d'une marée particulièrement basse mais n'a pas été associé à un événement sismique régional ni à l'arrivée d'un tsunami océanique. Un ouvrier affairé à la construction du quai a été emporté dans de l'eau et est décédé. Finalement, un autre exemple très connu de tsunami généré par un mouvement de masse sous-marin s'est produit dans le Golfe du Saint-Laurent, au large des Grands Bancs de Terre-Neuve, Canada en 1929 et a aussi eu des conséquences graves. Ce glissement sous-marin aurait impliqué un volume de près de 200 km³ de sédiments et subséquemment généré une vague de tsunami qui a causé la mort de

27 personnes (Piper et al. 1985), faisant de cet événement de mouvement de masse l'un des plus imposants et des plus meurtriers au Canada.

Plusieurs des mouvements de masse côtiers observés, du moins ceux qui sont récents, sont largement documentés et ont eu de lourdes conséquences comme par exemple les glissements ci-haut mentionnés de Nice, de Finneidfjord et de Skagway. Le déclenchement ou certains facteurs aggravants peuvent être directement reliés aux activités humaines. Dans les cas présentés le remblayage, le dragage ou encore le dynamitage pour la construction d'ouvrages, ont affecté la stabilité des pentes côtières. Avec le développement constant des activités humaines en mer et le long des côtes ainsi qu'avec la prise de conscience associée au danger des glissements côtiers et à la compréhension des mécanismes de génération de tsunami (Mosher 2008), il est primordial de mieux comprendre les facteurs qui contrôlent la stabilité des pentes et ceux qui déclenchent les instabilités subaquatiques et subaériennes en milieu côtier. La compréhension des processus associés au problème des instabilités côtières est donc d'importance pour une gestion sécuritaire du territoire.

1.2 Problématique générale

Au Québec, on retrouve d'importantes accumulations de dépôts meubles mis en place lors de l'immersion et du retrait des mers postglaciaires. L'une de ces mers, la mer de Goldthwait, a submergé les zones côtières au pourtour de l'estuaire et du golfe du Saint-Laurent (Gadd 1974; Dionne 1977). Lors de l'abaissement du niveau marin relatif qui a suivi cette immersion, jumelé à un important apport de sédiments remobilisés par l'incision des rivières, d'importantes séquences sédimentaires de dépôts meubles en bordure des côtes québécoises se sont mises en place (Hart and Long 1996). Le complexe deltaïque de la rivière Betsiamites (Figure 1.1) a été formé dans ce contexte et présente une stratigraphie changeante qui résulte des variations du régime sédimentaire selon les fluctuations du niveau marin relatif enregistré dans l'Estuaire et celles de l'apport sédimentaire au début de l'Holocène (Dionne 1977; Dionne 1988; Bernatchez 2003). Un abaissement rapide du niveau relatif de la mer en conjonction avec des taux de sédimentation très élevés peut causer la formation de pentes métastables et entraîner des mouvements de masse (e.g.,

Sultan et al. 2004b). Ces conditions sont fréquemment présentes dans les environnements postglaciaires deltaïques (McKenna et al. 1992; Christian et al. 1997).

Dans le secteur de la municipalité de Colombier sur la Côte-Nord de l'estuaire du Saint-Laurent, à l'est de l'embouchure de la rivière Betsiamites, une large cicatrice subaérienne et sous-marine de glissements de terrain est identifiée dans les dépôts meubles du delta de la rivière. Cette large cicatrice, ci-après nommée le complexe de glissements de terrain de Betsiamites, résulte de plusieurs épisodes de glissements de terrain.

La portion subaérienne du complexe de glissements de Betsiamites a été sommairement identifiée par Allard (1984). Cette énorme cicatrice subaérienne de 9.6 km², résultat d'un glissement par étalement vraisemblablement associé à une coulée argileuse, a été associée au séisme de 1663 (Bernatchez 2003). Cet événement est ci-après nommé glissement de Colombier. Le séisme du 5 février 1663 est un séisme historique violent connu au Québec dont la magnitude M est estimée entre 7 et 7.8 (Smith 1962; Locat 2011). L'immense cicatrice du glissement subaérien de Colombier n'a été que brièvement reportée (Allard 1984) et seulement les grandes caractéristiques géomorphologiques et sédimentologiques ont été décrites (Bernatchez 2003).

À la suite de ces observations préliminaires sur la côte, l'étude préliminaire de la zone sous-marine de l'Estuaire située directement en face du glissement subaérien de Colombier, à l'aide de levés multifaisceaux et de sismique réflexion marine a permis de mettre en évidence d'importantes cicatrices de mouvements de masse sous-marins et plusieurs structures associées à la déposition des débris du glissement subaérien de 1663 (Locat et al. 2004).

Ces observations préliminaires, qui témoignent de la présence de cicatrices de glissements de terrain aux dimensions considérables autant dans le domaine subaérien que sous-marin, ont donc servi de point de départ pour la mise en place d'une étude approfondie du complexe de glissements de terrain de Betsiamites. Les résultats et interprétations de cette étude sont présentés dans cette thèse, et viennent appuyer une première étude de la morphostratigraphie du secteur sous-marin du delta de la rivière Betsiamites (Cauchon-Voyer et al. 2008).

Dans un premier temps, les dimensions du complexe de glissements de terrain de Betsiamites sont imposantes. Si on évalue l'étendue de la zone de décrochement de la cicatrice dans la partie subaérienne et sous-marine sans distinction des différents événements, on obtient une superficie approximative de 80 km². Compte tenu des observations préliminaires (Bernatchez 2003; Cauchon-Voyer et al. 2008) qui indiquent qu'une épaisseur moyenne de 15 m de dépôts a été remobilisée, on peut estimer grossièrement un volume total de plus de 1.2 km³ (1200 million de m³) pour cette cicatrice. Le complexe de glissements de terrain de Betsiamites serait donc parmi les plus grandes cicatrices de glissements de terrain historiques connus au Québec et au Canada.

Si on considère seulement le segment subaérien de la cicatrice de Colombier, qui occupe une superficie de 9.6 km² et dont on estime l'épaisseur moyenne à 40 m, le volume impliqué est de 384 hm³ (1 hectomètre cube = 1 millions de m³) Ces dimensions font donc du glissement de Colombier un autre très grand glissement de terrain historique au Québec (Tableau 1.1), au même titre que celui de St-Jean Vianney de 1663 (Lasalle and Chagnon 1968; Potvin et al. 2001) et de St-Alban en 1894 qui avait fait 4 victimes (Laflamme 1900).

Tableau 1.1 Les grands glissements historiques au Québec

Glissements répertoriés	Superficie (km ²)	Volume (hm ³)	Volume (km ³)
Saint-Jean Vianney, 1663	20.6	204	0.204
St-Alban, 1894	6.5	225	0.225
Colombier, cicatrice subaérienne	9.6	384	0.384
Betsiamites, subaérien et sous-marins, plusieurs événements	80	1200	1.2

On a répertorié d'autres mouvements de masse importants dans la région de la Côte-Nord depuis la déglaciation et pendant l'Holocène (Tableau 1.2). Cependant, la superficie et le volume impliqués lors de ces événements sont d'un ordre de grandeur plus petit que ceux de Betsiamites. Par exemple, dans le milieu subaérien, on connaît l'existence de plusieurs glissements rotationnels, de coulées argileuses et d'étalement le long de la côte de l'Estuaire (dossier MTQ). Plusieurs autres glissements ont été répertoriés près du secteur de Betsiamites, par exemple, à Pointe-aux-Outardes (Allard 1982; Bernatchez 2003), dans

des dépôts aux caractéristiques similaires. De plus, d'importants glissements de terrain holocènes de taille kilométrique seraient survenus le long de la rivière St-Jean quelques kilomètres à l'ouest de Havre-Saint-Pierre et ont été répertoriés et datés entre 6.1 et 6.9 ka BP (Dubois 1977; Ferris 1986). Finalement, un glissement, qui pourrait être un étalement, s'est produit en 1981 à Havre-Saint-Pierre et une étude géotechnique complète de ce glissement a été entreprise (Locat et al. en préparation). Le glissement de Havre-Saint-Pierre s'est développé sur le bord du rivage dans des conditions potentiellement comparables à celles du site de Betsiamites mais les dimensions de l'événement de Havre-Saint-Pierre sont beaucoup plus petites.

Dans le domaine sous-marin de l'Estuaire, Syvitski et Praeg (1989) ainsi que Massé et Long (2001) ont répertorié plusieurs évidences d'instabilités de pentes sur des levés de sismique réflexion marine. Plus récemment encore, l'accès plus efficace aux levés bathymétriques aux multifaisceaux grâce à de récentes avancées technologiques a permis la reconnaissance de plusieurs traces d'instabilité sur le fond de l'estuaire du Saint-Laurent (Duchesne et al. 2003; Lajeunesse et al. 2007; Campbell et al. 2008; Gagné 2008; Locat et al. 2008; Mosher 2008). Dans le domaine sous-marin, comme dans le domaine subaérien, la superficie de la cicatrice sous-marine au site de Betsiamites dépasse les 74 km² sur le fond marin actuel et, à ce titre, surpasse tous les autres événements historiques répertoriés dans l'Estuaire.

Tableau 1.2. Glissements sous-marins et subaériens au début de l'Holocène dans l'Estuaire moyen du Saint Laurent et sur la Côte-Nord et la rive-Sud, à l'est de l'embouchure du fjord du Saguenay (liste non exhaustive).

Événement ou lieu	Subaérien (A) ou sous-marin (M)	Lat. (N)	Long. (W)	Date cal BP	Référence
Événement paraglacial Betsiamites	M	48°51'4"	68°44'36"	Avant 9250	(Cauchon-Voyer et al. 2008)
Lobe de débris de Rimouski	M	48°41'0"	68°33'54"	~8700	(Campbell et al. 2008)
Mitis / Grand Métis	A	48°38'45"	68°08'26"	Avant 8500	(Dionne and Coll 1995)
Événement de 7250 ans Betsiamites	M	48°50'38"	68°42'24"	~7250	(Cauchon-Voyer et al. 2008)
Rivière St-Jean - Havre-Saint-Pierre	A	50°19'24"	64°18'13"	Entre 7600 et 6300	(Dubois 1977; Ferris 1986)

Bien que plusieurs mouvements de masse soient répertoriés sur la Côte-Nord de l'Estuaire, autant dans le domaine subaérien que sous-marin, peu d'études complètes portent sur l'étude des causes et des mécanismes responsables de ces mouvements de terrain en milieu côtier. En fait, la majorité des études publiées se contentent de cartographier et de répertorier les événements. Dans un même ordre d'idée, étant peu fréquents et complexes, les très grands glissements dans les dépôts postglaciaires de l'est de l'Amérique sont aussi peu étudiés d'un point de vue géotechnique dans le but de déterminer les causes de la rupture et les processus associés aux comportements en post-rupture.

Au Québec, l'étude détaillée de tels mouvements subaériens et sous-marins est d'intérêt en raison des risques importants qu'ils représentent pour les infrastructures routières (*e.g.*, les routes côtières 138 et 132) et pour la sécurité civile des habitants de la Côte-Nord et de la Rive-Sud dans l'éventualité d'un tsunami déclenché par un glissement de terrain dans l'Estuaire du Saint-Laurent. La compréhension des causes de ces mouvements de masse prend donc toute son importance dans un contexte d'évaluation des risques naturels au Québec.

1.3 Problématique spécifique

Dans le secteur de Betsiamites, malgré l'ampleur de la cicatrice du complexe de glissements de terrain, les travaux effectués jusqu'à maintenant ont permis de répertorier, de décrire sommairement la morphologie subaérienne et de dater certaines des cicatrices et structures associées aux mouvements de masse. Les connaissances au sujet de la séquence des événements et des mécanismes responsables de la rupture présentent encore de nombreux questionnements qui seront présentés ci-après.

L'étude de doctorat poursuit l'analyse du secteur déjà entamée (Cauchon-Voyer et al. 2008) qui visait à faire l'analyse morpho-stratigraphique du secteur sous-marin de la cicatrice. Cette première étude a permis d'établir les caractéristiques morpho-sédimentologiques d'un secteur sous-marin couvrant plus de $\sim 500 \text{ km}^2$ à l'est du delta de la rivière Betsiamites. Cette analyse a aussi permis de répertorier plusieurs épisodes de glissements de terrain dont les traces ont été laissées sous l'eau dans la géomorphologie locale du fond marin et dans la colonne sédimentaire. Une analyse spatio-temporelle des mouvements de masse sous-marins a été présentée, c'est-à-dire que quatre couches de débris associés à des événements distincts ont été identifiées, et une chronologie établissant l'âge des ruptures de pente a été proposée. Les structures de mouvement de masses observées sont associées à au moins trois épisodes de glissement de terrain. Un premier mouvement de masse paraglaciale serait antérieur à 9280 cal BP¹ et a été identifié sur les profils de sismique réflexion marine. Un second aurait laissé de larges couloirs de glissement sur le plateau sous-marin ainsi qu'un cône de sédiments dans le Chenal laurentien (Figure 1.1) et daterait de 7250 ans cal BP. Cet événement est ci-après nommé dans cette thèse le glissement sous-marin de Betsiamites. Un troisième événement plus récent aurait été causé par le séisme de 1663 AD ($M \sim 7$) et serait associé au glissement subaérien visible sur la côte. Ce troisième événement est ci-après nommé le glissement de Colombier.

Plusieurs indices mettent donc en évidence des mouvements de masse qui ont eu lieu dans les environnements subaérien et sous-marin de Betsiamites (Cauchon-Voyer et al. 2008).

¹ cal BP indique que les dates ont été calibrées, c'est-à-dire que les dates en années radiocarbone obtenues au laboratoire ont été converties en années calendrier.

Cependant, les données morphologiques précises, comme par exemple les hauteurs et angles d'escarpement ou encore les distances de rétrogression, manquent pour déterminer la géomorphologie subaérienne de la zone côtière des cicatrices de glissements de terrain. Une analyse rigoureuse de la morphologie du glissement de Colombier est donc requise pour décrire la géométrie de la zone de départ, déterminer si la rupture s'est produite en plusieurs phases et finalement présenter la morphologie des débris.

Comme mentionné plus haut, les glissements de Betsiamites et Colombier se sont développés dans des sédiments maintenant émergés du delta postglaciaire de la rivière Betsiamites. Ces sédiments sont fortement stratifiés et possèdent une granulométrie et des structures sédimentaires variées (Bernatchez 2003), typiques des formations deltaïques (e.g., Hart and Long 1996). On a relevé la présence de cinq unités sismostratigraphiques régionales de sédiments postglaciaires dans l'Estuaire du Saint-Laurent (Syvitski and Praeg 1989) et ces mêmes cinq unités ont été interprétées dans le secteur sous-marin du delta de la rivière Betsiamites (Cauchon-Voyer et al. 2008). Cependant très peu de validations géologiques directes ont été obtenues afin de caractériser les unités sismiques de l'Estuaire (St-Onge et al. 2003; Cauchon-Voyer et al. 2008; Gagné 2008; St-Onge et al. 2008; Barletta et al. 2010) et ces études ne fournissent aucune information quant aux propriétés géotechniques des sédiments. De plus, les liens entre, d'une part, la sismostratigraphie et les propriétés sédimentologiques observées en mer et, d'autre part, les dépôts émergés dans lequel le glissement subaérien s'est développé n'ont pas été établis. Il manque donc une analyse qui intègre les observations obtenues en mer ainsi que de nouvelles investigations dans le domaine subaérien pour déterminer les propriétés sédimentologiques ainsi que la lithostratigraphie des glissements de terrain de Betsiamites et de ses environs. Finalement il faut déterminer l'architecture 3D des dépôts associés aux épisodes de glissements de terrain subaériens, c'est-à-dire préciser l'épaisseur des couches, leurs variations latérales et leur structure.

Les matériaux dans les glissements n'ont pas encore été documentés. Les études antérieures effectuées sur les matériaux dans le secteur subaérien ont permis seulement de documenter les caractéristiques sédimentologiques des dépôts de la ligne de rivage (Bernatchez 2003). Les analyses en milieu sous-marin ont permis de caractériser les

propriétés sédimentologiques de certaines unités (Cauchon-Voyer et al. 2008) . Toutefois, aucune caractérisation des matériaux n'a été faite pour ces deux milieux. Dans l'optique de faire une analyse à rebours complète des glissements, il est nécessaire de bien comprendre les caractéristiques et propriétés géotechniques des sédiments impliqués, autant dans les parties subaérienne que sous-marine.

La séquence des événements de glissements récents intervenus dans le domaine subaérien n'a pas été établie. Il a été soulevé par Bernatchez (2003) que l'étalement latéral aurait été suivi par une coulée argileuse. Par contre, ces observations ne prennent pas en considération les cicatrices du domaine sous-marin ni l'ensemble du complexe de glissements de terrain de Betsiamites. Une analyse fine de la morphologie permettra de déterminer le nombre de phases de rupture et de préciser la séquence des événements qui ont causé la grande cicatrice observée dans le domaine subaérien et des conditions requises pour de tels mouvements.

En fait, il a été reconnu que la cicatrice sous-marine de 74 km² s'est formée à la suite d'une ou de plusieurs ruptures sous-marines dont la principale est le glissement de Betsiamites daté à 7250 ans cal BP (Cauchon-Voyer et al. 2008); cependant le domaine d'influence de cet événement n'a pas été établi. En d'autres mots, il n'a pas été démontré si le glissement sous-marin de Betsiamites a eu un impact dans le domaine subaérien au moment où s'est produite la rupture. Par la suite, il a été démontré que les débris de l'événement de Colombier en 1663 se sont déposés sous l'eau (Cauchon-Voyer et al. 2008). Cependant, aucune information morphologique ne permettait d'établir si le déclenchement de la rupture subaérienne aurait pu avoir été initié dans un premier temps dans le domaine sous-marin.

La cicatrice subaérienne de Colombier a été associée au tremblement de terre historique de 1663 à l'aide de la datation de deux troncs d'arbre (Bernatchez 2003), des écrits des Jésuites et de la datation d'une couche de débris subaériens déposée dans l'Estuaire, faite à partir de mesures du taux de sédimentation (Cauchon-Voyer et al. 2008). On sait également que le séisme de 1663 (Smith 1962) a causé plusieurs mouvements de terrain un peu partout au Québec (e.g., Locat 2008; Locat 2011), mais pour le glissement de Colombier aucune analyse à rebours n'avait encore été entreprise pour confirmer cette hypothèse. Il est donc nécessaire de faire une caractérisation géotechnique complète du complexe de glissements

de terrain de Betsiamites afin d'établir les facteurs de prédisposition, aggravants ou déclenchants ainsi que les conséquences des ruptures. Dans toute analyse à rebours de la stabilité d'une pente, il est nécessaire de déterminer les facteurs déclencheurs ou aggravants. Les facteurs déclencheurs amènent la pente à la rupture tandis que les facteurs aggravants modifient les conditions de la stabilité de la pente. Finalement, une analyse de la mobilité du glissement de Colombier après la rupture permettra de décrire la masse en post-rupture.

L'interaction entre les mouvements de terrain subaérien et sous-marin à Betsiamites pose quelques difficultés. En effet, les cicatrices du complexe de glissements de terrain de Betsiamites, dans les milieux subaérien et sous-marin, sont adjacentes et complémentaires. Il faut donc procéder à une analyse mécanique, à rebours, de la stabilité du talus sous-marin afin de déterminer si les deux cicatrices sont reliées et surtout si un mouvement sous-marin aurait pu entraîner un mouvement subaérien, ou vice-versa. Les conclusions de cette étude devraient contribuer à l'évaluation des risques naturels sur la Côte-Nord, étant donné que de nombreux glissements sous-marins ont été répertoriés dans l'Estuaire sur le pourtour des côtes.

Finalement, encore dans une optique d'évaluation des risques naturels sur la Côte-Nord, il faudra établir quels sont les éléments qui ont eu un impact sur le comportement en post-rupture des mouvements associés aux événements de 1663.

1.4 Objectifs

Les résultats des travaux présentés dans cette thèse visent, pour le secteur du complexe de glissements de terrain de Betsiamites, à décrire l'évolution paléogéographique du secteur, à expliquer les processus mécaniques impliqués dans les mouvements de masse observés et à décrire les comportements en post-rupture.

Dans un premier temps, les objectifs sont orientés de façon à établir l'évolution paléogéographique du secteur afin d'interpréter les conditions avant les glissements de terrain et de décrire les formes associées aux glissements.

- Décrire la géomorphologie subaérienne et sous-marine des cicatrices de glissements de terrain et de ses environs.
- Déterminer les liens géomorphologiques entre les cicatrices subaériennes et sous-marines.
- Interpréter la séquence sismostratigraphique subaérienne le long du littoral et la corréler avec les interprétations sismostratigraphiques du domaine marin.
- Faire l'interprétation de l'architecture 3D de la lithostratigraphie du secteur, dans le domaine subaérien et sous-marin.
- Interpréter la géométrie de la zone de départ des glissements de terrain et présenter une séquence d'événements.
- Évaluer les caractéristiques géométriques et les volumes de chacune des phases de ruptures.
- Déterminer les unités lithostratigraphiques impliquées dans les glissements de terrain.

Dans un deuxième temps, les objectifs sont orientés de façon à effectuer une analyse à rebours de la stabilité et de la mobilité des événements.

- Déterminer les facteurs ayant pu contribuer à l'instabilité c'est à dire les facteurs révélateurs, les facteurs prédisposants, les facteurs aggravants et les facteurs déclencheurs
- Comprendre le développement de la rupture
- Évaluer la mobilité des débris
- Discuter de l'aléa du glissement côtier pour l'estuaire du Saint-Laurent

1.5 Contenu de la thèse

Les résultats des travaux effectués sont présentés et discutés dans quatre chapitres de la thèse. Les chapitres 2 à 4 forment le corps principal de la thèse. Ils sont organisés sous la forme d'articles scientifiques soumis ou à soumettre à des revues avec comité de lecture pour les chapitre 2 et 3 et à une conférence pour le chapitre 4. Le cinquième chapitre comprend une synthèse, des conclusions et recommandations.

Le premier article intitulé «*Large-scale subaerial and submarine Holocene and recent mass movements in the Betsiamites area, Quebec, Canada*» intègre les résultats d'études sur le terrain des environnements sous-marin et subaérien du delta de la Rivière Betsiamites ainsi que des essais laboratoires afin de comprendre l'évolution morpho-stratigraphique du secteur causée par les épisodes de glissement de terrain. Cet article est publié dans la revue *Engineering Geology*.

Le deuxième article intitulé «*Stability and mobility of the 1663 Colombier subaerial and submarine landslide event, Québec, Canada*» présente les résultats de la caractérisation géotechnique des matériaux impliqués dans le glissement de Colombier afin de proposer une analyse à rebours de la stabilité du secteur, de réaliser une étude paramétrique des mécanismes des ruptures et de caractériser le comportement en post-rupture de l'événement subaérien. Cet article sera soumis à la *Revue canadienne de géotechnique*.

Le troisième article intitulé «*Development and potential triggering mechanisms for a large Holocene landslide in the Lower St. Lawrence Estuary*», présente les résultats et interprétations en relation avec l'événement le glissement sous-marin de Betsiamites de 7250 cal BP. Cet article sera publié dans le compte-rendu du 5^{ème} symposium international de l'IGCP *Submarine Mass Movements and Their Consequences* qui aura lieu à Kyoto en octobre 2011.

Le dernier chapitre de la thèse expose les conclusions générales aux travaux de doctorat.

Cette thèse de doctorat approfondit les travaux effectués à la maîtrise et s'appuie sur l'article déjà publié dans la revue *Marine Geology* en 2008, «*Late-Quaternary morpho-sedimentology and submarine mass movements of the Betsiamites area, Lower St.*

Lawrence Estuary, Quebec, Canada ». Cet article, qui présente les travaux de maîtrise bonifiés de plusieurs précisions obtenues lors des premiers travaux de doctorat, est présenté en annexe.

En annexe de la thèse se trouve aussi un court article intitulé « *Morphological and stratigraphic analysis of the Colombier landslide area, Québec* » publié dans le compte-rendu de la 4^{ème} Conférence canadienne sur les géorisques: des causes à la gestion, qui a eu lieu à Québec en mai 2008. Cet article fait une brève présentation du glissement subaérien de Colombier et une première analyse des résultats.

Les annexes présentent aussi plusieurs résultats et analyses obtenus lors de la caractérisation du site de Colombier – Betsiamites.

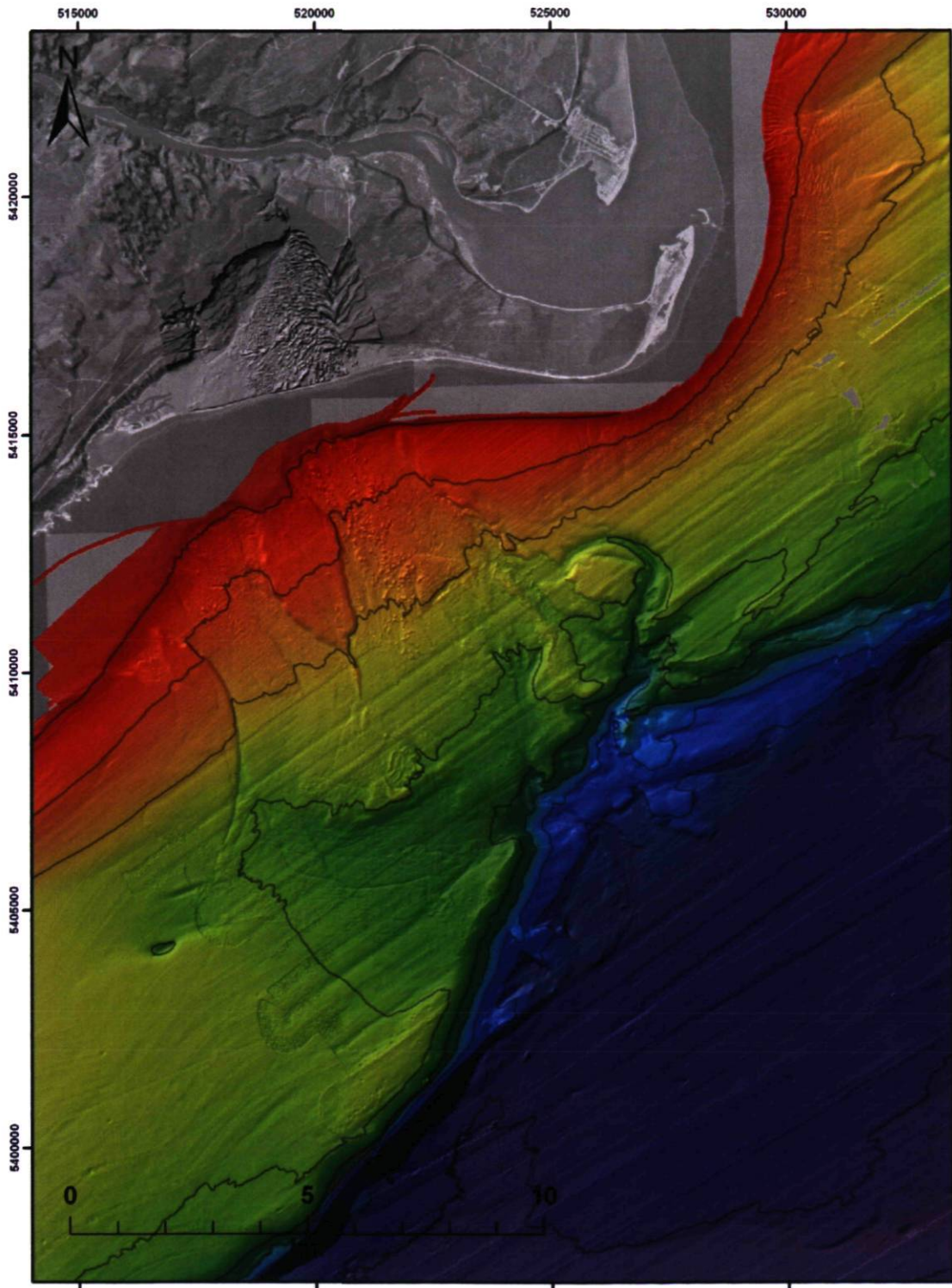


Figure 1.1. Modèle numérique de terrain du secteur d'étude

Chapitre 2 Large-scale subaerial and submarine Holocene and recent mass movements in the Betsiamites area, Quebec, Canada

2.1 Abstract

At least three major landslide events formed the submarine and subaerial Betsiamites (Québec, Canada) landslide complex and mobilized an estimated total volume of 2000 million m³ (2 km³). Linkage between offshore and onshore geophysical investigations with borehole data and *in situ* testing allows reconstruction of the architecture of the Betsiamites River delta area and leads to the identification of the main failure events. The submarine scar of the Betsiamites landslides complex may have resulted from a first failure, dated at about 9250 cal BP, which mobilized a minimum volume of 200 million m³. A second landslide dated at 7250 cal BP mobilized a volume of 1300 million m³ over an area of 54 km². The Betsiamites submarine landslide event dated at 7250 cal BP left the largest scar yet identified on the St. Lawrence estuary seafloor. Furthermore, this paper demonstrates that the subaerial scar of the Betsiamites landslides complex is a result of the Colombier landslide event, which was initiated by the 1663 earthquake and involved four successive failure phases: one submarine and three subaerial. The February 5th 1663 earthquake triggered a submarine landslide event, which reached the shoreline, and led in a short period of time successively to two subaerial flowslides in sensitive clayey material and a subaerial lateral spread. The four failure phases mobilized a possible total volume of about 530 million m³ over an area of 20 km². The Colombier landslide event is among the largest documented historic landslides in Canada. The presence of submarine scars left by the early Holocene events acted as predisposition factors for the development of the failure while the earthquake of 1663 was the main triggering factor of the first submarine failure.

2.2 Introduction

Human development and activities tend to occur along the coast, which justifies the relevance of studying coastal geologic hazards. In Eastern Canada (Figure 2.1), along the

St. Lawrence estuary, part of the coastline is interrupted by large deltaic complexes. These deltaic sediments were deposited in post-glacial seas where many regressive deltas were constructed in a time of falling relative sea-level (e.g., Hart and Long 1996). A rapid lowering of relative sea-level in conjunction with high sedimentation rates can create metastable slopes prone to mass movements (e.g., Sultan et al. 2004b) and such conditions are frequently met in post-glacial deltaic environments (McKenna et al. 1992; Christian et al. 1997).

Scars of such failures are present in the lifted and submerged Quaternary sediments of the Betsiamites River delta area, on the North Shore region of the Province of Quebec, Canada (Figure 2.1), close to the municipality of Colombier and about 400 km north-east of Quebec City. The Betsiamites landslides complex is the result of separate subaerial and submarine failure events (Bernatchez 2003; Cauchon-Voyer et al. 2008). The Colombier subaerial landslide scar, which is the subaerial part of the Betsiamites landslide complex, was first studied by Bernatchez (2003) who suggested, following aerial photo interpretation, that the scar may have resulted from at least two distinct failure events. Radiocarbon dating of a tree trunk and a marine shell allowed suggestion that both associated failures were triggered simultaneously by a strong earthquake ($M \sim 7$) (Bernatchez 2003) that occurred in the Province of Québec on February 5th, 1663 (Smith 1962; Locat 2011). This age estimation for the subaerial landslide is additionally supported by historical account of landslide events in the Betsiamites area (Thwaites 1959) and by dating, through ^{210}Pb derived sedimentation rates, of subaerial debris deposited offshore (Cauchon-Voyer et al. 2008). With an estimated area of 9.6 km^2 and more than 385 hm^3 (1 cubic hectometres = 1 million m^3) of mobilized material, the Colombier subaerial scar is likely to be one of the largest known to have occurred in the province of Quebec, comparable to the 1663 St-Jean Vianney subaerial landslide (e.g., Lasalle and Chagnon 1968; Potvin et al. 2001).

In addition to the Colombier subaerial scar, the adjacent submarine geomorphology of the area, between the Betsiamites River and Rimouski (Figure 2.1), is characterized by yet larger landslide scars and accumulation of debris. A 54 km^2 landslide scar, characterized by two topographic depressions on the submarine shelf separated by a 5 km^2 central butte of

intact deposits, and a 104 km² related debris lobe in the Laurentian Channel, makes up the most significant landslide scar identified in the St. Lawrence estuary (Cauchon-Voyer et al. 2008). This event, hereafter named the Betsiamites landslide event to differentiate it from the 1663 Colombier landslide event, was relatively dated at 7250 calibrated years (cal) BP (Cauchon-Voyer et al. 2008) by mapping seismic reflections from the top of the debris accumulation in the Laurentian Channel to the location of core MD99-2220 where a chronostratigraphy is available (St-Onge et al. 2003). Similar chronostratigraphic correlations were used to date another layer of buried debris flow deposits as older than 9250 cal BP. This layer is found below the 7250 cal BP Betsiamites submarine landslide scar on the shelf (Cauchon-Voyer et al. 2008). This correlation method introduces a possible error of a few hundred years, but regardless of these uncertainties, it provides enough evidence to attribute the large submarine landslide scars and debris deposits to the results of events well before the recent Colombier landslide. Elsewhere in the Estuary, other authors have identified and described submarine landslide scars (e.g., Massé and Long 2001; Duchesne et al. 2003; Lajeunesse et al. 2007; Campbell et al. 2008; Gagné 2008; Locat et al. 2008; Mosher 2008), but no other landslide scars of dimensions similar to the 7250 cal BP event have been observed on the seafloor.

Any in-depth analysis of large mass movements requires knowledge of the geomorphology, geometry, lithostratigraphy, and geotechnical characteristics of the sediments involved in the failures. For the Betsiamites landslide complex, studies onshore provided only a general description of the geomorphology and age estimation for the landslide event (Bernatchez 2003). Submarine morphosedimentological analysis led to the identification and dating of scars and subaerial debris deposited underwater (Cauchon-Voyer et al. 2008). These studies did not define the material involved nor the physical link and sequence between the subaerial and submarine events. Understanding the mechanisms involved in the failure of such large mass movements, which left related scars and debris above and below the shoreline, is necessary for coastal landslide hazard assessment. For example, Highway 138, which is the main road and lifeline on the North Shore of the St. Lawrence estuary, runs directly across the Colombier landslide scar and is constructed on many other similar deltaic complexes along the North Shore. This fact underscores the need for assessment of the probability of occurrence of similar events.

The objectives of this paper are to understand the events that produced the large Betsiamites landslides complex in order to assess the potential of coastal geohazards such as landslide in the St. Lawrence estuary. In this paper, the subaerial and submarine geomorphology of the Betsiamites landslides complex and its surroundings is presented first. The seismostratigraphic sequence obtained along the shoreline is then presented and correlated with lithostratigraphic and piezocone test data. These data are then integrated in order to interpret the morpho-stratigraphy prior to failure and define the landslide events and sequences that occurred in the area. The links between the subaerial and submarine scars are demonstrated. This paper comes as a first step for subsequent slope stability and post failure flow dynamics analyses (Cauchon-Voyer 2011).

2.3 Physical setting

2.3.1 Local physiography

The Betsiamites River flows eastward into the St. Lawrence estuary (Figure 2.1a) and truncates a large coastal plain that is about 7.5 km wide by 25 km long and interrupted by several marine terraces, bedrock outcrops, peat bogs, and raised beach ridges (Bernatchez 2003). The highest, but intermittent, raised marine terrace in the vicinity of the Colombier subaerial landslide scar is located at about 70 m, whereas bedrock outcrops reach elevations up to 140 m. Underwater, the regional morphology of the Estuary is divided into three physiographic regions: the shelf (SH) bounded by a shelf break (SB) lowering to the Laurentian Channel (LC) (Figure 2.1b). The shelf has an average width of 10 km and a maximum slope of 2° , with water depths ranging from the shoreline to about 150 m. The shelf break occurs between 150 and 200 m water depth, creating a slope of about 10° with maximum height of 200 m. The Laurentian Channel is a long sub-horizontal topographic depression in the seafloor of the Estuary with maximum water depth of 375 m and width of 45 km in the study area. The study area is located between the Lower St. Lawrence Seismic Zone (LSZ) and the Charlevoix Seismic Zone (CSZ) (e.g., Adams and Atkinson 2003), implying that the area frequently undergoes earthquakes. Since these seismic zones started being monitored in the late 19th century several earthquakes with magnitude ranging between 4.5 and 6.5 were recorded (e.g., Lamontagne et al. 2003; Lamontagne et al. 2008).

2.3.2 Late Quaternary history

The study area was covered by the Laurentide Ice Sheet during the late Wisconsinan. Following deglaciation, which started around 12 kyr BP in the area, the combined effect of the glacio-isostatic subsidence and eustatic sea-level rise resulted in the marine invasion of the Goldthwait Sea up to an elevation of 152 m above present sea-level around 11 kyr BP (Bernatchez 2003). Subsequent land emergence led to the erosion of deltaic plains resulting in the stair-like morphology of raised marine terraces visible onshore. At the time of the large submarine failure, dated at 7250 cal BP, relative sea level had reached more or less its present level (Dionne 2001; Bernatchez 2003).

It is generally accepted that the lithostratigraphic Quaternary sequence found on the subaerial portion of the delta and area is limited to deposits of the last glaciation and deglaciation (e.g., Dredge 1976; Dubois 1977; Dionne and Occhietti 1996; Bernatchez 2003). The coastal subaerial stratigraphy of the Betsiamites River area is simplified, from bottom to top, as a sequence of marine, prodeltaic, fluvio-deltaic, intertidal, and littoral deposits.

Offshore, many authors described the seismostratigraphy in the St. Lawrence estuary (e.g., Syvitski and Praeg 1989; Josenhans and Lehman 1999; Massé 2001; Duchesne et al. 2007; Duchesne et al. 2010). Such analyses provide an interpretation of the Quaternary stratigraphy based mostly on geophysical interpretation with limited geological validation (e.g., long boreholes). Syvitski and Praeg (1989) defined 5 seismic units and proposed a geological interpretation associated with the retreat of the Laurentide Ice Sheet in the Estuary, which is still used today. From the base to the top, these seismic units are interpreted as: (U1) ice-contact deposits including ice-loaded and ice-deposited sediments such as tills; (U2) ice proximal, coarser grained sediments deposited as a thin conformable layer during rapid retreat of an ice terminus; (U3) fine-grained ice-distal sediments probably correlated to the Goldthwait Sea clays (e.g., Dionne 1977); (U4) coarser paraglacial sediments transported from land to sea from a rapidly ablating subaerial ice-sheet; and (U5) postglacial sediments deposited under modern sea-level and oceanographic conditions. Cauchon-Voyer et al. (2008) identified the same seismostratigraphic sequence for the submarine portion of the Betsiamites River delta area. Despite these numerous

geophysical studies, very few provide geological validation with core data. St-Onge et al. (2003) studied and described a 51.6 m-long piston core located in the Estuary; MD99-2220 shown in Figure 2.1, and dated the deposition of two lithological units. They were interpreted as glaciomarine and postglacial sediments and subsequently correlated to seismic units U3 and U5 (Cauchon-Voyer et al. 2008; Barletta et al. 2010). Seismic unit U2 was sampled on the southern shelf of the Laurentian Channel and is also interpreted as ice-proximal glaciomarine sediments (St-Onge et al. 2008).

2.4 Data and methods

Onshore, the approach used to interpret the geometry of the area prior to the landslide events and the location of the failure surfaces included integration of piezocone soundings (CPTU), subaerial seismic reflection data, and boreholes. Offshore, integration of geophysical and sampling results allows the linkage of the submarine landslide morphostratigraphy to the subaerial observations (Syvitski and Praeg 1989; St-Onge et al. 2003; Cauchon-Voyer et al. 2008). It is important to notice that such integration of both onshore and offshore investigations is very seldom done and implies the use of many different techniques.

2.4.1 Digital terrain models

The description of the landslide complex includes a morphological analysis, aerial photo interpretation, and geometrical measurements carried out on the subaerial and submarine digital elevation models (DEM). The subaerial DEM was derived at a 1 m resolution from airborne laser scanning (LIDAR) and hypsometric lines at 1 m contour interval obtained from photogrammetry on 1:15000 aerial photos. Details on the bathymetric data used to obtain the submarine DEM are found in Cauchon-Voyer et al. (2008). Landslide volume calculations were carried with ArcGIS Spatial and 3D Analyst tools.

2.4.2 Seismic reflection data

A continuous seismic reflection profile was acquired over a total length of 5.2 km along the shoreline west of the Betsiamites River (see location on Figure 2.1) and offers a cross-section perpendicular to the north-south axis of progradation of the delta. Sub-bottom

profiling allows definition of seismic properties of subsurface materials from reflected seismic waves, from which geological interpretation such as sediment type and accumulation pattern are proposed. Seismic reflection data were acquired using an array of 24 geophones (40 Hz) at 5 m spacing. The source was a “Buffalo gun” firing 12-gauge blank charges that were in holes about 50 cm below the ground surface (Pullan and MacAulay 1987). The configuration for the survey was a repetition of 12 shots increasing at 5 m steps, the first shot being fired at 2.5 m away from the first geophone. The data were acquired with a Geometrics Strata Visor seismograph and processed with the WinSeis Turbo software. Normal moveout corrections were applied to account for changes in distance between the source and each receiver. Stacking velocities were determined during the processing and a constant speed of 1500 m/s was used to linearly convert two-way travel time to approximate depths. Band pass filtering (150-200 and 500-600 Hz) was also applied to the presented section. In addition, 750 km of high-resolution seismic reflection data (white lines on Figure 2.1) used in this study were obtained with an EG&G chirp system (2 to 12 kHz) mounted on board the Coriolis II research vessel (Cauchon-Voyer 2007). To simplify, sections and descriptions presented in this paper are directly converted to depths. Interpretation of subsurface data was performed with the Kingdom Suite software package. Distinct seismic facies were defined according to amplitude and geometry of the inner reflections and to characteristics of the upper transition of each facies. In definition of subaerial seismic facies, the upper 10 ms were considered to be impacted by surface waves and hence do not necessarily reveal the inner geometry of the first 7.5 m of the deposits.

2.4.3 Piezocone tests (CPTU)

Thirty-eight piezocone tests, i.e., cone penetration tests with pore water pressure measurement (CPTU), were performed on both shores of the Betsiamites River (Figure 2.1b). These tests provide continuous in-situ geotechnical measurements of soil resistance and pore water pressure induced by penetration of the cone (e.g., Lunne et al. 1997). They were carried out with a 15-tonne capacity cone with a 15 cm² base area. To obtain a better definition of the stratigraphy, the penetration rate was maintained at 10 mm/s and pore pressure measured immediately behind the tip (u_{base}) and tip resistance (q_c) were recorded

at 10 mm intervals. Tip resistance (q_c) was corrected for the pore pressure acting behind the tip to obtain (q_t). The penetration depth of the CPTUs varies from 3.35 to 59.9 m. Pore pressure dissipation tests were carried out when coarser layers of higher resistance were reached and at the end of all soundings. The distance over which the cone senses an interface increases with material stiffness, indicating that soft layers thinner than 10 cm can be detected whereas stiff layers may need to be as thick as 75 cm or more for the cone resistance to reach its representative value (Lunne et al. 1997). When sounding results are used for geotechnical correlations, tip resistance is presented in terms of net tip resistance ($q_t - \sigma_{vo}$). Variation with penetration of the values of net tip resistance and induced pore water pressure, in addition to the shape (e.g., continuous or highly layered) and the slope of the profiles were considered for correlations between soundings.

2.4.4 Core data

Two boreholes were performed in the area (Figure 2.1b). Borehole F46010, to a depth of 58.9 m, was performed in the accumulation zone of the subaerial landslide ($68^{\circ}44'20.1''W - 48^{\circ}53'46.9''N$) at a distance of 75 m from the shoreline and at an elevation of 7.8 meters above sea-level. Unless specified otherwise, all data are positioned corresponding to their elevation above (positive value) or below sea-level (negative value). Borehole F46006, to a depth of 54.4 m, was performed 400 m behind the escarpment of the Colombier subaerial landslide scar ($68^{\circ}46'6.9''W - 48^{\circ}54'12.0''N$) at an elevation of 47.6 m. One Nilcon vane test profile was carried out at site 46006 to estimate the *in situ* undrained shear strength. Samples were recovered with a split spoon sampler and Shelby sampling tubes (70 mm diameter x 76 cm length). Immediately after recovery, sediments were subsampled at all sample ends in order to measure water content and to assess sample preservation. Digital X-ray images of all samples before extrusion were obtained with computerized co-axial tomography (CAT-Scan). The samples were then cut in subsections of 5 to 15 cm, described, covered with a mixture of petroleum jelly and paraffin, and kept undisturbed in a cold room ($\sim 8^{\circ}$ and 88% humidity). Natural water contents, shear strength measured with the Swedish fall cone, Atterberg limits, and preconsolidation pressures were subsequently measured. The preconsolidation pressure (σ'_p) was determined by conventional 24 hrs oedometer tests with load increment of 0.5 using the Casagrande method. Grain size

distributions were obtained using a Beckman Coulter LS 13 320 laser diffraction particle size analyzer for the sediment fraction smaller than 2 mm. Sediment mineralogy was identified by X-ray diffraction analyses (XRD) from analyses on bulk samples and sediment fractions smaller than 2 μm . Salinity values were estimated by ion chromatography. Forty-six sediment samples were also recovered in the submarine segment of the delta (Cauchon-Voyer 2007) and the location of the sampling stations are also indicated on Figure 2.1b. Nine marine shell fragments from boreholes F46010 and F46006 were sampled and ^{14}C dated by accelerator mass spectrometry (AMS) at the AMS facility of the University of California, Irvine (Table 2.1). To account for the apparent age of the dissolved inorganic carbon reservoir, a correction of -400 years was applied ($\Delta R=0$). To convert the ^{14}C conventional ages to calendar years, the dates were calibrated using the CALIB 5.0.1 online software (Stuiver and Reimer 1993).

2.5 Surface geomorphology

The subaerial and submarine portions of the delta are characterized by various geomorphologic elements resulting from landslide events. In this section, the subaerial domain is presented first, followed by the description of the submarine domain, with emphasis on both the local morphology and the elements resulting from mass movement events.

2.5.1 Subaerial morphology

In the vicinity of the Colombier landslide scar, large outcrops of Late Proterozoic Grenvillian metamorphic rocks (Franconi et al. 1975) break the highest deltaic plains at elevations ranging between 60 to 140 m (Figure 2.2). One of these outcrops is located at a distance of 200 m north of the landslide scar at an elevation of 60 m. The bedrock outcrops also on the shoreline at sea-level on the west side of the site (Figure 2.2), implying that the bedrock surface drops for at least 60 m over a distance of about 1500 m.

The subaerial topography around the landslide scar is composed of 4 main levels of raised marine terraces at elevations ranging between 70 and 15 m (Figure 2.2). The upper 70 m terrace is found in disconnected sections above the landslide scar. The 60 m terrace is

completely truncated by the landslide scar. The terrain at 60 m is overlain by peat bogs and has a slope angle of less than 1° . West of the landslide scar, shown on the left side of Figure 2.3a, the 40 m terrace runs parallel to the terrace at 60 m and is also truncated by the landslide scar (Figure 2.3b). The slope of the terrain above the landslide on the 40 m terrace is around 0.5° . East of the scar, many well-defined raised beach ridges are visible on the surface of the 40 and 15 m terraces and their orientations shift as they lower in elevation (Figure 2.2). The 15 m terrace is seen mainly east of the landslide scar and its upper plain narrows as it approaches the 40 m terrace (Figure 2.2).

For the Colombier subaerial landslide body, four morphological zones are defined on the basis of their geomorphologic elements and are referred as the West, Central, East, and Accumulation zones (Figure 2.3a).

The West zone consists of a salt water marsh bounded to the north by a 45 to 50 m escarpment with an average slope of 15° . This escarpment runs parallel to the 60 m terrace for 3000 m, then drops to sea level and truncates the 40 m high marine terrace (Figure 2.3b). This escarpment is subjected to small shallow landslides. Bedrock outcrops are also found at sea-level in this area.

The Central zone is characterized by a regular southeast sloping terrain of average slope of 2.5° bounded to the north by an upper escarpment with a surface elevation decreasing from 60 to 45 m. The height of this escarpment ranges between 10 and 30 m and its slope angle varies between 15° and 25° . This escarpment and the underlying terrain are eroded by small creeks (Figure 2.2) which drain the northwest terrain above the landslide. In the lower portion of this zone there is an escarpment with a maximum height of 8 m (pointed by an arrow on Figure 2.3c) at an elevation of about 10 m. This escarpment has more or less the same orientation as the escarpment of the West zone and is truncated to the west by road works and gully erosion (Figure 2.3c).

The main morphological characteristic of the East zone is a succession of elongated ridges and depressions (Figure 2.2). This part of the Colombier landslide scar has a morphology typical of a spread such as described by Cruden and Varnes (1996). Three main orientations of ridges are observed. The first group, in the northern part (main ridges, yellow on Figure

2.2), has an E-W orientation (90°). These ridges have a typical height, width and length of 10 m, 40 m and 200 m, respectively. The second group, to the east (lateral ridges, purple on Figure 2.2), has an average orientation of 120° . These ridges are slightly larger than the E-W ridges and have an average length of 275 m and maximum heights and widths of 25 and 60 m. The largest ridges are still connected to the eastern flank. The height of the scarp in this area ranges between 25 and 30 m. The third group of ridges has (central ridges, green on Figure 2.2) an orientation of 230° .

The Accumulation zone of the landslide is defined as the subaerial area where the displaced material deposited. This zone includes a levelled and forested area with an average elevation of 5 m, and the beach near or at modern sea-level. Disorganized ridges are also observed in this zone (central ridges, green on Figure 2.2). This zone appears to be an extension of the landslide debris in the Estuary. On the beach at low tide, large blocks of deformed and rotated sediment beds (Figure 2.4) are observed. These blocks extend into the West zone and the position of westernmost block observed at low tide is marked by a blue square on Figure 2.2. As it will be demonstrated later, the northern limit of the Accumulation zone is approximately the interpreted location of the marine terrace prior to the landslide.

2.5.2 Submarine morphology

The main geomorphologic element on the shelf is a 54 km^2 landslide scar, with two main topographic depressions, the West depression and the East depression, separated by an intact butte with steep flanks and flat top (Figure 2.2). This submarine scar resulted from the Betsiamites landslide event dated at 7250 cal BP and was partly filled by debris of the 1663 Colombier landslide event (Cauchon-Voyer et al. 2008). It is assumed that the submarine scar resulted from one event dated at 7250 cal BP, but it may have resulted from more than one failure phase. Both depressions have widths ranging from 2 to 4 km, lengths of 7 km, and floor slopes of about 1° . The height of the flanks to the seafloor of both depression ranges from 12 to 20 m. The butte is 5 km^2 in area with a maximum length and width of 4.5 km and 1.6 km respectively (Figure 2.2). The average slope of the top of this butte is 1° . The depressions and the butte are overlain by 3 to 10 m of subaerial landslide debris. The scar extends from -10 m to -140 m (Figure 2.5).

The northernmost ship track of the bathymetric survey closest to the shore follows approximately the 5 m water depth contour line (Figure 2.2). This contour does not run parallel to the shoreline but instead moves seaward as it approaches the West depression. The upper portion of the West depression is smooth, has a fairly low slope of about 0.5° , and no apparent escarpment (Figure 2.2). The easternmost portion of the East topographic depression has a low gradient and is overlain by landslide blocks. The westernmost portion is bounded by a 20 m high escarpment having a slope of 8° and running parallel to the shoreline (Figure 2.2). As it will be demonstrated, this escarpment has a significant impact on the stability of the submarine area and is interpreted as the back escarpment of the submarine failure dated at 7250 cal BP. Fewer blocks appear at the toe of this escarpment than in the easternmost portion of the East topographic depression.

Offshore, in the Laurentian Channel (Figure 2.1), there is a large depositional lobe observed at an average water depth of 350 m covering an area of about 104 km^2 (Figure 2.5). It has a maximum width of 15 km and an average thickness of 9.4 m, thus has an estimated volume of $\sim 1 \text{ km}^3$. This lobe corresponds to the sediments mobilized from the shelf to the Laurentian Channel by the 7250 cal BP Betsiamites submarine landslide (Cauchon-Voyer et al. 2008). Seismic profiling and samples recovered from the lobe area indicate the presence of a few cm-thick turbidite layer associated with the 1663 Colombier landslide event on top of hemipelagic sediments covering the 7250 cal BP debris (Cauchon-Voyer et al. 2008).

2.6 Coastline seismostratigraphy

The 5.2 km-long subaerial seismic reflection profile shown in Figure 2.6a provides correlation between the boreholes and CPTUs in addition to linking the subaerial stratigraphy (Figure 2.6b) to the submarine seismostratigraphy (Figure 2.6c). Four seismic units and a reflector resulting from a strong acoustic impedance contrast, interpreted as bedrock, were identified on the seismic section (Figure 2.6b) and are summarized in Table 2.2. The lower four subaerial units correlate with the seismostratigraphy interpreted offshore for the Betsiamites River area (Figure 2.6c) (Cauchon-Voyer et al. 2008). For

consistency with previously published work, the numbering and interpretation proposed by Syvitski and Praeg (1989) are followed.

The sediment-bedrock interface is characterized by relatively continuous high amplitude reflections, where little energy penetrates below this boundary. The depth to the bedrock decreases west to east, from -120 to -30 m, on the profile. The bedrock drops at an angle of about 4° for the first 1000 m and then reaches a more gently sloping segment with an angle of less than 0.5° . Additionally, the bedrock outcrops on the beach 600 m west of the seismic profile, which supports the interpretation that the continuous high amplitude reflections correspond to the sediment-bedrock interface.

Seismic unit U1 is the lowermost seismostratigraphic unit characterized by moderate to strong amplitude reflections and poor or absent continuous internal reflecting horizons. The upper bounding surface is highly variable. The thickness of unit 1 ranges from 1 to 43 m and averages 29 m. This unit was associated to ice-contact deposits including ice-loaded and ice-deposited sediments (Syvitski and Praeg 1989).

Seismic unit U2 is characterized by highly variable acoustic reflections with strong and closely spaced reflecting horizons. The upper boundary of this seismic unit corresponds to a sharp decrease in amplitude of the reflecting horizons. The thickness of unit 2 ranges from 5 to 36 m and averages 17 m. On the easternmost 1500 m of the section, the thickness of U2 increases and has an average thickness value of 25 m. In this section, between 4500 and 5000 m, the reflecting horizons of the upper boundary have a V-shape dipping down 15 m over a total distance of 500 m, which is interpreted as a buried submarine channel. This unit was defined as a ice proximal, coarser grained sediments deposited as a thin conformable layer during the rapid retreat of an ice terminus (Syvitski and Praeg 1989). As it will be shown, the upper part of this unit has been sampled in borehole 46010.

Seismic unit U3 consists of low amplitude reflections and presents only few weak continuous reflecting horizons located in the lower portion of the seismic unit. The upper transition of this unit with U4 is weak and often absent, i.e., the change in acoustic impedance is too weak to obtain coherent reflections. The boundary was interpreted mostly on the general trend of reflection amplitude, i.e., U3 being generally weaker than U4. The

transition between both units is hence approximate. The thickness of U3 ranges between 7 to 34 m with an average of 22 m. This unit was interpreted as fine-grained ice-distal sediments (Syvitski and Praeg 1989) probably correlated to the Goldthwait Sea clays (e.g., Dionne 1977; Dredge 1983).

Seismic unit U4 is a stronger amplitude section with strong and coherent internal reflections. The thickness of U4 ranges between 8 and 44 m and averages 25. Within this seismic unit, there is a 2 to 4 m thick sequence of closely packed reflecting horizons, which is labelled R1 on Figure 2.6b. These reflecting horizons are due to strong acoustic impedance contrasts in the sedimentary succession that could result, among other causes, from a significant change in grain size distribution, e.g., clayey to sandy material. The maximum amplitude of this package of reflecting horizons is recorded at about -16.5 m. Similar reflecting horizons within Unit 4 were mapped on the submarine profiles on the submarine shelf (Figure 2.6c) (Cauchon-Voyer et al. 2008). This unit correlates to paraglacial sediments transported from land to sea from a rapidly ablating subaerial ice-sheet (Syvitski and Praeg 1989).

The uppermost seismic facies is apparent on Figure 2.6c in the westernmost part of the profile. Reflections are conformable on the irregular and hummocky unit 4. This facies is not numbered as it does not correspond to the post-glacial sediments defined by Syvitski and Praeg (1989) as unit 5. The average thickness of this seismic facies is 10 m. The seismic amplitude of this facies varies and based on seismic characteristics from the literature (e.g., Piper et al. 1999) is interpreted as subaerial landslide debris.

2.7 Lithological units

Two subaerial boreholes provide lithological data to validate seismic reflection interpretations. Sedimentological and geotechnical data obtained from borehole 46010 (Figure 2.7) and borehole 46006 (Figure 2.8) are summarized in Table 2.3 whereas the lithostratigraphic correlations are presented on Figure 2.9.

2.7.1 Borehole in subaerial slide debris - site 46010

Lithological and geotechnical data for the landslide debris and the deposits below the failure surface were obtained from the 58.9 m long borehole F46010 (Figure 2.7) carried out 40 m from CPTU C46010 (see location on Figure 2.2) at an elevation of 7.8 m along the shoreline. Six lithological units, with different sedimentological and geotechnical properties, were identified (Table 2.3).

The lowermost lithological unit (10-L2) consists of gravelly and bouldery sandy silt. On the CPTU profile, this lithological unit is characterized by more than 4 meters of closely spaced layers of moderate (3 MPa to 18 MPa) net tip resistance ($q_t - \sigma_{vo}$). Pore pressure dissipation tests carried out within this unit indicated hydrostatic conditions with reference to the water table at an elevation of 4.7 m. This unit corresponds to the upper portion of seismic unit U2 (Figures 2.6b and 2.9).

The second lithological unit (10-L3a) consists of grey laminated silt to silty sand with some clay with generally low net tip resistance. This unit is about 4 m thick and shows a decrease in net tip resistance with increasing depth. It correlates with the lower portion of seismic unit U3 (Figures 2.6b and 2.9).

The third unit (10-L3b) observed in this borehole comprises bioturbated grey silty clay. This unit is 21 m thick at elevations between -43 and -22 m. The natural water content ranges between 30 and 43%. The plasticity index ranges between 16 and 28 % and the liquidity index is lower than 1, with values between 0.7 and 0.9. The clay fraction (particles less than 2 μm) ranges between 29 and 50% and averages 37%. The sensitivity (S_t) values obtained with the Swedish fall cone for this layer are 14 and 56. Salinity values decrease with depth, from 16.4 to 6.3 g/L. Four marine shell fragments sampled within this lithological unit were dated and range between 10.2 and 10.7 ka cal BP (Table 2.1). This unit correlates also with seismic unit U3 (Figures 2.6b and 2.9).

The fourth lithological unit (10-L4a) consists of 14 m of highly stratified silty clay and silty clayey sand between -22 and -8 m. The CPTU pore pressure dissipation test performed in the coarser soil layers of higher resistance indicated hydrostatic conditions relative to the

water table. One broken shell fragment was dated in this unit and yielded an age of 10.2 ka cal BP. This lithological unit correlates with seismic unit U4 (Figure 2.6b) and corresponds to paraglacial prodeltaic sediments deposited in a time of falling relative sea-level (Syvitski and Praeg 1989; Bernatchez 2003). This interpretation explains why a date as old as the ones from the previous distal glaciomarine sediments unit (U3, 10-L3b) was sampled within this unit (U4, 10-L4a) since these finer paraglacial sediments are lifted distal glaciomarine sediments eroded and transported from land to sea, which possibly included this remobilized shell fragment.

The fifth lithological unit (10-Da) consists of chaotic facies of silty clay to sandy clayey silt. Evidence of sediment disturbance was observed in five samples, between -8.0 to 0.2 m. The boundary between this chaotic facies (10-Da) and the lower intact stratified silty clay and silty clayey sand (10-L4a) corresponds also to a change in the CPTU profile at -8 m (Figure 2.7). Three samples between -0.2 and 5.0 m show deformed silty clay clasts in a sandy clayey silt matrix, which is typical of a debris flow deposit (e.g., Mulder and Alexander 2001). A sample between -6.6 and -5.9 m presents distinctive subvertical 1 cm-thick laminations, implying that this sample was recovered from a displaced block, which had rotated about 90° and that this block was stiff enough to keep laminations intact. The sample recovered at an elevation between -8.0 and -7.4 m represents two facies; the upper 25 cm is a silty layer with subvertical structures sharply overlying a 33 cm-thick layer of silty clay clasts within a sandy muddy matrix. This lithological unit corresponds to the seismic facies interpreted as landslide debris deposits on the subaerial seismic profile (Figure 2.6b).

Finally, the upper 7.5 m of borehole F46010 contains moderately well-sorted brown sand (10-Db). The water table was 4.3 meters below the surface at an elevation of 4.7 m at the time of the soundings. This unit corresponds to regressive paraglacial sand (U4-sand) and, as it will also be demonstrated, was mobilized by the subaerial landslide.

2.7.2 Borehole outside the Colombier subaerial landslide scar – site 46006

Borehole F46006 (Figure 2.8) was carried out 400 m from the lateral escarpment of the Colombier subaerial landslide scar close to the West and Central zones (Figure 2.3). The borehole was located 23 meters from CPTU C46006. The CTPU sounding was stopped at 59.99 m, at an elevation of -12.37 m, whereas the borehole reached the bedrock at -6.7 m. This difference implies that the topography of the bedrock is irregular and could drop at a possible angle of 14° between the location of the CPTU and the borehole at site 46006. Four lithological units were defined in this borehole and their characteristics are summarized in Table 2.3.

The lowermost lithological unit (6-L3a) of borehole F46006 comprises ~20 meters of highly laminated clayey silt up to an elevation of 8 m. The clay content ranges between 24 and 53% and this variation results mostly from changes in grain sizes between cm-scale horizontal laminations. Four calcareous concretions were sampled between 4.95 and 4.25 m. They present carbon and oxygen isotope compositions ranging between $-16.8 > \delta^{13}\text{C} > -18.4$ ‰ and $0.43 > \delta^{18}\text{O} > 3.4$ ‰, vs V-PDB, implying that they are typical of glaciomarine concretions (Hillaire-Marcel and Causse 1989). This unit correlates to seismic unit U3.

The overlying layer (6-L3b and 6-L3c) consists of 20 m of bioturbated grey silty clay between 8 and 28 m. Despite comparable physical characteristics such as grain size distribution and sedimentary structures across depth; it has two layers with different geotechnical behaviour and thus is described as two subunits, 6-L3b and 6-L3c. Within both subunits, four marine shell fragments were sampled and dated between 10.1 and 10.6 ka cal BP (Table 2.1). This unit correlates with seismic unit U3.

Subunit 6-L3b ranges between 8 and 18 m. The natural water contents range between 24 and 31 %. The plasticity index ranges from 10 to 14 %, the liquidity index is slightly greater than 1.0, with values ranging between 1.1 and 1.2. The clay fraction is typically of 46 %. Sensitivity ranges between 35 and 67.

The upper 10-m thick subunit 6-L3c between 18 and 28 m has a natural water content ranging between 31 and 37 %. The plasticity index ranges between 7 and 10 % and the liquidity index is greater than 1, with values between 2.4 and 3.1. If a 1-cm thick sand bed at 26.8 m is ignored, the clay fraction ranges between 40 and 52 % and averages 46 %. The sensitivity values obtained with the Swedish cone, range between 406 and 1202.

According to the radiocarbon dates obtained, the physical characteristics, and the stratigraphic position in the sedimentary column of both subunits of bioturbated grey silty clay, 6-L3b and 6-L3c correlates to the unit (10-L3b) of bioturbated grey silty clay (Figure 2.9) observed in borehole 46010 (Figure 2.7). Despite similar sedimentological characteristics, the sensitivity of the material of this layer in 46006 is one order of magnitude greater than that of this layer at site 46010 (Table 2.2). The fourth lithological unit (6-L4a) within borehole 46006 consists of 14 m of highly stratified clayey silt and silty sand. The natural water contents range between 24 and 40 % and the liquidity index is greater than 1.0 with values ranging between 1.6 and 2.8. Some measured remoulded shear strength (C_{ur}) values are lower than 0.08 kPa, which corresponds to the limit of the Swedish cone apparatus, indicating that the liquidity index is at least equal or higher than 3.9 according to Leroueil et al. (1983). This lithological unit correlates with seismic unit U4.

The upper lithological unit (6-L4b) is a 5.0 m-thick sandy layer with a sand content ranging from 79 to 97 %. Some subsamples within this layer contain 15 to 19 % of rounded pebbles of size between 2 to 8 mm. The transition unit 06-L4b with the underlying stratified clayey silt and silty sand (6-L4a) likely corresponds to an erosive contact related to the lowering of the relative sea-level (e.g., Hart and Long 1996; Bernatchez 2003). This unit could correspond to seismic unit U4 according to the interpretation of Syvitski and Praeg (1989) and is labelled U4-sand in this study.

2.8 Assessment of failure surfaces and material involved in the 1663 Colombier landslide event

Onshore, the boreholes and adjacent CPTUs, provide lithological and geotechnical data inside and outside the Colombier subaerial landslide scar. The subaerial landslide boundaries were obtained from the morphological analysis whereas the seismic profiles

allowed the definition of the sequence of deposits and their lateral extension. Combined together, such information allows identification of the materials involved in the 1663 Colombier landslide and detecting the location of the failure surfaces.

2.8.1 Coastal correlations and failure surfaces

Four CPTUs were carried out along the shoreline (Figure 2.10) and correlated with borehole 46010. On the subaerial seismic profile (Figure 2.6a), the upper seismic facies interpreted as reworked sediments reached an elevation of -8.6 m at the location of borehole 46010 (Figure 2.6b), which is further confirmed by landslide debris identified in the sediment cores (Figure 2.7). Such lithological interpretation was correlated to the surrounding CPTUs to evaluate the location of a failure surface along the shoreline (Figure 2.10). The criterion to identify the failure surface on the CPTUs carried out along the current shoreline is the strong change in net tip resistance corresponding to the transition from the chaotic facies (lithological unit 10-Db) to the intact stratified silty clay and silty clayey sand (seismic unit U4 and 10-L4). On that cross section, the failure surface slightly dips toward the center of the delta with a maximum angle of 0.2° (Figure 2.10). Transitions between the lithological units, interpreted on the CPTUs, also dip toward the center of the delta implying that the failure surface could follow a stratigraphic level resulting from the conformable bedding pattern of the deltaic progradation in the valley. At the location of CPTU C46111 on the eastern side of the site (Figure 2.2), morphological observations indicate that this site was not impacted by mass movement as it is 1300 m outside the subaerial and submarine scars. The upper 5 m layer within CPTU 46111 is interpreted as regressive littoral sand (U4-sand). At an elevation of -17 m, there is a 35 cm-thick layer with net tip resistance reaching 28 MPa, which, according to Robertson's charts (1990), is likely composed of a mixture of clean sand to silty sand. The elevation to this sandy layer corresponds to the elevation of seismic reflector R1 identified at about -16.5 m in the subaerial seismic profile (Figure 2.6b) and correlates to the seismic reflector R1 identified on the submarine seismic profiles (Figure 2.6c).

2.8.2 North south correlations and failure surfaces

A sequence of 4 CPTUs (Figure 2.11) was carried out along the north-south axis of the subaerial landslide in the Central zone (Figure 2.2). The section on Figure 2.11 shows the topography prior to the landslide, estimated according to the location of the remaining terraces and raised beaches, the actual topography, and the location of the failure surface. The final topographic profile discloses an 8 m-high, 500 m long escarpment at 2500 m from the start of the profile (Figure 2.2). Along this section, from base to top, the four CPTUs present a 1 to 4 m-thick layer presenting the same attributes as coarse ice-proximal glaciomarine sediments (10-L2) identified at site 46010 (Figure 2.7). This layer is overlain by an uniform layer, likely composed of finer glaciomarine sediments similar to 10-L3a and 10-L3b (Figure 2.7). The elevation of the failure surface is evaluated on the CPTUs and is defined as the increase of net tip resistance in the profile (Figure 2.11c). In addition, no other significant irregularity in the profile is interpreted below this level. The failure surface is thus located just below a 3-4 m thick layer of debris. This fact implies that the landslide mass was more than 50 m thick in part of the Central zone but the failed material evacuated the area, which is typical of flow slides in sensitive clay.

A sequence of 6 CPTUs (Figure 2.12) was carried out in the East zone of the subaerial landslide (Figure 2.2). The initial topography is assumed according to the topography of the terrain outside the Colombier landslide scar. The elevation of the failure surface was evaluated on the CPTU profiles in the East zone when at least one of the three following criteria was met: (1) the profile reveals an apparent decrease in tip resistance (e.g., Figure 2.13a) as if the mass sliding above the failure surface was remoulded; (2) there is a sharp increase in tip resistance (e.g., Figure 2.13b), as it was seen for the coastal profiles (Figure 2.10), which could imply that the landslide eroded clayey material and left sandy material above the failure surface; or (3) there is a change in the preconsolidation pressure profile. With an empirical relationship [1] linking preconsolidation pressure (σ'_p) and net tip resistance ($q_t - \sigma_{v0}$) it is possible to emphasize the change in trend of the stratigraphic profiles. These changes can result from marine erosion, landslides or change in soil nature and composition (e.g., Locat et al. 2003).

$$[1] \quad \sigma'_p = \frac{q_t - \sigma_{vo}}{3.4} \quad (\text{Demers and Leroueil 2002})$$

For CPTU C46009 (Figure 2.13c), a 90 cm layer at -17 m is normally consolidated, implying that it could be a layer of remoulded and mobilized sediments above the failure surface. Since there is only one borehole (Figure 2.7) to validate the CPTUs interpretation along the north-south axis (Figure 2.12), it was not always obvious which criterion prevailed and actually corresponds to the failure surface. To account for this ambiguity, two scenarios presenting a shallow and a deeper failure surface are indicated on Figure 2.12. The deepest possible failure surface, shown in orange on Figure 2.12, developed over a length of about 3 km. The vertical exaggeration of Figure 2.12a is 20x, which greatly distorts the perception of the failure surface and emphasizes the fact that it did not need a high gradient to propagate. The slope of the failure surface between C46003 and C46005 is only 0.8°. The slope angle between the interpreted failure surface, which rises up between C46005 and C46010, is 0.45°.

2.9 Interpretation of seismic data

The subaerial and submarine seismic data show two main features in regard to the landslides that occurred in the Betsiamites area. First, the seismic data allow interpretation of subaerial and submarine depositional processes in the sedimentary succession and of the debris deposits. Secondly, the seismic data allow establishment of the architecture of the deposits along the shoreline and below sea-level and therefore identification of the units of sediments involved in the subaerial and submarine failures.

On the submarine profile shown on Figure 2.6c, the transparent seismic package between -110 to -80 m is interpreted as representing mass transport deposits associated with a landslide event dated at 9250 cal BP (Cauchon-Voyer et al. 2008). On the same submarine profile, the truncated reflectors correspond to lateral escarpments of the 7250 cal BP Betsiamites submarine landslide event (Cauchon-Voyer et al. 2008). The 9250 cal BP debris are interpreted within Unit 4 (Figure 2.6c) below reflector R1, which implies that the 9250 cal BP event occurred before the deposition of R1. The thickest accumulation of 9250 cal BP debris is observed within the central butte of intact deposits within the Betsiamites

submarine landslide scar. More than 200 hm³ of buried deposits over 22 km² occurring under seismic reflector R1 (Figure 2.6c) were mapped across the submarine shelf. The sediment accumulation rate was rapid, up to 34 m/kyr in the Estuary prior to 8500 cal BP (St-Onge et al. 2003), which implies that the depression resulting from the 9250 cal BP event was promptly filled, as seen on Figure 2.6c where about 25 m of highly stratified prodeltaic sediments cover reflector R1.

The Betsiamites submarine failure, which removed more than 25 m of deposit within seismic unit U4, occurred above the stratigraphic level of R1 (Figure 2.6c). On Figure 2.6c, the depth to the failure surface is about 20 m below the current seafloor. According to the seismic interpretation in the upper portion of the submarine scar (area shown on Figure 2.2), the failure surface developed a few meters above seismic reflector R1 in the West depression, whereas the failure developed on R1 in the East depression (Figure 2.6c). The location of the failure surface of the submarine event was mapped across the landslide scar and the previous topography was estimated according to the location of the lateral flanks. The volume estimate for the submarine scar reaches 1.3 km³, which implies an average escarpment height of 24 m across the area of the starting zone, which is 54 km².

Seismic surveys onshore and offshore allow the definition of seismic characteristics that correlate for the subaerial and submarine portions of the delta area. For the reconstitution of the landslide events, it becomes significant to recognize that seismic unit U3 on the subaerial and submarine profiles consists of low amplitude conformable reflections whereas Unit 4 contains parallel reflections on both onshore and offshore surveys and, on the submarine profiles, contains transparent reflection pattern and truncated reflectors. These observations imply that the sedimentological and geotechnical properties obtained from the coastal borehole (Figure 2.7) can be used to characterize the properties of the seismic subaerial and submarine units defined elsewhere around the Betsiamites landslide complex.

2.10 1663 Colombier landslide failure phases

Various indications suggest that several failures occurred at different times in the Betsiamites River area. In addition to the two early Holocene submarine failures dated as

older than 9250 and 7250 cal BP, the integration of the results allows distinguishing that the large Colombier subaerial scar was the result of a complex slide initiated by the 1663 earthquake. In this section, it is demonstrated that the 1663 Colombier landslide event resulted from four related failure phases which all probably occurred one after the other in a short period of time (hours or days). The sequence of events in the triggering and development of the failures is therefore presented.

2.10.1 Interpretation of initial topography and morpho-stratigraphy

The subaerial and submarine initial morpho-stratigraphy of the Colombier landslide area is interpreted on the basis of the CPTU results, borehole data and seismic profiling (Figure 2.14). Onshore, the slope of all three delta plains of the marine terraces was likely around 1° (Figure 2.15a), as it is for the surrounding terrain.

The lithological units involved in the Colombier subaerial landslide fine glaciomarine sediments (U3), stratified paraglacial prodeltaic sediments (U4), and littoral sand (U4-sand) (Figure 2.14). Sediment thickness increases toward the center of the delta and geotechnical properties of glaciomarine sediments (U3) change according to their elevation above sea-level. The upper sandy layer (U4-sand, 6-L4b) is only 5 m thick (Figure 2.8) west of the landslide, whereas it is about 25-30 m thick in the East area (see CPTU 46001 on Figure 2.12). This difference in sand accumulation is a result of the distance from the river; the thickest accumulation being proximal to the river, and had an impact on the type of mass movement developing in the slope. The transition to stratified facies (U4) is at lower elevation in the East zone, at about 5 m closer to the shoreline and potentially up to an elevation of 30 m higher upslope. In the Central (Figure 2.14b) and West zones this transition occurs at higher elevation, as identified at 42 m at site 46006 (Figure 2.8).

Below sea-level, the same lithostratigraphic units extend seaward (Figure 2.14). The upper part of the of 8° back scarp of the 7250 cal BP Betsiamites submarine failure (see position on Figure 2.2) is at an approximate water depth of -10 m. Reflector R1, which appears on the subaerial seismic profile (Figure 2.6a) and the submarine profiles (Figure 2.6c) is interpreted as a sandy later (Figure 2.10). This sandy layer probably came into sight in the lower portion of the back escarpment of the Betsiamites scar (Figure 2.14a). This sandy

layer (R1) also likely extended inland in the unit of stratified silty clay and silty clayey sand (U4, 4-L4) but the Colombier landslide event eroded it making its recognition with CPTU soundings onshore impossible. When reconstructing the topography prior to the 1663 Colombier landslides (Figure 2.15a), it is interpreted that the location of borehole F46010, now onshore, was a few meters below sea-level (Figure 2.14a).

2.11 Interpretation of the 1663 Colombier landslide phases

The Colombier subaerial landslide scar (Figure 2.3) is a complex slide resulting from at least three failure mechanisms: a submarine landslide event, a flowslide in sensitive clay and a lateral spread, as defined by Cruden and Varnes (1996). This landslide scar resulted from 4 distinct failure phases, which all probably occurred one after the other in a short period of time (hours or days). The submarine slide, Phase 1, occurred first. It was followed by a flowslide, Phase 2F in the West Zone, then by a second flowslide, Phase 3F in the Central zone, and finally, likely synchronously, by a spread, Phase 3S, in the East zone (Figure 2.15b).

2.11.1 Phase 1 – Submarine failure

Phase 1 occurred first underwater and mobilized part of the beach to an approximate location between the shoreline and the 40 m terrace (Figure 2.15b). Prior to this submarine failure, the 8° and 20 m high upper escarpment of the 7250 cal BP Betsiamites landslide scar (Figure 2.5) probably followed the -10 m contour line (Figure 2.2). Presumably, the 1663 earthquake liquefied a sandy layer, possibly R1 (Figure 2.10) or a layer similar to it, emerging in the submarine headwall at a water depth of -40 m (Figure 2.14a). This planar failure probably reached above the current shoreline up to at least the location of soundings C46036, C46010 and C46037 (Figure 2.10). On those shoreline CPTU soundings, the subaerial landslide debris deposits are interpreted at elevations ranging between -13.5 and -6 m. Large blocks of deformed and rotated sediment beds (Figure 2.4) are observable on the beach at low tide. The space below the current shoreline must have been made available for debris spread prior to the subaerial failures, hence supporting the hypothesis of a submarine failure occurring first. More than 145 hm³ of material were mobilized over an

approximate area of 9.3 km^2 , which implies an average height of 15.6 m for the submarine landslide body.

It is difficult, on the basis of available data, to define the exact lateral extension of the 1663 Colombier submarine failure (Phase 1). The back escarpment of the 7250 cal BP Betsiamites event in the East depression was eroded (Figure 2.2) by this submarine failure, which provides an approximate southern boundary. However, the absence of an escarpment on the bathymetric map in the West depression could suggest that: (1) the Colombier submarine failure also occurred on the crest of the Betsiamites submarine scar in the West depression and eroded this escarpment; or (2) the debris of the Colombier subaerial failures simply covers the back escarpment of the Betsiamites submarine scar. The rotated and deformed blocks along the shoreline (Figure 2.4) extend at least to the proposed boundary of the submarine failure 1 (Figure 2.15b). As a result, the volume estimation of 145 hm^3 for the submarine slide involves uncertainties.

2.11.2 Phase 2F – West flowslide

Shortly after the submarine failure (Phase 1), it is interpreted that a large subaerial flowslide (Figure 2.15b) developed in the West zone. The 40 m marine terrace is truncated by the western flank (Figure 2.3b) of the flowslide. This truncation provides the main evidence to interpret that this area was eroded by a flowslide. The bedrock outcrops on the shoreline (Figure 2.2) and is estimated around -10 m at site 46006. The presence of bedrock implies that the failure surface could not be much lower than sea-level and thus indicates that it was likely in the unit of laminated silt to silty sand (06-L3a) identified in borehole 46006 (Figure 2.8). The height of the back escarpment of the landslide is about 45 m, which is similar to the thickness of the landslide body estimated in the Central zone (Figure 2.11). The liquidity index of the soil in the upper portion of the slope (6-L4a and 6-L3c) is above 1.2 (Table 2.3), which likely facilitated development of a flowslide (e.g., Leroueil et al. 1996). If it is assumed that the failure surface developed only on land and stopped at the shoreline and that the failure surface was at sea-level, the estimated volume for this phase of the subaerial landslide is about 130 hm^3 . The retrogression distance from the interpreted shoreline ranges between 800 and 1200 m. This section of the subaerial scar has an area of 3.4 km^2 and an average width of 3.1 km. Landslide debris appear totally evacuated from the

subaerial scar and flowed into the estuary. On the marine seismic profile, the layer of debris related to this event is interpreted to be less than 10 m thick, thus less than 22% of the initial slope height.

2.11.3 Phase 3F – Central flowslide

Shortly after the first flowslide (Phase 2F), a second flowslide (Phase 3F) developed in the Central zone. Flowslide 2F acted in fact as an initial failure leaving an unstable backscarp in which flowslide 3F developed. The estimated area for flowslide 3F is 2.5 km² and the maximum retrogressive distance was likely between 2600 and 3000 m. The volume of displaced material in this area of the subaerial scar is 75 hm³. The debris of flowslide 3F moved westward into the open space created by flowslide 2F and into the scars of the submarine failures of 1663 (Phase 1) and 7250 cal BP. Only a 3-4 m thick layer of debris remains in the Central area of the subaerial scar, confirming that this phase is indeed a flowslide (Figure 2.11). Four CPTUs were carried out in the upper west Central area (Figure 2.2). Refusal was met at depths between 14.6 and 22.8 m, which is generally shallower than the soundings carried out in the East zone (Figure 2.12 and Figure 2.16), suggesting that the bedrock is not as deep in this area.

Few uncertainties remain in regard to the exact position of the failure surface. It appears that the failure surface of flowslide 3F was actually above the shoreline and did not follow the same level as the failure surface of the submarine failure (Phase 1) or the west flowslide 2F. The failure surface of the central flowslide 3F is interpreted to be at an elevation of 7.3 m on CPTU C46008, which was carried out at an elevation of 11.1 m. The location of the failure surface indicates that the 8 m high escarpment left in the western portion of the central scar (Figure 2.3c) could be in fact the lower part the headwall of the west flowslide 2F and where, subsequently, the failure surface of Phase 3F came into sight. The transition of $I_L > 1$ and $I_L < 1.2$ occurs at about 18 m (Figure 2.8) at borehole site 46006, 400 m west of the escarpment of Phase 3F and that the failure surface is located at 7.3 m at the position of CPTU 46008. The surface between this transition at borehole 46006 and the failure surface at site 46008 makes an angle of 0.4°. This surface where a significant change in liquidity index occurs could potentially correspond to the plane of retrogression of the failure.

2.11.4 Phase 3S – Lateral spread

As a result of the destabilization of the shoreline by the 1663 Colombier submarine failure (Phase 1) and associated flowslides 2F and 3F, Phase 3S occurred (Figure 2.15b). Flowslide 3F and the lateral spread 3S probably occurred more or less simultaneously but the remoulded material of the flowslide 3F evacuated the scar more rapidly and pushed east the sandy and stiffer blocks of spread 3S (green and yellow ridges on Figure 2.2). The boundary between the Phase 3S and 3F is approximate and based on the morphology of the debris remaining in the scar. The debris remaining in the scar of the lateral spread 3S is characterized by a repetitive pattern of ridges and troughs mostly oriented perpendicular to the direction of movement, which is typical of lateral spreads (Cruden and Varnes 1996). Few blocks of clayey material moved underwater toward the central butte and in the West depression of the 7250 cal BP Betsiamites landslide scar, but most of the blocks are found in the East depression. It is thought that these clayey materials were initially between the failure surface and the sandy layer (U4-sand, 6-L4b) above and were extruded under the weight of the sand layer. The maximum distance between the location of the interpreted location of the back scarp left by the submarine slide (Phase 1) and the back escarpment of the spread (phase 3S) is 2600 m. The approximate width of the landslide body of this phase 3S is about 1300 m. CPTU C46118 (Figure 2.16) is the only sounding directly in the center of the lateral spread and shows the failure surface to be at least at -13 m (Figure 2.2). In fact, since the area has a complex lithostratigraphy and there is no core validation, it is difficult to define exactly the position of the failure surface on CPTU 46118 (Figure 2.16). To account for the uncertainties in the failure surface location, a potential zone for its elevation is indicated. The topographic profile with CPTU results shown on Figure 2.12 lies more or less at the boundary between both the flowslide 2F and the spread 3S. The angle of the failure surface between soundings C46118 and C46002 along the section is only 1.9°. As observed for the cross-section along the shoreline, the failure surface likely followed a gently inclined bedding surface. The area of the lateral spread 3S is about 3.7 km² and mobilized an estimated slide volume of 180 hm³.

2.12 Conclusions

The prediction of landslide activity along the coast of the St. Lawrence estuary and the evaluation of the potential for submarine failures to reach the current shoreline is significant and should be integrated in geohazard mapping and coastal planning. This reconstruction of the sequence of landslide events of the Betsiamites landslides complex demonstrates that the 1663 submarine failure retrogressed upslope and destabilized the subaerial shoreline, which subsequently caused a large multi-component subaerial landslide. In this case, the stability of the slope prior to 1663 failure events was reduced by the presence of the 7250 cal BP Betsiamites submarine scars that acted as a predisposition factor by changing the general geometry of the slope. Mapping of previous shallow submarine scars should hence be integrated in subaerial landslide danger analysis.

In summary, this investigation of the coastal instabilities in the Betsiamites River delta area enabled the identification of a landslide complex of 74 km² in the subaerial and submarine domains. The Betsiamites landslides complex was likely formed by at least three landslide events. A first submarine landslide, dated at about 9250 cal BP, which involved at least 200 hm³ is followed by a second failure, the Betsiamites submarine landslide event dated at 7250 cal BP, which mobilized a volume of 1.3 km³ over an area of 54 km².

The third landslide event is the Colombier landslide initiated by the 1663 earthquake, which involved 4 successive failure phases: one submarine and three subaerial. The Colombier submarine slide (phase 1) involved a volume of 145 hm³ over 9.3 km² and was likely triggered by the 1663 earthquake. The second phase, flowslide 2F, developed in sensitive material and involved a volume of 130 hm³ over an area of 3.2 km². Phase 3F is a flowslide that occurred in the back headwall of flowslide 2F and mobilized 75 hm³ over more than 2.5 km². Phase 3S is a lateral spread, which extended over 3.8 km² with an estimated volume of 180 hm³. The total volume of material mobilized in 1663 is 530 hm³ over 20 km², which is among the largest documented subaerial landslides in Canada.

2.13 Acknowledgements

The authors wish to thank the Ministère des Transports du Québec (MTQ), NSERC and FQRNT for their financial support. We thank the MTQ for the permission to use their topographic and LIDAR surveys, borehole, and piezocone soundings data of the Colombier - Betsiamites area, and in particular to D. Robitaille and P. Locat for their involvement in the project. Many thanks to D. Turmel and C. Amiguet (Université Laval) for their valuable help during seismic reflection data acquisition and to A. Pugin (Geological Survey of Canada, Ottawa) for his assistance with seismic data processing. We recognize the contribution of Patrick Lajeunesse and all scientists and crew members on board the Coriolis II, F.G. Creed, and Guillemot vessels. The Canadian Hydrographic Service and GSC-Quebec are also acknowledged for their contribution to bathymetric data acquisition.

2.14 References

- Adams, J., and Atkinson, G. 2003. Development of seismic hazard maps for the proposed 2005 edition of the National Building Code of Canada. *Canadian Journal of Civil Engineering*, **30**(2): 255-271.
- Barletta, F., St-Onge, G., Stoner, J.S., Lajeunesse, P., and Locat, J. 2010. A high-resolution Holocene paleomagnetic secular variation and relative paleointensity stack from eastern Canada. *Earth and Planetary Science Letters*, **298**(1-2): 162-174.
- Bernatchez, P. 2003. Évolution littorale holocène et actuelle des complexes deltaïques de Betsiamites et de Manicouagan-Outardes : synthèse, processus, causes et perspectives. Ph.D. thesis, Université Laval, Québec.
- Campbell, C., Duchesne, M.J., and Bolduc, A. 2008. Geomorphological and geophysical evidence of Holocene instability on the Southern slope of the Lower St. Lawrence Estuary, Québec. *In 4e Conférence canadienne sur les géorisques: des causes à la gestion - 4th Canadian Conference on Geohazards : From Causes to Management*. Presses de l'Université Laval, Québec, pp. 367-374.
- Cauchon-Voyer, G. 2007. Morpho-sédimentologie et mouvements de masse au large de la Rivière Betsiamites, estuaire du Saint-Laurent, Québec. M.Sc. thesis, Université Laval, Québec.
- Cauchon-Voyer, G. 2011. Mouvements de masse en milieu côtier dans l'estuaire du Saint-Laurent, Québec, Canada: le cas du grand complexe des glissements de terrain de Betsiamites. Ph.D. thesis, Université Laval, Québec.
- Cauchon-Voyer, G., Locat, J., and St-Onge, G. 2008. Late-Quaternary morpho-sedimentology and submarine mass movements of the Betsiamites area, Lower St. Lawrence Estuary, Quebec, Canada. *Marine Geology*, **251**(3-4): 233-252.
- Christian, H.A., Mosher, D.C., Mulder, T., Barrie, J.V., and Courtney, R.C. 1997. Geomorphology and potential slope instability on the Fraser River Delta foreslope, Vancouver, British Columbia. *Canadian Geotechnical Journal*, **34**(3): 432-446.
- Cruden, D.M., and Varnes, D.J. 1996. Landslide Types and Processes. *In Landslides Investigation and Mitigation*. Edited by A.K. Turner and R.L. Schuster, Transportation Research Board, Washington DC. pp. 36-75.
- Demers, D., and Leroueil, S. 2002. Evaluation of preconsolidation pressure and the overconsolidation ratio from piezocone tests of clay deposits in Quebec. *Canadian Geotechnical Journal*, **39**(1): 174-192.
- Dionne, J.C. 1977. La Mer de Goldthwait au Québec. *Géographie Physique et Quaternaire*, **16**(1-2): 61-80.
- Dionne, J.C. 2001. Relative Sea-Level changes in the St. Lawrence estuary from deglaciation to present day. *In Deglacial History and Relative Sea-Level Changes, Northern New England and Adjacent Canada*. Edited by T.K. Weddle and M.J. Retelle, Geological Society of America Special Paper, Boulder, Colorado. pp. 271-284.
- Dionne, J.C., and Occhietti, S. 1996. Aperçu du Quaternaire à l'embouchure du Saguenay, Québec. *Géographie Physique et Quaternaire*, **50**: 5-34.
- Dredge, L.A. 1976. Quaternary geomorphology of the Quebec North Shore, Godbout to Sept-Iles. Ph.D. thesis, University of Waterloo, Waterloo.
- Dredge, L.A. 1983. Surficial Geology of the Sept-Îles area. Geological survey of Canada.

- Dubois, J.-M.M. 1977. La déglaciation de la Côte-Nord du Saint-Laurent. *Geographie Physique et Quaternaire*, **16**(3-4): 229-246.
- Duchesne, M., Pinet, N., Bolduc, A., Bédard, K., and Lavoie, D. 2007. Seismic stratigraphy of the lower St Lawrence River estuary (Quebec) Quaternary deposits and seismic signature of the underlying geological domains. Geological Survey of Canada.
- Duchesne, M., Pinet, N., Bédard, K., St-Onge, G., Lajeunesse, P., Campbell, D., and Bolduc, A. 2010. Role of the bedrock topography in the Quaternary filling of a giant estuarine basin: the Lower St. Lawrence Estuary, Eastern Canada. *Basin Research*, **22**(6): 933-951.
- Duchesne, M.J., Long, B.F., Urgeles, R., and Locat, J. 2003. New evidence of slope instability in the Outardes Bay delta area, Quebec, Canada. *Geo-Marine Letters*, **22**(4): 233-242.
- Franconi, A., Sharma, K.N.M., and Laurin, A.F. 1975. Région des rivières Betsiamites (Bersimis) et Moisie. Québec; Ministère des richesses naturelles, Direction générale des mines, Service de l'exploration géologique.
- Gagné, H. 2008. Géomorphologie et géologie marine du Quaternaire du secteur Trois-Pistoles-Forestville, estuaire du Saint-Laurent (Québec). M.Sc. thesis, Université Laval, Québec.
- Hart, B.S., and Long, B.F. 1996. Forced regressions and lowstand deltas: Holocene Canadian examples. *Journal of Sedimentary Research*, **66**(4): 820-829.
- Hillaire-Marcel, C., and Causse, C. 1989. Chronologie Th/U des concrétions calcaires des varves du lac glaciaire de Deschaillons (Wisconsinien inférieur). *Canadian Journal of Earth Sciences*, **26**(5): 1041-1052.
- Josenhans, H., and Lehman, S. 1999. Late glacial stratigraphy and history of the Gulf of St. Lawrence, Canada. *Canadian Journal of Earth Sciences*, **36**(8): 1327-1345.
- Lajeunesse, P., St-Onge, G., Locat, J., and Labbé, G. 2007. Multibeam bathymetry and morphostratigraphy of submarine gravity flows and slopes failures in the St. Lawrence Gulf and Lower Estuary (Québec, Canada). *In Submarine Mass Movements and Their Consequences*. Springer, p. 27.
- Lamontagne, M., Keating, P., and Perreault, S. 2003. Seismotectonic characteristics of the Lower St. Lawrence Seismic Zone, Quebec: insights from geology, magnetism, gravity, and seismics. *Canadian Journal of Earth Sciences*, **40**(2): 317-336.
- Lamontagne, M., Halchuk, S., Cassidy, J., and Rogers, G. 2008. Significant Canadian Earthquakes of the Period 1600-2006. *Seismological Research Letters*, **79**(2): 211.
- Lasalle, P., and Chagnon, J.-Y. 1968. An ancient landslide along the Saguenay River, Quebec. *Canadian Journal of Earth Sciences*, **5**(3): 548-549.
- Leroueil, S., Tavenas, F., and Le Bihan, J.-P. 1983. Propriétés caractéristiques des argiles de l'est du Canada. *Canadian Geotechnical Journal*, **20**(4): 681-705.
- Leroueil, S., Vaunat, J., Locat, J., Picarelli, L., Lee, H., and Faure, R. Geotechnical characterization of slope movements. *In 7th International Symposium on Landslides*, Trondheim, 1996, pp. 53-74.
- Locat, J. 2011. La localisation et la magnitude du séisme du 5 février 1663 (Charlevoix) revues à l'aide des mouvements de terrain. *Canadian Geotechnical Journal*, **In press**.
- Locat, J., Tanaka, H., Tan, T.S., Dasari, G.R., and Lee, H. 2003. Natural soils: geotechnical behaviour and geological knowledge. *In Characterisation & Engineering Properties*

- of Natural Soils Vol 1. *Edited by* T.S. Tan, K.K. Phoon, D.W. Hight, and S. Leroueil. pp. 3-28.
- Locat, J., Amiguet, C., Cauchon-Voyer, G., Bolduc, A., Demers, D., Mosher, D., Sanfaçon, R., Godin, A., Lajeunesse, P., and St-Onge, G. 2008. Instabilités sous-marines et côtières le long de la rive nord du Saint-Laurent, entre Pointe-des-Monts et Saint-Siméon : analyse préliminaire. *In* Quebec 2008: 400 Years of Discoveries. Joint Meeting of the Geological Association of Canada, Mineralogical Association of Canada, Society of Economic Geologists and the Society for Geology Applied to Mineral Deposits. *Revue des résumés*, Québec, p. 99.
- Lunne, T., Robertson, P.K., and Powell, J.J.M. 1997. Cone penetration testing in geotechnical practice. Blackie Academic - Chapman-Hall Publishers.
- Massé, M. 2001. Évolution générale des dépôts quaternaires sous l'estuaire du St-Laurent entre l'Îles aux Lièvres et Rimouski. M.Sc. thesis, Université du Québec à Rimouski, Rimouski.
- Massé, M., and Long, B. 2001. Slope instability seismic signatures in Quaternary sediments of the St. Lawrence estuary. *In* Proceedings of 2001 An Earth Odyssey, International Association of Hydrogeologists. The Canadian Geotechnical Society, pp. 784–791.
- McKenna, G.T., Luternauer, J.L., and Kostaschuk, R.A. 1992. Large-scale mass-wasting events on the Fraser River Delta front near sand heads, British Columbia. *Canadian Geotechnical Journal*, **29**(1): 151-156.
- Mosher, D.C. 2008. Submarine Mass Movements: Geohazards with far-reaching implications. *In* 4e Conférence canadienne sur les géorisques: des causes à la gestion - 4th Canadian Conference on Geohazards : From Causes to Management. Presses de l'Université Laval, Québec, pp. 55-62.
- Mulder, T., and Alexander, J. 2001. The physical character of subaqueous sedimentary density flows and their deposits. *Sedimentology*, **48**(2): 269-299.
- Piper, D.J.W., Hiscott, R.N., and Normark, W.R. 1999. Outcrop-scale acoustic facies analysis and latest Quaternary development of Hueneme and Dume submarine fans, offshore California. *Sedimentology*, **46**(1): 47-78.
- Potvin, J., Pellerin, F., Demers, D., Robitaille, D., La Rochelle, P., and Chagnon, J.-Y. 2001. Revue et investigation complémentaire du site du glissement de Saint-Jean-Vianney. *In* 54th Canadian Geotechnical Conference pp. 792–800.
- Pullan, S.E., and MacAulay, H.A. 1987. An in-hole shotgun source for engineering seismic surveys. *Geophysics*, **52**(7): 985-996.
- Robertson, P.K. 1990. Soil classification using the cone penetration test *Canadian Geotechnical Journal*, **27**(1): 151-158.
- Smith, W. 1962. Earthquakes of eastern Canada and adjacent areas, 1534-1927, Publications of the Dominion Observatory, Ottawa. pp. 271-301.
- St-Onge, G., Stoner, J.S., and Hillaire-Marcel, C. 2003. Holocene paleomagnetic records from the St. Lawrence Estuary, eastern Canada: centennial- to millennial-scale geomagnetic modulation of cosmogenic isotopes. *Earth and Planetary Science Letters*, **209**(1-2): 113-130.
- St-Onge, G., Lajeunesse, P., Duchesne, M., and Gagné, H. 2008. Identification and dating of a key Late Pleistocene stratigraphic unit in the St. Lawrence Estuary and Gulf (Eastern Canada). *Quaternary Science Reviews*, **27**(25-26): 2390-2400.

- Stuiver, M., and Reimer, P. 1993. Extended 14C database and revised CALIB radiocarbon calibration program. *Radiocarbon*, **35**(1): 215-230.
- Sultan, N., Cochonat, P., Canals, M., Cattaneo, A., Dennielou, B., Hafliðason, H., Laberg, J.S., Long, D., Mienert, J., Trincardi, F., Urgeles, R., Vorren, T.O., and Wilson, C. 2004. Triggering mechanisms of slope instability processes and sediment failures on continental margins: a geotechnical approach. *Marine Geology*, **213**(1-4): 291-321.
- Syvitski, J.P.M., and Praeg, D. 1989. Quaternary Sedimentation in the St. Lawrence Estuary and adjoining areas, Eastern Canada : an overview based on high resolution seismo-stratigraphy. *Géographie Physique et Quaternaire*, **43**(3): 291-310.
- Thwaites, R.G. 1959. *The Jesuit relations and allied documents : travels and explorations of the Jesuit missionaries in New France, 1610-1791 : the original French, Latin, and Italian texts, with English translations and notes.* Pageant Book Co, New York.

2.15 Tables

Table 2.1. Radiocarbon dates on shell fragments

Borehole	Elevation (m)	Conv. age ¹⁴ C (yr BP)	Conv. age ¹⁴ C - 400 yr (yr BP)	Calibrated age (cal BP)	Lab#
F46006	19.57	9265 ± 20	8865 ± 20	10136	UCIAMS-66258
F46006	15.55	9625 ± 25	9225 ± 25	10508	UCIAMS-60876
F46006	9.97	9725 ± 25	9325 ± 25	10570	UCIAMS-60872
F46006	9.41	9745 ± 25	9345 ± 25	10585	UCIAMS-60874
F46010	-15.27	9365 ± 20	8965 ± 20	10203	UCIAMS-66260
F46010	-24.17	9350 ± 25	8950 ± 25	10194	UCIAMS-60873
F46010	-32.07	9830 ± 20	9430 ± 20	10666	UCIAMS-66259
F46010	-34.97	9770 ± 25	9370 ± 25	10609	UCIAMS-60875
F46010	-38.05	9850 ± 25	9450 ± 25	10697	UCIAMS-66261

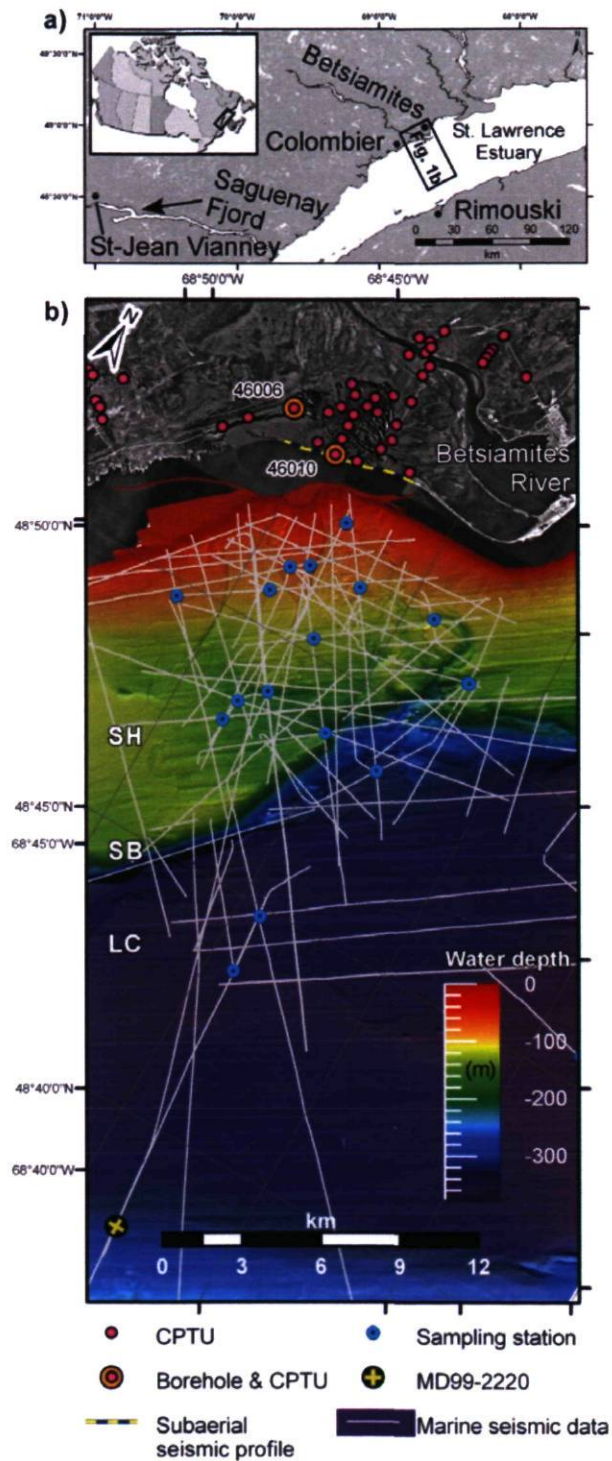
Table 2.2. Summary of seismic units on the subaerial profile.

Subaerial seismic units	Geological interpretations	Reflecting horizons pattern	Thickness (m) min (average) max
U1	Ice-contact deposits	Poor or absent continuous internal reflecting horizons	1 (29) 43
U2	Ice proximal, coarser grained sediments	Strong amplitude and closely spaced reflecting horizons	5 (17) 36
U3	Fine-grained ice-distal glacio-marine sediments	Weak continuous reflecting horizons	7 (22) 34
U4	Paraglacial prodeltaic sediments	Closely packed reflecting horizons	8 (25) 44
Upper facies	Landslide debris	Reflecting horizons are conformable on unit 4	5 (10) 19

Table 2.3. Summary of lithostratigraphy and geotechnical properties defined on site, with boreholes and seismic correlations. z = thickness of layer

Seismic unit	Geological interpretation	Borehole Layer	Layer on Fig. 7 and 8	Elevation (m)	z (m)	w_n (%)	l_p	IL	St	CF (%)
U2	Coarse ice-proximal glaciomarine sediments	46010	Gravelly and bouldery sandy silt	-50.6	>3.6	-	-	-	-	11
		10-L2		6-L to -47						
	Finer ice-proximal glaciomarine sediments	46010 10-L3a	Laminated silt to silty sand	-47 to -43	4	25	16	0.7	-	15
U3	Laminated ice-distal glaciomarine sediments	46006 6-L3a	Laminated clayey silt IL<1	8 to ~ -12	~20	34	27	0.7	(7-12)	38
		46010 10-L3b	Homogenous grey silty clay	-22 to -43	21	35	22	0.8	(14-56)	37
	Fine ice-distal glaciomarine sediments	46006 6-L3b	Homogenous grey silty clay IL~1	18 to 8	10	27	12	1.1	(35-67)	46
		46006 6-L3c	Homogenous grey silty clay IL>1.2	28 to 18	10	34	8	2.8	(406-1202)	45
		46010 10-L4a	Stratified silty clay and silty clayey sand	-8 to -22	14	29	14	1.2	(13-36)	31
U4-sand	Littoral sand	46006 6-L4b	Sand	47.6 to 42	5.6	-	-	-	-	1
Debris	Subaerial landslide debris, i.e., reworked U4-U3	46010 10-Da	Reworked stratified silty clay and silty clayey sand	-8 to 1.5	9.5	28	13	1.2	-	30
Debris	Subaerial landslide debris, i.e., reworked U4-sand	46010 10-Db	Reworked sand	1.5 to 9	7.5	-	-	-	-	0.3

2.16 Figures



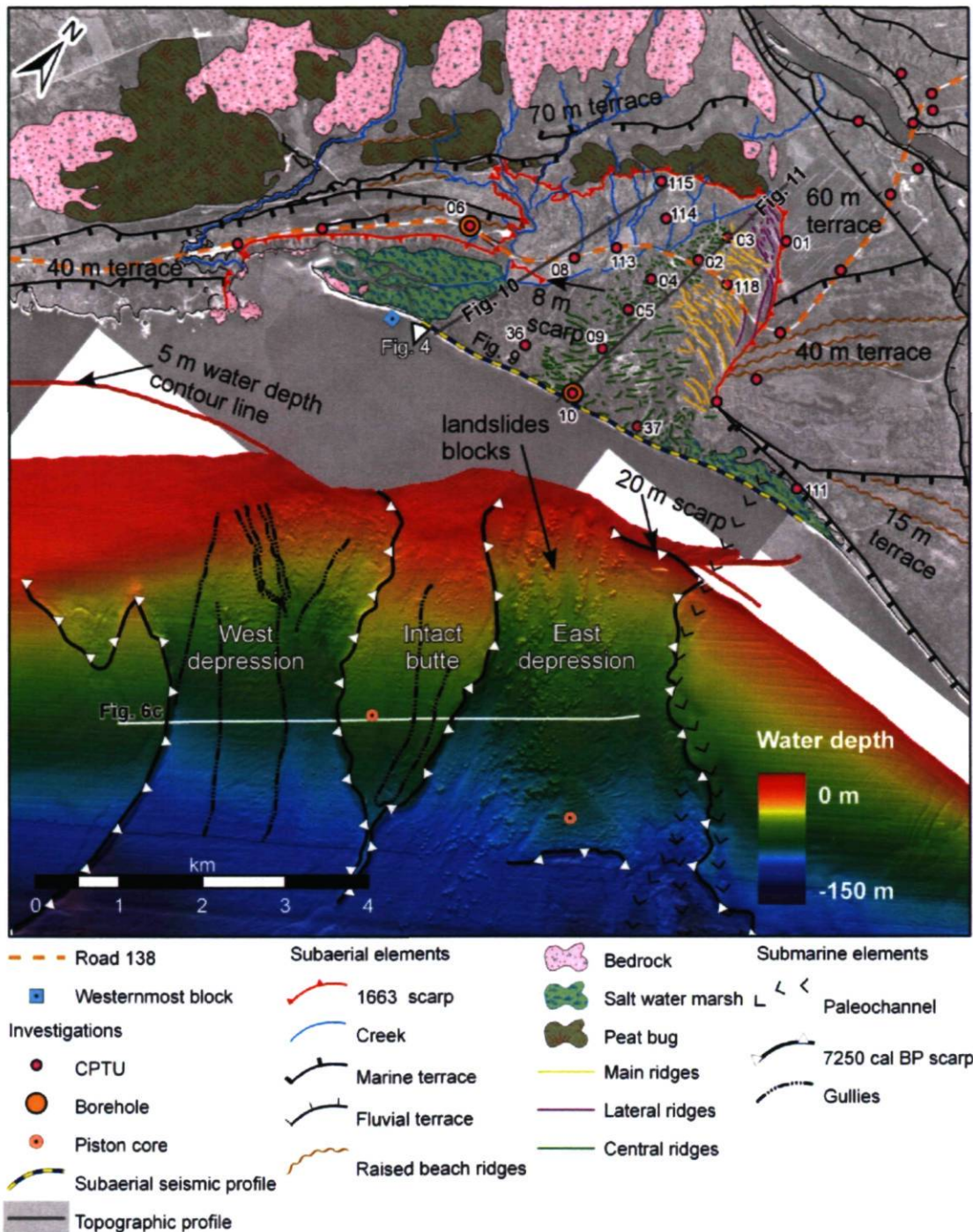


Figure 2.2. Geomorphologic interpretation of the Betsiamites landslides complex area.

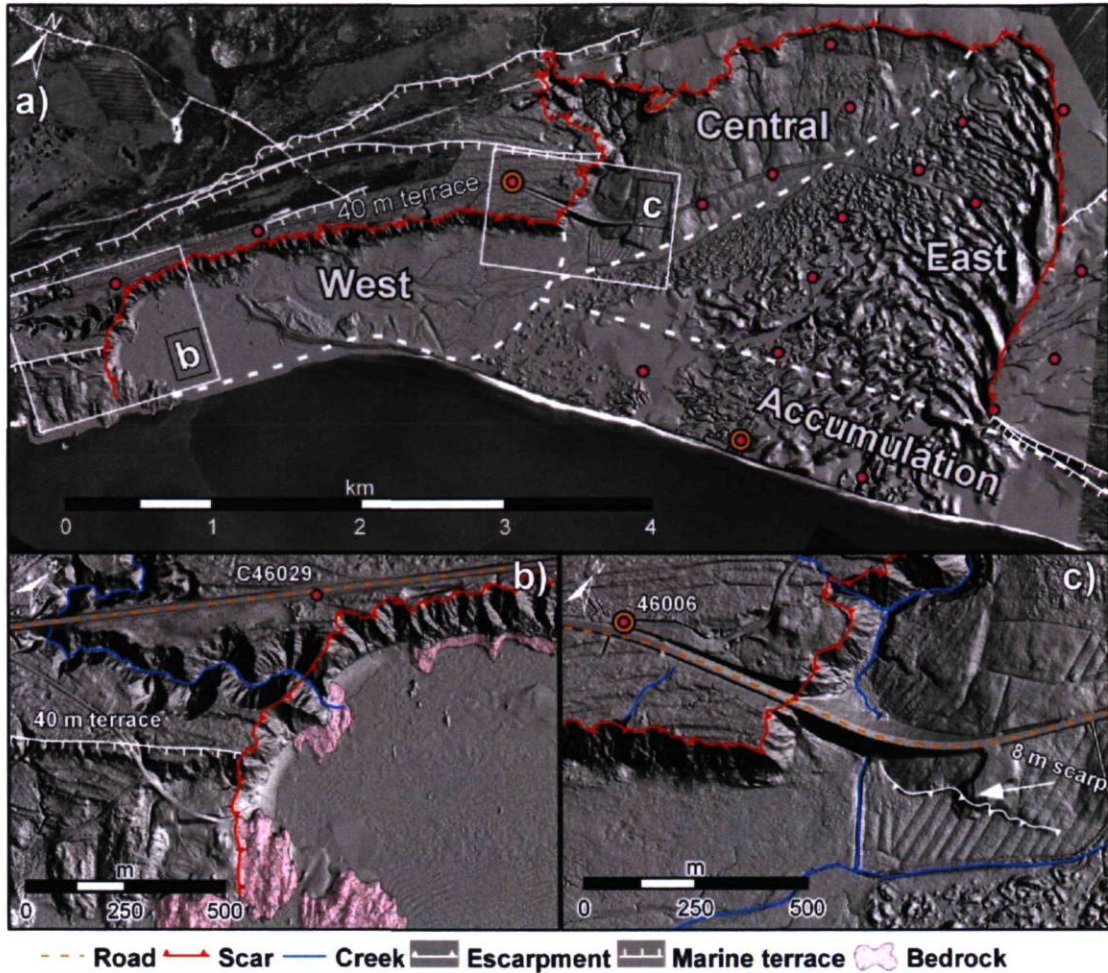


Figure 2.3. Digital elevation model of the Colombier subaerial scar. a) Morphological zones with geomorphologic characteristics within the subaerial landslide body and CPTUs locations. See text for details; b) enlargement of the western escarpment; c) enlargement of the area with the 8 m scarp within the central zone..

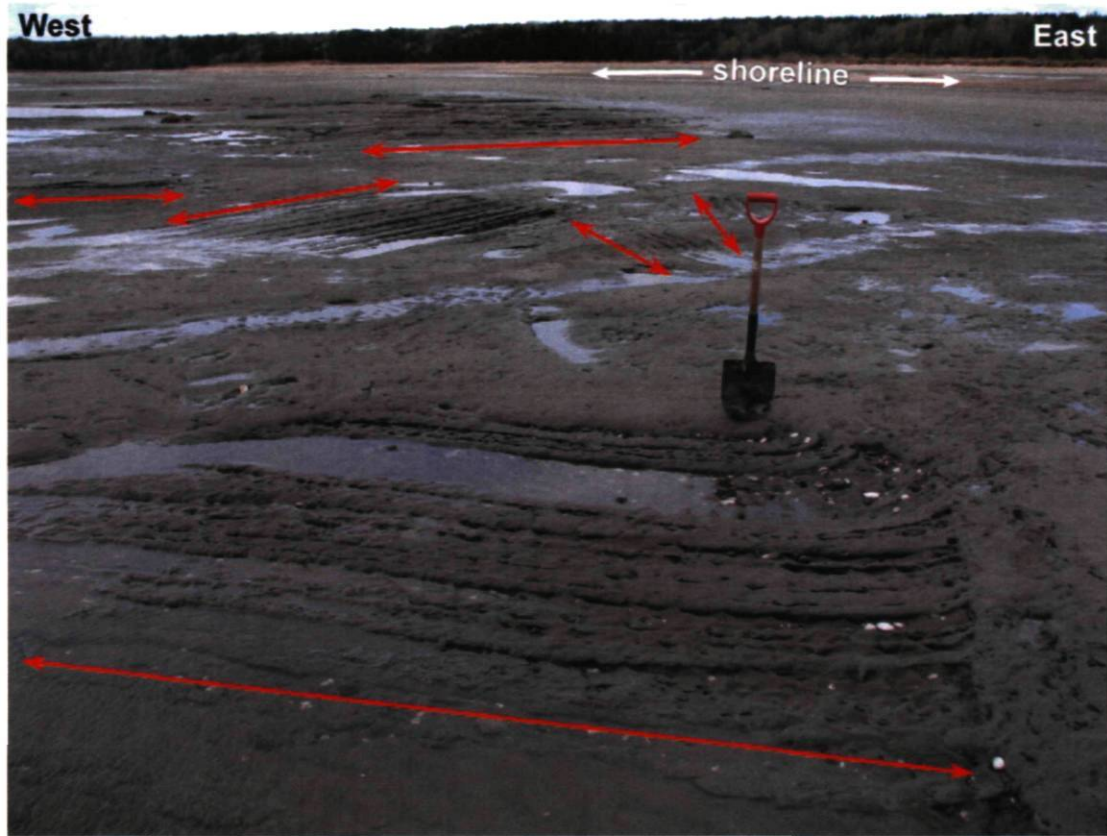


Figure 2.4. Beach at low tide revealing blocks of deformed clayey sediments currently eroded by marine action. Arrows are parallel to stratifications (typically 10 cm-thick) in the landslide blocks. Position of image is indicated on Figure 2.2 by a white triangle.

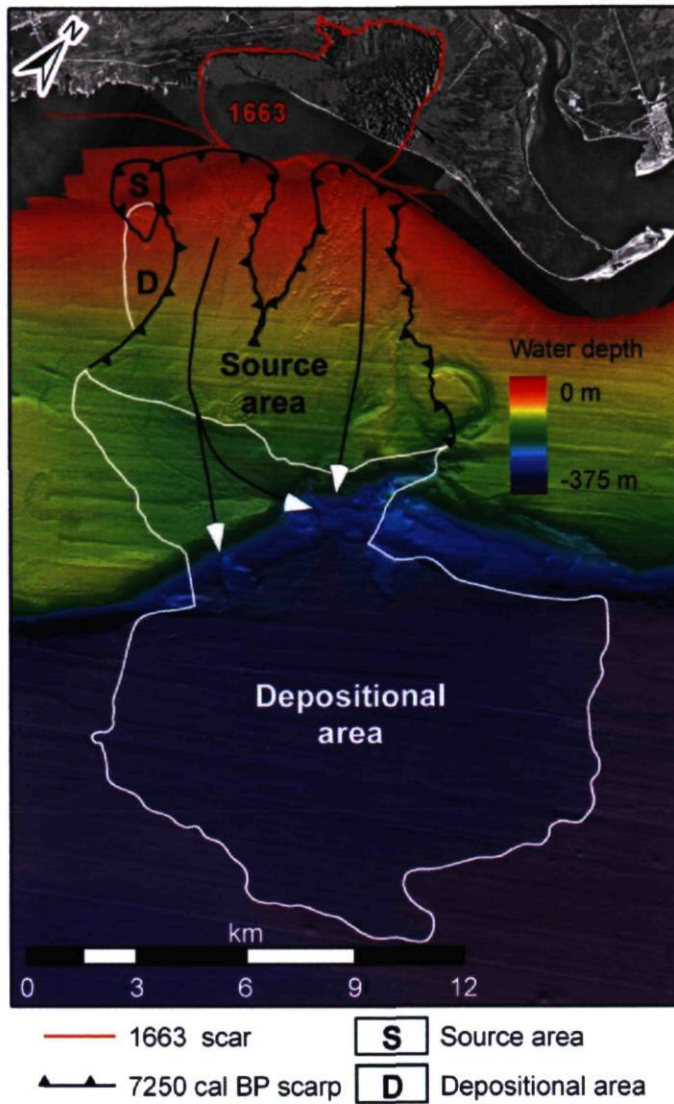


Figure 2.5. Source and depositional areas of the 7250 cal BP Betsiamites submarine landslide event.

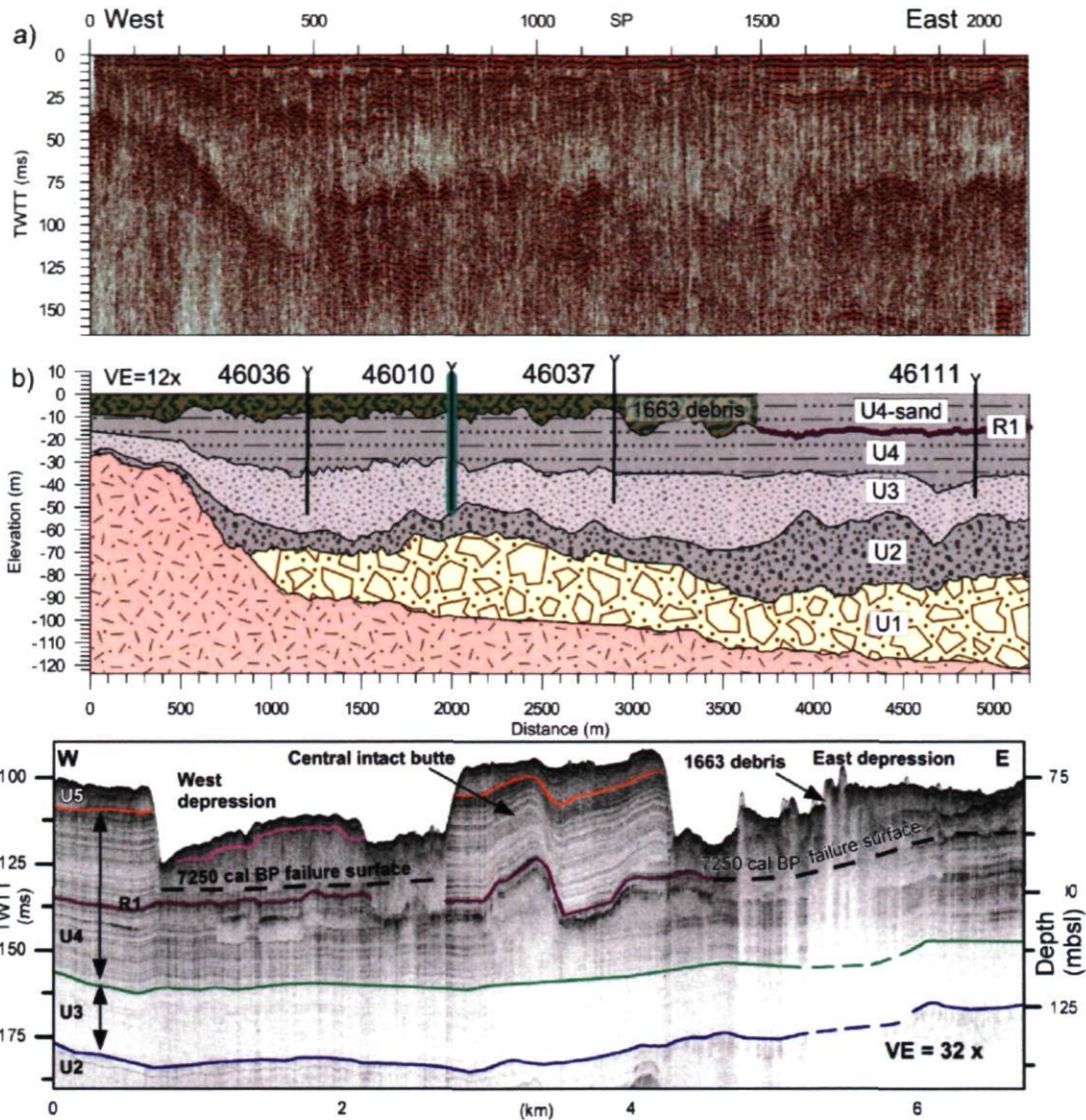


Figure 2.6. Seismostratigraphy of the Betsiamites landslide complex.

a) 5.2 km-long continuous subaerial seismic reflection profile;

b) Seismic interpretation. The vertical black lines indicate the locations and depths reached by the four CPTUs carried out close to the shoreline whereas the green line indicates the location and depth reached in borehole 46010. VE = 14x;

c) Submarine seismostratigraphy, modified from Cauchon-Voyer et al. (2008). 9250 corresponds to the seismic body interpreted as debris of a submarine landslide dated as older than 9250 cal BP (see text for details). TWTT = two way travel time. The depth scale was approximated using a constant velocity of 1500 m/s. Position of submarine profile is indicated on Figure 2.2, view looking north toward the head of the landslide.

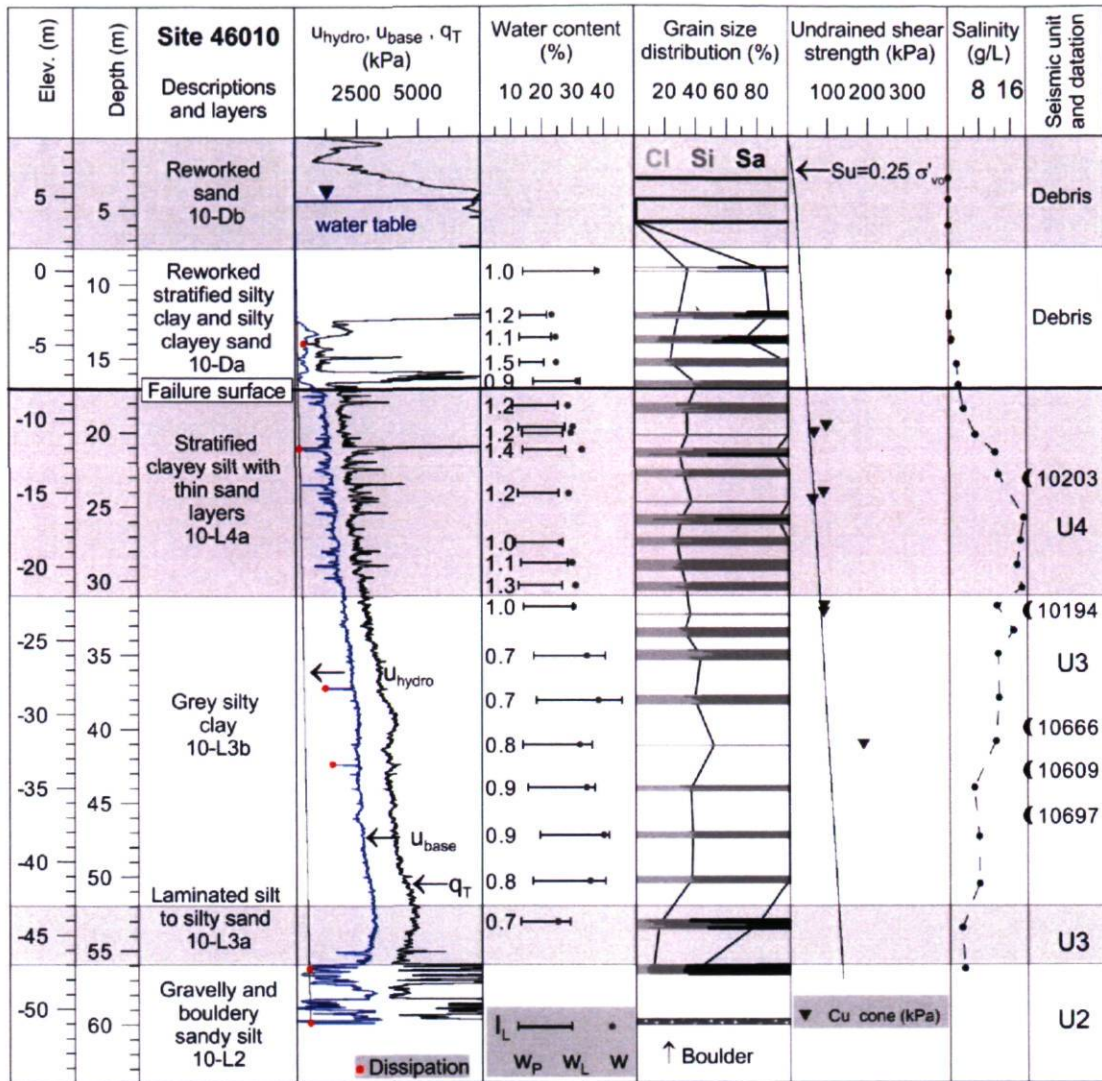


Figure 2.7. Geotechnical profile at site 46010 in the accumulation zone of the lateral spread (phase 3S) of the 1663 Colombier subaerial landslide.

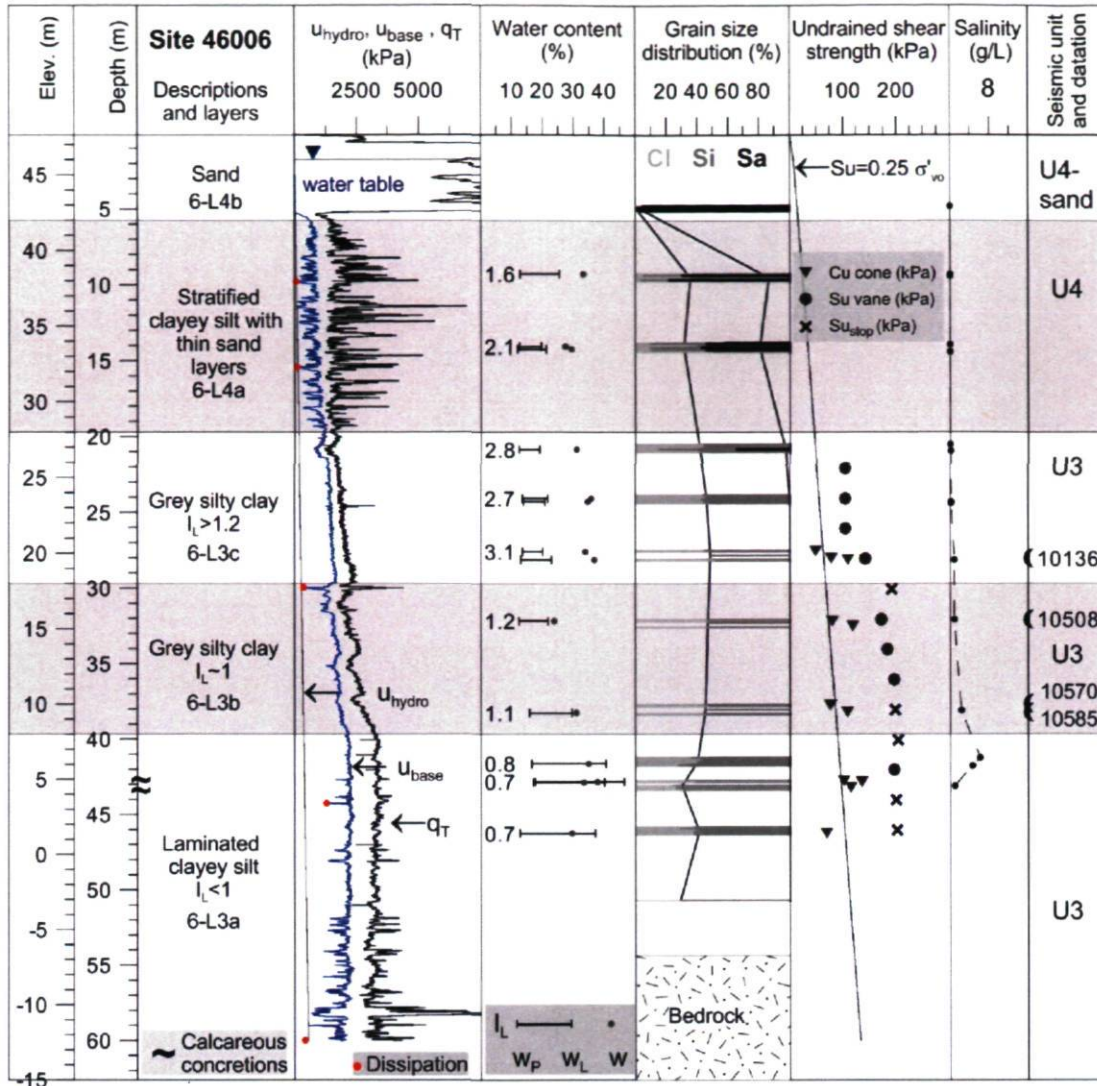


Figure 2.8. Geotechnical profile at site 46006 on the upper escarpment of the 1663 Colombier flowslides (phase 2F and 3F). Cone = Swedish fall cone. S_u = undrained shear strength measured with the vane. $S_{u_{min}}$ indicates that the test was stopped at the maximum value of 200 kPa.

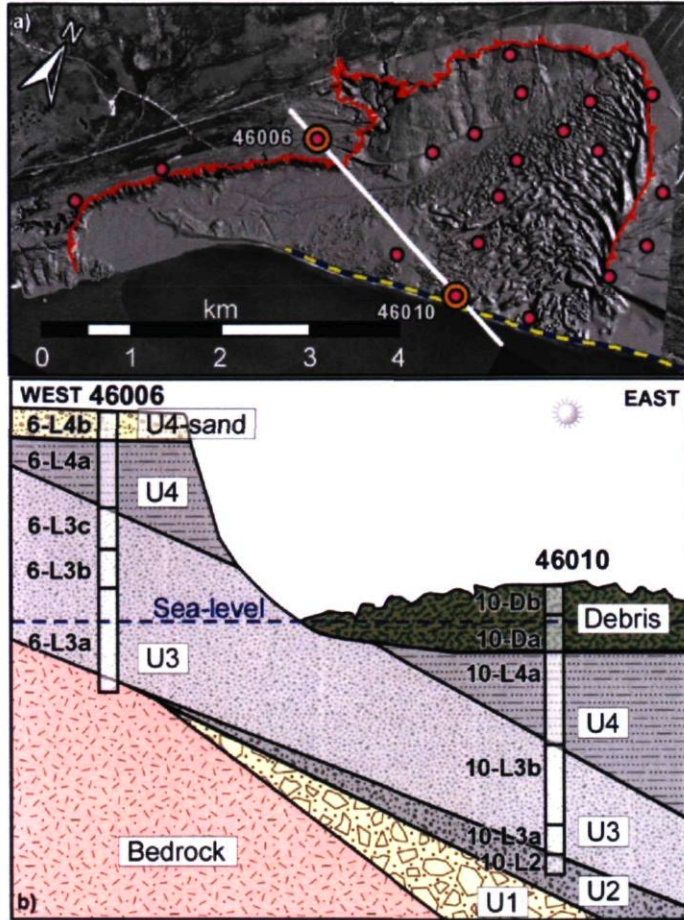


Figure 2.9. Schematic summary of the lithostratigraphy and seismostratigraphic interpretation between boreholes 46006 and 46010. Labels in square correspond to seismic units whereas other labels refer to lithological units. Not to scale.

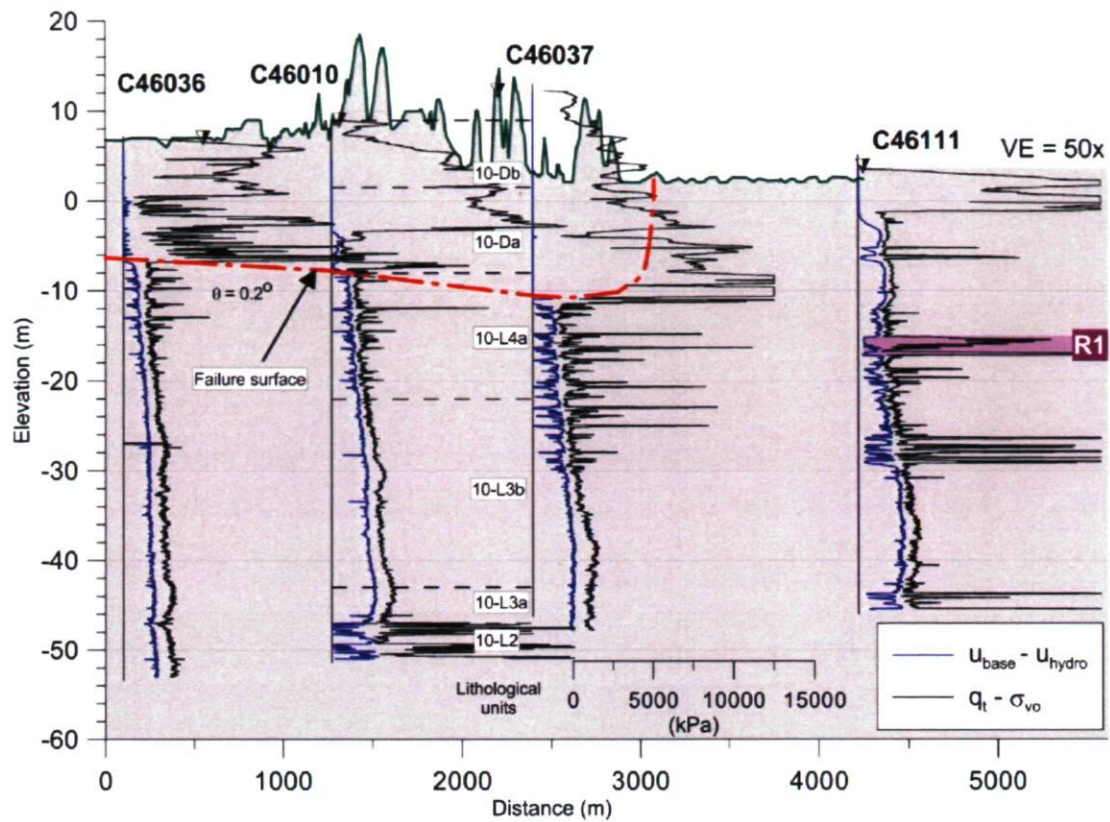


Figure 2.10. CPTUs and topographic section along the shoreline. Refer to the triangular symbols for exact CPTU profile locations and to Figure 2.2 for topographic profile location.

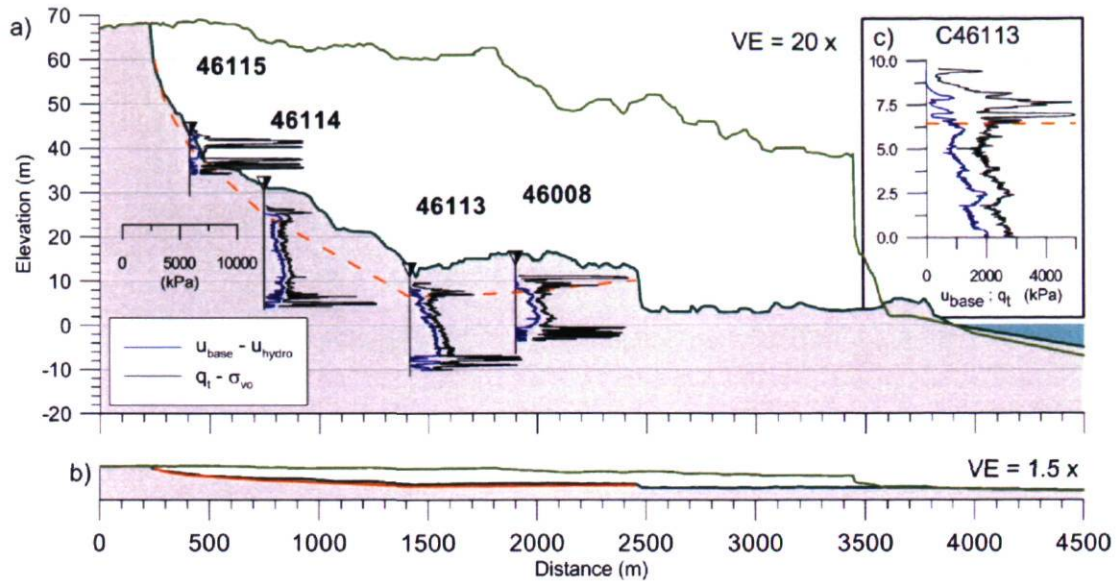


Figure 2.11. Sequence of 4 CPTUs carried out in the north south axis of the Colombier subaerial scar in the Central zone. a) CPTUs and topographic profile across the Central area (flowslide 3F); b) profile of the estimated topography prior to failure, failure surface in orange, and final topography at 1.5x vertical exaggeration; c) criterion to define the failure surface in the CPTUs of the central area.

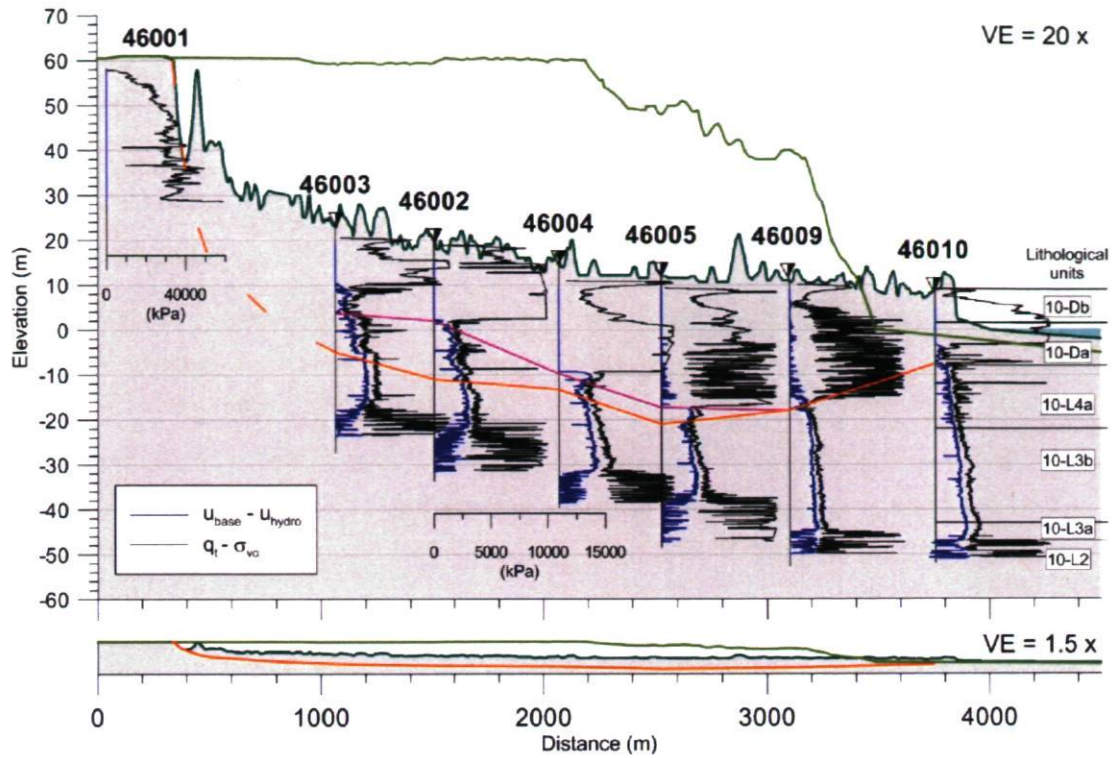


Figure 2.12. Sequence of 6 CPTUs carried out in the East zone of the Colombier subaerial scar. a) CPTUs and topographic profile across the East zone of the scar (spread 3S); b) Deepest possible failure surface with initial and final topography at VE = 1.5x.

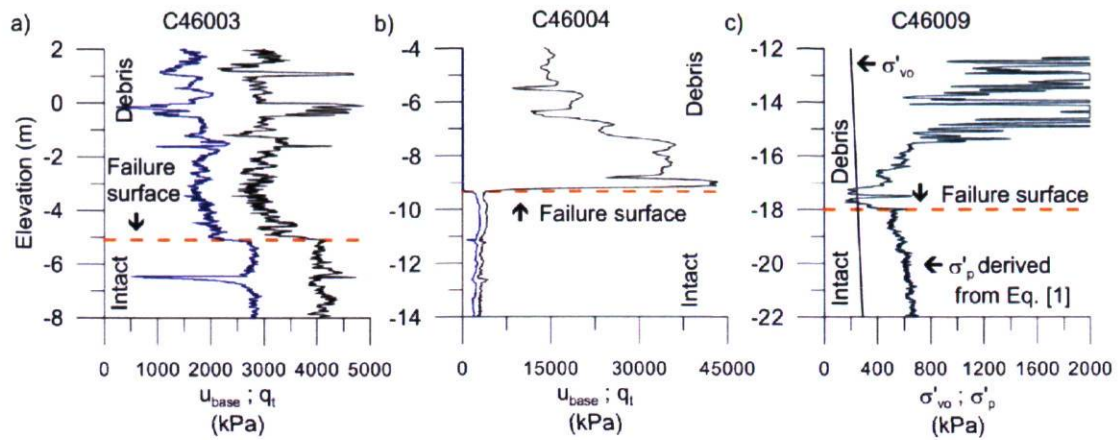


Figure 2.13. Criteria used to identify the elevation to the failure surface on the CPTU profiles carried out in the north south axis of the subaerial scar. a) Decrease in tip resistance above a level; b) sharp increase in net tip resistance above a level; c) decrease in calculated preconsolidation pressure.

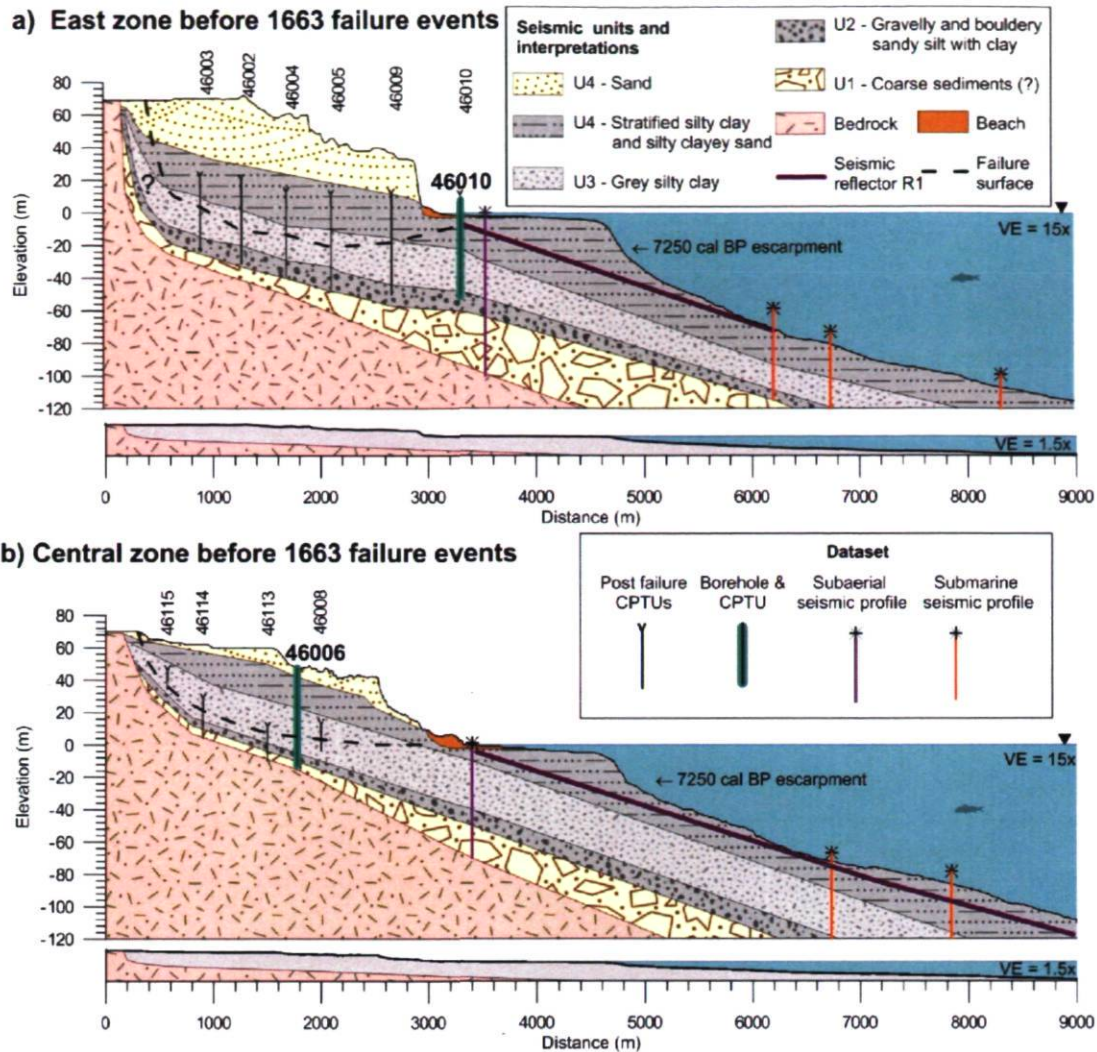


Figure 2.14. Lithostratigraphy prior to the 1663 failure phases for the a) East zone and b) Central zone. Lower sections present the topographic profiles at VE=1.5x.

Refer to Figure 2.15a for locations of the interpreted profiles.

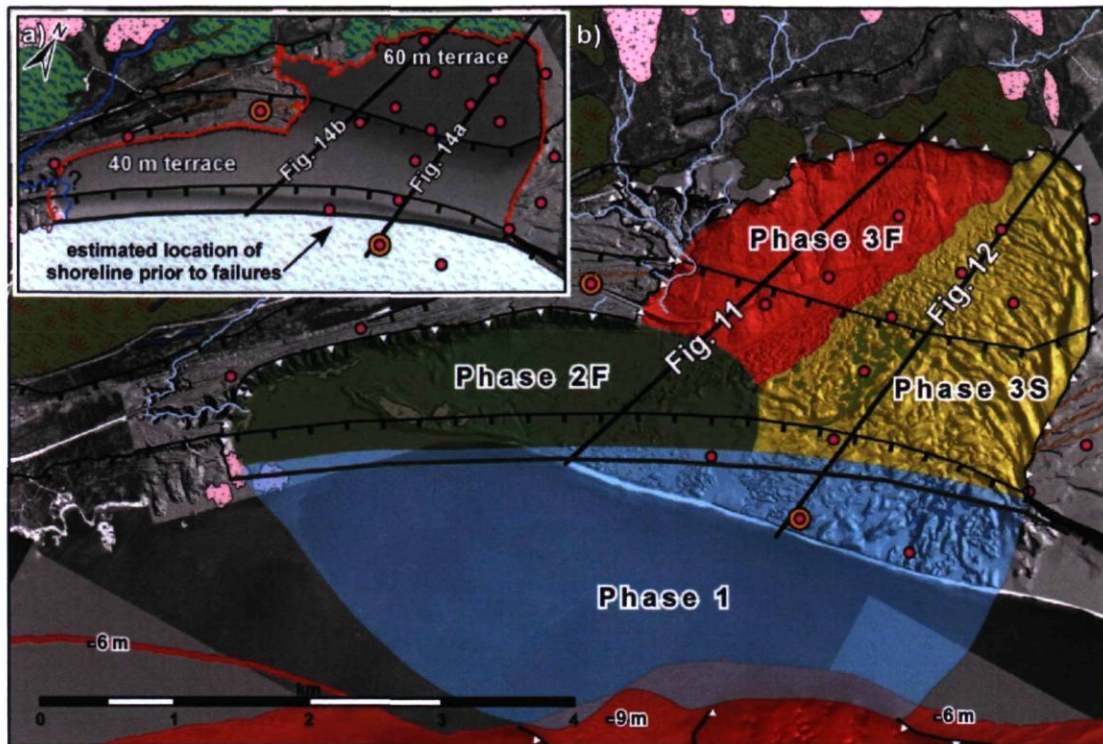


Figure 2.15. Initial topography and 1663 failure phases:

a) Subaerial topography prior to the 1663 complex slide;

b) Definition of boundaries of 1663 landslide slide phases. See Figure 2.2 for legend.

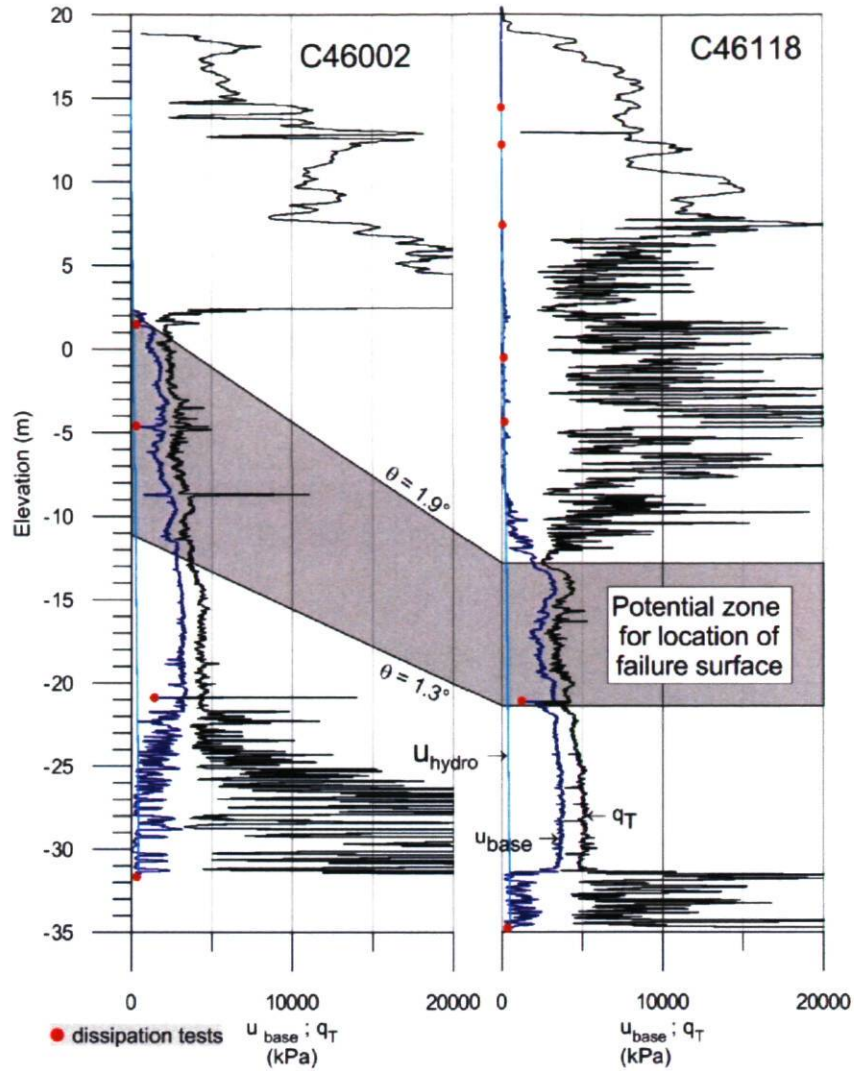


Figure 2.16. CPTU 46002 (left graph) and 46118 (right graph) carried out in the East zone. The failure surface is interpreted at a minimum of 2 m and at -13 m, which corresponds to an angle of 1.9° between both soundings.

Chapitre 3 Stability and mobility of the 1663 Colombier subaerial and submarine landslide event, Québec, Canada

3.1 Abstract

The Colombier landslide event (est. volume 530 million m³ over 20 km²) occurred in post-glacial clayey sediments in the area of the Betsiamites River delta, on the north coast of the St. Lawrence Estuary, in Québec, Canada following the 1663 earthquake. The Colombier landslide scar is part of the Betsiamites slide complex which extends also in the submarine domain and results from 3 main landslide events (9250 cal BP, 7250 cal BP and AD 1663). This paper focuses on the 1663 Colombier subaerial and submarine slide event, which involved four successive failure phases: one submarine and three subaerial. The geomechanical interactions between the 1663 failure phases are demonstrated. The back-analysis of the Colombier landslide scar area indicates that a first submarine undrained failure resulting from an earthquake reached the shoreline and triggered the development of a lateral spread (3S). The subaerial flowslide 2F acted as the triggering factor for flowslide (3F). This study presents an extremely large subaerial coastal landslide in sensitive clayey sediments, among the largest known historical landslide in sensitive clayey material in Canada, and it demonstrates that flowing and spreading mechanisms occurred simultaneously in the subaerial environment.

3.2 Introduction

3.2.1 Betsiamites slide complex

The North Coast of the St Lawrence Estuary (Quebec, Canada) (Figure 3.1) exhibits many areas with subaerial and submarine landslide scars. The largest scars are identified in the vicinity of the Betsiamites River delta, close to the municipality of Colombier, about 400 km northeast of Québec City. The Betsiamites slide complex scar extend over more than 64 km² (Figure 3.2) continuously in the subaerial and submarine environments. Detailed

analyses of the morphology and lithostratigraphy of the Betsiamites slide complex area showed that this landform resulted from three separate major landslide events (Bernatchez 2003; Cauchon-Voyer et al. 2008; Cauchon-Voyer et al. 2011b). The submarine scar of the Betsiamites slide complex resulted from a first submarine failure, dated at about 9250 calibrated calendar years (cal) BP, which mobilized a minimum volume of 200 million m³. A second major submarine event landslide, thereafter named Betsiamites slide event, dated at 7250 cal BP also shaped the complex. The submarine Betsiamites slide event mobilized a minimum volume of 1300 million m³ (1.3 km³). The deposition of the debris of both early Holocene events were dated (Cauchon-Voyer et al. 2008) by mapping seismic reflections from the top of the debris accumulation to the location of core MD99-2220 ~15 km away in the Laurentian Channel where a chronostratigraphy is available (St-Onge et al. 2003). The third event is the 1663 Colombier subaerial and submarine slide event and is the main focus of this paper.

The 1663 Colombier slide event left a large subaerial scar within the Betsiamites slide complex. The geomorphology of subaerial landslide scar was first described by Bernatchez (2003) who suggested on the basis of radiocarbon dates that it was triggered by the February 5th 1663 earthquake (M~7 to 7.8) (Smith 1962; Locat 2008; Locat 2011). This interpretation was further supported by dating to 1663, with ²¹⁰Pb-derived sedimentation rate of hemiplegic sediments, subaerial debris sampled offshore and associated to the Colombier event (Cauchon-Voyer et al. 2008). Historical accounts from the Jesuits missionaries in New France describe in great details the outcome of the 1663 earthquake and mention briefly “ravages wrought by the Earthquake” in the vicinity of the Betsiamites River (Thwaites 1959) also supports the interpretation.

Following a morphostratigraphic analysis of the area, Cauchon-Voyer et al (2011b) concluded that the Colombier slide event involved four successive failure phases: one submarine and three subaerial. The 1663 earthquake triggered a submarine slide, which reached the shoreline and led subsequently to three subaerial failure phases: two flowslides in sensitive clayey material and one subaerial lateral spread. The four failure phases, which have influenced the subaerial domain in 1663, have mobilized a total volume of more than 530 hm³ (h=100, thus 1 cubic hectometres = 1 million m³) over an area of 20 km². The

volume involved solely in the 3 subaerial failure phases is estimated at 385 hm³. The debris of the 1663 Colombier slide event, i.e., those that evacuated the subaerial scar, accumulated mostly in the 7250 cal BP Betsiamites submarine landslide scar.

The main focus of this paper is to define the mechanisms involved in the 1663 Colombier slide event and demonstrate the necessary triggering mechanisms to create such failures in those conditions. The main hypothesis that required to be confirmed with a back analysis is that an earthquake must have been required to trigger the Colombier slide event. Earthquakes are recognized as major triggering mechanism for landslides in Quebec, e.g. Saint-Thècle and Saint-Adelphe landslides (Lefebvre et al. 1992) triggered by the 1988 Saguenay earthquake ($M_s=5.9$), Sainte-Geneviève-de-Batiscan – rang des Lahaie landslide (Lamontagne et al. 2007), following the 1870 Charlevoix earthquake ($M = 6.5$), Saint-Jean-Vianney landslide (Lasalle and Chagnon 1968; Potvin et al. 2001), following the 1663 Charlevoix earthquake ($M 7$ to 7.8). A detailed review of the landslides triggered by the 1663 earthquake can be found in (Locat 2011). Despite the fact that landslide dating or direct observations led to the identification of earthquake as trigger mechanisms, very few sensitive clay landslides were analysed in the context of seismic triggering.

The purpose of the present paper is to summarize the morpho-stratigraphic characteristics of the 1663 landslide phases and to reconstruct the movement history. The triggering mechanisms of the landslide and post failure behaviour of the subaerial mass are defined to evaluate the conditions for failure, and assess the role of seismic triggering. The mobility of the failed mass is also discussed. The approach used in the paper follows the integration of an extensive dataset and resulting interpretations (Cauchon-Voyer et al. 2008; Cauchon-Voyer et al. 2011b) to select geotechnical and rheological parameters of the lithological units for limit equilibrium analysis of slope failure conditions and post-failure behaviour.

3.2.2 Setting and local morpho-stratigraphy

The post-glacial geology and geomorphology of the region was described by Dredge (1976), Dubois (1977), Dionne and Occhietti (1996), and Bernatchez (2003). The study area was covered by the Laurentide Ice Sheet during the Late Wisconsinan and, following deglaciation, the combined effect of the glacio-isostatic subsidence and eustatic sea-level

rise resulted in the marine invasion of the Goldthwait Sea up to an elevation of 152 m around 11 ka BP (Bernatchez 2003). In the area of the landslide scar, till probably cover the bedrock and is followed by a sequence of coarser ice-proximal marine sediments, glaciomarine sediments and deltaic sand. The regression of the Goldthwait Sea led to deposition of thick sequence of stratified silty sediments. The lowering of the relative sea-level also resulted in the edification of large sandy delta plains and 4 main levels of raised marine terraces at elevation of 70, 60, 40, and 15 m in the delta area (Figure 3.2).

The bedrock outcrops on the shoreline in the western area of the subaerial landslide scar close to the western lateral escarpment (Figure 3.2). Previous seismic investigations have demonstrated that the bedrock is located at a depth of -110 m (110 m below sea level) along the shoreline below the eastern lateral escarpment of the Colombier subaerial scar (Cauchon-Voyer et al. 2011b). Taken together, this implies that sediments thickness prior to the Colombier failure phases along the shoreline increased, from west to east, from a few meters to about 110 m. The bedrock also outcrops on the upper plain above the 60 m terrace, north of the landslide (Figure 3.2).

3.3 Data and methods

3.3.1 DEM and seismostratigraphic data

The subaerial digital elevation model (DEM) of the landslide area was derived at a 1 m resolution from airborne laser scanning (LIDAR) and hypsometric lines at 1 m contour interval obtained from photogrammetry on 1:15000 aerial photos. The submarine DEM is derived from high-resolution bathymetric surveys. A 5.2 km-long subaerial seismic reflection survey was carried out on the current beach and allowed the definition of the coastal seismostratigraphy (Cauchon-Voyer et al. 2011b). In addition, more than 750 km of seismic reflection survey allows the reconstruction of a seismostratigraphic model of the submarine seafloor and underlying deposits. Methodological details on the subaerial LIDAR, submarine bathymetric surveys, and subaerial and submarine geophysical data can be found in Cauchon-Voyer et al. (2008; 2011b).

3.3.2 Sampling and laboratory analysis

Two boreholes were performed in the area (see location on Figure 3.3). Borehole 46010, to a depth of 58.9 m, was performed in the accumulation zone of the Colombier subaerial landslide scar at a distance of 75 m behind the shoreline and at an elevation of 7.8 m above sea-level. Borehole 46006, to a depth of 54.4 m, was performed 400 m behind the escarpment of the subaerial landslide scar at an elevation of 47.6 m. Samples were recovered with a split spoon sampler and Shelby sampling tubes (70 mm diameter x 76 cm length). Immediately after recovery, sediments subsamples were taken at each ends of the sample in order to measure water content. The samples were then cut in subsections of 5 to 15 cm, described, covered with a mixture of petroleum jelly and paraffin, and kept undisturbed in a cold room (~8°C and 88% humidity). Natural water contents, shear strengths measured with the Swedish fall cone, Atterberg limits, and preconsolidation pressures were subsequently measured. The preconsolidation pressure (σ'_p) was determined by conventional 24 hrs oedometer tests with load increment ratio of 0.5. Grain size distributions were obtained using a Beckman Coulter LS 13 320 laser diffraction particle size analyzer for the sediment fraction smaller than 2 mm.

Unless specified otherwise, all data are positioned according to their elevation in meter above (positive value) or below sea-level (negative value). The soil profiles are described in function of the lithological units (physical properties of the sediments such as grain size and sedimentary structures) and geotechnical units (defined according to the lithological units and their geotechnical behaviour, index properties, and salt content). The labelling of the geotechnical units (e.g., 6-4b) identifies the borehole (6 for 46006 and 10 for 46010), correlates the units with their matching seismostratigraphic units (e.g., seismic unit 4) previously described (Cauchon-Voyer et al. 2011b) and hence describes the geotechnical units (e.g., 4b). The geotechnical units are presented in this paper from top to bottom but are numbered from bottom to top. This reverse labelling is used to be consistent with previous published work providing stratigraphic correlation and geological interpretations (Cauchon-Voyer et al. 2011b).

3.3.3 CPTUs

Thirty-eight cone penetration tests with pore water pressure measurement (CPTU) were carried out (Figure 3.3) with a 15-tonne capacity cone (15 cm² base area) at a penetration rate of 60 cm/min. Pore pressure values were measured immediately behind the tip (u_{base}) and tip resistance (q_c) were recorded at 10 mm intervals. The tip resistance (q_c) is corrected for the pore pressure acting behind the tip to obtain q_T . Pore pressure dissipation tests were carried out when coarser layers of higher resistance were reached and at the end of all soundings in order to define the local pore pressure conditions. Tests carried out in clayey layers were stopped before complete dissipation and hence are not necessarily representative of the *in situ* conditions. When the sounding results are used for geotechnical correlations, the tip resistance is presented in term of net tip resistance ($q_T - \sigma_{v0}$), in which σ_{v0} is the total vertical stress.

The CPTU data allows the estimation of the preconsolidation pressure profile with an empirical relationship [1] linking preconsolidation pressure (σ'_p) and net tip resistance ($q_T - \sigma_{v0}$):

$$[1] \quad \sigma'_p = \frac{q_T - \sigma_{v0}}{3.4}, \text{ (Demers and Leroueil 2002)}$$

3.3.4 *In situ* strength measurement

One Nilcon vane test profile was carried out at site 46006 to estimate the *in situ* field vane undrained shear strength. For 5 of the 13 measurements, the test was stopped at the limit value for the apparatus, i.e. about ~200 kPa. In addition three field shear vane profiles were also carried out about 10 km west of the Colombier landslide scar in similar post-glacial clayey deposits (elevation of profiles between 30 and 60 m) and all 4 profiles are considered to obtain a regional empirical cone factor N_{kt} (Lunne et al. 1997). In fact, CPTU measurements can be used for estimating sediment undrained shear strength using an N_{kt} value, which can be determined by calibrating net tip resistance with a known measured of S_u .

$$[2] \quad S_u = \frac{q_T - \sigma_{v0}}{N_{kt}}$$

For the study area, a value of $N_{kt} = 10.5$ appears to be reasonable and is used to derive S_u from other CPTUs around the landslide area (Cauchon-Voyer 2011).

3.3.5 Radiocarbon dating

Three tree branches were sampled and ^{14}C dated by accelerator mass spectrometry (AMS) at the AMS facility of the University of California, Irvine (Table 3.1). To convert the ^{14}C conventional ages to calendar years (cal), the dates were calibrated using the CALIB 5.0.1 online software program (Stuiver and Reimer 1993).

3.3.6 Slope stability evaluation

2D limit equilibrium slope stability analyses were carried out with the GeoStudio Slope/W commercial software package. It is assumed that the material failure behaviour follows a Mohr-Coulomb failure criterion such as:

$$[3] \quad \tau_f = c' + (\sigma - u)\tan\phi'$$

Where τ_f is the shear strength of material mobilized along the failure surface, c' the effective cohesion, σ the total normal stress, u the pore pressure along the failure surface, and ϕ' the effective friction angle. The factor of safety is calculated using a Limit equilibrium method. The effects of earthquakes are taken into account in a pseudostatic analysis by using the horizontal coefficient of seismic acceleration k to simulated the application of an horizontal pseudostatic seismic acceleration (α_h , PSA) to the soil mass:

$$[4] \quad k = \frac{\alpha_h}{g}$$

where g is the gravitational acceleration.

3.3.7 Post-failure analysis

For the Colombier area, rheological parameters, such as the yield strength, can be estimated from morphological observation and index properties. The yield strength can be obtained with the following equation (Hampton 1972; Johnson 1984):

$$[5] \quad \tau_c = H_f \gamma' \sin \beta_f$$

where H_f is the average thickness of the debris flow deposits (m), γ' is the buoyant unit weight of the debris flow material (kN/m^3), and β_f the slope of the gliding surface over which the debris flow material came to a rest (in degree). For the Colombier debris flow mixture a buoyant unit weight of 9.4 kN/m^3 is assumed. Eq. [5] can be used to obtain a range of critical values of yield strength required to create a debris lobe.

An estimation of the yield strength of the landslide mass can also be obtained from the relationship linking the liquidity indices to the viscosity and to the yield strength. Assuming that the flow behaves as a Bingham fluid, one can use the relationship between the plastic viscosity (η , in Pa.s) and yield strength (τ_c , in Pa) measured at various liquidity indices (Locat and Demers 1988; Locat 1997):

$$[6] \quad \eta = 0.52 \tau_c^{1.12}$$

The plastic viscosity can be obtained from the liquidity index (I_L):

$$[7] \quad \eta = \left(\frac{9.27}{I_L} \right)^{3.33}$$

3.4 Initial slope conditions prior to the 1663 event

The initial topography of the Betsiamites slide complex and the lithostratigraphy, geotechnical parameters, and strength properties of the slope deposits prior to the 1663 Colombier slide event are described in this section.

3.4.1 Initial topography

The interpreted subaerial topography prior to the 1663 Colombier slide event is shown on Figure 3.4 and characterized by two main terraces, at elevation of 60 and 40 m (Cauchon-Voyer et al. 2011b). The elevations of the terraces are interpreted taking into account the orientation of the remaining terraces on both sides of the landslide scar and of the raised beach observed outside the scar (Figure 3.2). The ground surface on the upper terrace plains is almost flat with slope angle between 0.5 and 2° .

Underwater, the main geomorphologic element on the shelf is a 54 km² landslide scar, with two main topographic depressions, the West depression and the East depression, separated by a 5 km² intact butte with flanks dipping between 5 to 15° and a nearly flat top (~1°) (Figure 3.4) extending to water depth of -140 m (Figure 3.2). Both depressions have widths ranging from 2 to 4 km, lengths of 7 km, and floor slopes of about 1°. It was demonstrated that this large scar resulted from the 7250 cal BP Betsiamites submarine slide, which involved about 1.3 km³ of material (Cauchon-Voyer et al. 2008). Prior to the 1663 failures, the back escarpment of the Betsiamites slide event was located at water depth of -10 m (Figures 3.2 and 3.4). Part of this escarpment is still preserved immediately east of the Colombier landslide scar and has a slope angle of 8° and an average height of 25 m (pointed by an arrow on Figure 3.2).

3.4.2 Lithostratigraphy and geotechnical parameters

The lithostratigraphy and the geotechnical parameters of the slope prior to the Colombier slide event are evaluated from 2 subaerial boreholes and 38 CPTU carried inside and outside the Colombier landslide scar (Figure 3.3).

Borehole 46006 is located at an elevation of 47.2 m outside the subaerial scar and complements a CPTU carried 23 m away (see location on Figure 3.3). Together, they provide soil data over a depth of 60 m. Borehole 46006 terminated on the bedrock at an elevation of -7 m whereas the CPTU met refusal at -12 m (Figure 3.5). Five main geotechnical units are identified and their characteristics are summarized in Table 3.2. The geotechnical profile consists, from top to bottom, of 5 m of sand (6-4b) over 24 m of sensitive clayey material (6-3c and 6-4a) overlying 10 m of grey silty clay (6-3b) and ~20 m of laminated clayey silt (6-3a).

Borehole 46010 was carried out in accumulation zone of the landslide scar and provides data over a depth of 60 m (Figure 3.6). Six main geotechnical units are defined and their properties are summarized in Table 3.3. From top to bottom, the lithostratigraphy at site 46010 consists of 17 m of mobilized deposits (10-Da and 10-Db) over 39 m of 3 types of fine clayey glacio-marine sediments (10-4a, 10-3b and 10-3a) underlying 3.6 m of coarser material (10-2).

Sedimentological and seismostratigraphic analyses combined with radiocarbon dating allowed establishing the correlations between the geotechnical units of both boreholes and provide geological interpretations (Cauchon-Voyer et al. 2011b). The same lithological units are found in both boreholes along the slope and the correlations for the units involved in the landslides are presented on Figure 3.7.

The upper sandy unit (6-4b) is found only in borehole 46006 (Figure 3.5 and Figure 3.7) and consists of coarse sand ($d_{50} \sim 0.5$ mm). The stratified clayey silt units (6-4a and 10-4a) contain on average 33% of clay (6-4a) and 31% of clay (10-4b). Several layers of fine sand less than 5-cm thick are identified within this unit. The water content is variable, from 22 to 40 %. The plasticity index ranges between 7 to 16 %, with the highest values found in borehole 46010. The liquidity index ranges between 1 and 1.4 for borehole 46010 and is greater than 1.2, with values ranging between 1.6 and 2.8, for borehole 46006 (Figure 3.7). The CPTU pore pressure dissipation tests performed in the coarser soil layers of higher resistance within these layers indicate hydrostatic conditions with the water table. Preconsolidation pressures (σ'_p), evaluated by a conventional oedometer test at -10.9 m (46010) is 400 kPa, leading to an overconsolidation ratio (OCR) of 2.

Geotechnical unit 6-3c is found only in borehole 46006 (Figure 3.7) and consists of grey silty clay (Figure 3.5). It has a natural water content ranging between 31 and 37 %. The plasticity index ranges between 7 and 10 % and the liquidity index is between 2.4 and 3.1. If a 1-cm thick sand bed at 26.8 m is ignored, the clay fraction ranges between 40 and 52 % and averages 46 %. The sensitivity values obtained with the Swedish cone, range between 406 and 1202. The σ'_p at an elevation of 20 m is 450 kPa, leading to an OCR of 1.8.

Unit 6-3b has similar grain size distributions as 6-3c, but higher plasticity and lower liquidity indices. The plasticity index ranges from 10 to 14 %, the liquidity index is slightly greater than 1.0, with values ranging between 1.1 and 1.2. The clay fraction is typically of 46 %. Sensitivity ranges between 35 and 67. σ'_p evaluated at an elevation of 9 m is 500 kPa, leading to an OCR of 1.7.

Unit 10-3b observed in borehole 46010 comprises also grey silty clay. The plasticity index ranges between 16 and 28 %, which is greater than for 6-3b and the liquidity index is lower

than 1, with values between 0.7 and 0.9. These differences in index properties indicate that for similar sedimentological properties, the geotechnical properties vary according to the position in the sedimentary column (Figure 3.7). The clay fraction ranges between 29 and 50% and average 37%. The sensitivity (S_t) values obtained with the Swedish fall cone for this layer are between 14 and 56. The CPTU data allows the estimation of the preconsolidation pressure profile at the location of borehole 46010 (Figure 3.6) with the empirical relationship [1]. The clayey layers of this deposit (10-4a and 10-3b), in comparison with a typical soil profile normally consolidated ($S_u=0.25\sigma'_{vo}$), appears overconsolidated with an approximate OCR of about 2.

The lowermost geotechnical unit (6-3a) of borehole 46006 comprises ~20 meters of highly laminated clayey silt. The clay content ranges between 24 and 53%. The plasticity index ranges between 23 and 29% and the natural water content ranges between 29 and 38 %. The liquid limit, always slightly above the natural water content, ranges between 37 and 46%, leading to liquidity index ranging between 0.7 and 0.8. Sensitivity, measured with the Swedish cone, ranges between 7 and 12, which is similar to marine deposits (e.g., Perret et al. 1995). The σ'_p at an elevation of 4.4 m reaches 700 kPa, which leads to an OCR of about 1.8.

3.4.3 Strength properties

The undrained shear strength (S_u) in the landslide area was evaluated from field shear vane test, Swedish fall cone measurements, and derived from CPTU profiles. For site 46006, layer 6-3c of grey silty clay, between elevation of 28 and 18 m, the S_u increases linearly from 125 to 165 kPa at a rate of 3 kPa/m, leading to a S_u/σ'_{vo} ratio of 0.3. The layer between 18 and 8 m (6-3b) is characterized by 3 sublayers with significant strength reductions. At 16 m S_u decreases to 110 kPa. These strength reductions are neither associated to major changes in grain size distribution, as the clay fraction of the layer between 28 and 18 m is 45% and 46%, nor to significant changes in sedimentary structures as the sediments remain homogenous and bioturbated deep sea-sediments. At 8 m, when the sediments change from homogenous grey silty clay (6-3b) to laminated clayey silt (6-

3a), S_u reduces from 250 to 175 kPa. This layer presents many thin sandy layers and also calcareous concretions (Cauchon-Voyer et al. 2011b).

By applying a N_{kt} factor of 10.5 to the profile carried out along the beach 46010 (Figure 3.6), the S_u increases fairly linearly in the stratified silty clay and silty clayey sand (10-4a) layer from 125 kPa to 200 kPa. This is thus a very stiff unit which strength increases at a S_u/σ'_{vo} ratio of 0.6 (rate 6 kPa/m). This rate of increase for site 46010 is significantly higher than the value of 0.3 obtained at site 46006, but was also evaluated at site 46111 and 46037. The strength of the grey silty clay layer (10-3b) also increases with depth according to a ratio of 0.6.

3.5 Dating

Three radiocarbon dates (Table 3.1) were obtained from 3 different tree branches recovered from the Colombier landslide debris on the tidal flat at low tide (Figure 3.8), about 100 m from the transition between the beach and the protected salt water marsh (see sampling location on Figure 3.3). The samples were recovered from the muddy tidal flat and the branches appeared fairly intact so it is interpreted that they were buried by the landslide. The AMS ^{14}C dates after calibration provide a probability that the subaerial debris and tree branches were mobilized somewhere between AD 1647 and AD 1801. This range reinforces the interpretation that the subaerial landslide was triggered by the 1663 earthquake.

3.6 1663 landslide morphologies and phases

The 1663 Colombier landslide results from 4 distinct failure phases: one submarine phase (1) leading successively to three subaerial phases (2F, 3F, 3S) (Figure 3.9). The subaerial failure phases (2F, 3F, 3S) occurred along the shoreline over a length of 6 km. The morphological observations inside and outside the scar area provide insight on failure mechanisms, the movements sequence, and the links between the failure phases. CPTU derived stratigraphy and strength characteristics provided evidence to locate the failure surfaces. This section summarizes the morpho-stratigraphic evidence in regard to the 1663

Colombier landslide failure phases proposed and discussed in Cauchon-Voyer et al. (2011b).

3.6.1 Submarine failure (Phase 1)

The submarine failure (1) developed in the back escarpment of the 7250 cal BP Betsiamites landslide scar (Figure 3.9). As presented on the geotechnical profile of site 46010 (Figure 3.6), debris are found to an elevation of -8 m in the borehole and this is further supported with CPTU soundings 36, 10, and 37 (see locations on Figure 3.3) where debris are interpreted to an elevation ranging between -6 to -13.5 m. This indicates that at least a section with a minimal thickness of 6 m must have been removed along the current shoreline prior to the subaerial events. On the basis of these observations, it was concluded that the submarine failure must have occurred slightly prior to the subaerial failures, otherwise this space would have been filled with sandy beach material carried out by longshore drift (Cauchon-Voyer et al. 2011b).

The failure surface of phase 1 likely developed on a stratigraphic level that daylighted in the back escarpment of the 7250 cal BP Betsiamites slide event (Figure 3.9). In fact, the Betsiamites event left a 35 m high escarpment (Figure 3.9) on the seafloor at -10 m water depth (Figure 3.4). This escarpment is currently only ~25 m high as about 10 m of subaerial debris from the Colombier failures are at its toe (Figure 3.10). If the failure surface developed in the bottom of the escarpment, then the maximum thickness of the failed layer of 1663 submarine failure phase is about 35 m. The area of the failure is estimated at 9.3 km² and the volume of material involved in the Colombier submarine failure is estimated at 145 hm³. The submarine failure impacted a length of 6 km along the shoreline and retrogressed to the previous shoreline or possibly onshore to an approximate location between the shoreline and the 40 m terrace, as indicated on Figure 3.9. Most of the debris of this failure phase evacuated in the 7250 cal BP Betsiamites scars.

3.6.2 West flowslide (Phase 2F)

After the submarine failure (1), a first subaerial flowslide (2F) occurred over a length of 3700 m and retrogressed over a distance of 1000 m from the previous shoreline (Figure

3.9). On the basis of the geometry of the failure surfaces of phases 3F and 3S, observations that will be presented later, this event is interpreted to have occurred after phase 1 and before phases 3F and 3S. The crown of flowslide 2F is located at an elevation of 40 to 45 m while the failure surface is interpreted to be located more or less at sea-level (Cauchon-Voyer et al. 2011b). This implies that at least a 40 m-thick section of soil was involved in the landslide. The area of this first failure is 3.7 km^2 and involved about 130 hm^3 of material (Cauchon-Voyer et al. 2011b).

The bottom of the subaerial scar of the 2F flowslide appears mostly free of debris, which reinforces that this landslide is indeed a flowslide and is supported by the high value of liquidity index. The debris were unconfined and flowed directly into the Estuary. Seismic reflections surveys offshore allowed establishing that the thickness of debris decreases from about 5 m to a few centimetres within the West channel of the Betsiamites landslide scar (Figure 3.10).

3.6.3 Central flowslide (Phase 3F) and lateral spread (3S)

The central flowslide (3F) and the lateral spread (3S) combined developed over a length of 3200 m and retrogressed over about 2500 m (Figure 3.9). Both failure phases likely occurred simultaneously and hence their morphologies are described together. Both failure phases cut into in the 60 and 40 m terraces. The area of these two failure phases is estimated at 5.9 km^2 .

For the flowslide area (3F), CPTU soundings allowed establishing that the failure surface decreases from approximately an elevation of 60 m in the back portion of the landslide scar to the north, to an elevation of 10 m at the boundary with the back escarpment of phase 2F (section presented on Figure 3.11). This decrease of elevation occurred over a distance of 2000-2500 m. Within the subaerial scar of failure phase 3F, an 8 m high cliff of intact deposits was left in the scar and appears to be a part of the back escarpment of flowslide 2F (pointed by an arrow on Figure 3.12). The height of the flowslide 3F body, in its thickest portion towards the lateral spread (3S) (vertical dashed line on Figure 3.11), increases, from the back toward the shoreline, from about 40 to 55 m. Flowslide 3F involved a volume

estimated at about 75 hm^3 over 2.5 km^2 . As with flowslide 2F, the bottom of the 3F subaerial scar appears mostly free of debris (Figure 3.10).

In the lateral spread area (3S) (Figure 3.9), which occurred over an area of 3.4 km^2 , the failure surface is identified at an approximate elevation of 10 m towards the back of the slide and at an elevation of about -17 to -20 m, closer to the shoreline (Figure 3.11). Part of the failure surface of this subaerial failure developed well below sea-level. The position of the failure surface implies also that the landslide body height increases approximately from 50 to 67 m toward the shoreline. The failure surface is inclined at an angle β_s decreasing from 8° to 0.9° and extends over a horizontal distance of about 2900 m. The volume of soil involved in this failure phase (3S) is about 180 hm^3 . The retrogression distance from the previous shoreline is about 2500 m.

The morphology of the lateral spread area is characterized by succession of elongated ridges and depressions (Figure 3.12a). Today, even if the failure occurred almost 350 years ago, the landslide blocks were large enough (with length up to 700 m and height above the ground surface of 30 m) that they are still well preserved. The scar of the lateral spread almost contains the thickest accumulation of debris above the failure surface, with maximal values of 48 m (Figure 3.10). Three main groups of ridges were mapped according to their size, orientation, and location within the landslide scar. The first group corresponds to large ridges (purple on Figure 3.12a), which are still partly connected to the lateral escarpment. The largest continuous ridge within this group has a length of about 700 m and a height of 30 m above the surrounding debris. The second group (red on Figure 3.12a) has an orientation of 90° , which appears perpendicular to the mean direction of the lateral spread movement. The ridges of the third group (green on Figure 3.12a) are located in the lower portion of the scar and are oriented more or less parallel to the back escarpment of the scar in the area of the flowslide (3F), which is a difference of 140° from the ridges of the second group. Underwater, blocks of heights ranging between 10 and 50 meters are visible on the seafloor as far as 8.5 km from the previous shoreline (Figure 3.2). The more mobile part of the lateral spread traveled in the runout zone for a distance L_R of about 8.5 km on a gliding surface of slope (β_f) ranging between 0.8 and 1° , leaving a debris flow

deposit of average thickness of 3-5 m and with maximal thickness of 10 m (H_f) in the East depression (Figure 3.10).

Few marine core samples were recovered and provide a minimal thickness of the layer of debris offshore (Figure 3.12). Core 45PC was recovered in the debris lobe of the debris of flowslide 3F and lateral spread 3S (Figure 3.10). This 5 m depth core shows very distinctive chaotic sedimentary structures, such as contorted laminae, on the CAT-Scan image resulting from the mobilization of the landslide mass. This is further validated with sedimentological observations of silty clay clasts in a sandy mud matrix (Cauchon-Voyer et al. 2008). The water contents measured in the debris range between 22 and 38% and average 28%. These values of water contents are value close to the values evaluated on shore in unit 10-4b, which range between 24 and 37% and average 29% (Figure 3.6).

The dispersal pattern of the debris of all four failure phases is presented on Figure 3.10. As the failures occurred sequentially in a short period of time, it is almost impossible to differentiate the events in the debris lobe. This accumulation map of debris deposits resulting from the 1663 Colombier event on the shelf (Figure 3.10) is interpolated from geophysical interpretation. The base and top of the debris were interpreted and mapped across all 2D surveys on the shelf (Figure 3.3) and the thickness of the debris subsequently was gridded by interpolation. The resulting grid is a 3D volume disclosing the pattern of accumulation on the shelf. Due to the irregular surveying pattern and the large area to be covered, lines are spread irregularly and this impacts the grid resolution. The seismic reflection surveys were carried out along the beach and at water depths below 30 mbsl and do not provide thickness estimates for the area between the shoreline and the -30 m contour line. This figure however shows that the thickest accumulation of debris is found in the East depression and that a thin layer of debris accumulated on top of the central butte. This analysis indicated also that for a total landslide volume of 530 hm^3 , 55% of the landslide mass (290 hm^3) remained within the source area above the failure surface and 45% (240 hm^3) evacuated the source area and flowed in the Estuary.

3.7 Morphosedimentological and geotechnical models

The approach to carry out the slope stability analyses of the 1663 Colombier slide event requires a morphosedimentological model (Figure 3.13) and estimates of the geotechnical properties of the sediments involved (Table 3.4) in order to establish a five layers geotechnical model (Figure 3.14).

3.7.1 Morphosedimentological model

The morphosedimentological models are composed of 5 main soil units and the bedrock (Figure 3.13). The lithological and geotechnical parameters, thickness, and elevation of the five main soil units were defined from CPTU data, borehole data, and seismic profiling and the location of the data source used to interpret the models is indicated on Figure 3.13b. Two models are defined due to significant changes in the lithostratigraphy, i.e., since bedrock elevation changes across the area, each lithostratigraphic unit has different elevation and thickness (e.g., Figure 3.7). The locations of the profiles prior to failure are indicated on Figure 3.4, which present the interpreted topography. These profiles of the inferred morphostratigraphy correspond to the slopes prior to the flowslide 2F and 3F (Figure 3.13a) and prior to the lateral spread (Figure 3.13b). As it will be demonstrated, this change in lithostratigraphy and geotechnical properties has a direct impact on movement mechanisms and corresponds to the most significant difference between both areas. Finally, it is worth noticing that the vertical exaggeration of Figure 3.13 is 15x, which greatly distorts the perception of the slope angles.

Prior to failure, the thickness of the sandy layer (5) increases from west to east. Up to 28 m of sand was identified on CTPU 46039 (Figure 3.11) carried out outside the scar, 400 m from the east lateral escarpment of the spread 3S (Figure 3.3), whereas only 5 m of sand were sampled at borehole 46006, 450 m west of flowslide 3F (Figure 3.5), about 3.6 km from the other. Based on the geometry of the landslide body, the failure surface of the three subaerial failure phases (2F, 3F, 3S) developed in the clayey soil layers (3 and 4) (Figure 3.13a).

For the submarine portion, in addition to the presence of the ~25 m high Betsiamites landslide back escarpment, previous seismostratigraphic analysis led to the interpretation of a 35 cm-thick layer sand to silty of sand (indicated by a purple line on Figure 3.13) within the stratified silty clay unit (soil layer 4) along the shoreline (Cauchon-Voyer et al. 2011b). This layer is also identified submarine seismic profiling (Cauchon-Voyer et al. 2008). This layer has a slope angle less than 1° . It was suggested that this layer, or at least that the fact that this unit (4) is highly stratified, may have controlled the development of the 7250 cal BP Betsiamites failure (Cauchon-Voyer et al. 2011a). Similarly, observation of the height of the submarine escarpment of the Betsiamites scar and the elevation of this sandy layer, the failure surface of the submarine failure (1) (Figure 3.13b) appears to have developed within in the soil layer 4 (10-4a) and could potentially have developed above this sandy layer.

3.7.2 Geotechnical model

The morphological model (Figure 3.13) is transferred in an equivalent geotechnical model with geotechnical parameters for the five soil layers (Figure 3.14) to conduct limit equilibrium analyses of slope failure conditions for long term processes (drained) and short term processes (undrained). The characteristics of the soil layers are summarized in Table 3.4 and correspond to the soil layers indicated to the right on Figure 3.5 and Figure 3.6. The locations of these profiles are shown on Figure 3.9, which are not exactly the same locations as the morphosedimentological models (Figure 3.4). The geotechnical models were defined parallel to the movement of the landslide for each simulation.

CPTU pore pressure measurements (u_{base}) and pore pressure dissipation tests carried along the CPTU soundings indicate that the water table is located within the upper sandy layer (e.g, 6-4b on Figure 3.5) in the upper part of the slope and that the conditions are essentially hydrostatic. CPTUs soundings demonstrate no apparent excess pore water pressures other than in the clayey layers were the tests were stopped before complete dissipation. Since the slopes of the terrain are very low ($<2^\circ$) and the distances so large (>2 km), the ground water flow regime is assumed to be hydrostatic for the analyses.

For the drained analysis, Mohr-Coulomb drained strength parameters are used for all 5 soils layers (Table 3.4). The sandy layer 5 is assumed cohesionless with a friction angle of 40° defined from CPTU correlation proposed by Robertson and Campanella (1983). For the clayey layers (4 and 3), the strength parameters are defined using the correlations proposed by Lefebvre (1981). In fact, for the stratified silty clay and silty clayey sand layer (layer 4), extrapolation from the preconsolidation pressure profile (Figure 3.6) defined with Eq. [1] allows estimating that the values of preconsolidation pressure from the failed layer along the shoreline likely increased with depth from 100 to 350 kPa. Following the work carried out by Lefebvre (1981) linking post-peak strength parameters to preconsolidation pressure for eastern Canada clays, the strength parameters can be estimated at $c'_m = 10$ kPa for cohesion and $\varphi'_m = 36^\circ$ for the friction angle. For the layer of grey silty clay (3), the same method allows establishing $c'_m = 10$ kPa and $\varphi'_m = 40^\circ$. The given values for layer 2 of laminated silt to silty sand with clay and layer 1 of gravelly and bouldery sandy silt are typical values (Table 3.4). These values can be roughly estimated as these layers (2 and 1) were not involved in any landslide failure phases in 1663.

For the undrained stability analyses, the strength parameters of layer 4 and layer 3 are specified with a function that allows the undrained shear strength to increase with depth, from 25 kPa at the surface with the rate of 3 kPa/m for the simulation of on the subaerial portion (obtained from site 46006, Figure 3.5) failure phases and from 25 kPa at the surface with the rate of 6 kPa/m for the submarine failure phase (obtained from site 46010, Figure 3.6). These values correspond to the slope of the S_u profile within layer 4 from CPTU data obtained with Eq. [2].

3.8 Back-analysis and movement phases

The movement sequence (Phase 1, 2F, 3F, 3S) was established only on the basis of morphological observations (Cauchon-Voyer et al. 2011b). In order to establish the destabilization processes and validate the morphological interpretation, slope back-analyses are carried out.

3.8.1 Submarine landslide (phase 1)

The limit equilibrium slope stability model allows to back-analyze the submarine slope failure (1), which developed prior to subaerial failures (2F, 3F, and 3S) (Figure 3.9). For this submarine failure (1), the initial conditions of slope stability are analyzed, using drained and undrained strength parameters.

Assuming that long term processes have influenced the submarine slope, a drained analysis (effective stress analysis) has to be carried out (Figure 3.14a). Without constraining the location of the failure surface, the lowest factor of safety for the submarine slope is 5.6, which indicates that the failure has not developed under drained conditions (Figure 3.14a). Under undrained conditions, the factor of safety of the submarine slope is 5.8. Both stability conditions (drained and undrained) confirm that the initial submarine slope should have been stable. However, morphological observations indicate that it failed so other mechanisms such as earthquake-generated high pore water pressures, degradation of strength due to earthquake shaking and/or presence of a liquefied layer interbedded in clayey material must be investigated to explain the development of the failure.

The influence of seismic shaking was first simulated with a pseudostatic approach, which applies a horizontal acceleration to the sediments. These simulations were done under undrained conditions with a S_u/σ'_{vo} ratio of 0.6 (6 kPa/m from Figure 3.6), as they are short term processes, and require a total stress analysis. The results for the slope prior to the submarine failure (phase 1) are shown in Figure 3.15 where the factor of safety is presented as a function of the coefficient of horizontal acceleration (PSA), expressed as a ratio of the gravitational acceleration. This analysis indicates that a PSA between 28 and 38%, which is likely for the area (Adams and Atkinson 2003), and a strength reduction less than 20% would be required for the failure. Despite that it does not directly prove that an earthquake was required to trigger the landslide, it supports the hypothesis that significant triggering forces must have come into play. Nevertheless, the hypothesis of an earthquake as main trigger for the failure remains likely the most probable triggering factor. In fact, when trying to estimate the required value of seismic force to trigger the failure, it is important to take into consideration that the failure developed in a clayey silt unit (geotechnical units 6-

4a and 10-4a) within which many thin silt and sand layers are observed (Figure 3.6) and that it may have played an important role in the failure development. Dan et al. (2009) demonstrated, with an example from the Algerian margin, that thin sand and silt beds were the main cause of sediment deformation and liquefaction during earthquakes and could also have occurred from the Colombier submarine failure. Similar observations were obtained in the laboratory by Konrad and Dubeau (2003). This phenomenon can also be emphasized by the fact that the water becomes trapped between impermeable sublayers of clayey material. Kokusho (1999) demonstrated that this behaviour can occur under seismic loading and lead to a soil mass that may glide above a water film. This mechanism may have played an important role in the generation of the submarine failure (phase 1). Similarly, Levesque et al. (2006) showed in the Saguenay fjord that many earthquake triggered failures occurred along bedding planes or parallel to them and led to the nearly complete removal of material above the failure surface.

In summary, evidences from the back analysis indicate that an earthquake was likely required to trigger the Colombier submarine landslide. The drained and undrained analyses indicate that the 1663 earthquake and its associated effects triggered the submarine failure (1).

3.8.2 Flowslide development (Phases 2F and 3F)

Four main conditions must be met to develop a flowslide in fine grained material (Tavenas 1984; Leroueil et al. 1996; Leroueil 2001). First, there must be an initial slope failure (1) leaving unstable backscarp in the slope. For example, this first failure can be initiated by an external trigger such as earthquakes or erosion. Then, the material of the slope must have the ability to be remolded (2). A $I_L > 1.2$ and $Cu_r < 1$ kPa is required to allow the remoulded material to flow (Leroueil 2001). This depends, in part, on the height of the slope (H) as it controls the potential energy available for remoulding. It also depends on the mechanical and physical characteristics of the material such as its plasticity and undrained shear strength (3). For an $I_p \sim 10$, the soil characteristics act as predisposition factor for failure given by a stability number $\gamma H/Cu > 4$ (Leroueil 2001). Finally, the

topography must be favourable to allow the failed mass to flow outside the landslide scar (4).

The morphology of the scar area indicates that the failure surface of the west flowslide 2F (Figure 3.9) is interpreted to be more or less at sea-level (Figure 3.13b) in material with S_u of about 200 kPa (geotechnical unit 6-3a on Figure 3.5). If the stability of the subaerial slope prior to flowslide 2F is analyzed using undrained strength parameters without pseudostatic seismic forces, the factor of safety of the submarine slope is 2.2 (Figure 3.14b). A PSA of 13% is apparently required to bring the slope to failure, indicating again that seismic forces were required cause a first failure leading to the development of flowslide 2F. This failure could either have resulted from the initial earthquake or a following aftershock. In fact, historical accounts reveal that the 1663 earthquake had few aftershocks in the following hours and days, and could potentially have influenced a thin layer of sandy material in the laminated clayey silt unit (unit 6-3a on Figure 3.5). This analysis also indicates that for phase 2, it is possible that the submarine failure did not necessary played a role in the development of failure 2F. When modeling the stability of the slope with the submarine mass prior to failure and after failure (as presented on Figure 3.14b), the FS and the most critical failure surface are not influenced.

According to the geometry of the failure surfaces, flowslide 3F probably developed quickly as a result of flowslide 2F. In fact, a remnant escarpment was identified within the scar (pointed by a black arrow on Figure 3.12). Flowslide 2F hence acted as first failure for flowslide 3F. In addition, for a stability number of 4, with a bulk density (γ) of 19 kN/m³ and average shear strength (S_u) of 150 kPa as it is the case for the slope prior to flowslide 3F, the minimal height that would remould the clay is 31.5 m. For flowslide 3F, the height of the slope above the failure surface is about 35 m (Figure 3.11) and implies that the slope met the elevation potential energy requirement. In addition, the material involved in failure 3F (6-4a and 6-3c) has a liquidity index greater than 1.2, implying that it gets easily remoulded and has the ability to flow outside the landslide scar into the estuary. As presented earlier, both geotechnical units on borehole 46006 between 42 and 18 m (6-4a and 6-3c) have a $I_L > 1.2$ and $Cu_r < 1$ kPa (Figure 3.5).

The failure surface of flowslide 3F was identified at an elevation of 8 m on CPTU 46008 (Figure 3.11). If this elevation is compared to the elevation of changes in index properties at the location of borehole 46006, it is possible to suggest that change in I_L controlled the development of the failure surface. The 3F failure surface hence could have propagated over a low angle of 0.4° in sensitive clayey sediments (6-4a and 6-3c) and left intact the higher resistance and less sensitive material below the failure surface (6-3b and 6-3a). Since the deposits above the failure surface are highly sensitive ($I_L > 1.2$) they easily flowed out of the crater once remoulded. After a first failure, the new exposed back scarp was unstable, failed, and then liquefied to lead to further retrogressive failures. The final halt was apparently controlled by the stratigraphy when the failure surface reached the coarser sediments draping the bedrock (Figure 3.13b). Finally, in this case, the topography was favourable for the evacuation of the liquefied clay. The space at the toe of the slope was already cleared by the first submarine failure (phase 1) and the debris could flow without constraint in the Estuary.

3.8.3 Lateral spread development (phase 3S)

The first submarine failure (Phase 1), which occurred as a result of the 1663 earthquake, unloaded rapidly the toe of the subaerial slope (Figure 3.14). If it is assumed that the submarine failure stopped close to the location of the previous shoreline (Figure 3.4), an undrained back-analysis indicates that the newly exposed subaerial slope in the eastern portion of the scar (25°) is barely stable with a factor of safety of 1.09 (Figure 3.14c). As for the submarine failure, it is important to realize that the failure developed in a unit of stratified sediments and could have behaved as “weak” layers during an earthquake. According to Cruden and Varnes (1996) spread may result from the liquefaction or flow (or extrusion) of softer material overlain by a stiffer layer. The movement is translational and often retrogressive and lead to a general subsidence of the overlying mass into the softer underlying material. In the case of the Colombier spread, the upper sandy layer prior to failure was dense (see CPTU 46039 outside the scar on Figure 3.11); so, after failure, the large blocks of coarser material sank into the remoulded layer of silty clay layer, forming grabens and generating a massive extrusion of material into the estuary. In fact, a thickness of more than 40 m of soil is missing in the upper portion of the landslide scar and more

than 30 m in the lower portion of the slope (cross-section shown on Figure 3.11). In the upper portion of the scar, CPTU 46002 (see location on Figure 3.3) was carried out at an elevation of 18.8 m and the elevation of the terrain prior to failure was estimated at 60 m (Figure 3.4), which demonstrates the powerful extrusion of material that prevailed since 40 m of soil is missing. In fact, it was established that most of the debris remaining in the scar are sandy material (Cauchon-Voyer et al. 2011b) as demonstrated by thickness up to 40 m (Figure 3.10). It is also possible that, in addition to the initial failure in the clayey layers (layers 3 and 4 on Figure 3.13), the overlying sandy layer acted as a weight helping the clayey material to get remolded and facilitated even more the extrusion of material from the slope into the Estuary in the space created by the submarine slide (1).

3.9 Mobility and post-failure analysis

The Colombier slide event generated a large volume of debris that traveled over a distance of nearly 8.5 km from the shoreline on the submarine shelf (Figure 3.10). About 45% of the debris evacuated the source area and flowed into the Estuary. In a context that coastal geohazards such as landslides and tsunamis need to be evaluated in the St. Lawrence Estuary, the runout characteristics of the failed mass in the submarine environment are investigated.

One main characteristic of the debris in the submarine area is the presence of large landslide blocks (Figure 3.12) implying that the debris mass was not completely remolded while being mobilized. As seen onshore in the lateral spread area (Figure 3.12), large ridges and blocks remain intact. With sizes up to 20×60×150 m for height, width and length respectively, landslide blocks flowed underwater on a gliding surface with very low slope angle ($\beta_f = 0.8-1^\circ$). The blocks seen on the central butte are nearly intact pieces of debris but remained in the debris area and did not flow ahead of the front as outrunner blocks would do (De Blasio et al. 2006). However, similarly to outrunner blocks, these blocks produced an erosion glide track about 1-2 m deep on the central butte (Figure 3.12b). These blocks probably benefited from water lubrication at the block-seafloor interface (De Blasio et al. 2006), helping to explain the large runout distance observed. In addition, the high mobility of the blocks may have been helped by the constraint of the

lateral escarpments of 7250 cal BP Betsiamites scar, thus concentrating mainly the flow within the East depression (Figure 3.10).

Overall, the debris mass of the Colombier slide event, the blocks and the remoulded material, flowed offshore. Field observations, such as thickness of debris from seismic profiling can be used to evaluate the yield strength, which can be considered as a first approximation to the remolded undrained shear strength of the failed mass (Locat and Demers 1988) with eq. [5]. This analysis is done in order to define the characteristics of the failed mass. The mobility analysis can be used to evaluate if the main parameter to generate a tsunami are met (e.g., landslide mass velocity, geometry and water depth of the failure) (Bardet et al. 2003). Based on this equation, to generate a flow thickness ranging between 3 and 5 m, the material must have a yield strength (τ_c) of ranging between 394 to 820 Pa (grey area on Figure 3.17).

A second estimation of the yield strength of the landslide mass can be obtained from the relationship linking the liquidity indices to the viscosity and to the yield strength (Locat 1997). The liquidity indices measured along the shoreline, i.e., in the lithological unit of stratified silty clay and silty clayey sand (10-4a) involved in the submarine landslide (phase 1), ranges between 1.0 and 1.4 (Figure 3.6). It was also demonstrated that the liquidity index changes around the landslide area according to the elevation of the material above sea-level (Figure 3.7). In the lateral escarpment, where the material has been leached since its deposition, it is assumed that the I_L of the material involved in the lateral spread 3S reaches values up to 3.1 (Figure 3.5). For such a range of liquidity indices values (1.0 to 3.1), according to Eqs. [6] and [7], the yield strength would range between 47 to 1346 Pa (Figure 3.17).

The coherence of the properties in the starting zone (borehole 46010) and the submarine depositional lobe can be supported by the fact that the average water content of 30% measured in the failed unit (10-4a) in the starting zone (Figure 3.6), and 29% in the lateral escarpment (Figure 3.5) correspond to the values measured offshore. In fact, core 45PC was recovered in the debris lobe of the debris of flowslide 3F and the lateral spread 3S (Figure 3.10) where the water content of the sediments range between 22 and 38% and average 28%. This indicates that little water was incorporated in the mass while flowing.

Submarine landslides can directly have an impact of coastal infrastructure, but also can generate tsunamis could potentially cause disastrous consequence onshore. Other landslides in the St. Lawrence Estuary (St-Simeon and Matane) have been recognized as tsunamigenic (Poncet et al. 2010). However, for the submarine phase of the Colombier event (phase 1), with a volume of 145 hm^3 over 9.3 km^2 , with depth of water above slide of less than 10 m and glided on a low angle of about 1° , it is difficult to demonstrate that such a landslide caused a significant tsunami. This analysis suggests that the 1663 Colombier slide event likely did not cause a significant tsunami wave but further analysis should be undertaken to evaluate if the 7250 cal BP Betsiamites slide event could have generated such a wave as such similar events were suggested for the St. Lawrence Estuary (Poncet et al. 2010).

3.10 Conclusions

The analysis of the 1663 Colombier landslide scar area demonstrates that this landslide event is the result of 4 failure phases. This analysis shows that in historical time in the St. Lawrence Estuary, a submarine failure occurred in association with subaerial failures. This analysis demonstrates that the 1663 Colombier slide event results from a first submarine landslide (phase 1), with estimated volume of 145 hm^3 , triggered by an earthquake. The first submarine failure (phase 1) is followed by a 3-phases significant subaerial landslide, hence demonstrating the submarine landslide hazard in the St. Lawrence Estuary to the subaerial environment.

The submarine slope (phase 1), which was stable (FS) under drained conditions, very probably failed following the 1663 earthquake. The triggering mechanism of the Colombier slide event, among the largest known historical subaerial landslides in sensitive clayey material in Canada, hence must have involved seismic loading and its effects on the strength of the material. Following the submarine failure, flowslide 2F developed in sensitive material also as the result of the earthquake and involved a volume of 130 hm^3 over an area of 3.2 km^2 . Flowslide 3F occurred in the back headwall of flowslide 2F and mobilized 75 hm^3 over more than 2.5 km^2 . This analysis suggests that change in I_L controlled the development of the failure surface for the subaerial flowslide 3F. Phase 3S

is a lateral spread, which extended over 3.8 km^2 with an estimated volume of 180 hm^3 and the first failure of this landslide could also be triggered by the earthquake. Part of the failure surface of this subaerial failure (3S) developed well below sea-level and it was possible to suggest that the submarine failure (1) left an unstable escarpment (FS ~1) in which failure 3S was initiated. Not only the Colombier slide event resulted partly in an extremely large subaerial landslide in sensitive clayey sediments triggered by a submarine failure, it is also an example where flowing and spreading mechanisms occurred simultaneously.

With regards to the post-failure behaviour of the landslide mass, the yield strength values obtained from the I_L values corresponds to the morphology described by the Hampton equation. In addition to the large blocks observed on the seafloor, the measured values of water content in the initial sliding mass and in the debris lobe correspond, which implies that slide material was not totally remoulded. This paper suggests that the 1663 Colombier slide event likely did not cause a significant tsunami wave but further analysis should be undertaken to evaluate if the 7250 cal BP Betsiamites slide event could have generated a tsunami wave. The case of Betsiamites slide demonstrates that the integration of morphological, field and laboratory investigation in the source area, allows matching the morpho-stratigraphic observations offshore in the depositional area.

3.11 Acknowledgements

The authors wish to thank the Ministère des Transports du Québec (MTQ), NSERC and FQRNT for their financial support. We thank the MTQ for the permission to use their topographic and LIDAR surveys, borehole, and piezocone soundings data of the Colombier - Betsiamites area, and in particular to D. Demers, D. Robitaille and P. Locat for their involvement in the project. We recognize the contribution of Patrick Lajeunesse and all scientists and crew members on board the Coriolis II, F.G. Creed, and Guillemot vessels. The Canadian Hydrographic Service and GSC-Quebec are also acknowledged for their contribution to bathymetric data acquisition.

3.12 References

- Adams, J., and Atkinson, G. 2003. Development of seismic hazard maps for the proposed 2005 edition of the National Building Code of Canada. *Canadian Journal of Civil Engineering*, **30**(2): 255-271.
- Bardet, J.P., Synolakis, C.E., Davies, H.L., Imamura, F., and Okal, E.A. 2003. Landslide tsunamis: Recent findings and research directions. *Pure and Applied Geophysics*, **160**(10-11): 1793-1809.
- Bernatchez, P. 2003. Évolution littorale holocène et actuelle des complexes deltaïques de Betsiamites et de Manicouagan-Outardes : synthèse, processus, causes et perspectives. Ph.D. thesis, Université Laval, Québec.
- Cauchon-Voyer, G. 2011. Mouvements de masse en milieu côtier dans l'estuaire du Saint-Laurent, Québec, Canada: le cas du grand complexe des glissements de terrain de Betsiamites. Ph.D. thesis, Université Laval, Québec.
- Cauchon-Voyer, G., Locat, J., and St-Onge, G. 2008. Late-Quaternary morpho-sedimentology and submarine mass movements of the Betsiamites area, Lower St. Lawrence Estuary, Quebec, Canada. *Marine Geology*, **251**(3-4): 233-252.
- Cauchon-Voyer, G., Locat, J., St-Onge, G., Leroueil, S., and Lajeunesse, P. Development and potential trigger mechanisms for a large Holocene landslide in the Lower St. Lawrence Estuary. 2011. *In* 5th International Symposium on Submarine Mass Movements and Their Consequences, Kyoto, Japan. Springer.
- Cauchon-Voyer, G., Locat, J., Leroueil, S., St-Onge, G., and Demers, D. 2011b. Large-scale subaerial and submarine Holocene and recent mass movements in the Betsiamites area, Quebec, Canada. *Engineering Geology*, **121**(1-2): 28-45.
- Cruden, D.M., and Varnes, D.J. 1996. Landslide Types and Processes. *In* Landslides Investigation and Mitigation. Edited by A.K. Turner and R.L. Schuster, Transportation Research Board, Washington DC. pp. 36-75.
- Dan, G., Sultan, N., Savoye, B., Deverchere, J., and Yelles, K. 2009. Quantifying the role of sandy-silty sediments in generating slope failures during earthquakes: example from the Algerian margin. *International Journal of Earth Sciences*, **98**(4): 769-789.
- De Blasio, F., Engvik, L., and Elverhøi, A. 2006. Sliding of outrunner blocks from submarine landslides. *Geophysical Research Letters*, **33**(6): L06614.
- Demers, D., and Leroueil, S. 2002. Evaluation of preconsolidation pressure and the overconsolidation ratio from piezocone tests of clay deposits in Quebec. *Canadian Geotechnical Journal*, **39**(1): 174-192.
- Dionne, J.C., and Occhietti, S. 1996. Aperçu du Quaternaire à l'embouchure du Saguenay, Québec. *Geographie Physique et Quaternaire*, **50**: 5-34.
- Dredge, L.A. 1976. Quaternary geomorphology of the Quebec North Shore, Godbout to Sept-Iles. Ph.D. thesis, University of Waterloo, Waterloo.
- Dubois, J.-M.M. 1977. La déglaciation de la Côte-Nord du Saint-Laurent. *Geographie Physique et Quaternaire*, **16**(3-4): 229-246.
- Hampton, M. 1972. The role of subaqueous debris flow in generating turbidity currents. *Journal of Sedimentary Petrology*, **42**(4): 775-793.
- Johnson, A.M. 1984. Debris flow. *In* Slope Instability. Edited by D. Brunsten and D. Prior, Wiley, New York. pp. 257-361.

- Kokusho, T. 1999. Water film in liquefied sand and its effect on lateral spread. *ASCE Journal of Geotechnical and Geoenvironmental Engineering*, **125**(10): 817-826.
- Konrad, J.M., and Dubeau, S. Cyclic strength of stratified soil samples. 2003. *In Submarine Mass Movements and their Consequences 1st International Symposium*. Kluwer Academic Publishers, pp. 47-57.
- Lamontagne, M., Demers, D., and Savopol, F. 2007. Description et analyse du glissement de terrain meurtrier du 25 octobre 1870 dans le rang des Lahaie, Sainte-Genève-de-Batiscan, Québec. *Canadian Journal of Earth Sciences*, **44**(7): 947-960.
- Lasalle, P., and Chagnon, J.-Y. 1968. An ancient landslide along the Saguenay River, Quebec. *Canadian Journal of Earth Sciences*, **5**(3): 548-549.
- Lefebvre, G. 1981. Fourth Canadian Geotechnical Colloquium: Strength and slope stability in Canadian soft clay deposits. *Canadian Geotechnical Journal*, **18**(3): 420-442.
- Lefebvre, G., Leboeuf, D., Hornych, P., and Tanguay, L. 1992. Slope failures associated with the 1988 Saguenay earthquake, Quebec, Canada. *Canadian Geotechnical Journal*, **29**(1): 117-130.
- Leroueil, S. 2001. Natural slopes and cuts: movement and failure mechanisms. *Géotechnique*, **51**(3): 197-243.
- Leroueil, S., Vaunat, J., Locat, J., Picarelli, L., Lee, H., and Faure, R. 1996. Geotechnical characterization of slope movements. *In 7th International Symposium on Landslides*, Trondheim, pp. 53-74.
- Levesque, C., Locat, J., and Leroueil, S. 2006. Dating submarine mass movements triggered by earthquakes in the Upper Saguenay Fjord, Quebec, Canada. *Norwegian Journal of Geology*, **86**(3): 231-242.
- Locat, J. 1997. Normalized Rheological Behaviour of Fine Muds and Their Flow Properties in a Pseudoplastic Regime. *In Debris-Flow Hazards Mitigation: Mechanics, Prediction, and Assessment*, Water Resources Engineering Division, American Society of Civil Engineers, New York. pp. 260-269.
- Locat, J. 2008. Localisation et magnitude du séisme du 5 février 1663 (Québec) revues à l'aide des mouvements de terrain. *In 4e Conférence canadienne sur les géorisques: des causes à la gestion - 4th Canadian Conference on Geohazards: From Causes to Management*. Presses de l'Université Laval, Québec, pp. 429-444.
- Locat, J. 2011. La localisation et la magnitude du séisme du 5 février 1663 (Charlevoix) revues à l'aide des mouvements de terrain. *Canadian Geotechnical Journal*, **In press**.
- Locat, J., and Demers, D. 1988. Viscosity, Yield Stress, Remolded Strength, and Liquidity Index Relationships for Sensitive Clays. *Canadian Geotechnical Journal*, **25**(4): 799-806.
- Lunne, T., Robertson, P.K., and Powell, J.J.M. 1997. Cone penetration testing in geotechnical practice. Blackie Academic - Chapman-Hall Publishers.
- Perret, D., Locat, J., and Leroueil, S. 1995. Strength development with burial in fine-grained sediments from the Saguenay Fjord, Quebec. *Canadian Geotechnical Journal*, **32**(2): 247-262.
- Poncet, R., Campbell, C., Dias, F., Locat, J., and Mosher, D. A Study of the Tsunami Effects of Two Landslides in the St. Lawrence Estuary. *In Submarine Mass Movements and Their Consequences 2010*. Springer Netherlands, pp. 755-764.

- Potvin, J., Pellerin, F., Demers, D., Robitaille, D., La Rochelle, P., and Chagnon, J.-Y. 2001. Revue et investigation complémentaire du site du glissement de Saint-Jean-Vianney. *In* 54th Canadian Geotechnical Conference pp. 792–800.
- Reimer, P., Baillie, M., Bard, E., Bayliss, A., Beck, J., Blackwell, P., Ramsey, C., Buck, C., Burr, G., and Edwards, R. 2009. IntCal09 and Marine09 radiocarbon age calibration curves, 0-50,000 years cal BP.
- Robertson, P., and Campanella, R. 1983. Interpretation of cone penetration tests. Part I: Sand. *Canadian Geotechnical Journal*, **20**(4): 718-733.
- Smith, W. 1962. Earthquakes of eastern Canada and adjacent areas, 1534-1927, Publications of the Dominion Observatory, Ottawa. pp. 271-301.
- St-Onge, G., Stoner, J.S., and Hillaire-Marcel, C. 2003. Holocene paleomagnetic records from the St. Lawrence Estuary, eastern Canada: centennial- to millennial-scale geomagnetic modulation of cosmogenic isotopes. *Earth and Planetary Science Letters*, **209**(1-2): 113-130.
- Stuiver, M., and Reimer, P. 1993. Extended ^{14}C database and revised CALIB radiocarbon calibration program. *Radiocarbon*, **35**(1): 215-230.
- Tavenas, F. Landslides in Canadian sensitive clays: a state-of-the-art. *In* Fourth International Symposium on Landslides, Toronto 1984. University of Toronto, pp. 141–153.

3.13 Tables

Table 3.1. Radiocarbon dates for the subaerial landslide.

Material dated ^a	Lab ID	¹⁴ C age yr BP	±	cal AD age ranges (2 sigma) ^d	Relative area under probability distribution ^e
Wood	UCIAMS-80034	215 ^b	20	1647 - 1680	0.393
				1763 - 1801	0.494
Wood	UCIAMS-80035	175 ^b	15	1667 - 1684	0.193
				1733 - 1783	0.525
Wood	UCIAMS-80036	160 ^b	15	1668 - 1692	0.165
				1728 - 1781	0.528
Wood	UL-2004	300 ^c	50	1462 - 1666	0.980
				1784 - 1795	0.020
Wood	UL-1922	310 ^c	60	1448 - 1668	0.973
				1782 - 1797	0.025

^a All wood samples were recovered along the shoreline at sea-level, see location of the 3 samples obtained in this study on Figure 3.3.

^b AMS ¹⁴C ages as reported from the laboratory after normalization for a $\delta^{13}\text{C}$ value of -25‰.

^c Radiocarbon dates as reported by Bernatchez (2003).

^d Calibrated to calendar years with CALIB6.0 (Stuiver and Reimer 1993) and INTCAL09 (Reimer et al. 2009) and presenting the 95.4 % (2 σ) probability distribution of the sample's true age.

^e Only the higher 2 probability distributions are presented.

Table 3.2. Properties of geotechnical units on the back escarpment of the 1663 flowslide 2F and lateral escarpment of flowslide 3F (borehole 46006), modified from Cauchon-Voyer et al. (2011b). z = thickness of layer. clay ($d < 2 \mu\text{m}$), silt ($2 < d < 63 \mu\text{m}$) and sand ($+63 \mu\text{m}$).

Geotechnical unit	Sediments type	Elevation (m)	z (m)	w (%)	I_p	I_L	S_t	Clay (%)	Silt (%)	Sand (%)
6-4b	Sand	47.6 to 42	5.6	-	-	-	-	0.5	2	97.5
6-4a	Stratified clayey silt with thin sand layers	42 to 28	14	30	10	1.9	-	33	50	17
6-3c	Grey silty clay $IL > 1.2$	28 to 18	10	34	8	2.8	(406-1202)	45	54	1
6-3b	Grey silty clay $IL \sim 1$	18 to 8	10	27	12	1.1	(35-67)	46	54	0
6-3a	Laminated clayey silt $IL < 1$	8 to ~ -12	~ 20	34	27	0.7	(7-12)	38	62	0

Table 3.3. Properties of geotechnical units at the foot of the lateral spread 3S (borehole 46010), modified from Cauchon-Voyer et al. (2011b)

Geotechnical unit	Sediments type	Elevation (m)	z (m)	w (%)	Ip	IL	St	Clay (%)	Silt (5)	Sand (%)
10-Db	Reworked sand	9 to 1.5	7.5	-	-	-	-	0.3	1	98.7
10-Da	Reworked stratified silty clay and silty clayey sand	1.5 to -8	9.5	28	13	1.2	-	30	59	11
10-4a	Stratified clayey silt with thin sand layers	-8 to -22	14	29	14	1.2	(13-36)	31	67	2
10-3b	Grey silty clay	-22 to -43	21	35	22	0.8	(14-56)	37	63	0
10-3a	Laminated silt to silty sand	-43 to -47	4	25	16	0.7	-	15	64	21
10-2	Gravelly and bouldery sandy silt	-47 to -50.6	>3.6	-	-	-	-	11	29	60

Table 3.4. Summary of the geotechnical and physical properties of the soil layers used in the limit equilibrium analyses, derived from the geotechnical units presented on Figure 3.5 and Figure 3.6. Estimation of drained friction angle (ϕ') of unit 5 is from CPTU sounding based on Robertson and Campanella (1983). Estimation of drained friction angle (ϕ') and cohesion (c) for clayey units 4 to 2 based on Lefebvre (1981). Properties of layer 1 are average values for coarse sand. Rate of increase of S_u , Phase 1: 6 kPa/m, Phases 2 and 3: 3 kPa/m.

Soil layer	Sediments type	Approximate thickness z		Water content w (%)	Unit weight γ (kN/m ³)	Drained friction angle (min) ϕ' ($^\circ$)	Cohesion (min) c' (kPa)
		min (avg)	max				
5	Sand	5 (30)	40	-	20	40	0
4	Stratified clayey silt with thin sand layers	4 (25)	45	30	19	36	10
3	Grey silty clay	5 (20)	35	35	18.5	40	10
2	Laminated silt to silty sand with clay	5 (10)	35	25	19	40	10
1	Gravelly and bouldery sandy silt	2 (30)	45	-	21	38	0

3.14 Figures

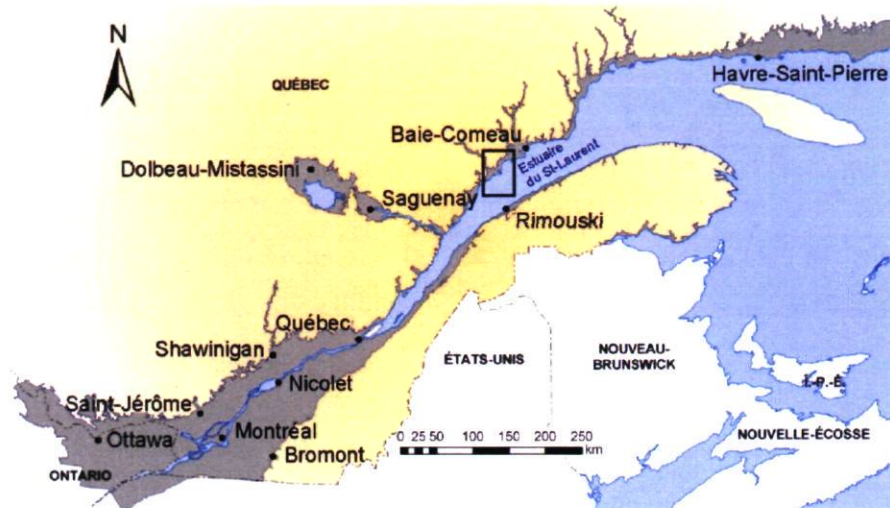


Figure 3.1. Map of the study area. The grey area indicates accumulation of glaciomarine sediments.

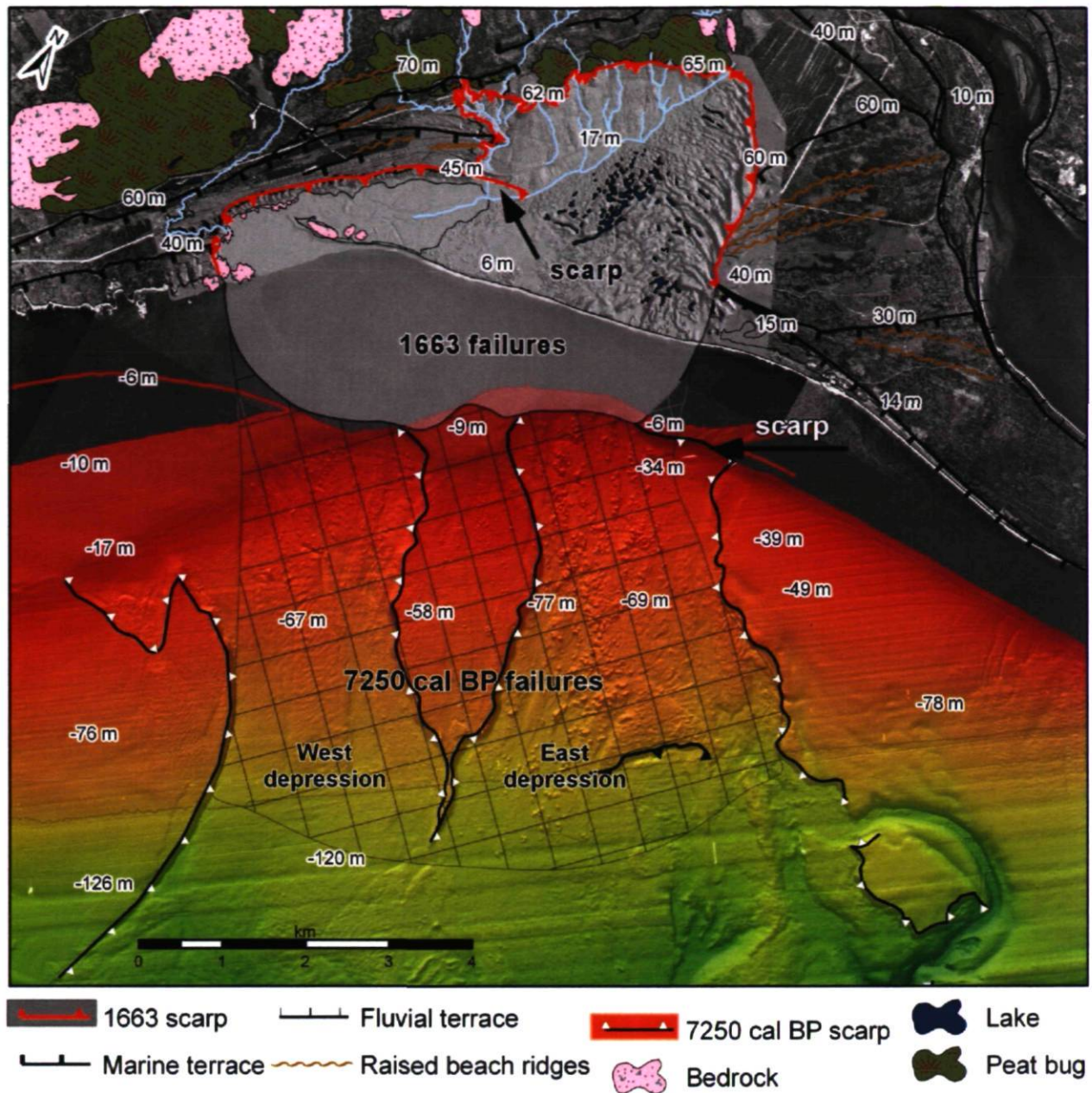


Figure 3.2. General view of the Betsiamites slide complex.

Grey shaded area onshore and in shallow water area corresponds to the depletion zone of the 1663 Colombier slide event. The submarine escarpments bound the 7250 cal BP Betsiamites failure event which extend over 54 km² on the submarine shelf. The back escarpment of the Betsiamites slide event is located at -10 m and its remnant is pointed by an arrow. Dashed submarine area corresponds to the debris accumulation of the Colombier event, with thickness > 1 m. Map layout is rotated 30°.

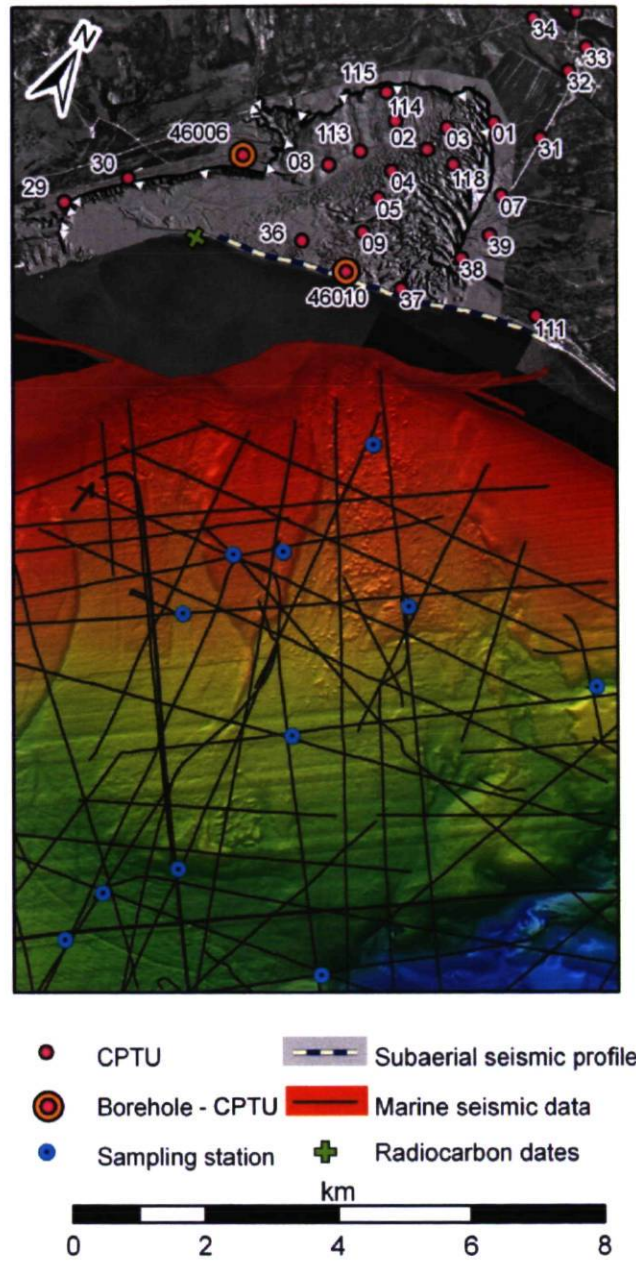


Figure 3.3. Investigation carried out in the subaerial and submarine area of the Betsiamites slide complex.

Numbers refer to CPTUs and 46006 and 46010 to boreholes.

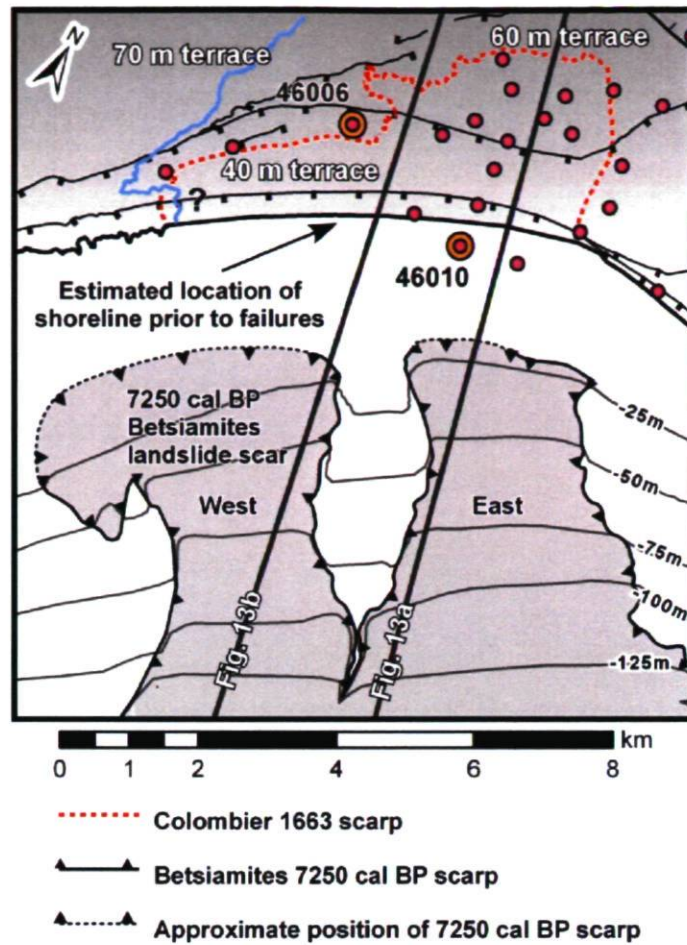


Figure 3.4. Interpreted topography prior to the 1663 Colombier slide event.

The question mark indicates that the location of the creek is assumed. Refer to Figure 3.1 and Figure 3.2 for legends and to Figure 3.1 for elevation values onshore.

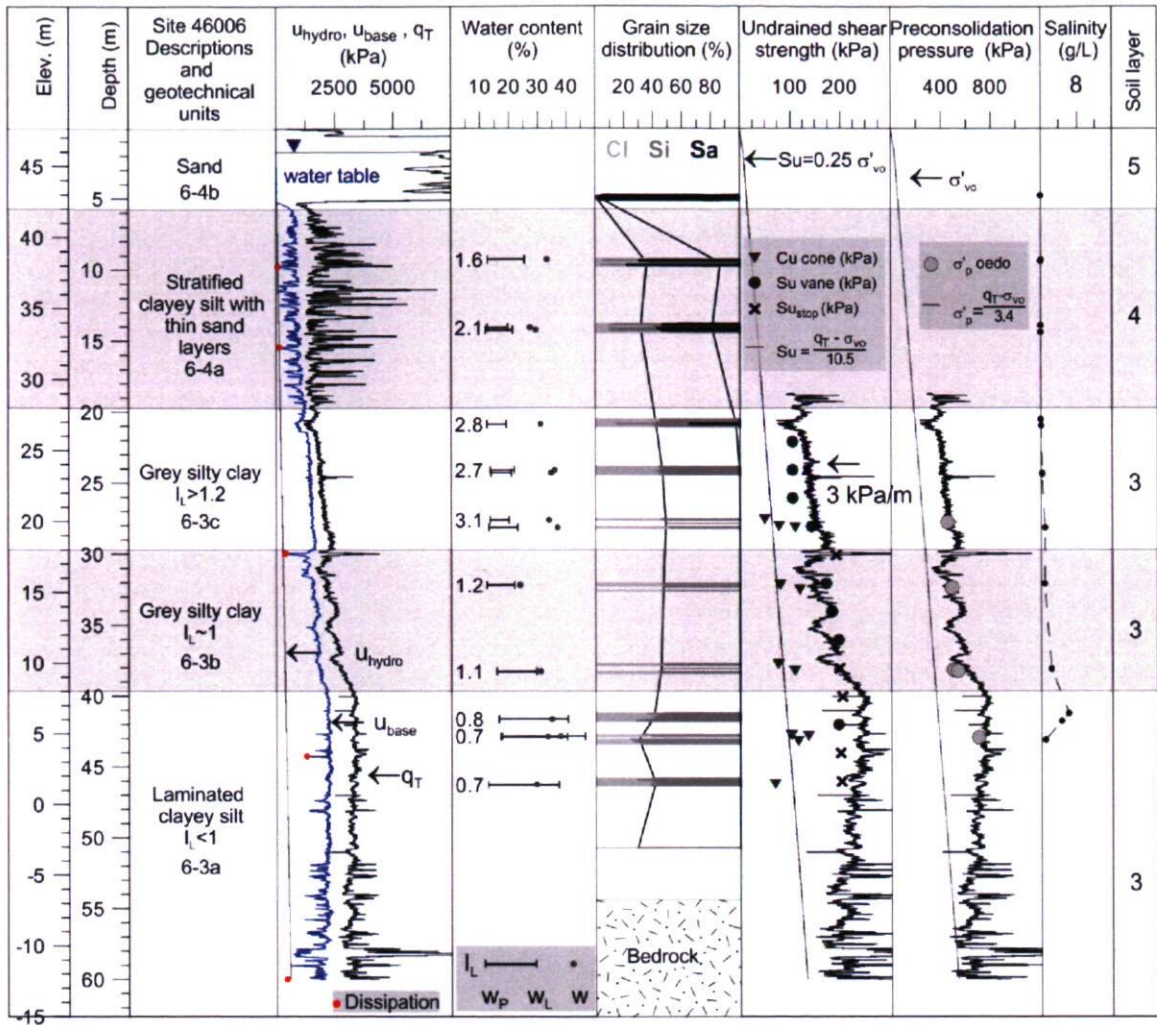


Figure 3.5 Geotechnical properties of borehole 46006.

The soil layer to the right of the graph corresponds to the layers defined in the geotechnical model.

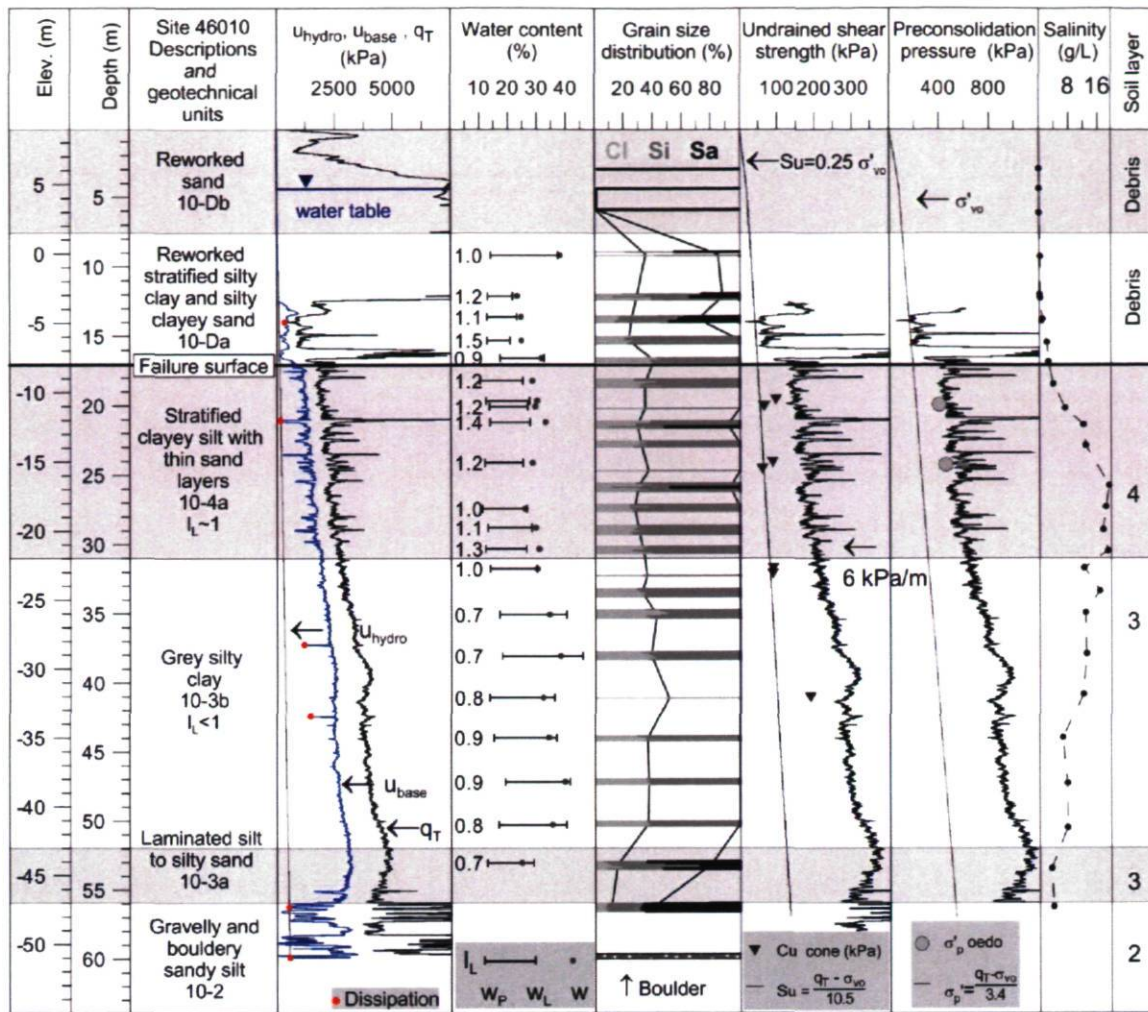


Figure 3.6 Geotechnical properties of borehole 46010.

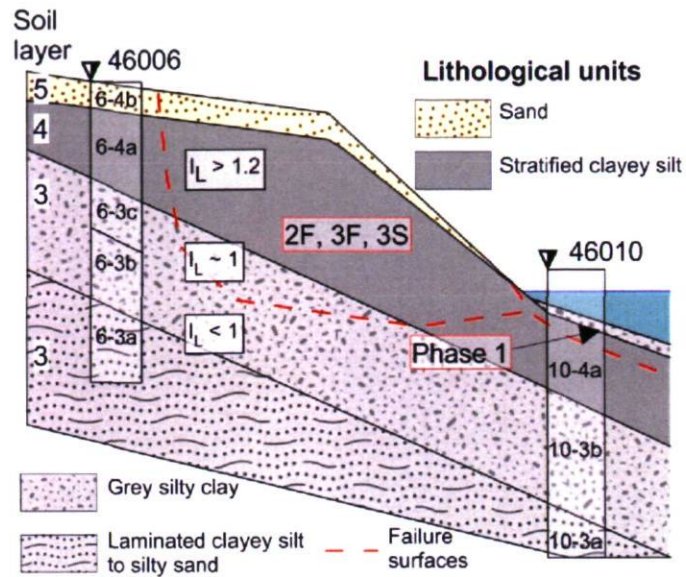


Figure 3.7 Schematic representation of the variation of the lithological and geotechnical units across the landslide area prior to the 1663 failure phases.

For similar sedimentary characteristics such as grain size distribution and internal structures, the liquidity index changes according to the elevation above sea-level. Numbers to the left of the figure indicate soil layers for stability analysis. The location of the failure surface of phases 2F, 3F, 3S is approximate and presents the soil layers involved in the landslides more than the exact location as three different failure surfaces developed. Not to scale.



Figure 3.8 Well preserved tree branches exposed at low tide.
See location on Figure 3.3. This patch of subaerial debris is located in the middle of the scar of flowslide 2F, 100 m from the upper water limit.

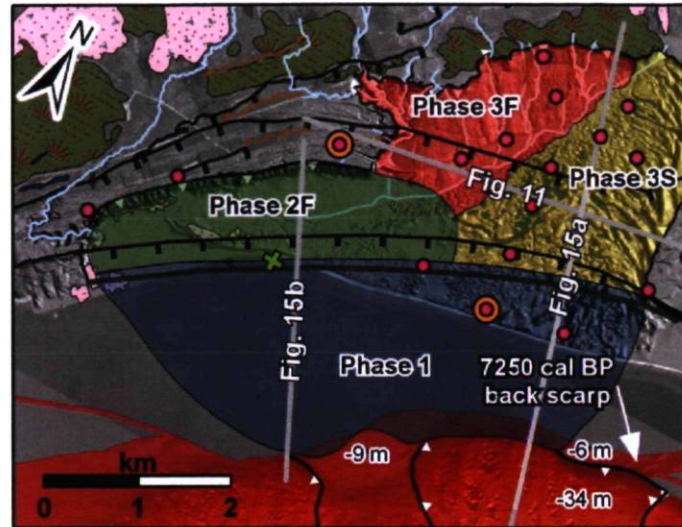


Figure 3.9 Landslide extent and failure phases of 1663 Colombier slide event.

The Colombier slide event involved four successive failure phases: one submarine and three subaerial. The lines with figure numbers refers to the CPTU cross-section (Figure 3.11) and the assumed location for the slope back analysis (Figure 3.14). Map layout is rotated 30° to the east. Refer to Figure 3.2 and Figure 3.3 for legend.

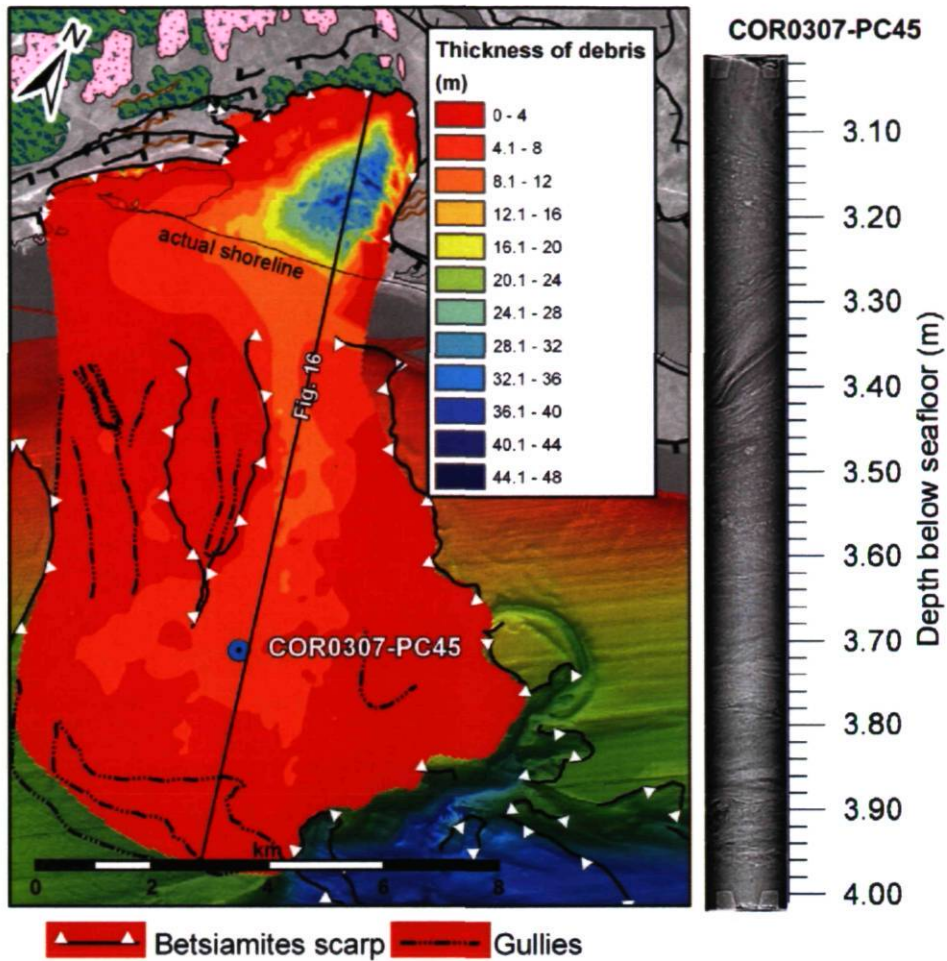


Figure 3.10 Thickness of debris and CAT-SCAN image of core COR0307-PC45 recovered offshore in debris area.

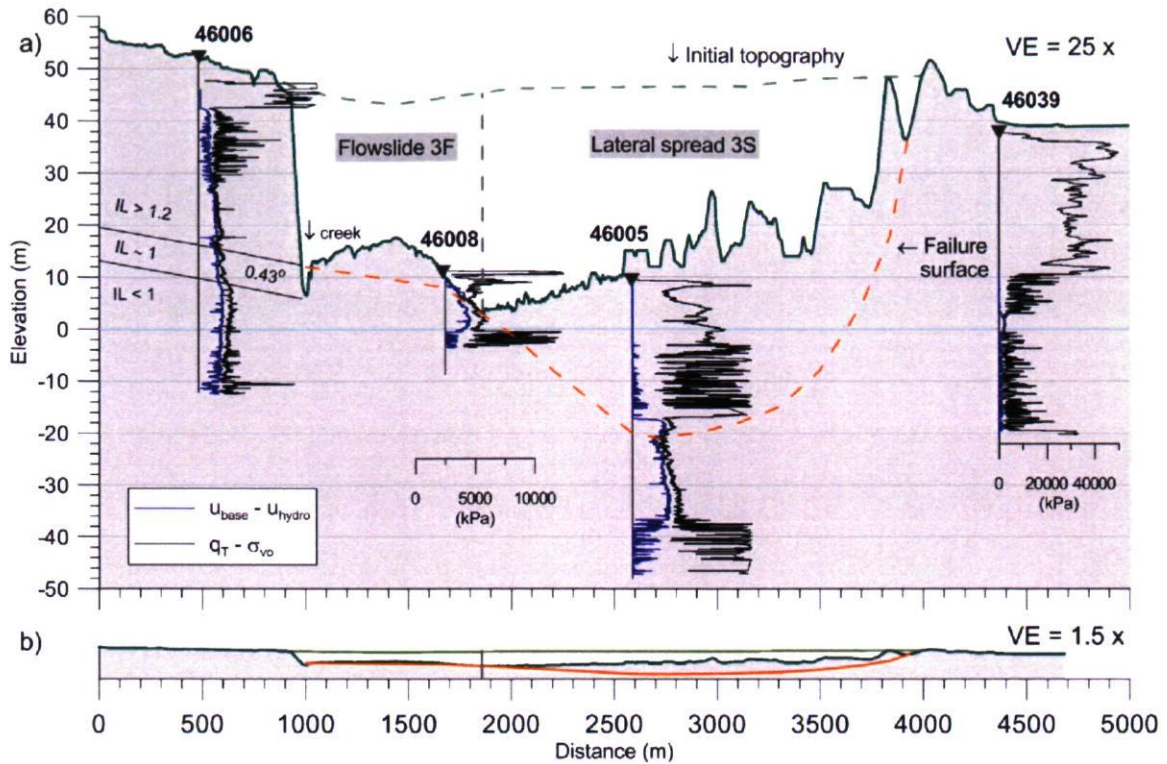


Figure 3.11 CPTUs and topographic cross-section in the subaerial flowslide 3F and 3S.

Triangular symbols refer to CPTU profile locations and the location of the topographic profile is shown on Figure 3.9. Refer to Figure 3.9 for profile location.

CPTUs and topographic profile at 20x vertical exaggeration. Notice that the scale increments for CTPU change for sounding 46039, demonstrating that the upper 28 m of sediments are dense sand with average tip resistance of 30 MPa. The vertical grey dashed line presents the approximate transition between the flowslide (3F) and the lateral spread (3S).

Profile of the estimated topography prior to failure, failure surface in orange, and final topography at 1.5x vertical exaggeration;

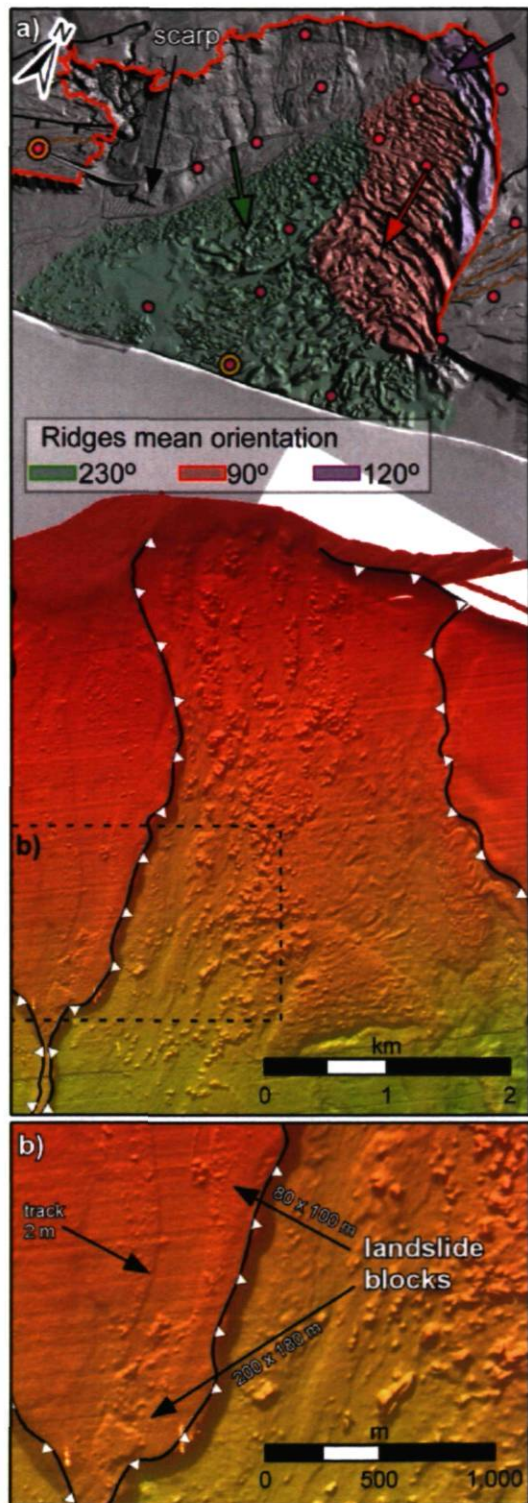


Figure 3.12 Morphology of the debris within the subaerial and submarine landslide scars.

Arrows indicate the direction of the movements of the subaerial ridges, which are assumed perpendicular to the orientation of the ridges. DEM is derived from combined LIDAR data and hypsometric lines at 1 m contour interval, accounting for the change in ground resolution within the scar.

Subaerial blocks dispersed underwater. On the central butte, the blocks produced an erosion glide track about 1-2 m deep.

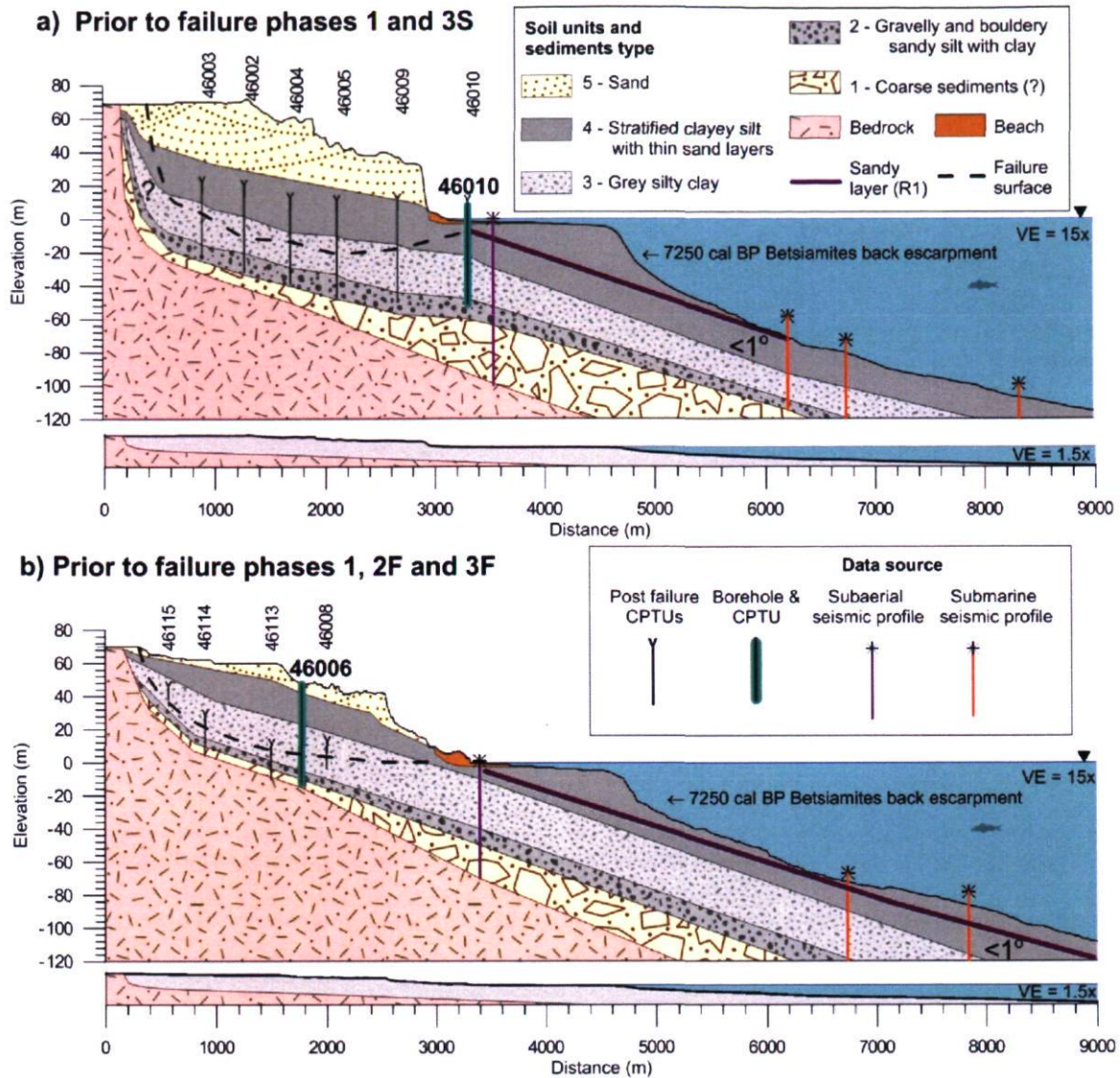


Figure 3.13 Inferred morphostratigraphy of the slope prior to failure and geomorphologic interpretations used for generating the geotechnical models shown in Figure 3.14, modified from Cauchon-Voyer et al. (2011b).

Locations of the profiles are presented on Figure 3.4. Lower graphs present the topography at a vertical exaggeration of 1.5x.

- a) Model prior to the submarine and lateral spread (3S) failure phases.
- b) Model prior to the submarine and flowslides (2F, 3F) failure phases.

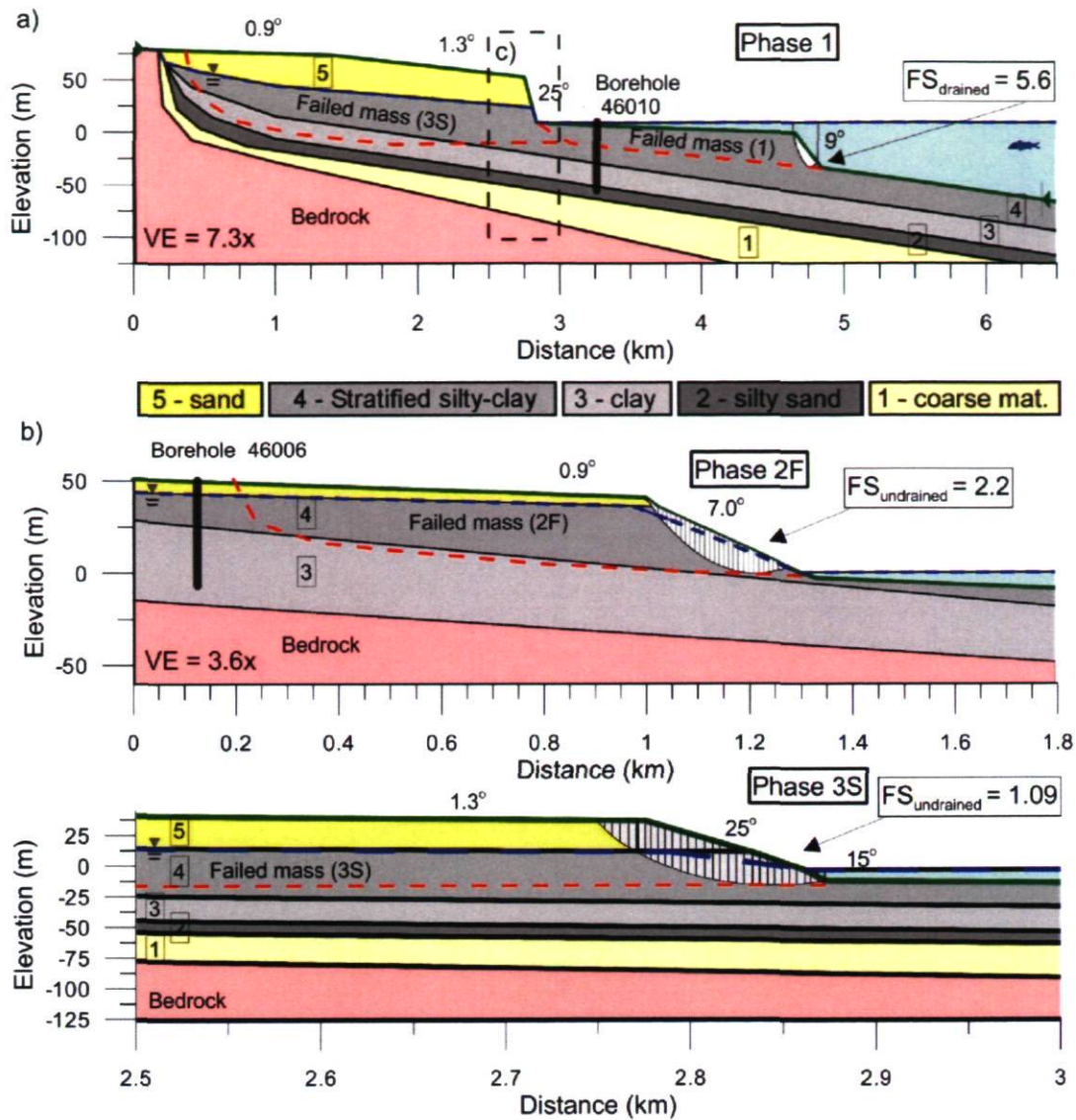


Figure 3.14 Simplified models used for slope stability analysis with SLOPE/W. Refer to Figure 3.9 for assumed location of these models and to Figure 3.13 for a topographic profile at 1.5x. Dashed lines corresponds to the location of the failure surfaces. a) For the submarine slide under drained conditions, showing the stratigraphic units (1 to 5, see text for explanation), and the slip surface with minimum calculated factor of safety (FS) of 5.7. b) Model representing the subaerial failure after the submarine failure (1) for an undrained analysis, with a FS of 2.0 under static loading for the central area (2F). c) Model representing a first failure required to trigger the large lateral spread 3S. Model corresponds to the slope after phase 1, shown on Figure 3.14a.

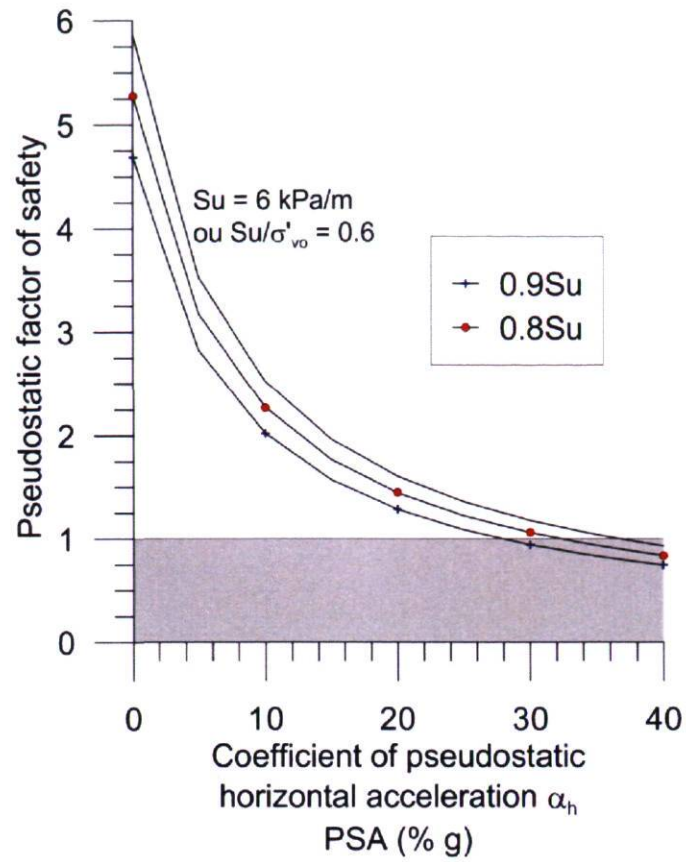


Figure 3.15 Factor of safety plotted as a function of the coefficient of horizontal acceleration, expressed as a ratio of the gravitational acceleration for the slope of the submarine failure (Phase 1).

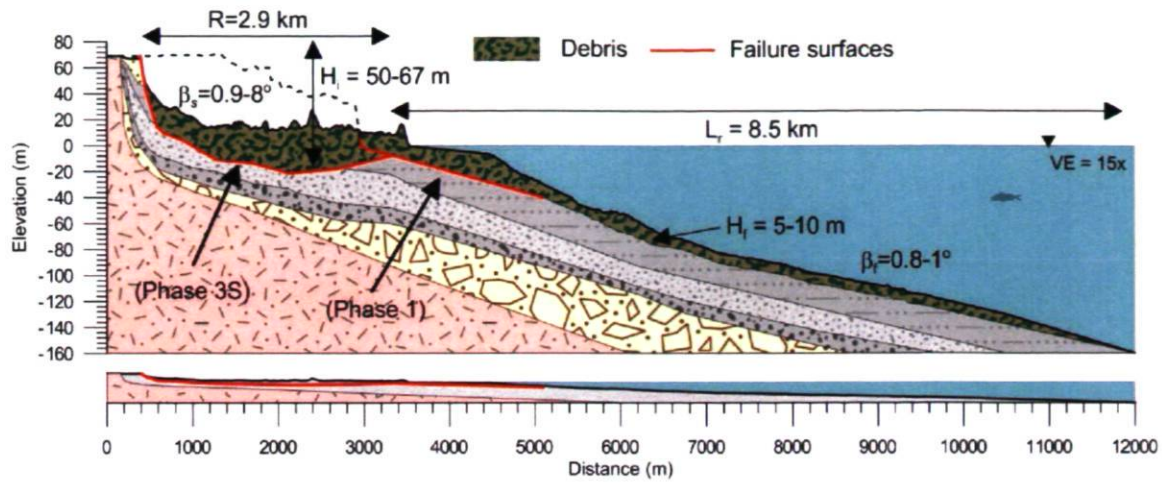


Figure 3.16 Thickness of debris interpreted from subaerial CPTUs and boreholes, submarine coring and subbottom profiling.

The thickness of the submarine lobe decreases from 10 m to few a centimetres over 8.5 km in the East channel at the toe of the lateral spread 3S.

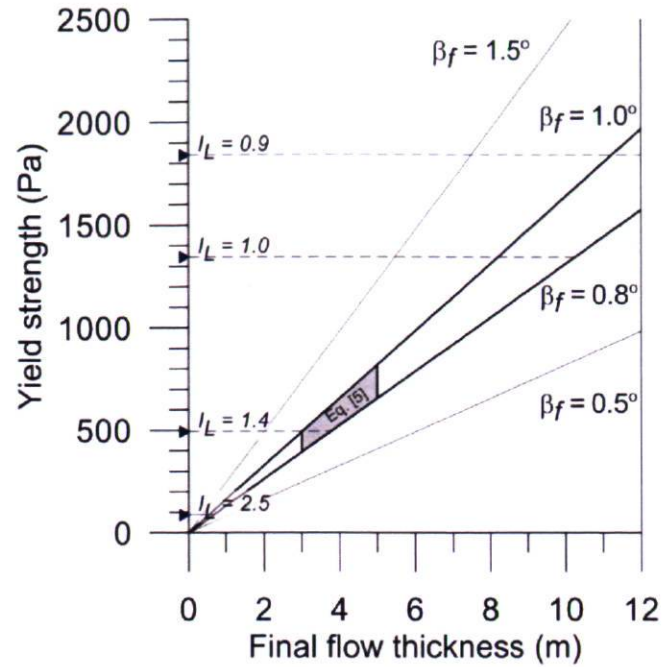


Figure 3.17 Evaluation of the yield strength using the relationship proposed by Johnson (1984) which uses the flow deposit thickness (H_f) in the runout zone Eq. [5] for various gliding surface angle (β_f).

The horizontal dashed lines indicate the range of values of yield strength evaluated from equations [6] and [7] according to the liquidity index, ranging between 0.9 and 2.5 for the failed mass.

Chapitre 4 Development and potential triggering mechanisms for a large Holocene landslide in the Lower St. Lawrence Estuary

4.1 Abstract

The Betsiamites 7250 cal BP submarine landslide mobilized a volume of 1.3 km³ in the St. Lawrence Estuary, Eastern Canada. The failure was initiated in shallow water between 10 and 140 mbsl and most likely developed in a unit stratified clayey silt deposits following a very strong earthquake. Most of the failed mass appears dislocated and evacuated the failure source area. This paper concludes that gas hydrates dissociation could not have influenced slope stability on the shelves of the Lower St. Lawrence Estuary in the Early Holocene and that despite the high sedimentation rates prior to the failure this condition did not act independently as a significant trigger for the Betsiamites failure.

4.2 Introduction

In Eastern Canada, submarine landslides have recently received more attention (e.g., Duchesne et al. 2003; Lajeunesse et al. 2007; Campbell et al. 2008; Cauchon-Voyer et al. 2008; Gagné 2008) and their consequences have been summarized (Mosher 2008). The Lower St. Lawrence Estuary is characterized by two ~10 km wide sub-horizontal 2° slope shelves breaking at water depth between 150 and 200 m (Figure 4.1) where many mass movement scars are observed. The deepest section of the Estuary, the Laurentian Channel at water depth of about between 350 and 375 m, is a long sub-horizontal NE-SW topographic depression.

The North Coast of the St. Lawrence Estuary exhibits areas with subaerial and submarine landslide scars with the largest located on the seafloor off the Betsiamites river delta (Figure 4.1). This delta was constructed in a time of falling relative sea-level as a result of the melting of the Laurentide Ice Sheet and glacio-isostatic rebound during the Late Wisconsinan, which transported great amounts of sediments from the continent into the Estuary. The Betsiamites landslide complex is the result of at least 3 distinct landslide

events, i.e. the submarine and subaerial Colombier failure in 1663, which extend is indicated on Figure 4.2, a large failure in 7250 cal BP and a failure in 9250 cal BP (Cauchon-Voyer et al. 2011b). Morphological analysis of the scar of the 7250 cal BP landslide event, thereafter named Betsiamites slide event, allows establishing that it occurred only in the submarine portion (Cauchon-Voyer et al. 2011b) when relative sea-level was about similar to present level (Bernatchez 2003).

4.2.1 Objectives

The 7250 cal BP Betsiamites submarine slide is the largest scar yet identified on the seafloor of the St. Lawrence Estuary. The main objective of this paper is to describe this massive submarine landslide and discuss its development and potential trigger mechanism.

4.3 Data and methods

Bathymetric data were acquired using a SIMRAD EM1000 multibeam echosounder. The seismic reflection profiles presented in this study were obtained with an EG&G chirp system (2-12 kHz). Technical details and results on the submarine bathymetric and geophysical data can be found in Cauchon-Voyer et al (2008). Forty-six sediments samples were recovered in the submarine segment of the delta and the locations of some sampling stations are indicated in Figure 4.1 and Figure 4.2. In addition, a cone penetration test with pore water pressure measurement (CPTU), providing tip resistance (q_T) and pore pressure measured immediately behind the tip (u_{base}) profiles, which can be compared to hydrostatic condition (u_{hydro}), and a 58-m long borehole (site 46010) were performed onshore along the current beach (Figs. 1-2). Detailed description of the CPTU and core data analysis and results can be found in (Cauchon-Voyer et al. 2011).

4.4 Morphology of the Betsiamites slide complex

The Betsiamites failure developed over an area of 54 km^2 at water depth from -10 mbsl to -140 mbsl (Figure 4.2) and mobilized about 1.3 km^3 of sediments, leading to an average landslide thickness of 24 m. This scar is made up of two main topographic depressions, the West depression and the East depression, separated by an intact butte with steep flanks (15-

20°) and flat top (Figs. 2 and 3). In the West and East depressions of the scar, the escarpment height ranges from 12 to 20 m above the seafloor. The floor of the landslide scar is overlain by up to 20 m of landslide debris deposits (Figure 4.3).

Based on core data and seismic profiling, the upper 3 to 10 m of these landslide debris deposits are associated with subaerial landslide debris resulting from the 1663 Colombier landslide event (Cauchon-Voyer et al. 2011). The intact butte within the central part of the scar extends over 5 km² with a maximum length and width of 4.5 km and 1.6 km respectively. The average slope of the top of this butte is 1°, which corresponds more or less to the slope of the seafloor prior to failure. In the Laurentian Channel, at water depths between 350 to 375 m, there is a large debris lobe covering an area of 115 km² with a maximum diameter of 15 km (Figure 4.2). With an average thickness of 9 m, the lobe has an estimated volume of 1 km³.

4.5 Lithostratigraphy and failure surface

The lithostratigraphy and the material involved in the 7250 cal BP Betsiamites slide are mostly assessed on the basis of geophysical surveys (Figure 4.3) as most of the sediment cores recovered offshore consist of 1663 landslide debris or post-glacial hemipelagic sediments deposited after the Betsiamites slide. The main challenge for offshore work on older landslides is to obtain geological validation and properly evaluate the *in situ* geotechnical properties. To counter this limitation in this coastal area, a subaerial CPTU and borehole (Figure 4.4) were carried out along the coastline. 6 main geotechnical units are identified at this site. The upper two are debris from the 1663 events. Unit 4 contains many ~5 cm-thick silty layers interbedded in clayey layers. Unit 3 is a homogenous grey silty clay, unit 3a is a thin layer of a laminated silt and unit 2 is a gravelly and bouldery silt.

The seismic profiling shows that the bedrock has an irregular topography and creates a sediment basin at the toe of the failure scar on the shelf (Figure 4.5). Prior to failure, the sediment layers deposited conformably on the underlying bedrock and allowed for little accumulation of sediments at the toe of the scar (Figure 4.5). Seismic interpretations (Figure 4.3) associated with core data (Figure 4.4) shows that the Betsiamites failure

developed in a unit of more than 25 m of stratified clayey silt deposit (Figure 4.5), labeled 4 (Figure 4.4 and Figure 4.5) and U4 on the seismic profiles (Figure 4.3). On average, unit 4 consist of 30% of clay ($d < 2 \mu\text{m}$), 67% of silt ($2 < d < 63 \mu\text{m}$) and 2% of sand ($+63 \mu\text{m}$).

The failure surface identified from the seismic profiles has a slope angle of about 1.3° . Local and regional chronostratigraphic and paleogeographic work (Bernatchez 2003; St-Onge et al. 2003; St-Onge et al. 2008; Cauchon-Voyer et al. 2011b) shows that the sequence of glaciomarine sediments (units 2-3-4) shown on Figure 4.3 was deposited approximately in about 4000 years between 11 to 7 cal ka in a time of significant sea-level fall. These very high sedimentation rates, averaging 15 mm/yr, occurred prior to the 7250 cal BP Betsiamites failure.

4.6 Movement development

The failure developed along a surface with a low angle of about 1 degree. According to the geometry of the slope, the failure was likely initiated at the bottom of the mass and propagated upslope (Figure 4.5).

Most of the failed mass appears to have moved outside the source area. In fact, when comparing the volume of the 54 km² scar on the shelf (1.3 km³) and the volume of the sediment lobe (1 km³) in the Laurentian Channel, only 20% of the debris remained in the source area and on the shelf. When the landslide mass reached the shelf break, it flowed down to the Laurentian Channel and appears on the seismic profile completely remolded. The height potential, more than 200 m, of the shelf break likely helped the sediments to remold, facilitating the mobility of the mass to create the debris fan. In fact, the material did not accumulate on the 8° slope which would have obstructed the movement and reduced the overall flow of the mass.

4.7 Triggering mechanisms

The Betsiamites failure developed over more than 8 km in deposits with slope angle of about 1 degree (Figure 4.5). To create such a large failure in these conditions, diverse factors could have contributed to the development of the failure, its propagation and the

evacuation of the failed mass. The effects of gas and excess pore water pressure resulting from high sedimentation rate or an earthquake are investigated in order to define their potential influence on the development of the Betsiamites failure. As the Betsiamites River had a configuration similar to what it is at present (Figure 4.1) at the time of the failure (Bernatchez 2003) and the water depth of the scar area range between -10 and -140 m, we assume that significant erosive currents did not form to influence the stability of the area. As the failure developed 7520 cal BP, is it difficult to assess if groundwater flow influenced the initiation.

Areas with greater amount of pockmarks in the vicinity of the Betsiamites landslides (Figure 4.2) have been identified (Cauchon-Voyer et al. 2008). The pockmarks in the St. Lawrence estuary have recently been studied and these studies suggest that they formed through the recent and still active release of gas from a reservoir within the Paleozoic sedimentary succession (Pinet et al. 2008; Pinet et al. 2009; Lavoie et al. 2010) and thus are not biogenic gas resulting from synchronous sedimentation of organic matter. Such observations led to the questioning that gas could have been a possible trigger for submarine landslides in the St. Lawrence Estuary (Campbell et al. 2008; Cauchon-Voyer et al. 2008; Pinet et al. 2008). Gas can have an effect on seafloor stability if gas hydrates dissociate (Sultan et al. 2004a) or if free gas influences the permeability and/or the structure of the sediments (Best et al. 2003). Along the North shelf (water <150 mbsl) of the Estuary where there are many failure scars, we can discard that gas hydrates dissociation acted as a trigger mechanism because the conditions for hydrate formation (mainly pressure and temperature), and thus dissociation, were likely never met following the last deglaciation (Pinet et al. 2008).

Another hypothesis for the origin of this failure would be that the very high sedimentation rates estimated prior to the failure could have generated high pore water pressure. For an average thickness (h) of 24 m of sediments having a buoyant unit weight (γ') of 9.7 kN/m³ deposited on an angle of 1.3°, a simple infinite slope stability analysis indicates that the pore pressure required to bring the slope to failure (FS=1), if no other mechanisms are involved, correspond to 0.98 of the weight of the sediment layer. This value corresponds to

230 kPa of overpressure, which is extremely high and hence would require that only 2% of dissipation and consolidation have occurred. Such high overpressures are obtained at much greater depth (more than 250 m with rate up to 35 mm/yr) with more advanced modeling (Hustoft et al. 2009). This simple demonstration indicates that pore water pressure resulting only from high sedimentation rates likely had the time to dissipate and hence did not play an important role in the development of the Betsiamites failure.

Pore pressures generated by rapid sedimentation might not cause failure on their own but could still contribute to failure through another mechanism, e.g. an earthquake. Earthquakes are known to generate slope failure by degrading the shear strength and increasing the pore pressure within a slope. Such mechanisms likely played an important role in the initial triggering of a failure on such a low slope (1°) for the Betsiamites failure. In fact, shaking could cause significant strength reduction in one or several layers within the stratified unit (labeled U4 on Figure 4.3). In the case of the Betsiamites failures, more study are required to investigate the cyclic behavior of the sediments involved, but similar demonstration of the influence of stratification on cyclic strength of stratified sand-silt samples were demonstrated (e.g., Konrad and Dubeau 2003; Dan et al. 2009). A related mechanism has been proposed by Kokusho (1999) who suggested that following the earthquake, the water expelled from the liquefied layer could become trapped between less permeable layers above, which may generate a water film over which the soil mass could start sliding. This mechanism could support the morphological observations within the landslide scar as the deposits were easily transported outside the scar. In fact, to account for the large scar observed on a low slope angle with less than 10 m of debris of the shelf (20%), a significant sliding mechanism must have been involved (Figure 4.3).

4.8 Concluding remarks and future work

The 7250 cal BP Betsiamites slide (1.3 km^3 over 54 km^2) is one of the largest landslides in the St. Lawrence Estuary. The failure surface developed in a thick stratified sequence clayey silt. This paper concludes that gas hydrates dissociation could not have influenced slope stability on the shelves of the St. Lawrence Estuary in the Early Holocene. The stability of the slope prior to failure does not appear to have been influenced by excess pore

pressures resulting independently from high sedimentation rates as dissipation in the deposits could occur efficiently. The most likely trigger for such a large failure would be excess pore pressures resulting from an earthquake. With a volume of more than 1.3 km^3 , it would be important to direct further analysis to determine if this event triggered a tsunami.

4.9 References

- Bernatchez, P. 2003. Évolution littorale holocène et actuelle des complexes deltaïques de Betsiamites et de Manicouagan-Outardes : synthèse, processus, causes et perspectives. Ph.D. thesis, Université Laval, Québec.
- Best, A., Clayton, C., Longva, O., and Szuman, M. 2003. The role of free gas in the activation of submarine slides in Finneidfjord. *In* Submarine Mass Movements and their Consequences 1st International Symposium. Dordrecht, Netherlands: Kluwer Academic Publishers, pp. 419-498.
- Campbell, C., Duchesne, M.J., and Bolduc, A. 2008. Geomorphological and geophysical evidence of Holocene instability on the Southern slope of the Lower St. Lawrence Estuary, Québec. *In* 4e Conférence canadienne sur les géorisques: des causes à la gestion - 4th Canadian Conference on Geohazards : From Causes to Management. Presses de l'Université Laval, Québec, pp. 367-374.
- Cauchon-Voyer, G., Locat, J., and St-Onge, G. 2008. Late-Quaternary morpho-sedimentology and submarine mass movements of the Betsiamites area, Lower St. Lawrence Estuary, Quebec, Canada. *Marine Geology*, **251**(3-4): 233-252.
- Cauchon-Voyer, G., Locat, J., Leroueil, S., St-Onge, G., and Demers, D. 2011. Large-scale subaerial and submarine Holocene and recent mass movements in the Betsiamites area, Quebec, Canada. *Engineering Geology*, **121**(1-2): 28-45.
- Dan, G., Sultan, N., Savoye, B., Deverchere, J., and Yelles, K. 2009. Quantifying the role of sandy-silty sediments in generating slope failures during earthquakes: example from the Algerian margin. *International Journal of Earth Sciences*, **98**(4): 769-789.
- Duchesne, M.J., Long, B.F., Urgeles, R., and Locat, J. 2003. New evidence of slope instability in the Outardes Bay delta area, Quebec, Canada. *Geo-Marine Letters*, **22**(4): 233-242.
- Gagné, H. 2008. Géomorphologie et géologie marine du Quaternaire du secteur Trois-Pistoles-Forestville, estuaire du Saint-Laurent (Québec). M.Sc. thesis, Université Laval, Québec.
- Hustoft, S., Dugan, B., and Mienert, J. 2009. Effects of rapid sedimentation on developing the Nyegga pockmark field: Constraints from hydrological modeling and 3-D seismic data, offshore mid-Norway. *Geochemistry Geophysics Geosystems*, **10**(6): Q06012.
- Kokusho, T. 1999. Water film in liquefied sand and its effect on lateral spread. *ASCE Journal of Geotechnical and Geoenvironmental Engineering*, **125**(10): 817-826.
- Konrad, J.M., and Dubeau, S. Cyclic strength of stratified soil samples. *In* Submarine Mass Movements and their Consequences 1st International Symposium 2003. Kluwer Academic Publishers, pp. 47-57.
- Lajeunesse, P., St-Onge, G., Locat, J., and Labbé, G. 2007. Multibeam bathymetry and morphostratigraphy of submarine gravity flows and slopes failures in the St. Lawrence Gulf and Lower Estuary (Québec, Canada). *In* Submarine Mass Movements and Their Consequences. Springer, p. 27.
- Lavoie, D., Pinet, N., Duchesne, M., Bolduc, A., and Larocque, R. 2010. Methane-derived authigenic carbonates from active hydrocarbon seeps of the St. Lawrence Estuary, Canada. *Marine and Petroleum Geology*, **27**(6): 1262-1272.

- Mosher, D.C. 2008. Submarine Mass Movements: Geohazards with far-reaching implications. *In* 4e Conférence canadienne sur les géorisques: des causes à la gestion - 4th Canadian Conference on Geohazards : From Causes to Management. Presses de l'Université Laval, Québec, pp. 55-62.
- Pinet, N., Duchesne, M., and Lavoie, D. 2009. Linking a linear pockmark train with a buried Palaeozoic structure: a case study from the St. Lawrence Estuary. *Geo-Marine Letters*: 517-522.
- Pinet, N., Duchesne, M., Lavoie, D., Bolduc, A., and Long, B. 2008. Surface and subsurface signatures of gas seepage in the St. Lawrence Estuary (Canada): Significance to hydrocarbon exploration. *Marine and Petroleum Geology*, **25**(3): 271-288.
- St-Onge, G., Stoner, J.S., and Hillaire-Marcel, C. 2003. Holocene paleomagnetic records from the St. Lawrence Estuary, eastern Canada: centennial- to millennial-scale geomagnetic modulation of cosmogenic isotopes. *Earth and Planetary Science Letters*, **209**(1-2): 113-130.
- St-Onge, G., Lajeunesse, P., Duchesne, M., and Gagné, H. 2008. Identification and dating of a key Late Pleistocene stratigraphic unit in the St. Lawrence Estuary and Gulf (Eastern Canada). *Quaternary Science Reviews*, **27**(25-26): 2390-2400.
- Sultan, N., Cochonat, P., Foucher, J., and Mienert, J. 2004. Effect of gas hydrates melting on seafloor slope instability. *Marine Geology*, **213**(1-4): 379-401.

4.10 Acknowledgments

The authors wish to thank the Ministère des Transports du Québec (MTQ), NSERC and FQRNT for their financial support. We thank the MTQ for the permission to use their topographic and LIDAR surveys, borehole, and piezocone soundings data of the Colombier - Betsiamites area. We recognize the contribution of all scientists and crew members on board the Coriolis II, F.G. Creed, and Guillemot vessels. The Canadian Hydrographic Service and GSC-Quebec are also acknowledged for their contribution to bathymetric data acquisition. We thank Homa Lee and Jean-Sébastien L'Heureux for their constructive comments.

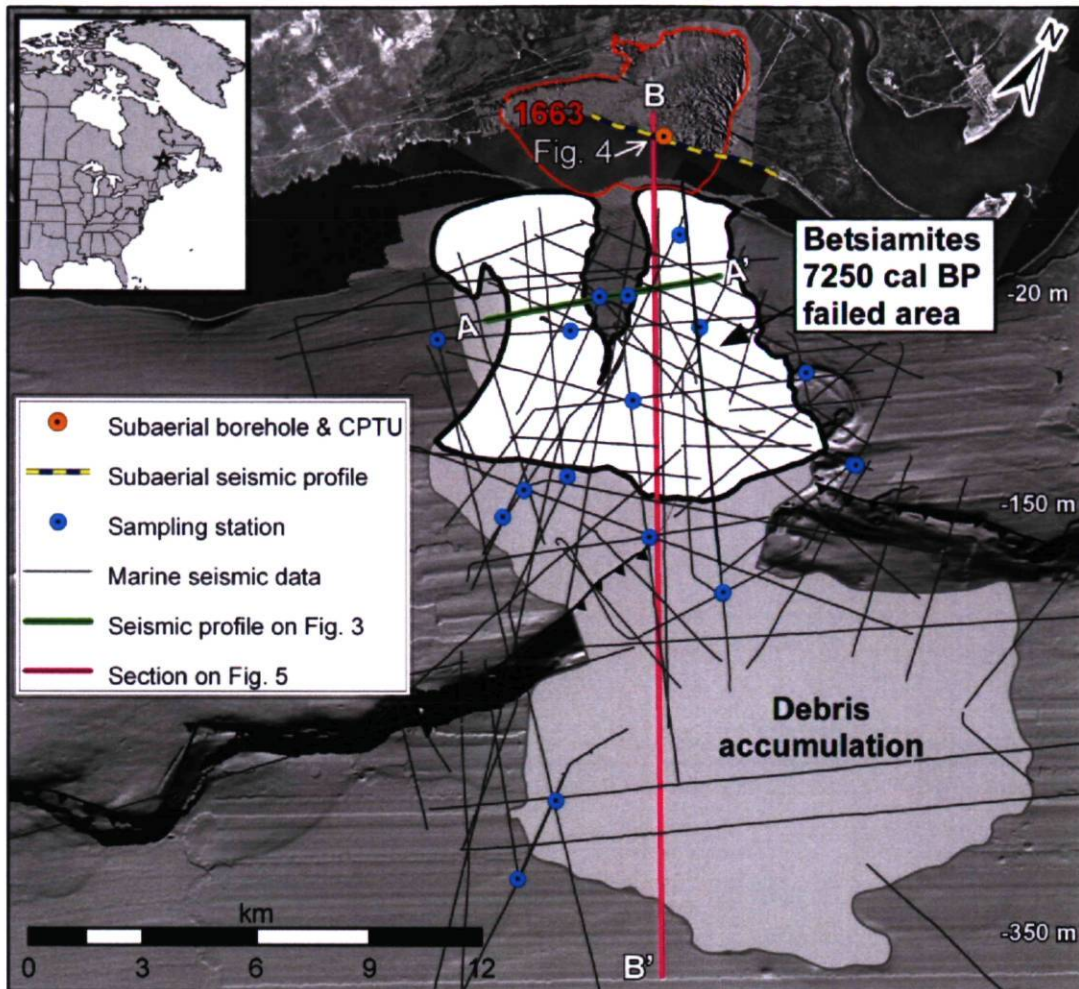


Figure 4.1 Study site and extent of the Betsiamites landslide scar.

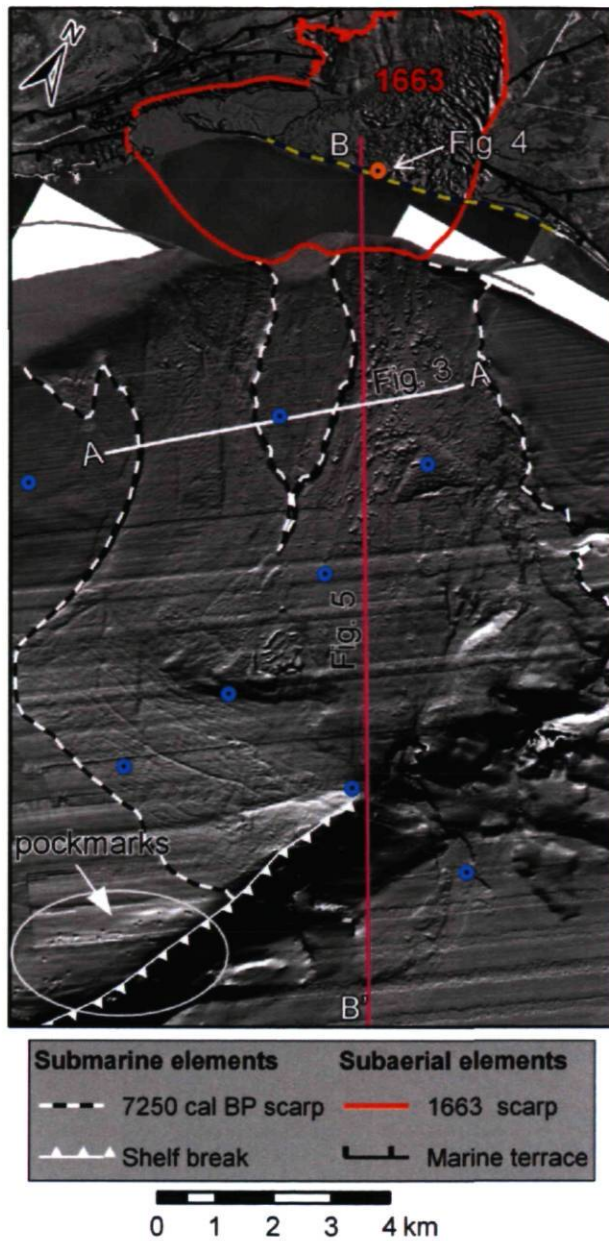


Figure 4.2. Geomorphology of the Betsiamites scar, see Figure 4.1 for legend of data source

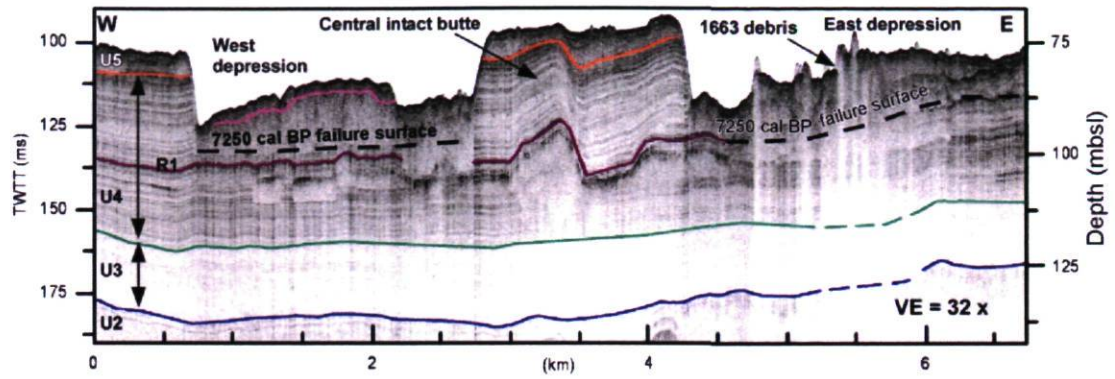


Figure 4.3. Seismic profile across the Betsiamites landslide scar, along line A-A', on Figure 4.2 (Modified from Cauchon-Voyer et al. 2008).

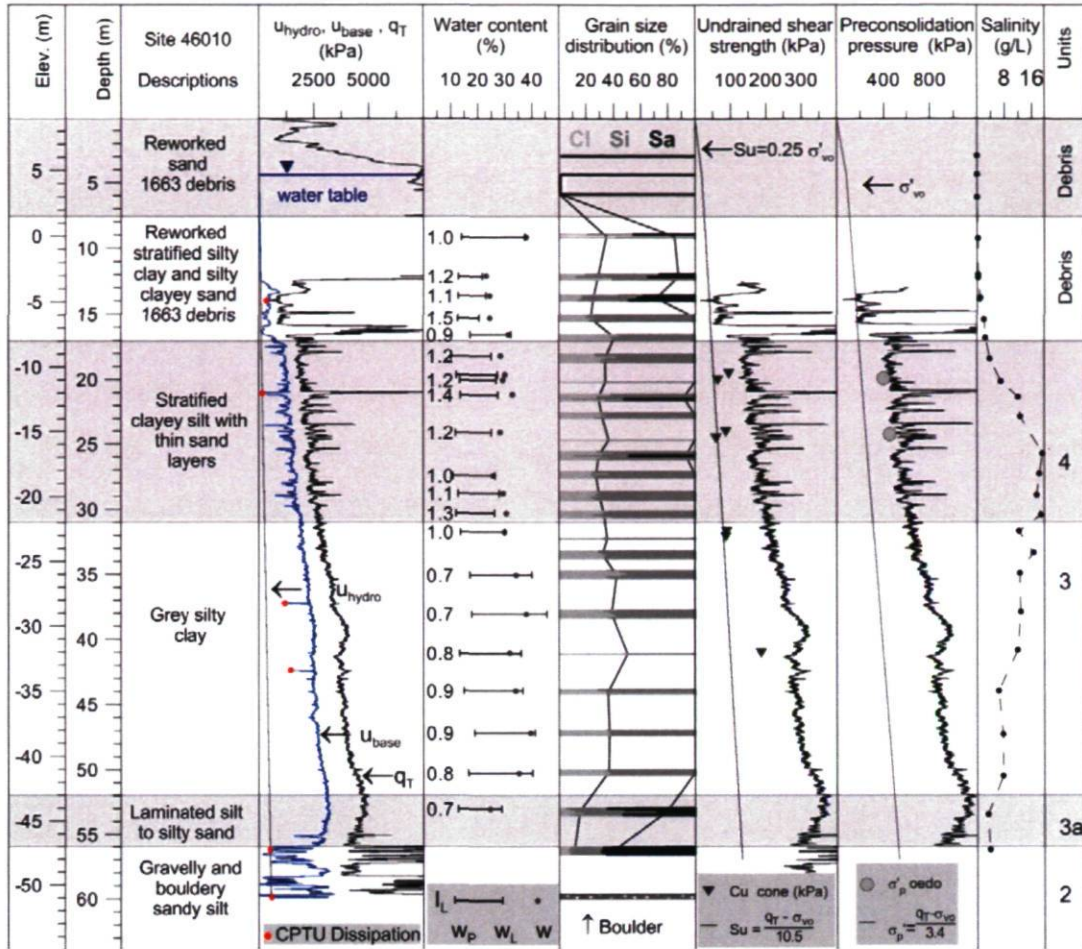


Figure 4.4. Geotechnical profile carried out onshore along the shoreline, modified from (Cauchon-Voyer et al. 2011b). This borehole is located outside the 7250 cal BP scar but inside 1663 failure scar. The 7250 cal BP failure developed within unit 4. Shear strength and preconsolidation pressure profiles are estimated from CPTU results.

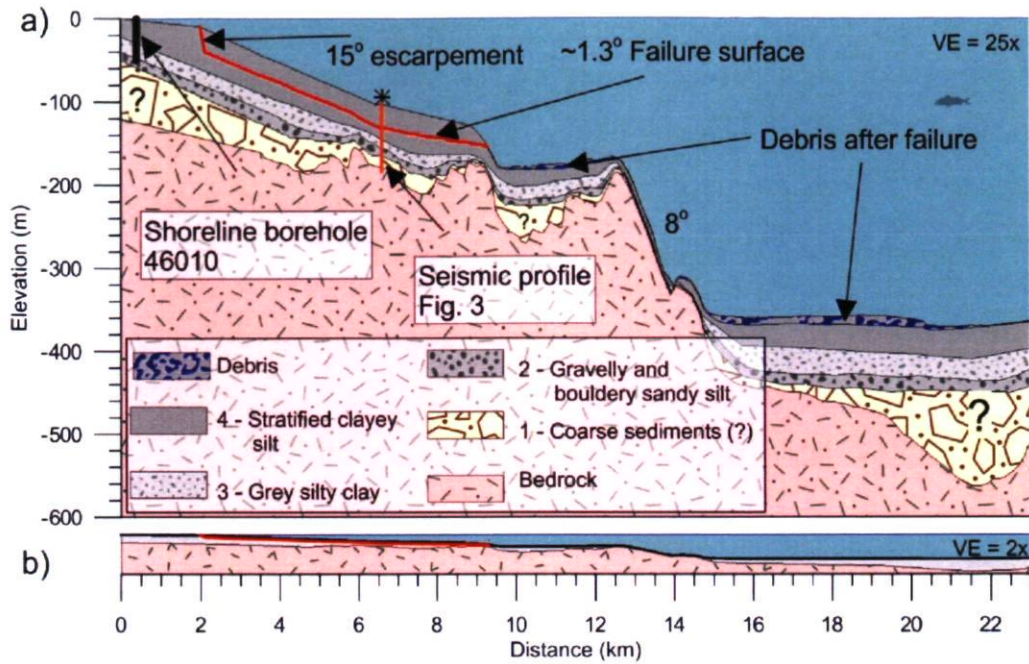


Figure 4.5. a) Morphostratigraphic reconstitution of the Betsiamites landslide showing the topography prior to failure and the accumulation of debris after failure. See location on Figure 4.1, profile B-B'. b) Same profile at VE=2x

Chapitre 5 Synthèse, conclusions et recommandations

Dans l'est du Canada, au pourtour de l'Estuaire du Saint-Laurent, les glissements subaériens (Allard 1984; Locat et al. en préparation) et sous-marins (Duchesne et al. 2003; Lajeunesse et al. 2007; Campbell et al. 2008; Cauchon-Voyer et al. 2008; Gagné 2008; Locat et al. 2008; Mosher 2008) commencent à être mieux documentés et mieux étudiés. L'étude du complexe de glissements de terrain de Betsiamites fournit une occasion d'appliquer une approche d'évaluation des glissements de terrain dans l'estuaire du Saint-Laurent qui intègre divers éléments de l'analyse des mouvements de masse, y compris la définition des conditions en pré-rupture, rupture et post-rupture. Cette approche est nécessaire dans l'optique de mieux définir le danger de glissements de terrain côtiers. De plus, on sait que certains glissements sous-marins peuvent générer d'importants tsunamis et doivent donc être intégrés dans une analyse globale des aléas en milieu côtier. L'analyse de tels événements de tsunamis dans l'Estuaire a été initiée avec la modélisation des mouvements de l'eau induit par les glissements sous-marins de Matane et de St-Siméon (Poncet et al. 2010). Cependant, autant dans l'Estuaire du Saint-Laurent qu'ailleurs dans le monde, très peu d'études traitent principalement sur les glissements dans l'environnement côtier (Christian et al. 1997; L'Heureux 2009; Barnhardt et al. 2010; L'Heureux et al. 2010).

5.1 Synthèse des glissements de Betsiamites

Dans cette thèse, une analyse approfondie des glissements du complexe de Betsiamites a été effectuée. Il a été démontré qu'au moins trois événements de glissement de terrain ont formé le complexe de glissements de terrain de Betsiamites et deux de ces événements ont été étudiés en détails (Figure 5.1). Le plus ancien, peu documenté faute de données, est daté à plus vieux que 9250 cal BP. L'événement de glissement de terrain sous-marin de Betsiamites daté de 7250 cal BP serait le résultat d'un séisme qui aurait généré une surface de rupture dans un dépôt de silt argileux stratifiée. D'un volume de près de 1.3 km³, il est l'un des plus grands glissements répertoriés dans l'Estuaire. Par la suite, l'événement de glissement sous-marin et subaérien de Colombier aurait été causé par le séisme du 5 février 1663. Ce tremblement de terre aurait causé une première rupture dans l'environnement sous-marin. Le glissement de Colombier s'est déroulé en quatre phases successives dont la

première a eu lieu dans le domaine sous-marin. Deux grandes coulées argileuses et un étalement latéral se seraient par la suite déclenchés.

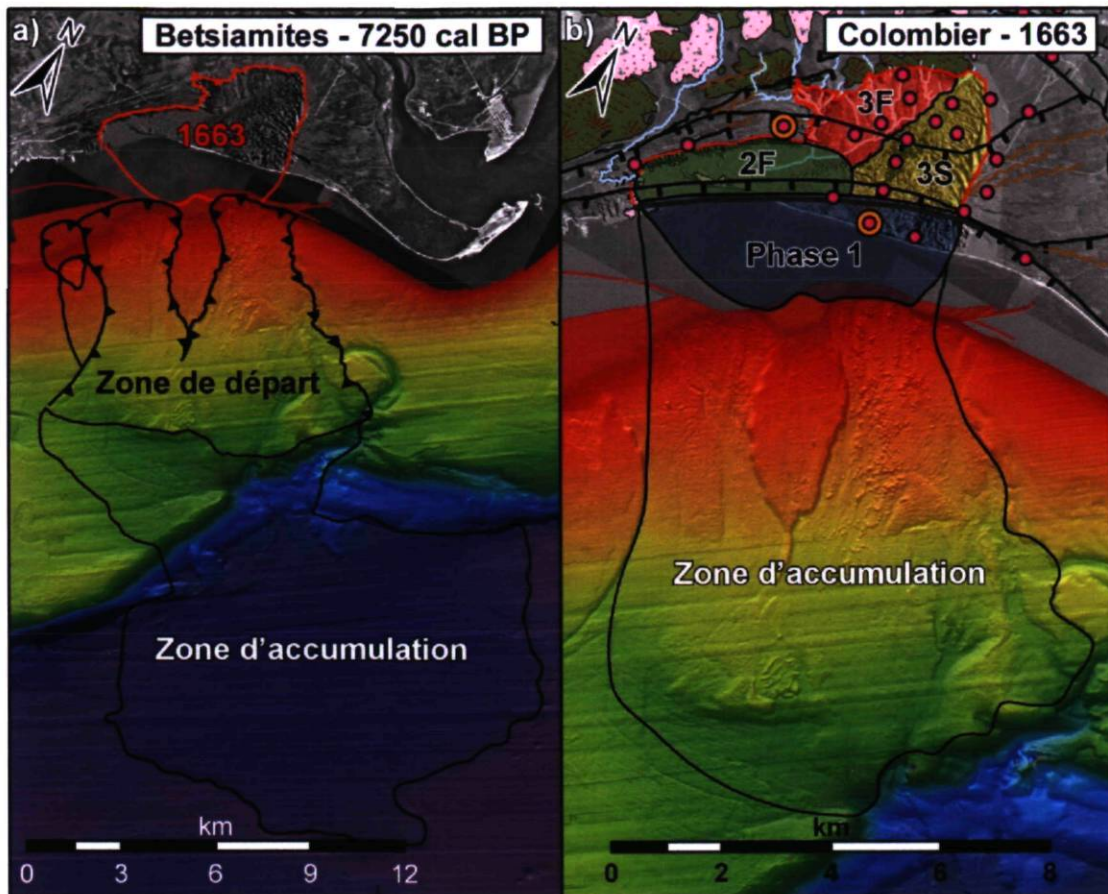


Figure 5.1. Délimitation a) du glissement sous-marin de Betsiamites daté à 7250 cal BP et b) du glissement subaérien et sous-marin de Colombier daté à 1663, qui composent le complexe de glissements de terrain de Betsiamites. Le glissement de Colombier est le résultat de quatre phases de glissement : une rupture sous-marine (1), deux coulées argileuses (2F, 3F) et un étalement latéral (3S).

L'interprétation complète de la séquence des dépôts quaternaires du secteur d'étude, autant dans le domaine subaérien que sous-marin, a été effectuée afin de définir la lithostratigraphie du complexe de glissements de Betsiamites. Dans l'Est du Canada, au retrait de l'inlandsis Laurentidien, la conjonction de l'abaissement glacio-isostatique avec le relèvement eustatique a créé des mers postglaciaires, dont la mer de Goldthwait dans l'estuaire du Saint-Laurent (Dionne 1977). Le delta de la rivière Betsiamites s'est formé

lors d'une période d'abaissement du niveau marin relatif laissant une séquence typique reliée à la déglaciation du continent.

La lithostratigraphie quaternaire des dépôts de l'estuaire du Saint-Laurent a principalement été décrite à l'aide de levés de sismique réflexion. Ces analyses ont été intégrées dans l'étude du complexe de glissements de terrain de Betsiamites. Régionalement, plusieurs auteurs ont présenté des séquences sismostratigraphiques (e.g., Syvitski et Praeg 1989; Josenhans et Lehman 1999; Massé 2001; Duchesne et al. 2007; Duchesne et al. 2010). Par contre, la validation géologique des unités sismiques de l'Estuaire est plutôt limitée en raison de la difficulté de récupérer de longues carottes. Les couches de dépôts hémipélagiques postglaciaires, l'unité sismique 5 selon la numérotation de Syvitski and Praeg (1989), et les dépôts glaciomarins de Goldthwait (unité 3) et les dépôts associés à la régression de celle-ci (unité 4) sont facilement récupérable (e.g, Hart 1987; d'Anglejan 1990; Hein et al. 1993; St-Onge et al. 2003; Gagné 2008; Barletta et al. 2010), mais les couches plus anciennes sont souvent enfouies sous d'importantes épaisseurs de sédiments. Des dépôts glaciomarins proximaux (unité 2), qui auraient été déposés pendant ou avant l'événement climatique du Dryas récent (11 100–10 000 yr BP), ont aussi été identifiés et datés dans l'Estuaire à la hauteur de St-Simon (St-Onge et al. 2008). Par contre, ces études ne permettent pas de valider en continu la séquence sismostratigraphique identifiée dans l'Estuaire ni de définir les propriétés géotechniques des matériaux.

Dans le cadre de l'analyse effectuée dans cette thèse, le forage côtier, fait en association avec un levé de sismique réflexion terrestre, a permis d'échantillonner trois des principales unités sismiques reconnues régionalement. Cette étude procure donc une validation géologique pour l'unité de dépôts paraglaciales prodeltaïques (unité 4), l'unité de dépôts glaciomarins distaux (unité 3) et une unité de dépôts marins proximaux (unité 2). Des dates au ^{14}C variant entre 9265 à 9850 ans ^{14}C (10 136 to 10 697 cal BP) ont aussi été obtenues dans les sédiments glaciomarins distaux (unité 3). Une caractérisation géotechnique de ces 3 unités sismostratigraphiques et lithostratigraphiques a été faite.

Quant aux glissement de Betsiamites, l'intégration des analyses sédimentologiques et géotechniques a permis de reconnaître que la rupture de Betsiamites s'est développée dans

l'unité 4 qui est fortement stratifiée et que ces caractéristiques lithostratigraphiques auraient agi en temps qu'éléments prédisposants au déclenchement de la rupture.

Pour les ruptures de l'événement de Colombier, il a été démontré que la rupture sous-marine (phase 1) s'est aussi développée dans l'unité stratifiée (unité 4), que les coulées argileuses et l'étalement latéral se sont développés dans des matériaux argileux sensibles. Il a aussi été suggéré que la position de la surface de la grande coulée 3F, qui se serait déclenchée suite à la rupture 2F, a été contrôlée par le changement d'indice de liquidité de l'argile dans la pente. L'analyse au site de Betsiamites-Colombier a mis en lumière un site où, pour une même unité lithostratigraphique, les propriétés géotechniques (i.e., l'indice de liquidité et, par le fait même, la sensibilité) sont fortement influencées par leur position dans la colonne stratigraphique par rapport au niveau de la mer. En fait, il a été démontré que l'indice de liquidité est influencé par le lessivage des sédiments, qui en retour est influencé par la position dans la colonne sédimentaire. Finalement, il a été reconnu que les escarpements latéraux de la cicatrice subaérienne sont pratiquement enlignés avec les escarpements latéraux de la cicatrice de l'événement de Betsiamites.

L'analyse de la stabilité des talus à l'aide de la méthode à l'équilibre limite a démontré que pour les deux événements principaux de glissements de terrain, les forces sismiques ont été nécessaires pour déclencher la rupture. Ces tremblements de terrain ont donc agi en temps qu'élément déclencheur des glissements. Finalement, l'analyse a aussi démontré que les glissements subaériens de l'événement de Colombier (phases 2F, 3S et 3S) dans les dépôts d'argile sensibles ont été déclenchés par le déchargement en pied de talus causé par la première rupture sous-marine (phase 1).

5.1.1 Données morphométriques des glissements de terrain du complexe de Betsiamites

Les données morphométriques (Figure 5.2) des événements de glissements de terrain du complexe de Betsiamites sont résumées au Tableau 5.1.

Tableau 5.1. Données morphométriques des événements de glissements de terrain du complexe de Betsiamites.

Événement	Phase	A_s	A_f	V		H_b	$H_i =$								
		km^2	km^2	km^3	hm^3	m	V/A_s	H_f	ΔH	β_s	R	L_r	L	β_f	$\Delta H/L$
9250 cal BP	*debris seulement	-	52	0.2	200	-	-	3.8	-	-	-	-	9.5	1.2	-
Betsiamites 7250 cal BP	Ruptures est et ouest	54	185	1.3	1276	40	24	9.5	365	1.3	8	12	20		0.018
Colombier 1663	Sous-marine (1)	9.3	36	0.15	145	10	15.6	4.1	150	0.9	1.9	6.1	8	-	0.019
	Coulée argileuse (2F)	3.4	31	0.13	130	45	38	4.6	200	0.6	1	9.0	10		0.020
	Coulée argileuse (3F)	2.5	38	0.075	75	40	30	2.1	220	0.9	2.8	8.7	11.5		0.019
	Étalement latéral (3S)	3.7	39	0.18	180	50	48	5.1	220	0.9	2.5	9.0	11.5		0.019

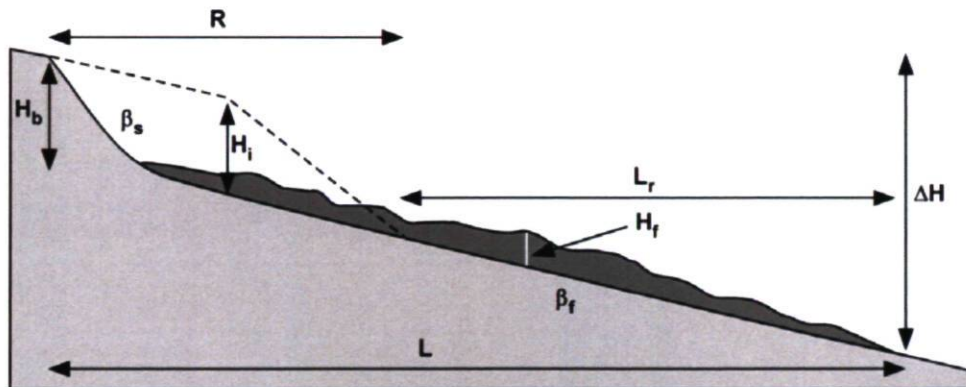


Figure 5.2 Définition des paramètres morphométriques.

5.2 Conclusions

Les travaux présentés dans cette thèse documentent les grands glissements répertoriés dans l'estuaire du Saint-Laurent au pourtour du delta de la rivière Betsiamites. Cette étude présente une reconstitution complète de l'évolution paléogéographique intégrant le domaine

subaérien et marin de la région de Betsiamites. Les principales conclusions au sujet de l'étude sont les suivantes :

- La lithostratigraphie du secteur du delta de la rivière Betsiamites est composée d'unités principales mises en place lors de la déglaciation du continent, l'invasion de la mer de Goldthwait et l'émersion des terres qui a suivie. Quatre de ses unités ont été étudiées en détails.
- Le complexe de glissements de terrain de Betsiamites est formé d'au moins trois événements dont deux sont majeurs et ont laissé des traces significatives dans la morphostratigraphie locale.
- L'événement de glissement de terrain sous-marin de Betsiamites, daté de 7250 cal BP, a impliqué un volume de 1.3 km³ et aurait été déclenché par un séisme. La surface de rupture de cet événement est localisée dans une unité fortement stratifiée de silt argileux.
- L'événement de glissement de terrain sous-marin et subaérien de Colombier date de 1663.
- L'intégration des analyses géomorphologiques, lithostratigraphiques, sismostratigraphiques, géotechniques, dans les domaines subaérien et sous-marin, couplée avec des analyses à rebours de la stabilité des pentes, indique que le glissement de Colombier s'est déroulé en quatre phases successives dont la première a eu lieu dans le domaine sous-marin.
- Deux grandes coulées argileuses et un étalement latéral se seraient déclenchés à la suite de la première rupture sous-marine.
- En créant de l'espace en bas de talus, la première rupture sous-marine (1) a permis le développement d'une surface de rupture passant sous le niveau de la mer pour l'étalement latéral (3S).

- L'analyse à rebours de la stabilité de la pente sous-marine de l'événement de 1663 indique que cette rupture n'aurait probablement pas été déclenchée sans l'action d'un séisme.
- Cette étude a aussi mis en relief les variations en post-déposition de certaines propriétés géotechniques au sein d'une même unité lithostratigraphique en fonction de la position dans la colonne sédimentaire.
- Cette étude présente de plus un cas où certaines propriétés géotechniques des dépôts dans la zone de départ et la zone accumulation sont demeurées constantes.
- L'événement de 1663 de Colombier est l'un des plus grands glissements subaériens documentés au Canada.
- La phase 1 du glissement de Colombier indique que des glissements du domaine marin peuvent mettre à risque des infrastructures côtières.

Cette étude a démontré le caractère particulier du secteur de Betsiamites – Colombier. Le grand complexe de glissements de terrain de Betsiamites s'est formé en raison d'une association de plusieurs facteurs de prédispositions et déclencheurs causant une série d'événements de glissements de terrain et n'est pas nécessairement représentatif de l'ensemble de la côte le long des berges de l'estuaire du Saint-Laurent. Cette étude a par contre démontré que dans une stratégie globale de reconnaissances des glissements côtiers il est requis de prendre en considération l'environnement sous-marin adjacent.

5.3 Recommandations

Voici quelques recommandations générales quant à l'orientation de projets de recherche futurs au pourtour de l'estuaire du Saint-Laurent et du delta de la rivière Betsiamites :

- Modéliser la vague de tsunami que le glissement de 7250 cal BP aurait pu générer.
- Effectuer des relevés de terrain sur la rive-sud du Saint-Laurent afin de répertorier une couche de tsunamite potentiellement laissée par l'événement de 7250 cal BP.

- Investiguer le rôle des concrétions calcaires sur le comportement des matériaux.
- Définir le comportement dynamique des sédiments fins (argile et silt) ayant de minces stratifications de sable par rapport à des sédiments argileux homogènes.
- Investiguer le rôle de la stratification dans le lessivage de l'argile marine.
- Investiguer le rôle du gaz libre s'échappant des événements de gaz sur la stabilité des pentes sous-marines.

Bibliographie de la thèse

- Adams, J., and Atkinson, G. 2003. Development of seismic hazard maps for the proposed 2005 edition of the National Building Code of Canada. *Canadian Journal of Civil Engineering*, **30**(2): 255-271.
- Allard, J.-D. 1984. Zones exposées aux mouvements de terrain, région de Chutes-aux-Outardes, Ministère de l'Énergie et des Ressources, Québec.
- Bardet, J.P., Synolakis, C.E., Davies, H.L., Imamura, F., and Okal, E.A. 2003. Landslide tsunamis: Recent findings and research directions. *Pure and Applied Geophysics*, **160**(10-11): 1793-1809.
- Barletta, F., St-Onge, G., Stoner, J.S., Lajeunesse, P., and Locat, J. 2010. A high-resolution Holocene paleomagnetic secular variation and relative paleointensity stack from eastern Canada. *Earth and Planetary Science Letters*, **298**(1-2): 162-174.
- Barnhardt, W., Jaffe, B., Kayen, R., and Cochrane, G. 2010. Influence of near-surface stratigraphy on coastal landslides at Sleeping Bear Dunes National Lakeshore, Lake Michigan, USA.
- Bernatchez, P. 2003. Évolution littorale holocène et actuelle des complexes deltaïques de Betsiamites et de Manicouagan-Outardes : synthèse, processus, causes et perspectives. Ph.D. thesis, Université Laval, Québec.
- Best, A., Clayton, C., Longva, O., and Szuman, M. The role of free gas in the activation of submarine slides in Finneidfjord. *In Submarine Mass Movements and their Consequences 1st International Symposium 2003*. Dordrecht, Netherlands: Kluwer Academic Publishers, pp. 419-498.
- Blott, S.J., and Pye, K. 2001. GRADISTAT: A grain size distribution and statistics package for the analysis of unconsolidated sediments. *Earth Surface Processes and Landforms*, **26**(11): 1237-1248.
- Boespflug, X., Long, B.F.N., and Occhietti, S. 1995. Cat-Scan in Marine Stratigraphy - a Quantitative Approach. *Marine Geology*, **122**(4): 281-301.
- Campbell, B.A., and Nottingham, D. 1999. Anatomy of a Landslide-Created Tsunami at Skagway, Alaska November 3, 1994. *Science of Tsunami Hazards*, **17**(1): 19-48.
- Campbell, C., Duchesne, M.J., and Bolduc, A. 2008. Geomorphological and geophysical evidence of Holocene instability on the Southern slope of the Lower St. Lawrence Estuary, Québec. *In 4e Conférence canadienne sur les géorisques: des causes à la gestion - 4th Canadian Conference on Geohazards : From Causes to Management*. Presses de l'Université Laval, Québec, pp. 367-374.
- Cauchon-Voyer, G. 2007. Morpho-sédimentologie et mouvements de masse au large de la Rivière Betsiamites, estuaire du Saint-Laurent, Québec. M.Sc. thesis, Université Laval, Québec.
- Cauchon-Voyer, G., Locat, J., and St-Onge, G. 2008. Late-Quaternary morpho-sédimentology and submarine mass movements of the Betsiamites area, Lower St. Lawrence Estuary, Quebec, Canada. *Marine Geology*, **251**(3-4): 233-252.
- Cauchon-Voyer, G., Locat, J., St-Onge, G., Leroueil, S., and Lajeunesse, P. 2011a. Development and potential trigger mechanisms for a large Holocene landslide in the Lower St. Lawrence Estuary *In 5th International Symposium on Submarine Mass Movements and Their Consequences*, Kyoto, Japan. Springer.

- Cauchon-Voyer, G., Locat, J., Leroueil, S., St-Onge, G., and Demers, D. 2011b. Large-scale subaerial and submarine Holocene and recent mass movements in the Betsiamites area, Quebec, Canada. *Engineering Geology*, **121**(1-2): 28-45.
- Chapman, H.D. 1695. Cation exchange capacity. *In Methods of Soil Analysis, Part 2. Edited by C.A. Black, American Society of Agronomy.* pp. 891-901.
- Christian, H.A., Mosher, D.C., Mulder, T., Barrie, J.V., and Courtney, R.C. 1997. Geomorphology and potential slope instability on the Fraser River Delta foreslope, Vancouver, British Columbia. *Canadian Geotechnical Journal*, **34**(3): 432-446.
- Cruden, D.M., and Varnes, D.J. 1996. Landslide Types and Processes. *In Landslides Investigation and Mitigation. Edited by A.K. Turner and R.L. Schuster, Transportation Research Board, Washington DC.* pp. 36-75.
- d'Anglejan, B. 1990. Recent sediments and sediment transport processes in the St. Lawrence Estuary. *In Oceanography of a Large-Scale Estuarine System-The St. Lawrence. Edited by M.I.a.S. El-Sabh, N., Springer-Verlag, New York.* pp. 109-129.
- Dan, G., Sultan, N., and Savoye, B. 2007. The 1979 Nice harbour catastrophe revisited: Trigger mechanism inferred from geotechnical measurements and numerical modelling. *Marine Geology*, **245**(1-4): 40-64.
- Dan, G., Sultan, N., Savoye, B., Deverchere, J., and Yelles, K. 2009. Quantifying the role of sandy-silty sediments in generating slope failures during earthquakes: example from the Algerian margin. *International Journal of Earth Sciences*, **98**(4): 769-789.
- De Blasio, F., Engvik, L., and Elverhøi, A. 2006. Sliding of outrunner blocks from submarine landslides. *Geophysical Research Letters*, **33**(6): L06614.
- Demers, D., and Leroueil, S. 2002. Evaluation of preconsolidation pressure and the overconsolidation ratio from piezocone tests of clay deposits in Quebec. *Canadian Geotechnical Journal*, **39**(1): 174-192.
- Dionne, J.C. 1977. La Mer de Goldthwait au Québec. *Géographie Physique et Quaternaire*, **16**(1-2): 61-80.
- Dionne, J.C. 1988. Holocene Relative Sea-Level Fluctuations in the St Lawrence Estuary, Quebec, Canada. *Quaternary Research*, **29**(3): 233-244.
- Dionne, J.C. 2001. Relative Sea-Level changes in the St. Lawrence estuary from deglaciation to present day. *In Deglacial History and Relative Sea-Level Changes, Northern New England and Adjacent Canada. Edited by T.K. Weddle and M.J. Retelle, Geological Society of America Special Paper, Boulder, Colorado.* pp. 271-284.
- Dionne, J.C., and Coll, D. 1995. Le niveau marin relatif dans la région de Matane (Québec), de la déglaciation à nos jours. *Géographie Physique et Quaternaire*, **49**(3): 363-380.
- Dionne, J.C., and Occhietti, S. 1996. Aperçu du Quaternaire à l'embouchure du Saguenay, Québec. *Géographie Physique et Quaternaire*, **50**: 5-34.
- Dredge, L.A. 1976. Quaternary geomorphology of the Quebec North Shore, Godbout to Sept-Iles. Ph.D. thesis, University of Waterloo, Waterloo.
- Dredge, L.A. 1983. Surficial Geology of the Sept-Îles area. Geological survey of Canada.
- Dreimanis, A. 1962. Quantitative gasometric determination of calcite and dolomite by using Chittick apparatus. *Journal of Sedimentary Research*, **32**(3): 520-529.

- Dubois, J.-M.M. 1977. La déglaciation de la Côte-Nord du Saint-Laurent. *Geographie Physique et Quaternaire*, **16**(3-4): 229-246.
- Duchesne, M., Pinet, N., Bolduc, A., Bédard, K., and Lavoie, D. 2007. Seismic stratigraphy of the lower St Lawrence River estuary (Quebec) Quaternary deposits and seismic signature of the underlying geological domains. Geological Survey of Canada.
- Duchesne, M., Pinet, N., Bédard, K., St-Onge, G., Lajeunesse, P., Campbell, D., and Bolduc, A. 2010. Role of the bedrock topography in the Quaternary filling of a giant estuarine basin: the Lower St. Lawrence Estuary, Eastern Canada. *Basin Research*, **22**(6): 933-951.
- Duchesne, M.J., Long, B.F., Urgeles, R., and Locat, J. 2003. New evidence of slope instability in the Outardes Bay delta area, Quebec, Canada. *Geo-Marine Letters*, **22**(4): 233-242.
- Ferris, L. 1986. Les grands glissements de terrain de Rivière-Saint-Jean, Moyenne Côte-Nord du Saint-Laurent: hypothèse du tremblement de terre, Undergraduate thesis Université de Sherbrooke.
- Franconi, A., Sharma, K.N.M., and Laurin, A.F. 1975. Région des rivières Betsiamites (Bersimis) et Moisie. Québec; Ministère des richesses naturelles, Direction générale des mines, Service de l'exploration géologique.
- Gadd, N.R. 1974. Limites maximales de la submersion marine au tardiglaciaire dans le bassin du Saint-Laurent - 18 cartes manuscrites à 1:250 000, p. 6.
- Gagné, H. 2008. Géomorphologie et géologie marine du Quaternaire du secteur Trois-Pistoles-Forestville, estuaire du Saint-Laurent (Québec). M.Sc. thesis, Université Laval, Québec.
- Hampton, M. 1972. The role of subaqueous debris flow in generating turbidity currents. *Journal of Sedimentary Petrology*, **42**(4): 775-793.
- Hart, B.S. 1987. The Evolution of the Outardes Estuary. M.Sc. thesis, Université du Québec à Rimouski, Rimouski.
- Hart, B.S., and Long, B.F. 1996. Forced regressions and lowstand deltas: Holocene Canadian examples. *Journal of Sedimentary Research*, **66**(4): 820-829.
- Hein, F.J., Syvitski, J.P.M., Dredge, L.A., and Long, B.F. 1993. Quaternary Sedimentation and Marine Placers Along the North Shore, Gulf of St-Lawrence. *Canadian Journal of Earth Sciences*, **30**(3): 553-574.
- Hillaire-Marcel, C., and Causse, C. 1989. Chronologie Th/U des concrétions calcaires des varves du lac glaciaire de Deschaillons (Wisconsinien inférieur). *Canadian Journal of Earth Sciences*, **26**(5): 1041-1052.
- Hustoft, S., Dugan, B., and Mienert, J. 2009. Effects of rapid sedimentation on developing the Nyegga pockmark field: Constraints from hydrological modeling and 3-D seismic data, offshore mid-Norway. *Geochemistry Geophysics Geosystems*, **10**(6): Q06012.
- Johnson, A.M. 1984. Debris flow. *In Slope Instability. Edited by D. Brunsten and D. Prior*, Wiley, New York. pp. 257-361.
- Josenhans, H., and Lehman, S. 1999. Late glacial stratigraphy and history of the Gulf of St. Lawrence, Canada. *Canadian Journal of Earth Sciences*, **36**(8): 1327-1345.
- Kokusho, T. 1999. Water film in liquefied sand and its effect on lateral spread. *ASCE Journal of Geotechnical and Geoenvironmental Engineering*, **125**(10): 817-826.

- Konrad, J.M., and Dubeau, S. Cyclic strength of stratified soil samples. *In* Submarine Mass Movements and their Consequences 1st International Symposium 2003. Kluwer Academic Publishers, pp. 47-57.
- L'Heureux, J.-S. 2009. A multidisciplinary study of shoreline landslides: From geological development to geohazard assessment in the bay of Trondheim, Mid-Norway. Ph.D. thesis, Norwegian University of Science and Technology, Trondheim, Norvège.
- L'Heureux, J.-S., Hansen, L., Longva, O., Emdal, A., and Grande, L. 2010. A multidisciplinary study of submarine landslides at the Nidelva fjord delta, Central Norway—implications for geohazards assessment. *Norw. J. Geol.*, **90**: 1–20.
- Laflamme, J.C.K. 1900. Modifications remarquables causées à l'embouchure de la rivière Sainte-Anne par l'éboulement de St-Alban, *Transactions de la Société royale du Canada* IV. pp. 175-177.
- Lajeunesse, P., St-Onge, G., Locat, J., and Labbé, G. 2007. Multibeam bathymetry and morphostratigraphy of submarine gravity flows and slopes failures in the St. Lawrence Gulf and Lower Estuary (Québec, Canada). *In* Submarine Mass Movements and Their Consequences. Springer, p. 27.
- Lamontagne, M., Keating, P., and Perreault, S. 2003. Seismotectonic characteristics of the Lower St. Lawrence Seismic Zone, Quebec: insights from geology, magnetics, gravity, and seismics. *Canadian Journal of Earth Sciences*, **40**(2): 317-336.
- Lamontagne, M., Demers, D., and Savopol, F. 2007. Description et analyse du glissement de terrain meurtrier du 25 octobre 1870 dans le rang des Lahaie, Sainte-Geneviève-de-Batiscan, Québec. *Canadian Journal of Earth Sciences*, **44**(7): 947-960.
- Lamontagne, M., Halchuk, S., Cassidy, J., and Rogers, G. 2008. Significant Canadian Earthquakes of the Period 1600-2006. *Seismological Research Letters*, **79**(2): 211.
- Lasalle, P., and Chagnon, J.-Y. 1968. An ancient landslide along the Saguenay River, Quebec. *Canadian Journal of Earth Sciences*, **5**(3): 548-549.
- Lavoie, D., Pinet, N., Duchesne, M., Bolduc, A., and Larocque, R. 2010. Methane-derived authigenic carbonates from active hydrocarbon seeps of the St. Lawrence Estuary, Canada. *Marine and Petroleum Geology*, **27**(6): 1262-1272.
- Lefebvre, G. 1981. Fourth Canadian Geotechnical Colloquium: Strength and slope stability in Canadian soft clay deposits. *Canadian Geotechnical Journal*, **18**(3): 420-442.
- Lefebvre, G., Rosenberg, P., Paquette, J., and Lavallee, J.G. 1991. The September 5, 1987, landslide on the La Grande River, James Bay, Quebec, Canada *Canadian Geotechnical Journal*, **28**(2): 263-275.
- Lefebvre, G., Leboeuf, D., Hornych, P., and Tanguay, L. 1992. Slope failures associated with the 1988 Saguenay earthquake, Quebec, Canada. *Canadian Geotechnical Journal*, **29**(1): 117-130.
- Leroueil, S. 2001. Natural slopes and cuts: movement and failure mechanisms. *Géotechnique*, **51**(3): 197-243.
- Leroueil, S., Tavenas, F., and Le Bihan, J.-P. 1983. Propriétés caractéristiques des argiles de l'est du Canada. *Canadian Geotechnical Journal*, **20**(4): 681-705.
- Leroueil, S., Vaunat, J., Locat, J., Picarelli, L., Lee, H., and Faure, R. Geotechnical characterization of slope movements. *In* 7th International Symposium on Landslides, Trondheim, 1996, pp. 53–74.

- Levesque, C., Locat, J., and Leroueil, S. 2006. Dating submarine mass movements triggered by earthquakes in the Upper Saguenay Fjord, Quebec, Canada. *Norwegian Journal of Geology*, **86**(3): 231-242.
- Locat, J. 1997. Normalized Rheological Behaviour of Fine Muds and Their Flow Properties in a Pseudoplastic Regime. *In Debris-Flow Hazards Mitigation: Mechanics, Prediction, and Assessment*, Water Resources Engineering Division, American Society of Civil Engineers, New York. pp. 260-269.
- Locat, J. 2008. Localisation et magnitude du séisme du 5 février 1663 (Québec) revues à l'aide des mouvements de terrain. *In 4e Conférence canadienne sur les géorisques: des causes à la gestion - 4th Canadian Conference on Geohazards : From Causes to Management*. Presses de l'Université Laval, Québec, pp. 429-444.
- Locat, J. 2011. La localisation et la magnitude du séisme du 5 février 1663 (Charlevoix) revues à l'aide des mouvements de terrain. *Canadian Geotechnical Journal*, **In press**.
- Locat, J., and Demers, D. 1988. Viscosity, Yield Stress, Remolded Strength, and Liquidity Index Relationships for Sensitive Clays. *Canadian Geotechnical Journal*, **25**(4): 799-806.
- Locat, J., and Lee, H.J. 2002. Submarine landslides: advances and challenges. *Canadian Geotechnical Journal*, **39**(1): 193-212.
- Locat, J., Tanaka, H., Tan, T.S., Dasari, G.R., and Lee, H. 2003. Natural soils: geotechnical behaviour and geological knowledge. *In Characterisation & Engineering Properties of Natural Soils Vol 1*. Edited by T.S. Tan, K.K. Phoon, D.W. Hight, and S. Leroueil. pp. 3-28.
- Locat, J., Levesque, C., Locat, P., Cauchon-Voyer, G., Leroueil, S., Godin, A., and Sanfaçon, R. Aperçu des mouvements de masse sous-marins au large de la rivière Betsiamites, estuaire du Saint-Laurent, Québec, Canada. *In Conférence Canadiane de Géotechnique*, Québec, 2004.
- Locat, J., Amiguet, C., Cauchon-Voyer, G., Bolduc, A., Demers, D., Mosher, D., Sanfaçon, R., Godin, A., Lajeunesse, P., and St-Onge, G. 2008. Instabilités sous-marines et côtières le long de la rive nord du Saint-Laurent, entre Pointe-des-Monts et Saint-Siméon : analyse préliminaire. *In Quebec 2008: 400 Years of Discoveries*. Joint Meeting of the Geological Association of Canada, Mineralogical Association of Canada, Society of Economic Geologists and the Society for Geology Applied to Mineral Deposits. *Revue des résumés*, Québec, p. 99.
- Locat, P., Leroueil, S., Locat, J., and Demers, D. en préparation. Analyse du glissement de terrain de Havre-Saint-Pierre, avril 1980, Québec, Canada.
- Longva, O., Janbu, N., Blikra, L.H., and Boe, R. 2003. The 1996 Finneidfjord Slide, seafloor failure and slide dynamics. *In Submarine Mass Movements and Their Consequences*. Kluwer Academic Publishers, pp. 531– 538.
- Lunne, T., Robertson, P.K., and Powell, J.J.M. 1997. Cone penetration testing in geotechnical practice. Blackie Academic - Chapman-Hall Publishers.
- Massé, M. 2001. Évolution générale des dépôts quaternaires sous l'estuaire du St-Laurent entre l'Îles aux Lièvres et Rimouski. M.Sc. thesis, Université du Québec à Rimouski, Rimouski.
- Massé, M., and Long, B. 2001. Slope instability seismic signatures in Quaternary sediments of the St. Lawrence estuary. *In Proceedings of 2001 An Earth Odyssey*,

- International Association of Hydrogeologists. The Canadian Geotechnical Society, pp. 784–791.
- McKenna, G.T., Luternauer, J.L., and Kostaschuk, R.A. 1992. Large-scale mass-wasting events on the Fraser River Delta front near sand heads, British Columbia. *Canadian Geotechnical Journal*, **29**(1): 151-156.
- Mosher, D.C. 2008. Submarine Mass Movements: Geohazards with far-reaching implications. *In* 4e Conférence canadienne sur les géorisques: des causes à la gestion - 4th Canadian Conference on Geohazards : From Causes to Management. Presses de l'Université Laval, Québec, pp. 55-62.
- Mulder, T., and Alexander, J. 2001. The physical character of subaqueous sedimentary density flows and their deposits. *Sedimentology*, **48**(2): 269-299.
- Mulder, T., Savoye, B., and Syvitski, J.P.M. 1997. Numerical modelling of a mid-sized gravity flow: The 1979 Nice turbidity current (dynamics, processes, sediment budget and seafloor impact). *Sedimentology*, **44**(2): 305-326.
- Perret, D., Locat, J., and Leroueil, S. 1995. Strength development with burial in fine-grained sediments from the Saguenay Fjord, Quebec. *Canadian Geotechnical Journal*, **32**(2): 247-262.
- Pinet, N., Duchesne, M., and Lavoie, D. 2009. Linking a linear pockmark train with a buried Palaeozoic structure: a case study from the St. Lawrence Estuary. *Geo-Marine Letters*: 517-522.
- Pinet, N., Duchesne, M., Lavoie, D., Bolduc, A., and Long, B. 2008. Surface and subsurface signatures of gas seepage in the St. Lawrence Estuary (Canada): Significance to hydrocarbon exploration. *Marine and Petroleum Geology*, **25**(3): 271-288.
- Piper, D.J.W., Hiscott, R.N., and Normark, W.R. 1999. Outcrop-scale acoustic facies analysis and latest Quaternary development of Hueneme and Dume submarine fans, offshore California. *Sedimentology*, **46**(1): 47-78.
- Piper, D.J.W., Shor, A.N., Farre, J.A., Oconnell, S., and Jacobi, R. 1985. Sediment Slides and Turbidity Currents on the Laurentian Fan - Sidescan Sonar Investigations near the Epicenter of the 1929 Grand Banks Earthquake. *Geology*, **13**(8): 538-541.
- Poncet, R., Campbell, C., Dias, F., Locat, J., and Mosher, D. A Study of the Tsunami Effects of Two Landslides in the St. Lawrence Estuary. *In* Submarine Mass Movements and Their Consequences 2010. Springer Netherlands, pp. 755-764.
- Potvin, J., Pellerin, F., Demers, D., Robitaille, D., La Rochelle, P., and Chagnon, J.-Y. 2001. Revue et investigation complémentaire du site du glissement de Saint-Jean-Vianney. *In* 54th Canadian Geotechnical Conference pp. 792–800.
- Prior, D.B., Bornhold, B.D., and Johns, M.W. 1984. Depositional Characteristics of a Submarine Debris Flow. *Journal of Geology*, **92**(6): 707-727.
- Pullan, S.E., and MacAulay, H.A. 1987. An in-hole shotgun source for engineering seismic surveys. *Geophysics*, **52**(7): 985-996.
- Reimer, P., Baillie, M., Bard, E., Bayliss, A., Beck, J., Blackwell, P., Ramsey, C., Buck, C., Burr, G., and Edwards, R. 2009. IntCal09 and Marine09 radiocarbon age calibration curves, 0-50,000 years cal BP.
- Robertson, P., and Campanella, R. 1983. Interpretation of cone penetration tests. Part I: Sand. *Canadian Geotechnical Journal*, **20**(4): 718-733.

- Robertson, P.K. 1990. Soil classification using the cone penetration test. *Canadian Geotechnical Journal*, **27**(1): 151-158.
- Santamarina, J.C., Klein, K.A., Wang, Y.H., and Prencke, E. 2002. Specific surface: determination and relevance. *Canadian Geotechnical Journal*, **39**(1): 233-241.
- Smith, W. 1962. Earthquakes of eastern Canada and adjacent areas, 1534-1927, Publications of the Dominion Observatory, Ottawa. pp. 271-301.
- St-Onge, G., Stoner, J.S., and Hillaire-Marcel, C. 2003. Holocene paleomagnetic records from the St. Lawrence Estuary, eastern Canada: centennial- to millennial-scale geomagnetic modulation of cosmogenic isotopes. *Earth and Planetary Science Letters*, **209**(1-2): 113-130.
- St-Onge, G., Mulder, T., Francus, P., and Long, B. 2007. Continuous physical properties of cored marine sediments. *In Proxies in Late Cenozoic Paleocyanography. Edited by C. Hillaire-Marcel and A. De Vernal, Elsevier Science.* pp. 63-98.
- St-Onge, G., Lajeunesse, P., Duchesne, M., and Gagné, H. 2008. Identification and dating of a key Late Pleistocene stratigraphic unit in the St. Lawrence Estuary and Gulf (Eastern Canada). *Quaternary Science Reviews*, **27**(25-26): 2390-2400.
- Stuiver, M., and Reimer, P. 1993. Extended ¹⁴C database and revised CALIB radiocarbon calibration program. *Radiocarbon*, **35**(1): 215-230.
- Sultan, N., Cochonat, P., Foucher, J., and Mienert, J. 2004a. Effect of gas hydrates melting on seafloor slope instability. *Marine Geology*, **213**(1-4): 379-401.
- Sultan, N., Cochonat, P., Canals, M., Cattaneo, A., Dennielou, B., Haflidason, H., Laberg, J.S., Long, D., Mienert, J., Trincardi, F., Urgeles, R., Vorren, T.O., and Wilson, C. 2004b. Triggering mechanisms of slope instability processes and sediment failures on continental margins: a geotechnical approach. *Marine Geology*, **213**(1-4): 291-321.
- Syvitski, J.P.M., and Praeg, D. 1989. Quaternary Sedimentation in the St. Lawrence Estuary and adjoining areas, Eastern Canada : an overview based on high resolution seismo-stratigraphy. *Géographie Physique et Quaternaire*, **43**(3): 291-310.
- Tavenas, F. Landslides in Canadian sensitive clays: a state-of-the-art. *In Fourth International Symposium on Landslides, Toronto 1984.* University of Toronto, pp. 141-153.
- Thwaites, R.G. 1959. The Jesuit relations and allied documents : travels and explorations of the Jesuit missionaries in New France, 1610-1791 : the original French, Latin, and Italian texts, with English translations and notes. Pageant Book Co, New York.
- Watts, P., Grilli, S., Kirby, J., Fryer, G., and Tappin, D. 2003. Landslide tsunami case studies using a Boussinesq model and a fully nonlinear tsunami generation model. *Natural Hazards and Earth System Sciences*, **3**(5): 391-402.

Annexes

A Article “Late-Quaternary morpho-sedimentology and submarine mass movements of the Betsiamites area, Lower St. Lawrence Estuary, Quebec, Canada”.

Cauchon-Voyer, G., Locat, J., and St-Onge, G. 2008. Late-Quaternary morpho-sedimentology and submarine mass movements of the Betsiamites area, Lower St. Lawrence Estuary, Quebec, Canada. Marine Geology, 251(3-4): 233-252.



Late-Quaternary morpho-sedimentology and submarine mass movements of the Betsiamites area, Lower St. Lawrence Estuary, Quebec, Canada

Geneviève Cauchon-Voyer ^{a,*}, Jacques Locat ^a, Guillaume St-Onge ^{b,c}

^a Université Laval, Département de géologie et de génie géologique, Québec, Québec, Canada G1K 7P4

^b Institut des sciences de la mer de Rimouski (ISMER), Université du Québec à Rimouski, 310 allée des Ursulines, Rimouski, Québec, Canada G5L 3A1

^c Centre de recherche en géochimie et géodynamique (GEOTOP-UQAM-McGill), Université du Québec à Montréal, C.P. 8888, Succ. Centre-Ville, Montréal, Québec, Canada H3C 3P8

ARTICLE INFO

Article history:

Received 25 June 2007

Received in revised form 12 February 2008

Accepted 4 March 2008

Keywords:

submarine mass movements

morpho-sedimentology

multibeam bathymetry

seismic reflection

earthquakes

St. Lawrence Estuary

Betsiamites River

ABSTRACT

A complex submarine geomorphology was revealed from multibeam bathymetry and seismic reflection surveys conducted between 2001 and 2007 in the Lower St. Lawrence Estuary offshore Betsiamites River, Quebec, Canada. In this paper, we describe the submarine morpho-sedimentology of an area of ~500 km² with focus on the consequences of four mass movement events. The general morpho-sedimentology of the area and submarine features resulting from mass movement processes, channel erosion and gas seepage are described. A spatio-temporal sequence for the occurrence of the mass movements and a chronology for the failures are established. We propose dates for four of the observed mass movement deposits. A buried paraglacial debris flow deposit is dated as older than 9280 cal BP, whereas a major landslide scar characterized by two topographic depressions on the shelf and a sediment lobe in the Laurentian Channel were dated around 7250 cal BP. Morphological observations and sediment core analyses allow us to identify a least two different recent (i.e., less than 500 yr old) debris flow accumulations associated with two recent earthquakes: (1) the AD 1663 (M~7) and (2) AD 1860 (M~6) or AD 1870 (M~6.5) earthquakes. In addition to a complex geomorphology influenced by mass movements, we have identified several regions on the shelf and on the Laurentian Channel with evidence of pockmarks, which could potentially influence submarine slope stability in the Estuary.

© 2008 Elsevier B.V. All rights reserved.

1. Introduction

Investigating submarine mass movements in order to evaluate slope stability for a region is required when carrying out risk assessment related to natural hazards. With the development of coastal and offshore activities there is an essential need to improve our understanding of the factors maintaining slope stability and those triggering mass movements. This has major implications on the coastal environment as most of the human and economical activities are gathered around the coasts. Slope instability is generally caused by erosion, sedimentation, gas hydrate dissociation, earthquake shaking, diapirism, sea-level change and/or wave action (Prior et al., 1984; Locat and Lee 2002) and can generate submarine landslides, which occasionally result in tsunamis. Such consequences of slope instability can damage man-made infrastructures, such as the rupture of submarine telecommunication cables (Hampton et al., 1996), and influence public safety (Piper et al., 1985).

Submarine mass movements are widespread geomorphological processes occurring in many different oceanographic settings (Locat

and Lee 2002; Canals et al., 2004). In Quebec, comprehensive analyses of submarine mass movements have mostly been carried out in the Saguenay Fjord (Urgeles et al., 2002; Locat et al., 2003; St-Onge et al., 2004; Levesque et al., 2006). In the St. Lawrence Estuary (Fig. 1), Duchesne et al. (2003) and Hart and Long (1996) have presented geomorphological and geophysical evidence of slope instability for the Outardes River deltaic system, whereas Syvitski and Praeg (1989) and Massé (2001) have identified several local slope failures using high resolution seismic reflection profiles. However, no exhaustive study has been undertaken with the primary goal of understanding submarine mass movements in the Estuary. As part of the COSTA-Canada project (COntinental slope STABILITY) (Locat and Mienert, 2003), intensive field work was carried out in the St. Lawrence Estuary between the Betsiamites and Manicouagan deltaic systems (Duchesne et al., 2003; Locat et al., 2004; Cauchon-Voyer, 2007). This work led to the recognition of significant evidence of submarine mass movements west of the Betsiamites River mouth (Fig. 2). Considering the number of historic earthquakes known to have caused landslides across Eastern Canada since the last deglaciation (Smith 1962; Shilts and Clague 1992; Aylsworth et al., 2000; St-Onge et al., 2004; Levesque et al., 2006) and the extent of the irregular geomorphological features observed in the Betsiamites–Rimouski area (Locat et al., 2004; Cauchon-Voyer, 2007), more than one slope failure event could be

* Corresponding author. Tel.: +1 418 656 2131x8604; fax: +1 418 656 7339.
E-mail address: genevieve.cauchon-voyer.1@ulaval.ca (G. Cauchon-Voyer).

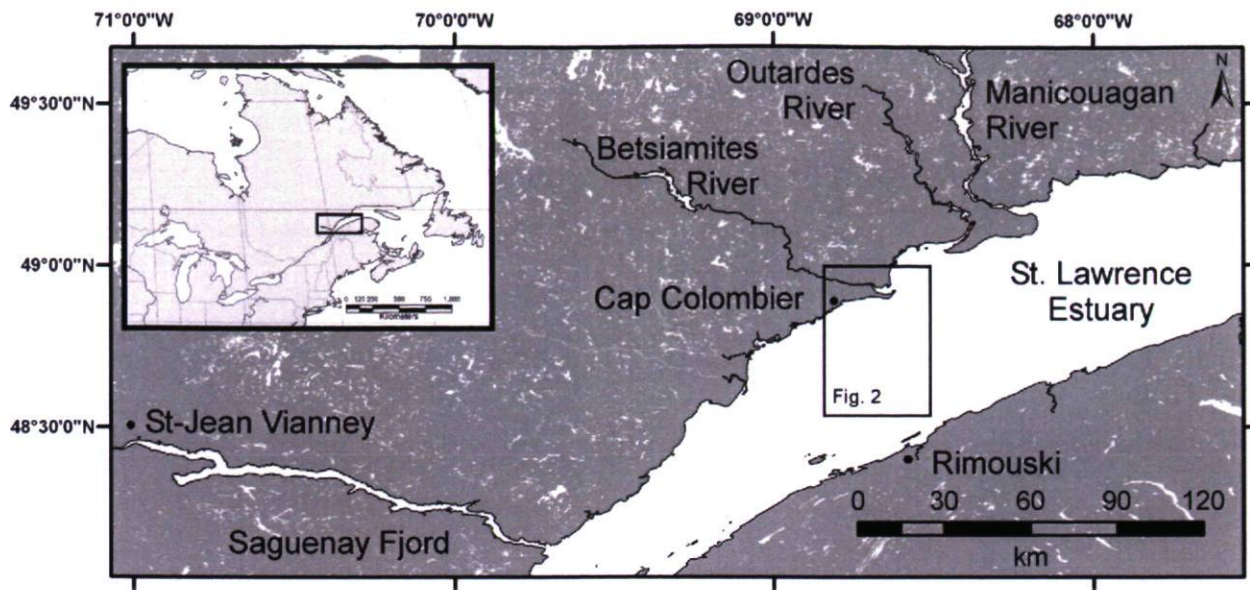


Fig. 1. Map of the St. Lawrence Estuary, with indication of the locations discussed in this paper. Black rectangle indicates location of the Betsiamites–Rimouski study area presented on Fig. 2. Inset is a map of Eastern Canada.

expected to have influenced the area. A better understanding of previous slope failure events and their timing is required to assess of the landslide hazard potential in the St. Lawrence Estuary.

The aim of this study is to present results of a seismostratigraphic and morpho-sedimentological analysis of the seafloor in the Betsiamites–Rimouski area in the Lower St. Lawrence Estuary. These analyses, integrated with results of studies presenting radiocarbon dates (Bernatchez, 2003) and describing the Holocene magnetic and sedimentological sequences of the St. Lawrence Estuary (St-Onge et al., 2003), will provide the basis for a spatio-temporal sequence and a chronology for the occurrence of at least 4 slope failure events.

2. Regional setting

2.1. St. Lawrence Estuary morphology

The study area is located along the North Shore of the Lower St. Lawrence Estuary, Quebec, Canada, 400 km northeast of Québec City close to the small community of Cap Colombier (Fig. 1). The regional morphology of the Estuary can be divided into three physiographic regions: the shelf (SH), slope (SL), and the Laurentian Channel (LC) (Fig. 2). The water depth in the study area ranges from shoreline down to 375 m in the Laurentian Channel. The shelf at the mouth of the Betsiamites River is a sub-horizontal surface and has an average width of 10 km and a maximum slope of 2°. The shelf break occurs between 150 and 200 m water depth. The slope has a height of 200 m. The Laurentian Channel is a long sub-horizontal topographic depression in the seafloor of the Estuary. It is interpreted as the result of a pre-Quaternary drainage system subsequently overdeepened by successive glaciations (Loring and Nota, 1973). It has a maximum water depth of 375 m and a width of 45 km in the study area. The topography of the Laurentian Channel in this area is generally uniform and leveled, with local variations due to landslide debris and pockmarks (Locat et al., 2004; Pinet et al., 2008). The underlying bedrock in this part of the Estuary is likely made up of Cambrian–Ordovician sedimentary rocks of the St. Lawrence Lowlands.

2.2. Late Quaternary geology

The glaciation and deglaciation cycles in Eastern Canada have caused a complex geomorphology in the Estuary. The north shore of

the St. Lawrence Estuary is characterized today by large deltaic systems discharging into the Estuary. These large deltaic complexes are linked to the northward retreat of the Laurentide Ice Sheet during the Late Wisconsinan. The Betsiamites River deltaic system, along with the Manicouagan and Outardes Rivers, was an important outlet for meltwater during deglaciation of Quebec and Labrador, partly accounting for the great volume of paraglacial sediments accumulated in the Estuary (Syvitski and Praeg, 1989). Deglaciation of the North shore of the Estuary took place at about 12 ka BP or ~14 ka cal BP (Shaw et al., 2006) and at 11.7 ka BP (~13.2 ka cal BP) (Bernatchez, 2003) in the study area of the Betsiamites River. Bernatchez (2003) established a regional relative sea-level (RSL) curve for the last 11 ka BP (~12.6 ka cal BP) for the North shore of the St. Lawrence Estuary. This curve, along with other proposed curves for the South shore of the Estuary (Locat, 1977; Lortie and Guilbault, 1984; Dionne, 2001), reflects the combined effect of a highly complex isostatic rebound history with global sea level changes. In the Estuary, the RSL fluctuations due to postglacial submergence of the coastal areas were not synchronous on both shores, making a generalized curve for the whole Estuary difficult to derive (Dionne, 2001). Sea level reached a maximum at about 150 m above sea level in the vicinity of the study area and lowered to the present sea level at around 7500 BP (~8000 cal BP) (Bernatchez, 2003). Fluctuations of the sea level on the order of 10 m were observed in the mid to late Holocene (Dionne, 2001). Glacio-isostatic rebound was significant in this area between 11 ka and 8 ka BP (~12.6 and ~8.5 ka cal BP) with an average annual rate of 47 mm/yr and as fast as 94 mm/yr between 11 and 10 ka BP (~12.6 and ~10.9 ka cal BP) (Bernatchez, 2003).

Onshore, Bernatchez (2003) described the Holocene coastal stratigraphy of the area as a sequence of emerged glacio-marine, prodeltaic, deltaic, fluvial and littoral deposits. Offshore, Syvitski and Praeg (1989) provided a regional seismostratigraphic framework for the late Quaternary sedimentation in the St. Lawrence Estuary by establishing a seismostratigraphic sequence with associated geological interpretations for each unit. Other authors have presented analyses of the Quaternary sedimentation (Josenhans and Lehman, 1998; Massé, 2001; Duchesne et al., 2007) for the Gulf and St. Lawrence Estuary, but the interpretations of Syvitski and Praeg (1989) best match the observations made in the study area and will be used hereafter in our analysis. They defined 5 units associated with the retreat of the Laurentide Ice Sheet. From the base to the top, they are

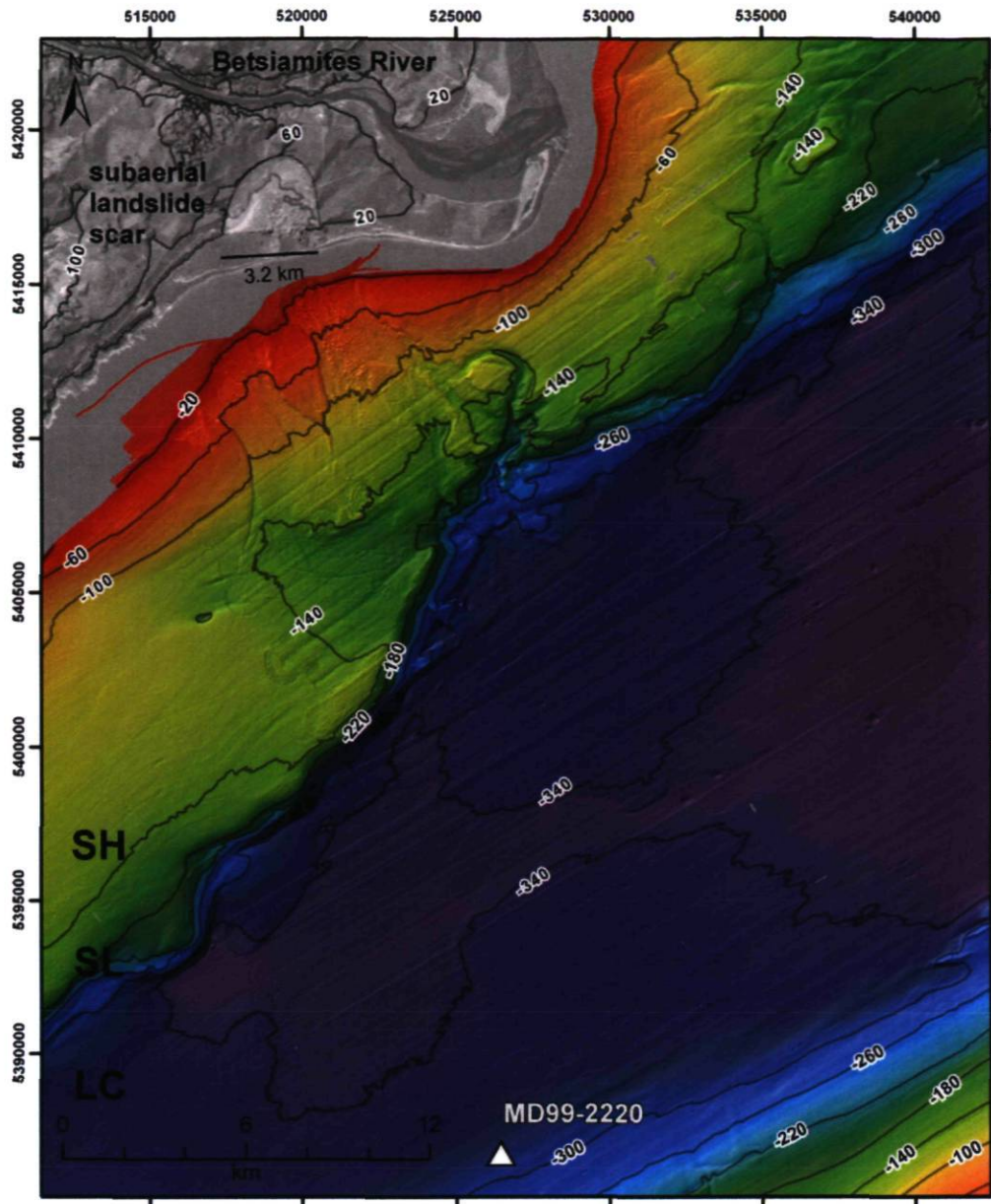


Fig. 2. Bathymetric coverage of the study area, ranging from 5 to 375 m water depth. Bathymetric contour lines are at 40 m interval starting at 20 m depth. The three physiographic regions are indicated: shelf (SH), slope (SL), and Laurentian Channel (LC). Note the location of the subaerial landslide scar, the Betsiamites River, and the MD99-2220 coring station. The landslide scar has a maximum width of 2000 m and length of 3280 m. The satellite image is the Landsat 7 Orthoimage 012026_0100_010525 from the Centre for Topographic Information, Geomatics Canada. Digital Elevation Model on land was computed from files 022B-G of the National Topographic Data Base (1:250 000), Geomatics Canada. Elevation contour lines are at 40 m interval starting at an elevation of 20 m.

interpreted as: (1) ice-contact deposits including ice-loaded and ice-deposited sediments; (2) ice proximal, coarser grained sediments deposited as a thin conformable layer during the rapid retreat of an ice terminus; (3) fine-grained ice-distal sediments probably correlated to the Goldthwait Sea clays (e.g., Dredge, 1983); (4) coarse paraglacial sediments transported from land to sea from a rapidly ablating subaerial ice-sheet; and (5) postglacial sediments deposited under modern sea-level and oceanographic conditions.

2.3. Subaerial landslide scar

Many subaerial mass movements have been previously identified onshore in the vicinity of the study area (Allard, 1984; Bernatchez, 2003). A subaerial landslide scar with an area of 6.5 km² is observed on shore, west of the Betsiamites River (Fig. 2). The landslide scar has a maximum width and length of 2000 m and 3280 m, respectively. Its

head scarp is located in a marine terrace at 60 m above sea level and the debris reach the tidal flat, which is composed of deformed prodeltaic silts with incorporated and sporadic pockets of organic matter and wood (Bernatchez, 2003). The lowermost section of the subaerial landslide scar is made of hills ranging from 5 to 15 m high and depressions filled with standing water. These hills are interpreted as large rafted and tilted blocks of well-preserved or intact stratified prodeltaic sediments mobilized by the landslide (Bernatchez, 2003). With an area of 6.5 km² and a volume of more than 300 million m³, it is one of the biggest historical subaerial landslide that has occurred in Québec, comparable to the 1663 Saint-Jean-Vianney (Fig. 1) landslide (Lasalle and Chagnon, 1968). According to three ¹⁴C dates and Jesuits writings (Thwaites, 1959), Bernatchez (2003) suggested that this landslide was triggered by the major earthquake ($M \approx 7$) that struck the province of Québec on February 5th 1663 (Smith, 1962). A well preserved conifer tree branch with remaining bark was found among

other landslide debris within the prodeltaic silts of the tidal flat and was dated at 310 ± 60 ^{14}C yr BP (UL-1922). This provides the best radiocarbon dating evidence linking this landslide to the earthquake of 1663. This also indicates that the slope failure occurred during subaerial exposure when the RSL was at present level.

The Jesuits, who had been living in the area since the early 1600s, recall in their documents details supporting this hypothesis. They indicate that many landslides were triggered by the 1663 earthquake, as they comment on the amount of sediments in suspension in the St. Lawrence River: “and our great river Saint Lawrence appeared all whitish as far as the neighborhood of Tadoussacq – a prodigy truly astonishing and fitted to surprise those who know the volume of water carried by this great stream below the Island of Orleans, and how much matter it must have taken to whiten it.” In the area of Betsiamites, the Jesuit Fathers observed debris flowing from the Betsiamites River: “We saw in passing the ravages wrought by the Earthquake in the rivers of Port neuf; the water coming therefrom is all yellow, and it retains this color far into the great rivers, as does that of the Bersiamites [Betsiamites]. The Savages could no longer navigate these two rivers”. Although the Jesuits provided valuable descriptions of the extent, magnitude, and outcomes of the 1663 earthquake and resulting landslides in the province of Quebec, they unfortunately do not directly link the 1663 earthquake to the landslide scar we observe today west of the Betsiamites river mouth (Fig. 2). Nevertheless, the existing published dates obtained from the debris of the subaerial landslide and the mention of the Betsiamites River in the Jesuits writings provide reasonable evidence to link this landslide to the 1663 earthquake. However, a much more detailed and rigorous investigation must be undertaken to unequivocally demonstrate their association.

3. Data and methods

3.1. Bathymetric data

High-resolution bathymetric mapping of the St. Lawrence Estuary started in 2000 in the deltas of the Outardes and Betsiamites rivers as part of the COSTA-Canada project (Urgeles et al., 2001) in collaboration with the Canadian Hydrographic Service (CHS). Subsequent surveys (2001–2004) in the Betsiamites-Manicouagan deltas area were obtained through collaboration between the CHS, the Interdisciplinary Centre for the Development of Ocean Mapping (CIDCO), and Laval University through COSTA-Canada. Between 2005 and 2006, the Geological Survey of Canada (GSC), in partnership with the CHS, led the “Geoscientific Mapping of the St. Lawrence Estuary Project” (Campbell et al., 2005, 2006; Bolduc et al., 2006), which allowed the coverage of the remaining portions of the Estuary. Finally, in 2007, the shallow area between 5 and 20 m water depth in the Betsiamites area was surveyed through collaboration between the GSC, the CHS, and Laval University. The deeper water data was obtained before 2005 using a Kongsberg EM1000 and later with a Kongsberg EM 1002 multibeam echosounder system mounted on board the Canadian Coast Guard (CCG) vessel Frederick G. Creed. The shallow area was surveyed with a Kongsberg EM3002 mounted on board the CCG vessel Guillemot. The data were positioned using differential and kinematic GPS. The data was processed with the Caris HIPS/SIPS software. Data visualization and shaded relief bathymetric images was obtained with Generic Mapping Tool (GMT) and ArcMap 9.2. All grids shown in this paper have a cell size of 10 m. Artifacts on the multibeam data are due to complex tide corrections between non continuous surveys, swath misalignment and coverage less than 100% for certain areas. The 140 m contour line was slightly smoothed to remove erroneous variations of seafloor depth due to artifacts.

3.2. Seismic data

The high resolution seismic reflection data used in this study were obtained with an EG&G chirp system mounted on board the Coriolis II

research vessel with frequencies ranging from 2 to 12 kHz (Fig. 3). 600 km of seismic profiles were acquired during three cruises between 2003 and 2006. Sound wave velocity for time-depth conversion in water and in sediments was estimated at 1500 m/s, hence all depth values are approximated. Interpretation of subsurface data was performed with the Kingdom Suite software package.

3.3. Sediment sampling and core analyses

10 box cores, 6 Lehigh gravity cores, 8 trigger weight cores, and 9 piston cores were recovered during three cruises (COR0307, COR0503, and COR0602) between 2003 and 2006 on board the R/V Coriolis II at 15 sampling stations (Table 1, Fig. 3). Core positioning was obtained using the acoustic tracking system Trackpoint II. Low field volumetric magnetic susceptibility (k) and wet bulk density derived from gamma ray attenuation were measured on board using a GEOTEK MSCL (Multi Sensor Core Logger) system at 1 cm intervals. Immediately after recovery, a few grams of sediments were sampled at all section ends in order to measure water content for geotechnical purposes and to later assess core preservation. Digital X-ray images of all cores were obtained with computerized co-axial tomography (CAT-Scan) with a pixel resolution of 1 mm. The resulting grey scale images allow us to extract profiles of tomographic intensity: darker and lighter zones representing lower and higher X-ray attenuation, respectively (e.g., St-Onge et al., 2007). The CT number relates to the mineralogy, organic matter content, grain size, and bulk density of the sediments (Boespflug et al., 1995; St-Onge et al., 2007). Cores were split, described and photographed. Grain size measurements were made using a Beckman Coulter LS 13 320 laser diffraction particle size analyzer for

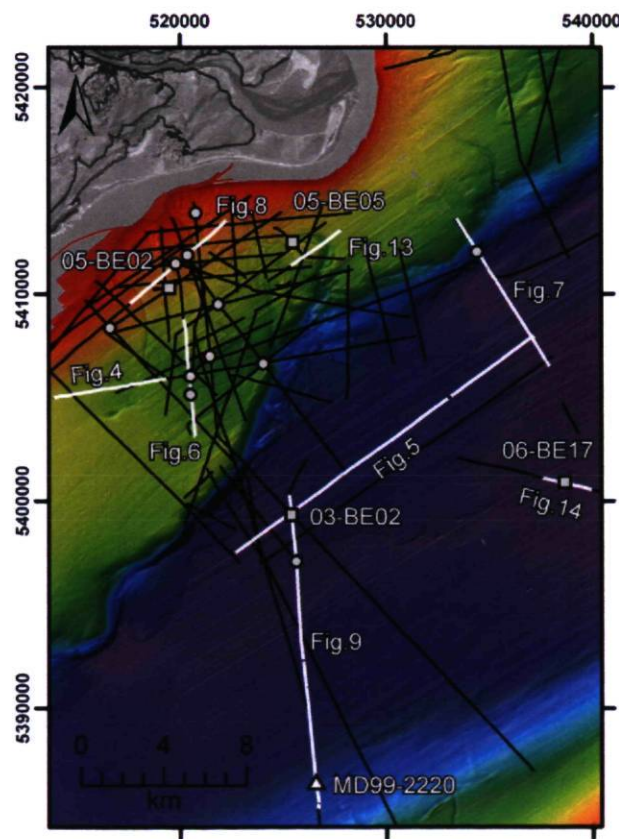


Fig. 3. Location of the 15 sediments sampling stations described in Table 1 and positions of all the high resolution seismic reflection profiles acquired in the study area between 2003 and 2006. The stations represented with a grey square and labeled are presented in this paper. The stations represented with a grey circle are described in Cauchon-Voyer (2007). The white seismic reflection profiles are presented in this paper.

Table 1
Position of the sampling stations and length of the sediments cores recovered in the Betsiamites area

Station	Core type and sample length (cm)				Features targeted	Latitude (N)	Longitude (W)	Water depth (m)
	Piston	Trigger weight	Lehigh gravity	Box				
03-BE01	505	101	–	44	Shelf edge	48°48.742	68°40.374	192
03-BE02	724	131	–	52	Laurentian Channel – debris lobe	48°44.812	68°39.318	347
03-BE03	501	–	–	49	Landslide scar (E)	48°50.309	68°42.143	123
03-BE12	–	–	134	48	Landslide scar (E)	48°52.687	68°43.030	54
05-BE01	776	95	–	–	Laurentian Channel	48°43.585	68°39.123	352
05-BE02	–	127	–	40	Landslide scar (W)	48°50.725	68°44.064	97
05-BE04	–	–	30	37	Butte 1	48°51.568	68°43.351	73
05-BE05	–	–	–	38	Paleomeander	48°51.886	68°39.179	129
05-BE06	–	–	205	32	Slope landslide	48°51.628	68°31.867	320
05-BE07	–	–	–	43	Rugged surface	48°48.430	68°43.230	165
06-BE15	592	13	128	–	Butte 1	48°51.359	68°43.803	73
06-BE16	708	–	90 & 235	–	Rugged surface	48°47.960	68°43.250	151
06-BE17	882	262	–	–	Laurentian Channel pockmark	48°45.578	68°28.444	370
06-BE18	597	33	–	–	Rugged surface	48°48.908	68°42.355	169
06-BE19	501	6	–	39	West shelf	48°49.700	68°46.440	85

The first two digits of the stations number refer to the year of the sampling cruise, 03 for cruise COR0307 in 2003, 05 for cruise COR0503 in 2005 and 06 for cruise COR0602 in 2006. Water depth values correspond to depth to the seafloor at sampling time.

the sediment fraction smaller than 2000 μm . The grain size data were processed with the Gradistat program and calculations of grain size statistics were done with the geometric method of moments (Blott and Pye, 2001). Sedimentation rates were derived from ^{210}Pb measurements within sediments of two box cores (05-BE02-02BC, 05-BE05-05BC). The measurements were obtained after chemical treatment, purification, and deposition on a silver disk and alpha counting of the daughter ^{210}Po following routine procedures at the GEOTOP-UQAM-McGill research center (e.g., Zhang, 2000).

4. Observations and results

4.1. Stratigraphic analysis

The seismostratigraphic analysis was done in order to temporally correlate morphological features and establish a time sequence for the mass movement events. Since this study aims to focus on the timing and on the consequences of mass movements, we will be consistent with the work of Syvitski and Praeg (1989) for the sequence-stratigraphy interpretations and will not attempt to provide a new interpretation. Based on seismic facies analysis rather than mapping unconformities, 5 seismic units were identified in this study. These units were defined according to their reflections, geometry of the inner reflecting horizons, amplitude, and attributes of the upper transition of each body. The seismic attributes of these five units match the seismic interpretations previously suggested by Syvitski and Praeg (1989) so we will use their associated sequence-stratigraphy interpretations, which is from base to top: (1) ice-contact sediments; (2) ice-proximal sediments; (3) ice-distal sediments; (4) paraglacial sediments; and (5) postglacial sediments (Table 2, Fig. 4). This sequence is interpreted on the shelf (Fig. 4) and in the Laurentian Channel (Fig. 5). The characteristic of each seismostratigraphic unit are described below and summarized in Table 2. In addition, five main reflecting horizons were mapped and are recognized regionally in the seismostratigraphic sequence of the study area. These reflecting horizons are coherent and laterally continuous reflections due to strong acoustic impedance contrasts in the sedimentary succession. They are labeled, from the deepest to shallowest, as R1, R2, R3, R4 and R5.

4.1.1. Bedrock signature

The bedrock surface at the base of the sequence is a relatively continuous high amplitude reflecting horizon with variable relief. There is no signal penetration below this reflecting horizon. On the shelf, this reflecting horizon can have a stair-like geometry (Fig. 6) or a

more leveled topography (Fig. 4). On the slope, the sedimentary drape is thinner and discloses the morphological control of the bedrock on the slope (Fig. 7). In the Laurentian Channel, the chirp system did not provide enough signal penetration to obtain a coherent bedrock reflection. The transition between the top of the bedrock and Unit 1, when visible, is sharp.

4.1.2. Ice-contact sediments – Unit 1

This unit is acoustically uniform with moderate amplitude. Coherent reflections are absent and there is absorption of acoustic energy. The upper transition of Unit 1 is a high amplitude discontinuous reflecting horizon of variable relief. Unit 1 overlies bedrock, which is visible only when this unit is thin (Figs. 4 and 6). Unit 1 is the lowermost unconsolidated body, so it is interpreted as ice contact sediments (Syvitski and Praeg, 1989).

Table 2
Summary of seismic attributes of the 5 seismostratigraphic units

Seismostratigraphic sequence and geological interpretations	Seismic attributes
Unit 5 Postglacial sediments	R: Medium to strong reflections G: Few internal reflecting horizons conformable with Unit 4 A: Medium to strong amplitude U: Sharp sediment–water contact
Unit 4 Paraglacial sediments	R: Strong high frequency reflections G: Closely packed reflecting horizons, conformable with Unit 3 A: Alternating low to strong amplitude U: Sharp or gradational transition from Unit 4 to Unit 5
Unit 3 Ice distal sediments	R: Weak reflections G: When apparent, reflecting horizons conformable with Unit 2 A: Low amplitude U: Sharp transition from Unit 3 to Unit 4
Unit 2 Ice proximal sediments	R: Strong and high frequency reflections G: Closely packed reflecting horizons conformable with Unit 1 A: Alternating low to medium amplitude U: Sharp transition from Unit 2 to Unit 3
Unit 1 Ice contact sediments	R: Absent reflections and absorption of acoustic energy G: No reflecting horizon A: Medium amplitude U: Sharp transition from Unit 1 to Unit 2

R refers to inner reflections, G to the geometry of the reflecting horizons, A to amplitude, and U to the attributes of the upper transition of the units.

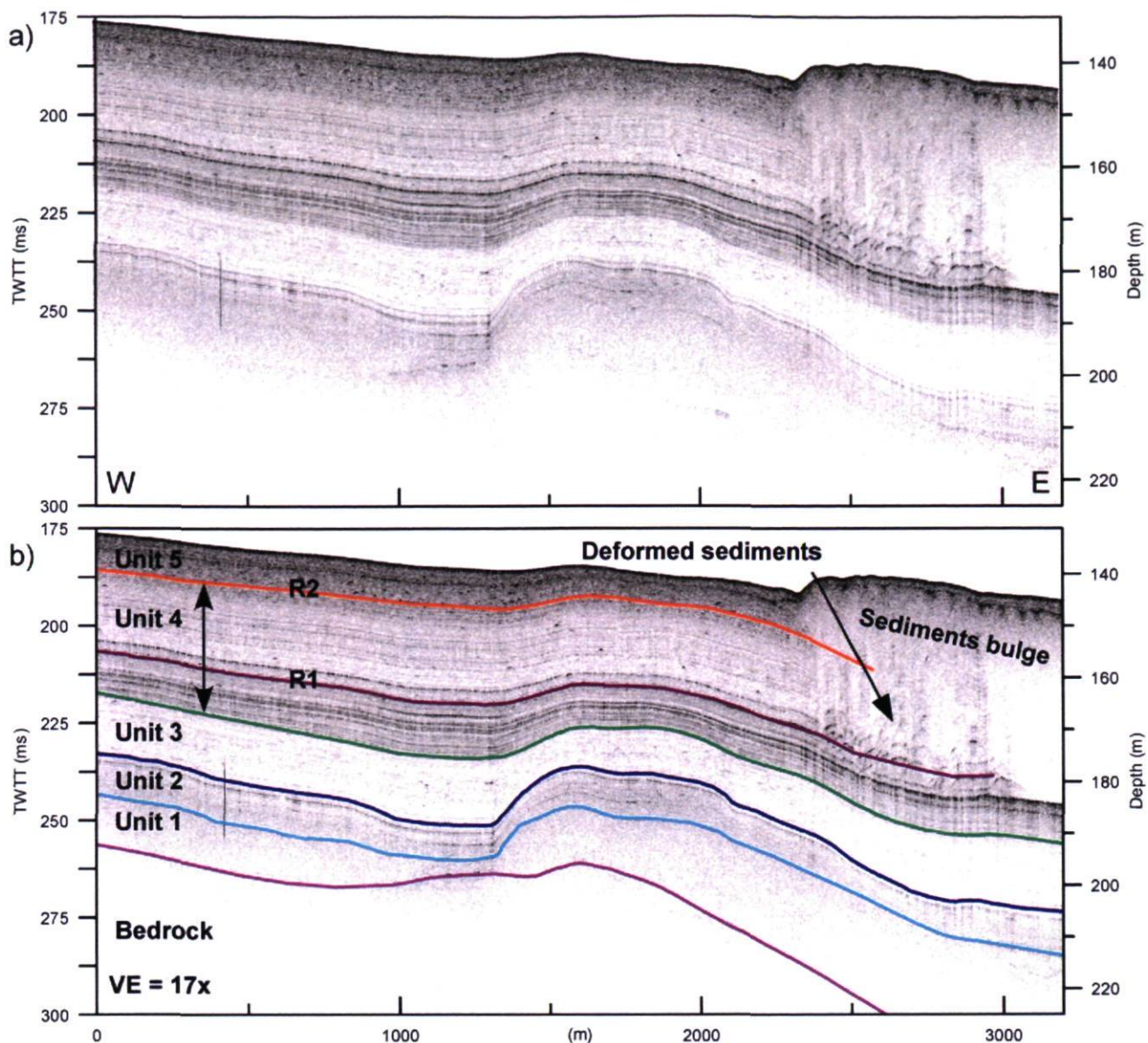


Fig. 4. (a) Profile be06_109 on the shelf outside and inside the large landslide scar area. The profile is 3.2 km long. The vertical exaggeration is 17 \times . Left scale is in milliseconds two way travel time (TWTT) and right scale is approximate depth in meters. (b) Interpretations showing the typical seismostratigraphic sequence for the study area: Unit 5 postglacial sediments, Unit 4 paraglacial sediments, Unit 3 ice distal sediments, Unit 2 ice proximal sediments, and Unit 1 ice contact sediments. R1 is a high amplitude reflecting horizon interpreted regionally on the shelf and in the Laurentian Channel in the study area. R2 is the reflecting horizon marking the limit between Unit 4 and Unit 5. Note the bulge of seismically transparent deposits and deformed reflecting horizons. Location of this section is shown on Figs. 3 and 12.

4.1.3. Ice-proximal sediments – Unit 2

Unit 2 is a sequence of closely packed reflecting horizons with alternating low to high amplitude. It is conformable with Unit 1. An upper reflecting horizon marks a sharp transition between Units 2 and 3. This unit is related to the ice-proximal sedimentation associated with high deposition rates of relatively coarse particles close to a major discharge outlet along the face of a glacier (Syvitski and Praeg, 1989).

4.1.4. Ice-distal sediments – Unit 3

This unit is a thick body with distinctive low amplitude and weak reflections (Fig. 4). A few high frequency and weak reflecting horizons are visible. They are conformable with Unit 2. The transition between Units 3 and 4 is sharp and is mostly recognized by the contrast in amplitude. Unit 3 is interpreted as ice-distal sediments (Syvitski and Praeg, 1989). Ice-distal sedimentation is interpreted as the accumulation of fine glaciomarine sediments deposited in a low-energy glacial sea environment when sea-ice cover may have been present up to 8 months per year (de Vernal et al., 1993).

4.1.5. Paraglacial sediments – Unit 4

Unit 4 is characterized by a sequence of strong high frequency reflections. Unit 4 has dense closely packed reflecting horizons conformable with Unit 3. The amplitude of this unit varies between low and high. Reflecting horizon R1 is observed within this unit (Fig. 4). This high amplitude reflecting horizon R1 is also recognized regionally on the shelf and in the Laurentian Channel (Figs. 5, 6, 7, 8, 9, and 14). The transition between Unit 4 and Unit 5 is sharp, mostly recognized by a change in amplitude and fewer coherent reflecting horizons. When present, the reflecting horizon marking the limit between Unit 4 and Unit 5 is indicated as R2 within the sequence (Fig. 4). Unit 4 is interpreted as paraglacial sediments (Syvitski and Praeg, 1989). Paraglacial sedimentation occurs when high volumes of coarse sediments are transported from land to sea from a rapidly ablating terrestrial ice-sheet. The Betsiamites River, Manicouagan and Outardes rivers deltaic systems were important fluvial discharge outlet during the last deglaciation, partly accounting for the great volume of paraglacial sediments accumulated in the Estuary resulting

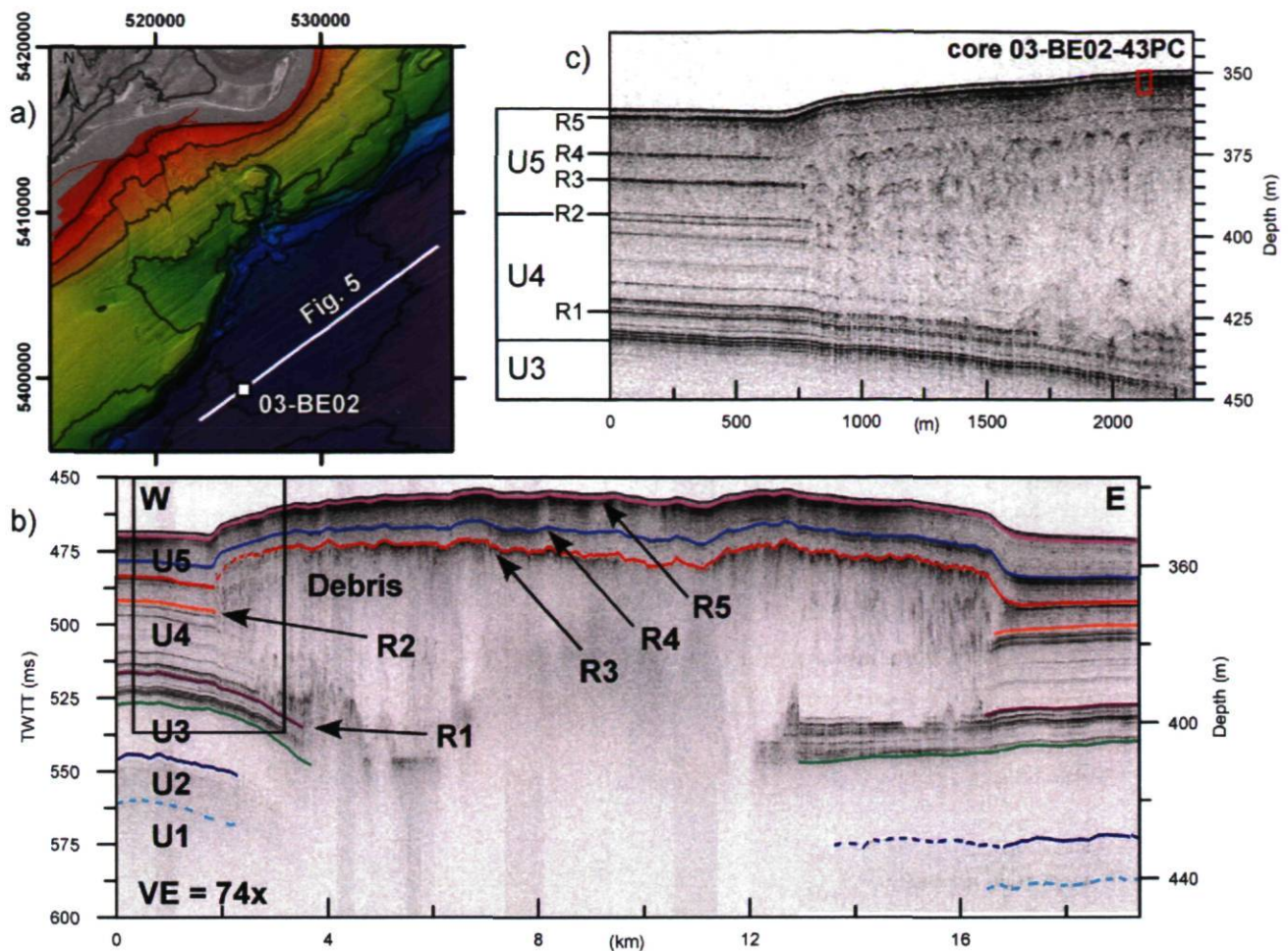


Fig. 5. (a) Bathymetric image of the landslide area and the buried debris lobe in the Laurentian Channel. Position of seismic profile presented in b) and position of core presented in Fig. 19. (b) Seismic reflection profile 03_bet2 across the debris flow lobe. Line is 19.4 km long. U1 to U5 refer to the 5 seismostratigraphic units and R1 to R5 refer to the 5 reflecting horizons identified in the study area, see text for explanations. Note also the debris flow deposit with seismically transparent to acoustically impermeable seismic attributes and resulting deformation structures on the reflecting horizons. (c) Enlargement on the western limit of the debris flow lobe. Note the deformation structures resulting from the debris flow. The red rectangle represents the position of the 724 cm-long piston core recovered from the 03-BE02 sampling location. The upper 112 cm of this core is presented in Fig. 19.

in high sedimentation rates. These sediments were transported offshore via slumps, slides, and turbidity currents. This is a higher energy environment than the finer glaciomarine environment leading to the deposition of Unit 3 (Syvitski and Praeg, 1989). Debris flow deposits are identified in Unit 4 (Fig. 8). These bodies are recognized on the seismic profiles by the chaotic and highly variable seismic attributes, ranging from seismically transparent to acoustically impermeable.

4.1.6. Postglacial sediments – Unit 5

The seismic attributes of Unit 5 consist of medium to strong amplitude reflections with few coherent reflecting horizons contrasting with the lower amplitude background, such as reflecting horizons R3, R4 and R5 (Figs. 5, 6, 8, and 14). Debris flow deposits are also recognized within Unit 5 and present seismically transparent to acoustically impermeable seismic attributes (Fig. 5). Unit 5 makes up the uppermost unconsolidated sediments of the study area and is interpreted as postglacial sediments. This unit corresponds to the sediments deposited under modern (post-glacial) sedimentation patterns of lowered RSL and complete retreat of the Laurentide Ice Sheet (Syvitski and Praeg, 1989).

4.1.7. Correlation to the sampling location of core MD99-2220

Seisimostratigraphic correlations to the sampling location of core MD99-2220 (48°38.32 N/68°7.93 W, water depth 320 m, length

51.6 m) (Fig. 2) were made to provide support for the timing of the seismostratigraphic sequence and for the chronology of the slope failure events between the Betsiamites River and Rimouski in the St. Lawrence Estuary. A 17 km long chirp profile was acquired between the study area and core MD99-2220 sampling location (Fig. 9). The five seismostratigraphic units and the reflecting horizons R1, R4 and R5 were identified on this profile. For reflecting horizons R2 and R3, the low contact in acoustic impedance in the sedimentary succession at core MD99-2220 sampling location, in conjunction with the low quality of our data due to waves and technical problems during data acquisition, did not allow us to map them precisely all the way to the core location. However, we were able to provide approximate depths for their stratigraphic positions. These approximate depths are 15 ms (11.3 m) for R3, 20 ms (15.0 m) for R2 and for 76 ms (57.0 m) for R1 (Fig. 9). St-Onge et al. (2003) established from 17 AMS ¹⁴C dates an age model for core MD99-2220 (Fig. 10) and dated the transition between glaciomarine and postglacial sediments (R2 between Unit 4 and Unit 5 of this study) at ~8500 cal BP at a depth of 14.97 m.

4.2. Morpho-sedimentology

A wide variety of submarine features are revealed from seafloor investigations (Fig. 11). A combination of morphological, seismostratigraphic, and sedimentological analyses within the three physiographic regions allow us to define the general morpho-sedimentology

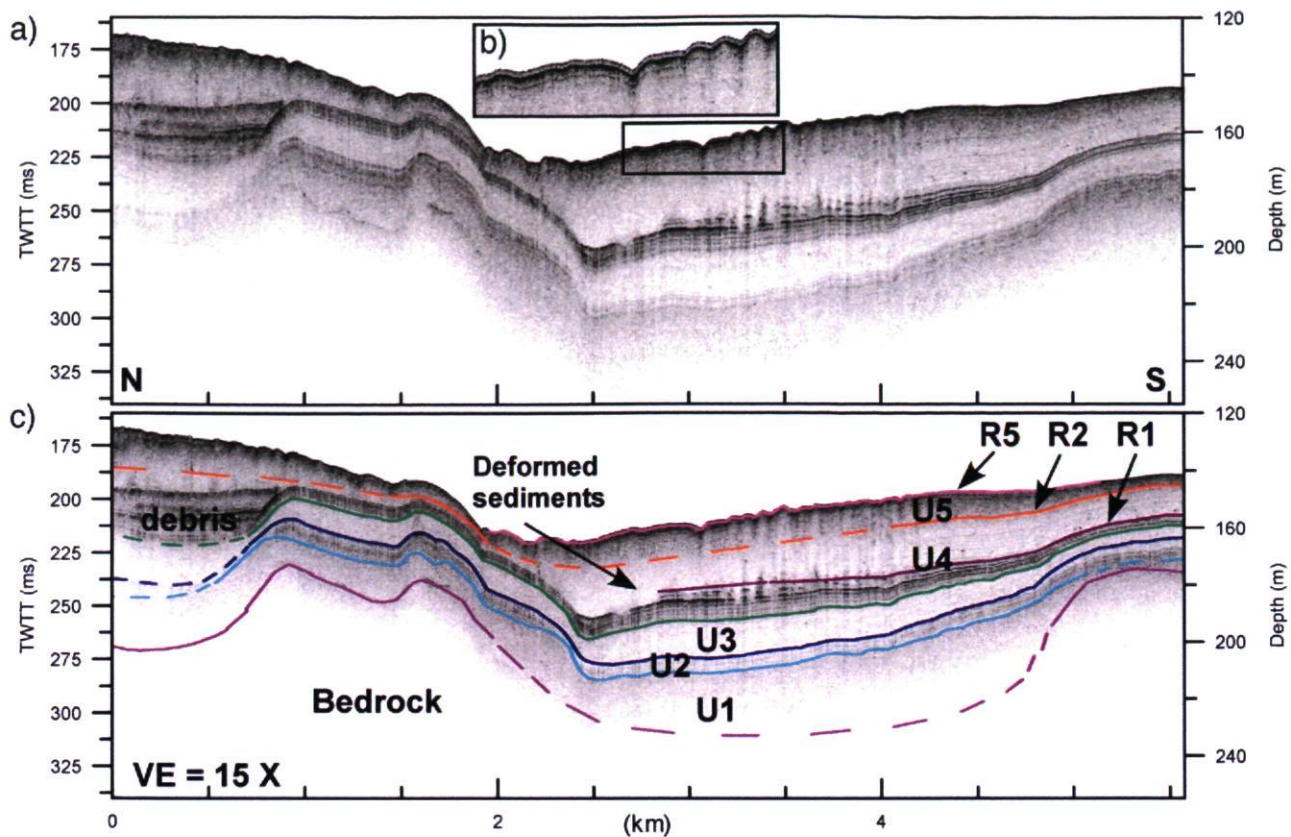


Fig. 6. (a) Seismic reflection profile be06_102 across the landslide scar and the rugged area. Line is 5.6 km long. (b) Enlargement of surface of the seismic reflection profile. The groove corresponds to the deepest channels of the rugged area and is indicated by the black rectangle on Fig. 12. The shallow reflecting horizon identified at 75 ms below seafloor is interpreted at R5. (c) Interpretations of the seismic reflection profile. U1 to U5 refer to the seismostratigraphic units and R1, R2 and R5 refer to the 3 reflecting horizons identified in the study area, see text for explanations. Note the stair-like geometry of the bedrock. Sediment deformations are observed within Unit 4. These deformations could be caused by accumulation of debris above R2 and relate to the sediments bulge identified on Fig. 4. A complex geometry of the reflecting horizons is identified within Unit 4 and is likely related to the Paraglacial landslide event, see text.

of the area. In this section, we describe the morpho-sedimentology of the area. The features are presented with regards to the physiographic regions within which they are observed, from the shelf to the Laurentian Channel. In addition, submarine features resulting from mass movement processes, channel erosion and gas seepage are also described.

The main physiographic regions of the study are the shelf, the slope and the Laurentian Channel. The shelf is a sub-horizontal surface and has an average width of 10 km and a maximum slope of 2°. Sediment thickness ranges from a few meters to 125 m on the shelf (Fig. 4). The shelf break occurs between 150 and 200 m water depth. The orientation of the slope scarp is structurally controlled by the underlying bedrock (Fig. 7). The slope scarp has two main orientations of lineaments (A and B on Fig. 11). Group A has an average SSW–NNE orientation (022°N) and group B has a WSW–ENE orientation (082°N). The slope has a height of 200 m with a sedimentary drape ranging from 0 to 50 m (Fig. 7). The Laurentian Channel is a flat area with large pockmarks (Fig. 11) and debris lobes (Fig. 5). More than 150 m of unconsolidated Quaternary sediments are found in the Laurentian Channel in the studied area (Fig. 9).

4.2.1. Mass movements

Mass movement processes have modified the shelf, the slope, and the Laurentian Channel. In this section, we present the features resulting most likely from more than one slope failure event on the shelf. It is composed of a large scar characterized by two topographic depressions, buttes with steep flanks and flat tops overlain by landslide debris, and areas with a rugged surface and channels. The large scar, with an area of 70 km², is located west of the Betsiamites

River mouth (Fig. 2), away from its present discharge, indicating that the river does not have a direct effect on the morphology of the landslide scar.

Two topographic depressions, West and East, separated by a butte of stratified deposits make up the upper sector of the landslide scar (Fig. 8). As it will be presented below, these depressions are interpreted as scars due to landsliding. The West depression has a width ranging from 2 to 3 km and a length of 5 km. The slope of the West depression floor is 1°. The height of the western flank of the West depression ranges from 12 to 18 m with an average slope of 12°. For the eastern flank, heights range between 10 to 20 m with an average slope of 5°. The width of the East depression varies from 2 to 4 km, has a length of 5 km, and a floor slope of 1°. The height of the western flank of the East depression ranges from 15 to 20 m with an average slope of 15°. The morphology of the eastern flank of the East depression is irregular. The East depression appears to be a continuity of the subaerial landslide (Fig. 2).

Two buttes with steep flanks and flat tops are observed within the landslide scar (1 and 2 on Figs. 11 and 12). Butte 1 is the largest one and is located in the center of the landslide scar marking the separation between the topographic depressions. It extends over 5 km² with a maximum length and width of 4.5 km and 1.6 km, respectively (Fig. 8). The average slope of the top of butte 1 is 1°. A sequence of truncated parallel reflecting horizons is observed on the seismic profiles (Fig. 8) of butte 1, implying that it was kept mostly intact when the two topographic depressions were carved and that it is neither a bedrock-controlled feature nor a displaced block. We can identify the high amplitude seismic reflecting horizon R1 in the buttes and in the deposits outside the large landslide scar (Fig. 8). Butte 2

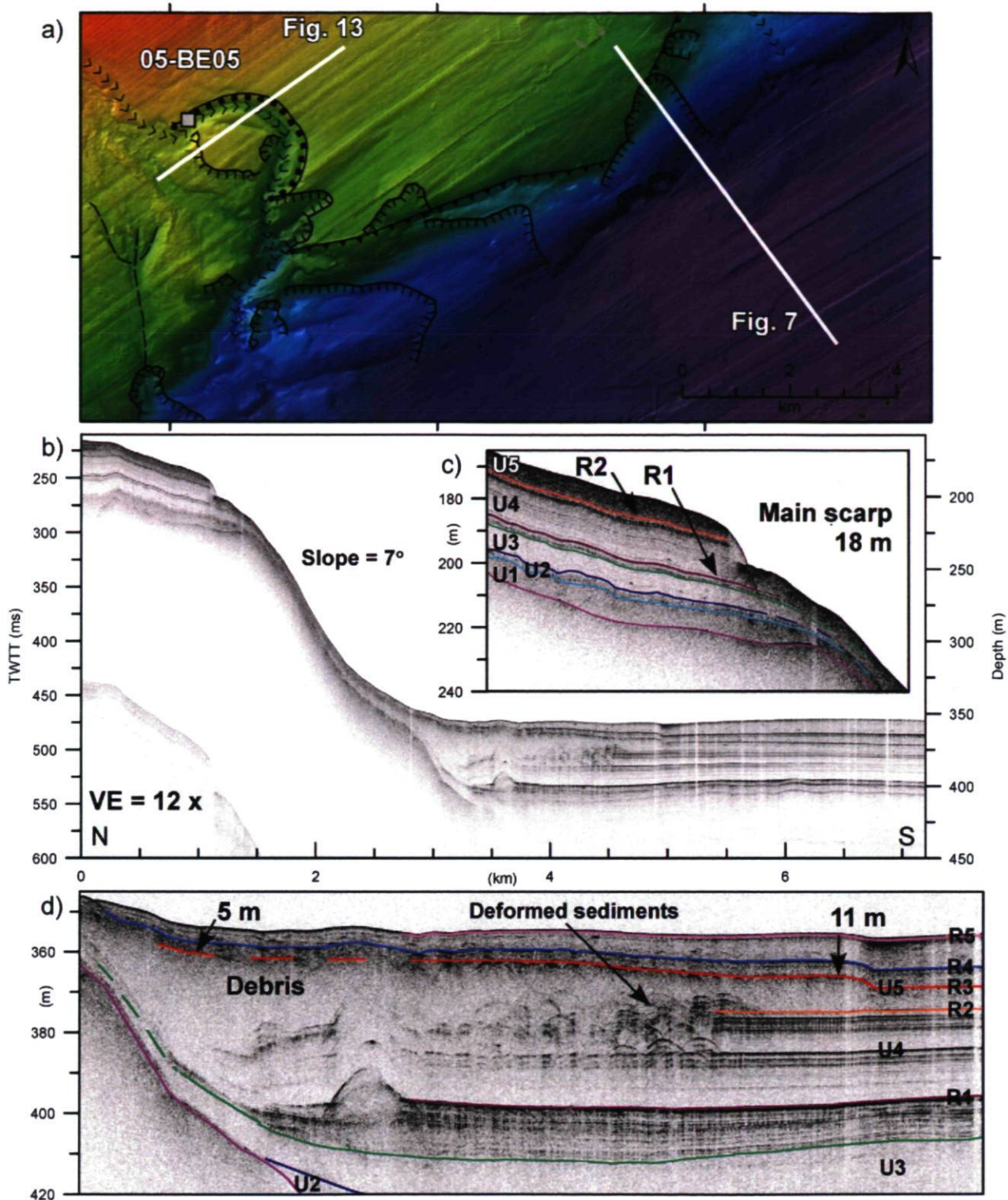


Fig. 7. (a) Bathymetric image of the slope and landslides. Refer to Fig. 11 for legend of symbols. Position of seismic profile presented in b) is indicated. (b) Seismic reflection profile be06_118 with enlargement of the headwall and the debris. The failure plane has an average slope of about 7° . Note the morphological control of the bedrock on the slope. Line is 7.2 km long and enlargement is 1.4 km long. (c) Enlargement of the main scarp area, which is 18 m high at this location. R1 is interpreted as the failure plane within the highly stratified sediments of Unit 4. (d) Enlargement on the debris area. 5 m and 11 m refer to the thickness of hemipelagic sediments draping the debris flow, assuming a sound wave velocity of 1500 m/s. Sediment deformations are observed within Unit 4.

(Fig. 11) is found in the lower section of the landslide scar. It has an area of 0.15 km^2 , an average length of 300 m and a width of 500 m. The slope of the flanks of the butte ranges between 5° and 15° . Butte 2 has similar seismic attributes as butte 1 (i.e., truncated parallel reflecting horizons).

The floor of the upper section of both topographic depressions is a rough and undulated surface (Fig. 8). This surface is also observed on top of butte 1 and characterized by the presence of large blocks, with sizes of up to $20 \times 60 \times 150 \text{ m}$ (Fig. 8) dispersed across a defined area (Fig. 11). The blocks extend up to 8 km downslope from the shoreline

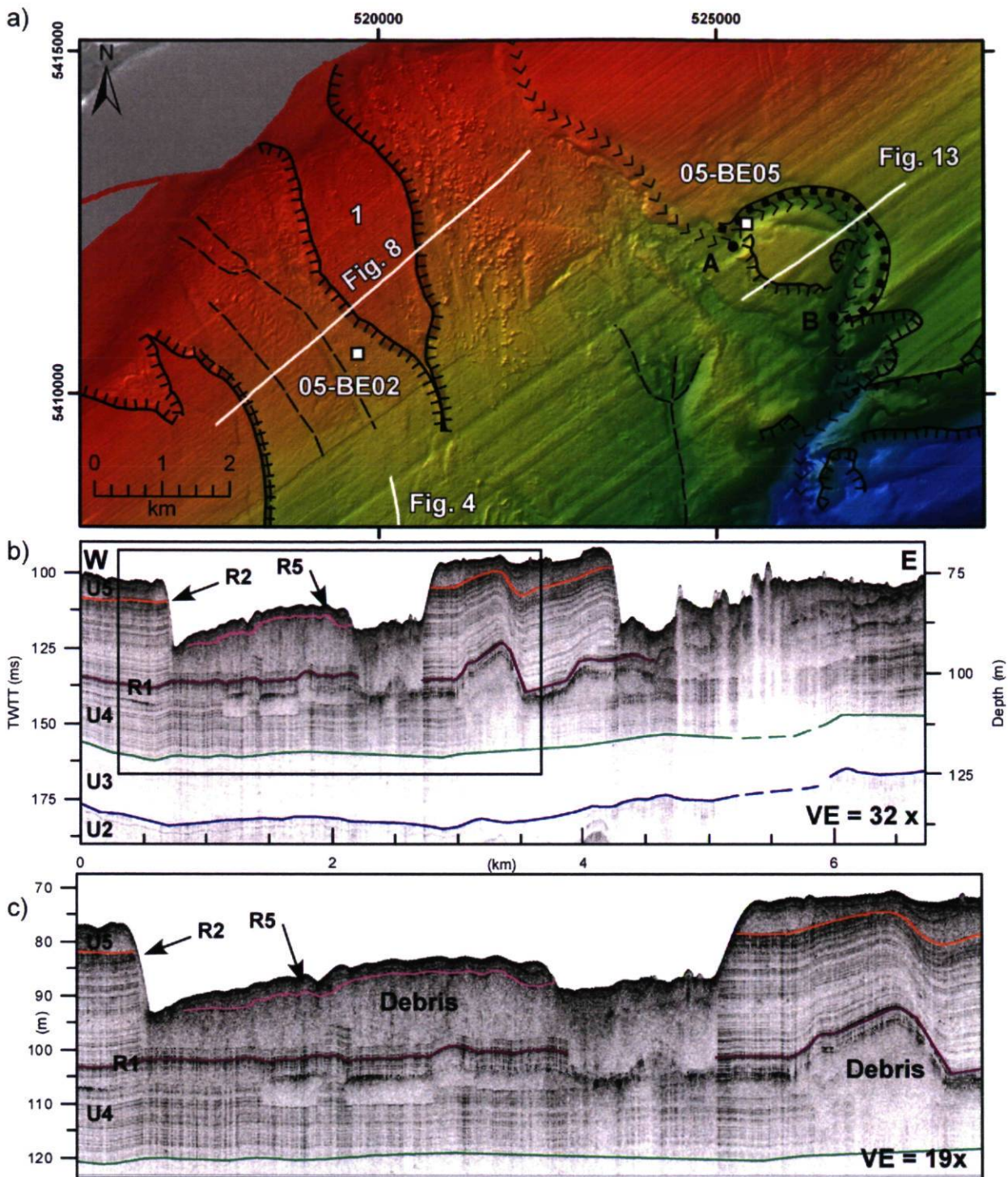


Fig. 8. (a) Bathymetric image of the upper shelf. Refer to Fig. 11 for legend of symbols. Position of seismic profile presented in b) is indicated. Note the large blocks on the surface of the upper shelf. (b) High resolution seismic profile be06_111 across the landslide scar and butte 1. The profile has a length of 6.7 km. U1 to U5 refer to the 5 seismostratigraphic units and R1 to R5 refer to the 5 reflecting horizons identified in the study area, see text for explanations. Note the debris flow deposits interpreted in Unit 4 below R1. The butte is a sequence of closely packed reflecting horizons (Unit 4). (c) Enlargement of the western depression. Note the high frequency and shallow highly undulated reflecting horizon at less than 2 m below seafloor. R5 is truncated in the 600 m wide and 5 m deep furrow of the West depression.

(Fig. 11). Some of the blocks are located in small grooves with depths of 1.5 m in the surface sediments (Fig. 8). These grooves are oriented parallel to the slope and could be the result of the displacement of the blocks. A furrow of 600 m wide and 5 m deep is found in the West depression, which is visible by the change in the shape of the 60 m contour line (Fig. 2). In addition, small channels are observed among the blocks and the matrix (Figs. 8 and 11). These channels have an

average width of 50 m and are more organized in the West depression (Fig. 11). The surface of both topographic depressions is a layer with transparent to acoustically impermeable seismic attributes, i.e. the blocks impede seismic signal penetration whereas the surrounding matrix is uniform and acoustically transparent (Fig. 8). Attempts to sample sediments from one targeted block led to the recovery of coarse sand, contrasting with the finer sandy mud matrix sampled

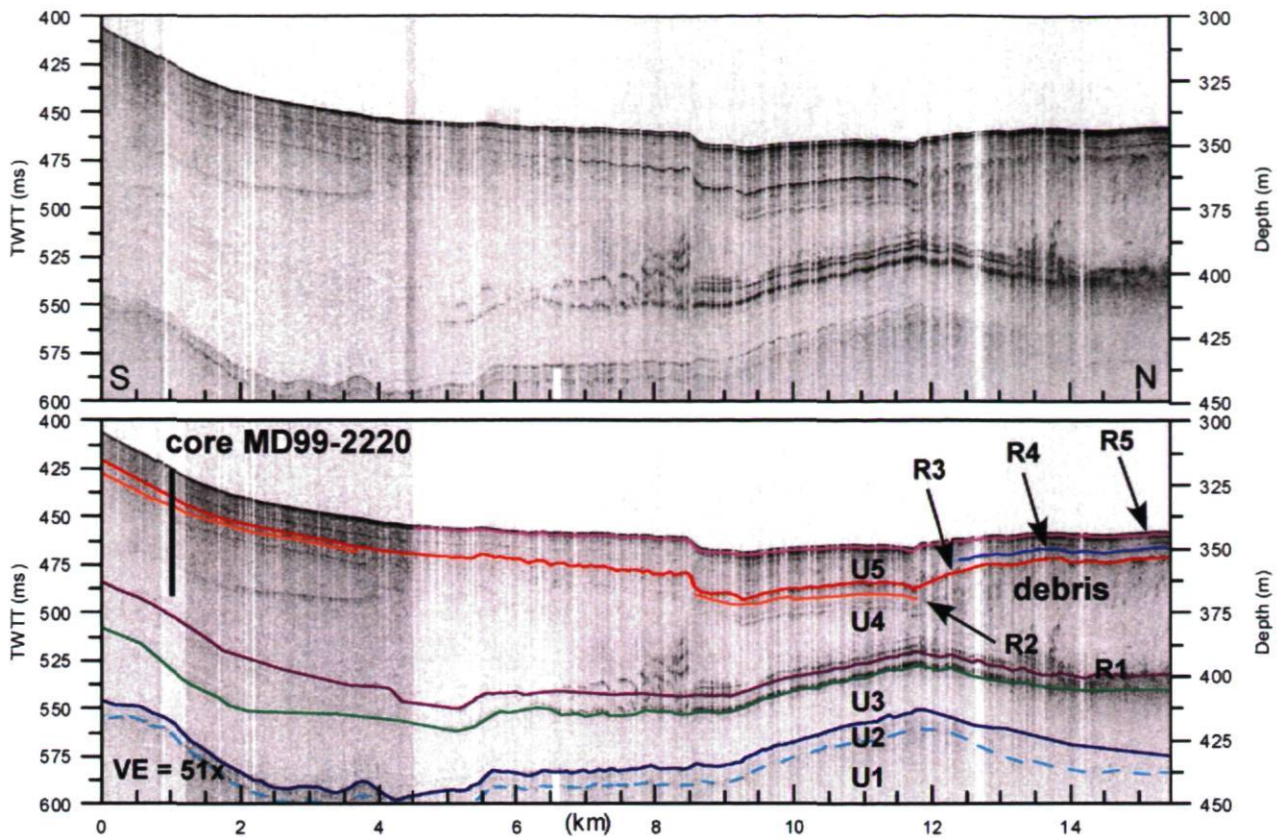


Fig. 9. (a) High resolution seismic profile 05_bet_01 providing a spatial correlation between the debris flow lobe and core MD99-2220 sampling location. Position of line 05_bet_01 is indicated on Fig. 3. The line is 15.4 km long. (b) Seismic interpretations, see text for explanations. The approximate depth at the MD99-2220 core location for R3 is 15 ms (11.3 m), 20 ms (15.0 m) for R2 and for 76 ms (57.0 m) for R1.

between the blocks. Small wood branches with bark and peat were found in the sediments recovered from the sandy mud matrix.

The lowermost portion of the landslide scar has an irregular rugged surface incised by small subparallel channels (Fig. 12). This ~20 km² area is located at the bottom of a drop in the relief of the West depression of the scar (Fig. 6) and ends at the shelf break before a bedrock ridge (Fig. 12). There is an apparent limit between the rugged area and the leveled surface outside the scar area (white dashed line on Fig. 12). The channels have a subparallel pattern and an orientation more or less perpendicular to the axis of the West depression. The largest channels have depths up to 2 m on the seafloor. In the seismic profiles, a shallow high amplitude reflecting horizon (R5 on Fig. 6) is observed at about 1 ms (75 cm) below the seafloor. The reflecting horizon R5 is conformable with the rugged morphology and drapes the channels, implying that the channels are not currently active. A bulge of seismically transparent deposits and deformed reflecting horizons are also identified in this area (Fig. 4).

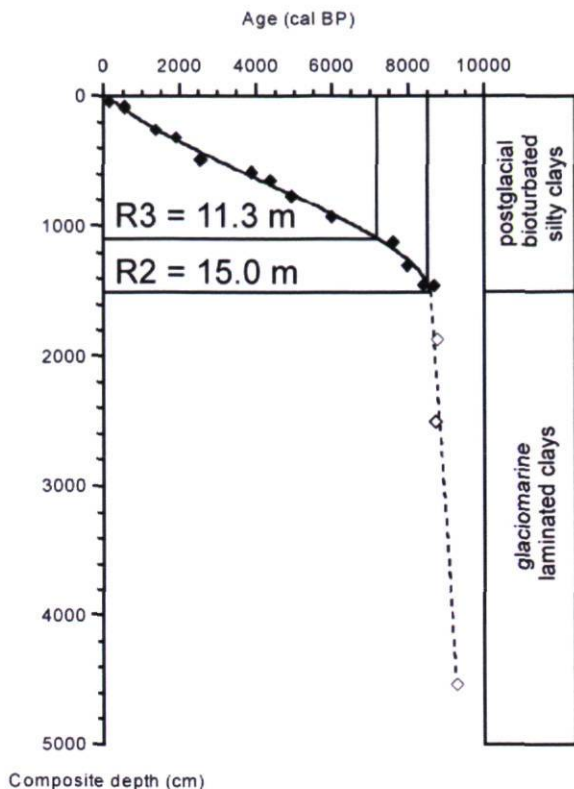
The Estuary slope also shows evidence of slope failure (Fig. 7) where many landslide scars are identified (Fig. 11). The largest landslide scar on the slope is found at water depths ranging from 180 m at the head scarp to 340 m at its toe (Fig. 7). The failure plane has an average slope of about 7°. The landslide scar has a maximum width and length of 1200 m and 1700 m, respectively and extends over an area of 1.8 km². The head scarp has a horseshoe shape and is on average 16 m high. The volume of displaced material is estimated at 13.8 million m³. The failure plane was interpreted on the seismic reflection profiles as the high amplitude reflecting horizon R1 within the highly stratified sediments of Unit 4 (Fig. 7c). The resulting debris are interpreted on the seismic reflection profiles (Fig. 7d) and are buried downslope under a layer of sediments, which ranges from 5 m in thickness at the foot of the slope to 11 m at the end of the depo-

sitional lobe. The upper limit of this debris flow deposit is interpreted as the reflecting horizon R3.

The Laurentian Channel was also influenced by mass movement events, given that we can observe accumulations of debris on the seafloor and within the seismostratigraphic sequence. In the study area, a large depositional lobe is observed at a water depth of 350 m (Fig. 5). This lobe has its apex downslope from the break in the shelf edge where the lineaments A and B in the bedrock meet (Fig. 11). The lobe covers an area of 115 km² and has a maximum diameter of 15 km. With an average thickness of 9 m, the lobe has an estimated volume of ~1 km³. Seismic reflection profiles allow us to interpret this lobe as a result, in part, of an important accumulation of debris following at least one major slope failure event (Fig. 5c). The lobe is recognized within Unit 5 (postglacial sediments) of the seismo-stratigraphic sequence. An undulated high amplitude seismic reflecting horizon (R3 on Figs. 5 and 9) is interpreted as related to a debris flow deposit. This strong reflecting horizon also extends out of the limit of the debris lobe (Fig. 5). This large debris flow is buried under an average of 20 ms (15 m) of deposits, which are interpreted as postglacial sediments (Unit 5). The acoustic signature of the buried debris flow deposit is variable, either transparent around the edges or acoustically impermeable in the central portion of the lobe (Fig. 5). Deformation structures in a soft-sediment fold-and-thrust belt manner (Schnellmann et al., 2005) can be interpreted in the sequence below the debris flow deposits, where the parallel reflecting horizons are deformed and displaced (Fig. 5).

4.2.2. Paleochannel

A paleo-submarine channel and its meander are identified on the shelf east of the landslide scar (Figs. 8, 11 and 13). This submarine channel is not related to the modern Betsiamites River discharge



(Modified from St-Onge et al., 2003)

Fig. 10. Age model with indication of depth of seismic reflecting horizon R3 at 1130 cm and R2 at 1500 cm with corresponding age of 7250 and ~9280 cal BP (modified from St-Onge et al., 2003).

(Fig. 2) and the position of the upper part of the paleochannel corresponds more or less to the eastern edge of the large landslide scar on the shelf (Fig. 11). Evans and Brooks (1994) made a similar observation for the South River Nation subaerial slide in the Ottawa region as that the area of the landslide was confined between two creeks. The meander length, measured along the center of the meander between point A and B (Fig. 8), is 3.4 km. The linear distance between point A and B is 1.9 km. The channel meander has depths of 20 m and 35 m and widths of 280 m and 545 m at points A and B, respectively. The water depth in the meander at point A is 130 m and 170 m at point B. This represents a gradient of 2% for this section of the paleochannel. Terraces are seen on both sides of the meander on the bathymetric images and seismic interpretation reveals conformable stratifications on buried terrace levels (Fig. 13). Upslope from the meander, cross-sections of buried submarine channels can be interpreted in the seismic profiles, implying that the channel base level shifted in time. Paraglacial (Unit 4) and postglacial sediments (Unit 5) have draped the inactive channel after its erosive stage (Fig. 13). Due to absorption of the acoustic energy, it is impossible to observe the seismostratigraphic sequence below Unit 4 (Fig. 13). In the meander, the uppermost reflecting horizons of Unit 4 are conformable on the channel topography, indicating its inactivity since at least the paraglacial sedimentation phase.

4.2.3. Pockmarks

Pockmarks were identified on the bathymetric data and seismic profiles of the shelf and Laurentian Channel regions (Figs. 11, 14 and 15). The pockmarks identified in the St. Lawrence Estuary are likely due to gas seepage (Pinet et al., 2008). On the shelf, they are mostly concentrated in areas at water depths around 140 m, close to the shelf break (Fig. 11). Their diameter ranges between 50 and 75 m with depths from 2 to 4 m. In the Laurentian Channel, the pockmarks are

significantly larger, some of them having diameters of up to 400 m with a depth of 12 m (Fig. 14), which is consistent with general descriptions of pockmarks (Hovland et al., 2002). Smaller pockmarks are observed at the surface of the buried debris lobe, but the largest are located outside the extent of this lobe. Core samples of surface sediments recovered above the buried debris lobe (e.g., station 03-BE02) show very little gas disturbance on the CAT-Scan images (Fig. 19), indicating that the debris lobe could act like an impermeable layer to gas escape or may have disturbed previous seismic chimneys. Station 06-BE17 (Fig. 15) was chosen in order to sample sediments from a large pockmark. With size of 400 m and depth of 12 m and the use of the acoustic tracking system Trackpoint II, it was possible to successfully target this feature. The 882-cm long piston core 06-BE17-06PC recovered was very disturbed when raised to ambient condition due to degassing. A large amount of intact shells (Fig. 15) was observed within the sediment core.

4.3. Spatio-temporal sequence of mass movement events

Bathymetric data, seismic reflection surveys, and sediment core data reveal that at least 4 major non-synchronous slope failure events have shaped the area. In this section, we describe morphologic and stratigraphic evidence for the occurrence of the landslides and expose the seismic interpretations that lead us to define a spatio-temporal sequence for these events.

4.3.1. Paraglacial event

The lowermost debris flow deposit interpreted on the seismic profiles of the study area is located in the upper section of the shelf. It is identified within Unit 4 below reflecting horizon R1 (Fig. 8) as a seismic body with an irregular geometry. The upper reflecting horizon of the deposit has an undulated relief. This debris flow deposit is acoustically transparent or acoustically opaque when thick. This event also likely relates to the complex geometry of the reflecting horizons within Unit 4 upslope on Fig. 6. Since other subsequent events may have eroded away this debris flow deposit, it is not possible to delimitate the spatial extension of this event on the shelf.

4.3.2. Debris lobe event

A second event, with the greatest impact in the study area, caused the formation of part of the large debris lobe in the Laurentian Channel. For a volume estimated at ~1 km³ for the debris lobe, one could expect to observe a significant landslide scar in the vicinity of this lobe. The positions of the large landslide scar on the shelf and the debris lobe in the Laurentian Channel are oriented along the same central axis (Fig. 11). The debris lobe in the Laurentian Channel is observed in Unit 5 above R2, which represents the limit between Unit 4 (paraglacial sedimentation) and Unit 5 (postglacial sedimentation). On the shelf, the large landslide scar is carved in the closely packed reflecting horizons of the paraglacial sedimentation Unit 4. In addition, a topographic bulge is interpreted above the reflecting horizon R2 (Fig. 4), implying that this bulge was formed during the postglacial sedimentation phase (Unit 5).

4.3.3. Recent landslides

Morphological observations, seismic interpretations and core data led us to establish that multiple landslides (i.e., less than 500 yr old) have occurred in the area. On the surface of the large landslide scar of the shelf, blocks and channels are identified. Numerous channels are oriented parallel to the axis of the slope (Figs. 8 and 11) and are interpreted as preferential pathways for downslope transport of the fluidized portion of the mass movement. In the seismic profiles of the upper shelf, two high amplitude and shallow highly undulated reflecting horizons at less than 4 ms below seafloor are interpreted (Fig. 8), the deepest being R5. This reflector is truncated in the 600 m wide and 5 m deep furrow of the West depression (Fig. 8).

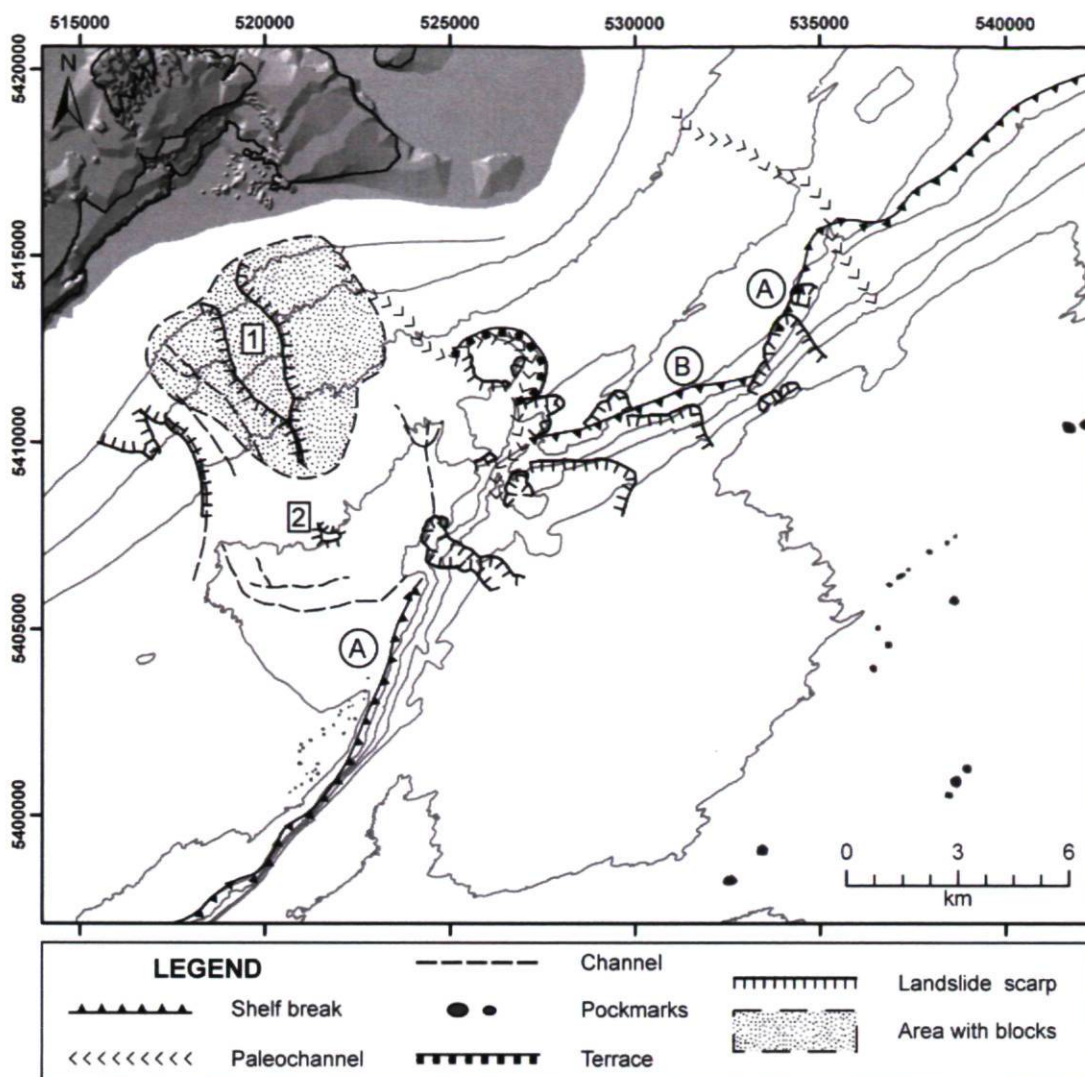


Fig. 11. Geomorphological interpretations of the area. 1 and 2 refer to the buttes, and A and B to the families of lineaments, see text. Bathymetric contour lines are at 40 m interval starting at 20 m depth.

Three cores were sampled from the large landslide scar on the shelf and analyzed (Figs. 8, 16, 17 and 18). A 127-cm long trigger weight core recovered from the West depression (05-BE02-02TWC) is composed of two facies (Fig. 16). The upper facies, between 0 and 30 cm, is a bioturbated sandy mud with a mean grain size of 15 μm with 14% clay, 70% silt, and 16% sand contents. The average density is 1.75 g/cm^3 and magnetic susceptibility values range between 250 and 390 $\times 10^{-5}$ SI. The second facies, from 30 to 127 cm, is composed of silty clay clasts in a sandy mud matrix, typical of a debris flow deposit (e.g., Mulder and Alexander, 2001). A clast, sampled between 38 and 39 cm, has a mean grain size of 1.8 μm and composed of 56% clay and 44% silt contents. The contrasting sandy mud matrix has a mean grain size of 16 μm with 20% clay, 50% silt, and 30% sand contents. Broken shells, a wood branch of $\sim 2 \times 2 \times 2$ cm and a small root were also identified in the second facies of this core. A box core (05-BE02-02BC) was sampled at the same station in the West depression (Figs. 8 and 17) and presents only one facies. The 40-cm long box core is also composed of sandy mud. The mean grain size is 17 μm with 14% of clay, 64% of silt and 22% of sand. The average density of the sediments is 1.8 g/cm^3 and magnetic susceptibility values range between 200 and 350 $\times 10^{-5}$ SI. ^{210}Pb measurements were carried out on the sediments of this box core. Three different horizons can be identified in the ^{210}Pb activity profile of core 05-BE02-02BC (Fig. 17): the active mixing upper horizon between 0

and 4.5 cm, the central radioactive decay horizon between 4.5 and 22.5 cm and the background horizon, which was reached at 22.5 cm. These measurements indicate that this uppermost 22.5 cm of sediments contains unsupported ^{210}Pb and that a sedimentation rate of 0.29 cm yr^{-1} can be calculated from the slope of the $\ln(^{210}\text{Pb}_{\text{excess}})$ (Fig. 17).

Analysis of the sediment properties recovered from a box core (05-BE05-05BC) sampled in the meander area (Fig. 8) led to the identification of a facies of bioturbated sandy mud and a coarser rapidly deposited layer characterized by sand laminations (Fig. 18). The first facies within this box core, between 0 to 30.5 cm and 34.5 to 38 cm, is composed of bioturbated sandy mud lacking apparent sedimentary structures. The mean grain size in the upper facies is 25 μm with 10% of clay, 60% of silt and 30% of sand. The density and magnetic susceptibility values are stable across the profiles: average magnetic susceptibility of 350 $\times 10^{-5}$ SI and average density of 1.8 g/cm^3 , indicating fairly stable hemipelagic sedimentary conditions in the meander. ^{210}Pb activity was measured within this box core and the results indicate that the uppermost 15.5 cm contain unsupported ^{210}Pb . Similarly to the box core sampled in the West depression, a sedimentation rate of 0.11 cm yr^{-1} was calculated from the slope of the $\ln(^{210}\text{Pb}_{\text{excess}})$ for the interval of radioactive decay between 4.5 and 22.5 cm (Fig. 18). A sharp transition occurs between the sandy mud

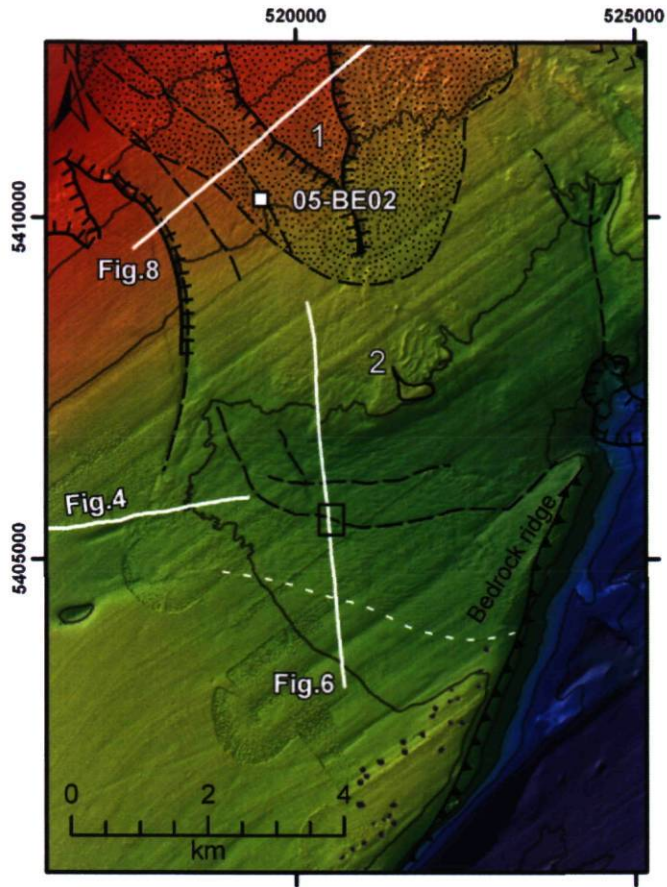


Fig. 12. Bathymetric image of the rugged area and the landslide scar with position of seismic profile presented on Figs. 4 and 6. Note the pockmarks located close to the shelf edge. The water depth of the rugged area ranges between 130 and 170 m. The rectangle corresponds to the enlargement of the seismic profile shown in Fig. 6b. The white dashed line is the apparent limit between the rugged area and the leveled surface outside the scar area. 1 and 2 refer to the buttes.

and the coarser layer at 30.5 cm. This 4-cm thick sand layer is normally graded (fining upward) with parallel laminations (Fig. 18), typical of normally graded turbidites (Bouma, 1962). The mean grain size decreases from 100 μm at the base to 49 μm at top of the layer. Two 0.5-cm thick layers of sand mixed with organic matter, most likely peat, were identified in the laboratory and are visible on the CAT-Scan at 30.5 and 32.5 cm by their darker color (Fig. 18).

In addition, a rapidly deposited layer, contrasting sharply from surrounding sediments, is observed close to the seafloor surface within the sediment sequence of the Laurentian Channel. On the seismic profiles, this layer is characterized by a high amplitude reflecting horizon contrasting with the uniform background attributes of seismostratigraphic Unit 5 (Fig. 5). This high amplitude reflecting horizon R5 is observed at an average depth of 1.33 ms (1 m) (Fig. 5). Its spatial extent is not related to the debris lobe, as it extends outside of the limit of the lobe (Fig. 5). A piston core (03-BE02-43PC) was sampled above the buried debris lobe in a sampling site located in the Laurentian Channel. One main facies is identified in this 724 cm-long core and is characterized by massive dark grey bioturbated clays with a few thin interbedded coarser layers. This facies has an average density of 1.5 g/cm³ and an average CT number of 1055. At a depth of 55 cm, a sharp-based 5 cm-thick sandy layer is observed (Fig. 19). This sandy layer presents peaks in the bulk density and magnetic susceptibility profiles and is interpreted as the sedimentary facies of reflecting horizon R5.

5. Discussion

5.1. Chronology of mass movement events

In North America, the historical earthquake record from eye-witnesses is fairly short (no more than 400 yr) and one way to extend this record past historic archives is to rely on the sediment record. The studied area is located within the Lower St. Lawrence Seismic Zone (LSZ) and close to the Charlevoix Seismic Zone (CSZ) (Adams and Atkinson, 2003; Lamontagne et al., 2003), suggesting that the occurrence of slope instability may be influenced by this locally enhanced seismic activity. We have shown for the Betsiamites–Rimouski area that many different slope failure events have occurred. Factors reducing slope stability such as highly stratified deposits and high sedimentation rates (i.e., Unit 4) or gas escape from pockmarks (Figs. 14 and 15) are found in this area of the Estuary. The failure of the debris lobe event (Fig. 8) and the landslide on the slope (Fig. 7) occurred within Unit 4. These highly variable seismic attributes could indicate different sediments composition, such as the alternation of silty clay and sand layers. Such changes in grain size across a sedimentary column could influence material permeability and create a weak layer in the case of an earthquake. If the sand liquefies following earthquake shaking, an upward flow of excess pore pressure can be trapped by relatively impermeable sublayers (e.g., silty clay) and forms a water film beneath it (Kokusho, 1999). There is no shear resistance along the water film and this will create a weak layer acting as a sliding surface for lateral spreading failure. Such liquefaction has

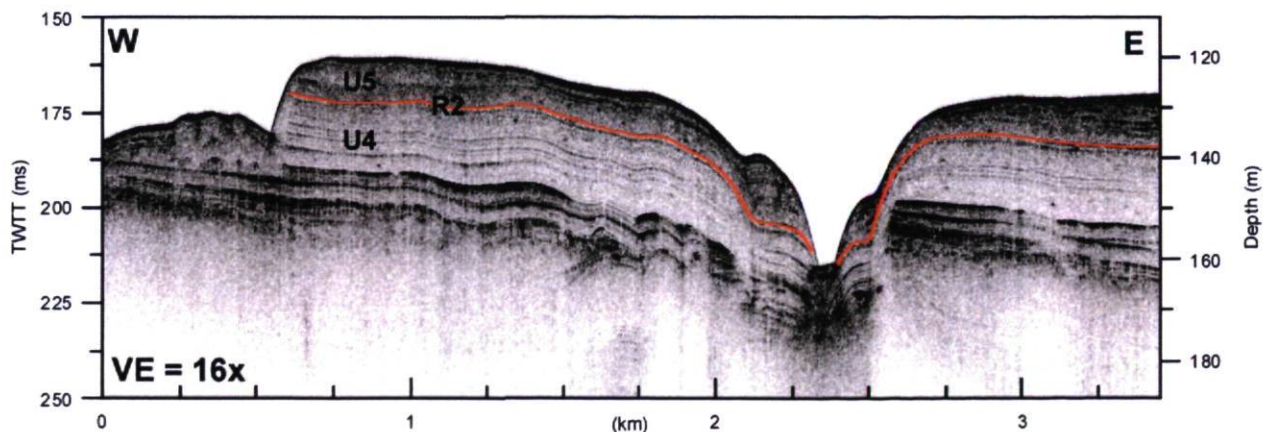


Fig. 13. Seismic profile 05_bet_12 across the paleochannel. Line is 3.5 km long. Seismic U4 and U5 refer to seismostratigraphic units (paraglacial and postglacial) and R2 is the transition between these two units. Seismic interpretation reveals conformable stratifications on buried terrace levels.

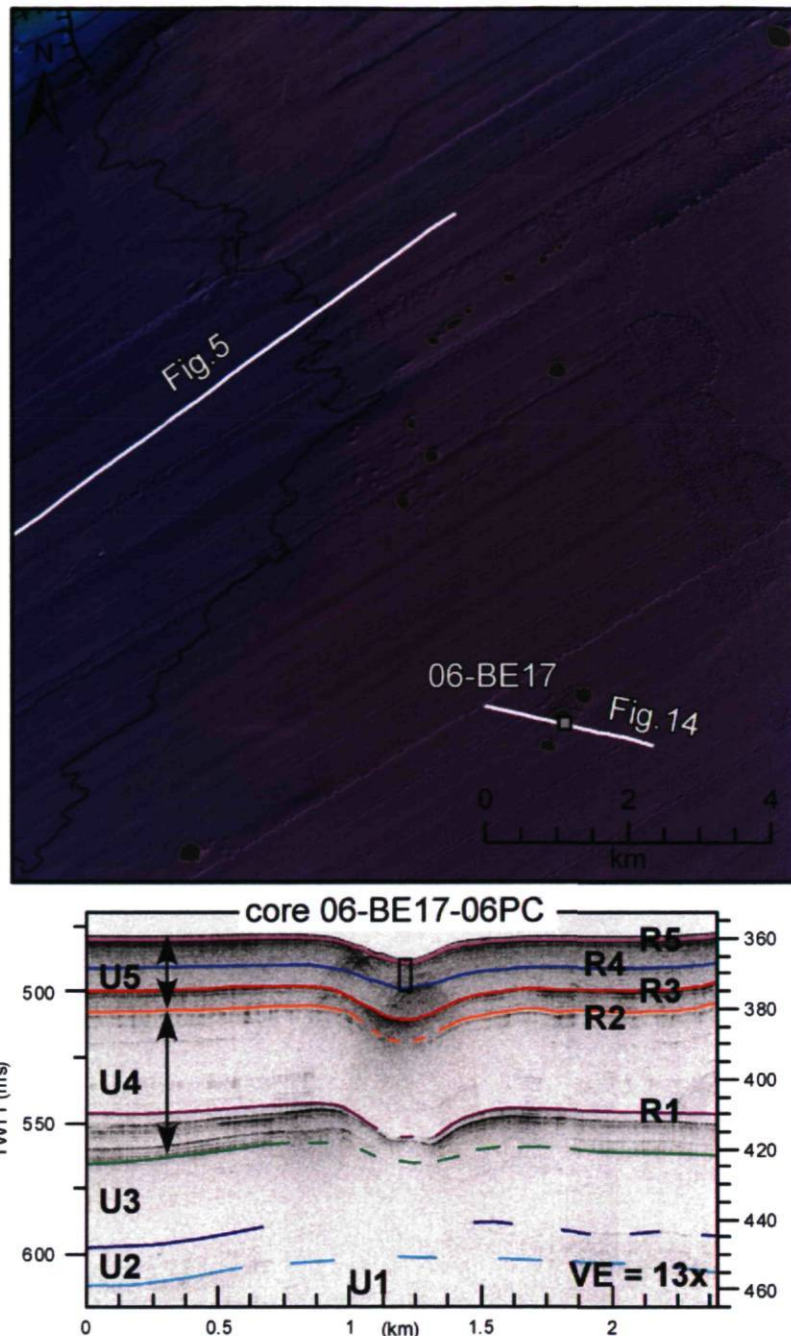


Fig. 14. (a) Bathymetric image of the Laurentian Channel pockmarks. The water depth range from 330 to 350 m. The pockmark has a diameter of 400 m with a depth of 12 m. Note that more pockmarks are observed outside the debris lobe. Station 06-BE17 and position of line are indicated. (b) Seismic reflection profile be06_112 across the pockmark. Line is 2.4 km long. U1 to U5 refer to the 5 seismostratigraphic units and R1 to R5 refer to the 5 reflecting horizons identified in the study area, see text for explanations.

likely occurred for the slide presented on Fig. 7, as little sediments remained on the failure plane.

Assuming that the failures in the Betsiamites–Rimouski have been triggered by earthquakes, we can now propose a chronology for some of these failure events. In our analysis, we have identified one event occurring during the phase of paraglacial sedimentation (seismostratigraphic Unit 4), the paraglacial event, and a second event during the early postglacial sedimentation (seismostratigraphic Unit 5), the debris lobe event. The oldest date obtained by St-Onge et al. (2003) is ~9280 cal BP sampled at a depth of 45.35 m. In our seismostratigraphic analysis, we have identified the reflecting horizon R1 at an estimated depth of 57.0 m at the core MD99-2220 sampling location (Fig. 9) and that the paraglacial event is observed on the shelf below

reflecting horizon R1 (Fig. 8). This would imply that the paraglacial event is older than 9280 cal BP. The level of the reflecting horizon R3, interpreted as the upper boundary of the debris flow deposits, can be mapped to the sampling location of core MD99-2220 in the Laurentian Channel (Fig. 9). This level is observed at a depth of 1130 cm, leading to an age estimate of about 7250 cal BP (Fig. 10). This age estimate is consistent with other observations linking earthquake triggered landslides at about the same time and suggests that this landslide may have been triggered by a major earthquake in a time of important glacio-isostatic rebound. For example, in the Saguenay Fjord, St-Onge et al. (2004) suggested that at least 4 rapidly deposited layers, possibly caused by earthquakes, occurred between 6800 and 7200 cal BP. Similarly, Aylsworth et al. (2000) associated observations of very

COR0602-BE17-06PC - Laurentian Channel pockmark

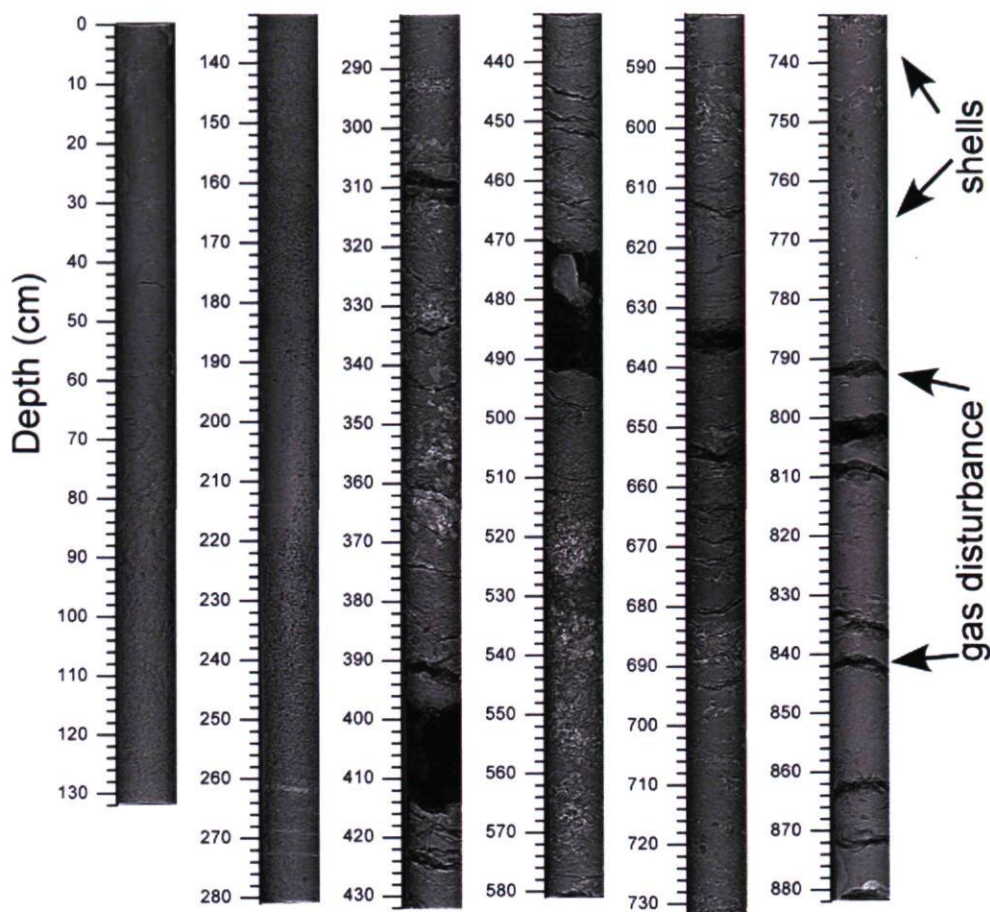


Fig. 15. CAT-scan image of the 882-cm long piston 06-BE17-06PC sampled in a large pockmark in the Laurentian Channel. Sample position is presented in Fig. 14. Note the substantial gas disturbance and amount of intact shells.

disturbed terrain in a flat erosional plain in the Ottawa Valley to earthquake deformations and liquefaction of sensitive clays and estimated the date of occurrence of this large earthquake to ca. 7060 yr BP (~7860 cal BP).

For the recent events, the age estimates were obtained from sedimentation rates derived from ^{210}Pb measurements (Figs. 17 and 18). As described previously, many landslides elsewhere in Quebec are related to the AD 1663 earthquake (Saguenay Fjord, Levesque et al., 2006 and St-Onge et al., 2004; Saint-Jean Vianney, Lasalle and Chagnon, 1968), as it is also suggested for the Betsiamites subaerial landslide (Bernatchez, 2003). In our analysis of core 05-BE05-05BC sampled in the paleomeander (Figs. 8 and 18), we have identified a turbidite layer at 30.5 cm and calculated a sedimentation rate of 0.11 cm yr^{-1} from the slope of the $\ln(^{210}\text{Pb}_{\text{excess}})$ for the 18-cm interval of radioactive decay between 4.5 and 22.5 cm (Fig. 18). 5 cm of compaction was recorded when the 10 cm diameter push core was subsampled from the $50 \times 50 \text{ cm}$ square box corer. This implies that the turbidite at this location is buried under a minimum of 35.5 cm. Considering that the effect of compaction due to sampling is usually higher in the upper centimeters where unconsolidated sediments have higher water content (e.g., Perret et al., 1995) and that the sedimentation rate was calculated for a 18-cm interval below the mixing zone, it is reasonable to apply the rate of 0.11 cm yr^{-1} to obtain an age estimate for the turbidite buried under 35.5 cm. This turbidite is dated at about AD 1681, which implies that it could possibly have been triggered by the AD 1663 earthquake. After the AD 1663 event, the following significant earthquake in Eastern Canada ($M \sim 5.8$)

occurred in AD 1732 in Montreal (Smith, 1962) about 600 km west of the study area, which is too far to have triggered the landslide.

The rapidly deposited layer (R5 on Fig. 5) identified in the Laurentian Channel presented above can also be related to the AD 1663 event. It is buried at an average depth of 1 m in the sediments and using the ^{210}Pb derived sedimentation rate of 0.28 cm yr^{-1} determined by St-Onge et al. (2003) on box core AH00-2220 13 km from our coring station (Fig. 3), we can estimate a date of occurrence at AD 1646, which can reasonably be linked to the AD 1663 earthquake. The work of Filion et al. (1991) in the Rivière du Gouffre in the Charlevoix region, 200 km southwest from our study area also supports the hypothesis that some of the observed recent landslides were triggered by the AD 1663 earthquakes. In fact, Filion et al. (1991) established a radiocarbon-based chronology of landslide activity from tree trunks buried in debris flow material. The radiocarbon dates indicate that most landslides were triggered before 600 ^{14}C yr BP. In addition, tree-ring dating allowed them to conclude that two large landslides within this area were caused by the AD 1663 earthquake.

For station 05-BE02 in the West depression, the debris flow was not identified in the 40-cm long ^{210}Pb -dated box core 05-BE02-02BC (Fig. 17), but was identified at a depth of 30 cm in the trigger weight core 05-BE02-02TWC (Fig. 16) of this same location. The 10 cm difference is explained by some loss due to sampling associated with the gravity coring. We can not determine precisely the depth of the debris flow in the trigger weight core. However, based on the sedimentation rate estimated at this station on the box core 05-BE02-02BC (0.29 cm yr^{-1} , Fig. 17) a depth of 40 cm would lead to AD 1872 for

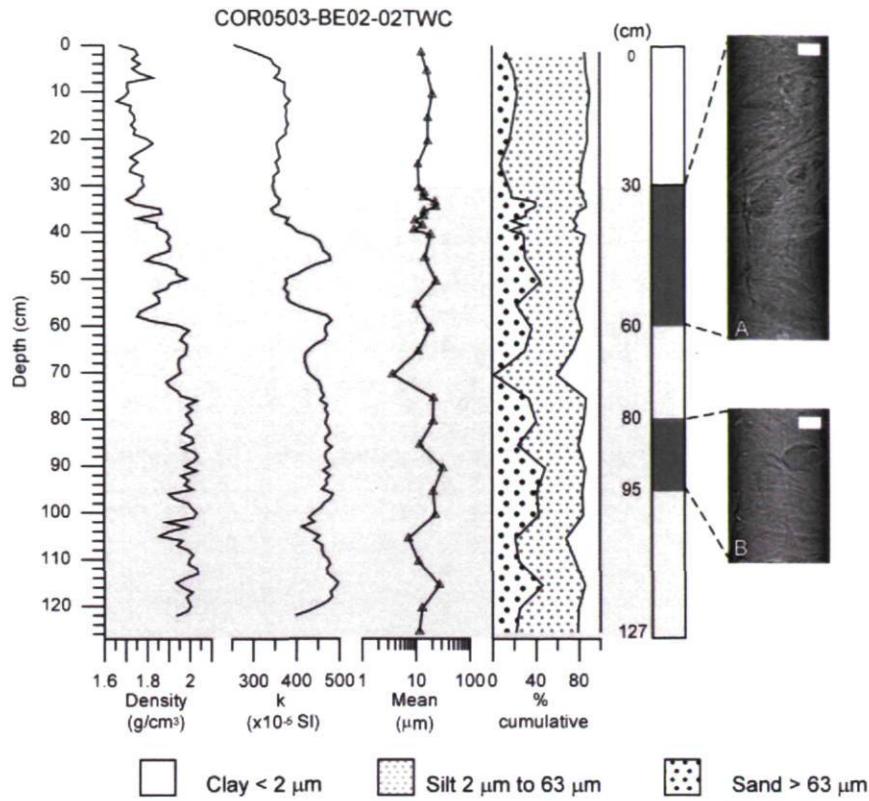


Fig. 16. Bulk density, magnetic susceptibility, mean grain size and cumulative fraction for clay, silt and sand for core 05-BE02-02TWC. The grey horizon highlights a debris flow deposit (see text for details). CAT-scan image A is 10×30 cm and corresponds to depths between 30 and 60 cm, B is 10×15 cm and corresponds to depths between 80 and 85 cm. The white scale bar represents 2×1 cm.

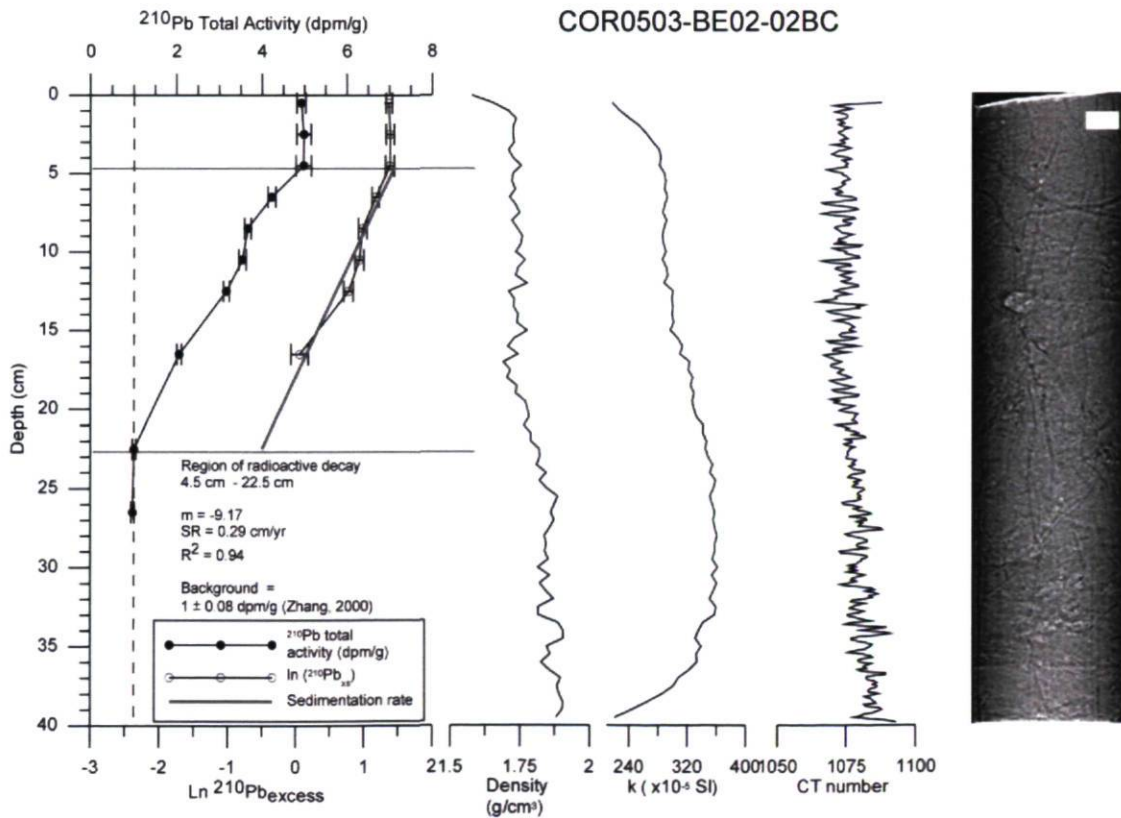


Fig. 17. ^{210}Pb measurements and physical properties in box core 05-BE02-02BC sampled in the West depression of the large landslide scar. Fig. 8 indicates location of the sampling station. Also shown is the CAT-scan image. k =magnetic susceptibility. The white scale bar represents 2 cm×1 cm.

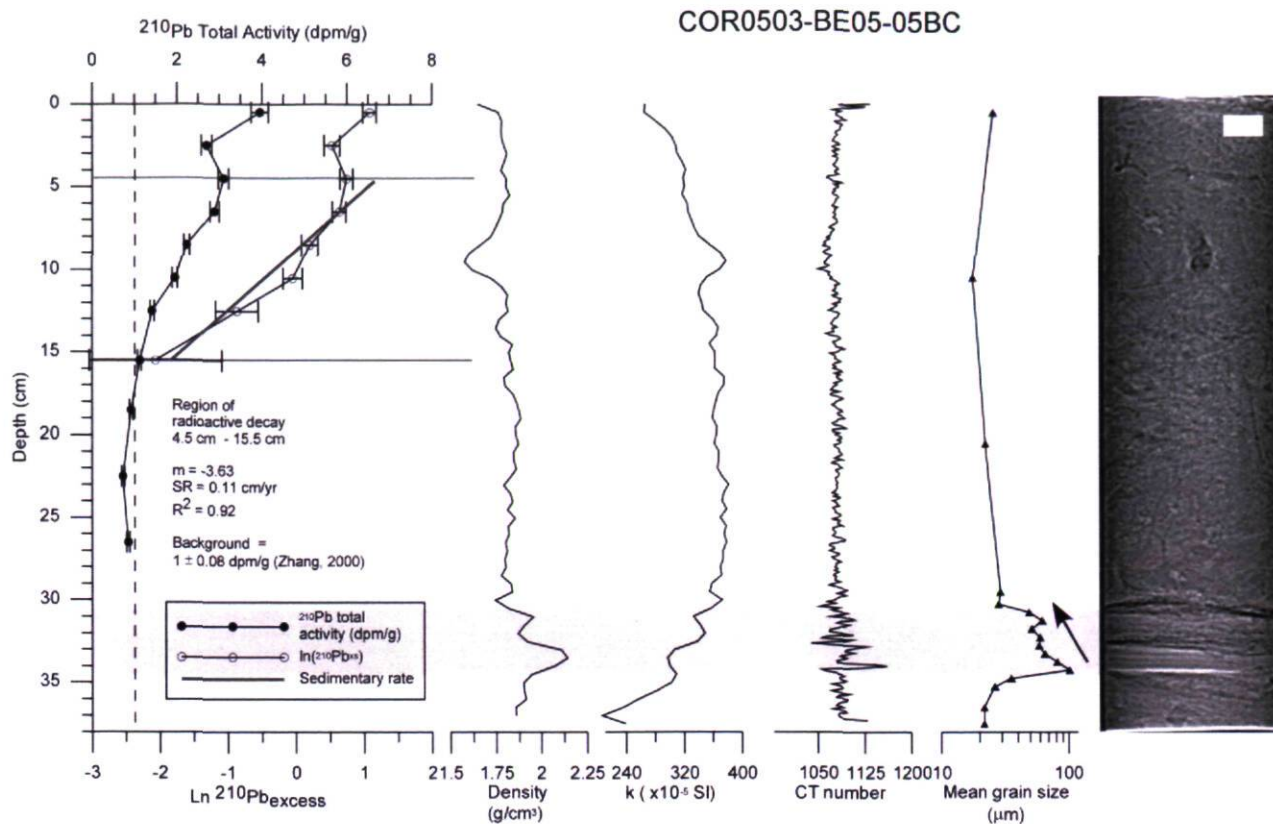


Fig. 18. ^{210}Pb measurements and physical properties in box core 05-BE05-05BC from the paleochannel. Also shown is the CAT-scan image. The grey area highlights the sand bed associated with the 1663 event (see text for details). k = magnetic susceptibility. The white scale bar represents 2 cm \times 1 cm.

the event, whereas a depth of 45 cm to AD 1855. Despite the fact that we can not provide a precise date, it nevertheless discards the hypothesis that this last event is associated with the AD 1663 earthquake.

In fact, with an average sedimentation rate of 0.29 cm yr^{-1} , the debris flow would have to be buried under at least 100 cm of hemipelagic sediments to be dated around AD 1663, which is too far from the minimum estimated depth of 40 cm for this coring station. Dates for submarine landslides that do not all correlate with the AD 1663 event were also observed by Levesque et al. (2006) in the Saguenay Fjord. They have compiled many ^{210}Pb -dated landslides and concluded that not all landslides can be associated with the AD 1663 event. Furthermore, two significant earthquakes were recorded in the Charlevoix Seismic Zone (CSZ) (Smith, 1962): a first one on October 17, 1860 ($M \sim 6$) and a second one on October 20, 1870 ($M \sim 6.5$). The epicenters for the 1860 and 1870 events are evaluated at 180 km and 200 km from the Betsiamites area, respectively.

6. Conclusions

The main objective of this study was to define a framework accounting for the evolution of the morpho-sedimentology observed in the Betsiamites–Rimouski area in the St. Lawrence Estuary. This was done by presenting a geomorphological analysis of the area and by proposing a spatio-temporal sequence for the occurrence of the mass movements. Finally, we propose a chronology for the related failures in the area.

In addition to the general morphology of the Estuary, submarine features resulting from mass movement processes, channel erosion and gas seepage are also described. This paper demonstrates that more than one failure events have influenced the morphology of the area during the Holocene. At least four events remobilized massive volumes of sediments, creating the complex geomorphology observed in the area. The first paraglacial event, estimated to have occurred before 9280 cal BP, left buried traces in the deposits of the shelf. The second event is dated at ca. 7250 cal BP and had the greatest consequences in the area. We attribute to this event the large landslide

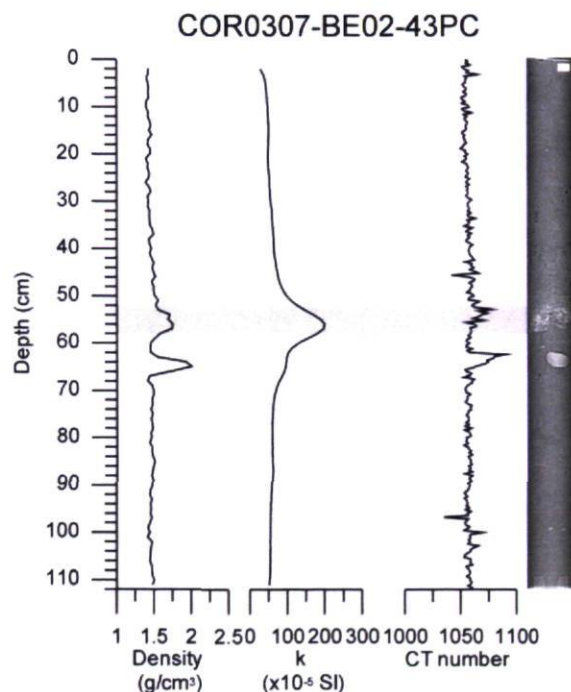


Fig. 19. Bulk density, magnetic susceptibility (k) and CT number profiles for the upper section of piston core 03-BE02-43PC. Also shown is the CAT-scan image. The sand layer highlighted around 55 cm is interpreted as the shallow reflecting horizon R5 (see text for details).

scar characterized by the two depressions and the buried debris lobe of the Laurentian Channel. The third event is linked to the AD 1663 (M~7) earthquake. ²¹⁰Pb-dated subaerial landslide debris were identified and related to a subaerial event dated on shore (Bernatchez, 2003). Our results lead us to link the submarine and the subaerial events to one another and support the hypothesis that the subaerial event occurred following the AD 1663 earthquake. Debris flow deposits associated with the AD 1663 earthquake are also identified in the Laurentian Channel. In addition, morphological observations indicate that a smaller landslide is younger than the AD 1663 event. In fact, ²¹⁰Pb analyses and historical earthquakes in Eastern Quebec allow us to estimate that this event could be related to the AD 1860 (M~6) or AD 1870 (M~6.5) earthquakes.

In our chronology, we were able to link 4 main mass movement events (older than 9280 cal BP, 7250 cal BP, AD 1663, and AD 1860 or AD 1870) to slope instability (i.e., not to catastrophic river discharge), and to differentiate them from one another based on a sequential stratigraphy point of view and on ²¹⁰Pb or radiometric dates. Our analysis has raised many other questions such as the tsunamigenic potential of these events and the threat of future similar events elsewhere in the Estuary. There is thus a need to pursue our research to clearly define the mechanisms responsible for slope failures and to describe post-failure behavior in order to assess slope stability in the St. Lawrence Estuary. Investigating bedrock faults influence and gas escape on sediments stability will also lead to a better understanding of the area.

Acknowledgements

The authors wish to thank the NSERC for their financial support for the Costa-Canada project and for ship time allocation. Many thanks to Roger Côté, André Godin, and Richard Sanfaçon (Canadian Hydrographic Service, Maurice Lamontagne Institute), Patrick Lajeunesse, Christiane Levesque, Pierre Therrien (Université Laval), Ben DeMol and Roger Urgeles (University of Barcelona), Bassam Ghaleb (GEOTOP UQAM-McGill), Andrée Bolduc and Mathieu Duchesne (GSC-Quebec), Calvin Campbell (GSC-Atlantic) and finally to all the crew members on board the F.G. Creed, Coriolis II and Guillemot vessels. Constructive reviews by David J.W Piper, editor, F. Anselmetti and an anonymous reviewer greatly improved the quality of this paper.

References

- Adams, J., Atkinson, G., 2003. Development of seismic hazard maps for the proposed 2005 edition of the National Building Code of Canada. *Can. J. Civ. Eng.* 30, 255–271.
- Allard, J.-D., 1984. Zones exposées aux mouvements de terrain, région de Chutes-aux-Outardes. Ministère de l'Énergie et des Ressources, Québec. 42 pp.
- Aylsworth, J.M., Lawrence, D.E., Guertin, J., 2000. Did two massive earthquakes in the Holocene induce widespread landsliding and near-surface deformation in part of the Ottawa Valley, Canada? *Geology* 28, 903–906.
- Bernatchez, P., 2003. Évolution littorale holocène et actuelle des complexes deltaïques de Betsiamites et de Manicouagan-Outardes : synthèse, processus, causes et perspectives. Ph.D Thesis, Université Laval, Québec. 460 pp.
- Bolduc, A., Campbell, D.C., Côté, R., Girouard, P., Duchesne, M.J., Beaulieu, S., 2006. F.G. CREED EXPEDITION 2005-075: Multibeam and magnetometer survey of the St. Lawrence Estuary west of Rimouski, October 27th to November 28th 2005. GSC Open File Report 5390. 28 pp.
- Blott, S.J., Pye, K., 2001. GRADISTAT: a grain size distribution and statistics package for the analysis of unconsolidated sediments. *Earth Surf. Processes Landf.* 26, 1237–1248.
- Boespflug, X., Long, B.F.N., Occhietti, S., 1995. Cat-scan in marine stratigraphy – a quantitative approach. *Mar. Geol.* 122, 281–301.
- Bouma, A.H., 1962. Sedimentology of some flysch deposits. A graphic approach to facies interpretation. Elsevier, Amsterdam. 168 pp.
- Campbell, D.C., Hayward, S., Côté, R., Poliquin, L., 2005. F.G. Creed expedition 2005-038: multibeam and magnetometer survey of the St. Lawrence Estuary north of Rimouski – June 5th to 17th 2005. GSC Open File Report 4966. 22 pp.
- Campbell, D.C., Duchesne, M., Poliquin, L., Côté, R., 2006. F.G. Creed expedition 2005-066: multibeam and magnetometer survey of the St. Lawrence Estuary north of Mont-Joli, Aug 27th to Sept 8th 2005. GSC Open File Report 5078. 23 pp.
- Canals, M., Lastras, G., Urgeles, R., Casamor, J.L., Mienert, J., Cattaneo, A., De Batist, M., Hafidason, H., Imbo, Y., Laberg, J.S., Locat, J., Long, D., Longva, O., Masson, D., Sultan, N., Trincardi, F., Bryn, P., 2004. Slope failure dynamics and impacts from seafloor and sub seafloor shallow geophysical data: an overview. *Mar. Geol.* 213, 9–72.
- Cauchon-Voyer, G., 2007. Morpho-sédimentologie et mouvements de masse au large de la Rivière Betsiamites, estuaire du Saint-Laurent, Québec. M.Sc. Thesis, Université Laval, Québec. 204 pp.
- Dionne, J.C., 2001. Relative sea-level changes in the St. Lawrence Estuary from deglaciation to present day. In: Weddle, T.K., Retelle, M.J. (Eds.), *Deglacial History and Relative Sea-Level Changes, Northern New England and Adjacent Canada*. Geological Society of America Special Paper, Boulder, Colorado, pp. 271–284.
- Dredge, L., 1983. Surficial Geology of the Sept-Îles area, Quebec North Shore. Geological survey of Canada Memoir, 408. 40 pp.
- Duchesne, M.J., Long, B.F., Urgeles, R., Locat, J., 2003. New evidence of slope instability in the Outardes Bay delta area, Quebec, Canada. *Geo-Mar. Lett.* 22, 233–242.
- Duchesne, M.J., Pinet, N., Bolduc, A., Bédard, K., Lavoie, D., 2007. Seismic stratigraphy of the lower St. Lawrence River estuary (Quebec) Quaternary deposits and seismic signature of the underlying geological domains. Geological Survey of Canada, Current Research 2007-D2, 14 pp.
- Evans, S.G., Brooks, G.R., 1994. An earthflow in sensitive Champlain Sea sediments at Lemieux, Ontario, June 20, 1993, and its impact on the South Nation River. *Can. Geotech. J.* 31, 384–394.
- Filion, L., Quinly, F., Bégin, C., 1991. A chronology of landslide activity in the valley of Rivière Du Gouffre, Charlevoix, Quebec. *Can. J. Earth Sci.* 28, 250–256.
- Hampton, M.A., Lee, H.J., Locat, J., 1996. Submarine landslides. *Rev. Geophys.* 34, 33–59.
- Hart, B.S., Long, B.F., 1996. Forced regressions and lowstand deltas: Holocene Canadian examples. *J. Sediment. Res.* 66, 820–829.
- Hovland, M., Gardner, J.V., Judd, A.G., 2002. The significance of pockmarks to understanding fluid flow processes and geohazards. *Geofluids* 2, 127–136.
- Josenhans, H., Lehman, S., 1999. Late glacial stratigraphy and history of the Gulf of St. Lawrence. *Can. J. Earth Sci.* 36, 1327–1345.
- Kokusho, T., 1999. Water film in liquefied sand and its effect on lateral spread. *J. Geotech. and Geoenviron. Eng.* 125, 817–826.
- Lamontagne, M., Keating, P., Perreault, S., 2003. Seismotectonic characteristics of the Lower St. Lawrence Seismic Zone, Quebec: insights from geology, magnetics, gravity, and seismics. *Can. J. Earth Sci.* 40, 317–336.
- Lasalle, P., Chagnon, J.-Y., 1968. An ancient landslide along the Saguenay River, Quebec. *Can. J. Earth Sci.* 5, 548–549.
- Levesque, C.L., Locat, J., Leroueil, S., 2006. Dating submarine mass movements triggered by earthquakes in the Upper Saguenay Fjord, Quebec, Canada. *Nor. J. Geol.* 86, 231–242.
- Locat, J., 1977. L'émersion des terres dans la région de Baie-des-Sables/Trois-Pistoles. *Géographie Physique Quaternaire* 31, 297–306.
- Locat, J., Lee, H.J., 2002. Submarine landslides: advances and challenges. *Can. Geotech. J.* 39, 193–212.
- Locat, J., Levesque, C., Locat, P., Cauchon-Voyer, G., Leroueil, S., Godin, A., Sanfaçon, R., 2004. Aperçu des mouvements de masse sous-marins au large de la rivière Betsiamites, estuaire du Saint-Laurent, Québec, Canada. Conférence Canadienne de Géotechnique, Québec. 10 pp.
- Locat, J., Martin, F., Locat, P., Leroueil, S., Levesque, C., Konrad, J.-M., Urgeles, R., Canals, M., Duchesne, M.J., 2003. Submarine Mass Movements in the Upper Saguenay Fjord, (Québec, Canada), triggered by the 1663 earthquake. In: Locat, J., Mienert, J. (Eds.), *Submarine Mass Movements and their Consequences*, 1st International Symposium. Kluwer Academic Publishers, Dordrecht, The Netherlands, pp. 509–520.
- Locat, J., Mienert, J. (Eds.), 2003. *Submarine Mass Movements and their Consequences* 1st International Symposium. Kluwer Academic Publishers, Dordrecht, The Netherlands. 540 pp.
- Loring, D.H., Nota, D.J.G., 1973. Morphology and sediments of the Gulf of St. Lawrence. Bulletin of the Fisheries Research Board of Canada 182, Ottawa. 147 pp.
- Lortie, G., Guilbault, J.P., 1984. Les diatomées et les foraminifères de sédiments marins post-glaciaires du Bas Saint-Laurent (Québec): Analyse comparée des assemblages. *Naturaliste Canadien* 111, 297–310.
- Massé, M., 2001. Évolution générale des dépôts quaternaires sous l'estuaire du St-Laurent entre Îles aux Lièvres et Rimouski. M.Sc. Thesis, Université du Québec à Rimouski, Rimouski, 129 pp.
- Mulder, T., Alexander, J., 2001. The physical character of subaqueous sedimentary density flows and their deposits. *Sedimentology* 48, 269–299.
- Perret, D., Locat, J., Leroueil, S., 1995. Strength development with burial in fine-grained sediments from the Saguenay Fjord, Quebec. *Can. Geotech. J.* 32, 247–262.
- Pinet, N., Duchesne, M.J., Lavoie, D., Bolduc, A., Long, B., 2008. Surface and subsurface signatures of gas seepage in the St. Lawrence Estuary (Canada): Significance to hydrocarbon exploration. *Marine and Petroleum Geology* 25, 271–288.
- Piper, D.J.W., Shor, A.N., Farre, J.A., O'Connell, S., Jacobi, R., 1985. Sediment slides and turbidity currents on the Laurentian Fan – sidescan sonar investigations near the epicenter of the 1929 Grand Banks earthquake. *Geology* 13, 538–541.
- Prior, D.B., Bornhold, B.D., Johns, M.W., 1984. Depositional characteristics of a submarine debris flow. *J. Geol.* 92, 707–727.
- Schnellmann, M., Anselmetti, F.S., Giardini, D., McKenzie, J.A., 2005. Mass movement-induced flood-and thrust belt structures in unconsolidated sediments in Lake Lucerne (Switzerland). *Sedimentology* 52, 271–289.
- Shaw, J., Piper, D.J.W., Fader, G.B.J., King, E.L., Todd, B.J., Bell, T., Batterson, M.J., Liverman, D.G.E., 2006. A conceptual model of the deglaciation of Atlantic Canada. *Quat. Sci. Rev.* 25, 2059–2081.
- Shilts, W.W., Clague, J.J., 1992. Documentation of earthquake-induced disturbance of lake-sediments using subbottom acoustic profiling. *Can. J. Earth Sci.* 29, 1018–1042.
- Smith, W., 1962. Earthquakes of eastern Canada and adjacent areas, 1534–1927. Publications of the Dominion Observatory, Ottawa, 26, pp. 271–301.

- St-Onge, G., Mulder, T., Piper, D.J.W., Hillaire-Marcel, C., Stoner, J.S., 2004. Earthquake and flood-induced turbidites in the Saguenay Fjord (Quebec): a Holocene paleoseismicity record. *Quat. Sci. Rev.* 23, 283–294.
- St-Onge, G., Mulder, T., Francus, P., Long, B., 2007. Continuous physical properties of cored marine sediments. In: Hillaire-Marcel, C., de Vernal, A. (Eds.), 2007. Proxies in Late Cenozoic Paleoceanography, Elsevier, pp. 63–98.
- St-Onge, G., Stoner, J.S., Hillaire-Marcel, C., 2003. Holocene paleomagnetic records from the St. Lawrence Estuary, eastern Canada: centennial- to millennial-scale geomagnetic modulation of cosmogenic isotopes. *Earth Planet. Sci. Lett.* 209, 113–130.
- Syvitski, J.P.M., Praeg, D., 1989. Quaternary sedimentation in the St. Lawrence Estuary and adjoining areas, Eastern Canada: an overview based on high resolution seismostratigraphy. *Géographie physique et Quaternaire* 43, 291–310.
- Thwaites, R.G. (Ed.), 1959. The Jesuit relations and allied documents: travels and explorations of the Jesuit missionaries in New France, 1610–1791: the original French, Latin, and Italian texts, with English translations and notes. Pageant Book Co, New York.
- Urgeles, R., Duchesne, M.J., Héroux, M.-C., 2001. Levés multifaisceaux au large des rivières Betsiamites et Outardes. Laboratoire d'études sur les risques naturels. Département de géologie et de génie géologique, Université Laval, Québec, internal report. 45 pp.
- Urgeles, R., Locat, J., Lee, H.J., Martin, F., 2002. The Saguenay Fjord, Quebec, Canada: integrating marine geotechnical and geophysical data for spatial seismic slope stability and hazard assessment. *Mar. Geol.* 185, 319–340.
- de Vernal, A., Guiot, J., Turon, J.-L., 1993. Late and postglacial paleoenvironments of the Gulf of St. Lawrence: marine and terrestrial palynological evidence. *Géographie physique et Quaternaire* 47, 167–180.
- Zhang, D., 2000. Fluxes of Short-lived Radioisotopes in the Marginal Marine Basins of Eastern Canada. Ph.D Thesis, Université du Québec à Montréal, Montréal, 193 pp.

B Article “Morphological and stratigraphic analysis of the Colombier landslide area, Québec”.

Cauchon-Voyer, G., Locat, J., Demers, D., Robitaille, D., and Locat, P. 2008. Morphological and stratigraphic analysis of the Colombier landslide area, Québec. In 4e Conférence canadienne sur les géorisques: des causes à la gestion - 4th Canadian Conference on Geohazards : From Causes to Management. Presses de l'Université Laval, Québec, pp. 271-278.

MORPHOLOGICAL AND STRATIGRAPHIC ANALYSIS OF THE COLOMBIER LANDSLIDE AREA, QUÉBEC

Geneviève Cauchon-Voyer, Jacques Locat

Laboratoire d'Études sur les Risques Naturels, Département de géologie et de génie géologique, Université Laval, Québec, QC, G1K 7P4, genevieve.cauchon-voyer.1@ulaval.ca

Denis Demers, Denis Robitaille, Pascal Locat

Service Géotechnique et Géologie, Ministère des Transports du Québec, 930 Chemin Ste-Foy, Québec, QC, G1S 4X9

RÉSUMÉ

Une cicatrice de glissement de terrain subaérien de 6.5 km² est identifiée dans les sédiments quaternaires situés à l'ouest du complexe deltaïque de la rivière Betsiamites, près de la municipalité de Colombier, sur la Côte-Nord de l'estuaire du St-Laurent au Québec. Une analyse morphologique et stratigraphique du secteur du glissement de Colombier, intégrant des données morphologiques, des résultats d'essais au piézocone et des interprétations d'une campagne de sismique réflexion, a été entreprise afin de définir les caractéristiques de glissements de terrain. Trois zones générales avec différentes caractéristiques géomorphologiques ont été définies dans la cicatrice de glissement: la zone Ouest avec un terrain en pente sud-ouest régulier, la zone Est avec une succession des crêtes allongées et de dépressions et finalement la zone d'accumulation de débris qui semble être le prolongement des débris dans l'Estuaire. La stratigraphie du secteur se compose de dépôts aux caractéristiques variables latéralement, résultant d'épisode de glissements de terrain et de la progradation deltaïque lors de la dernière phase régressive du niveau marin relatif. Quatre unités sismostratigraphiques et un réflecteur avec un fort contraste d'impédance acoustique, interprété comme la roche en place, ont été identifiés sur la section de sismique réflexion obtenue sur la plage. Trois de ces unités sismostratigraphiques corréleront potentiellement avec 3 couches de sol identifiés par les essais au piézocone.

ABSTRACT

A 6.5 km² subaerial landslide scar is identified in the Quaternary sediments located west of the Betsiamites River deltaic system at Colombier, on the north shore of the St. Lawrence estuary in Québec. A morphological and stratigraphic analysis of the Colombier landslide area, integrating morphological data, piezocone data and results from a seismic reflection survey, has been initiated in order to define the characteristics of the slope failure events. Three general zones with different geomorphological characteristics within the subaerial landslide scar were defined: the West zone with a regular southwest sloping terrain, the East zone with succession of elongated ridges and depressions and finally the accumulation zone of the landslide which likely appears to be an extension of the landslide debris in the Estuary. The stratigraphy of the area consists of deposits with laterally variable characteristics resulting from landslide events and deltaic progradation during the last relative sea-level regressive phase. Five seismic units and a reflector with a strong acoustic impedance contrast, interpreted as the bedrock, were identified on a seismic section obtained on the beach. Three of these seismostratigraphic units potentially correlate to 3 soil layers identified in the piezocone soundings.

1. INTRODUCTION

Numerous landslides have occurred in Eastern Canada in the sediments deposited following the retreat of the Laurentide Ice Sheet. These deposits are mostly located in the coastal areas around the St. Lawrence River valley (Fig. 1), where most of the population is gathered. Landslides constitute a risk for the population as well as for man-made infrastructures and the Colombier landslide is a striking example of the destructive potential of such events. The 6.5 km² Colombier subaerial landslide scar is located in the Quaternary sediments 3 km west of the Betsiamites River on the North Shore region of the province of Quebec. Highway 138, which is the main road and lifeline on the North Shore of Quebec, runs directly across the landslide scar (Fig. 2). This subaerial landslide scar is likely to be the second largest known to have occurred in the province of Quebec, after the 1663 St-Jean Vianney landslide (Lasalle and Chagnon, 1968). Understanding the triggering factors for mass movements in this coastal environment is necessary for landslide risk assessment on the Quebec

North Shore in the area in order to identify similar environments along the St. Lawrence Estuary.

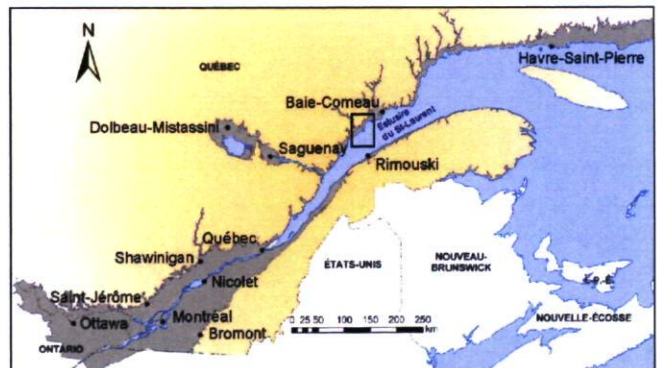


Figure 1. Localisation of the study area and limit of the marine submersion associated with the last deglaciation. Modified from Gadd, 1974.

The Colombier landslide was first described by Bernatchez (2003) who provided a general description of the landslide scar geomorphology and stratigraphy. He observed that the scar may have resulted from at least two different failure events and proposed that part of this landslide was triggered by the major earthquake (M~7) that occurred in the province of Québec on February 5th 1663 (Smith, 1962). In addition to this landslide, other subaerial mass movements have been previously identified in the vicinity of the study area (e.g., Chute-aux-Outardes, Allard, 1984).

The aim of this paper is to present ongoing work carried out in the Colombier landslide area in order to define the characteristics of the slope failure events. We first present new data revealing the morphology of the landslide scar area. Secondly, we suggest an interpretation from a seismic reflection survey integrated with piezocone soundings results to propose a preliminary description of the stratigraphy of the area. Finally, we make a few concluding remarks on this ongoing research.

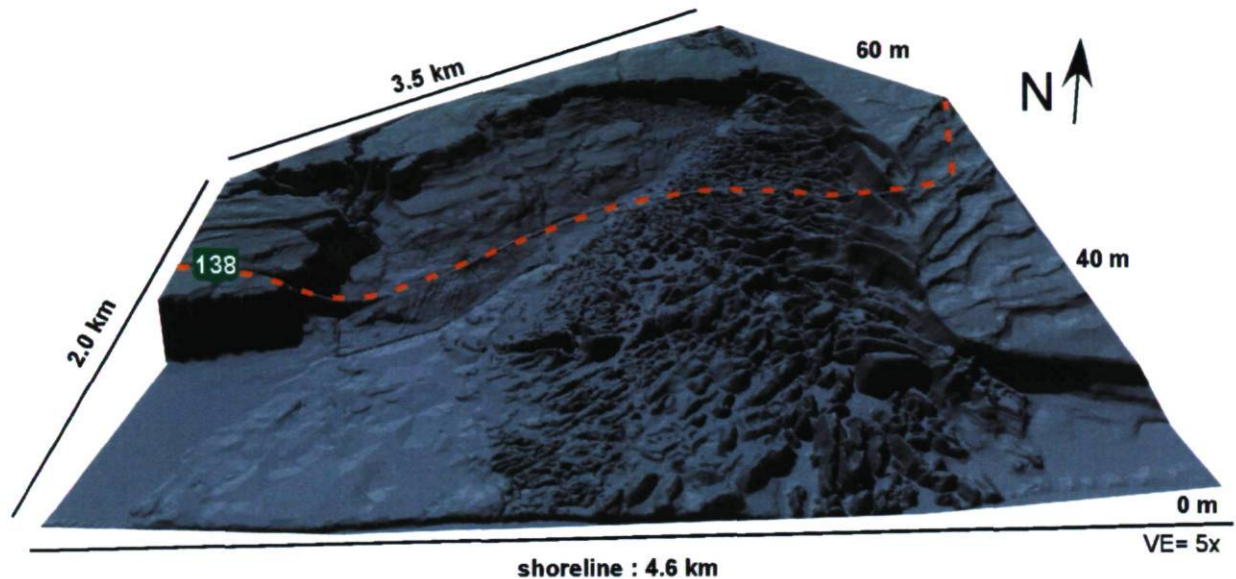


Figure 2. Shaded digital elevation model of the Colombier landslide scar area with indication of the position of Highway 138, which is the lifeline of the Quebec North Shore. The elevation ranges from the shoreline to 60 m. VE= 5x

2. REGIONAL SETTING

The Colombier area is located on the North Shore of the Lower St. Lawrence Estuary at about 400 km northeast of Québec City (Fig. 1). This area was submerged by the Goldthwait Sea (Dredge, 1983) and subsequently influenced by large deltaic complexes linked to the northward retreat of the Laurentide Ice Sheet during the Late Wisconsinan. Sea level reached a maximum at about 150 m above sea level in the vicinity of the study area and lowered to the present sea level at around 7.5 ka BP in ^{14}C years (~8 ka cal BP) (Bernatchez, 2003). Today, the Colombier area is a large coastal plain interrupted by several terrace levels and truncated by the Betsiamites River. The coastline in the area has a N-S and a W-E orientation, east and west of Betsiamites River, respectively. The Betsiamites River flows into the St. Lawrence Estuary with a W-E direction. The tides in Baie-Comeau, the reference station for the area, are semidiurnal with average amplitude of 3.8 m. The largest tides are in the order of 4.3 m (Canadian Tide and Current Tables). The study area is located between the Lower St. Lawrence Seismic Zone (LSZ) and the Charlevoix Seismic Zone (CSZ) (Adams and Atkinson, 2003).

Bernatchez (2003) described the Holocene coastal stratigraphy of the Betsiamites and Manicouagan-Outardes deltaic complexes. He described the Holocene coastal stratigraphy of the Betsiamites River area as a sequence of emerged glacio-marine, prodeltaic, deltaic, fluvial and littoral deposits. Syvitski and Praeg (1989) provided a regional seismostratigraphic framework for the late Quaternary sedimentation offshore in the St. Lawrence Estuary. Cauchon-Voyer *et al.* (2008) integrated both analyses to describe the sequence of deposits found in the submarine portion of the Betsiamites River deltaic complex.

Offshore, the regional seafloor morphology of the Estuary can be divided into three physiographic regions: a sub-horizontal shelf, a slope and the Laurentian Channel. The shelf has an average width of 10 km and a maximum slope of 2° , with water depths ranging from the shoreline to about 150 m. The shelf break occurs between 150 and 200 m water depth, creating a slope with maximum height of 200 m. The Laurentian Channel is a long sub-horizontal topographic depression in the seafloor of the Estuary and has a maximum water depth of 375 m and a width of 45 km in the study area. Cauchon-Voyer *et al.*, (2008) have described the submarine geomorphology of the area between the Betsiamites River and Rimouski and have

identified several landslide scars and accumulation of debris. They have proposed a chronology for 4 mass movement events in the submarine area that lies in immediate proximity to the Colombier landslide (Fig. 3). These 4 failures are dated as older than 9280 cal BP, 7250 cal BP, AD 1663, and AD 1860 or AD 1870.

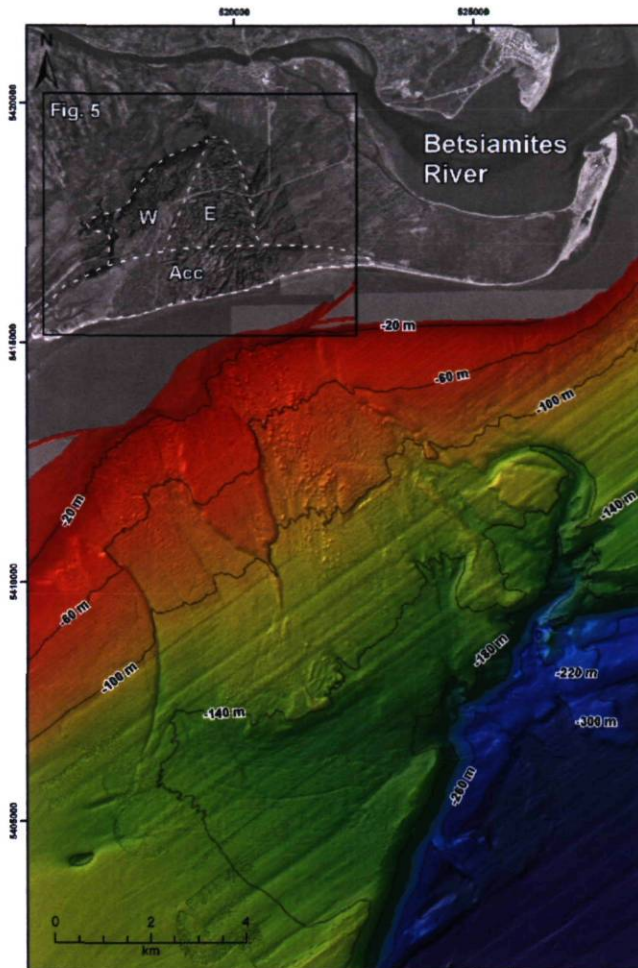


Figure 3. Bathymetric coverage of the study area, ranging from 5 to 325 m water depth. Bathymetric contour lines are at 40 m interval starting at 20 m depth. On shore, W, E and Acc indicate the position of the three zones within the landslide scar and insert refers to Figure 5.

3. DATA AND METHODS

The description of the landslide follows a morphological analysis, aerial photo interpretation and geometrical measurements carried out on the digital elevation model (DEM) (Fig. 2). The DEM was computed at a 1 m resolution from hypsometric lines at 1 m contour interval obtained from photogrammetry on 1:15000 aerial photos taken in 1996 (Q96312_008-011 and Q96311_195-198).

In order to obtain a 2D image of the stratigraphy of the disturbed area on the beach, a continuous seismic reflection

profile was produced over a total length of 5.2 km. Seismic reflection data were acquired using an array of 24 geophones (40 Hz) at 5 m spacings. The configuration for the survey is a repetition of 12 shots increasing at 5 m steps, the first shot being fired at 2.5 m away from the first geophone (Fig. 4). The source was a "Buffalo gun" firing 12-gauge blank charges in holes about 50 cm below the ground surface (Pullan and MacAulay, 1987). The data were acquired with a Geometrics Strata Visor seismograph.

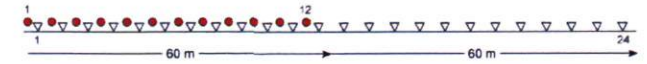


Figure 4. Diagram of the configuration of the geophone (triangles) and the 12 shot locations (circles).

The seismic data were processed with the software WinSeis Turbo. Normal moveout corrections were applied to correct for changes in distance between the source and each receiver. Stacking velocities were determined during the processing and the constant speed of 1575 m/s was used to linearly convert two-way travel time to approximate depths for the section presented in this paper. Band pass filtering (150, 200, 500, 600 Hz) was also applied to the presented section. Interpretation of the data was performed with the Kingdom Suite software package.

Sixteen piezocone tests were performed in the area of the scar (Fig. 5) between September and October 2006. They were carried out with a 15T apparatus with a 15 cm² base area. To obtain a better definition of the stratigraphy, the penetration rate was of 60 cm/min and the pore pressure (u_{base}) and tip resistance (q_T) were recorded at 10 mm intervals.

4. LANDSLIDE MORPHOLOGIES

The Colombier landslide is located within a large coastal plain of about 7.5 km wide by 25 km long interrupted by several terrace levels. They were established during the last submergence of the coastal area, which started around 11,000 BP in ¹⁴C years (Bernatchez, 2003). The highest, but intermittent, terrace in the vicinity of the landslide scar is located at about 70 m of elevation (Fig. 5). A second terrace is located at 60 m of elevation and corresponds also to the highest point of the Colombier landslide scar. Large bedrock (Grenvillian province) outcrops are visible above the highest terrace, at elevation ranging between 80 and 140 m. Bedrock outcrops are also present at a distance of 200 m from the main scarp and on the beach, west of the landslide scar (Fig. 5). Flat peat bogs are found west of the landslide scar at elevation ranging between 60 and 80 metres. Many well-defined paleo-beach ridges are visible on the surface of the 30 and 15 m terraces east of the scar.

The landslide scar has a horseshoe shape with a maximum width of 3200 m and length of 2400 m. The elevation of the main scar decreases from 60 m to 40 m and has an average height of 30 m. We defined three general zones with different geomorphological characteristics within the

landslide scar and we will refer to them as the West (W), the East (E) and the accumulation zones (Acc) (Fig. 3).

The West zone extends over 2.8 km² and is characterized by a regular southeast sloping terrain (Fig. 2). The main scarp height range between 10 and 30 m and its slope angle varies between 15° and 25°. The western flank was eroded by small creeks (Fig. 5), which drain the northwest terrain above of the landslide. The slope of the terrain has an average slope of 2.5° with minor relief variation.

The main morphological characteristic of the East zone is a succession of elongated ridges and depressions (Fig. 2). Two main orientations of ridges can be observed. The first group has a W-E orientation (270°N), which is parallel to the direction of the landslide (red on Fig. 5). They have average height, width and length of 10 m, 40 m and 200 m, respectively. The second group has an ESE-WNW orientation (300°N) (purple on Fig. 5). These ridges are slightly larger than the W-E ridge and have an average length of 275 m and maximal heights and widths of 25 and 60 m. They appear to be a continuity of the western flank. Both groups of ridges are likely constituted of stratified sandy material, which is similar to the material found in the upper 60 m terrace and rest on remoulded clayed sediments (Bernatchez, 2003). Many small and elongated lakes are found between the ridges. These lakes are depressions filled with standing water. In contrast with the West zone, no organized drainage system was identified in the East zone.

The accumulation zone of the landslide is defined as the subaerial area where the displaced material has accumulated. This zone includes the salt water marshes on either side of the landslide scar, a levelled and forested area with average elevation of 5 m and the sandy beach. Ridges are also observed (green ridges on Fig. 5) in this zone and have a different orientation than in the East zone. They are mostly disorganized but have a general NE-SW (215°N) trend. This zone appears to be an extension of the landslide debris in the Estuary, *i.e.*, the debris were deposited on the seafloor. The northern limit of this zone is the estimated position of the marine terrace prior to the landslide.

Offshore (Fig. 3), the general morphology of the shelf can be summarized as a large landslide scar characterized by two topographic depressions separated by a butte with steep flanks and a flat top. The flanks of the scar have an average height of 15 m and the butte is constituted of intact deposits (Cauchon-Voyer *et al.*, 2008). A rough estimate for the volume of this 40 km² submarine scar on the shelf is ~600 x 10⁶ m³. The landslide scar is overlain by landslide blocks, with sizes of up to 20 x 60 x 150 m. These blocks extend up to 8 km downslope from the shoreline. It was proposed by Cauchon-Voyer *et al.* (2008) that the scar and the overlaying debris result from two different failure events; the large landslide scar was dated at 7250 cal BP and the debris deposited in the pre-existing depressions were dated at AD 1663.

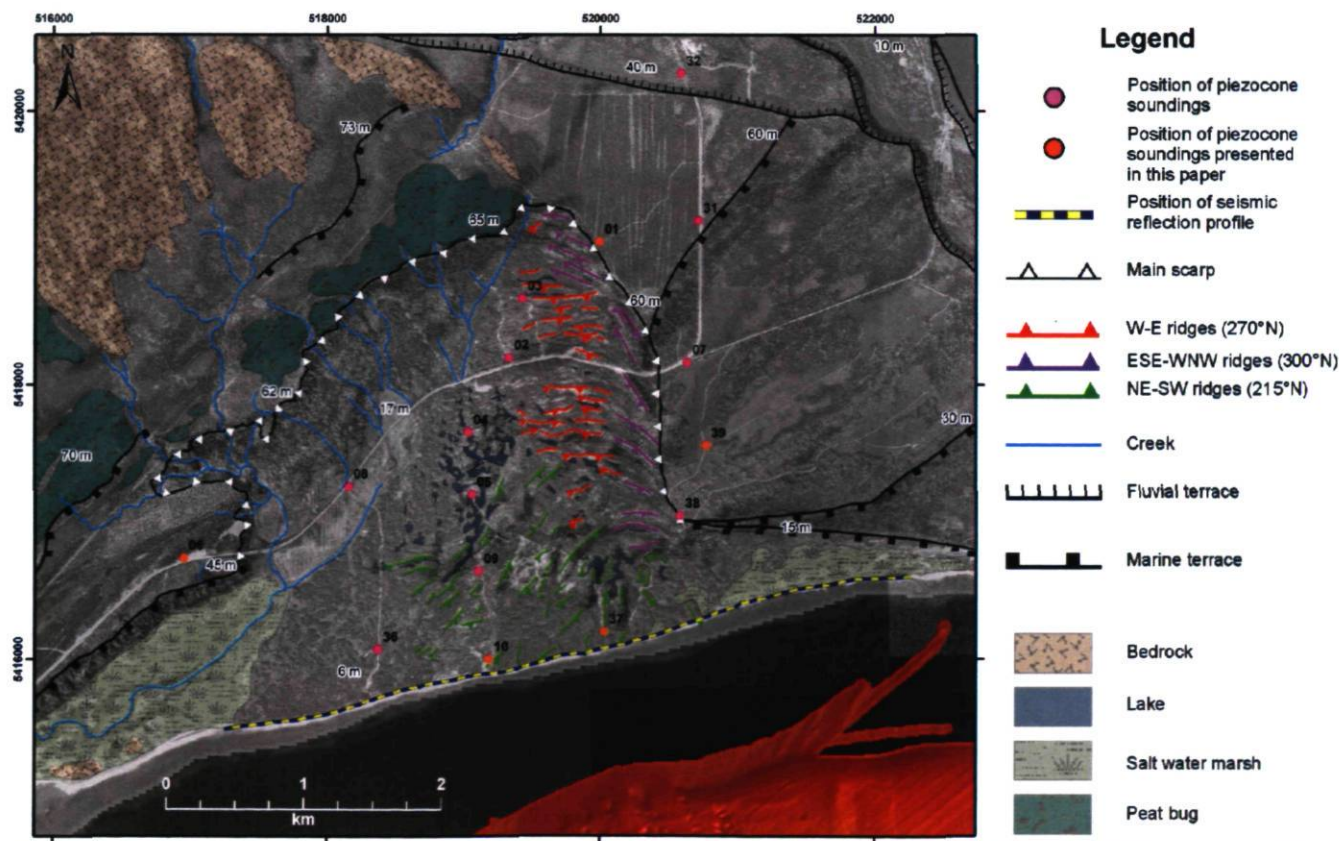


Figure 5. Geomorphological interpretation of the Colombier landslide. The black numbers refer to the piezocone soundings. The black and white elevation values represent the elevation at the point exactly below the label.

5. STRATIGRAPHIC ANALYSIS

As a second step in understanding the failure events that have shaped this landslide scar, it is necessary to describe the stratigraphic sequence of original deposits. In this section, we present results from piezocone soundings integrated with seismic reflection interpretation along the coastline to propose a description of the original stratigraphy of the area.

Original stratigraphy

Sixteen piezocone tests were carried out in the vicinity of the landslide scar and provide a basis for a general description of the stratigraphy of the area. The complex stratigraphy resulting from the deltaic sedimentation in the Betsiamites River area is reflected in the piezocone sounding results. The piezocone profiles present laterally variable characteristics resulting from landslide events and also by the highly variable depositional pattern known to develop in prograding deltaic complexes (Hart and Long, 1996).

Seven piezocone soundings were performed outside the landslide area, 6 on the eastern flank and 1 in the western flank on the landslide (Fig. 5). Piezocone C46001 (Fig. 6) was performed 50 m away from the main scarp on the marine terrace at 60 m of elevation. The profile consists of 29 m of material with very high tip resistance ranging between 30000 and 40000 kPa and almost null pore-water pressure (~ 5 kPa), which indicates that it is a sandy deposit.

Piezocone profiles 32, 31, 07, 39 and 38 show similar high tip resistance and very low pore-water pressure for the upper soil layer, which thickness ranges between 15 and 30 m for these 5 profiles. On profile C46039 (Fig. 6) performed at 37.7 m above sea-level (asl), this sandy layer is 27 m thick. At 10 m of elevation in this profile, there is a change in soil properties, which results in decreasing values of tip resistance ranging between 5000 and 20000 kPa. This layer is interpreted as a stratified silt and sand deposit. At an elevation of 0 m, there is a 3 metres thick layer of soil with regular trends of tip resistance and pore water pressure. Under this layer, the deposit is composed of stratified layers of soil, likely silt and sand.

On the western flank, the profile C46006 is 60 m long (Fig. 6), which is the maximal possible length for these piezocone soundings. The test was performed at an elevation of 47.6 m asl. For the upper 6 metres, which is composed of sand, the tip resistance average 8000 kPa with a peak up to 30000 kPa. At 5 m depth (42.7 m asl), a change in material results in a decrease in tip resistance and an increase in pore water pressure. The tip resistance values are highly variable, ranging between 1500 to 5000 kPa, which likely results from alternating layers of silty and sandy material. At an elevation of 26 m, the tip resistance and the pore water pressure profiles have regular trends, which is characteristic of uniform material. The interval between the elevation of 18 m and -15 m below sea level, shows variable characteristics, which imply that the material is also stratified.

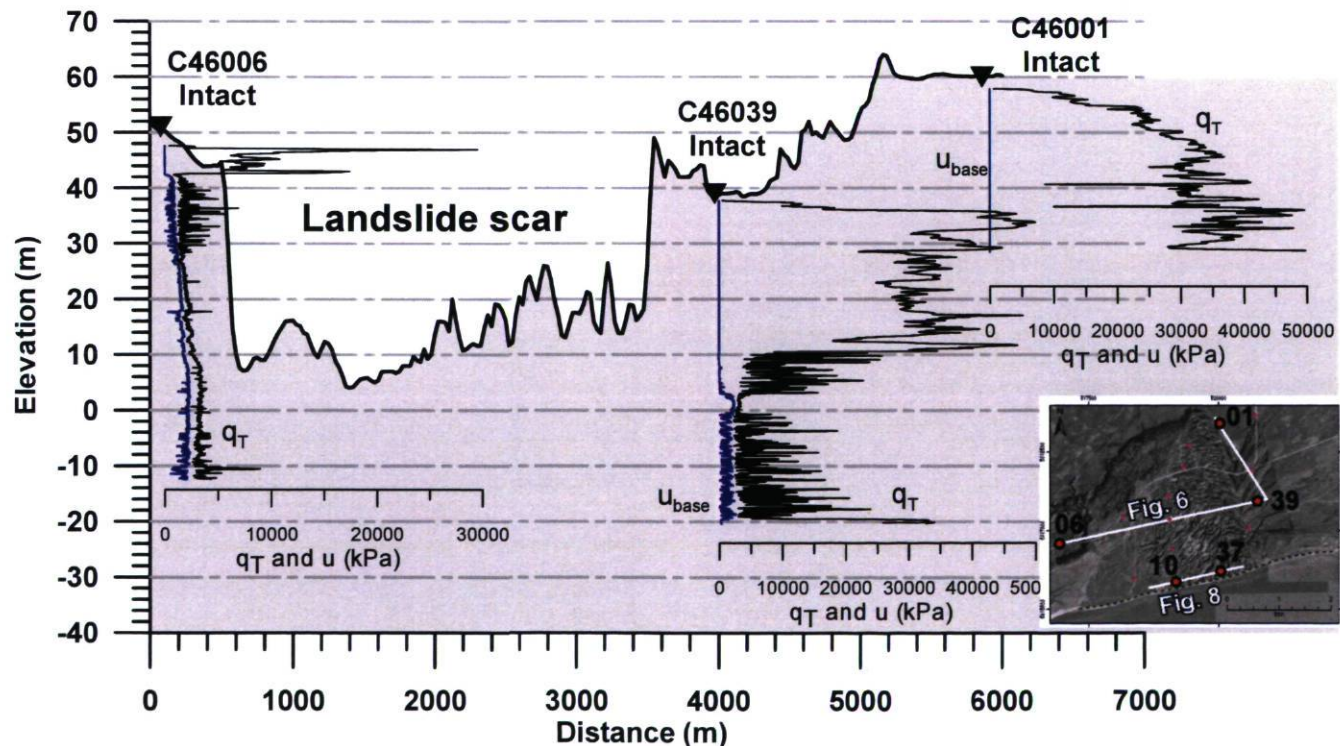


Figure 6. Piezocone soundings in the intact deposits outside the landslide scar. Black line with grey filling corresponds to the topographic profile. Insert indicates the position of the topographic profiles and piezocone soundings shown in Figs. 6 and 8.

The stratigraphy around the landslide head scarp can be simplified to an upper layer of sandy material, which thickness increases from 6 to about 30 metres from west to east respectively. The lower sections of the presented piezocone soundings (Fig. 6) indicate that there are highly stratified deposits changing with depth into a more uniform soil with less stratification. The failure plane of the landslide events likely occurred within the stratified soil layer.

Stratigraphy along the coastline

The seismic reflection data allows the definition of a preliminary seismostratigraphic sequence along the coastline. The reflections have central frequencies in the

range of 300 Hz, which is typical for marine sediments (Hunter *et al.*, 2000). The interpretation of this sequence will be validated with upcoming boreholes and piezocone soundings planned for summer 2008. Four seismic units and a reflector with a strong acoustic impedance contrast, interpreted as the bedrock, were identified on the seismic section. These 4 units were defined according to the amplitude and geometry of the inner reflections and to the attributes of the upper transition of each body. Preliminary stratigraphic interpretation is derived from the work carried out offshore by Syvitski and Praeg (1989), which was later integrated by Cauchon-Voyer *et al.* (2008) for the submarine segment of the Colombier and Betsiamites River area.

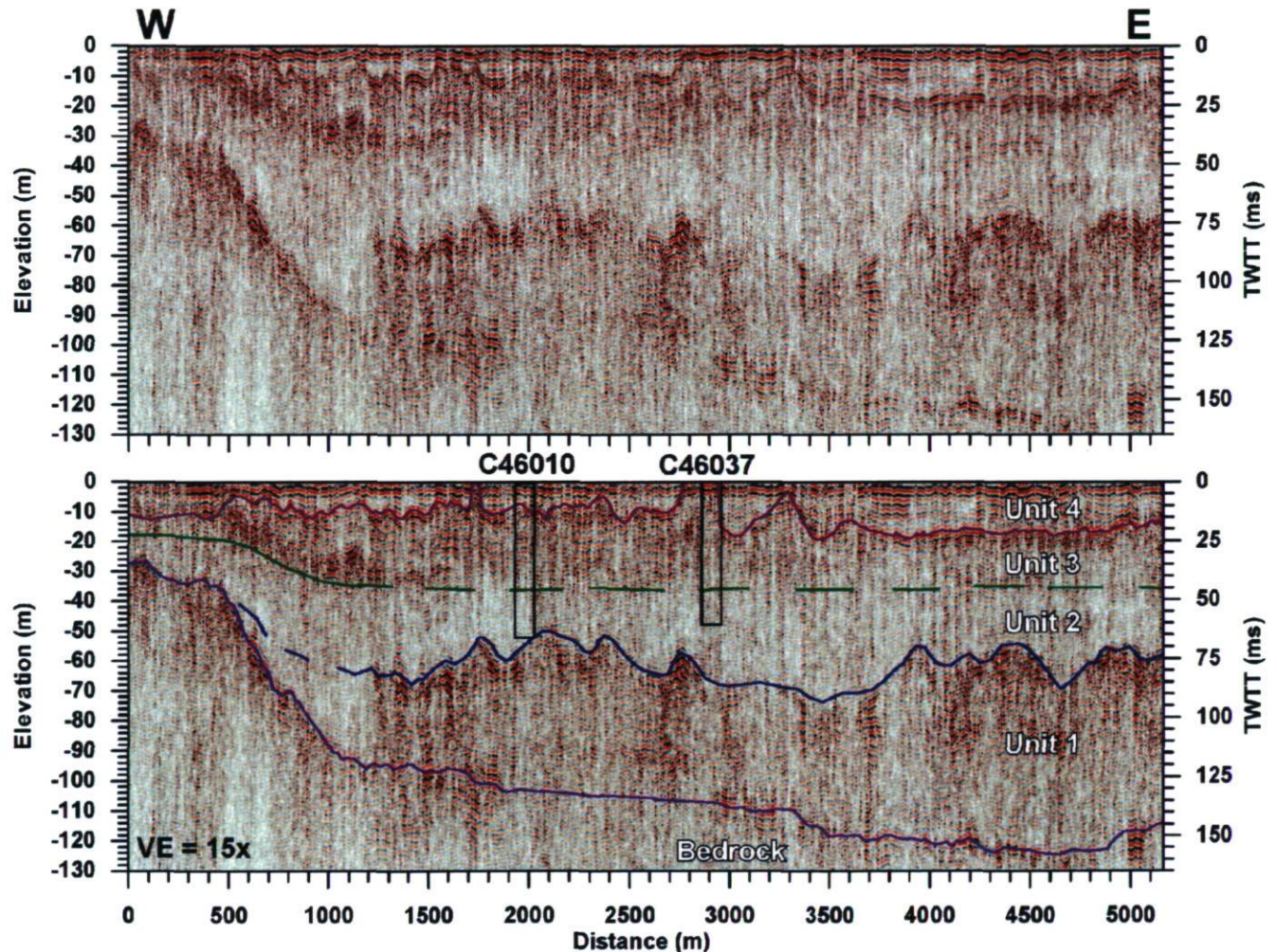


Figure 7. 5.2 km-long continuous seismic reflection profile. Right scale is in milliseconds two way travel time (TWTT) and left scale is approximate depth in metres (elevation), linearly converted using a constant speed of 1575 m/s. The black rectangles indicate the positions and depths reached by the two piezocone soundings carried out close to the shoreline.

The sediment-bedrock interface is characterized by relatively continuous high amplitude reflections, where little energy penetrates below this boundary. The depth to the bedrock increases from 125 m to 30 m (Fig. 7). This interpretation is coherent with the fact that a bedrock

outcrop is visible on the beach at about 600 m from the western end of the seismic line.

Unit 1 is a highly variable acoustic body with strong internal reflections. The upper boundary of this body is irregular and

its thickness ranges between a few metres to 60 m. In light of our current work, it is difficult to propose a definite interpretation for this body, but we can suggest that the lower part of this body may be constituted of till and ice-proximal sediments (Syvitski and Praeg, 1989). Upcoming work will help precise the geological interpretation for this unit.

Unit 2 is a very low amplitude body and presents only few weak reflections. The upper transition of this unit is weak and often absent, *i.e.*, the contact in acoustic impedance is too weak to obtain coherent reflections. Its thickness ranges between 10 to 30 m. This facies could correlate to the Goldthwait Sea sediments (Syvitski and Praeg, 1989).

Unit 3 is a stronger amplitude body with strong internal reflections and an irregular upper boundary. This facies could correspond to the highly stratified paraglacial deposits identified in the Estuary (Syvitski and Praeg, 1989). However, the irregular relief of the upper boundary of this body, which often reaches the surface of the section, indicates that the upper part of this seismic body may correspond to the landslide debris. This could imply that the debris were deposited on the stratified sediments and that the impedance contact between both bodies is too weak to obtain a clear boundary. This hypothesis must be validated with core data.

Unit 4 has dense closely packed sub-horizontal reflectors conformable with Unit 4. The amplitude of this unit varies between low and high. This unit could represent landslide debris reworked by littoral processes (*e.g.*, tides, wave action and longshore drift).

Two piezocone soundings, C46010 and C46037, were performed in the accumulation zone of landslide debris, at about 100 metres from the position of the seismic reflection profile on the beach (Fig. 7). The beach is an eroded surface reworked by littoral processes with an erosion terrace of about 5 to 10 metres high. Both profiles were performed above this terrace level, at 9.4 m asl for C46010 and 12.9 m asl for C46037 (Fig. 8). Both soundings were 60 m long and penetrate below the layer of debris.

For piezocone C46010, there is a 12 metres thick layer of sand with tip resistance increasing up to 15000 kPa. The layer between 3 to 7 m bsl has variable characteristics, likely resulting from stratifications and landslide disturbance. At 12 m bsl, there is a 15 cm thick layer with tip resistance increasing from 2000 to 10000 kPa. Below this layer, the tip resistance and pore-water pressure profiles have regular trends, with few peaks likely resulting from soil stratifications. The higher values of tip resistance obtained at 48 m bsl could potentially correlate to seismostratigraphic Unit 1, which has strong internal reflections.

Sounding C46037 (Fig. 8) has three main layers. The first layer has tip resistance increasing to 25000 kPa, the second layer with general regular trends of tip resistance and pore-water pressure with few peaks, and the third layer which is mostly uniform. The second and third layer could correlate to seismostratigraphic Unit 3 and Unit 2, respectively.

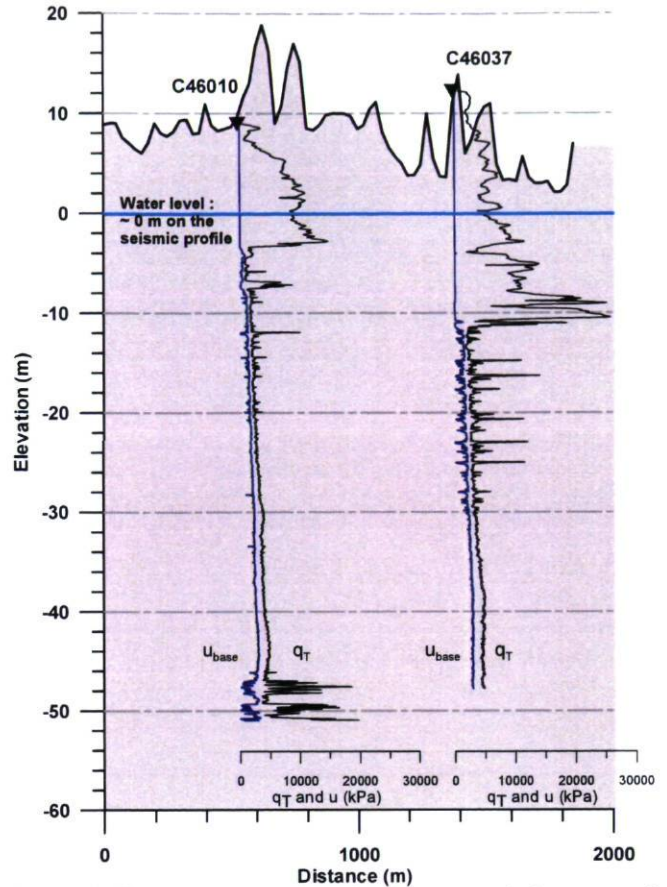


Figure 8. Piezocone soundings in the accumulation zone of landslide debris, at about 100 metres from the position of the seismic reflection profile on the beach. See Figure 6 for position of the profile.

6. CONCLUDING REMARKS

This analysis of the Colombier landslide area was initiated in order to define the morphological and geomorphological characteristics of the slope failure events. This important analysis will provide a geological framework for a future slope stability analysis. The observations and results derived from this ongoing work allow us to make a few general concluding remarks:

- The stratigraphy of the site of the landslide varies from west to east and may have influenced the morphology of the landslide.
- The irregular bedrock morphology in the area may have had a significant control on the extent of the landslide scar.
- Considering the effect of such a landslide on the North Shore of Quebec if it was to occur today, there is a need to pursue our research in the area and identify similar environments along the St. Lawrence Estuary.

7. ACKNOWLEDGEMENTS

The authors wish also to thank the Ministère des Transports du Québec (MTQ), NSERC and the FQRNT for their financial support. We would like to thank the reviewers S. Leroueil and G. St-Onge for their comments. Many thanks to D. Turmel and C. Amiguet (Université Laval) for their valuable help during seismic reflection data acquisition and to A. Pugin (Geological Survey of Canada, Ottawa) for his assistance with seismic data processing. We would finally like to thank the MTQ for the permission to use their topographic and piezocone soundings data of the landslide area.

8. REFERENCES

- Adams, J. and Atkinson, G., 2003. Development of seismic hazard maps for the proposed 2005 edition of the National Building Code of Canada. *Canadian Journal of Civil Engineering* 30, 255-271.
- Allard, J.-D., 1984. Zones exposées aux mouvements de terrain, région de Chutes-aux-Outardes, Ministère de l'Énergie et des Ressources, Québec, 42 pp.
- Bernatchez, P., 2003. Évolution littorale holocène et actuelle des complexes deltaïques de Betsiamites et de Manicouagan-Outardes : synthèse, processus, causes et perspectives, Ph.D Thesis, Université Laval, Québec, 460 pp.
- Cauchon-Voyer, G., Locat, J. and St-Onge, G., 2008. Late-Quaternary morpho-sedimentology and submarine mass movements of the Betsiamites area, Lower St. Lawrence Estuary, Quebec, Canada. *Marine Geology*, In press.
- Dredge, L., 1983. Surficial Geology of the Sept-Îles area, Quebec North Shore. Geological survey of Canada Memoir 408, 40 pp.
- Gadd N.R., 1974. Limites maximales de la submersion marine au tardiglaciaire dans le bassin du Saint-Laurent. Commission géologique du Canada, document manuscrit. 6 p. et 18 cartes au 1/250000.
- Hart, B.S. and Long, B.F., 1996. Forced regressions and lowstand deltas: Holocene Canadian examples. *Journal of Sedimentary Research*, 66, 820-829.
- Hunter, J.A., Burns, R.A., Aylsworth, J.M. and Pullan S.E., 2000. Near-surface seismic-reflection studies to outline a buried bedrock basin in eastern Ontario. *GSC Current Research 2000-E13*, 9 pp.
- Lasalle, P. and Chagnon, J.-Y., 1968. An ancient landslide along the Saguenay River, Quebec. *Canadian Journal of Earth Sciences* 5, 548 -549.
- Pullan, S. E. and MacAulay, H. A., 1987. An in-hole shotgun source for engineering seismic surveys. *Geophysics*, 52, 985-996.
- Smith, W., 1962. Earthquakes of eastern Canada and adjacent areas, 1534-1927. Publications of the Dominion Observatory, Ottawa 26, pp. 271-301.
- Syvitski, J.P.M. and Praeg, D., 1989. Quaternary Sedimentation in the St. Lawrence Estuary and adjoining areas, Eastern Canada: an overview based on high resolution seismo-stratigraphy. *Géographie physique et Quaternaire*, 43, 291-310.

C Démarche de traitement des données de sismique réflexion avec le logiciel WinSeis

Les données de sismique réflexion ont été obtenues au Cap Colombier, sur la Côte Nord du Québec en août 2007. 87 séries de 12 tirs enregistrées par 24 géophones pour former 1059 fichiers (pas de tirs et espacement des géophones de 5 m) ont été recueillies. Ce présent résumé a pour objectif de présenter les étapes effectuées lors du traitement des données. Ce résumé se veut un document complémentaire au manuel d'instruction de WinSeis. Les travaux de traitements de données de sismique réflexion ont été effectués à Ottawa en novembre 2007 avec M. André Pugin, de la Commission Géologique du Canada.

1. Conversion du format SEG2 vers le format KGS

La première étape consiste à faire le changement de format de fichier obtenu sur le terrain (SEG2) vers le format KGS. Tous les fichiers ont été placés dans le même répertoire afin de faciliter leur manipulation. L'utilitaire convert.exe a été utilisé pour cette opération. Nous suggérons de lire le fichier Convert.exeTutorial01.doc de l'utilitaire. Pour agglomérer les fichiers il faut s'assurer qu'ils ont été sélectionnés de façon décroissante dans la boîte de dialogue afin que ceux-ci se présentent de façon croissante dans la liste des fichiers. Lors de toutes les manipulations de toutes les étapes du traitement, il est plus prudent de toujours nommer les fichiers avec un maximum de 8 caractères. L'opération de conversion nous permet aussi d'augmenter l'intervalle d'enregistrement de 62.5 us à 125 us en sélectionnant un enregistrement sur deux dans la boîte de dialogue. Il est aussi utile de conserver le même SSN.

2. Configuration de l'ordinateur de travail

Afin de minimiser les problèmes possiblement encourus avec l'utilisation de WinSeis dans Windows, nous avons installé Norton Commander sur l'ordinateur. De plus, nous avons dû modifier la majorité des options de compatibilité des utilitaires .exe. En fait, il faut indiquer dans les paramètres d'affichage que l'utilitaire doit être exécuté avec une résolution d'écran de 640 x 480.

3. Réduction de la fenêtre d'écoute

Puisque les fichiers ont été enregistrés sur une longueur de 0.6, 1 et 1.5 secondes, il est important de : 1) s'assurer qu'ils ont la même longueur de fenêtre d'écoute; et 2) que nous conservons seulement la partie pertinente pour l'interprétation, i.e. jusqu'à la limite inférieure de cohérence acoustique. Cette limite a été établie visuellement en observant quelques traces. Cet exemple permet de sous-échantillonner 300 ms des 1000 premiers enregistrements de 16_315.dat.

```
a_resa.dek
>>START
*INPF 16_315.dat 0 1000 300
*OUTF a_res.dat
>>END
```

4. Géométrie du levé

La prochaine étape consiste à définir la géométrie du levé. La routine SORT est utilisée pour cette étape. La routine SORT doit être utilisée avec les commandes PTRN et SHOT, qui définissent l'arrangement spatial des géophones (PTRN) et la position des tirs (SHOT). C'est aussi à l'aide de cette opération qu'il est possible de corriger les problèmes de géométrie lors de l'acquisition. En fait, lors de notre levé, une série de 12 enregistrements avait été inversée, i.e la flûte 1-12 avait été connectée à l'embout 13-24 et vice-versa, et ce pour les 12 tirs de cette configuration.

```
a_sorted.SRT
>>START
*INPF a_res.dat
*SORT 92 19 1 1
PTRN 5 24 1
PN 1 100 101 24 1
PN 2 101 101 24 1
...
SHOT
SN 16 16 1 2.5
SN 17 17 2 2.5
*OUTF a_sorted.dat
>>END
```

La commande *SORT nécessite au moins 4 arguments. La première valeur 92 indique que les enregistrements seront classés en fonction de leur numéro de source séquentiel (SSN), i.e l'ordre dans lequel ils ont été acquis sur le terrain. La deuxième valeur 19 (common offset) indique que les enregistrements seront triés en fonction de leur éloignement de la source, i.e les fichiers auront tous le même aspect car les traces des enregistrements sont classées selon 2.5 m, 5 m, 7 m etc. de la source, peu importe la position de celle-ci. Voir le manuel de WinSeis pour les 3 autres arguments.

La commande PTRN possède 3 arguments qui sont l'espacement des géophones (5), le nombre de canaux (24) et finalement le système d'unité de mesure dans laquelle le levé a été effectué (1, pour mètre). La commande PTRN doit être utilisée avec PN.

Pour la commande PTRN, il faut définir autant de PN (pattern number) qu'il y a de possibilités d'arrangement tir-géophones. Dans notre cas, nous aurions dû avoir seulement 12 PN puisque nous tirions 12 tirs pour chaque configuration de géophones. Par contre, puisque nous avons fait une erreur de géométrie, il faut concevoir 12 autres PN pour corriger cette situation.

La commande PN possède 5 arguments. Le premier est le numéro associé à ce PN (1, 2, 3, etc.). Le deuxième est un numéro séquentiel (et non une distance ni une position) qui réfère à la station du tir. Dans notre cas de 12 tirs pour une même configuration, ce numéro augmentera séquentiellement par pas de 1 pour chaque tir (100, 101, 102, etc.). Le troisième argument est le numéro associé au premier géophone de la série de 24 géophones. Dans notre cas, ce numéro ne changera pas car la station du premier géophone reste constante pour les 12 tirs de la série (101, 101, 101 etc.). Le quatrième argument indique le nombre de stations-géophones du levé (24). Le cinquième argument indique le pas d'avancement et la direction entre chaque station (1). Lorsque le chiffre est 1, il n'est pas nécessaire d'indiquer le signe positif.

Puisque nous avons inversé les câbles connecteurs dans l'embout du système d'acquisition (1-12 dans l'embout 13-24), il a fallu définir 12 autres PN (13, 14, 15, etc.). Le deuxième

argument reste le même car la position du tir n'a pas changé (100, 101, 102, etc.). C'est la position relative du premier géophone qui est changée, celle-ci est devenue 124 et est restée constante pour les 12 PN. Le cinquième argument est -1 car l'ordre du pas d'avancement est inverse.

	G1	G2	G3	G4	G5	G6	G7	G8	G9	G10	G11	G12	G13	G14	G15	G16	G17	G18	G19	G20	G21	G22	G23	G24
Terrain	1	2	3	4	5	6	7	8	9	10	11	12	13	14	15	16	17	18	19	20	21	22	23	24
Fichier	24	23	22	21	20	19	18	17	16	15	14	13	12	11	10	9	8	7	6	5	4	3	2	1

La commande SHOT permet de définir la géométrie associée aux tirs. Elle doit être utilisée avec SN (shot number). SN contient 4 arguments. Le premier est le SSN. Dans notre cas, c'est le numéro du premier enregistrement (16). Le deuxième argument est dans notre cas le même que le premier argument. Le troisième argument est le PN associé à ce tir. Le quatrième argument est l'espacement entre le tir et le géophone le plus proche, dans notre cas cette valeur est de 2.5 m. C'est cette opération qui attribuera un CDP à chacune des traces.

Au départ, afin de faciliter la manipulation des fichiers, la ligne avait été séparée en 4 sous-fichiers. Maintenant que ceux-ci ont été réduits (fenêtre d'écoute et intervalle d'enregistrement), il est possible de les agglomérer ensemble dans NC :

```
Copy /b a_sorted.dat+b_sorted.dat+c_sorted.dat+d_sorted.dat sorted.dat
```

5. Inversion de la polarité

Au milieu du levé, nous avons dû changer un des deux câbles connecteur de géophones. Étant des modèles différents, ceux-ci ne transmettaient pas des polarités concordantes. Par exemple, les amplitudes des premières arrivées des traces 1-12 pouvaient être positives tandis qu'elles étaient négatives pour les traces 13-24. Il fallait donc faire une inversion de ces traces avant de les sommer (stack). La première étape a été de reconnaître les traces ayant subi des inversions. Nous avons identifié visuellement tous les sismographes qui avaient une inversion.

Début fichier/SSN	Fin fichier/SSN	1-12	13-24
244	255		x
256	267	X	
268	279		x

Par la suite, la commande INVERSE.BAS a été faite à partir d'une routine de A. Pugin en langage BASIC pour l'inversion des traces, dont les grandes lignes correspondent à :

```
a = 92 (SSN)
b = 8 (common recording channel, i.e géophone)
if a > 244 and <256 and b >= 13 and b <= 24 then inversion.
```

Le fichier sortant de cette opération est `sortedi.dat`

6. Sommation en Common Depth Point (CDP)

Maintenant que la géométrie a été incorporée aux fichiers, que le CDP a été calculé et que ceux-ci ont été corrigés pour les problèmes d'inversion de polarité, il est possible de les sommer (stack) selon leur CDP. La commande RSRT (resort) est utilisée avant cette tâche. Cette commande indique simplement que le fichier doit être reclassé selon la valeur d'entête 12 (CDP number) et 19 (offset). Le manuel d'instruction fait un commentaire pertinent sous la rubrique RSRT qui explique la différence entre SORT et RSRT.

```
rsrt_cdp.DEK
>>Start
*inpf sortedi.dat
*rsrt 12 19 1 1
*Outf cdp.dat
>>End
```

Le fichier `cdp.dat` est donc un fichier classé selon le CDP.

L'étape suivante est d'effectuer la sommation avec la commande STAK. Cette commande requière qu'un argument (2) mais plusieurs autres paramètres doivent être intégrés

préalablement à cette commande, le plus important étant les corrections pour le normal move-out (NMO). Cette étape est aussi variable, c'est-à-dire que c'est en modifiant certains paramètres et en répétant l'opération qu'il est possible d'améliorer le traitement des données.

to_stak.dek

>>Start		Tâche
*inpf cdp.dat		
*f_filt bp 150 200 500 600	1	Filtrer les données du fichier cdp.dat qui sont reclassées (RSRT) en CDP et offset (12-19).
*edmt 92 19	2	Appliquer un mute adouci sur 10 ms sur les données classées en fonction des enregistrements (byte 92) à partir de l'offset (byte 19) de 2.5 m sur 6 à 300 ms etc.
tapr 10		
mute 16 25 6 300 275 60 300 625 300 300		
*scal 250 1 500	3	Appliquer un AGC sur chacune des traces.
*Nmot .1	4	Appliquer une correction pour les changements entre les distances sources-géophones en considérant une vitesse de propagation des ondes des 1500 m/s. Cette étape doit être raffinée par la suite.
velf 2 30 1500		
*edmt 12 19	5	Un second mute est appliqué cette fois pour les données classées en fonction de leur CDP (byte 12) et de l'offset (byte 19).
tapr 10		
mute 200 25 0 0 1175 0 50		
*Stak 2	6	Opération qui somme les traces.
*f_filt bp 150 200 500 600	7	Les données sommées sont filtrées.
*Outf stak.dat		
>>End		

Il est logique de partitionner cette commande afin de valider chacune des étapes. En fait, en ajoutant des ! avant les commandes, celles-ci deviennent inactives et en inscrivant un fichier de sortie temporaire :

```
*outf temp.dat
>>end
```

Trois fichiers temporaires de validation devraient être faits; après l'étape 3 afin de valider le premier mute sur les données en SSN, après l'étape 4 pour valider le normal move-out et après l'étape 5 du second mute des données en CDP.

Le fichier de sortie de cette étape est **stak.dat**

7. Mixage des traces

Une fois la ligne sommée en CDP, une routine a été effectuée afin de mixer les traces avoisinantes et ainsi de réduire l'intensité des traces blanches entre celles-ci. L'utilitaire MIXEVF.EXE a été utilisé avec le fichier MCA.MIF. Le fichier MCA.MIF contient le fichier d'entrée, le fichier de sortie, le nombre de traces à mixer et la proportion de chacune de ces traces qui doit être considérée :

```
stak.dat
mix.dat
3
25
50
25
```

8. Analyse des vitesses

L'utilitaire VSCNF.EXE (Velocity Scan) permet de faire l'analyse des vitesses d'onde dans les couches du milieu. Les fichiers d'entrée doivent être reclassés (RSRT) en 12 19 (CDP et offset). Les fichiers sommés en CDP (stak.dat) et de sortie (vscn.dat) peuvent être en format .dat ou .evf. La première étape consiste à trouver une série de 50 CDP consécutifs sur la ligne qui semble représentative du terrain.

VSCNF.EXE requiert plusieurs entrées :

```
Nom du fichier d'entrée : stak.dat
Nom du fichier de sortie : vscn.dat
First CDP (of CDP-group#1) ? -> 1500
Last CDP (of CDP-group#1) ? -> 1600
```

of (CDP) Groups to be processed ? -> 1

Record length (ms)? -> current = 299:

Allowable sample stretch ratio (min=0.2;max=0.99) -> current = 0.50:

Stack? (0=DONOT STACK; 1=STACK; -> current = 0:

Après il faut saisir les vitesses de propagation, le maximum étant de 20 vitesses d'essai.

9. Conversion en format .sgy

Une fois les fichiers complétés, il est possible de les convertir en sgy afin de pouvoir les visualiser plus facilement. La commande FPT2SEGY.EXE est utilisée et ne requière qu'un fichier d'entrée et de sortie.

10. Lexique

Série: Une série comprend 12 tirs enregistrés par 24 géophones. Une série a 12 sismographes différents de 24 traces.

Tir: Un tir

Sismographe: Un enregistrement de 24 traces.

Trace: Une trace est l'enregistrement du signal à un géophone.

D Sondages au piézocône

D.1 Tableau des positions des sondages au piézocône

Numéro de sondage	X	Y	Élévation (m)	Profondeur atteinte (m)	Raison de l'arrêt
C46001-005-06	519992.6	5419044.3	57.86	29.27	R
C46002-005-06	519328.8	5418198.8	18.84	50.52	R
C46003-005-06	519427.3	5418628.1	20.56	44.12	R
C46004-005-06	519032.5	5417654.3	10.87	49.51	R
C46005-005-06	519057.4	5417201.1	9.33	56.54	R
C46006-005-06	516958.5	5416735.9	47.62	60.00	V
C46007-005-06	520634.9	5418161.2	49.82	30.90	R
C46008A-005-06	518160.2	5417256.0	11.09	14.60	R
C46009-005-06	519108.9	5416643.1	10.06	60.00	V
C46010-005-06	519183.8	5416003.8	8.95	59.92	R
C46029-005-06	514952.4	5414786.6	47.00	46.17	R
C46030-005-06	515615.3	5415579.1	50.51	57.64	R
C46031-005-06	520714.4	5419200.3	61.16	19.48	R
C46032-005-06	520588.5	5420278.5	39.85	14.37	R
C46033-005-06	520647.4	5420726.6	31.62	23.95	R
C46034-005-06	519739.2	5420699.1	24.29	20.81	R
C46036-005-06	518374.0	5416073.4	6.98	60.00	V
C46037-005-06	520029.5	5416199.1	12.23	60.00	V
C46038-005-06	520582.1	5417045.3	37.56	49.06	R
C46039-005-06	520775.8	5417556.2	37.72	58.04	R
C46100B-005-06	520250.6	5421106.3	27.80	26.63	R
C46101-005-06	520198.3	5421518.2	55.73	5.91	R
C46101B-005-06	520198.3	5421518.2	55.73	3.35	R
C46102-005-06	520451.2	5422140.4	63.18	57.51	R
C46103-005-06	522506.8	5423116.6	52.18	60.00	V
C46104-005-06	524022.9	5422181.6	33.97	58.00	V
C46105-005-06	519766.3	5421467.7	55.74	36.07	R
C46106B-005-06	520336.1	5421371.5	53.99	35.47	V
C46107-005-06	522400.2	5422453.0	32.83	60.00	V
C46108-005-06	522364.0	5422283.2	33.47	60.00	V
C46109-005-06	522351.8	5422069.2	33.30	60.00	V
C46110-005-06	522334.1	5421831.3	32.76	60.00	V
C46111-005-06	521979.7	5416861.6	3.84	49.33	R
C46113-005-06	518474.2	5417672.7	9.56	19.65	R

Numéro de sondage	X	Y	Élévation (m)	Profondeur atteinte (m)	Raison de l'arrêt
C46114-005-06	518707.9	5418328.2	26.93	22.76	R
C46115B-005-06	518381.4	5418631.4	44.17	10.00	R
C46118-005-06	519778.9	5418200.4	20.44	55.19	V

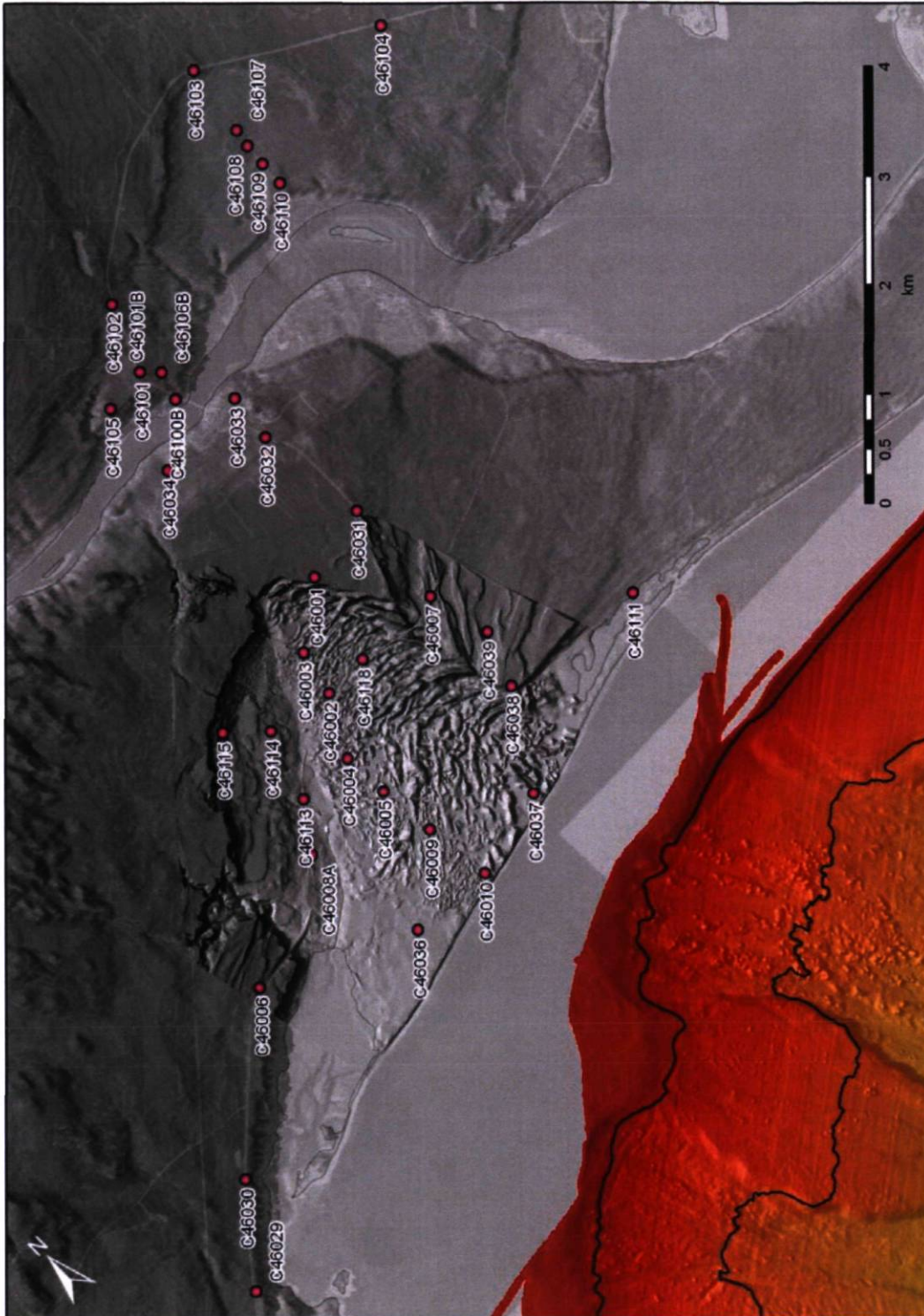
Raison de l'arrêt :

R = Refus sur une couche impénétrable

V = Arrêt volontaire

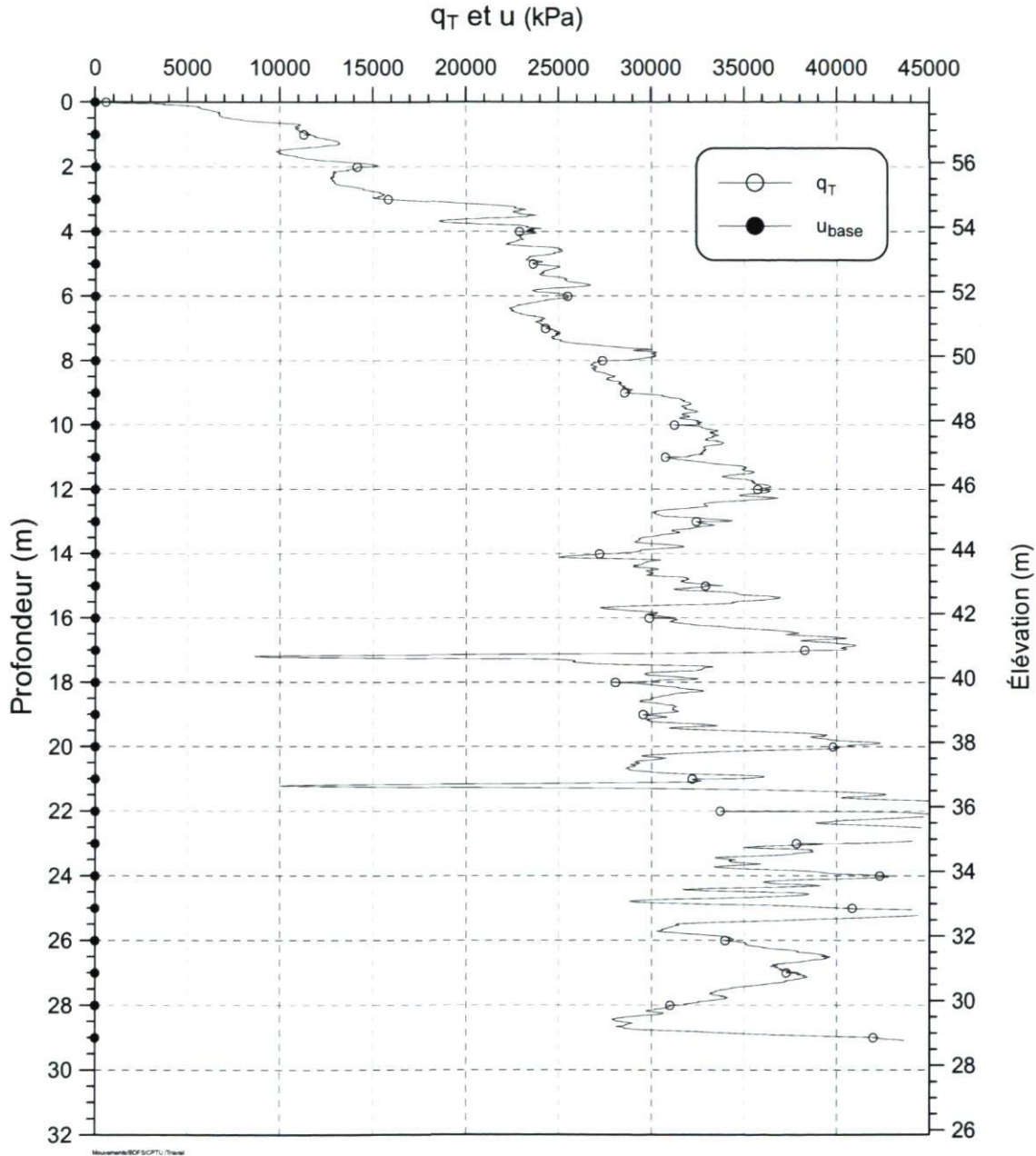
Les coordonnées X et Y sont en UTM 19N (m).

D.2 Carte de localisation des sondages au piézocône



D.3 Résultats des sondages

MINISTÈRE DES TRANSPORTS - ESSAI AU PIÉZOCÔNE			
SITE: Bersimis	ESSAI: C46001-005-06		
ÉLÉVATION T.N.: 57.860 m	AVANT-TROU: 0 m	PROF. ATTEINTE: 29.271 m [R]	DATE: 2006-09-21



SONDE: Hogentogler 5T (Techmat)

VITESSE: 60 cm/min

INCÉMENT: 1,0 cm

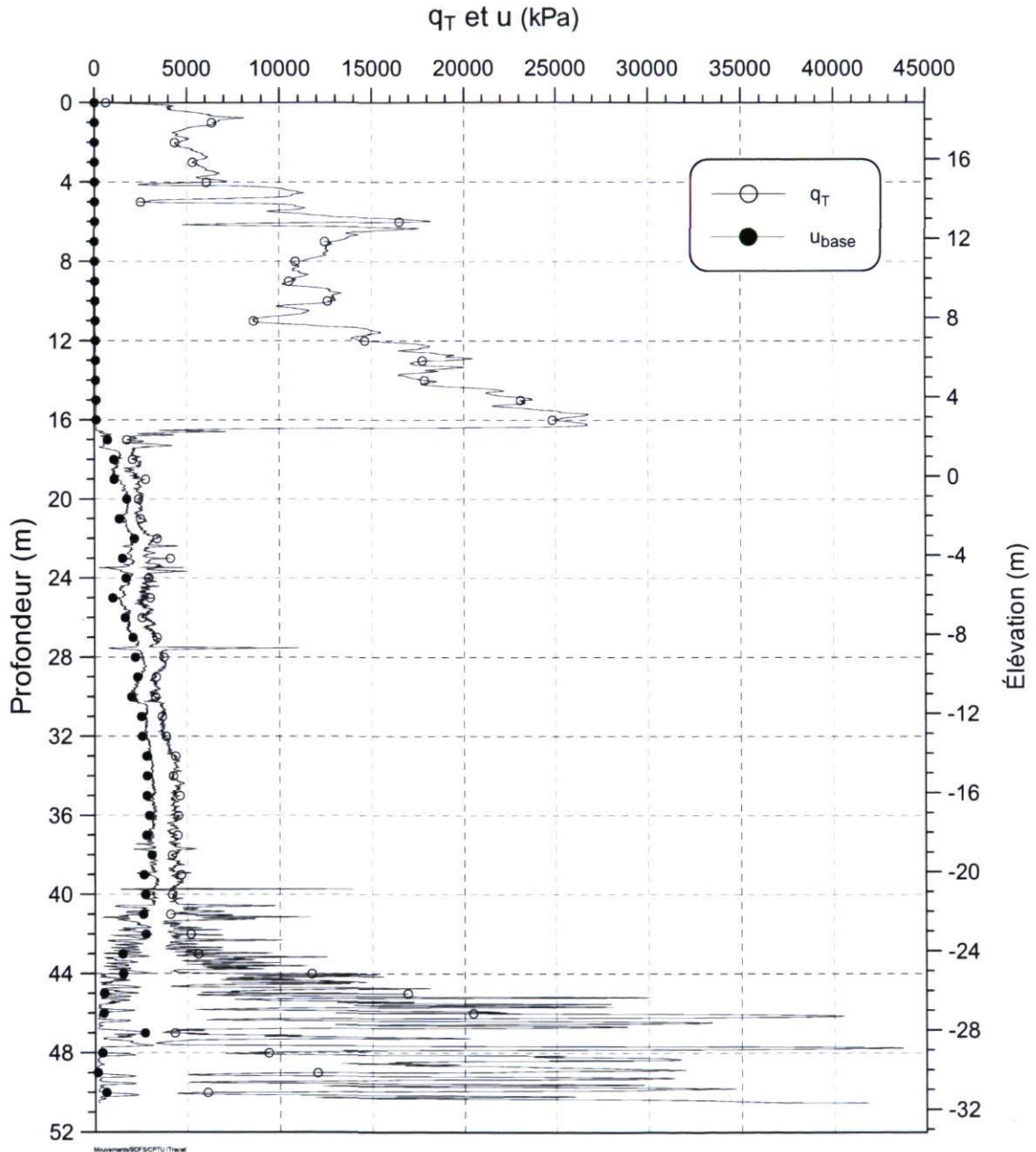
MINISTÈRE DES TRANSPORTS - ESSAI AU PIÉZOCÔNE

SITE: Colombier

ESSAI: C46002-005-06

ÉLÉVATION T.N.: 18.840 m AVANT-TROU: 0 m

PROF. ATTEINTE: 50.518 m [R] DATE: 2006-09-25



SONDE: Hogentogler 5T (Techmat)

VITESSE: 60 cm/min

INCRÉMENT: 1,0 cm

MINISTÈRE DES TRANSPORTS - ESSAI AU PIÉZOCÔNE

SITE: Colombier

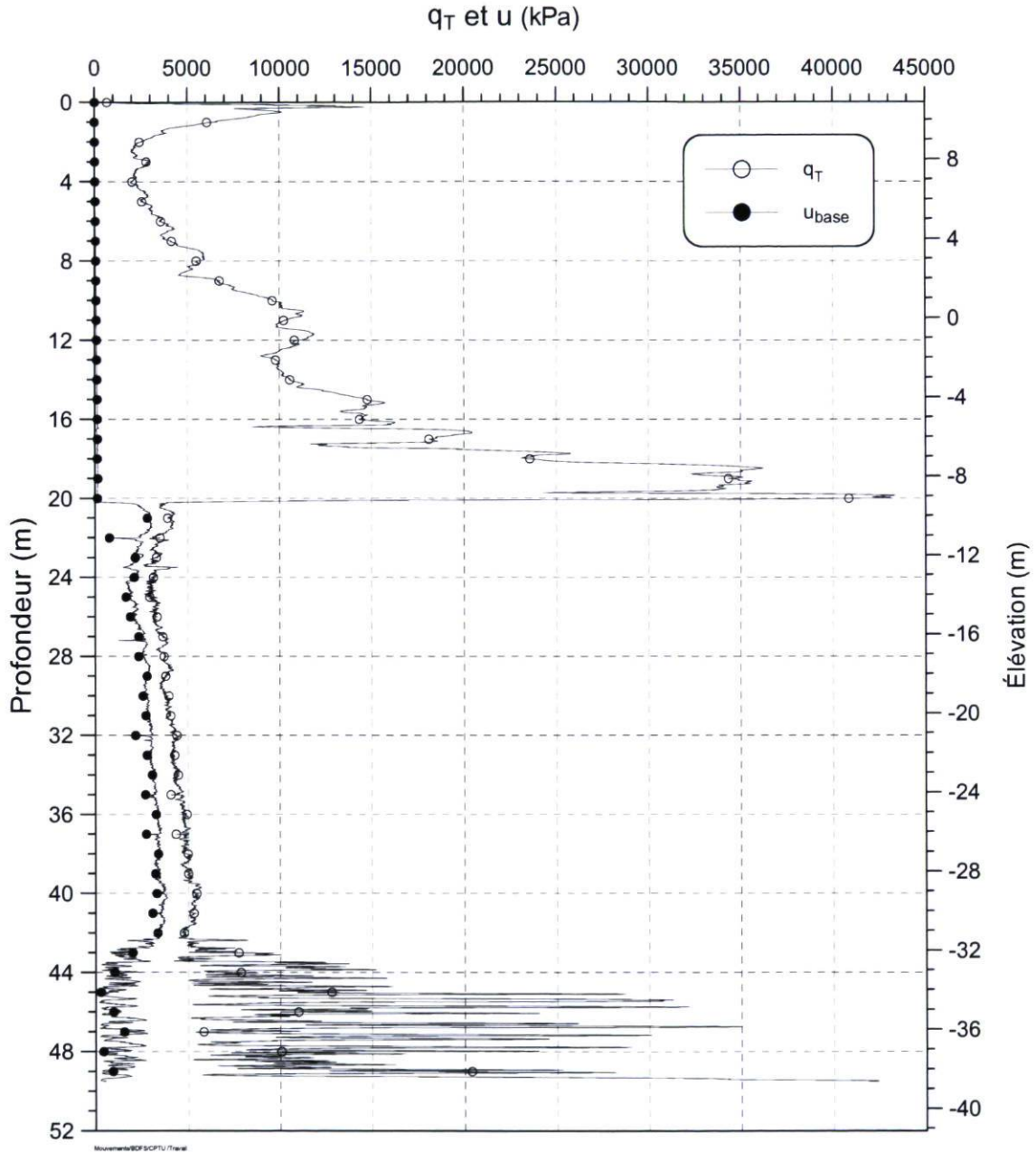
ESSAI: C46004-005-06

ÉLÉVATION T.N.: 10.870 m

AVANT-TROU: 0 m

PROF. ATTEINTE: 49.508 m [R]

DATE: 2006-09-26



SONDE: Hogentogler 5T (Techmat)

VITESSE: 60 cm/min

INCRÉMENT: 1,0 cm

MINISTÈRE DES TRANSPORTS - ESSAI AU PIÉZOCÔNE

SITE: Colombier

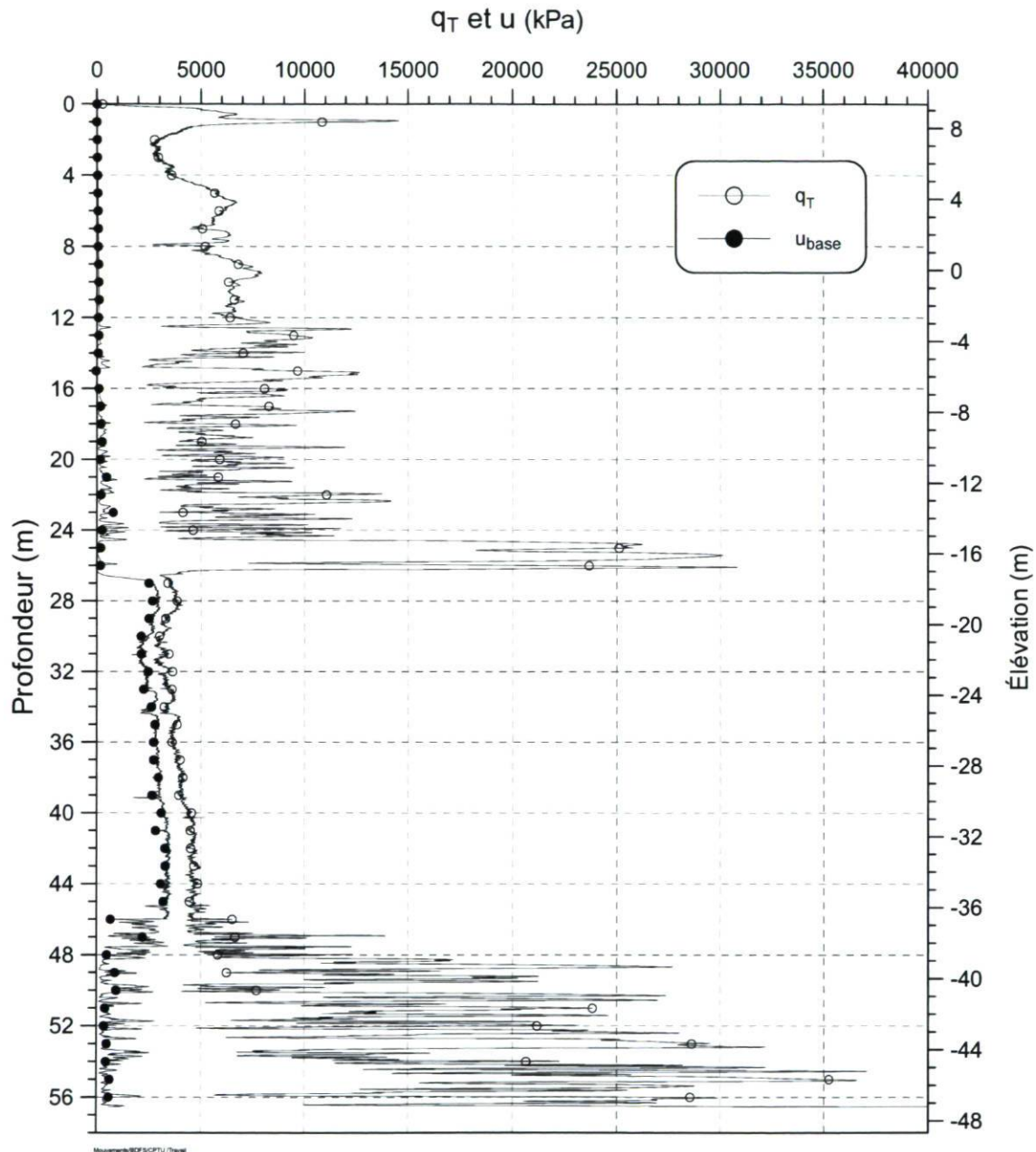
ESSAI: C46005-005-06

ÉLÉVATION T.N.: 9.330 m

AVANT-TROU: 0 m

PROF. ATTEINTE: 56.537 m [R]

DATE: 2006-09-26



SONDE: Hogentogler 5T (Techmat)

VITESSE: 60 cm/min

INCRÉMENT: 1,0 cm

MINISTÈRE DES TRANSPORTS - ESSAI AU PIÉZOCÔNE

SITE: Colombier

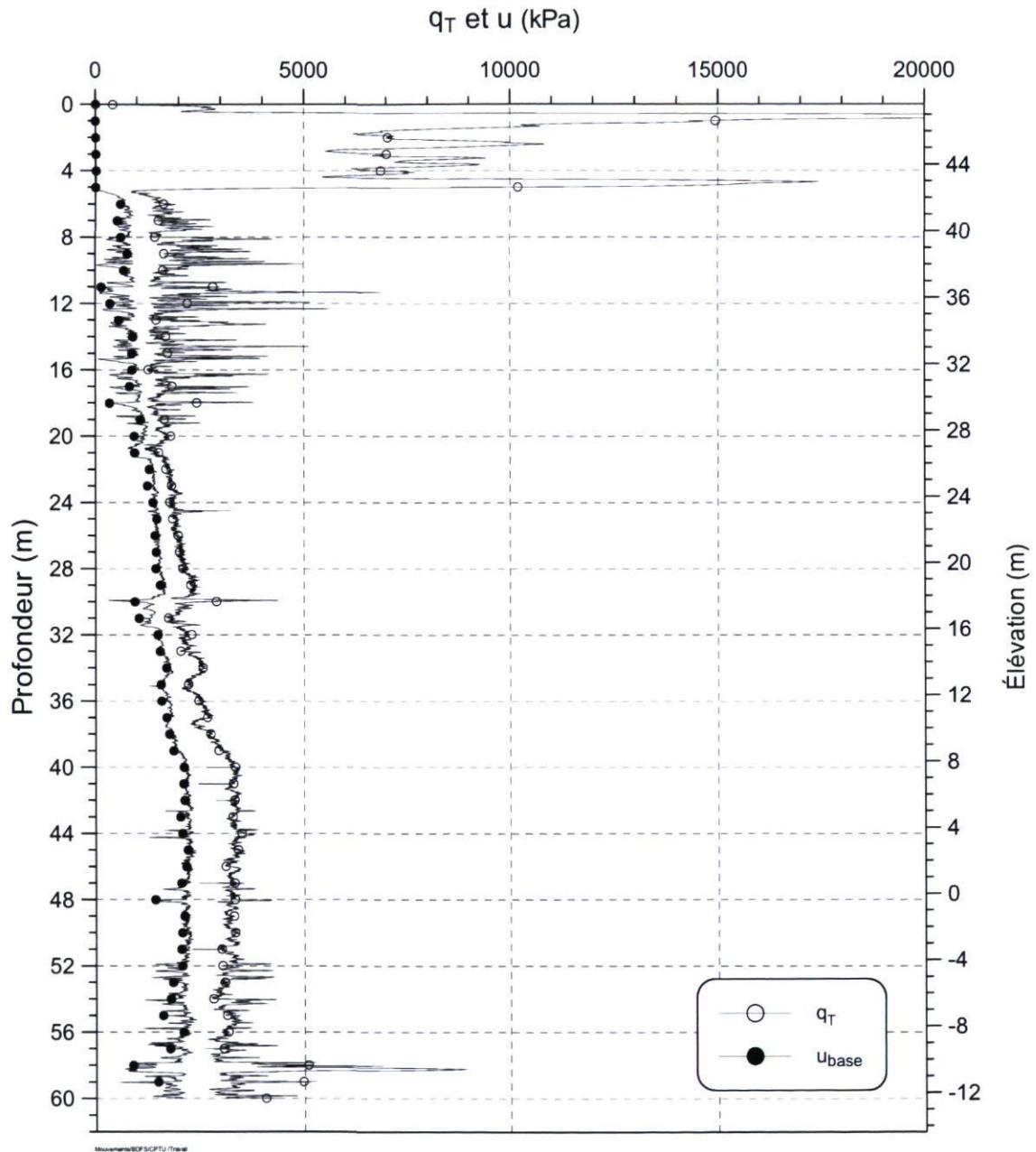
ESSAI: C46006-005-06

ÉLÉVATION T.N.: 47.620 m

AVANT-TROU: 0 m

PROF. ATTEINTE: 59.996 m [V]

DATE: 2006-09-28



SONDE: Hogentogler 5T (Techmat)

VITESSE: 60 cm/min

INCRÉMENT: 1,0 cm

MINISTÈRE DES TRANSPORTS - ESSAI AU PIÉZOCÔNE

SITE: Rivière Bersimis

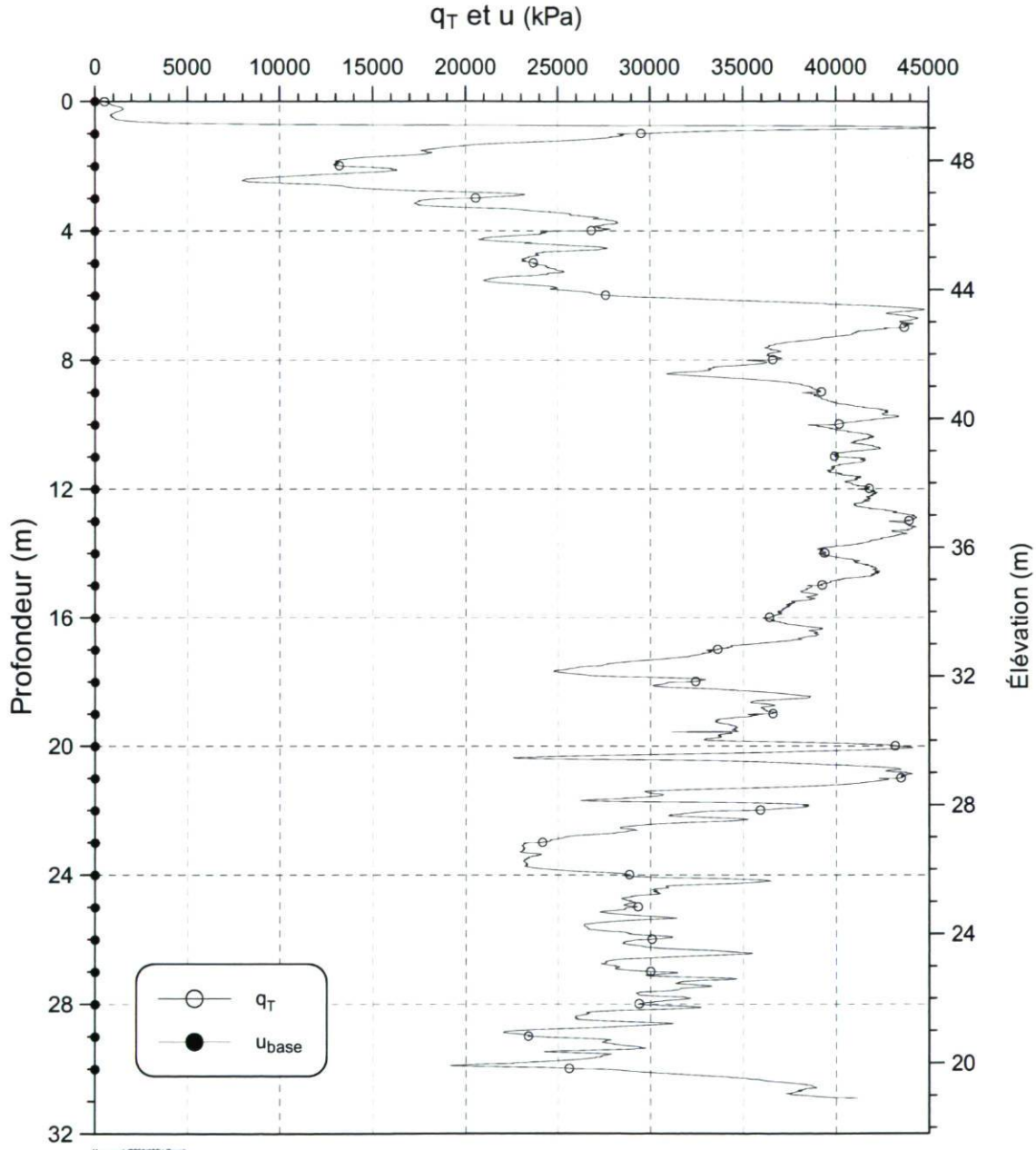
ESSAI: C46007-005-06

ÉLÉVATION T.N.: 49.820 m

AVANT-TROU: 0 m

PROF. ATTEINTE: 30.901 m [R]

DATE: 2006-09-22



SONDE: Hogentogler 5T (Techmat)

VITESSE: 60 cm/min

INCRÉMENT: 1,0 cm

MINISTÈRE DES TRANSPORTS - ESSAI AU PIÉZOCÔNE

SITE: Colombier

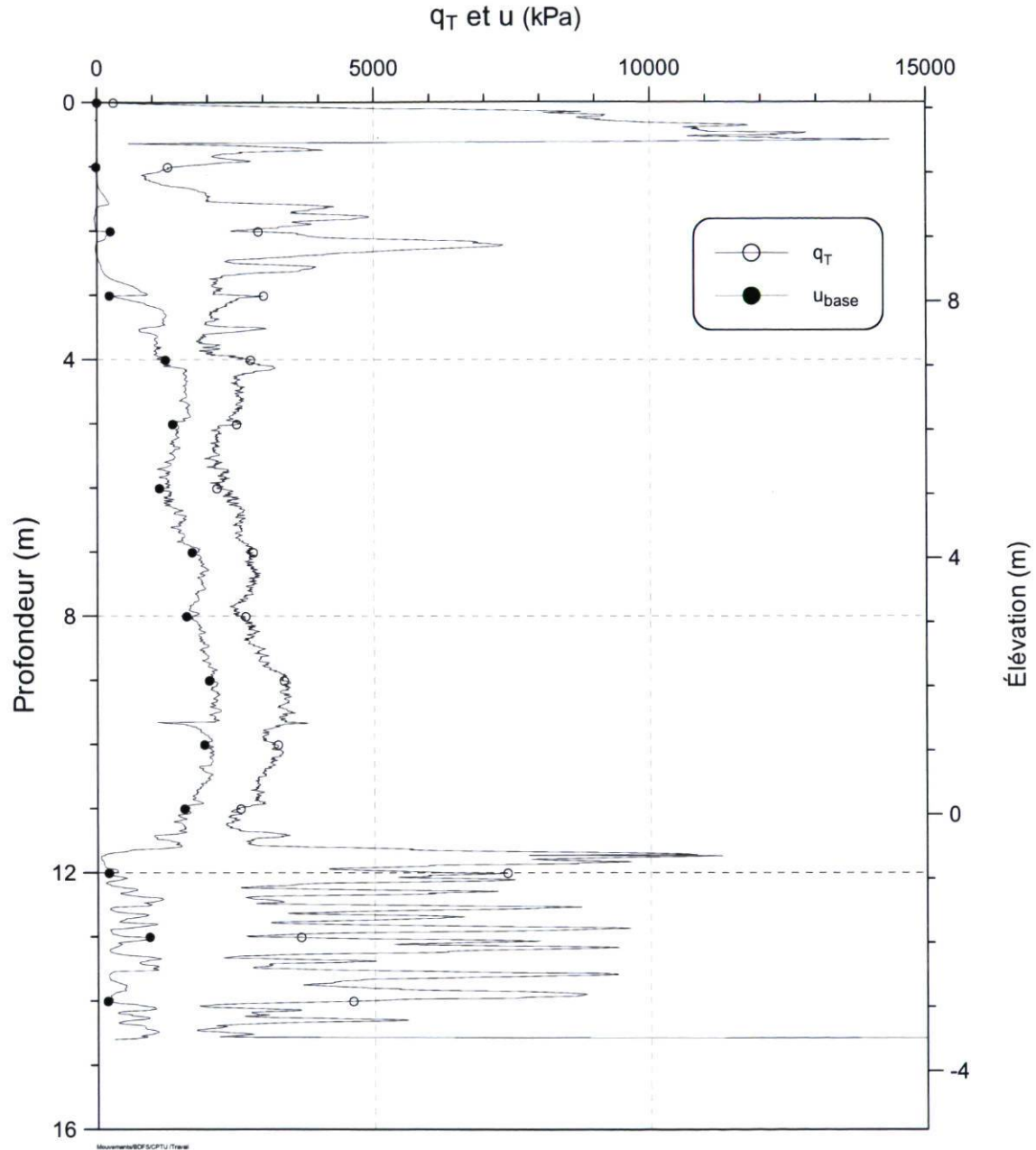
ESSAI: C46008A-005-06

ÉLÉVATION T.N.: 11.090 m

AVANT-TROU: 0 m

PROF. ATTEINTE: 14.600 m [R]

DATE: 2006-09-28



SONDE: Hogentogler 5T (Techmat)

VITESSE: 60 cm/min

INCRÉMENT: 1,0 cm

MINISTÈRE DES TRANSPORTS - ESSAI AU PIÉZOCÔNE

SITE: Colombier

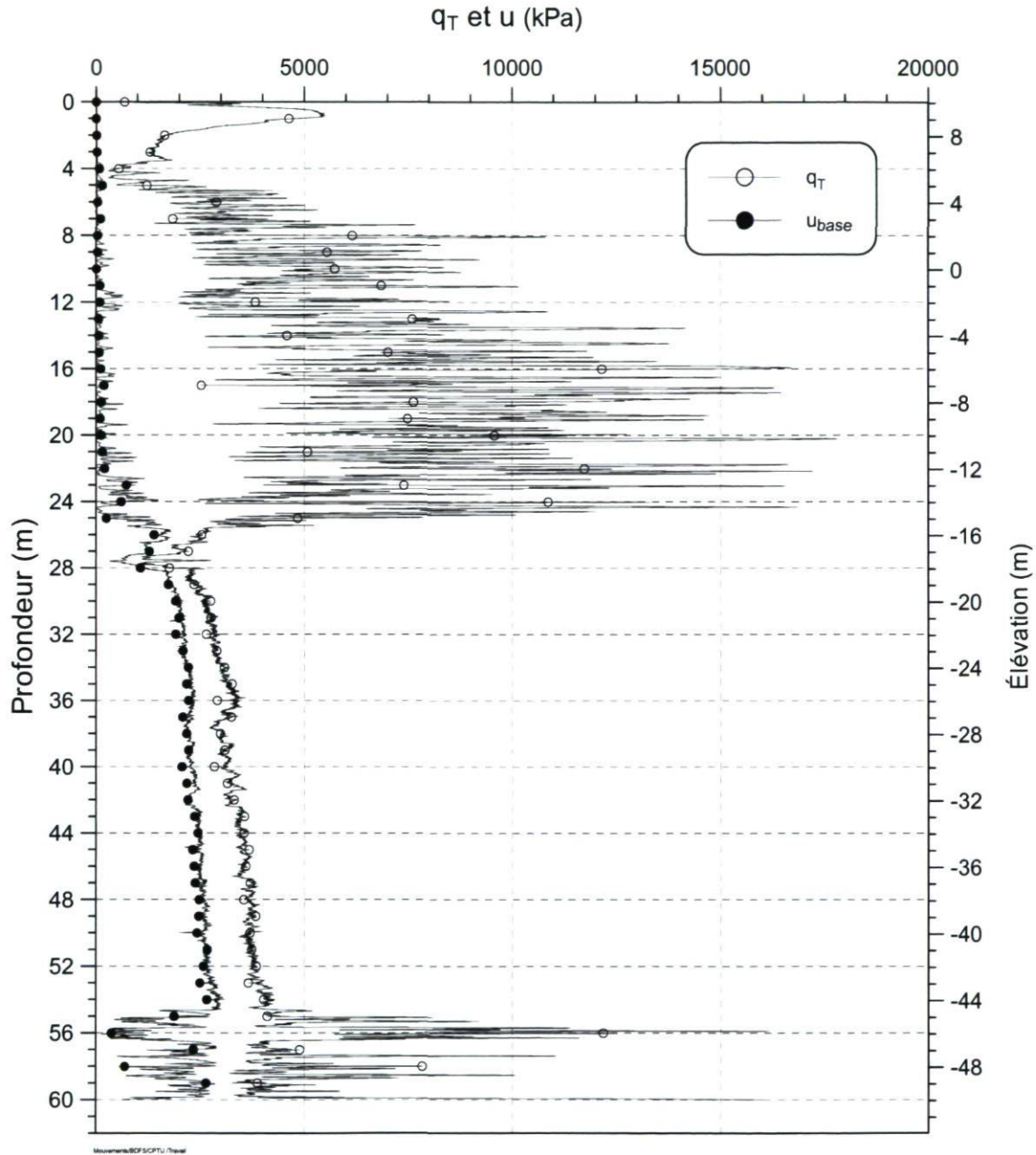
ESSAI: C46009-005-06

ÉLÉVATION T.N.: 10.060 m

AVANT-TROU: 0 m

PROF. ATTEINTE: 59.996 m [V]

DATE: 2006-09-27



SONDE: Hogentogler 5T (Techmat)

VITESSE: 60 cm/min

INCRÉMENT: 1,0 cm

MINISTÈRE DES TRANSPORTS - ESSAI AU PIÉZOCÔNE

SITE: Colombier

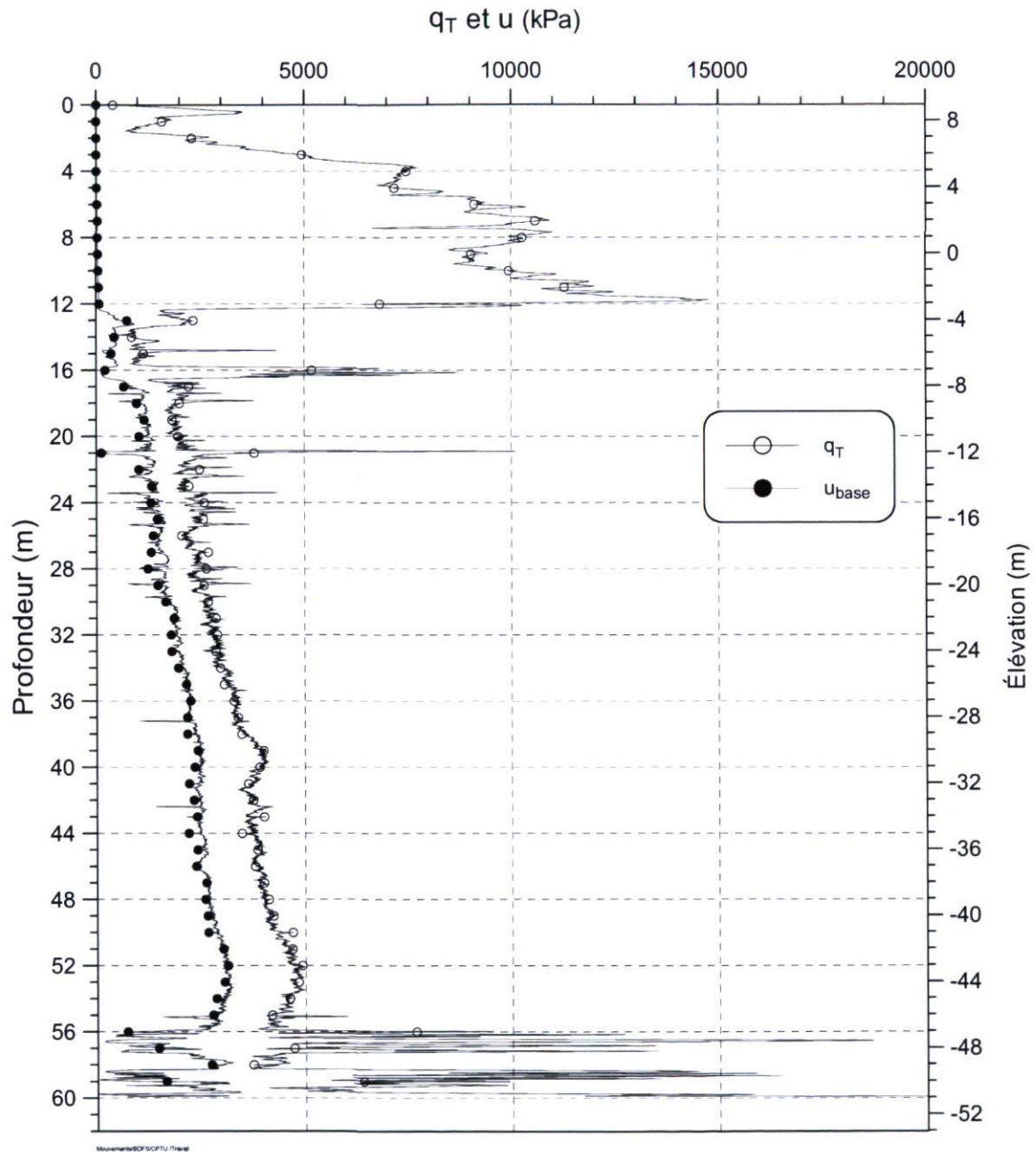
ESSAI: C46010-005-06

ÉLÉVATION T.N.: 8.950 m

AVANT-TROU: 0 m

PROF. ATTEINTE: 59.916 m [R]

DATE: 2006-09-27



SONDE: Hogentogler 5T (Techmat)

VITESSE: 60 cm/min

INCRÉMENT: 1,0 cm

MINISTÈRE DES TRANSPORTS - ESSAI AU PIÉZOCÔNE

SITE: Colombier

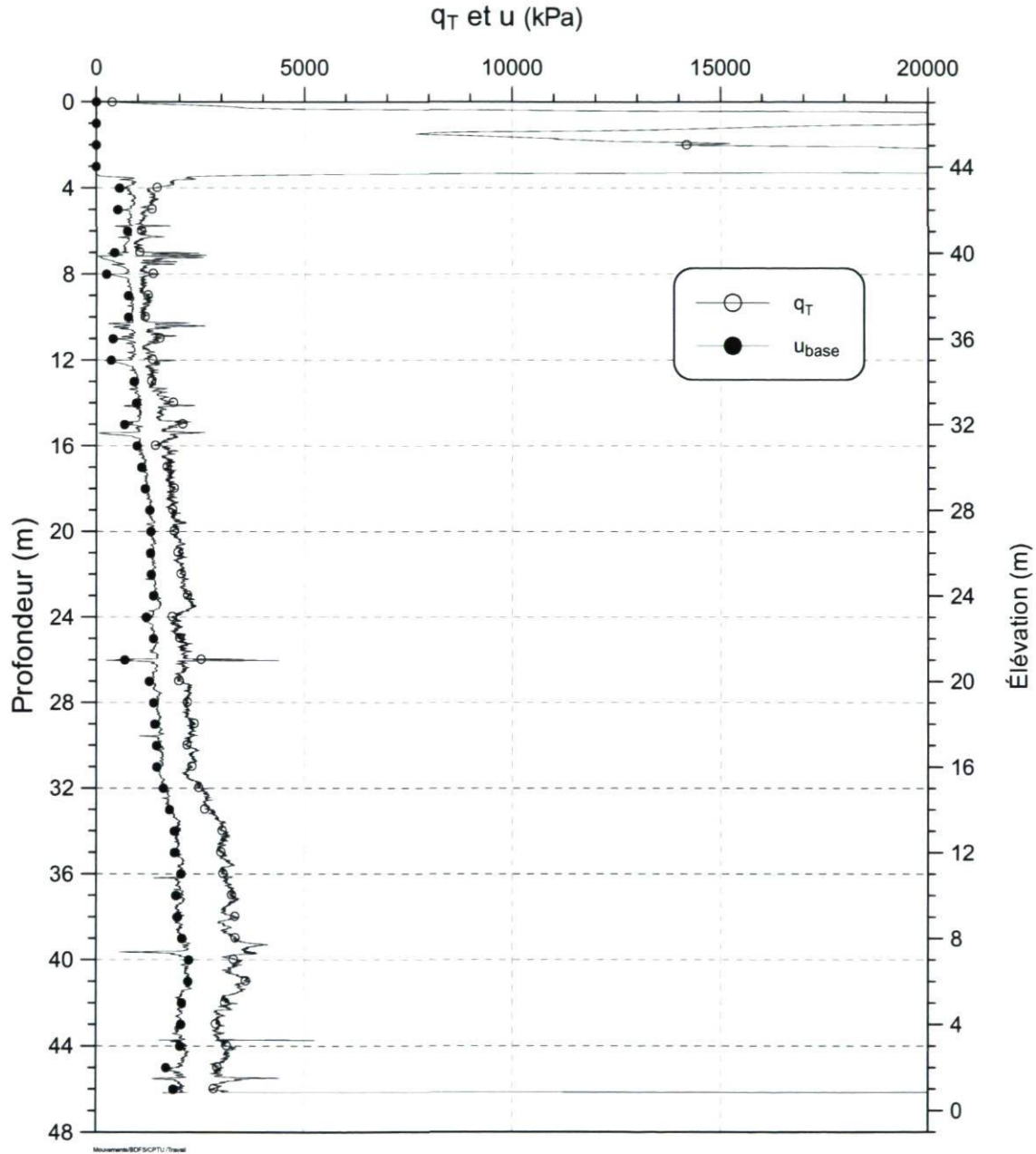
ESSAI: C46029-005-06

ÉLÉVATION T.N.: 47.000 m

AVANT-TROU: 0 m

PROF. ATTEINTE: 46.168 m [R]

DATE: 2006-10-02



SONDE: Hogentogler 5T (Techmat)

VITESSE: 60 cm/min

INCRÉMENT: 1,0 cm

MINISTERE DES TRANSPORTS - ESSAI AU PIÉZOCÔNE

SITE: Colombier

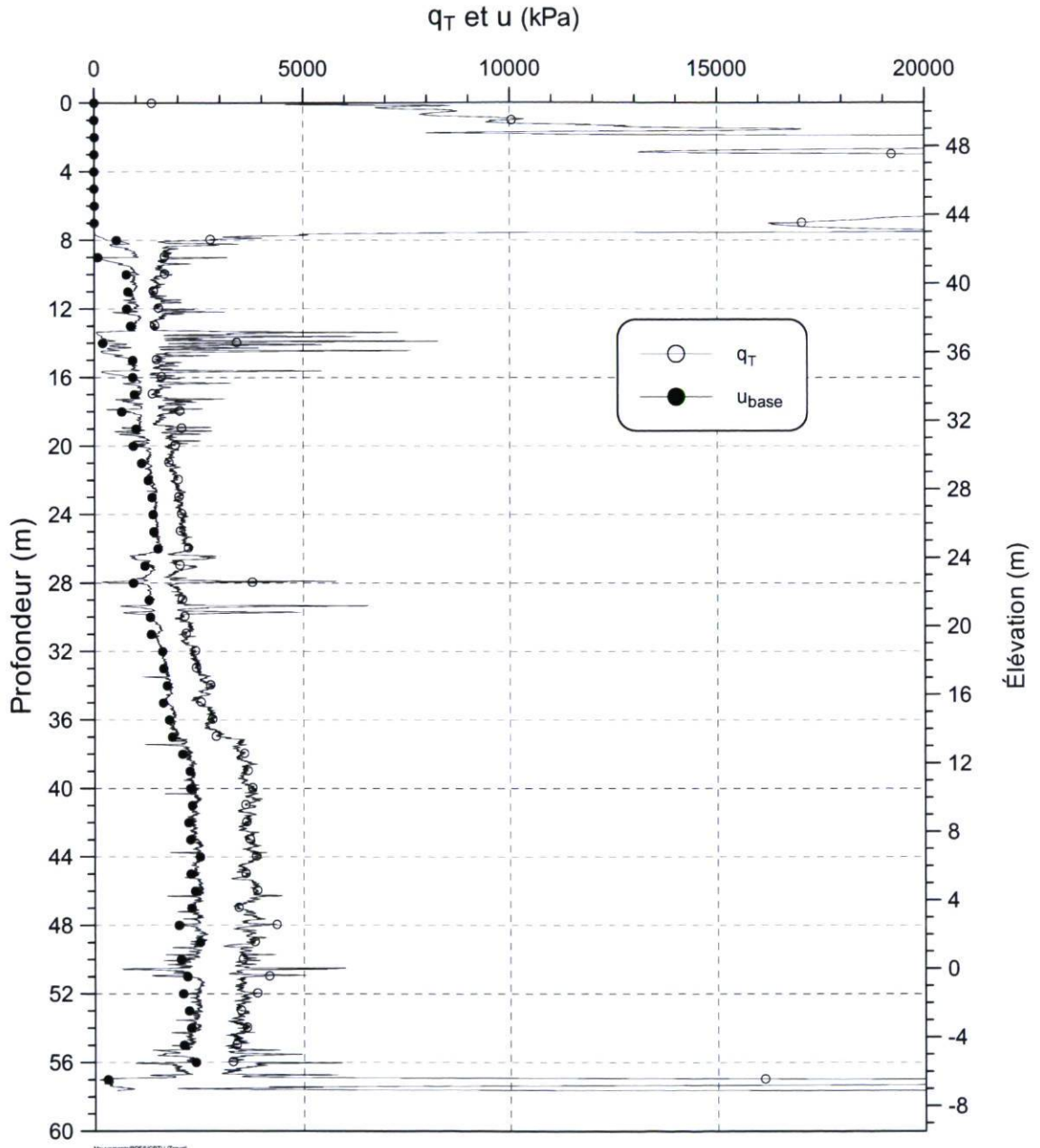
ESSAI: C46030-005-06

ÉLÉVATION T.N.: 50.510 m

AVANT-TROU: 0 m

PROF. ATTEINTE: 57.636 m [R]

DATE: 2006-09-29



SONDE: Hogentogler 5T (Techmat)

VITESSE: 60 cm/min

INCRÉMENT: 1,0 cm

MINISTÈRE DES TRANSPORTS - ESSAI AU PIÉZOCÔNE

SITE: Rivière Bersimis

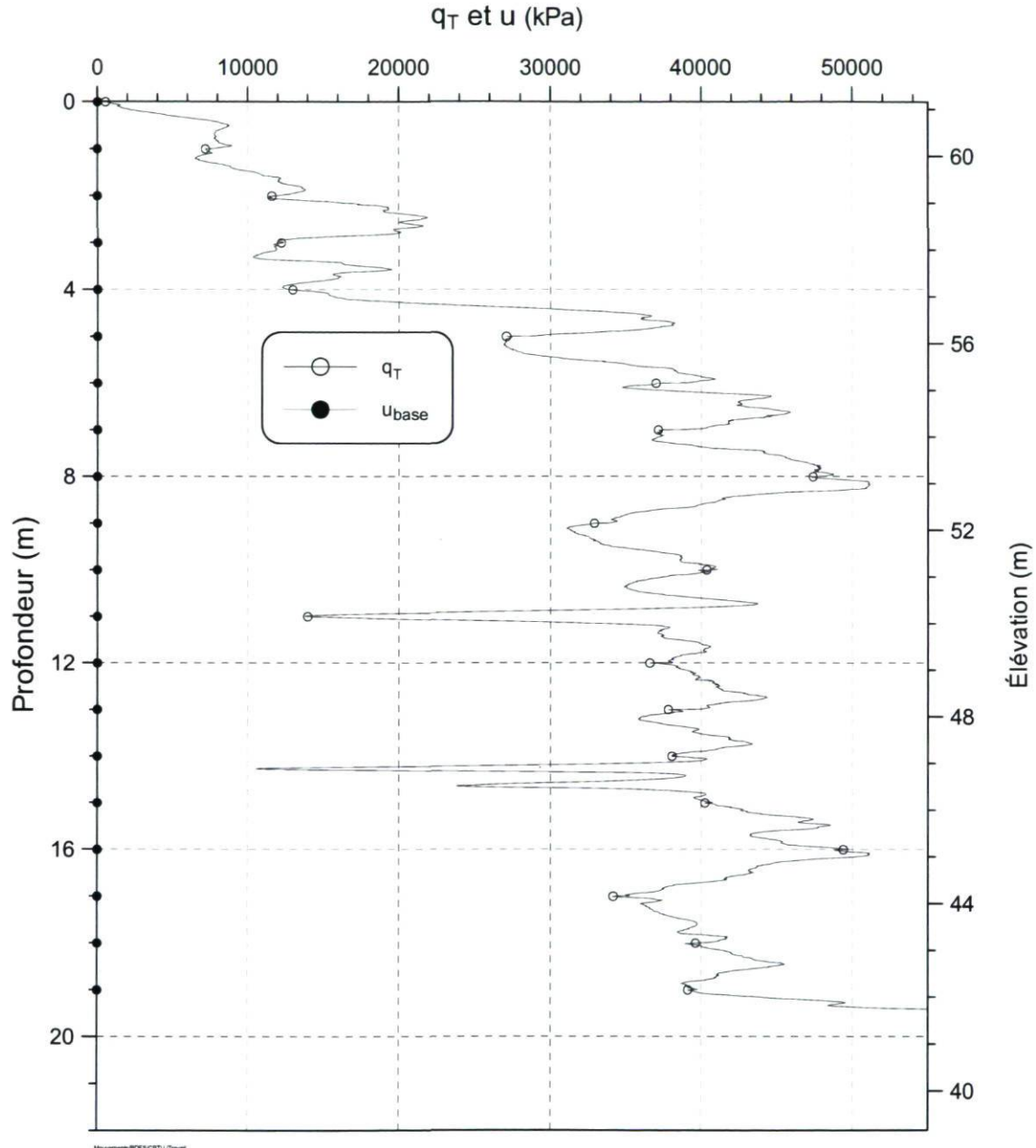
ESSAI: C46031-005-06

ÉLÉVATION T.N.: 61.160 m

AVANT-TROU: 0 m

PROF. ATTEINTE: 19.480 m [R]

DATE: 2006-09-21



SONDE: Hogentogler 5T (Techmat)

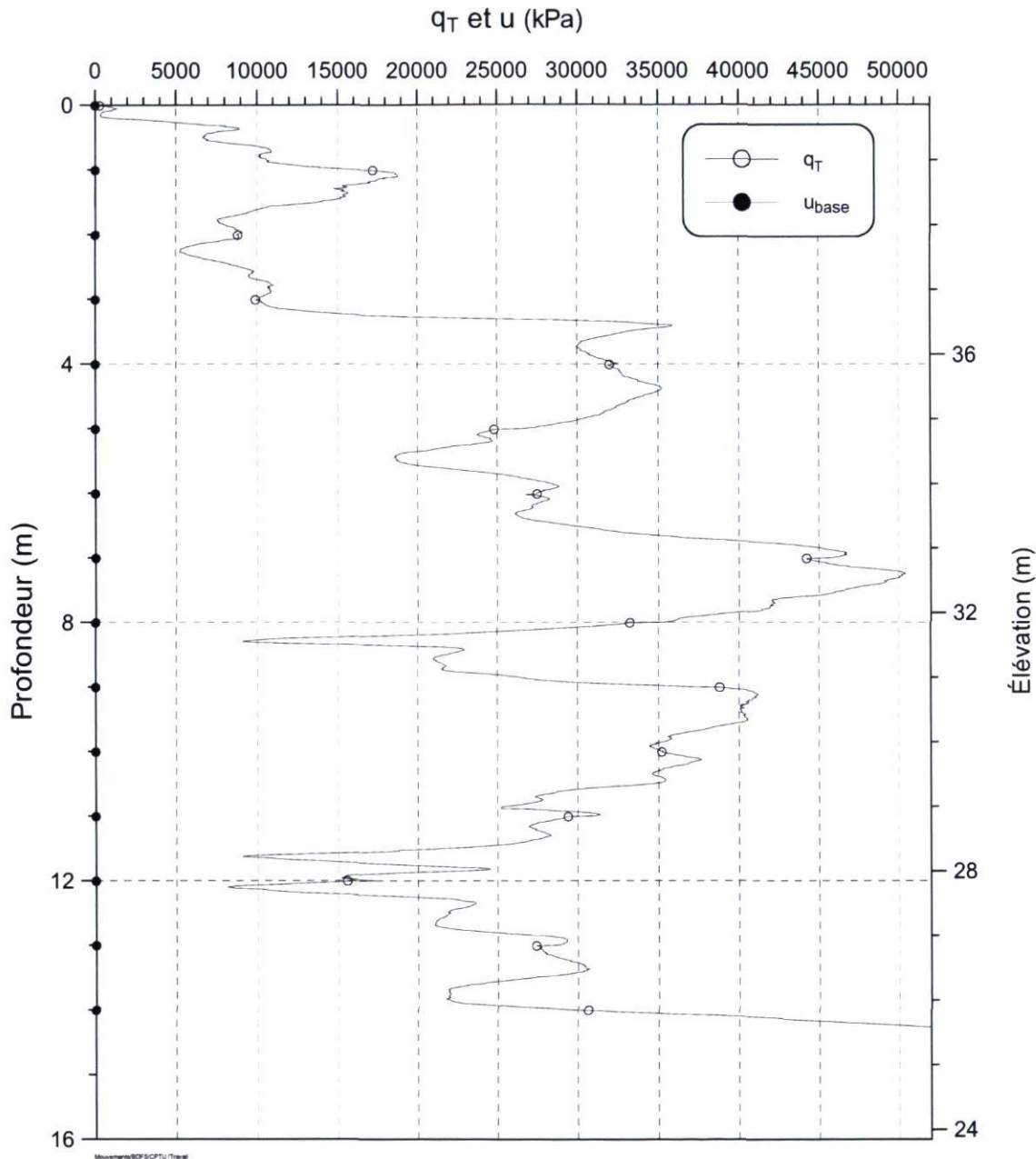
VITESSE: 60 cm/min

INCÉMENT: 1,0 cm

MINISTÈRE DES TRANSPORTS - ESSAI AU PIÉZOCÔNE

SITE: Rivière Bersimis ESSAI: C46032-005-06

ÉLÉVATION T.N.: 39.850 m AVANT-TROU: 0 m PROF. ATTEINTE: 14.370 m [R] DATE: 2006-09-21



SONDE: Hogentogler 5T (Techmat) VITESSE: 60 cm/min INCRÉMENT: 1,0 cm

MINISTÈRE DES TRANSPORTS - ESSAI AU PIÉZOCÔNE

SITE: Rivière Bersimis

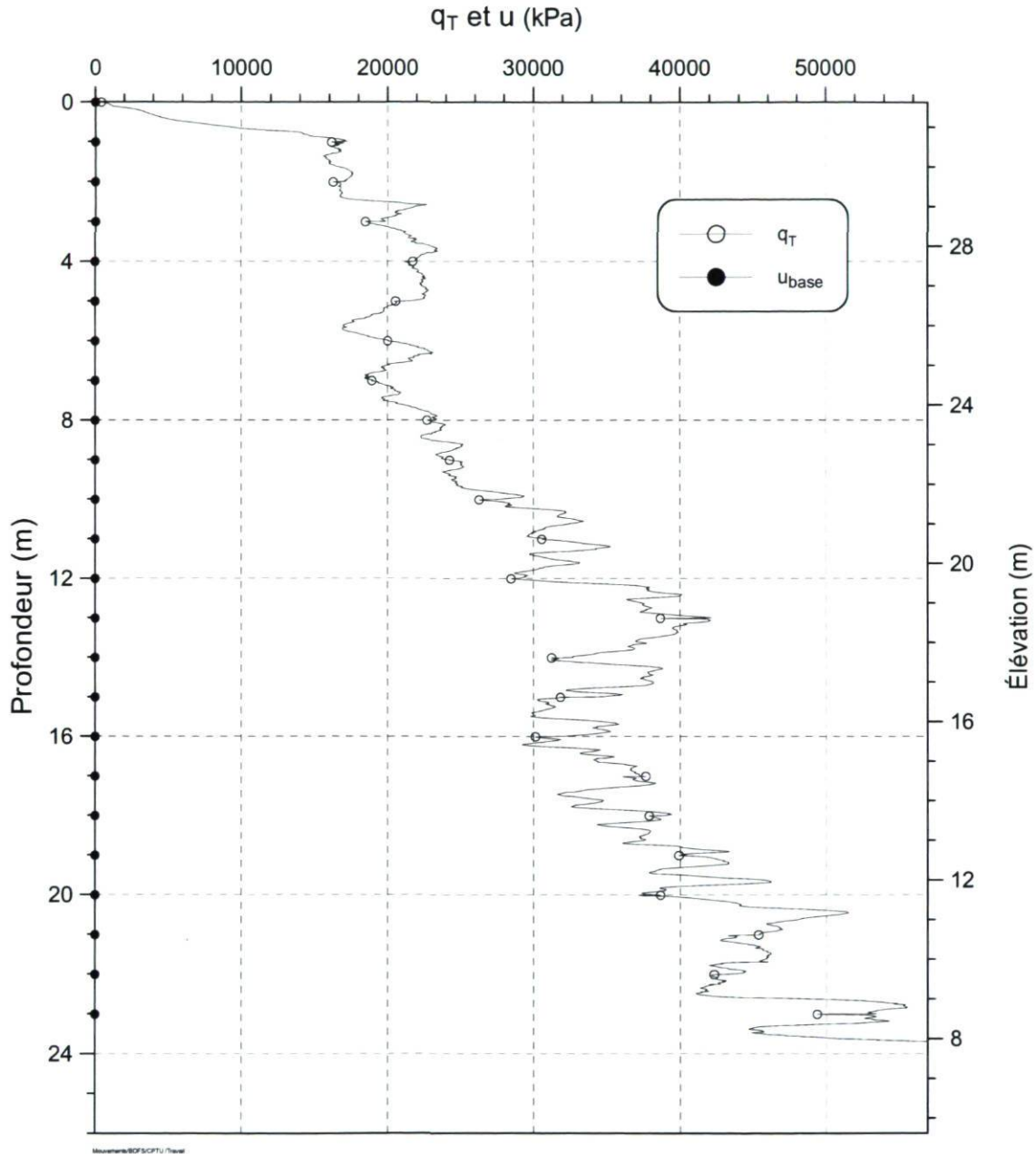
ESSAI: C46033-005-06

ÉLÉVATION T.N.: 31.620 m

AVANT-TROU: 0 m

PROF. ATTEINTE: 23.950 m [R]

DATE: 2006-09-20



SONDE: Hogentogler 5T (Techmat)

VITESSE: 60 cm/min

INCRÉMENT: 1,0 cm

MINISTÈRE DES TRANSPORTS - ESSAI AU PIÉZOCÔNE

SITE: Rivière Bersimis

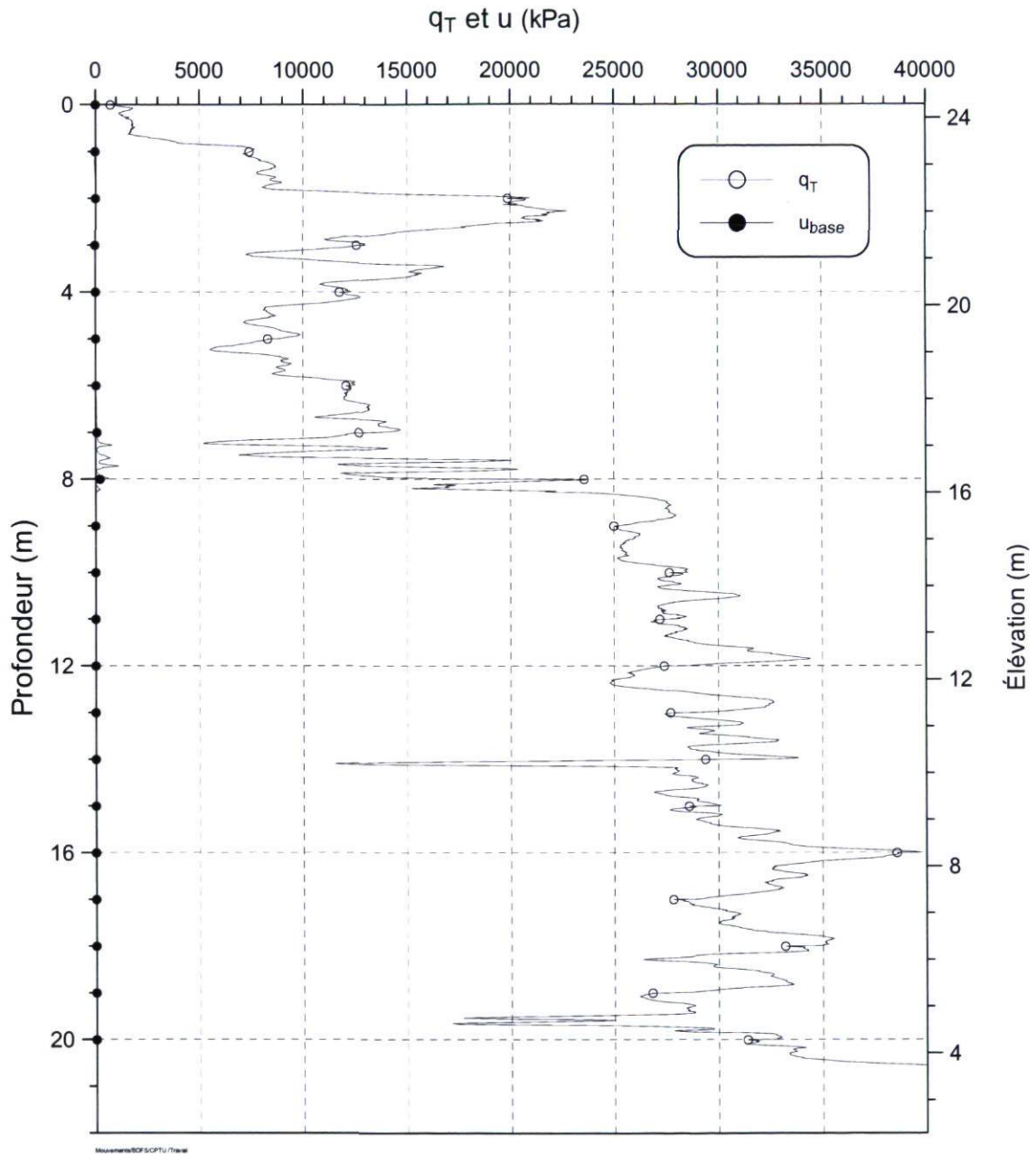
ESSAI: C46034-005-06

ÉLÉVATION T.N.: 24.290 m

AVANT-TROU: 0 m

PROF. ATTEINTE: 20.810 m [R]

DATE: 2006-09-21



SONDE: Hogentogler 5T (Techmat)

VITESSE: 60 cm/min

INCRÉMENT: 1,0 cm

MINISTÈRE DES TRANSPORTS - ESSAI AU PIÉZOCÔNE

SITE: Colombier

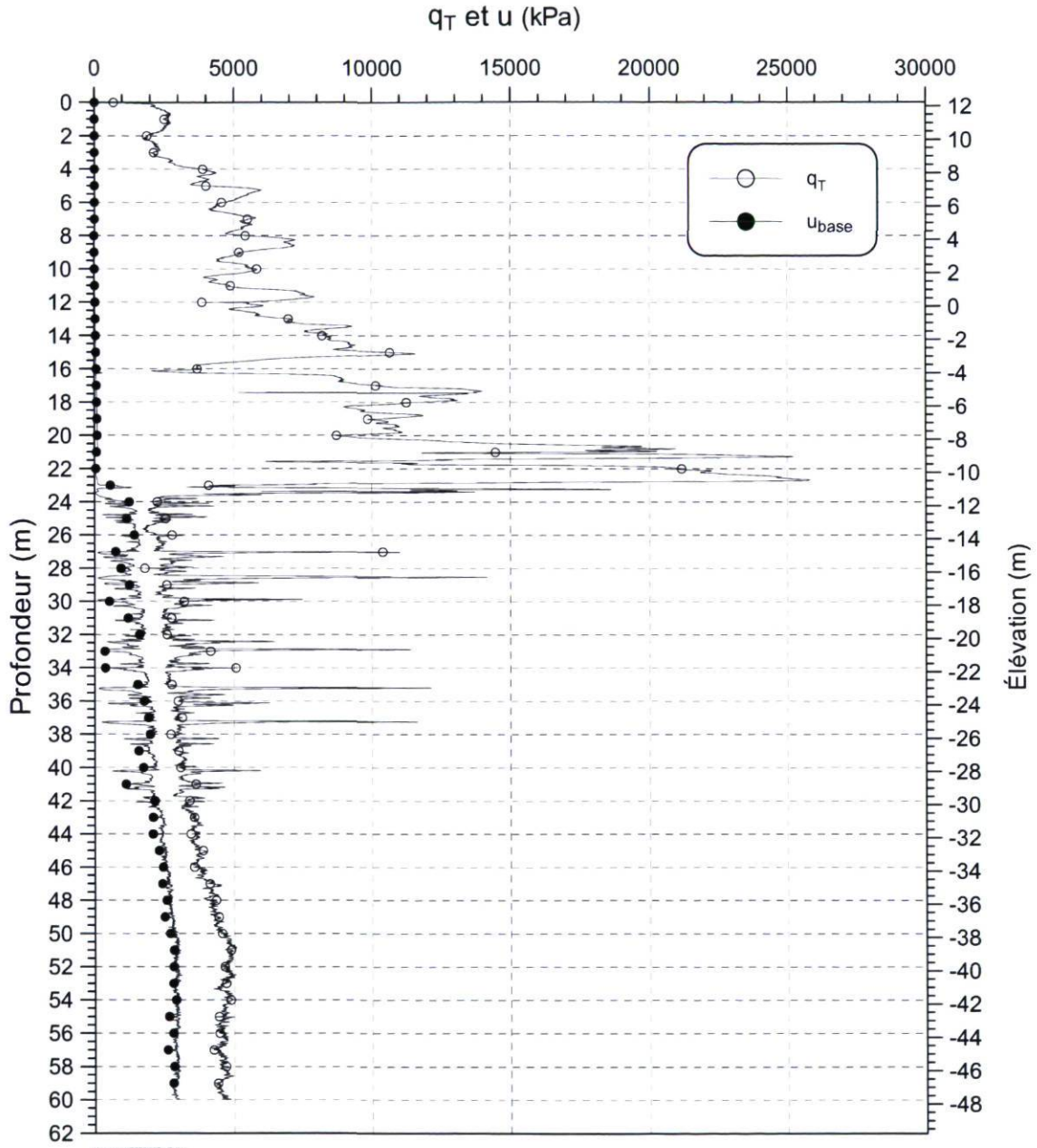
ESSAI: C46037-005-06

ÉLÉVATION T.N.: 12.230 m

AVANT-TROU: 0 m

PROF. ATTEINTE: 59.996 m [V]

DATE: 2006-10-12



SONDE: Hogentogler 5T (Techmat)

VITESSE: 60 cm/min

INCRÉMENT: 1,0 cm

MINISTÈRE DES TRANSPORTS - ESSAI AU PIÉZOCÔNE

SITE: Colombier

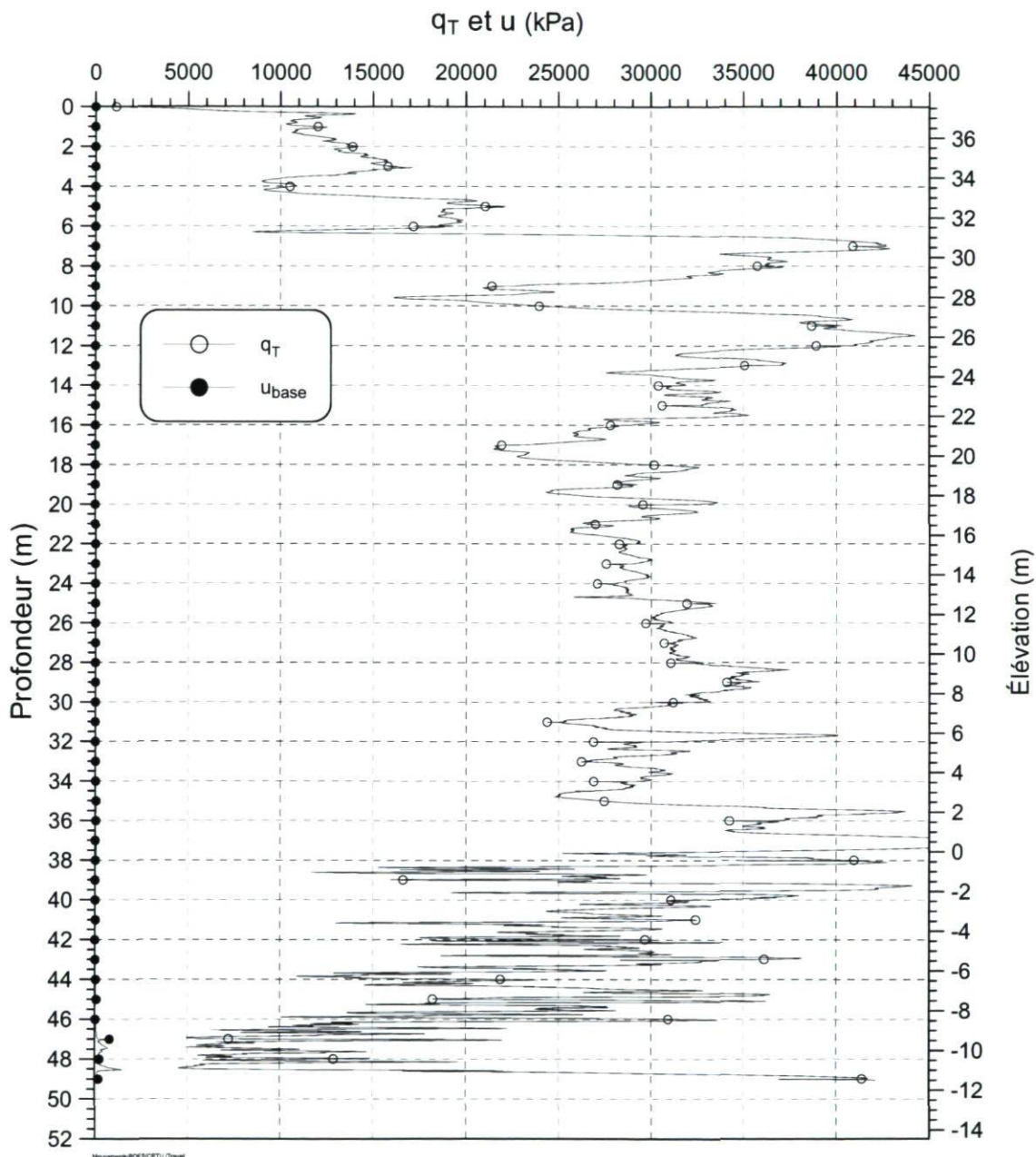
ESSAI: C46038-005-06

ÉLEVATION T.N.: 37.560 m

AVANT-TROU: 0 m

PROF. ATTEINTE: 49.058 m [R]

DATE: 2006-10-12



SONDE: Hogentogler 5T (Techmat)

VITESSE: 60 cm/min

INCRÉMENT: 1,0 cm

MINISTÈRE DES TRANSPORTS - ESSAI AU PIÉZOCÔNE

SITE: Colombier

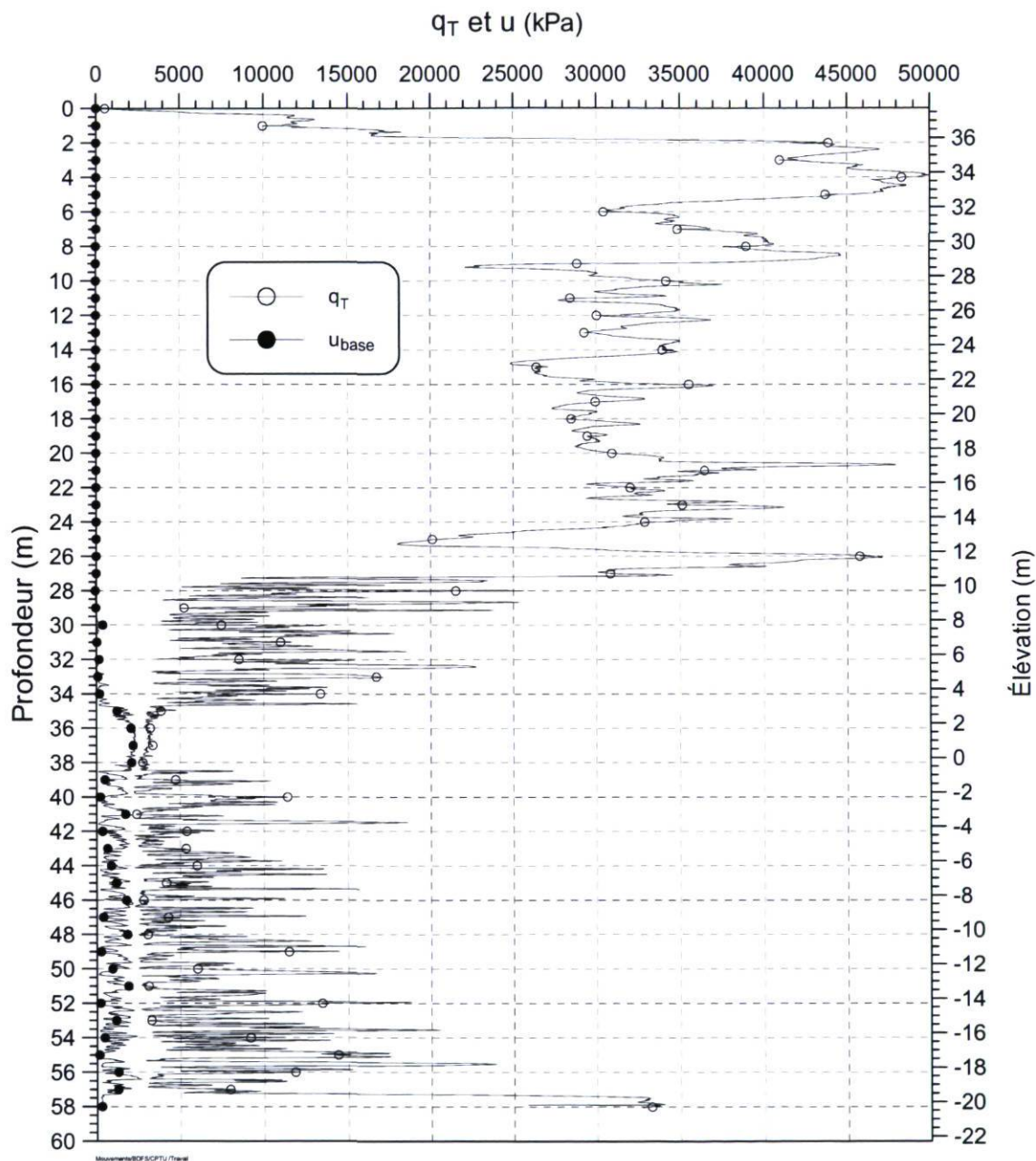
ESSAI: C46039-005-06

ÉLÉVATION T.N.: 37.720 m

AVANT-TROU: 0 m

PROF. ATTEINTE: 58.036 m [R]

DATE: 2006-10-13



SONDE: Hogentogler 5T (Techmat)

VITESSE: 60 cm/min

INCRÉMENT: 1.0 cm

MINISTÈRE DES TRANSPORTS - ESSAI AU PIÉZOCÔNE

SITE: Betsiamites

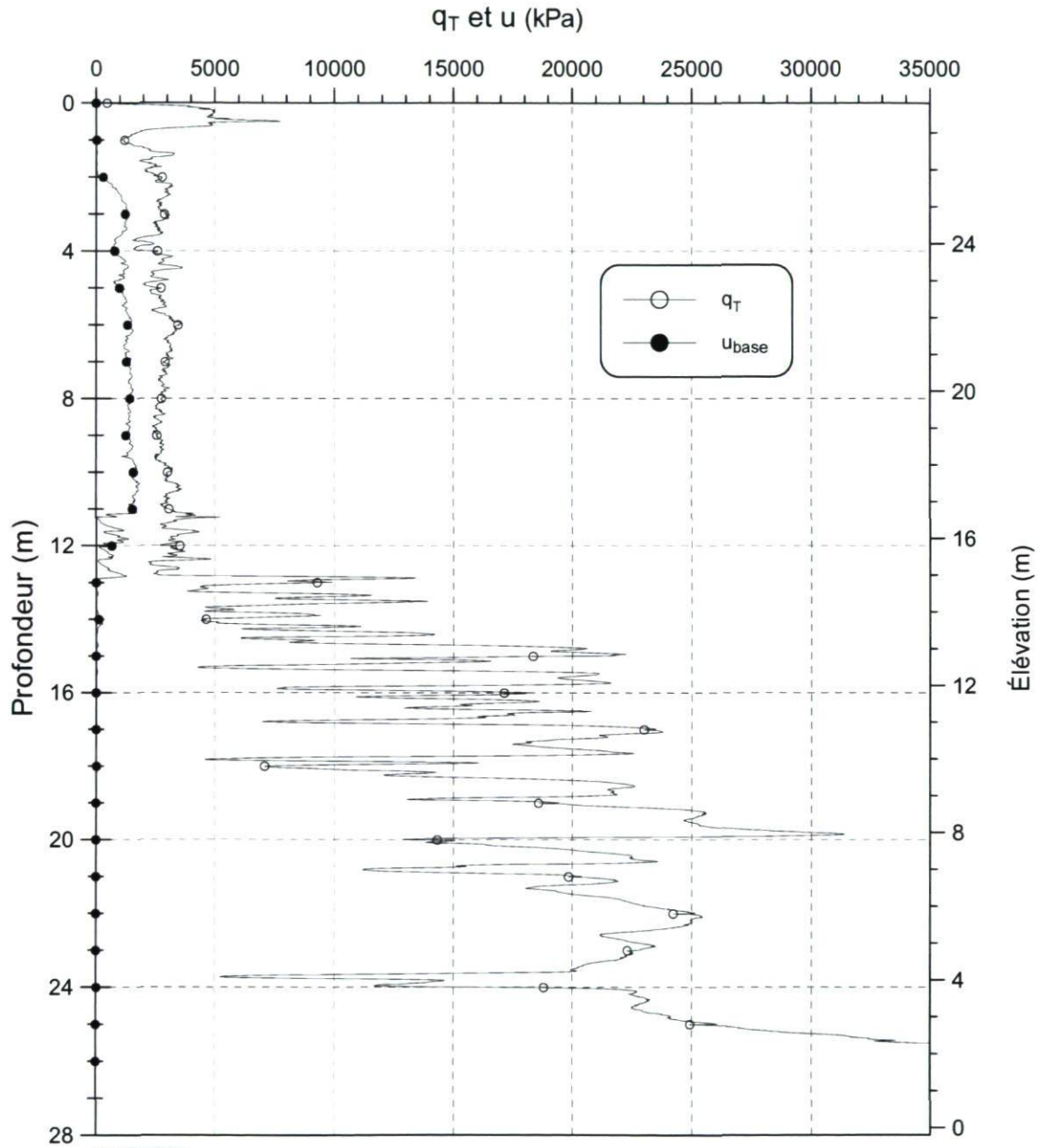
ESSAI: C46100B-005-06

ÉLÉVATION T.N.: 27.800 m

AVANT-TROU: 0 m

PROF. ATTEINTE: 26.631 m [R]

DATE: 2006-09-20



SONDE: Hogentogler 5T (Techmat)

VITESSE: 60 cm/min

INCRÉMENT: 1,0 cm

MINISTÈRE DES TRANSPORTS - ESSAI AU PIÉZOCÔNE

SITE: Betsiamites

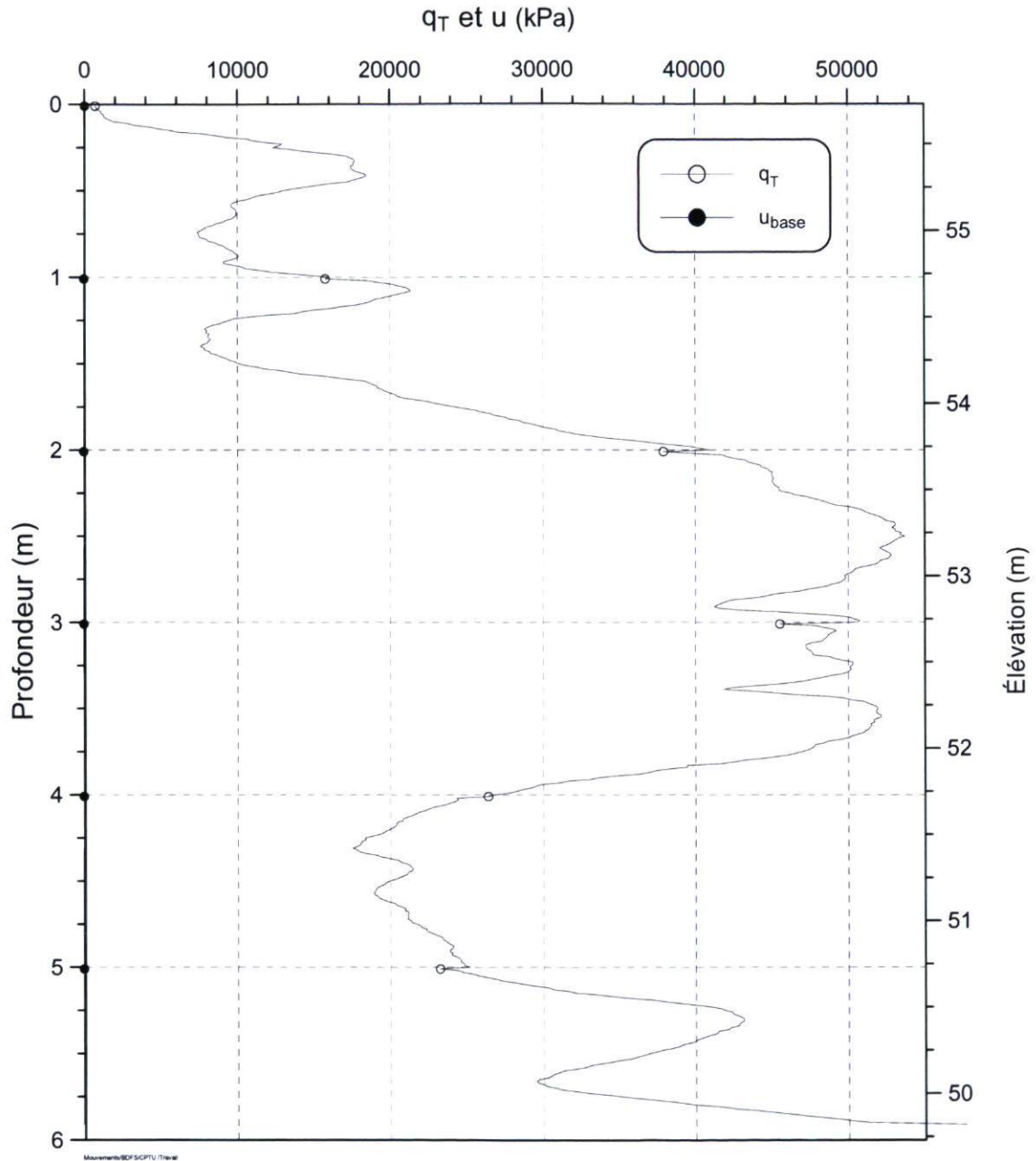
ESSAI: C46101-005-06

ÉLÉVATION T.N.: 55.730 m

AVANT-TROU: 0 m

PROF. ATTEINTE: 5.910 m [R]

DATE: 2006-09-15



SONDE: Hogentogler 5T (Techmat)

VITESSE: 60 cm/min

INCRÉMENT: 1,0 cm

MINISTÈRE DES TRANSPORTS - ESSAI AU PIÉZOCÔNE

SITE: Betsiamites

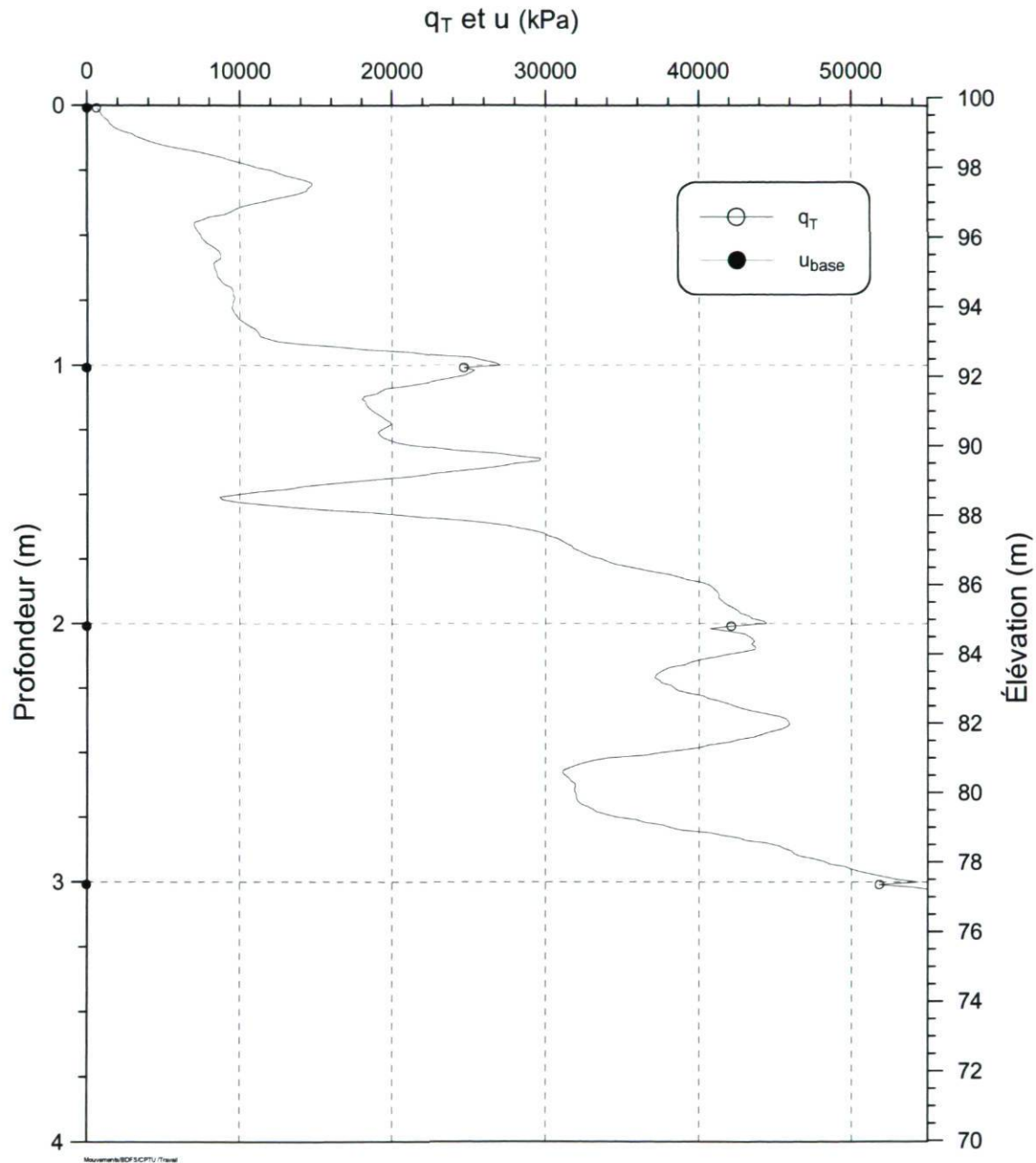
ESSAI: C46101B-005-06

ÉLÉVATION T.N.: 55.73 m

AVANT-TROU: 0 m

PROF. ATTEINTE: 3.350 m [R]

DATE: 2006-09-15



SONDE: Hogentogler 5T (Techmat)

VITESSE: 60 cm/min

INCRÉMENT: 1,0 cm

MINISTÈRE DES TRANSPORTS - ESSAI AU PIÉZOCÔNE

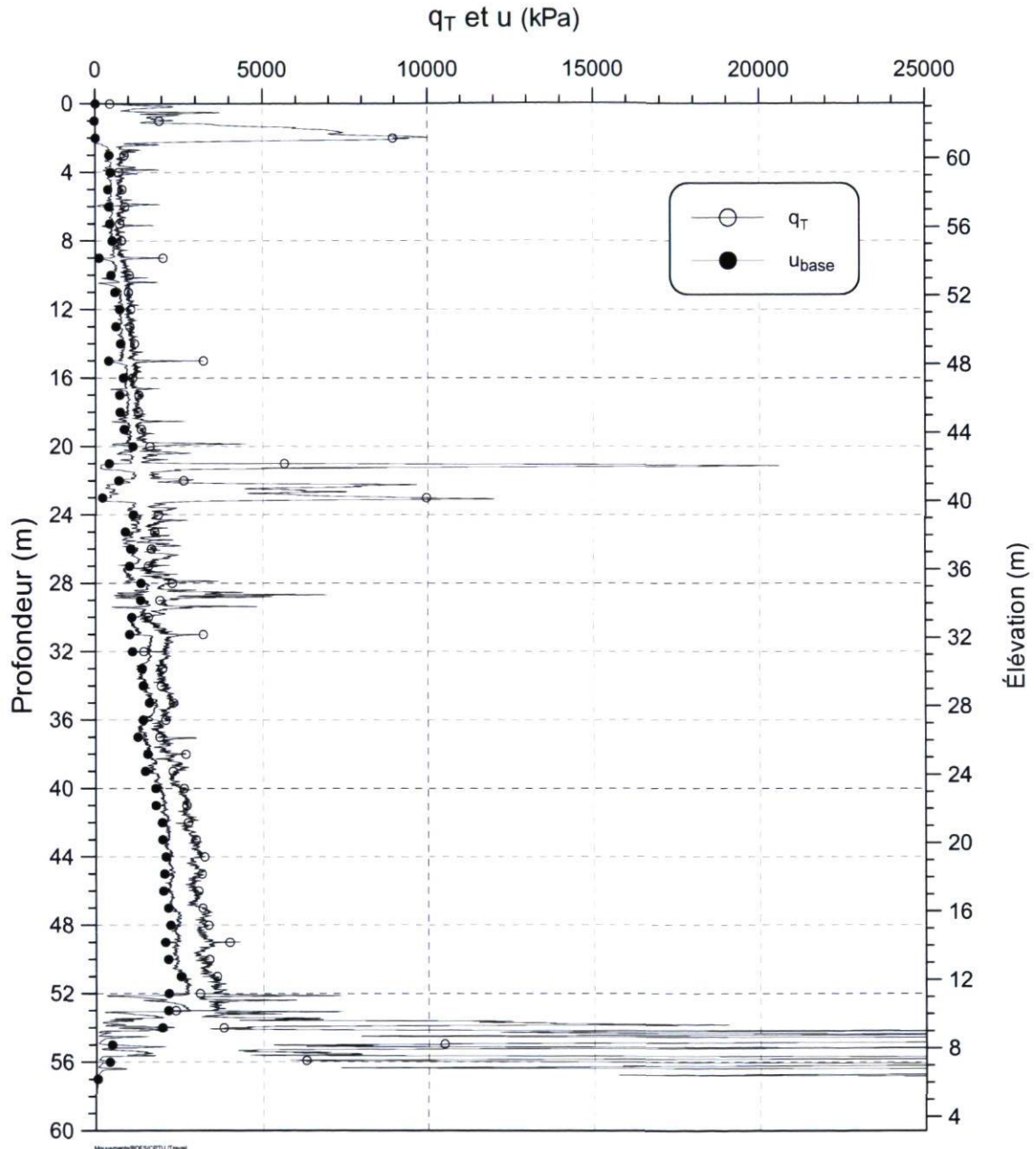
SITE: Betsiamites

ESSAI: C46102-005-06

ÉLÉVATION T.N.: 63.180 m AVANT-TROU: 0 m

PROF. ATTEINTE: 57.506 m [R]

DATE: 2006-09-14



SONDE: Hogentogler 5T (Techmat)

VITESSE: 60 cm/min

INCRÉMENT: 1,0 cm

MINISTÈRE DES TRANSPORTS - ESSAI AU PIÉZOCÔNE

SITE: Bersimis

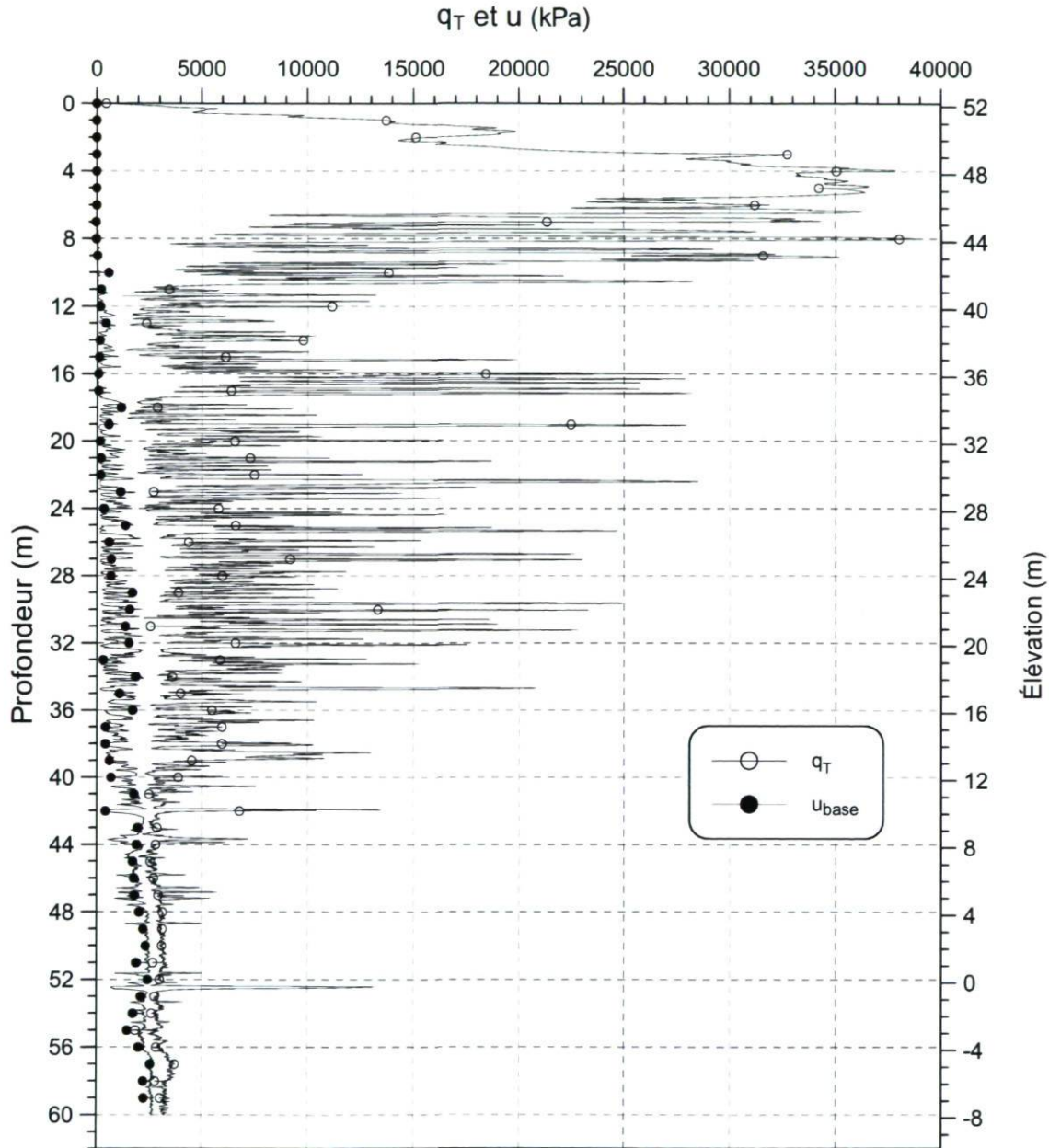
ESSAI: C46103-005-06

ÉLÉVATION T.N.: 52.180 m

AVANT-TROU: 0 m

PROF. ATTEINTE: 59.996 m [V]

DATE: 2006-09-13



SONDE: Hogentogler 5T (Techmat)

VITESSE: 60 cm/min

INCRÉMENT: 1,0 cm

MINISTÈRE DES TRANSPORTS - ESSAI AU PIÉZOCÔNE

SITE: Betsiamites

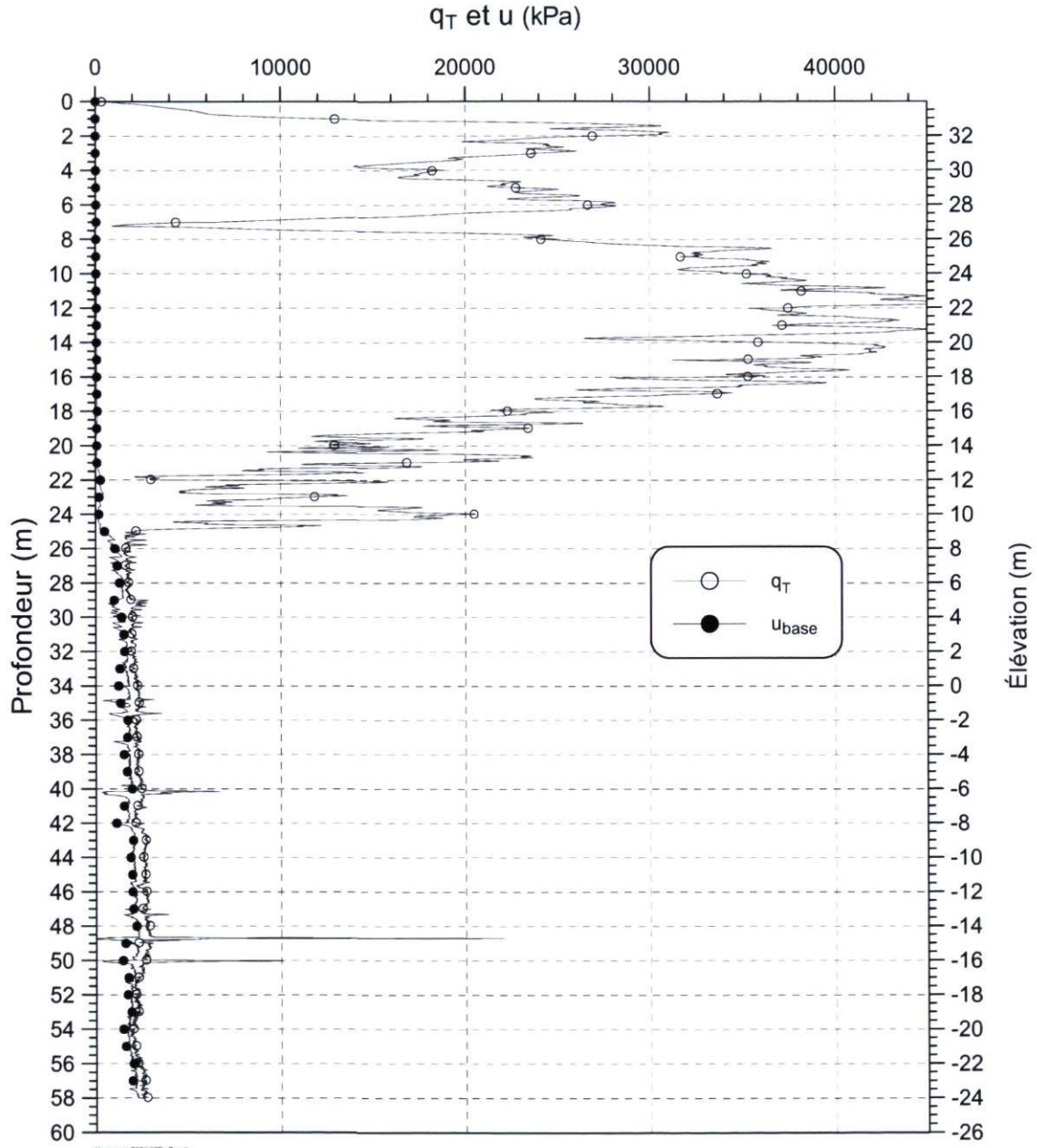
ESSAI: C46104-005-06

ÉLÉVATION T.N.: 33.970 m

AVANT-TROU: 0 m

PROF. ATTEINTE: 57.996 m [V]

DATE: 2006-09-08



SONDE: Hogentogler 5T (Techmat)

VITESSE: 60 cm/min

INCRÉMENT: 1.0 cm

MINISTÈRE DES TRANSPORTS - ESSAI AU PIÉZOCÔNE

SITE: Betsiamites

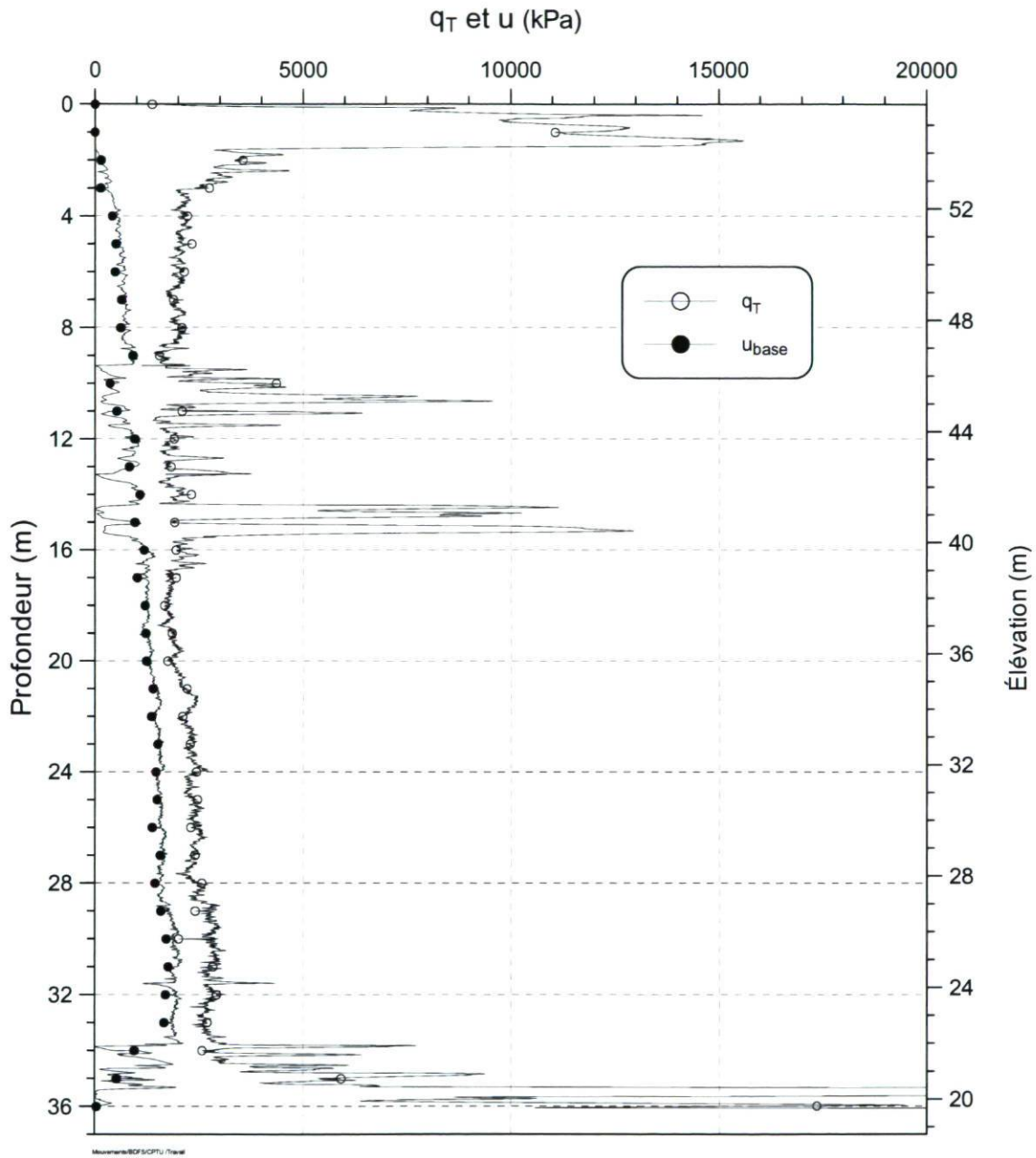
ESSAI: C46105-005-06

ÉLÉVATION T.N.: 55.740 m

AVANT-TROU: 0 m

PROF. ATTEINTE: 36.070 m [R]

DATE: 2006-09-14



SONDE: Hogentogler 5T (Techmat)

VITESSE: 60 cm/min

INCRÉMENT: 1,0 cm

MINISTÈRE DES TRANSPORTS - ESSAI AU PIÉZOCÔNE

SITE: Betsiamites

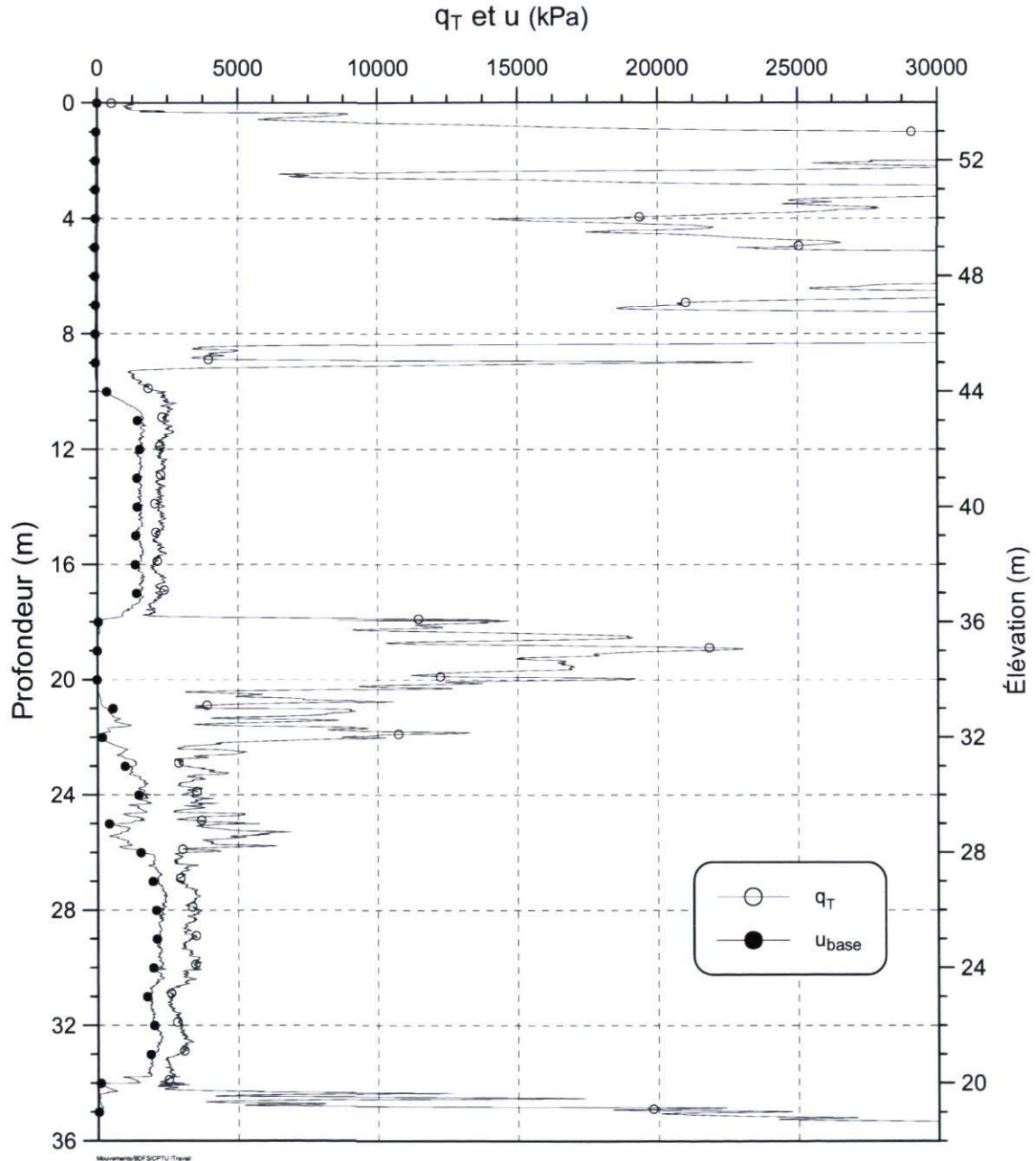
ESSAI: C46106B-005-06

ÉLÉVATION T.N.: 53.990 m

AVANT-TROU: 0 m

PROF. ATTEINTE: 35.470 m [V]

DATE: 2006-09-19



SONDE: Hogentogler 5T (Techmat)

VITESSE: 60 cm/min

INCRÉMENT: 1,0 cm

MINISTÈRE DES TRANSPORTS - ESSAI AU PIÉZOCÔNE

SITE: Betsiamites

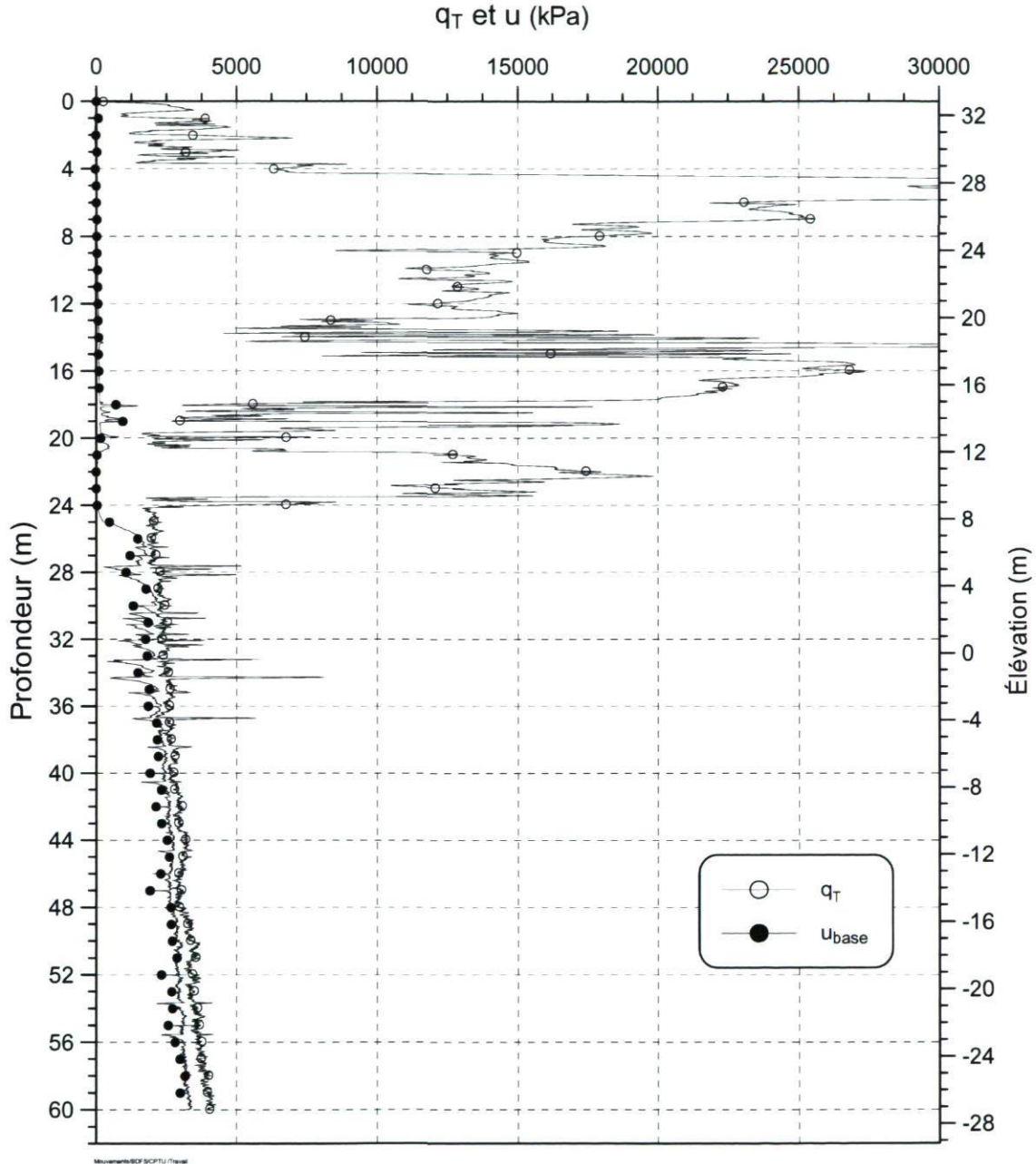
ESSAI: C46107-005-06

ÉLÉVATION T.N.: 32.830 m

AVANT-TROU: 0 m

PROF. ATTEINTE: 59.996 m [V]

DATE: 2006-09-11



SONDE: Hogentogler 5T (Techmat)

VITESSE: 60 cm/min

INCRÉMENT: 1,0 cm

MINISTÈRE DES TRANSPORTS - ESSAI AU PIÉZOCÔNE

SITE: Betsiamites

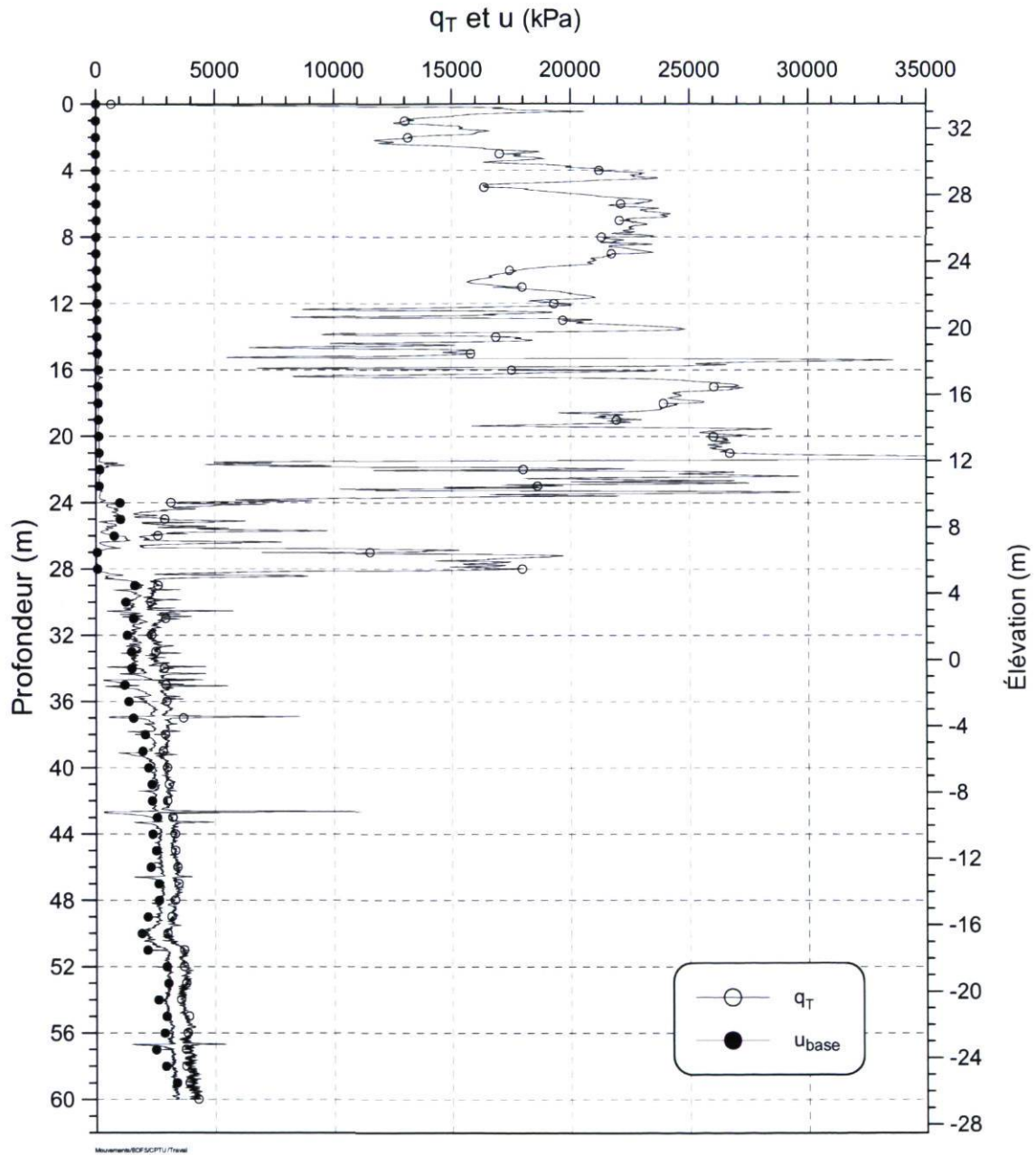
ESSAI: C46108-005-06

ÉLÉVATION T.N.: 33.470 m

AVANT-TROU: 0 m

PROF. ATTEINTE: 59.996 m [V]

DATE: 2006-09-12



SONDE: Hogentogler 5T (Techmat)

VITESSE: 60 cm/min

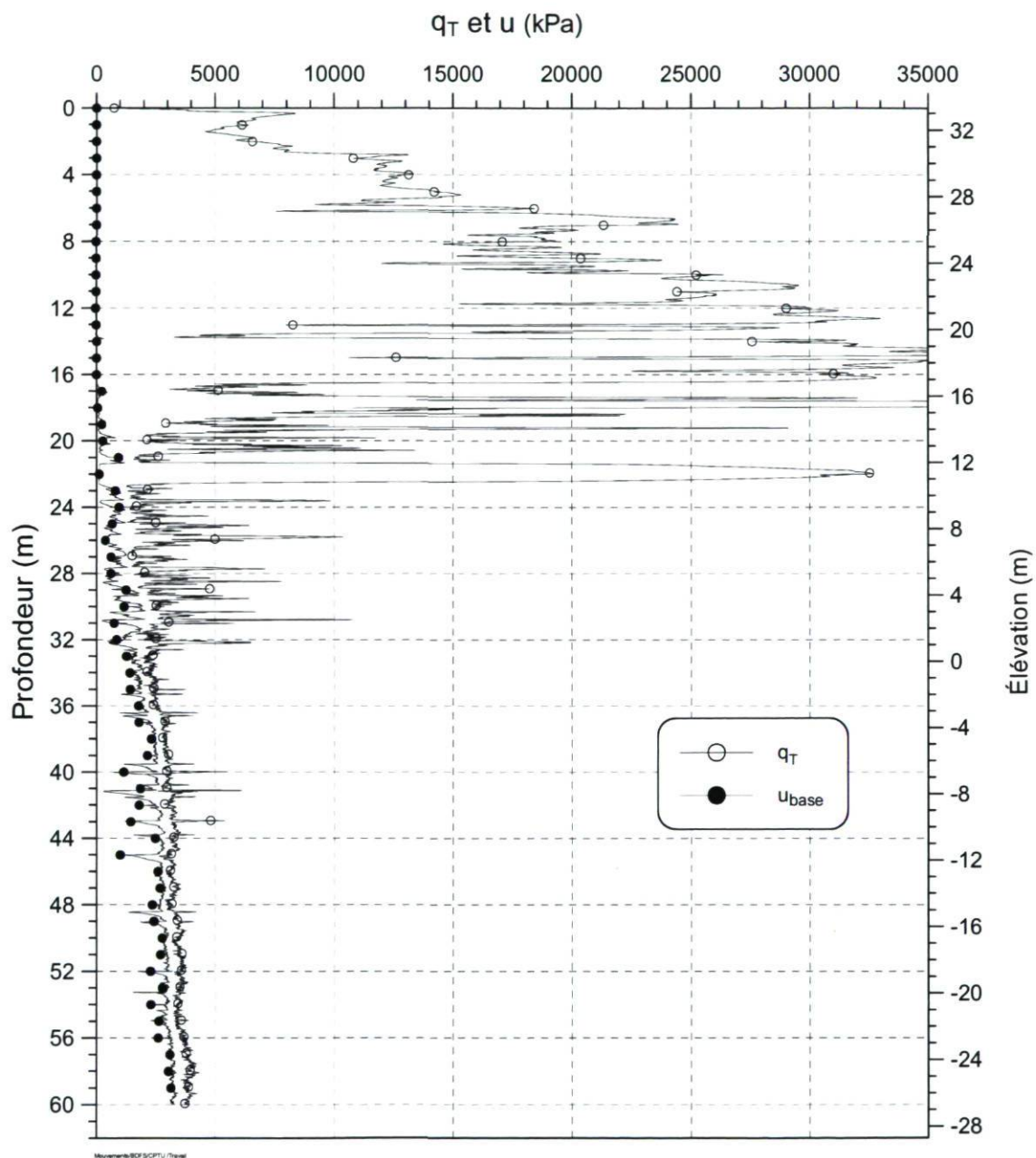
INCRÉMENT: 1,0 cm

MINISTÈRE DES TRANSPORTS - ESSAI AU PIÉZOCÔNE

SITE: Betsiamites

ESSAI: C46109-005-06

ÉLÉVATION T.N.: 33.300 m AVANT-TROU: 0 m PROF. ATTEINTE: 59.996 m [V] DATE: 2006-09-12



SONDE: Hogentogler 5T (Techmat)

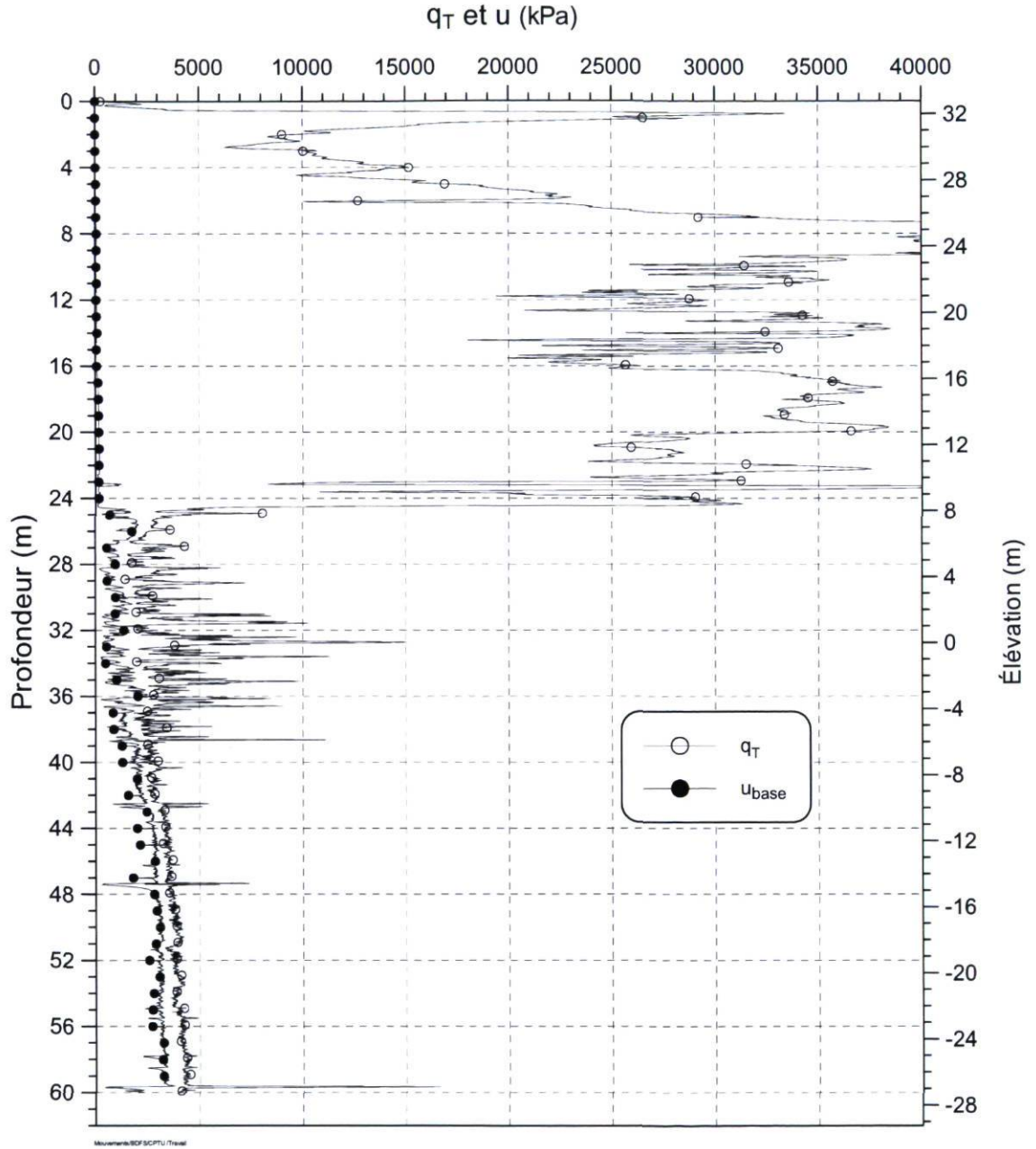
VITESSE: 60 cm/min

INCRÉMENT: 1,0 cm

MINISTÈRE DES TRANSPORTS - ESSAI AU PIÉZOCÔNE

SITE: Betsiamites ESSAI: C46110-005-06

ÉLÉVATION T.N.: 32.760 m AVANT-TROU: 0 m PROF. ATTEINTE: 59.996 m [V] DATE: 2006-09-13



SONDE: Hogentogler 5T (Techmat) VITESSE: 60 cm/min INCRÉMENT: 1.0 cm

MINISTÈRE DES TRANSPORTS - ESSAI AU PIÉZOCÔNE

SITE: Colombier

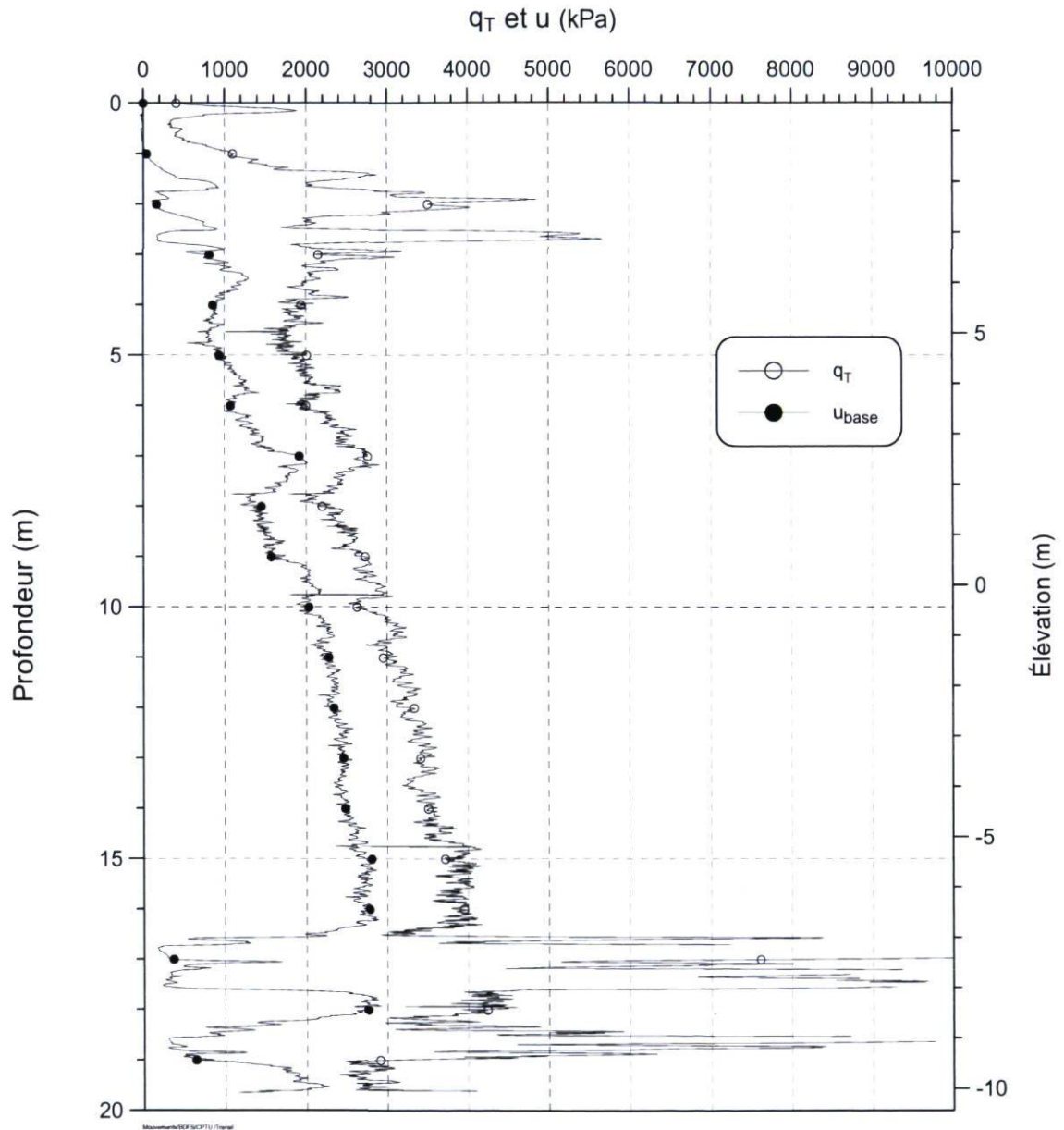
ESSAI: C46113-005-08

ÉLÉVATION T.N.: 9.564 m

AVANT-TROU: 0 m

PROF. ATTEINTE: 19,65 m [R]

DATE: 2008-08-19



SONDE: Hogentogler 15T (Techmat)

VITESSE: 60 cm/min

INCRÉMENT: 1,0 cm

MINISTÈRE DES TRANSPORTS - ESSAI AU PIÉZOCÔNE

SITE: Colombier

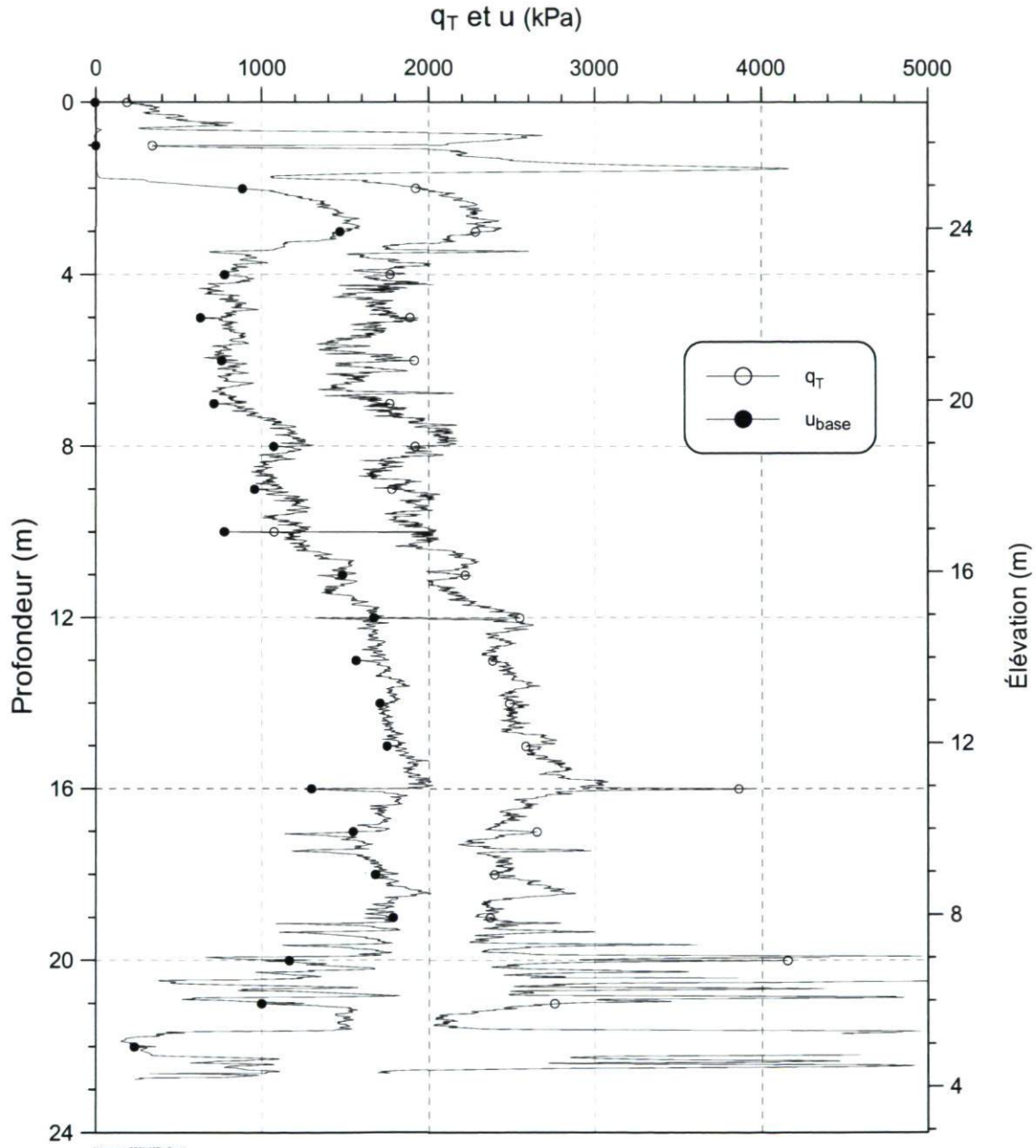
ESSAI: C46114-005-08

ÉLÉVATION T.N.: 26.927 m

AVANT-TROU: 0 m

PROF. ATTEINTE: 22,76 m [R]

DATE: 2008-08-19



SONDE: Hogentogler 15T (Techmat)

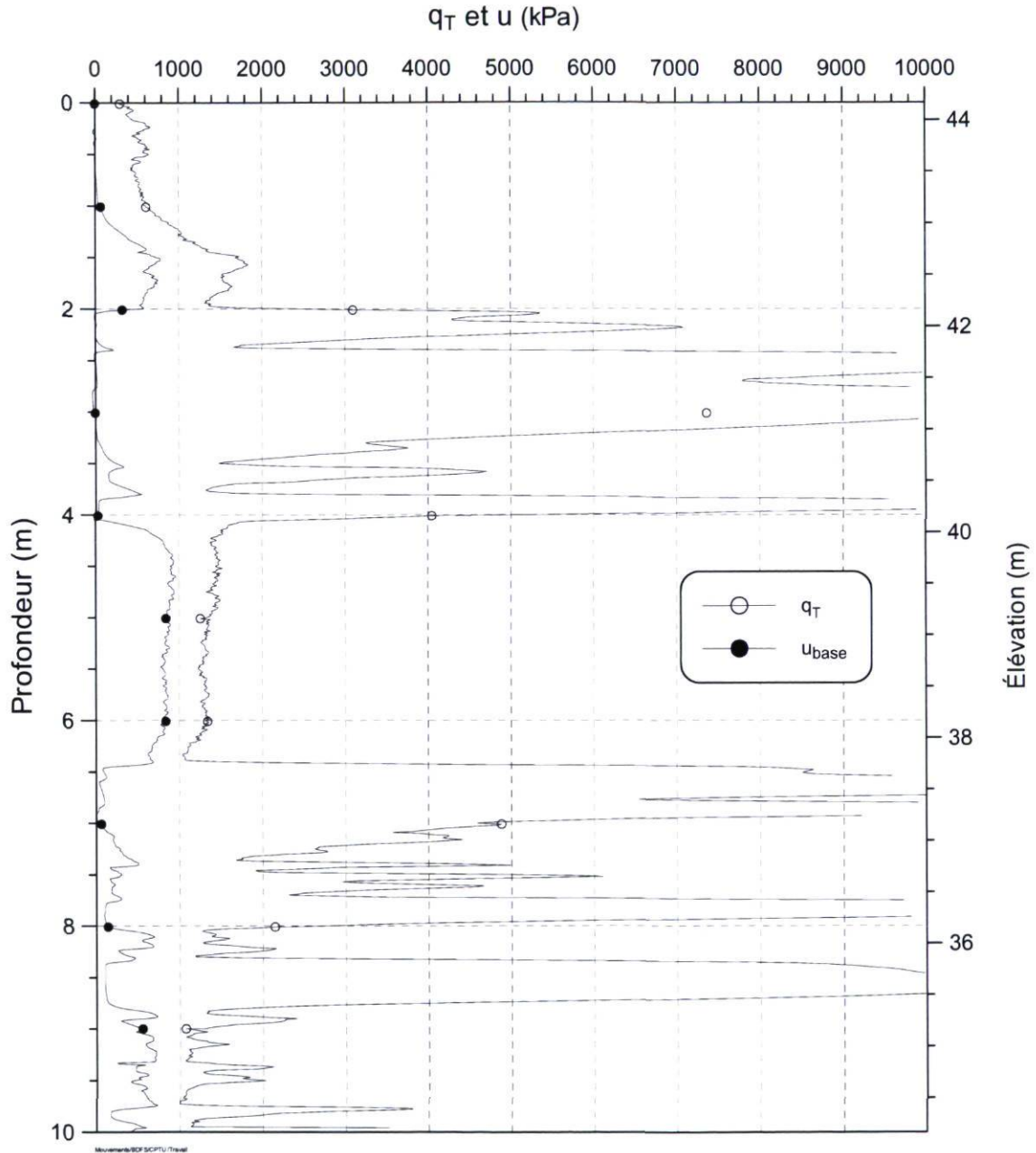
VITESSE: 60 cm/min

INCRÉMENT: 1,0 cm

MINISTERE DES TRANSPORTS - ESSAI AU PIÉZOCÔNE

SITE: Colombier ESSAI: C46115b-005-08

ÉLÉVATION T.N.: 44.17 m AVANT-TROU: 0 m PROF. ATTEINTE: 10,00 m [R] DATE: 2008-08-20



SONDE: Hogentogler 15T (Techmat) VITESSE: 60 cm/min INCRÉMENT: 1.0 cm

MINISTÈRE DES TRANSPORTS - ESSAI AU PIÉZOCÔNE

SITE: Colombier

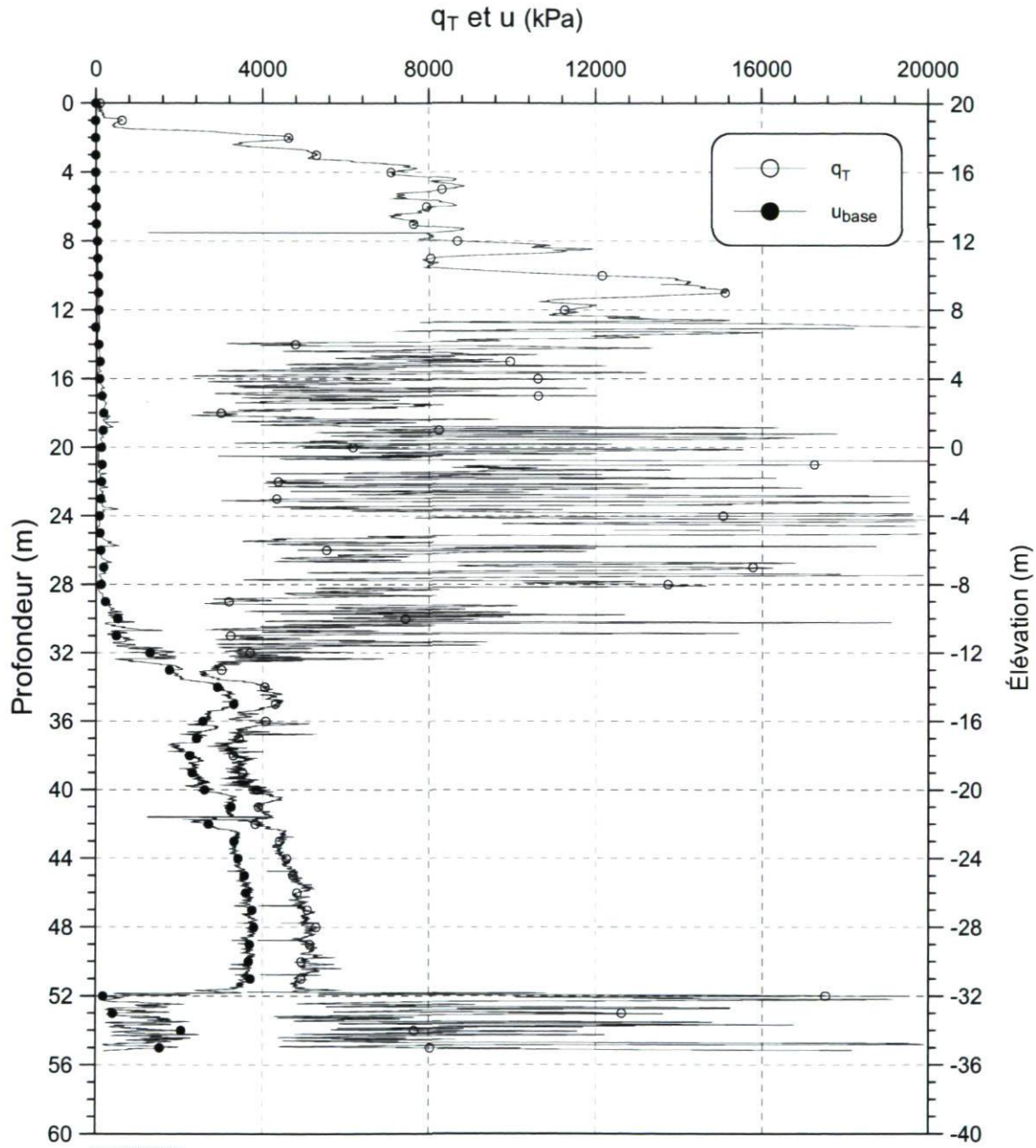
ESSAI: C46118-005-08

ÉLÉVATION T.N.: 20.435 m

AVANT-TROU: 0 m

PROF. ATTEINTE: 55,19 m [V]

DATE: 2008-08-22



SONDE: Hogentogler 15T (Techmat)

VITESSE: 60 cm/min

INCÉMENT: 1,0 cm

D.4 Tableau des essais de dissipation

Fichier	Sondage	Élévation (m)	Profondeur (m)	Pression finale (kPa)	État
460CP01.293	C46001	28.55	29.31	0	complet
460CP02.173	C46002	1.47	17.37	320	arrêt
460CP02.234	C46002	-4.62	23.46	340	moyen
460CP02.397	C46002	-20.89	39.73	1400	complet
460CP02.505	C46002	-31.68	50.52	345	complet
460CP03.50	C46003	15.50	5.06	40	complet
460CP03.117	C46003	8.82	11.74	108	complet
460CP03.206	C46003	-0.12	20.68	260	incomplet
460CP03.383	C46003	-17.80	38.36	260	incomplet
460CP03.423	C46003	-21.78	42.34	235	complet
460CP03.441	C46003	-23.56	44.12	253	complet
460CP04.80	C46004	2.84	8.00	67	complet
460CP04.220	C46004	-11.16	22.00	770	arrêt
460CP04.271	C46004	-16.34	27.18	1300	arrêt
460CP04.319	C46004	-21.15	31.99	1500	incomplet
460CP04.495	C46004	-38.67	49.51	415	complet
460CP05.231	C46005	-13.81	23.14	230	complet
460CP05.391	C46005	-29.80	39.13	1765	arrêt
460CP05.475	C46005	-38.25	47.58	445	complet
460CP05.565	C46005	-47.21	56.54	505	complet
460CP06.96	C46006	37.96	9.66	70	complet
460CP06.153	C46006	32.29	15.33	120	complet
460CP06.298	C46006	17.72	29.90	385	incomplet
460CP06.442	C46006	3.40	44.22	1280	arrêt
460CP06.600	C46006	-12.38	60.00	450	complet
460CP07.309	C46007	18.88	30.94	2	complet
460CP08A.96	C46008A	1.44	9.65	1090	arrêt
460CP08A.117	C46008A	-0.63	11.72	135	incomplet
460CP08A.146	C46008A	-3.51	14.60	185	complet
460CP09.63	C46009	3.74	6.32	52	complet
460CP09.127	C46009	-2.67	12.73	115	complet
460CP09.194	C46009	-9.43	19.49	178	complet
460CP09.241	C46009	-14.06	24.12	230	complet
460CP09.551	C46009	-45.11	55.17	503	complet
460CP10.138	C46010	-4.92	13.87	345	arrêt
460CP10.210	C46010	-12.05	21.00	170	complet
460CP10.372	C46010	-28.25	37.20	1180	arrêt
460CP10.423	C46010	-33.43	42.38	1450	arrêt
460CP10.562	C46010	-47.30	56.25	520	complet
460CP10.599	C46010	-50.97	59.92	575	complet
460CP11.90	C46011	37.99	9.01	43	complet

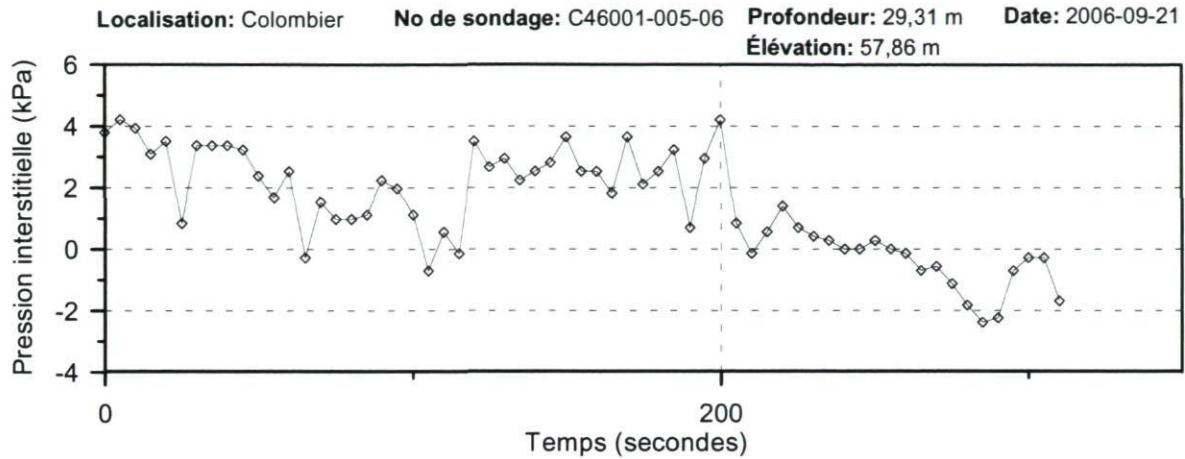
Fichier	Sondage	Élévation (m)	Profondeur (m)	Pression finale (kPa)	État
460CP11.233	C46011	23.65	23.35	170	complet
460CP11.320	C46011	14.93	32.07	280	incomplet
460CP11.359	C46011	11.02	35.98	230	complet
460CP30.90	C46030	41.51	9.00	115	incomplet
460CP30.133	C46030	37.17	13.34	75	complet
460CP30.279	C46030	22.59	27.92	255	incomplet
460CP30.374	C46030	13.09	37.42	1200	arrêt
460CP30.505	C46030	-0.03	50.54	910	arrêt
460CP30.577	C46030	-7.13	57.64	435	complet
460CP31.195	C46031	41.68	19.48	3	complet
460CP32.143	C46032	25.48	14.37	0	complet
460CP33.240	C46033	7.67	23.95	4	complet
460CP34.208	C46034	3.48	20.81	1	complet
460CP36.87	C46036	-1.74	8.72	75	complet
460CP36.167	C46036	-9.75	16.73	150	complet
460CP36B.600	C46036	-53.02	60.00	1450	arrêt
460CP37B.233	C46037	-11.13	23.36	150	complet
460CP37B.298	C46037	-17.60	29.83	200	complet
460CP37B.352	C46037	-22.97	35.20	250	complet
460CP37B.600	C46037	-47.77	60.00	1650	arrêt
460CP38.485	C46038	-11.03	48.59	200	complet
460CP39.320	C46039	5.72	32.00	120	incomplet
460CP39.384	C46039	-0.77	38.49	160	complet
460CP39.442	C46039	-6.49	44.21	200	complet
460CP39.520	C46039	-14.28	52.00	270	complet
460CP39.581	C46039	-20.32	58.04	315	arrêt
461CP00B.112	C46100B	16.59	11.21	50	incomplet
461CP00B.130	C46100B	14.80	13.00	0	complet
461CP00B.266	C46100B	1.17	26.63	0	arrêt
461CP02.59	C46102	57.24	5.94	85	incomplet
461CP02.104	C46102	52.72	10.46	110	incomplet
461CP02.170	C46102	46.18	17.00	360	incomplet
461CP02.212	C46102	41.94	21.24	155	complet
461CP03.113	C46103	40.79	11.39	58	complet
461CP03.156	C46103	36.55	15.63	100	complet
461CP03.223	C46103	29.87	22.31	190	complet
461CP03.305	C46103	21.68	30.50	290	complet
461CP03.419	C46103	10.24	41.94	415	complet
461CP04.348	C46104	-0.87	34.84	505	arrêt
461CP04.402	C46104	-6.23	40.20	360	complet
461CP04.487	C46104	-14.82	48.79	950	arrêt
461CP05.93	C46105	46.38	9.36	35	complet
461CP05.132	C46105	42.47	13.27	60	complet
461CP05.338	C46105	21.90	33.84	125	incomplet

Fichier	Sondage	Élévation (m)	Profondeur (m)	Pression finale (kPa)	État
461CP05.361	C46105	19.60	36.14	31	incomplet
461CP06B.179	C46106B	36.06	17.93	30	incomplet
461CP06B.340	C46106B	19.95	34.04	140	incomplet
461CP06B.355	C46106B	18.48	35.51	0	complet
461CP07.192	C46107	13.56	19.20	150	incomplet
461CP07.214	C46107	11.35	21.41	225	complet
461CP07.276	C46107	5.08	27.68	275	incomplet
461CP07.333	C46107	-0.56	33.32	400	incomplet
461CP08.220	C46108	11.47	22.00	160	complet
461CP08.251	C46108	8.29	25.18	480	arrêt
461CP08.346	C46108	-1.22	34.69	310	incomplet
461CP08.426	C46108	-9.22	42.69	350	complet
461CP09.193	C46109	13.96	19.34	85	complet
461CP09.236	C46109	9.63	23.67	155	complet
461CP09.308	C46109	2.49	30.81	240	complet
461CP09.411	C46109	-7.83	41.13	320	complet
461CP09.532	C46109	-19.97	53.27	1590	incomplet
461CP10.282	C46110	4.53	28.23	275	arrêt
461CP10.317	C46110	1.02	31.74	395	incomplet
461CP10.361	C46110	-3.42	36.18	265	complet
461CP10.473	C46110	-14.59	47.35	350	complet
46CP111.38	C46111	0.01	3.83	24	complet
46CP111.100	C46111	-6.16	10.00	130	complet
46CP111.207	C46111	-16.94	20.78	290	incomplet
46CP111.318	C46111	-27.93	31.77	405	complet
46CP111.382	C46111	-34.32	38.16	1530	arrêt
46CP113.167	C46113	-7.27	16.83	175	complet
46CP113.196	C46113	-10.11	19.67	235	incomplet
46CP114.218	C46114	5.08	21.85	165	complet
46CP114.227	C46114	4.30	22.63	250	incomplet
46CP115B.25	C46115B	41.64	2.53	12	complet
46CP115B.39	C46115B	40.21	3.96	28	complet
46CP115B.66	C46115B	37.51	6.66	93	complet
46CP115B.78	C46115B	36.29	7.88	100	complet
46CP115B.85	C46115B	35.60	8.57	101	complet
46CP115B.100	C46115B	34.13	10.04	155	incomplet
46CP118.60	C46118	14.435	6.00	6	complet
46CP118.82	C46118	12.155	8.28	27	complet
46CP118.130	C46118	7.365	13.07	70	incomplet
46CP118.210	C46118	-0.565	21.00	150	complet
46CP118.248	C46118	-4.385	24.82	185	complet
46CP118.415	C46118	-21.135	41.57	1240	incomplet
46CP118.551	C46118	-34.775	55.21	360	complet

D.4.1 Exemples d'essais de dissipation

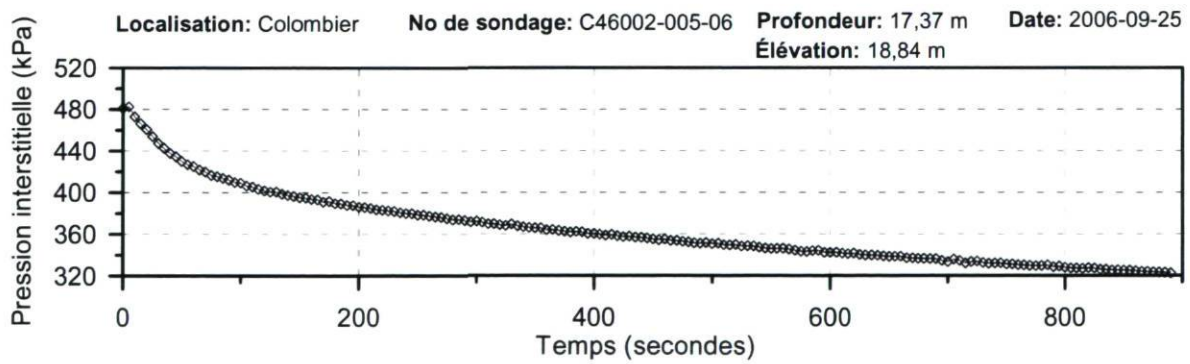
Exemple d'un essai de dissipation complétée (complet) :

SONDAGE AU PIÉZOCÔNE - ESSAI DE DISSIPATION



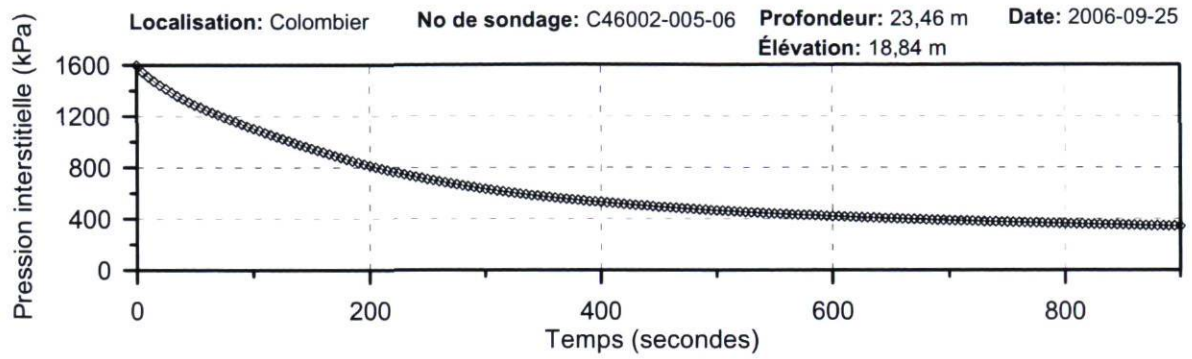
Exemple d'un essai de dissipation arrêté sans que la dissipation ne soit complétée (arrêt) :

SONDAGE AU PIÉZOCÔNE - ESSAI DE DISSIPATION



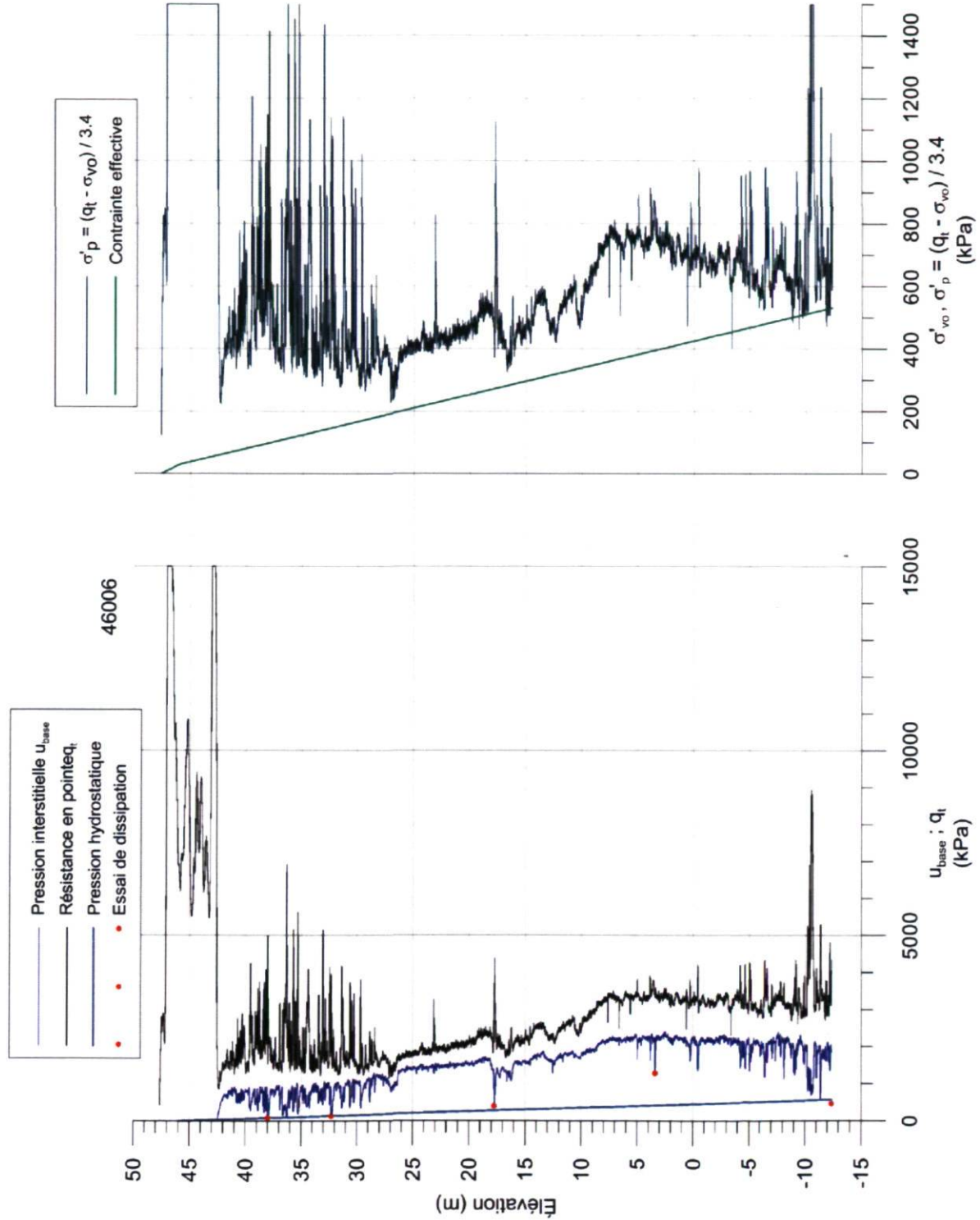
Exemple d'un essai de dissipation tendant pratiquement vers la stabilisation, mais arrêté avant la dissipation complète (incomplet).

SONDAGE AU PIÉZOCÔNE - ESSAI DE DISSIPATION

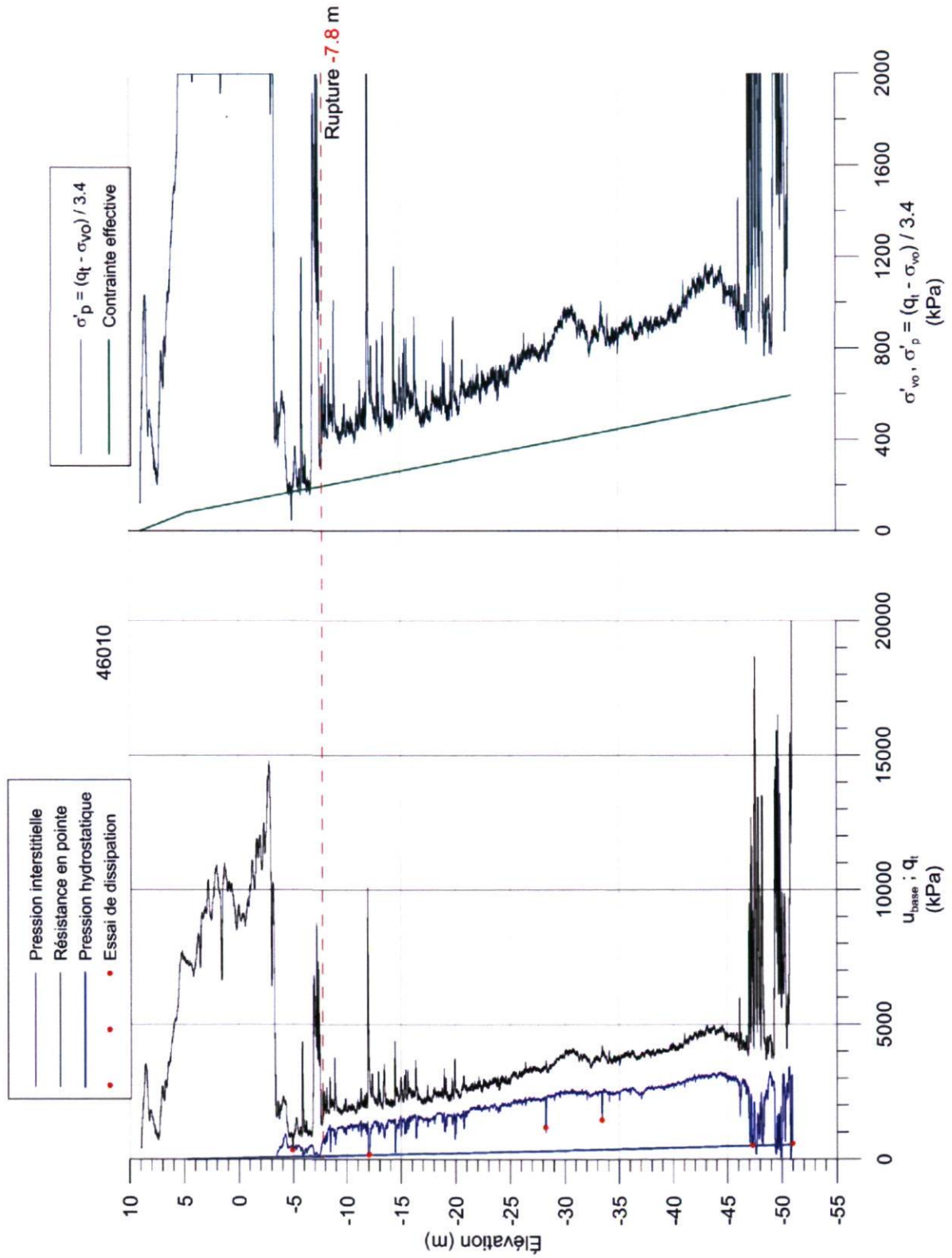


E Profils de pression de préconsolidation estimés à l'aide du piézocône

E.1 Site 46006



E.2 Site 46010



F Résultats de l'essai au scissomètre de chantier S46006**F.1 Tableau des résultats**

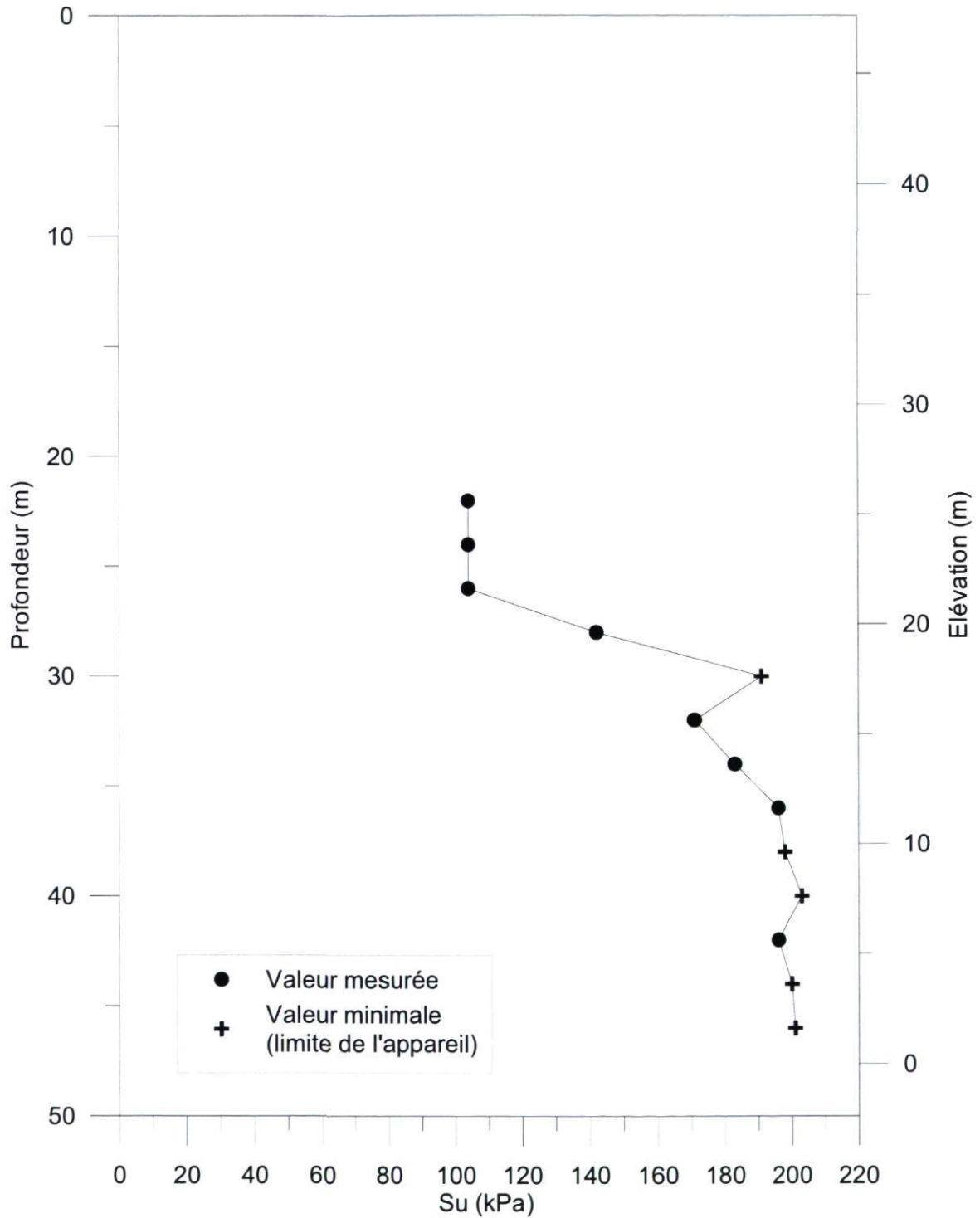
Essai	Prof (m)	Élévation (m)	Su (kPa)
M1	22	25.62	104
M2	24	23.62	104
M3	26	21.62	104
M4	28	19.62	142
M5	30	17.62	191
M6	32	15.62	171
M7	34	13.62	183
M8	36	11.62	196
M9	38	9.62	198
M10	40	7.62	203
M11	42	5.62	196
M12	44	3.62	200
M13	46	1.62	201

F.2 Profil de l'essai au scissomètre de chantier

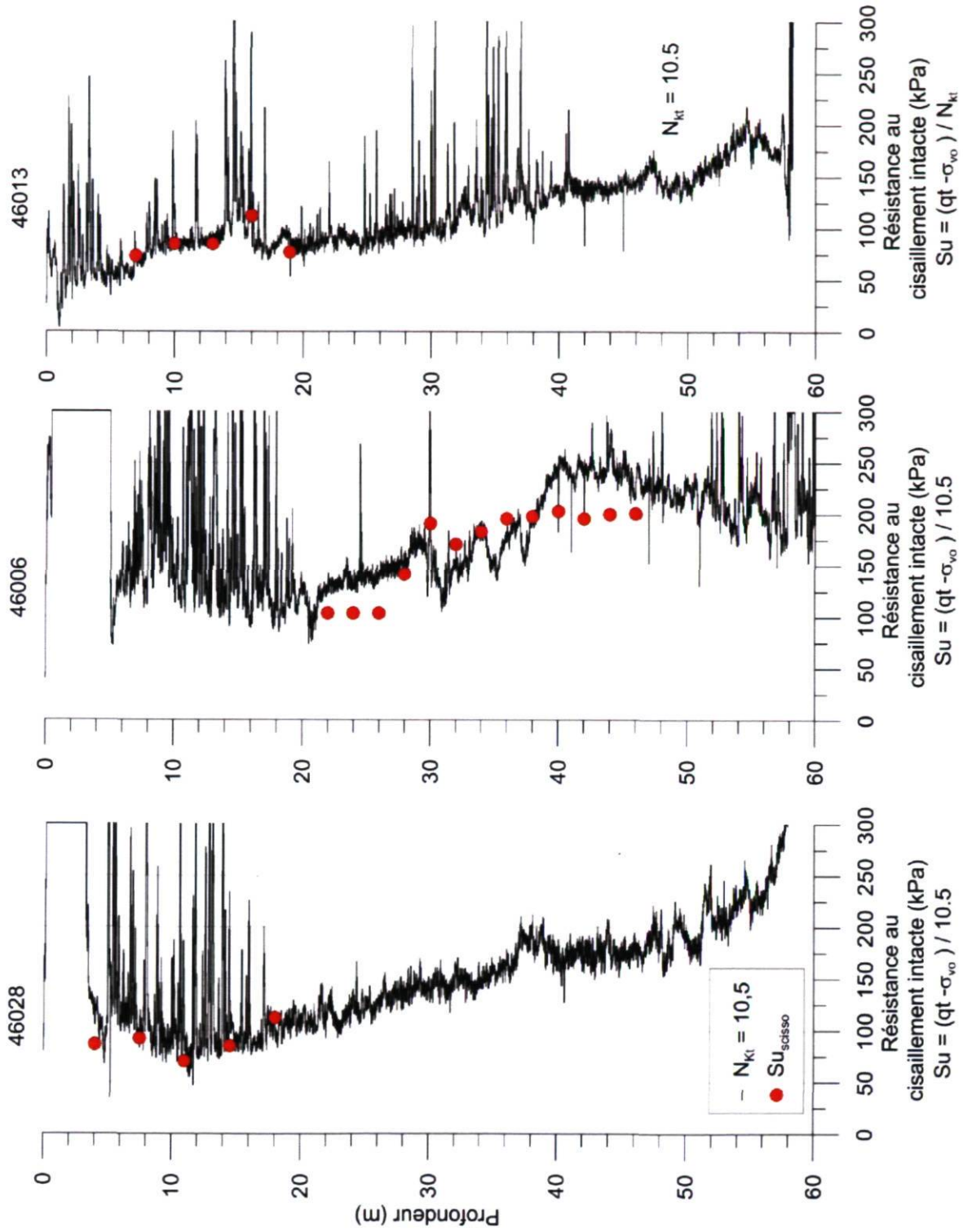
ESSAI AU SCISSOMÈTRE DE CHANTIER

Essai : S46006

Date: 2008-06-26

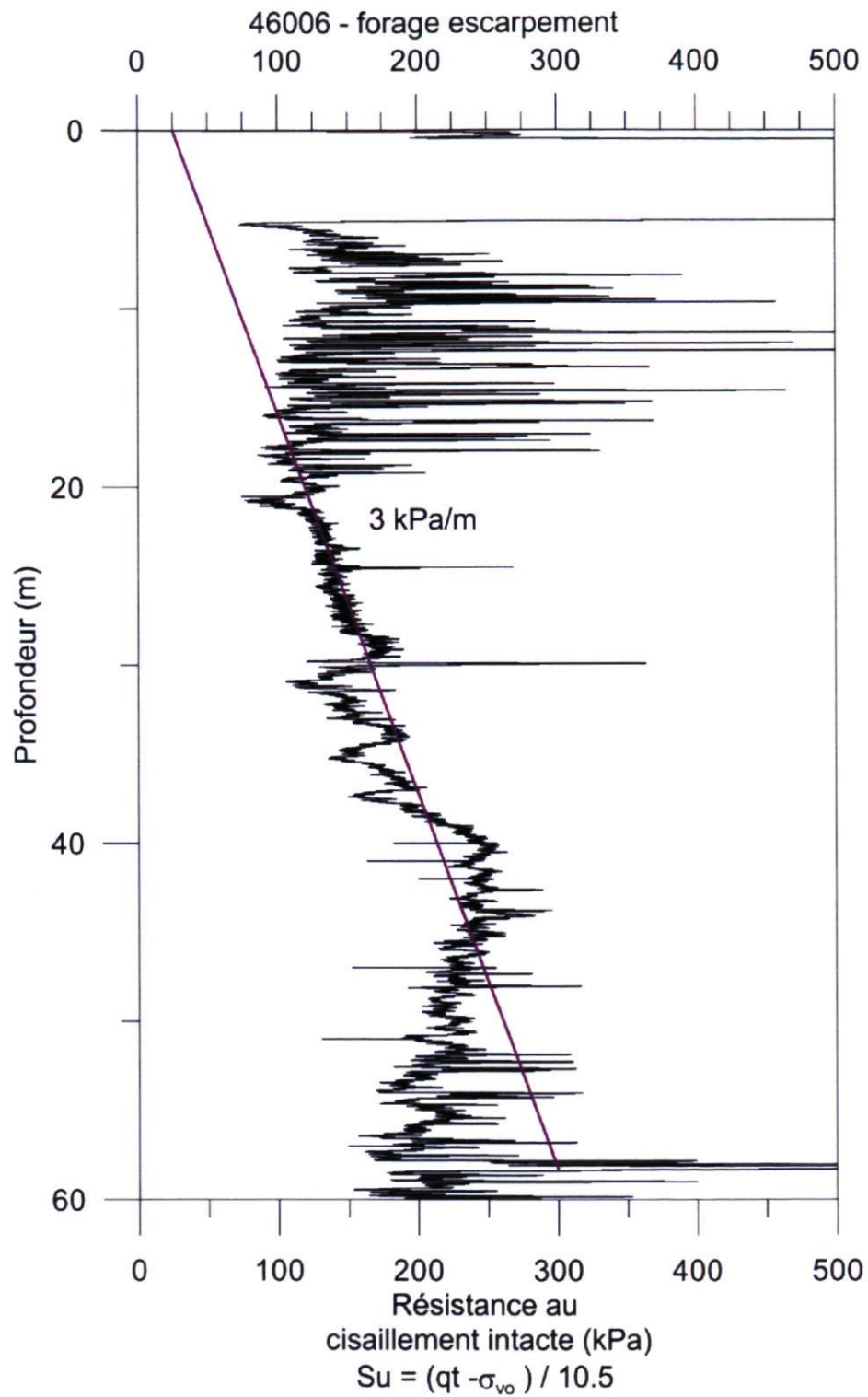


F.3 Détermination du facteur N_{kt}

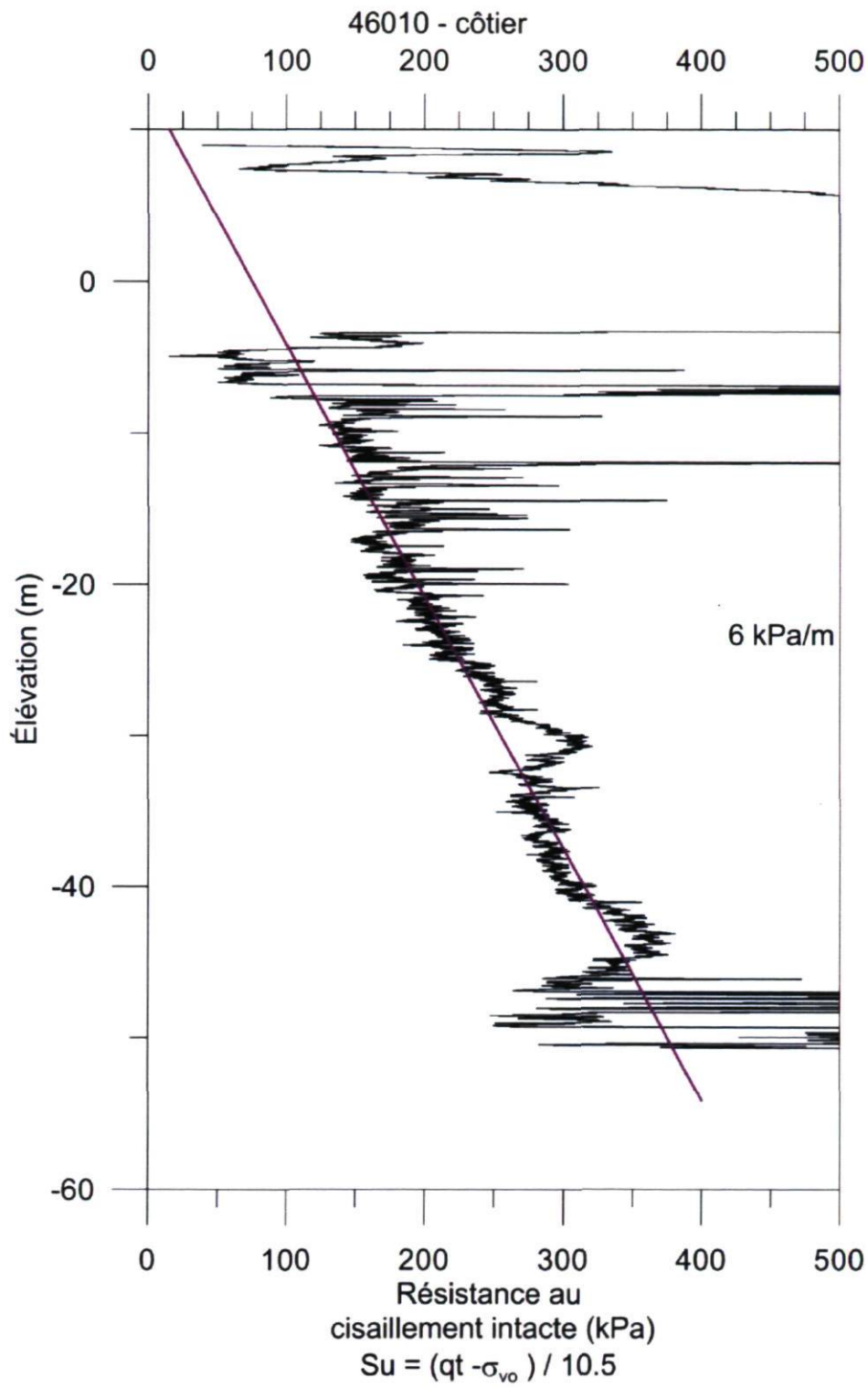


F.4 Estimation de la valeur de résistance au cisaillement à l'aide du piézocône

F.4.1 Site 46006



F.4.2 Site 46010



G Forages et échantillons prélevés

G.1 Localisation des forages

Forage	X (UTM 19)	Y (UTM 19)	Élévation du forage (m)	Profondeur atteinte (m)
F46006	516958	5416735	47.62	55.87
F46010	519128	5415969	7.84	58.92

G.2 Forage F46006

Échantillon	Récupération (cm)	Prof. du haut de l'échantillon (m)	Prof. du bas de l'échantillon (m)	Élévation du haut de l'échantillon (m)	Élévation du bas de l'échantillon (m)	Extraction
CF1	46	4.57	5.03	43.05	42.59	CF
CF2	52	9.14	9.66	38.48	37.96	CF
CF3	60	13.72	14.32	33.90	33.30	CF
CF4	55	20.40	20.95	27.22	26.67	CF
CF5	60	23.75	24.35	23.87	23.27	CF
TM6	70	27.43	28.13	20.19	19.49	V
TM7	61	32.00	32.61	15.62	15.01	V
TM8	69	37.65	38.34	9.97	9.28	V
CF9	60	41.15	41.75	6.47	5.87	CF
TM10	70	42.67	43.37	4.95	4.25	V
TM11	65	45.72	46.37	1.90	1.25	V
TM12	38	50.31	50.69	-2.67	-3.07	intact
CR13	152	54.35	55.87	-6.73	-8.25	roche

Extraction des échantillons

CF : Cuillère fendue, généralement sous-échantillonnée sur le terrain en intervalles de 5 cm;

V : Extraction verticale au laboratoire de géotechnique de l'Université Laval avec un vérin hydraulique;

H : Extraction horizontale avec un piston et transfert dans un tube de polycarbonate pour analyses sédimentologiques, manipulations faites au laboratoire de sédimentologie de l'ISMER à Rimouski.

G.3 Forage F46010

Échantillon	Récupération (cm)	Prof. du haut de l'échantillon (m)	Prof. du bas de l'échantillon (m)	Élévation du haut de l'échantillon (m)	Élévation du bas de l'échantillon (m)	Extraction
CFA	36	1.52	1.88	6.31	5.95	CF
CFB	13	3.05	3.18	4.79	4.66	CF
CF1	36	4.57	4.93	3.26	2.90	CF
CF2	50	7.62	8.12	0.22	-0.29	CF
CF3	47	10.67	11.14	-2.83	-3.30	CF
CF4	60	12.19	12.79	-4.36	-4.96	CF
TM5	69	13.72	14.41	-5.88	-6.57	H
TM6	58	15.24	15.82	-7.41	-7.99	H
TM7	70	16.76	17.46	-8.93	-9.63	H
TM8	68	18.29	18.97	-10.45	-11.13	V
TM9	68	19.81	20.49	-11.98	-12.66	H
TM10	50	21.34	21.84	-13.50	-14.00	H
TM11	63	22.86	23.49	-15.03	-15.66	V
TM12	64	24.38	25.02	-16.55	-17.19	H
TM13	57	25.91	26.48	-18.07	-18.64	H
TM14	64	27.43	28.07	-19.60	-20.24	H
TM15	59	28.96	29.55	-21.12	-21.71	H
TM16	61	30.48	31.09	-22.65	-23.26	V
TM17	68	32.00	32.68	-24.17	-24.85	H
TM18	60	33.53	34.13	-25.69	-26.29	H
TM19	66	36.58	37.24	-28.74	-29.40	H
TM20	35	39.62	39.97	-31.79	-32.14	V
TM21	30	42.67	42.97	-34.84	-35.14	H
CF22	60	45.72	46.32	-37.89	-38.49	CF
CF23	60	48.77	49.37	-40.93	-41.53	CF
CF24	60	51.82	52.42	-43.98	-44.58	CF
CF25	60	54.86	55.46	-47.03	-47.63	CF
CR26	40	58.52	58.92	-50.69	-51.09	roche

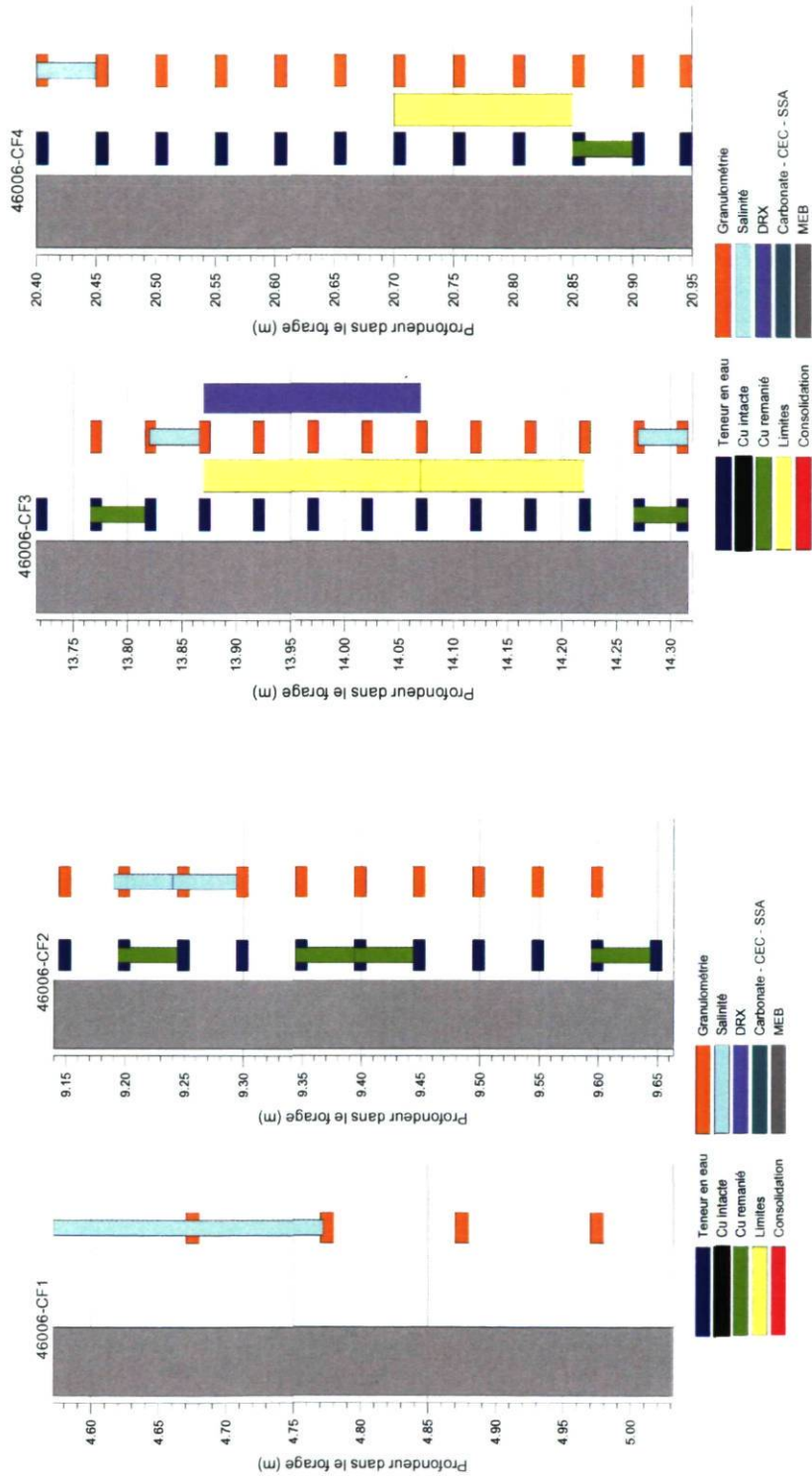
H Résultats d'essais de laboratoire

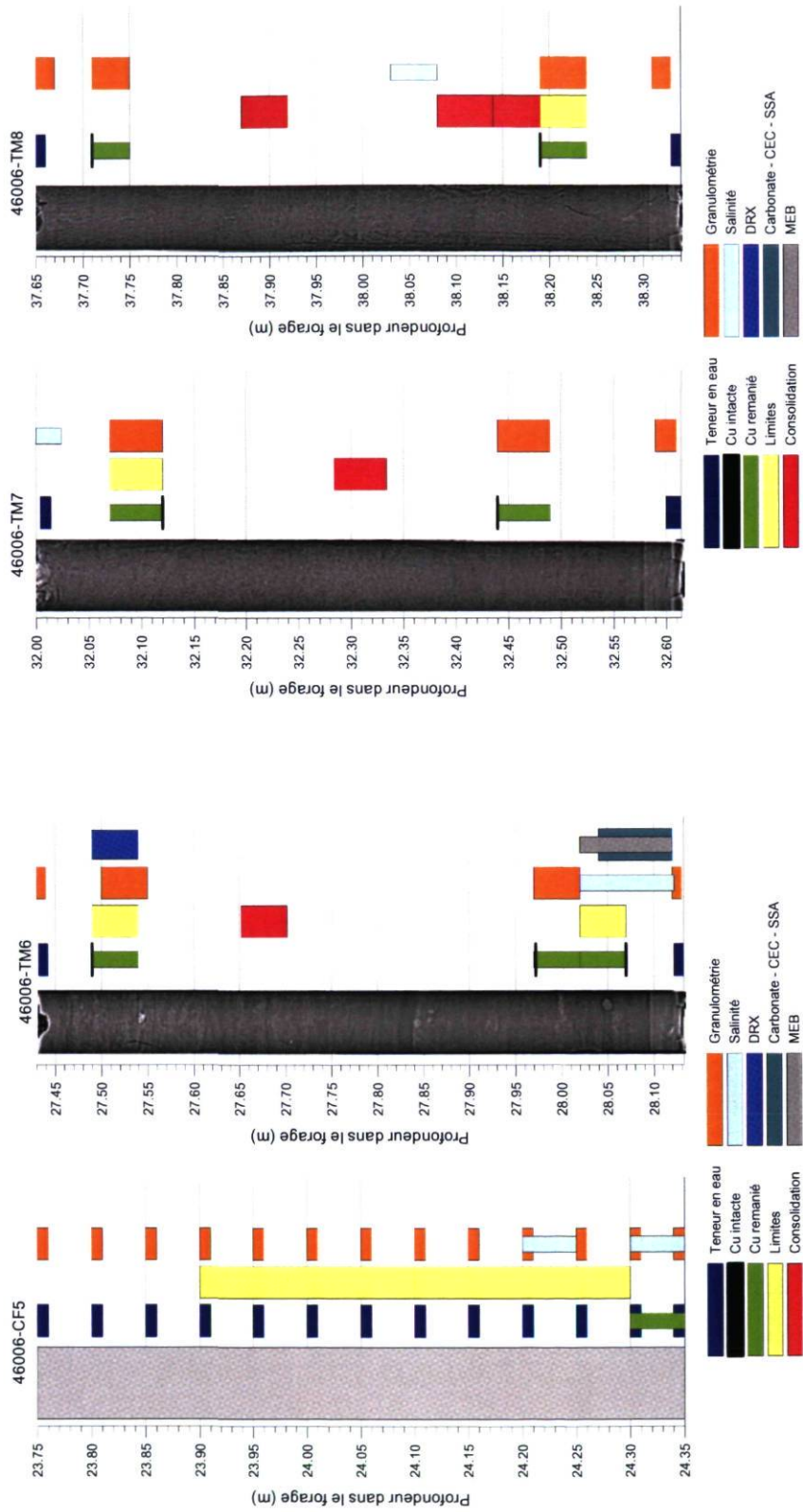
H.1 Compilation des données géotechniques obtenues lors de l'extraction des carottes.

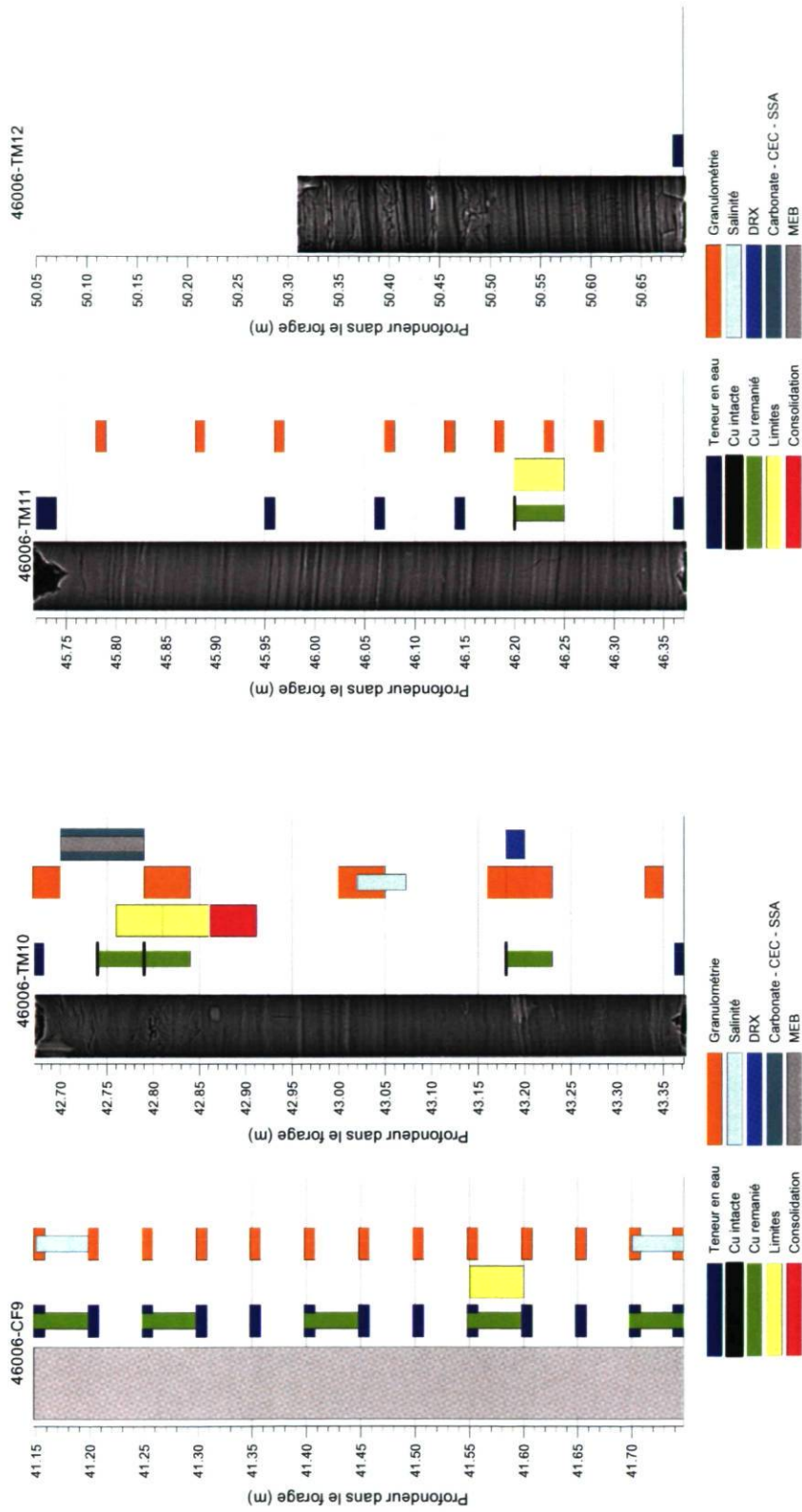
H.1.1 Tableau descriptif des analyses et essais géotechniques effectués

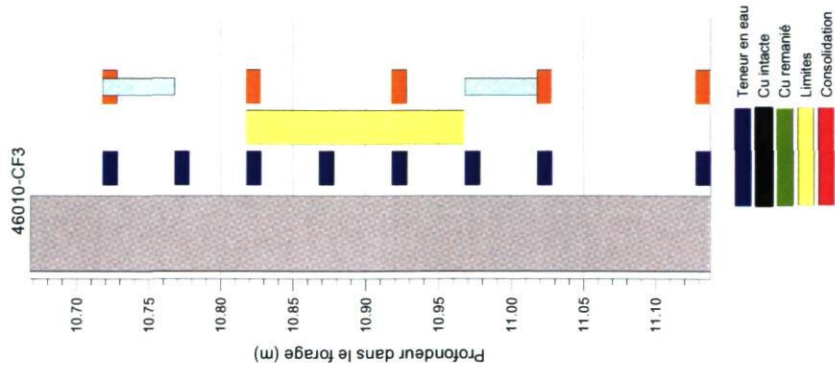
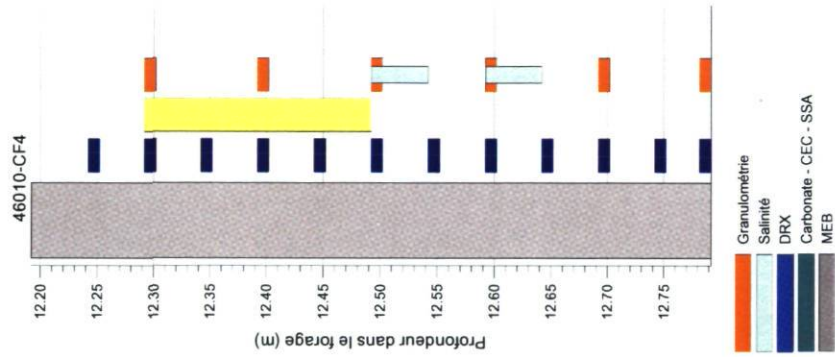
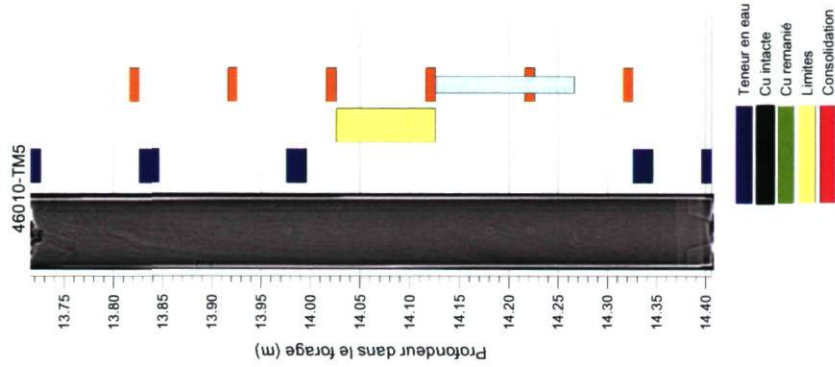
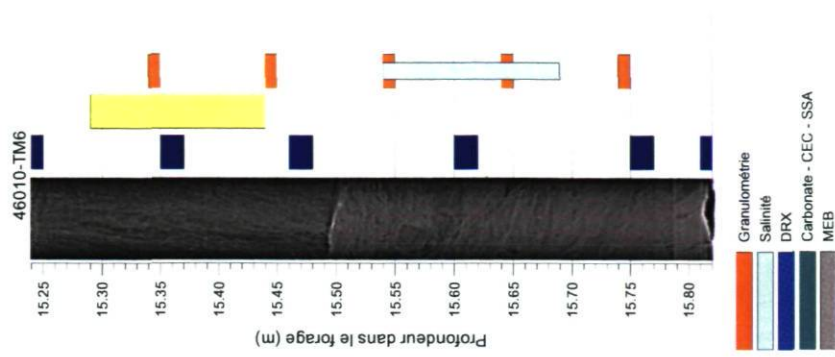
Résultats	Descriptions
Teneur en eau	Mesure de teneur en eau sur le terrain ou mesure additionnelle au laboratoire, supplémentaire aux mesures associées au Cu/Cur ou aux limites de consistance
Cu intact	Mesure de résistance au cisaillement non drainée intacte, au cône suédois
Cu remanié	Mesure de résistance au cisaillement non drainée remaniée, au cône suédois
Limites	Évaluation des limites de liquidité et de plasticité
Consolidation	Essais de consolidation oedométrique à chargement par paliers de 24 heures
Granulométrie	Mesure de la distribution granulométrique des particules par diffraction au laser. Analyses effectuées à l'ISMER.
Salinité	Chromatographie ionique de l'eau interstitielle pour la mesure du Cl ⁻ , F ⁻ , Br ⁻ et de SO ₄ ²⁻
DRX	Analyses minéralogiques par diffraction des rayons X (DRX)
Carbonate	Dosage de la calcite et de la dolomite, à l'aide de l'appareil Chittick (e.g., Dreimanis 1962).
CEC	Capacité d'échange cationique (e.g., Chapman 1965)
SSA	Surface spécifique au bleu de méthylène (e.g., Santamarina et al. 2002)
MEB	Analyse microstructurale à l'aide du microscope électronique à balayage

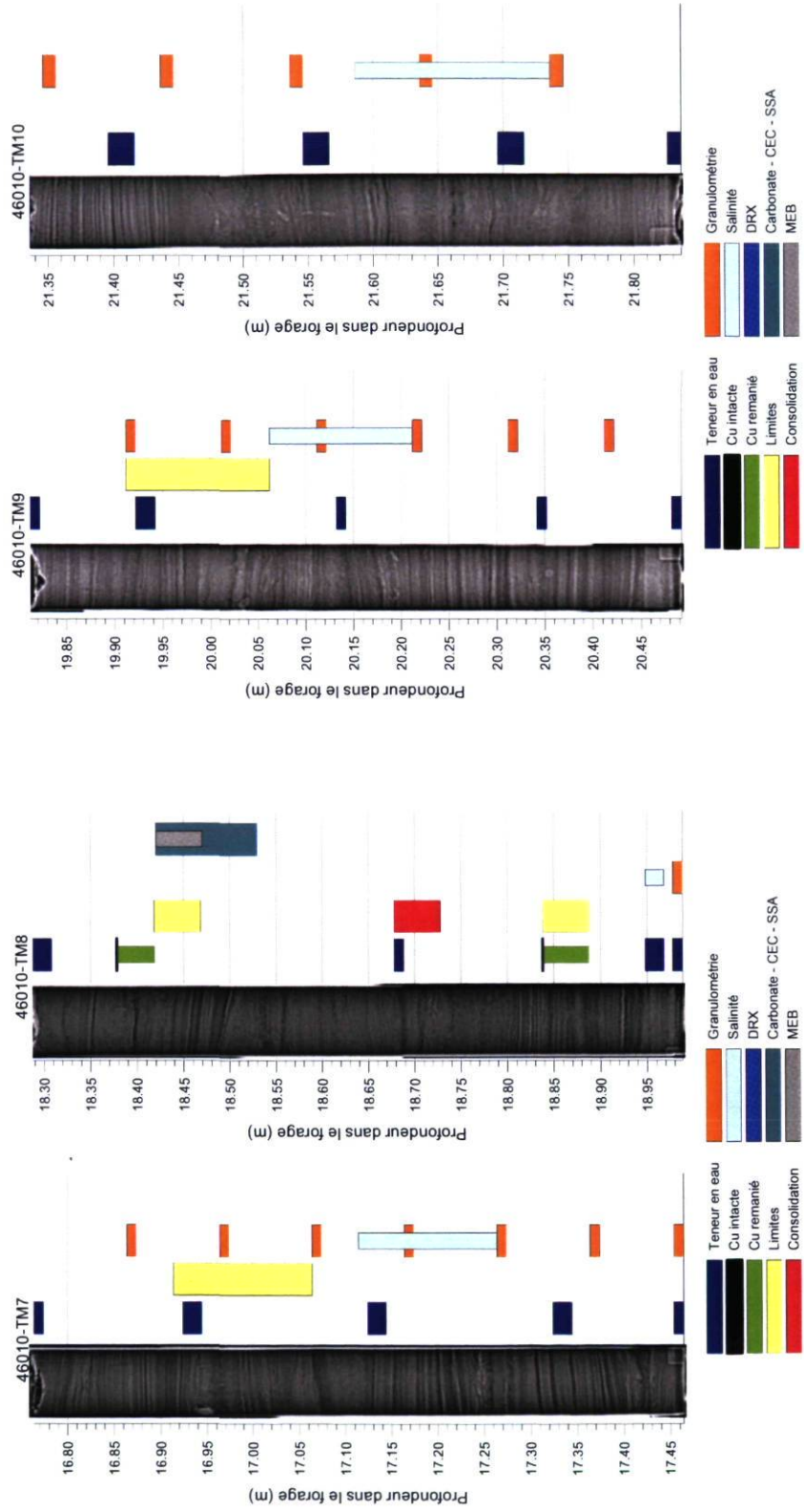
H.1.2 Compilation des essais géotechniques effectués – F46006

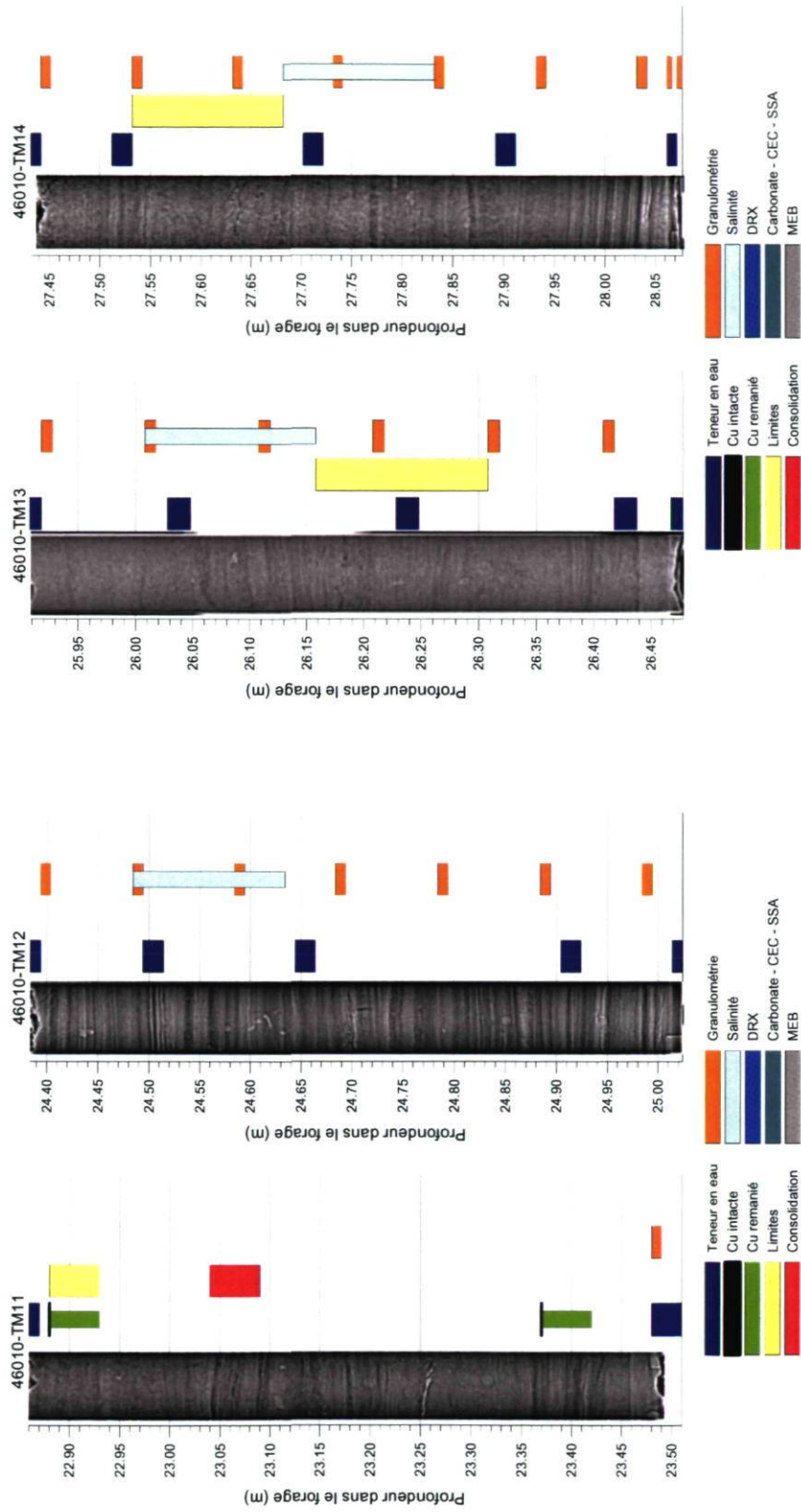


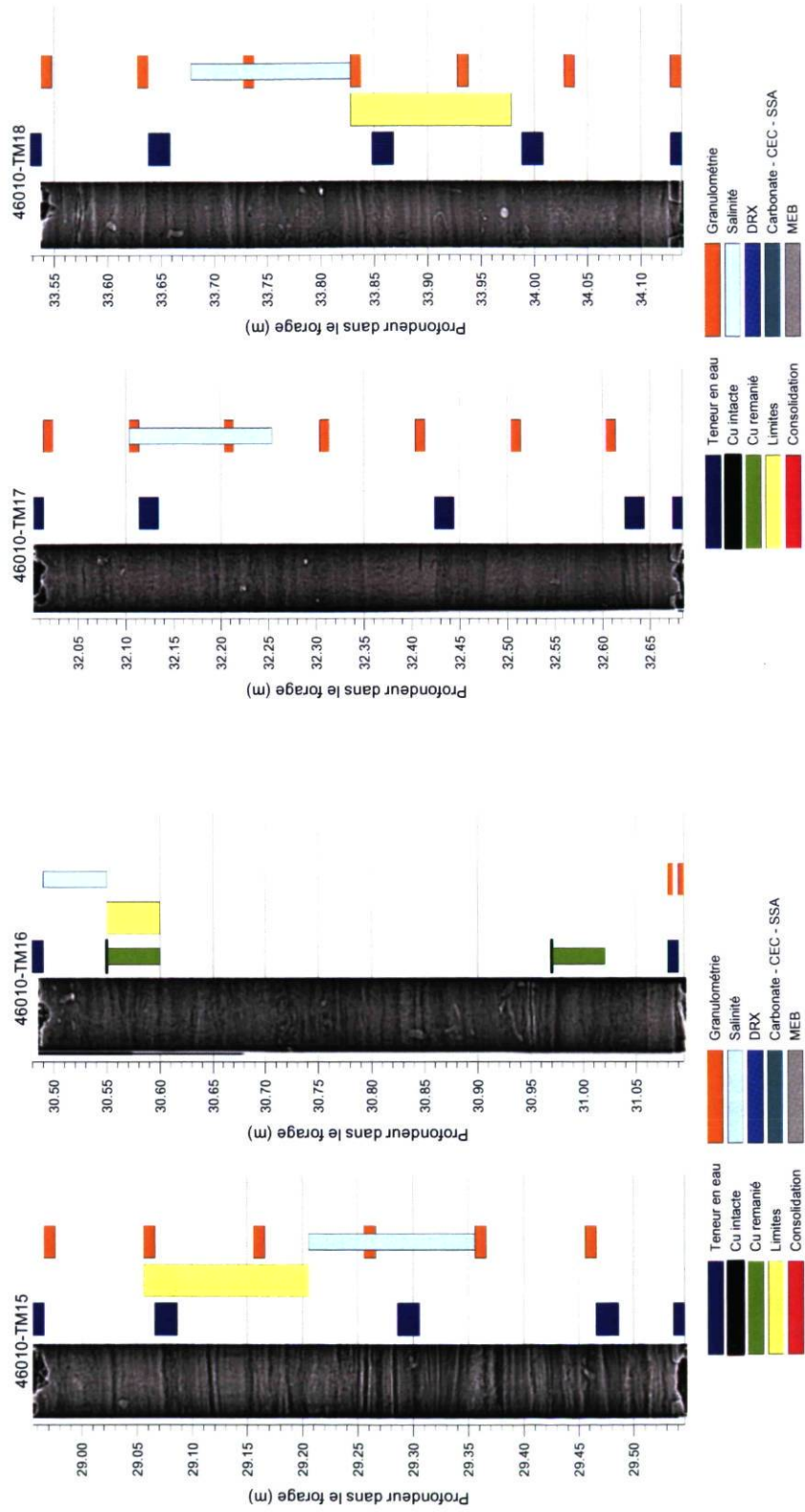


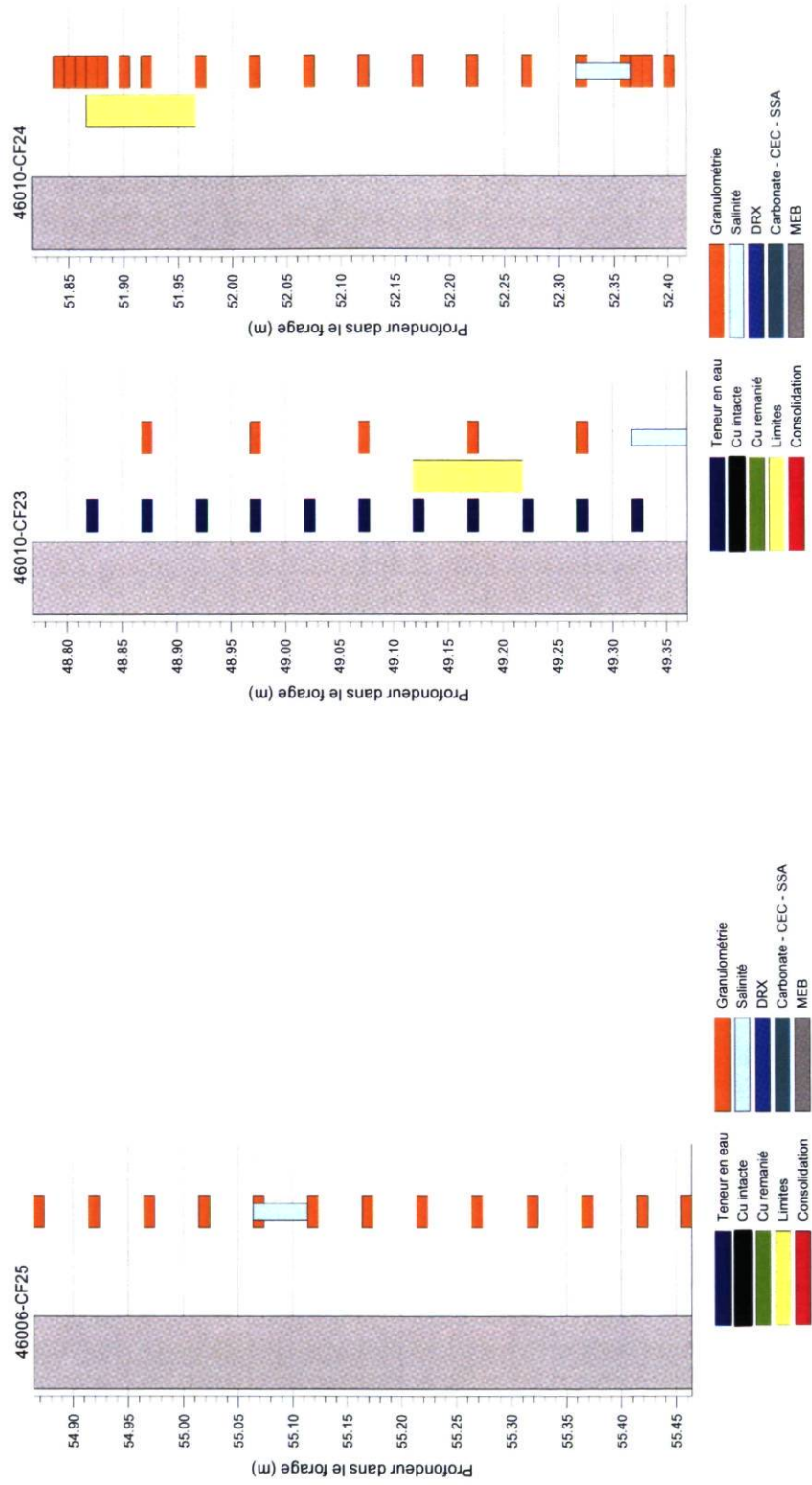












H.2 Mesures au cône suédois

H.2.1 Résultats des essais au cône suédois – F46006

Echantillon	Prof min (m)	Prof max (m)	Prof. moy. (m)	w _n (%)	W (g)	P1	P2	P3	P4	P5	Cu (kPa)	W (g)	P1	P2	P3	P4	P5	P4	P5	Cu (kPa)	W (g)	P1	P2	P3	P4	P5	Cur (kPa)	IL	St	Commentaires			
CF2	9.19	9.24	9.22	31%								10	5.50	5.50	5.00	5.00	5.00					10	5.50	5.50	5.00	5.00	1.06	1.2					
CF2	9.34	9.39	9.37	35%								10	3.50	3.00	3.50	3.25	3.25					10	3.50	3.00	3.50	3.25	2.69	0.8					
CF2	9.39	9.44	9.42	33%								10	6.00	5.75	5.50	5.00	5.25					10	6.00	5.75	5.50	5.00	0.97	1.2					
CF2	9.59	9.64	9.62	33%								10	4.75	4.75	4.50	4.25	4.50					10	4.75	4.75	4.50	4.50	1.42	1.0					
CF3	13.77	13.82	13.79	28%								10	20.00									10	20.00				0.07	3.9					
CF3	14.27	14.32	14.29	32%								10	20.00									10	20.00				0.07						
CF4	20.85	20.90	20.88	33%								10	20.00									10	20.00				0.07						
CF5	24.30	24.35	24.33	38%								10	20.00									10	20.00				0.07						
TM6	27.49	27.49	27.49	34%	400	9.50	8.50	8.75	9.00		49.0	400	17.00	15.00	14.75								10	17.00	15.00	14.75	0.12	3.1	406		à 5 cm du haut du tube		
TM6	27.49	27.54	27.52	32%								400	7.25	7.75	6.50	6.75						78.2	400	7.25	7.75	6.50	6.75	0.14	2.9	560		à bas 15 cm du bas du tube	
TM6	27.97	27.97	27.97	38%								400	6.00	6.00	6.00							108.9	400	6.00	6.00						à 6 cm du bas, pour MEB		
TM6	28.07	28.07	28.07	38%								400	6.00	6.00	6.00								10	18.00	19.00	17.00	0.09	3.5	1202				
TM6	28.02	28.07	28.05	37%								400	7.00	7.25	7.25	6.75	6.75					79.9	400	7.00	7.25	7.25	6.75	6.75				à 12 cm du haut du tube	
TM7	32.12	32.12	32.12	23%								60	11.00	11.00	10.75	10.50							60	11.00	11.00	10.75	1.51	1.0	53				
TM7	32.07	32.12	32.10	24%								60	11.00	11.00	10.75	10.50							60	11.00	11.00	10.75	1.51	1.0	53				à 17 cm du bas du tube
TM7	32.44	32.44	32.44	29%	400	5.50	5.75	5.75	5.75	6.00	118.5	400	5.50	5.75	5.75	5.75	6.00						60	10.25	10.00	9.75	1.76	1.0	67				
TM7	32.44	32.49	32.47	28%								60	10.25	10.00	9.75								60	10.25	10.00	9.75	1.76	1.0	67				
TM8	37.71	37.71	37.71	28%	400	5.75	8.50	6.75	7.75	6.75	76.4	400	5.75	8.50	6.75	6.75	6.75						60	9.25	9.00	8.75	2.18	0.9	35				Mesures par stagiaire
TM8	37.71	37.75	37.73	29%								400	5.75	8.50	6.75	6.75	6.75						60	9.25	9.00	8.75	2.18	0.9	35				Mesures par stagiaire
TM8	38.19	38.19	38.19	31%	400	6.50	5.50	5.50	6.50	6.00	108.3	400	6.50	5.50	5.50	6.50	6.00						60	10.00	9.00	9.50	1.90	0.9	57				Mesures par stagiaire
TM8	38.19	38.24	38.22	31%								60	10.00	9.00	9.50	10.00							60	10.00	9.00	9.50	1.90	0.9	57				Mesures par stagiaire
CF9	41.15	41.20	41.17	39%								60	4.75	4.75	4.75	4.25	4.00						60	4.75	4.75	4.75	4.00	8.7	0.5				Très difficile à remanier
CF9	41.25	41.30	41.27	35%								60	3.00	3.50	3.50	3.00	3.25						60	3.00	3.50	3.50	3.25	16.6	0.5				Très difficile à remanier

Echantillon	Prof min (m)	Prof max (m)	Prof. moy. (m)	w _n (%)	W (g)	P1	P2	P3	P4	P5	Cu (kPa)	W (g)	P1	P2	P3	P4	P5	Cur (kPa)	IL	St	Commentaires
CF9	41.40	41.45	41.42	37%								60	3.75	3.50	3.25	3.50	3.00	15.2	0.5		
CF9	41.55	41.60	41.57	35%								60	3.25	3.00	3.00	3.00	2.75	19.5	0.4		
CF9	41.70	41.75	41.72	30%								60	3.75	3.75	3.50	3.50	3.25	14.0	0.5		
TM10	42.74	42.74	42.74	37%	400	7.00	6.25	5.25	6.25		101.4		9.75	9.75	9.25	9.50		10.71	0.5	9	Échantillon TM10 avec concrétions et lits de sables
TM10	42.74	42.79	42.77	38%								100	10.00	9.75	9.75	8.75	9.00	10.95	0.5	12	
TM10	42.79	42.79	42.79	33%	400	5.50	5.25	5.00	5.75		135.3		10.00	9.75	9.75	8.75	9.00	10.95	0.5	12	
TM10	42.79	42.84	42.84	35%								100	10.00	9.75	9.75	8.75	9.00	10.95	0.5	12	
TM10	43.18	43.18	43.18	36%	400	6.25	6.00	6.00	5.00		115.2		10.00	9.75	9.75	8.75	9.00	10.95	0.5	12	
TM10	43.18	43.23	43.21	36%								100	8.50	8.75	8.50	8.50		13.36	0.5	9	
TM11	46.20	46.20	46.20	27%	400	7.00	7.50	8.00			69.5		10.00	10.25	10.00	10.00		9.68	0.5	7	Échantillon très fracturé
TM11	46.20	46.25	46.23	31%								100	10.00	10.25	10.00	10.00		9.68	0.5	7	

H.2.2 Résultats des essais au cône suédois – F46010

Echantillon	Prof min (m)	Prof max (m)	Prof. moy. (m)	w _n (%)	W (g)	P1	P2	P3	P4	P5	Cu (kPa)	W (g)	P1	P2	P3	P4	P5	Cur (kPa)	IL	St	Commentaires		
TM8	18.38	18.38	18.38	27.7	400	6.25	6.50	6.50			95.2											silt argileux très stratifié	
TM8	18.38	18.42	18.40									60	9.25	8.25	7.75	7.75	7.75	2.64		36			
TM8	18.84	18.84	18.84	29.8	400	7.75	7.75	8.00			63.9												
TM8	18.84	18.89	18.86	28.9								60	8.25	7.50	7.75	7.50	7.50	2.97		21			
TM11	22.88	22.88	22.88	29.4	400	6.00	6.75	8.00	6.00	6.75	86.3												silt argileux stratifié
TM11	22.88	22.93	22.91	27.1								60	7.00	7.00	7.00	7.00		3.60		24			
TM11	23.37	23.37	23.37	27.5	400	8.50	9.00	8.00	7.00		58.9												
TM11	23.37	23.42	23.40	29.8								60	5.50	7.00	6.75	5.50		4.55		13			
TM16	30.55	30.55	30.55	29.5	400	7.00	7.50	6.00	6.00		88.5												argile silteuse
TM16	30.55	30.6	30.58	30.6								60	5.50	4.75	4.75	5.75	6.00	6.11		14			
TM16	30.97	30.97	30.97	29.7	400	6.25	7.75	6.25	6.25	7.00	86.6												
TM16	30.97	31.02	31.00									60	5.75	5.50	5.25	5.25	5.25	6.04		14			
TM20	39.9	39.9	39.90	32.4	400	4.25	4.75	5.25	4.00		186.3												argile silteuse bioturbée
TM20	39.9	39.95	39.93	31.5								100	9.50	9.00	9.50	9.75		10.99		17			

H.2.3 Limites de consistance – F46006

Échantillon	Prof. minimum (m)	Prof. maximale (m)	Limite de liquidité (%)	Limite de plasticité (%)	Indice de plasticité (%)	Teneur en eau moyenne (%)	Indice de liquidité
CF2	9.14	9.19	25.4	12.7	12.7	33.2	1.6
CF3	13.87	14.07	19.6	12.6	7.0	27.3	2.1
CF3	14.07	14.22	21.1	11.8	9.2	29.4	1.9
CF4	20.70	20.85	19.0	12.3	6.7	31.0	2.8
CF5	23.90	24.10	21.8	13.5	8.4	35.7	2.7
CF5	24.10	24.30	20.9	13.7	7.1	34.7	2.9
TM6	27.49	27.54	20.0	13.5	6.5	33.8	3.1
TM6	28.02	28.07	23.0	12.9	10.1	36.7	2.4
TM7	32.07	32.12	21.9	12.3	9.6	24	1.2
TM8	38.19	38.24	29.5	15.8	13.7	30.9	1.1
CF9	41.55	41.60	40.4	16.4	24.0	34.8	0.8
TM10	42.76	42.81	46.4	17.5	28.8	37.7	0.7
TM10	42.81	42.86	40.0	16.9	23.1	33.3	0.7
TM11	46.20	46.25	37.0	12.7	24.3	29.4	0.7

H.2.4 Limites de consistance – F46010

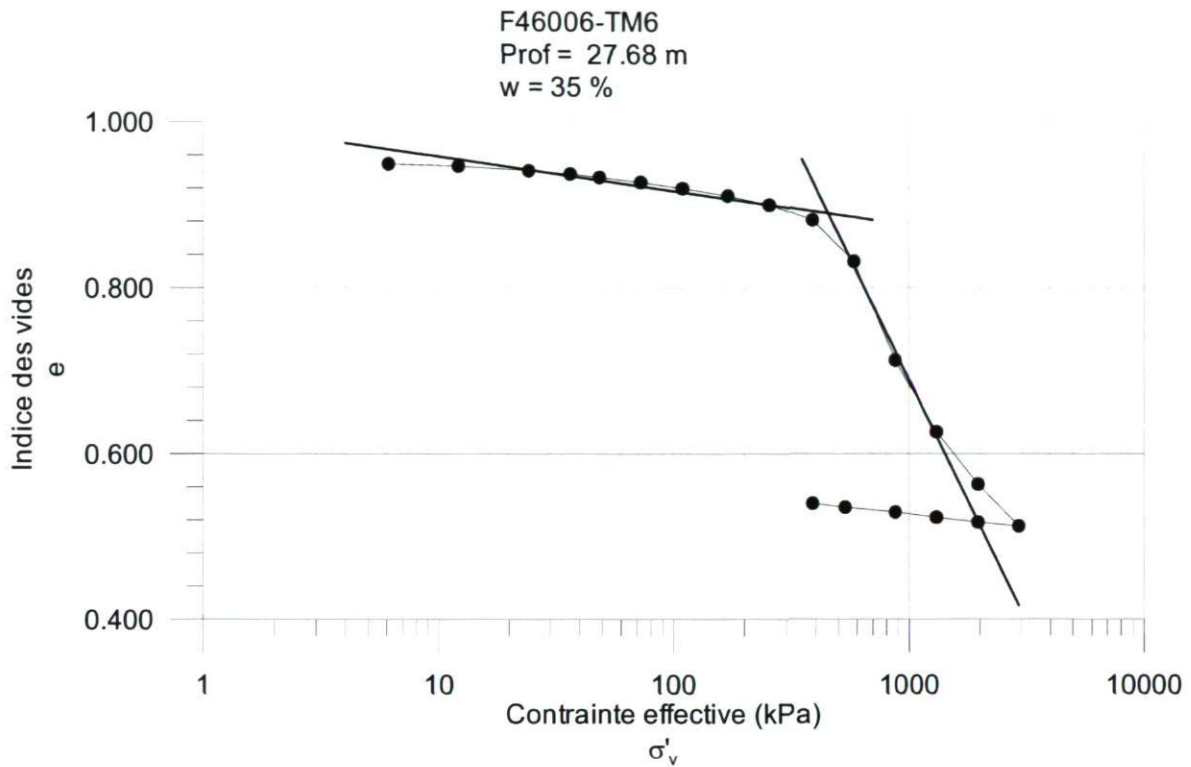
Échantillon	Prof. minimum (m)	Prof. maximale (m)	Limite de liquidité (%)	Limite de plasticité (%)	Indice de plasticité (%)	Teneur en eau moyenne (%)	Indice de liquidité
CF2	7.8	8.1	37.2	13.9	23.3	37.9	1.0
CF3	10.8	11.0	21.5	12.9	8.7	23.1	1.2
CF4	12.3	12.5	22.9	12.6	10.3	24.5	1.1
TM5	14.0	14.1	20.6	12.6	8.0	24.5	1.5
TM6	15.3	15.4	32.4	17.2	15.2	31.4	0.9
TM7	16.9	17.1	25.1	10.3	14.8	28.4	1.2
TM8	18.4	18.5	27.4	12.2	15.2	30.0	1.2
TM8	18.8	18.9	26.8	13.5	13.2	29.3	1.2
TM9	19.9	20.1	27.5	13.6	13.9	32.8	1.4
TM11	22.9	22.9	25.0	11.9	13.2	28.3	1.2
TM13	26.2	26.3	26.4	10.8	15.6	25.7	1.0
TM14	27.5	27.7	28.0	12.9	15.1	29.4	1.1
TM15	29.1	29.2	26.2	12.0	14.2	30.6	1.3
TM16	30.6	30.6	29.9	13.6	16.3	30.0	1.0
TM18	33.8	34.0	40.1	17.0	23.1	34.2	0.7
TM19	36.8	37.0	45.6	17.8	27.8	37.9	0.7
TM20	39.9	40.0	35.9	13.3	22.6	31.9	0.8
TM21	42.7	42.9	36.6	14.9	21.7	34.0	0.9
CF22	46.0	46.1	41.2	18.8	22.4	39.5	0.9
CF23	49.1	49.2	40.1	16.6	23.5	35.2	0.8
CF24	51.9	52.0	28.7	12.8	15.9	24.6	0.7

H.3 Compressibilité (essais oedométriques)

H.3.1 Tableau résumé des essais

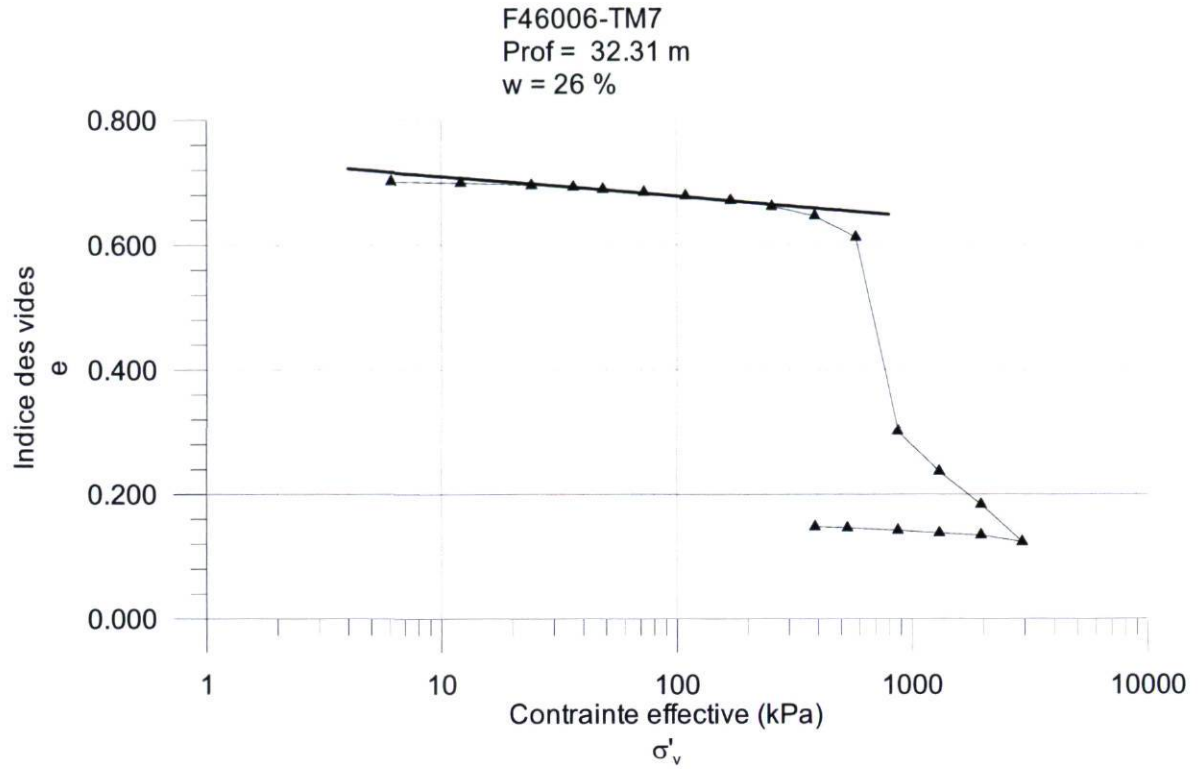
Forage	Tube	Profondeur moyenne (m)	Élévation moyenne (m)	Teneur en eau (%)	Indice des vides initial (e_0)	Indice des vides final (e_f)	Qualité de l'essai
F46006	TM6	27.68	19.5	35%	0.96	0.61	Bonne
F46006	TM7	32.31	14.9	26%	0.71	0.53	Mauvaise
F46006	TM8	38.11	9.1	32%	0.86	0.66	Bonne
F46006	TM8	38.17	9.0	31%	0.84	0.67	Moyenne
F46006	TM10	42.84	4.4	39%	1.05	0.77	Moyenne
F46010	TM8	18.70	-10.9	28%	0.77	0.57	Moyenne
F46010	TM11	23.07	-15.3	30%	0.83	0.61	Mauvaise

H.3.2 Résultats des essais oedométriques du forage F46006



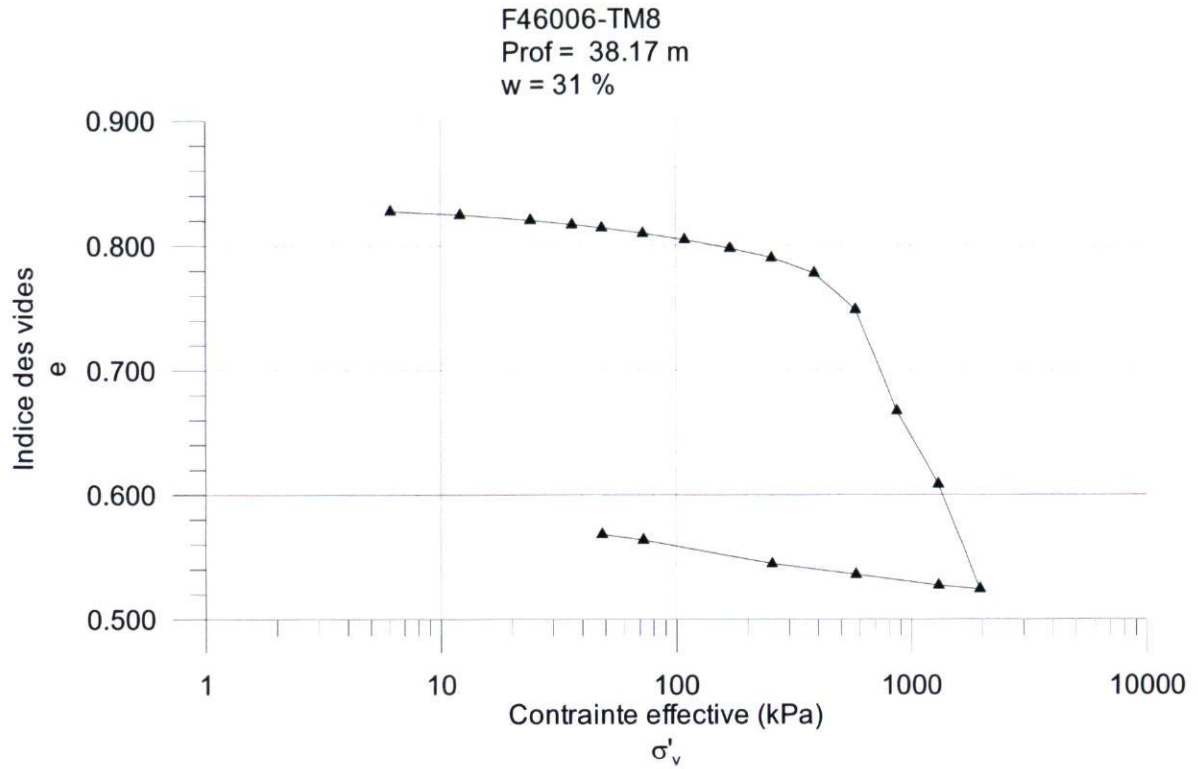
Caractéristiques géotechniques:

Indice des vides initial (e_0) :	0.96
Teneur en eau initiale (w) :	35 %
Poids volumique humide initial (γ_T):	18.6 kN/m ³
Degré de saturation initial (S_r)	100%
Pression de préconsolidation (σ'_p):	450 kPa



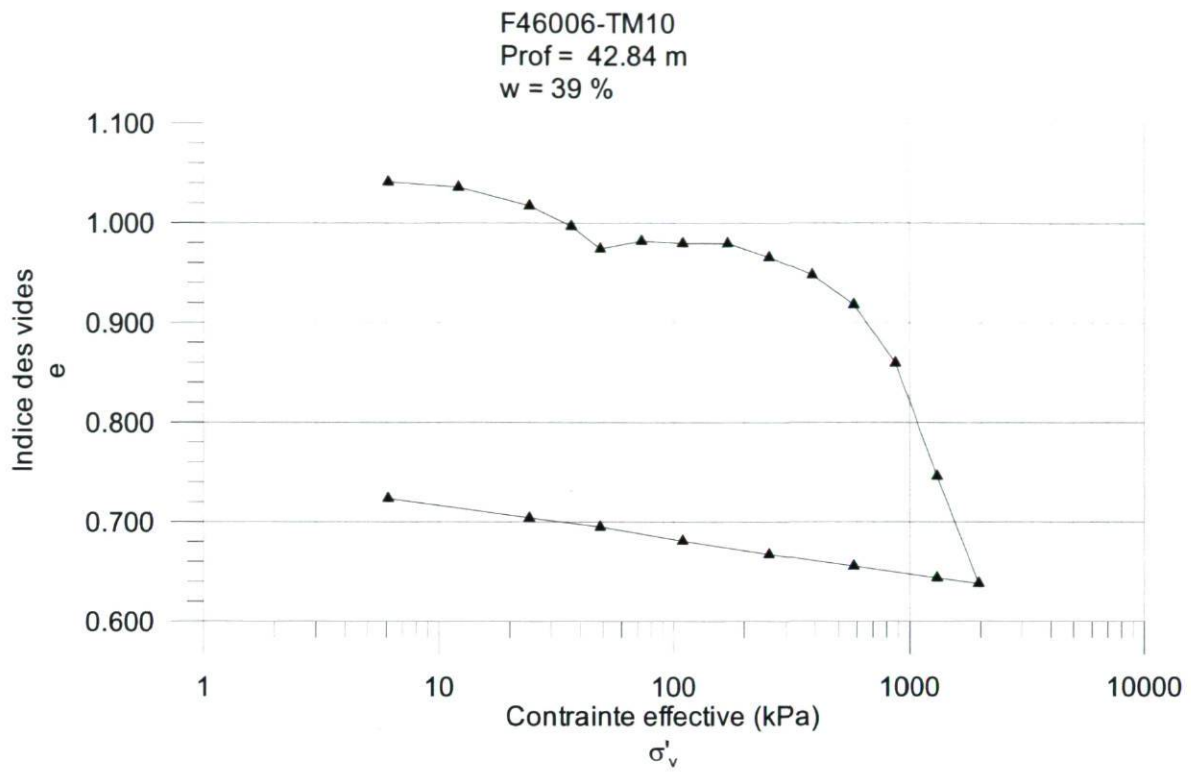
Caractéristiques géotechniques:

Indice des vides initial (e_0) :	0.71
Teneur en eau initiale (w) :	26%
Poids volumique humide initial (γ_T) :	19.6
Degré de saturation initial (S_r)	100%
Pression de préconsolidation (σ'_p):	485 kPa



Caractéristiques géotechniques:

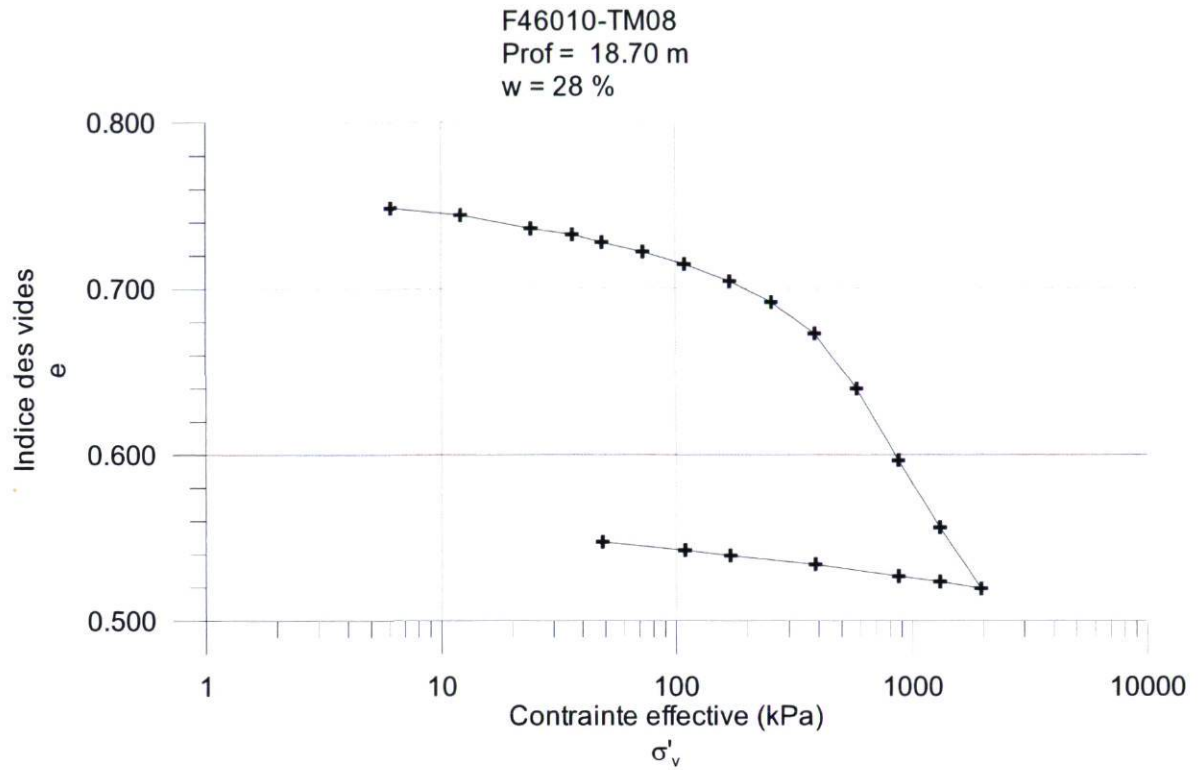
Indice des vides initial (e_0) :	0.84
Teneur en eau initiale (w) :	31%
Poids volumique humide initial (γ_T) :	19.0
Degré de saturation initial (S_r)	100%
Pression de préconsolidation (σ'_p):	530 kPa



Caractéristiques géotechniques:

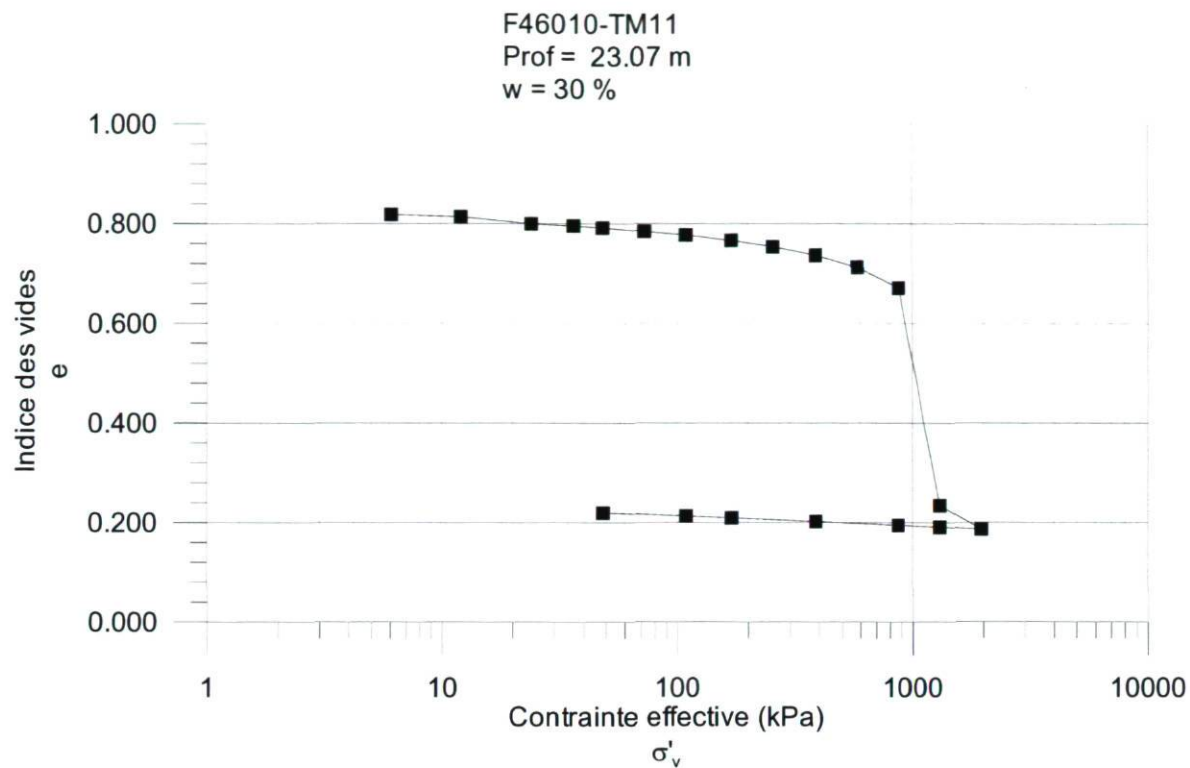
Indice des vides initial (e_0) :	1.05
Teneur en eau initiale (w) :	39%
Poids volumique humide initial (γ_T) :	18.2
Degré de saturation initial (S_r)	100%
Pression de préconsolidation (σ'_p):	700 kPa

H.3.3 Résultats des essais oedométriques du forage F46010



Caractéristiques géotechniques:

Indice des vides initial (e_0) :	0.77
Teneur en eau initiale (w) :	28%
Poids volumique humide initial (γ_T) :	20.4
Degré de saturation initial (S_r)	100%
Pression de préconsolidation (σ'_p):	400 kPa



Caractéristiques géotechniques:

Indice des vides initial (e_0) :	0.83
Teneur en eau initiale (w) :	30%
Poids volumique humide initial (γ_r) :	19.9
Degré de saturation initial (S_r)	100%
Pression de préconsolidation (σ'_p):	450 kPa

H.4 Analyses granulométriques

H.4.1 Distributions granulométriques - F46006

Échantillon	Profondeur minimale (m)	Profondeur maximale (m)	Sable (%)	Silt (%)	Argile (%)	Moyenne (µm)
CF1	4.67	4.68	95.5	3.4	1.1	410.0
CF1	4.77	4.78	83.3	1.3	0.2	708.9
CF1	4.87	4.88	79.3	1.2	0.2	788.0
CF1	4.97	4.98	97.4	2.2	0.4	439.0
CF2	9.14	9.15	0.0	63.9	36.1	3.3
CF2	9.19	9.20	0.0	56.2	43.8	2.3
CF2	9.24	9.25	69.8	25.4	4.8	57.2
CF2	9.29	9.30	0.0	69.4	30.6	4.1
CF2	9.34	9.35	0.0	51.8	48.2	2.1
CF2	9.39	9.40	0.0	56.6	43.4	2.3
CF2	9.44	9.45	0.0	57.3	42.7	2.4
CF2	9.49	9.50	0.0	51.5	48.5	2.1
CF2	9.54	9.55	78.1	18.2	3.7	76.8
CF2	9.59	9.60	0.0	56.5	43.5	2.3
CF2	9.64	9.65	0.0	53.5	46.5	2.2
CF3	13.72	13.73	42.1	45.1	12.8	24.7
CF3	13.77	13.78	53.7	37.3	9.0	35.9
CF3	13.82	13.83	0.0	60.4	39.6	2.6
CF3	13.87	13.88	0.0	59.2	40.8	2.6
CF3	13.92	13.93	0.0	54.8	45.2	2.3
CF3	13.97	13.98	0.0	64.5	35.5	3.3
CF3	14.02	14.03	57.1	33.4	9.5	36.6
CF3	14.07	14.08	43.4	39.8	16.7	20.3
CF3	14.12	14.13	0.0	55.4	44.6	2.2
CF3	14.17	14.18	54.0	36.4	9.6	34.9
CF3	14.22	14.23	0.0	55.0	45.0	2.3
CF3	14.27	14.28	0.0	49.8	50.2	2.0
CF3	14.31	14.32	0.0	49.8	50.2	1.9
CF4	20.40	20.41	0.0	55.9	44.1	2.3
CF4	20.45	20.46	0.0	55.6	44.4	2.2
CF4	20.50	20.51	0.0	54.7	45.3	2.3
CF4	20.55	20.56	0.0	55.9	44.1	2.2

Échantillon	Profondeur minimale (m)	Profondeur maximale (m)	Sable (%)	Silt (%)	Argile (%)	Moyenne (µm)
CF4	20.60	20.61	0.0	53.6	46.4	2.1
CF4	20.65	20.66	0.0	51.0	49.0	1.9
CF4	20.70	20.71	0.0	57.9	42.1	2.4
CF4	20.75	20.76	34.6	50.5	14.9	19.9
CF4	20.80	20.81	0.0	59.9	40.1	2.7
CF4	20.85	20.86	0.0	58.7	41.3	2.5
CF4	20.90	20.91	0.0	55.7	44.3	2.4
CF4	20.94	20.95	0.0	53.5	46.5	2.2
CF5	23.75	23.76	0.0	56.4	43.6	2.3
CF5	23.80	23.81	0.0	50.6	49.4	2.0
CF5	23.85	23.86	0.0	53.4	46.6	2.2
CF5	23.90	23.91	0.0	54.9	45.1	2.4
CF5	23.95	23.96	0.0	50.1	49.9	2.0
CF5	24.00	24.01	0.0	54.7	45.3	2.2
CF5	24.05	24.06	0.0	57.6	42.4	2.5
CF5	24.10	24.11	0.0	55.3	44.7	2.5
CF5	24.15	24.16	0.0	52.8	47.2	2.1
CF5	24.20	24.21	0.0	52.9	47.1	2.1
CF5	24.25	24.26	0.0	55.8	44.2	2.3
CF5	24.30	24.31	0.0	51.0	49.0	2.1
CF5	24.34	24.35	0.0	51.8	48.2	2.0
TM6	27.43	27.44	0.0	55.2	44.8	2.4
TM6	27.50	27.55	0.0	52.3	47.7	2.2
TM6	27.97	28.02	0.0	49.7	50.3	2.0
TM6	28.12	28.13	0.0	48.4	51.6	1.9
TM7	32.00	32.02	0.0	53.4	46.6	2.1
TM7	32.12	32.17	0.0	52.2	47.8	2.1
TM7	32.49	32.54	0.0	53.3	46.7	2.2
TM8	37.65	37.67	0.0	55.3	44.7	2.2
TM8	37.75	37.80	0.0	52.2	47.8	2.0
TM8	38.23	38.27	0.0	56.3	43.7	2.4
TM8	38.34	38.35	0.0	54.5	45.5	2.2
CF9	41.15	41.16	0.0	52.9	47.1	2.1
CF9	41.20	41.21	0.0	64.1	35.9	3.2
CF9	41.25	41.26	0.0	56.7	43.3	2.4
CF9	41.30	41.31	0.0	53.8	46.2	2.1

Échantillon	Profondeur minimale (m)	Profondeur maximale (m)	Sable (%)	Silt (%)	Argile (%)	Moyenne (µm)
CF9	41.35	41.36	0.0	57.8	42.2	2.5
CF9	41.40	41.41	0.0	53.2	46.8	2.1
CF9	41.45	41.46	0.0	55.8	44.2	2.4
CF9	41.50	41.51	0.0	54.4	45.6	2.3
CF9	41.55	41.56	0.0	59.4	40.6	2.8
CF9	41.60	41.61	0.0	63.1	36.9	3.1
CF9	41.65	41.66	0.0	67.3	32.7	3.9
CF9	41.70	41.71	0.0	72.1	27.9	5.0
CF9	41.74	41.75	0.0	64.7	35.3	3.3
TM10	43.33	43.35	0.0	68.5	31.5	3.8
TM10	43.18	43.23	0.0	72.5	27.5	4.5
TM10	43.16	43.18	0.0	74.1	25.9	5.2
TM10	43.00	43.05	0.0	76.3	23.7	5.4
TM10	42.79	42.84	0.0	61.3	38.7	3.0
TM10	42.67	42.70	0.0	67.1	32.9	3.7
TM11	46.30	46.31	0.0	62.2	37.8	3.0
TM11	46.28	46.29	0.0	57.0	43.0	2.5
TM11	46.23	46.24	0.0	55.9	44.1	2.3
TM11	46.18	46.19	0.0	51.2	48.8	2.0
TM11	46.13	46.14	0.0	62.1	37.9	3.0
TM11	46.07	46.08	0.0	47.1	52.9	1.8
TM11	45.96	45.97	0.0	59.8	40.2	2.8
TM11	45.88	45.89	0.0	71.1	28.9	4.4
TM11	45.78	45.79	0.0	61.0	39.0	2.7
TM12	50.68	50.69	0.0	70.9	29.1	4.0

La moyenne granulométrique est calculée selon la « Geometric method of moments » avec l'application Gradistat (Blott and Pye 2001) et la limite du silt-sable se situe à 63 µm.

H.4.2 Distributions granulométriques - F46010

Échantillon	Profondeur minimale (m)	Profondeur maximale (m)	Sable (%)	Silt (%)	Argile (%)	Moyenne (µm)
CFA	1.52	1.88	98.5	1.2	0.3	375.9
CFB	3.05	3.18	98.7	1.0	0.3	375.4
CF1	4.70	4.93	98.7	1.0	0.3	375.4
CF2	7.62	7.77	45.4	33.6	21.0	17.7
CF2	7.77	8.12	0.0	57.6	42.4	2.5
CF2	7.77	8.12	0.0	58.8	41.2	2.6
CF3	10.72	10.73	26.7	54.0	19.3	13.7
CF3	10.82	10.83	0.0	65.5	34.5	3.2
CF3	10.92	10.93	34.9	52.9	12.2	21.0
CF3	11.02	11.03	0.0	61.2	38.8	2.7
CF3	11.13	11.14	0.0	61.4	38.6	2.9
CF4	12.29	12.30	0.0	56.6	43.4	2.3
CF4	12.39	12.40	38.4	45.2	16.4	18.9
CF4	12.49	12.50	42.5	41.0	16.5	21.5
CF4	12.59	12.60	42.9	41.3	15.9	21.4
CF4	12.69	12.70	48.9	37.0	14.1	29.4
CF4	12.78	12.79	0.0	55.4	44.6	2.6
TM5	13.82	13.83	0.0	73.8	26.2	4.8
TM5	13.92	13.93	0.0	79.2	20.8	6.7
TM5	14.02	14.03	0.0	80.0	20.0	6.9
TM5	14.12	14.13	0.0	73.7	26.3	4.8
TM5	14.22	14.23	0.0	76.7	23.3	6.2
TM5	14.32	14.33	0.0	77.4	22.6	6.0
TM6	15.34	15.35	0.0	57.7	42.3	2.6
TM6	15.44	15.45	0.0	55.4	44.6	2.3
TM6	15.54	15.55	0.0	62.3	37.7	3.1
TM6	15.64	15.65	0.0	60.7	39.3	2.8
TM6	15.74	15.75	0.0	61.2	38.8	3.0
TM7	16.86	16.87	0.0	73.3	26.7	4.9
TM7	16.96	16.97	0.0	73.0	27.0	4.9
TM7	17.06	17.07	0.0	58.0	42.0	2.6
TM7	17.16	17.17	0.0	64.8	35.2	3.3
TM7	17.26	17.27	0.0	68.3	31.7	3.9
TM7	17.36	17.37	0.0	54.4	45.6	2.3

Échantillon	Profondeur minimale (m)	Profondeur maximale (m)	Sable (%)	Silt (%)	Argile (%)	Moyenne (µm)
TM7	17.45	17.46	0.0	69.4	30.6	4.2
TM8	18.98	18.99	0.0	65.7	34.3	3.5
TM9	19.91	19.92	0.0	62.0	38.0	3.0
TM9	20.01	20.02	0.0	62.1	37.9	3.0
TM9	20.11	20.12	0.0	72.1	27.9	4.9
TM9	20.21	20.22	0.0	72.0	28.0	4.6
TM9	20.31	20.32	52.3	38.0	9.7	32.7
TM9	20.41	20.42	0.0	66.0	34.0	3.6
TM10	21.35	21.36	0.0	68.4	31.6	4.1
TM10	21.44	21.45	0.0	65.3	34.7	3.5
TM10	21.54	21.55	0.0	69.1	30.9	4.3
TM10	21.64	21.65	0.0	65.4	34.6	3.3
TM10	21.74	21.75	0.0	73.7	26.3	5.6
TM11	23.48	23.49	0.0	63.5	36.5	2.9
TM12	24.39	24.40	0.0	72.2	27.8	5.0
TM12	24.48	24.49	0.0	60.8	39.2	2.9
TM12	24.58	24.59	0.0	67.7	32.3	3.6
TM12	24.68	24.69	48.4	40.2	11.4	27.3
TM12	24.78	24.79	0.0	69.0	31.0	4.3
TM12	24.88	24.89	0.0	63.3	36.7	3.0
TM12	24.98	24.99	0.0	71.8	28.2	4.4
TM13	25.92	25.93	0.0	73.4	26.6	6.1
TM13	26.01	26.02	0.0	76.1	23.9	6.1
TM13	26.11	26.12	0.0	63.4	36.6	3.0
TM13	26.21	26.22	0.0	76.1	23.9	5.9
TM13	26.31	26.32	0.0	73.2	26.8	4.6
TM13	26.41	26.42	0.0	74.2	25.8	5.8
TM14	27.44	27.45	0.0	71.3	28.7	4.5
TM14	27.53	27.54	0.0	70.2	29.8	4.4
TM14	27.63	27.64	0.0	71.5	28.5	4.4
TM14	27.73	27.74	0.0	73.2	26.8	4.7
TM14	27.83	27.84	0.0	68.7	31.3	4.2
TM14	27.93	27.94	0.0	75.7	24.3	5.5
TM14	28.03	28.04	0.0	69.8	30.2	4.4
TM14	28.06	28.06	0.0	74.1	25.9	5.5
TM14	28.07	28.07	0.0	63.0	37.0	3.0

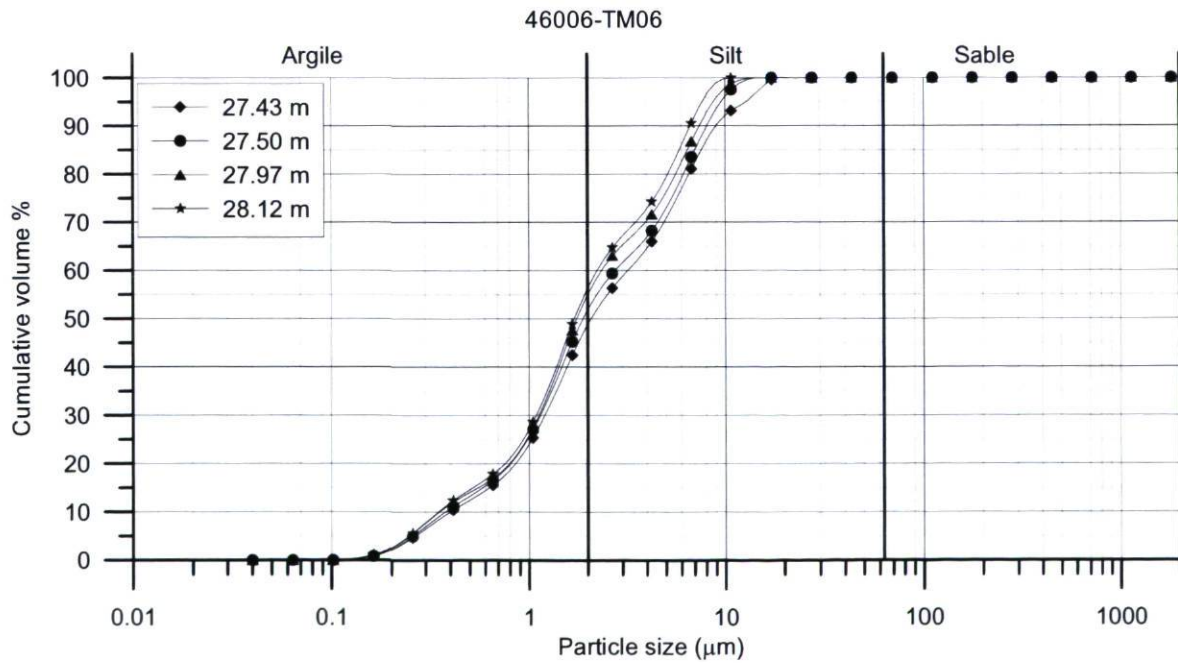
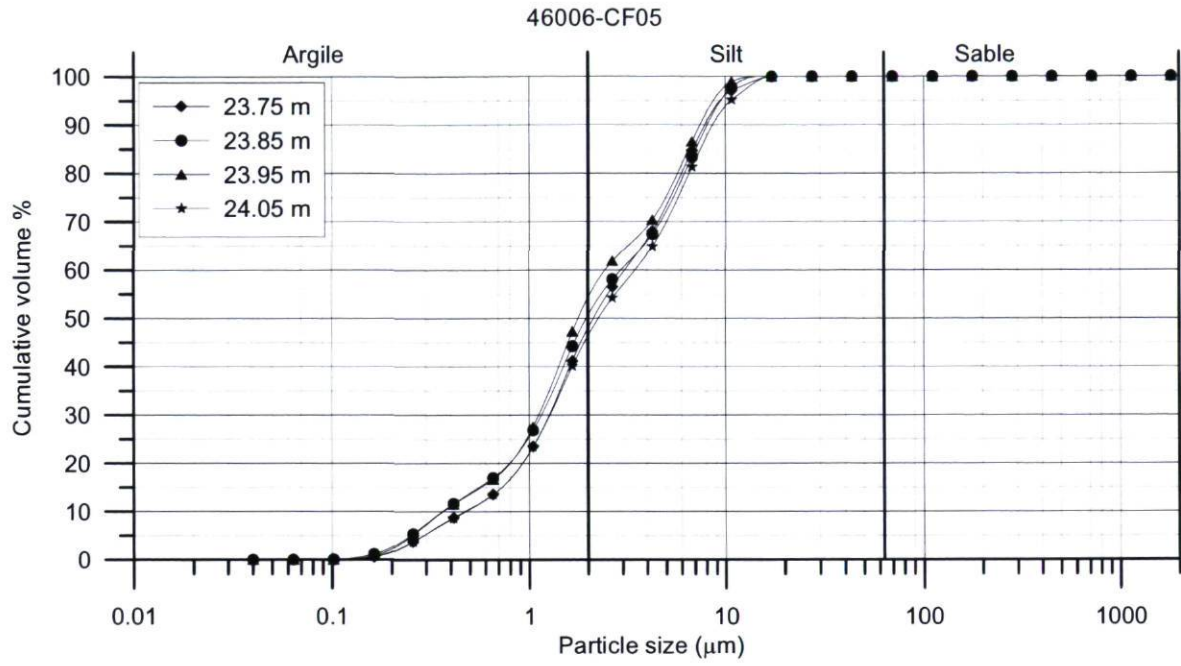
Échantillon	Profondeur minimale (m)	Profondeur maximale (m)	Sable (%)	Silt (%)	Argile (%)	Moyenne (µm)
TM14	28.10	28.10	0.0	63.9	36.1	3.2
TM15	28.97	28.98	0.0	64.1	35.9	3.0
TM15	29.06	29.07	0.0	67.4	32.6	4.0
TM15	29.16	29.17	0.0	66.2	33.8	3.4
TM15	29.26	29.27	0.0	74.5	25.5	5.6
TM15	29.36	29.37	0.0	67.9	32.1	3.6
TM15	29.46	29.47	0.0	61.0	39.0	3.1
TM16	31.08	31.08	0.0	67.6	32.4	4.5
TM16	31.09	31.09	0.0	64.9	35.1	3.6
TM16	31.12	31.12	0.0	61.2	38.8	2.9
TM17	32.01	32.02	0.0	71.1	28.9	5.2
TM17	32.10	32.11	0.0	71.2	28.8	4.1
TM17	32.20	32.21	0.0	69.0	31.0	3.8
TM17	32.30	32.31	0.0	65.8	34.2	3.7
TM17	32.40	32.41	0.0	66.5	33.5	3.7
TM17	32.50	32.51	0.0	65.7	34.3	3.7
TM17	32.60	32.61	0.0	66.8	33.2	3.8
TM18	33.54	33.55	0.0	65.9	34.1	3.6
TM18	33.63	33.64	0.0	55.9	44.1	2.4
TM18	33.73	33.74	0.0	51.6	48.4	2.1
TM18	33.83	33.84	0.0	49.7	50.3	1.9
TM18	33.93	33.94	0.0	54.8	45.2	2.3
TM18	34.03	34.04	0.0	65.3	34.7	3.5
TM18	34.13	34.14	0.0	57.1	42.9	2.6
TM18	34.14	34.14	0.0	63.2	36.8	3.1
TM18	34.17	34.17	0.0	56.8	43.2	2.4
TM19	36.59	36.60	0.0	57.6	42.4	2.6
TM19	36.68	36.69	0.0	68.0	32.0	3.7
TM19	36.78	36.79	0.0	63.1	36.9	3.1
TM19	36.88	36.89	0.0	60.7	39.3	2.8
TM19	36.98	36.99	0.0	58.8	41.2	2.7
TM19	37.08	37.09	0.0	58.4	41.6	2.5
TM19	37.18	37.19	0.0	64.0	36.0	3.0
TM20	39.96	39.97	0.0	49.5	50.5	1.9
TM21	42.72	42.73	0.0	71.4	28.6	4.1
TM21	42.77	42.78	0.0	68.6	31.4	3.8

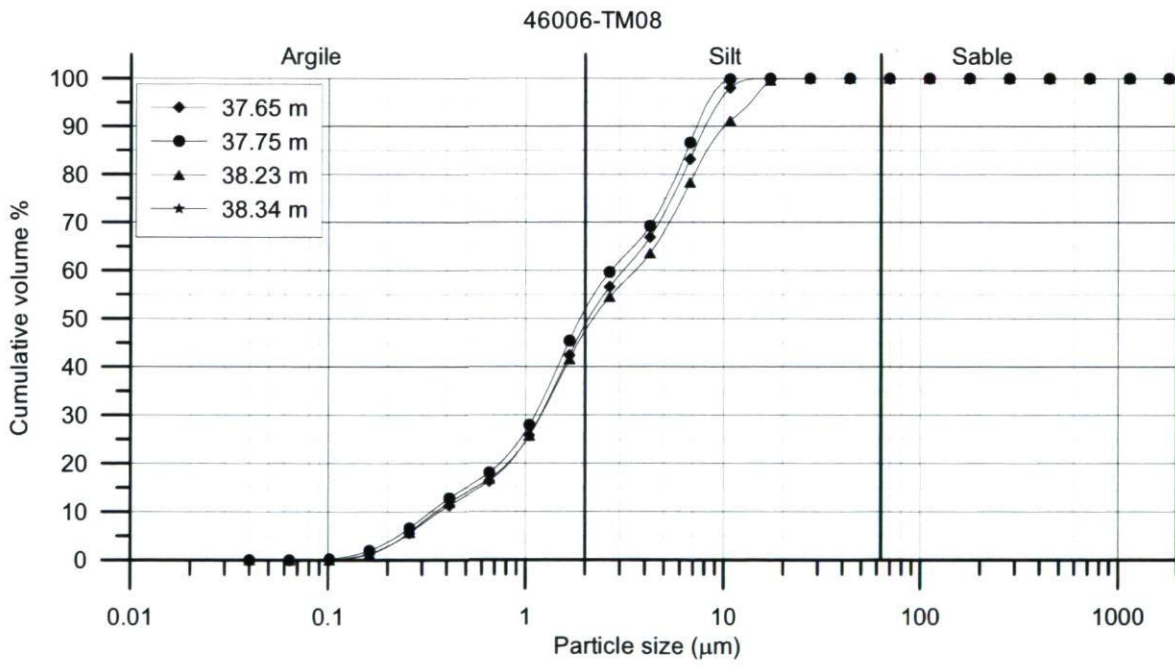
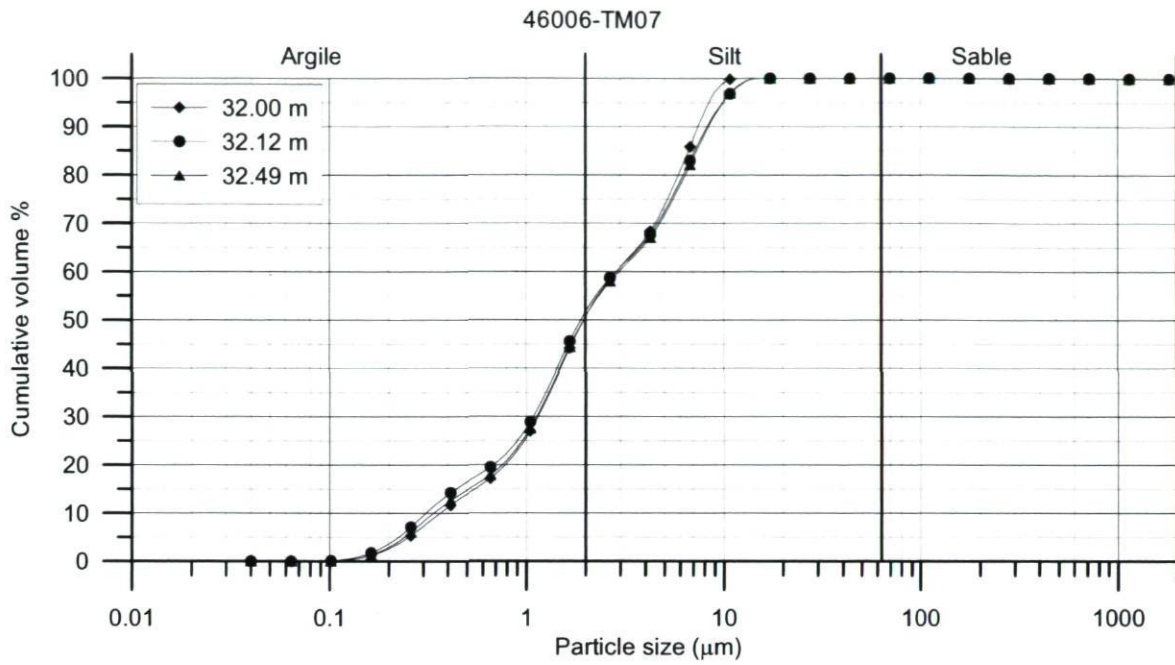
Échantillon	Profondeur minimale (m)	Profondeur maximale (m)	Sable (%)	Silt (%)	Argile (%)	Moyenne (µm)
TM21	42.82	42.83	0.0	63.0	37.0	3.0
TM21	42.87	42.88	0.0	65.1	34.9	3.3
TM21	43.01	43.01	0.0	54.8	45.2	2.1
TM21	43.02	43.02	0.0	60.3	39.7	2.7
TM21	43.04	43.04	0.0	65.1	34.9	3.1
CF22	45.82	45.83	0.0	65.1	34.9	3.2
CF22	45.92	45.93	0.0	62.2	37.8	2.9
CF22	46.02	46.03	0.0	63.8	36.2	3.1
CF22	46.12	46.13	0.0	62.8	37.2	3.0
CF22	46.22	46.23	0.0	61.9	38.1	2.9
CF23	48.87	48.88	0.0	64.5	35.5	3.2
CF23	48.97	48.98	0.0	64.4	35.6	3.2
CF23	49.07	49.08	0.0	63.2	36.8	3.2
CF23	49.17	49.18	0.0	62.0	38.0	3.0
CF23	49.27	49.28	0.0	64.2	35.8	3.2
CF24	51.84	51.85	15.2	72.0	12.8	13.2
CF24	51.85	51.86	44.4	47.7	7.9	27.0
CF24	51.86	51.87	64.8	29.9	5.3	45.8
CF24	51.87	51.88	47.1	44.4	8.5	29.1
CF24	51.88	51.89	8.9	77.3	13.8	11.8
CF24	51.90	51.91	37.7	54.0	8.4	24.9
CF24	51.92	51.93	0.0	70.9	29.1	4.4
CF24	51.97	51.98	14.0	73.2	12.8	12.6
CF24	51.97	51.98	51.9	40.1	8.1	36.0
CF24	52.02	52.03	2.0	81.3	16.7	8.5
CF24	52.07	52.08	0.0	77.8	22.2	5.9
CF24	52.12	52.13	28.2	60.6	11.2	19.4
CF24	52.17	52.18	0.0	77.0	23.0	5.4
CF24	52.22	52.23	0.1	81.8	18.1	7.3
CF24	52.27	52.28	0.0	80.8	19.2	6.7
CF24	52.32	52.33	0.0	74.3	25.7	4.4
CF24	52.36	52.37	53.3	38.1	8.6	33.8
CF24	52.37	52.38	45.9	46.2	7.8	29.8
CF24	52.38	52.39	0.0	80.7	19.3	7.0
CF24	52.40	52.41	0.0	71.4	28.6	3.7
CF25	54.86	54.87	17.7	46.1	32.0	6.7

Échantillon	Profondeur minimale (m)	Profondeur maximale (m)	Sable (%)	Silt (%)	Argile (%)	Moyenne (µm)
CF25	54.91	54.92	61.7	29.2	9.1	82.8
CF25	54.96	54.97	67.0	24.6	8.4	91.0
CF25	55.01	55.02	37.7	42.2	20.0	16.8
CF25	55.06	55.07	67.9	24.2	7.9	108.5
CF25	55.11	55.12	67.2	25.7	7.1	130.1
CF25	55.16	55.17	64.7	28.0	7.3	95.3
CF25	55.21	55.22	68.9	21.1	10.1	151.5
CF25	55.26	55.27	61.0	28.6	10.4	73.9
CF25	55.31	55.32	68.6	24.0	7.4	178.9
CF25	55.36	55.37	66.1	25.8	8.1	126.3
CF25	55.41	55.42	65.7	26.0	8.3	144.3
CF25	55.45	55.46	65.7	25.9	8.4	138.0

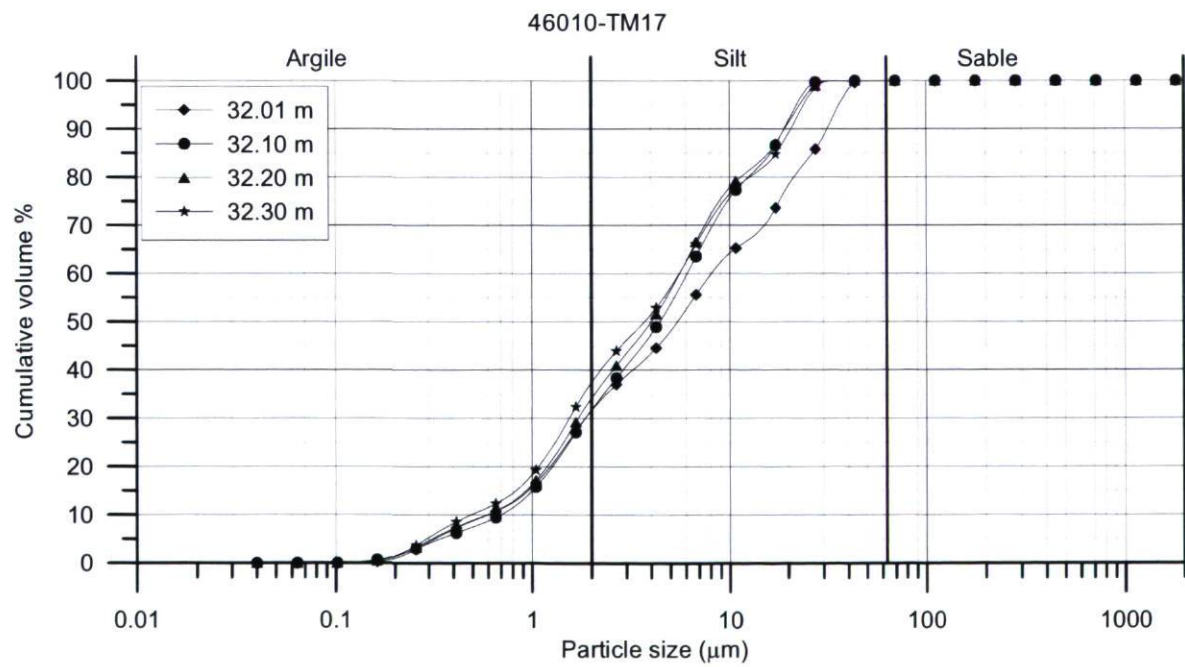
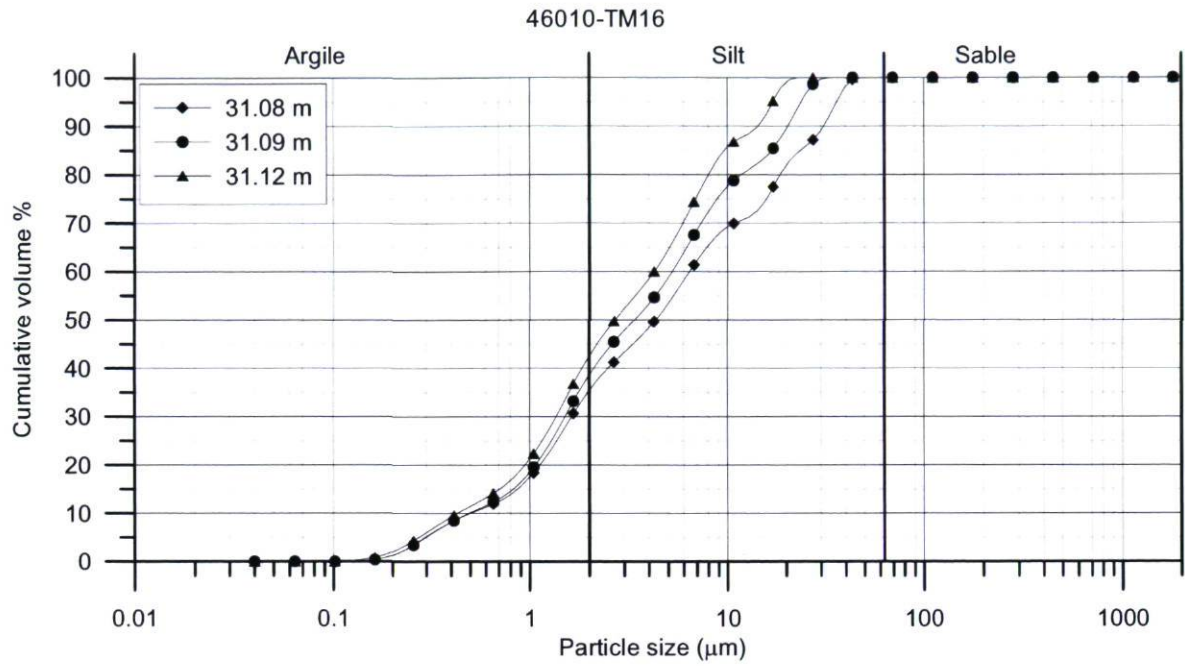
H.4.3 Distributions granulométriques de la couche d'argile marine U3

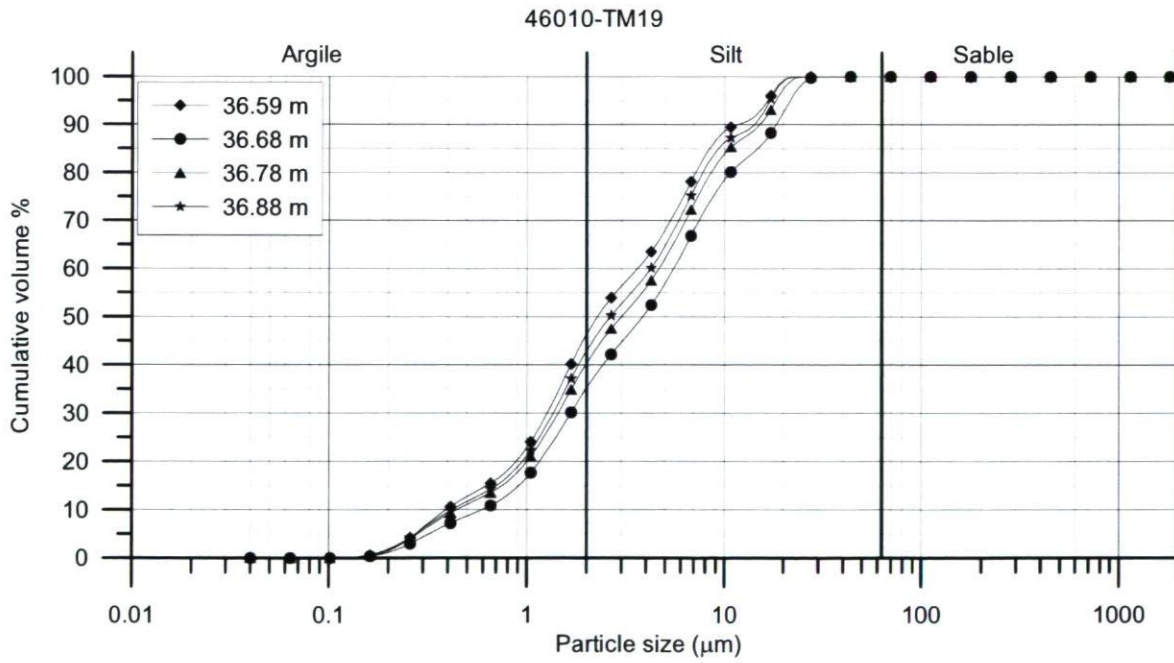
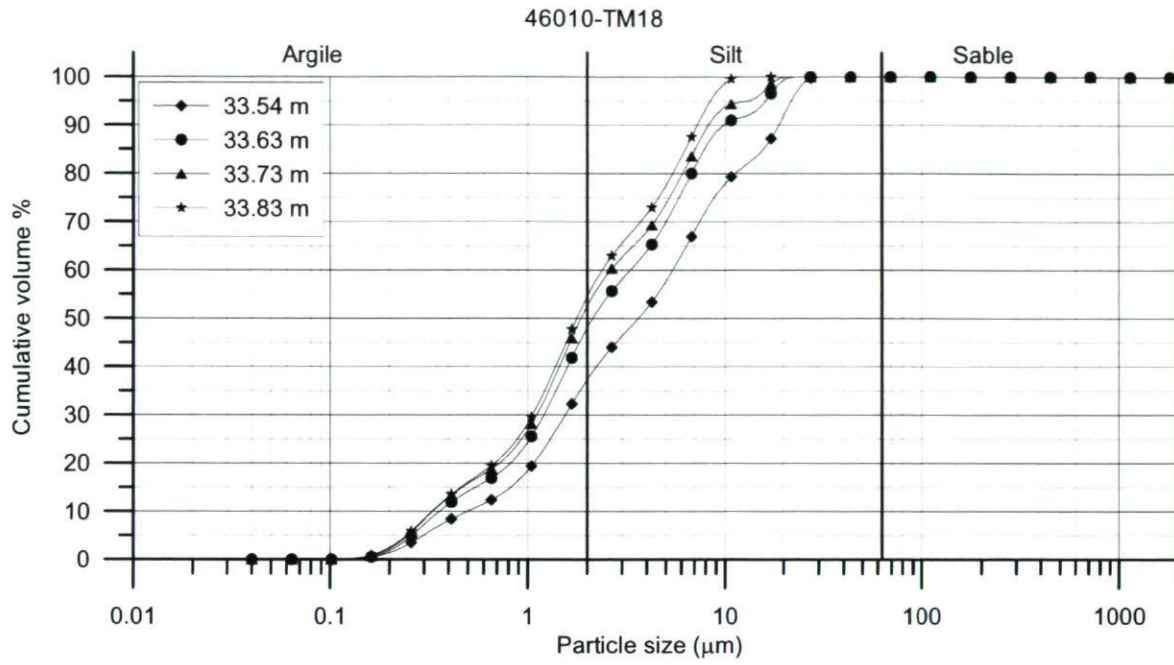
H.4.3.1 Forage 46006

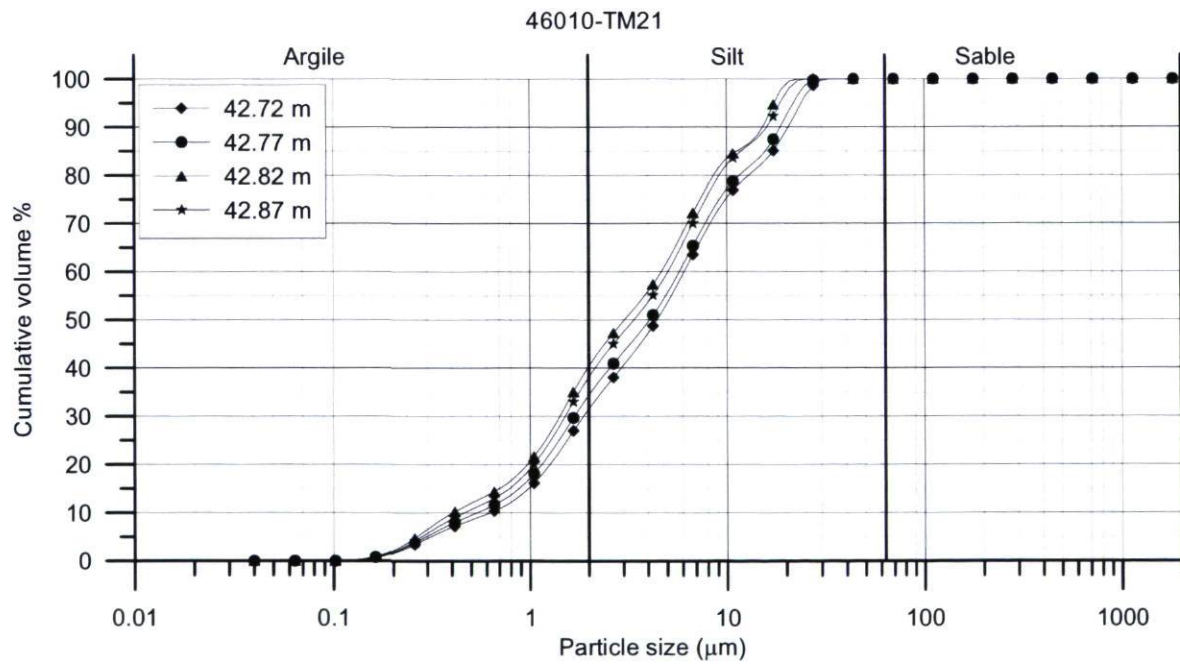
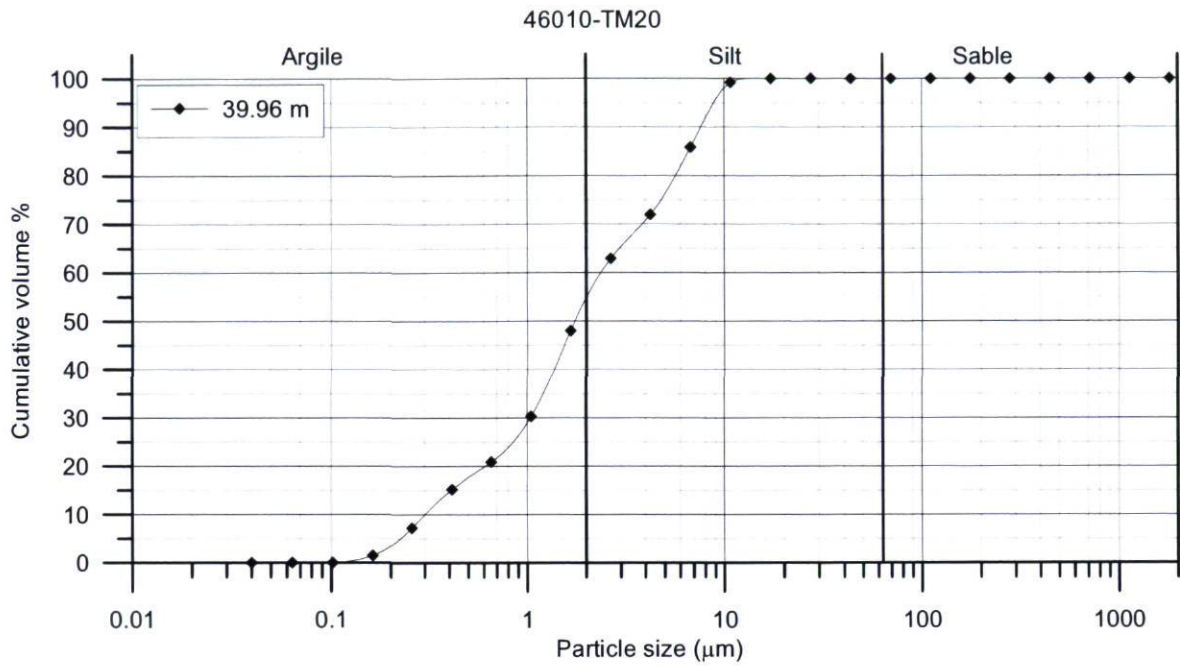


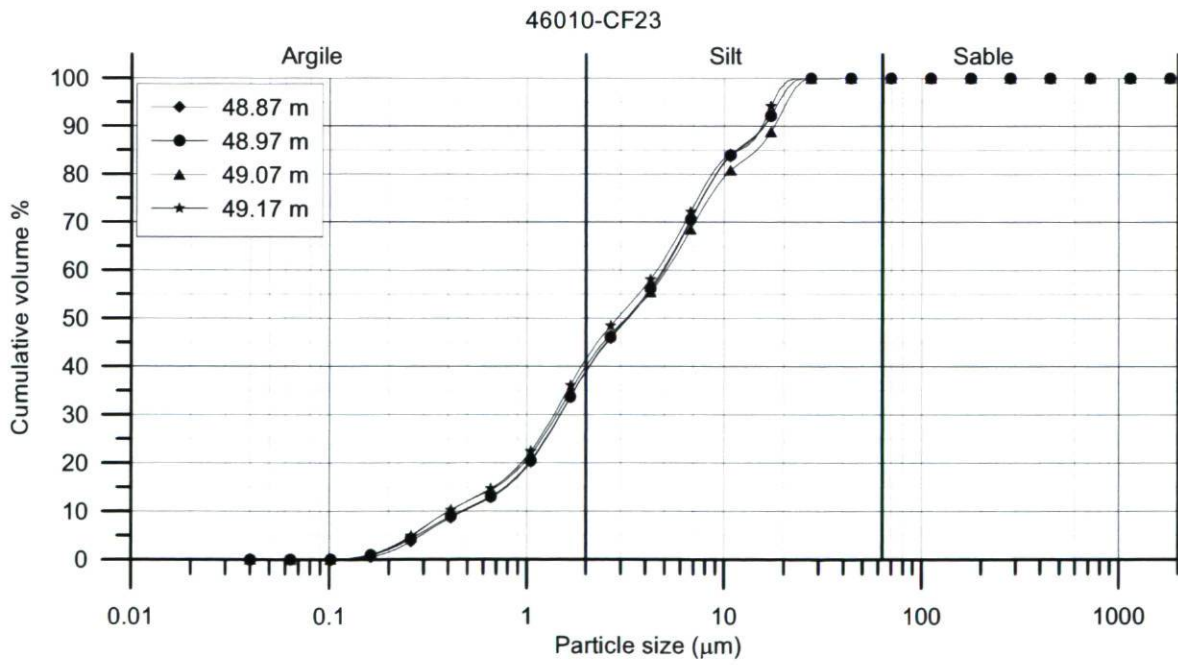
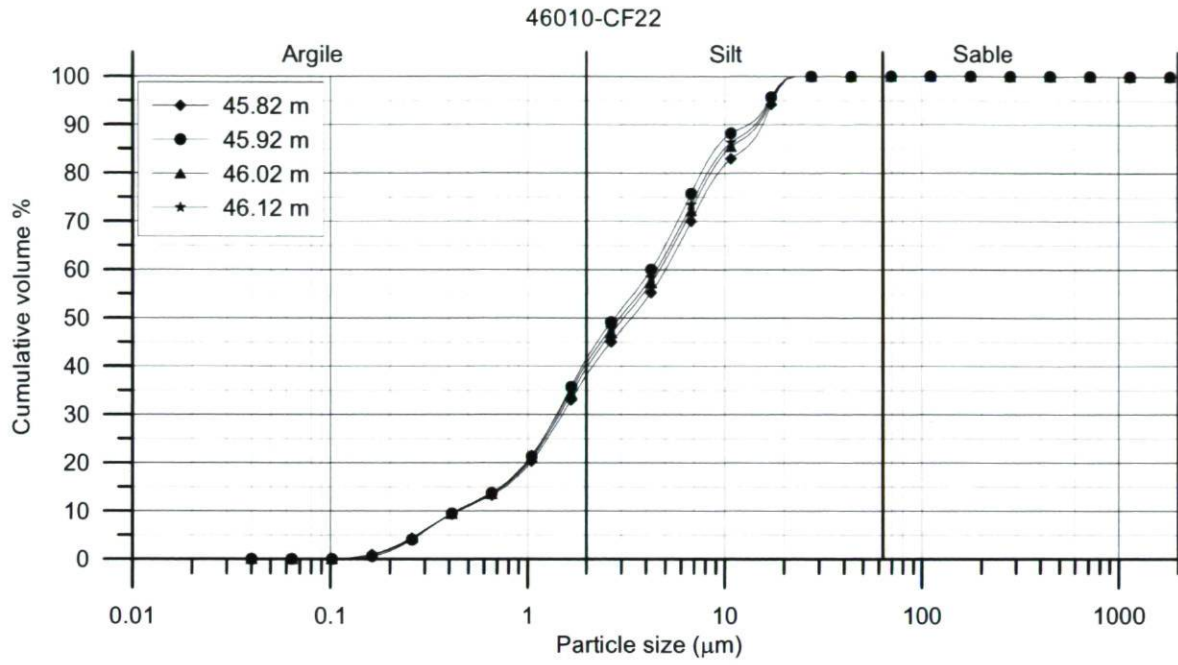


H.4.3.2 Forage 46010









H.5 Propriétés physico-chimiques

H.5.1 Chromatographie ionique de l'eau interstitielle - F46006

Échantillon	Profondeur minimum (m)	Profondeur maximale (m)	F ⁻ (mg/L)	Cl ⁻ (mg/L)	Br ⁻ (mg/L)	SO ₄ ²⁻ (mg/L)	Salinité (g/L)
CF1	4.57	4.77	0.0	28		24.1	0.03
CF2	9.19	9.24	0.6	33		291.8	0.03
CF2	9.24	9.29	1.4	14		159.2	0.01
CF3	13.82	13.87	0.5	9		241.1	0.01
CF3	14.27	14.32	1.1	12		206.1	0.01
CF4	20.40	20.45	4.0	28		227.1	0.03
CF4			4.6	97		665.0	0.10
CF5	24.20	24.25	6.4	255		138.1	0.25
CF5	24.30	24.35	5.1	239		197.5	0.24
TM6	28.02	28.12		878		100.3	0.88
TM7	32.00	32.02		809		3159.9	0.81
TM8	38.03	38.08		2272		72.6	2.27
CF9	41.15	41.20		6106	20.6	711.1	6.11
CF9	41.70	41.75	59.2	4511		199.7	4.51
TM10	43.02	43.07		937		40.4	0.94
TM11	45.72	45.72					
TM12							

H.5.2 Chromatographie ionique de l'eau interstitielle - F46010

Échantillon	Profondeur minimum (m)	Profondeur maximale (m)	F ⁻ (mg/L)	Cl ⁻ (mg/L)	Br ⁻ (mg/L)	SO ₄ ²⁻ (mg/L)	Salinité (g/L)
CFA	1.62	1.72		26		35.9	0.03
CFB	3.05	3.18		16			0.02
CF1	4.77	4.93		15		18.0	0.02
CF2	7.92	8.12		248		356.5	0.25
CF3	10.72	10.77		175		401.0	0.17
CF3	10.97	11.02		215		274.1	0.22
CF4	12.49	12.54		874		460.8	0.87
CF4	12.59	12.64		677	57.7	302.2	0.68
TM5	14.13	14.27		2087			2.1
TM6	15.54	15.69		2480			2.5
TM7	17.11	17.26		3750			3.7
TM8	18.95	18.97		6945			6.9
TM9	20.06	20.21		11934		52.7	11.9
TM10	21.59	21.74		12567		297.8	12.6
TM11							
TM12	24.48	24.63		19084		15.7	19.1
TM13	26.01	26.16		18157		55.0	18.2
TM14	27.68	27.83		17336		51.3	17.3
TM15	29.21	29.36		18631		30.7	18.6
TM16	30.49	30.55		12148		35.0	12.1
TM17	32.10	32.25		16413			16.4
TM18	33.68	33.83		12432			12.4
TM19	36.68	36.83		12693			12.7
TM20	39.65	39.69		11876	1914.0	103.3	11.9
TM21	42.72	42.92		6336			6.3
CF22	46.12	46.17		7546			7.5
CF23	49.32	49.37		7625		1803.4	7.6
CF24	52.32	52.37		3173			3.2
CF25	55.06	55.11		3791			3.8

H.5.3 Dosage de la calcite et de la dolomite

Forage	Échantillon	Profondeur minimum (m)	Profondeur maximale (m)	% calcite	% dolomite
F46006	TM6	28.04	28.12	0.000	2.84
F46006	TM10	42.70	42.79	0.000	2.31
F46010	TM08	18.42	18.53	0.000	1.36
COR0307-BET2-LEH-42		1.18	1.26	1.3	1.8

H.5.4 Surface spécifique au bleu de méthylène

Forage	Échantillon	Profondeur minimum (m)	Profondeur maximale (m)	Surface spécifique (m ² /g)
F46006	TM6	28.04	28.12	43.80
F46006	TM10	42.70	42.79	39.89
F46010	TM08	18.42	18.53	20.82
F46010	TM08	18.42	18.53	24.14
COR0307-BET2-LEH-42		1.18	1.26	88

H.5.5 Capacité d'échange cationique

Forage	Échantillon	Profondeur minimum (m)	Profondeur maximale (m)	CEC (méqu/100g)
F46006	TM6	28.04	28.12	9.1
F46006	TM10	42.70	42.79	7.9
F46010	TM08	18.42	18.53	1.2

H.6 Minéralogie

H.6.1 Tableau des analyses minéralogiques par diffraction des rayons X (DRX)

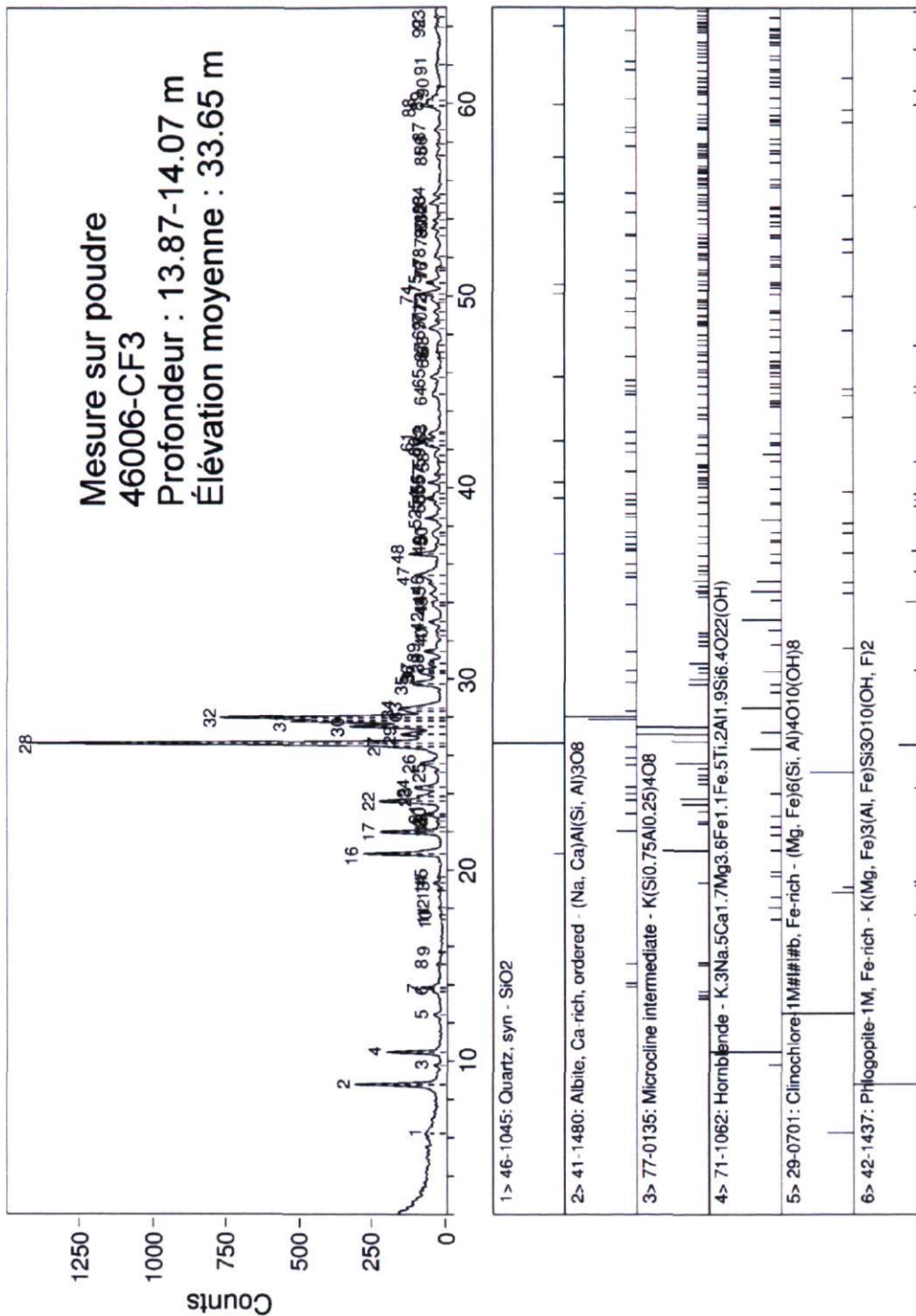
Nom de l'échantillon	X	Y	Profondeur minimum dans le forage (m)	Profondeur maximale dans le forage (m)	Élévation moyenne de la mesure (m)
F46006-CF3	516984	5416743	13.87	14.07	33.65
F46006-TM6	516984	5416743	27.49	27.54	20.10
F46006-TM10	516984	5416743	43.18	43.20	4.43
COR0307-BET2-LEH-42	525308	5399450	1.18	1.26	-345.8

En regardant globalement le spectre de chaque échantillon, on retrouve les pics associés à l'illite, au quartz, à l'albite et à la chlorite. Pas de kaolinite n'a été observée.

H.6.2 Spectres de diffraction-X obtenus sur les échantillons en poudre

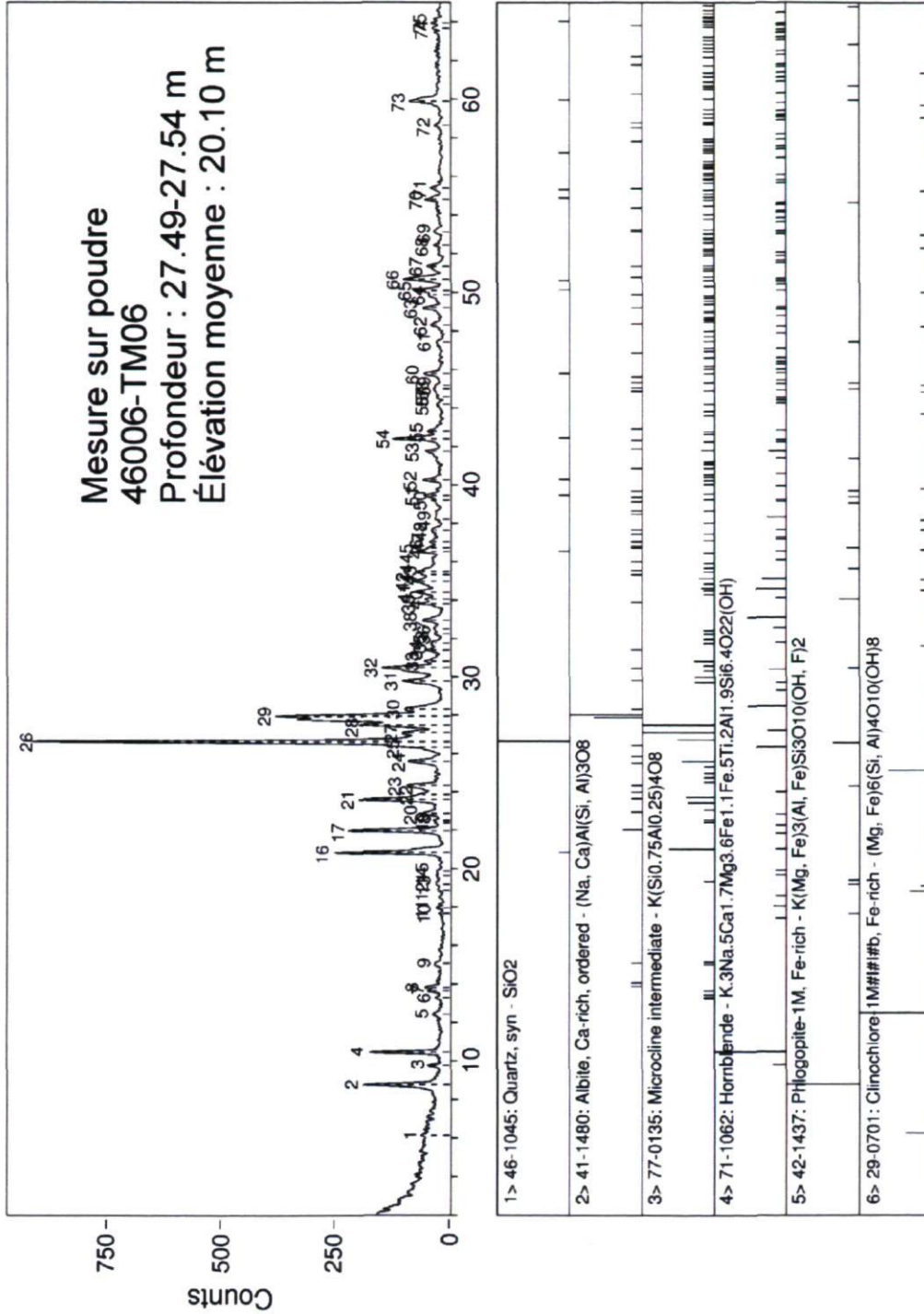
Nom de l'échantillon	Fichier sur poudre	Date d'analyse
F46006-CF3	9C24NN01	24 mars 2009
F46006-TM6	9C24OR01	24 mars 2009
F46006-TM10	9C25IN01	25 mars 2009
COR0307-BET2-LEH-42	4L03IS03	3 décembre 2004

ID: 9C24NN01, 24-Mar-2009 14:45
 File: 9C24NN01.RAW Scan: 2-65/02/ 1.2/#3151, Anode: CU

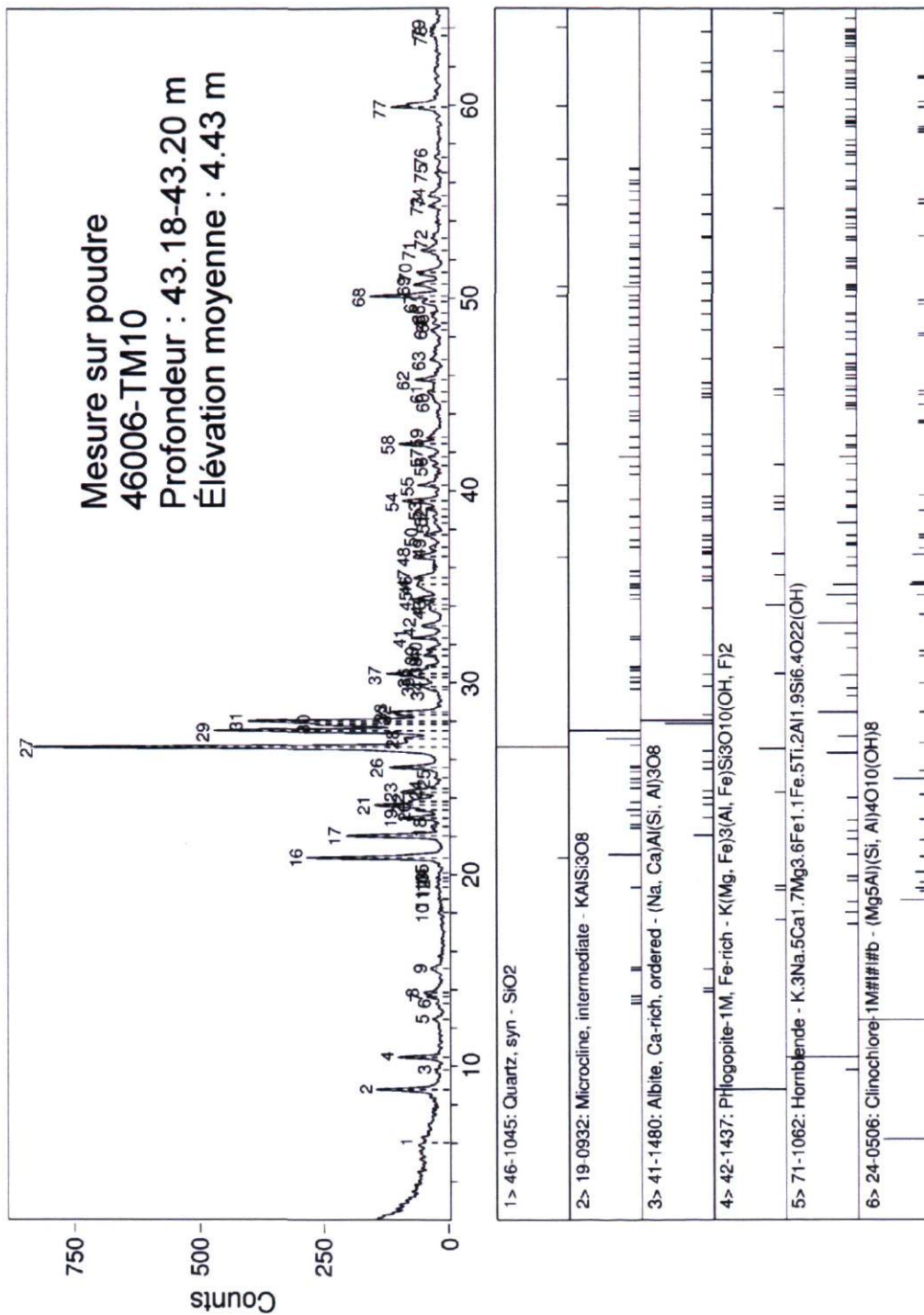


ID: 9C24OR01, 24-Mar-2009 15:57
 File: 9C24OR01.RAW Scan: 2-65/02/ 1.2/#3151, Anode: CU

Mesure sur poudre
 46006-TM06
 Profondeur : 27.49-27.54 m
 Élévation moyenne : 20.10 m

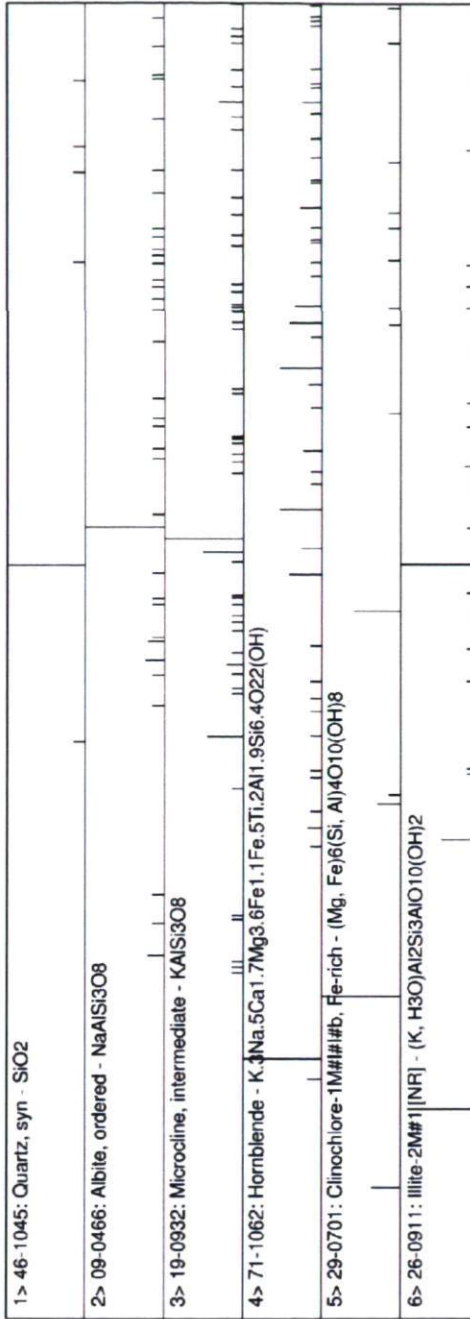
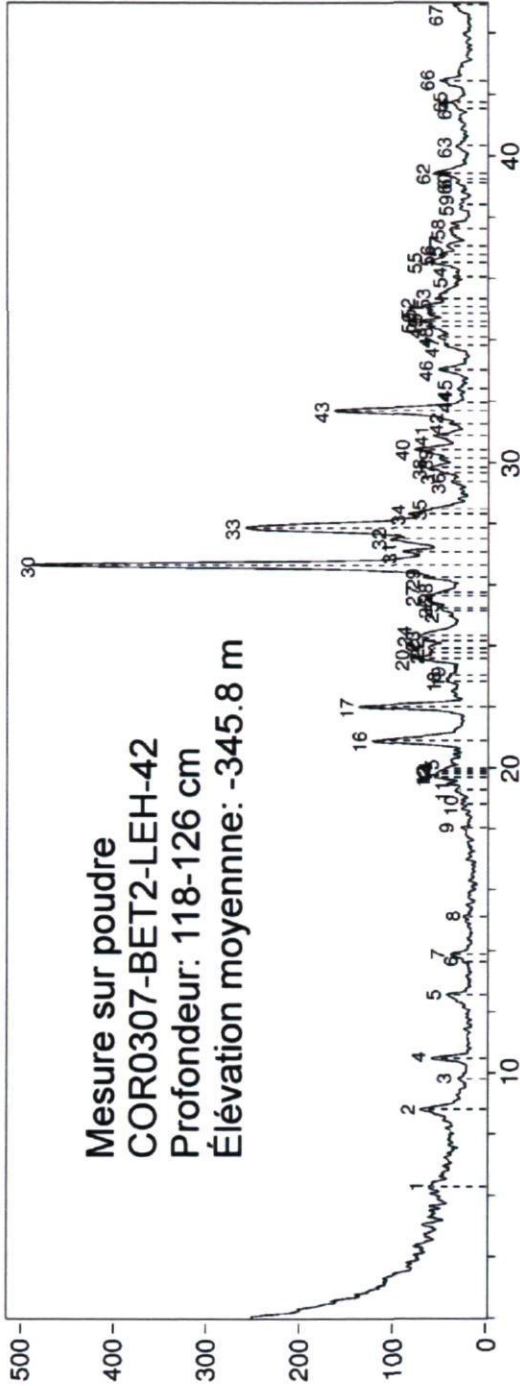


ID: 9C25IN01, 25-Mar-2009 09:44
 File: 9C25IN01.RAW Scan: 2-65/02/ 1.2/#3151, Anode: CU 2T(0)= .02



ID: 4L03IS03, 03-Dec-2004 11:08
 File: 4L03IS03.RAW Scan: 2-45/.02/ 1.2/#2151, Anode: CU 2T(0)=-.02

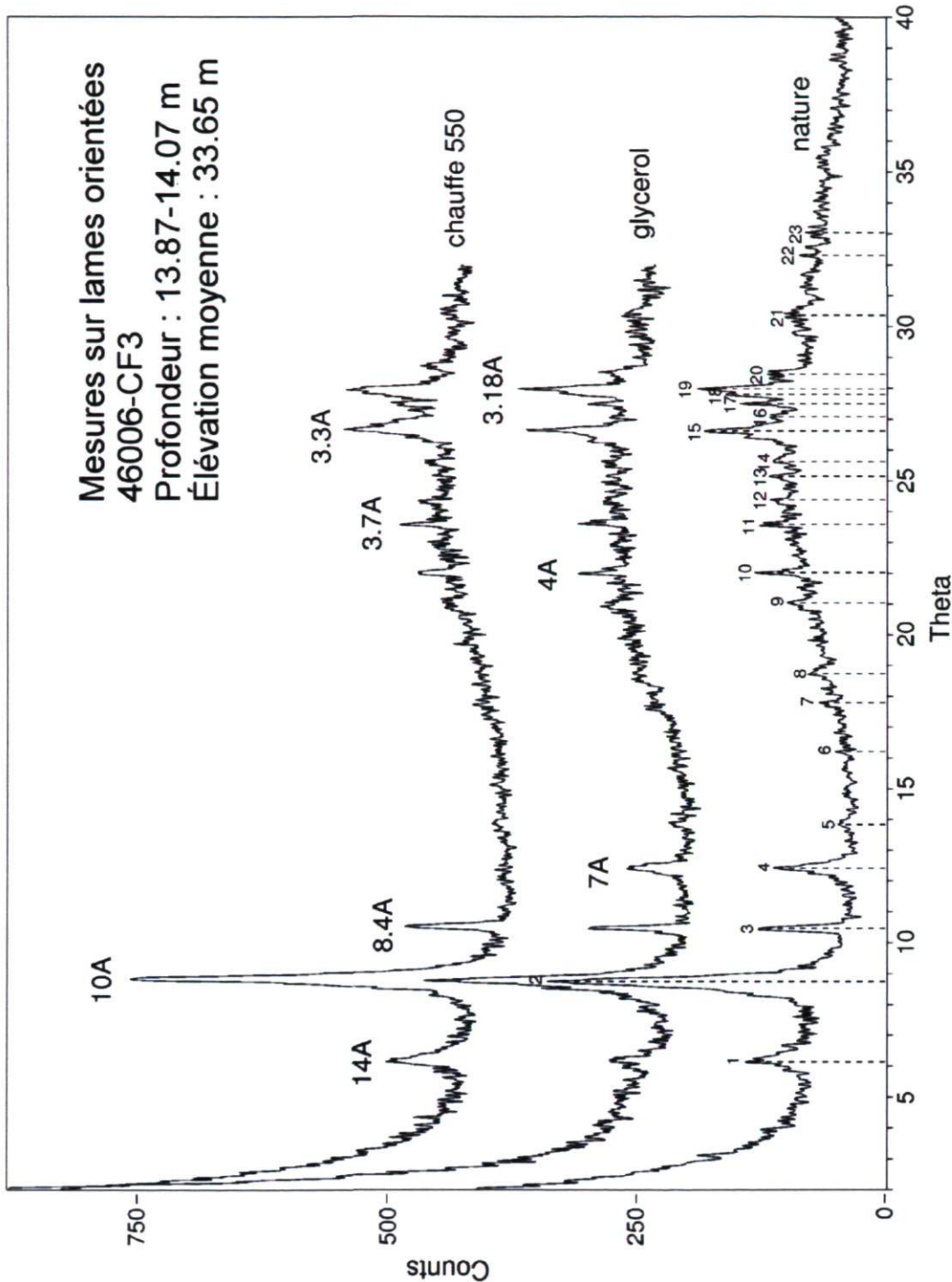
Mesure sur poudre
 COR0307-BET2-LEH-42
 Profondeur: 118-126 cm
 Élévation moyenne: -345.8 m



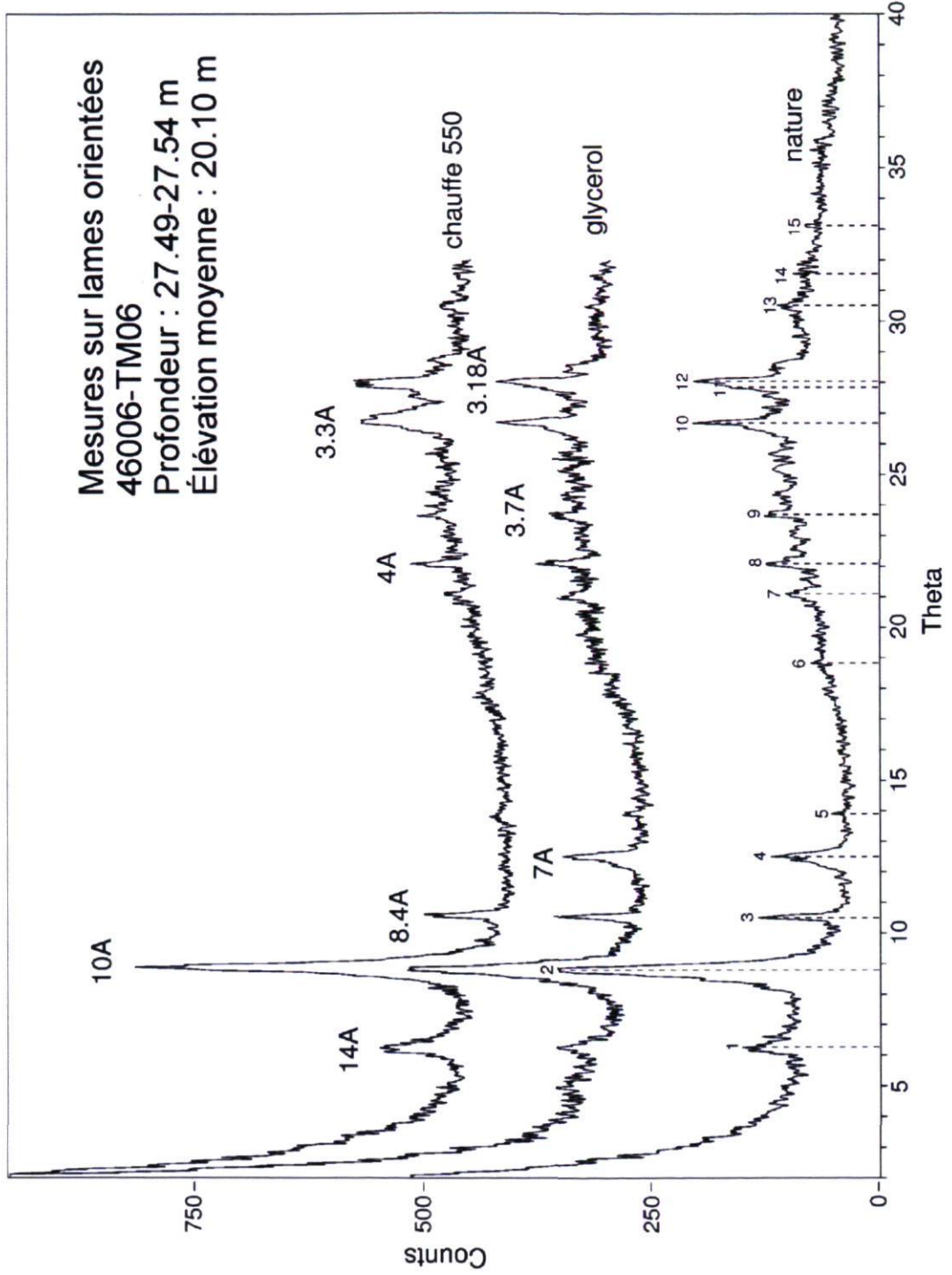
H.6.3 Spectres de diffraction-X des échantillons sur lames orientées

Nom de l'échantillon	Lame orientée nature	Lame orientée glycérolée	Lame orientée chauffée	Dates d'analyse
F46006-CF3	9C25KC01	9C26IE01	9C26NQ01	25, 26 mars 2009
F46006-TM6	9C25KC02	9C26IE02	9C26NQ02	25, 26 mars 2009
F46006-TM10	9C25KC03	9C26IE03	9C26NQ03	25, 26 mars 2009
COR0307-BET2-LEH-42	4L02OM03	4L03ND03	4L06LQ03	2, 3 et 6 décembre 2004

ID: 9C25KC01, 25-Mar-2009 10:46
File: 9C25KC01.DIF Scan: 2-40/.02/ 1.2/#1901, Anode: CU



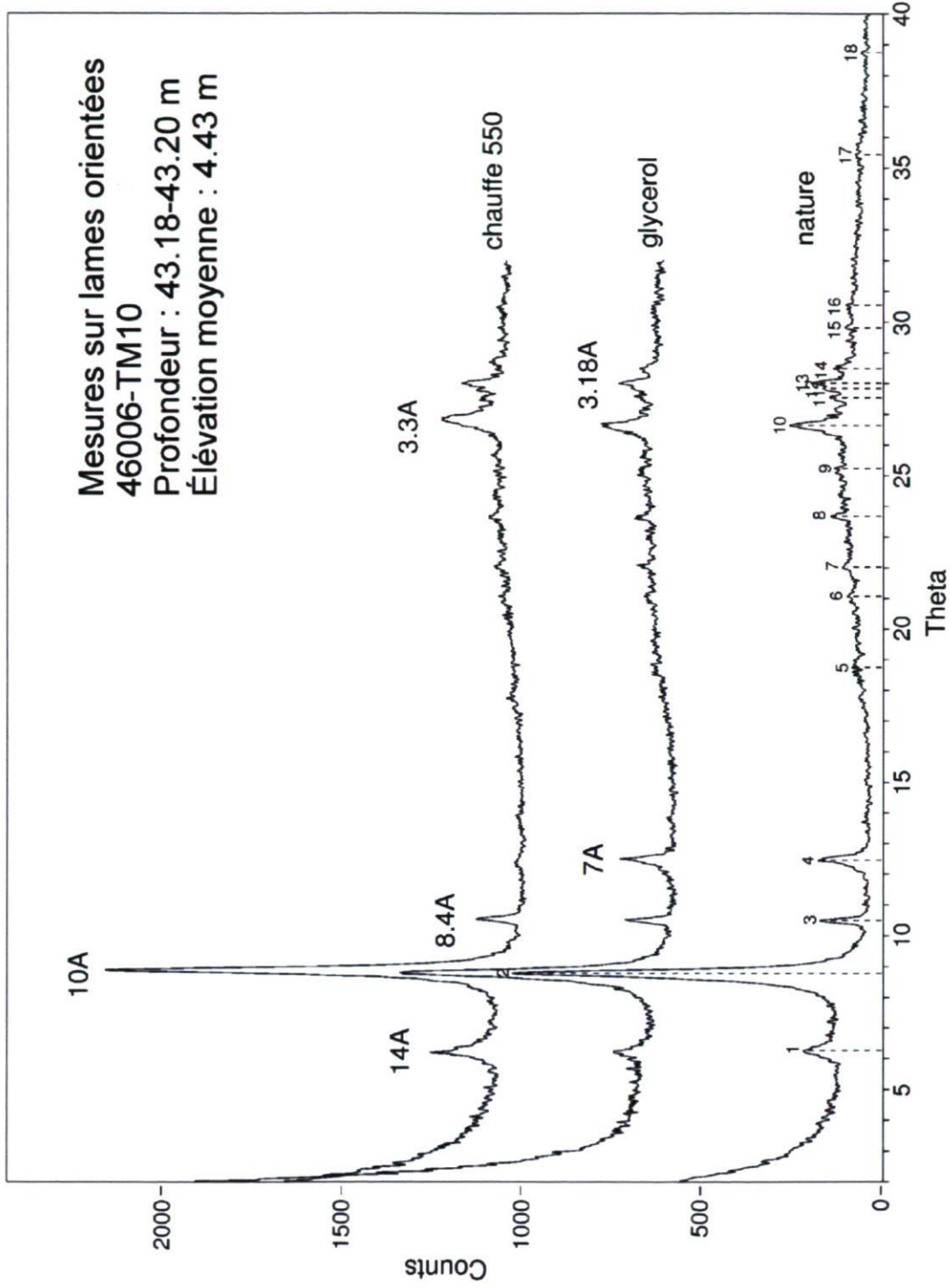
ID: 9C25KC02, 25-Mar-2009 11:25
File: 9C25KC02.DIF Scan: 2-40/.02/ 1.2/#1901, Anode: CU



ID: 9C25KC03, 25-Mar-2009 12:03

File: 9C25KC03.DIF

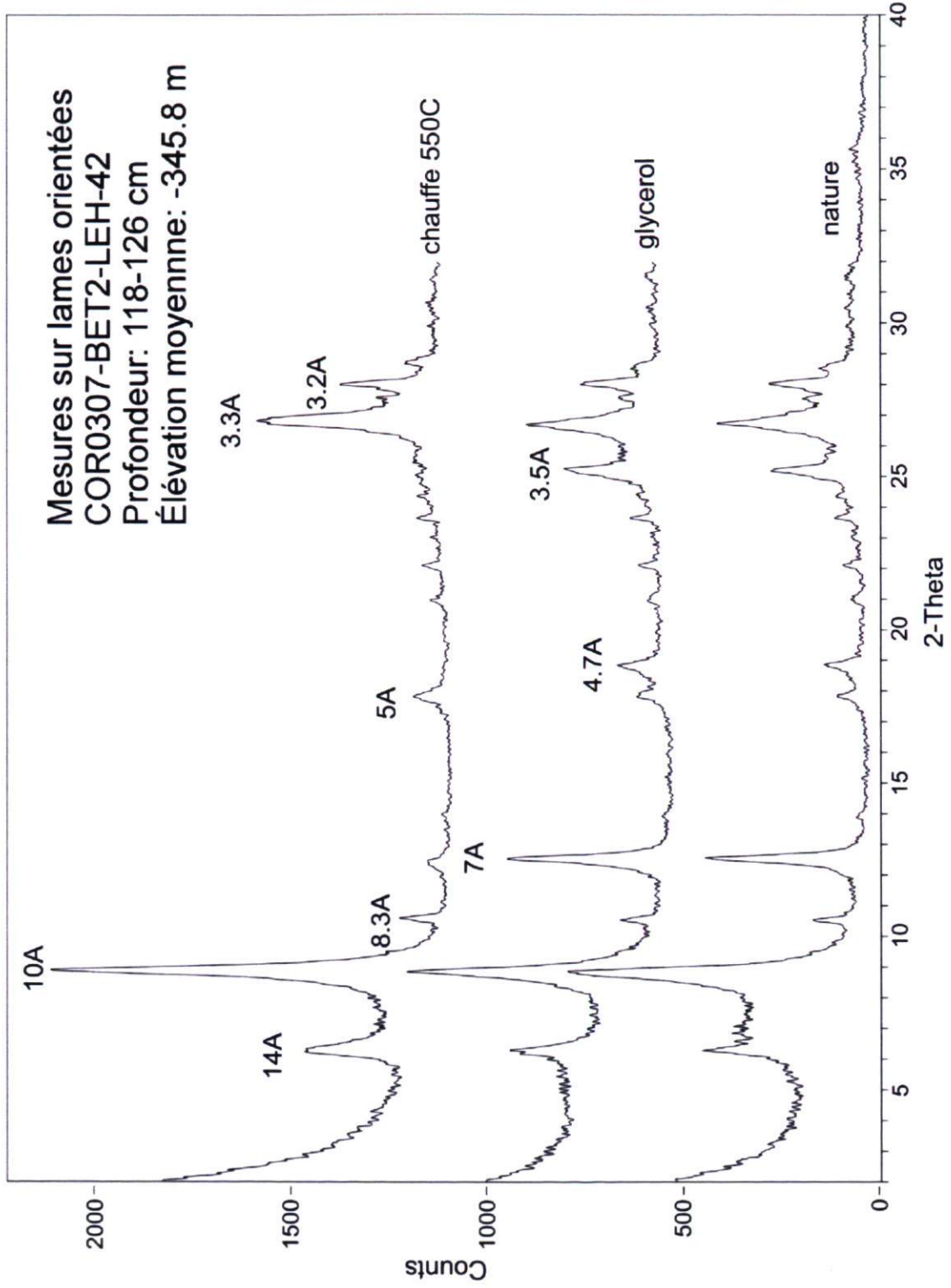
Scan: 2-40/.02/ 1.2/#1901, Anode: CU



ID: 4L02OM03, 02-Dec-2004 16:34

File: 4L02OM03.DIF

Scan: 2-40/02/ 1.2/#1901, Anode: CU



H.7 Analyse microstructurale à l'aide du microscope électronique à balayage

H.7.1 Tableau des analyses au MEB

Nom de l'échantillon	X	Y	Profondeur minimum dans le forage (m)	Profondeur maximale dans le forage (m)	Élévation moyenne (m)
F46006-TM6	516984	5416743	28.02	28.12	19.55
F46006-TM10	516984	5416743	42.70	42.79	4.85
F46010-TM8	519128	5415969	18.42	18.47	-10.61
BET2-LEH-42	525308	5399450	1.18	1.26	-345.8

H.7.2 Grille d'analyses F46006-TM06

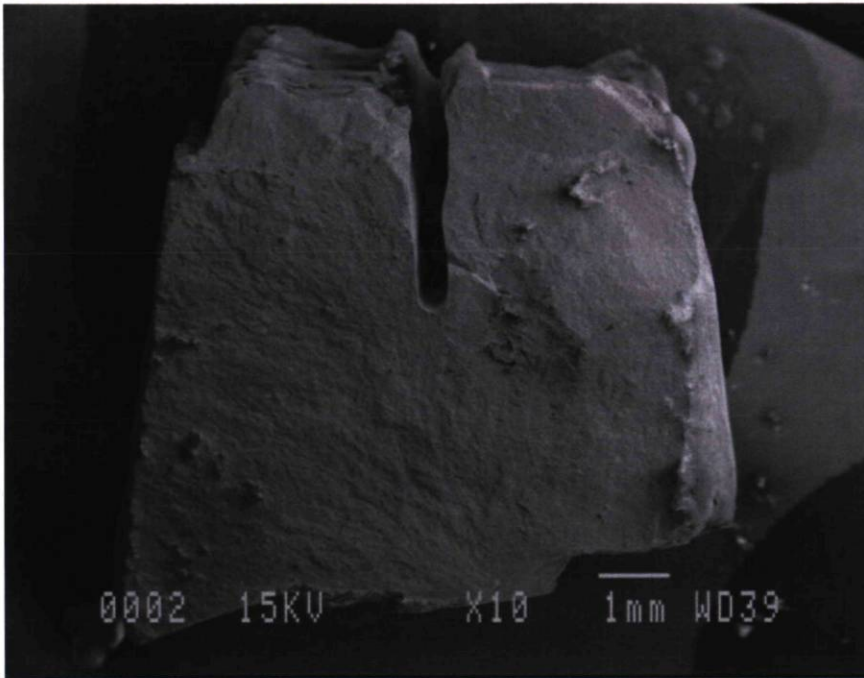
IDENTIFICATION

Site	Forage	Échantillon	Profondeur	Élévation moyenne
Colombier - escarpement	F46006	TM06	28.02-28.12 m	19.55 m

PROPRIÉTÉS

w _n	w _p	w _L	I _L	I _p	Fraction argile	Activité	Cu	Cur	St
37 %	13 %	23 %	2.4	10 %	50.5 %	0.20	109 kPa	0.09 kPa	1202

PHOTOS DE L'ÉCHANTILLON



Salinité	0.88 g/L
SS	43.80 m ² /g
CEC	9.1 equ/100 g
Calcite	0 %
Dolomite	2.84 %

QUALITE DE LA PREPARATION

COMMENTAIRES

Gel/Séchage	Bonne	
État de la surface :	Plane	
Coupe (H ou V)	Verticale	
Polarité	Conservée	
Remarque :		

ÉCHANTILLON : F46006-TM06 ÉLÉVATION MOYENNE : 19.55 m

PARTICULES ELEMENTAIRES, TYPE ET FORME

		Sable 2mm – 63 um	Silt 63 – 2 um	Argile < 2 um	Matière organique	Diatomée	Foram.
	Quantité	Trace	Présence	Abondance		Trace	
Particules	Arrondie						
	Angulaire	x	x	x			
	Plate		x	x			
	Flocon			x			
Micro-organismes	Centrique					X	
	Pennée					Brisées (?)	
	Tubulaire						
	Aiguille						
	Brisé					x	
	Taille (mm)						
	Remarque	Silt très angulaire, traces de diatomées brisées					

MICROFABRIQUE DE L'ASSEMBLAGE

	Taille (um)	Rond	Angulaire	Orientation aléatoire	Orientation stratifiée
Agrégats	2-10	X		X	
Flocons			x		
Pellets					
Remarque					

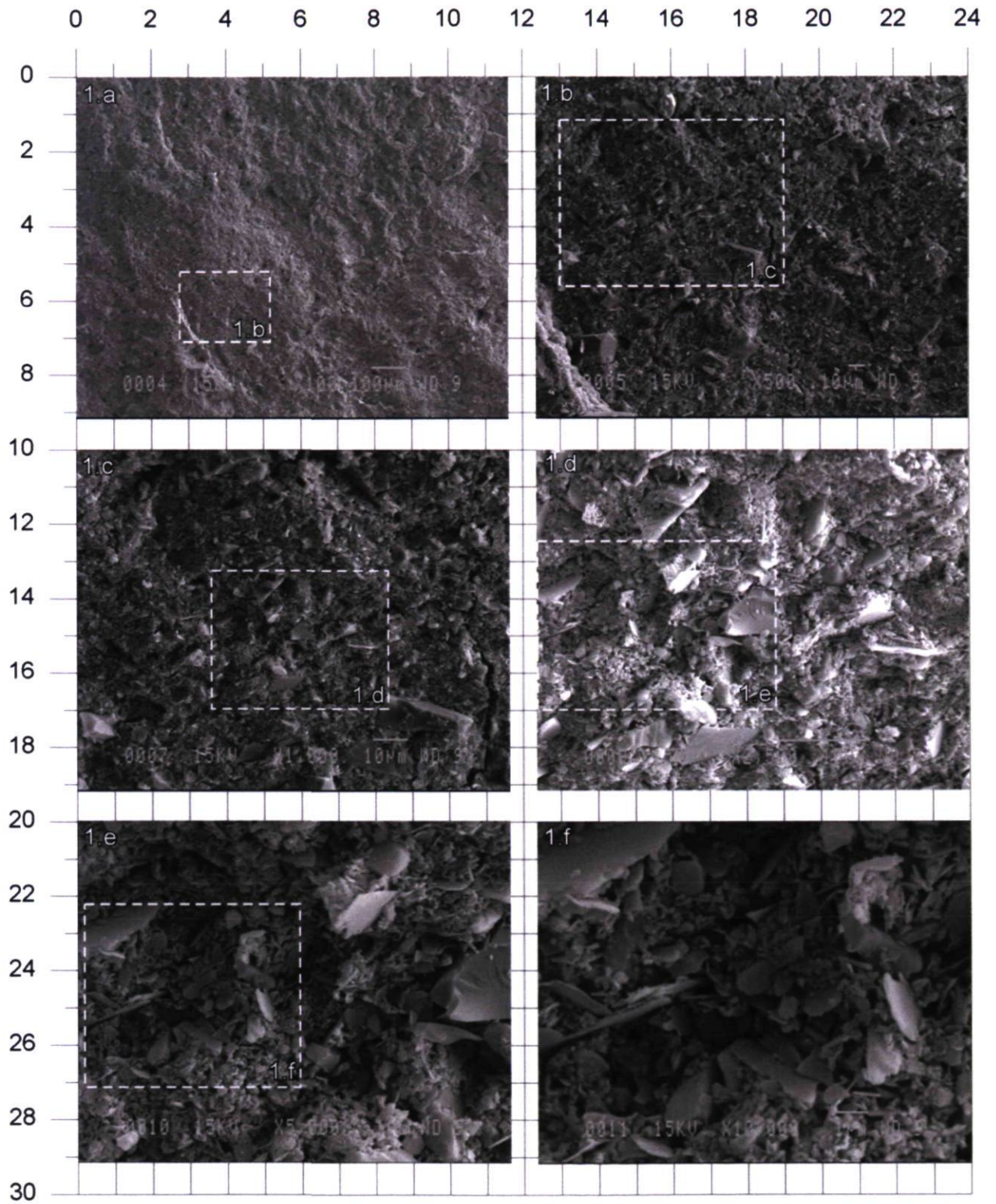
PORES

	Inter-agrégats	Intra- agrégats	Intra-squelettique	Squelettique
Diamètre	0.5 – 5 um	< 0.5 um	1-10 um	< 1 um
Rond				x
Irrégulier	x	x	x	
Remarque				

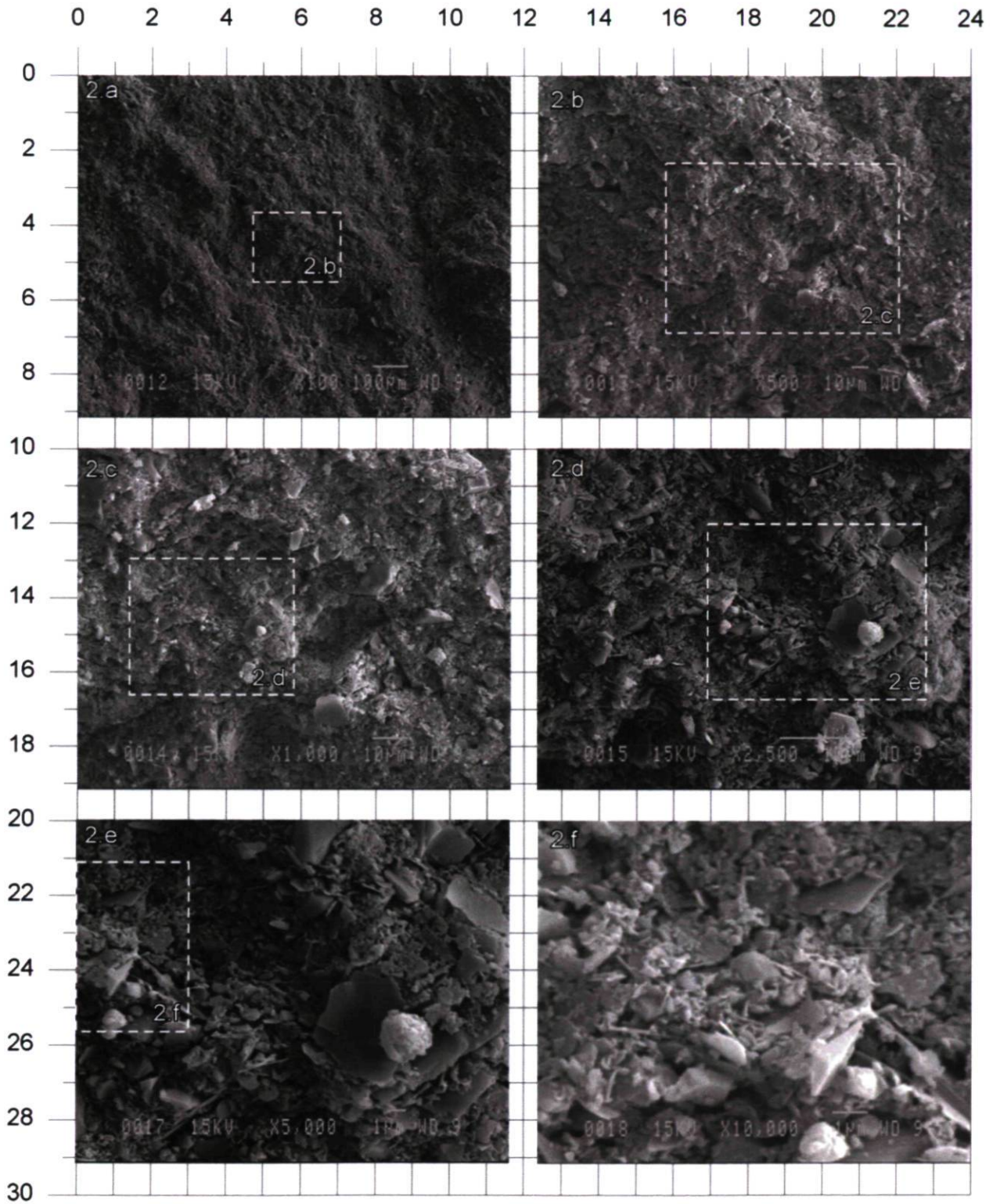
AUTRES ELEMENTS MICROSTRUCTURAUX

	Ouverture	Longueur	Épaisseur	Orientation aléatoire	Orienté
Fissures	1 um	> 10 um		x	
Ponts					
Vides					
Remarque					

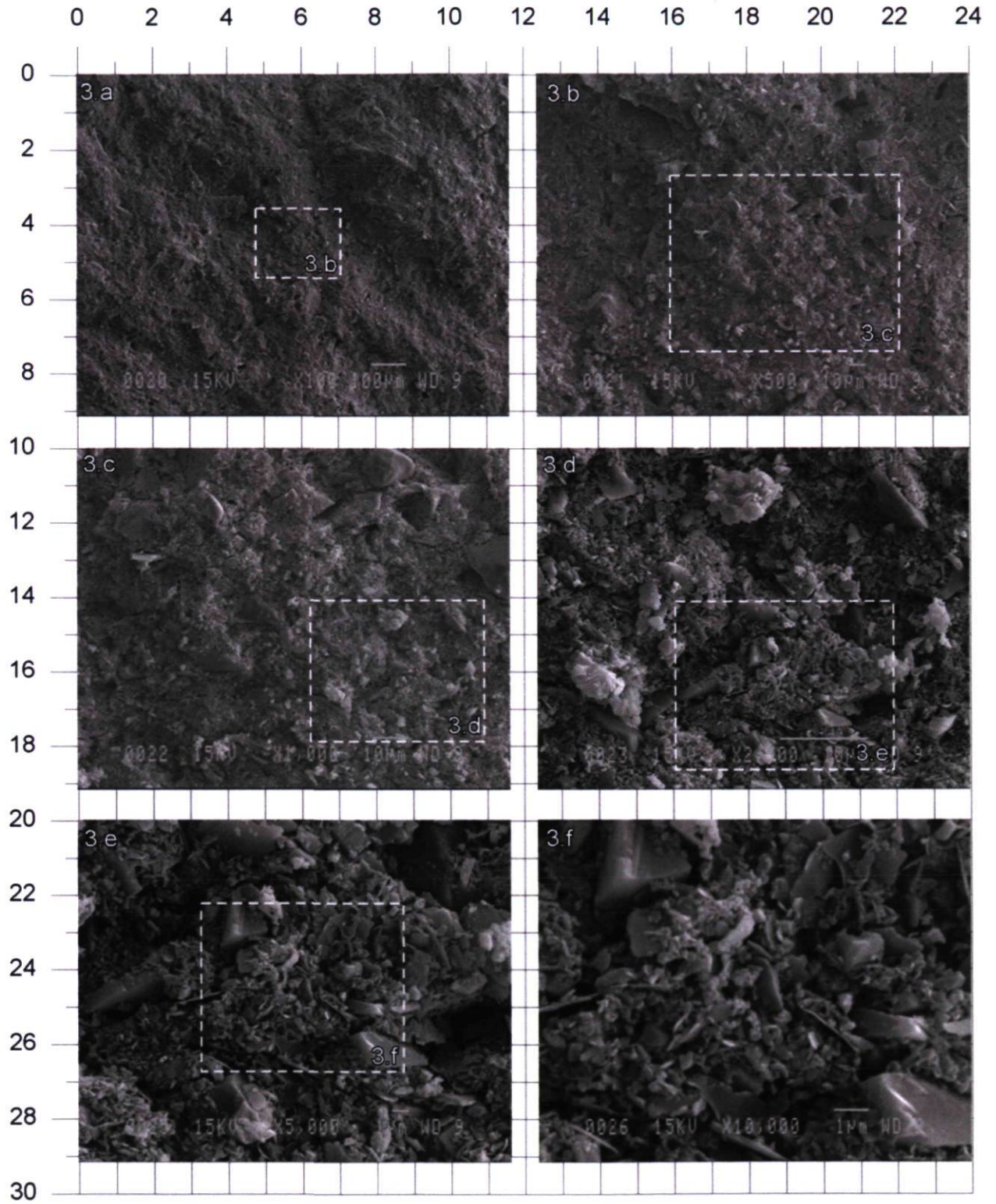
Échantillon : F46006-TM06 Série : 1
Élévation moyenne : 19.55 m Images : a à f



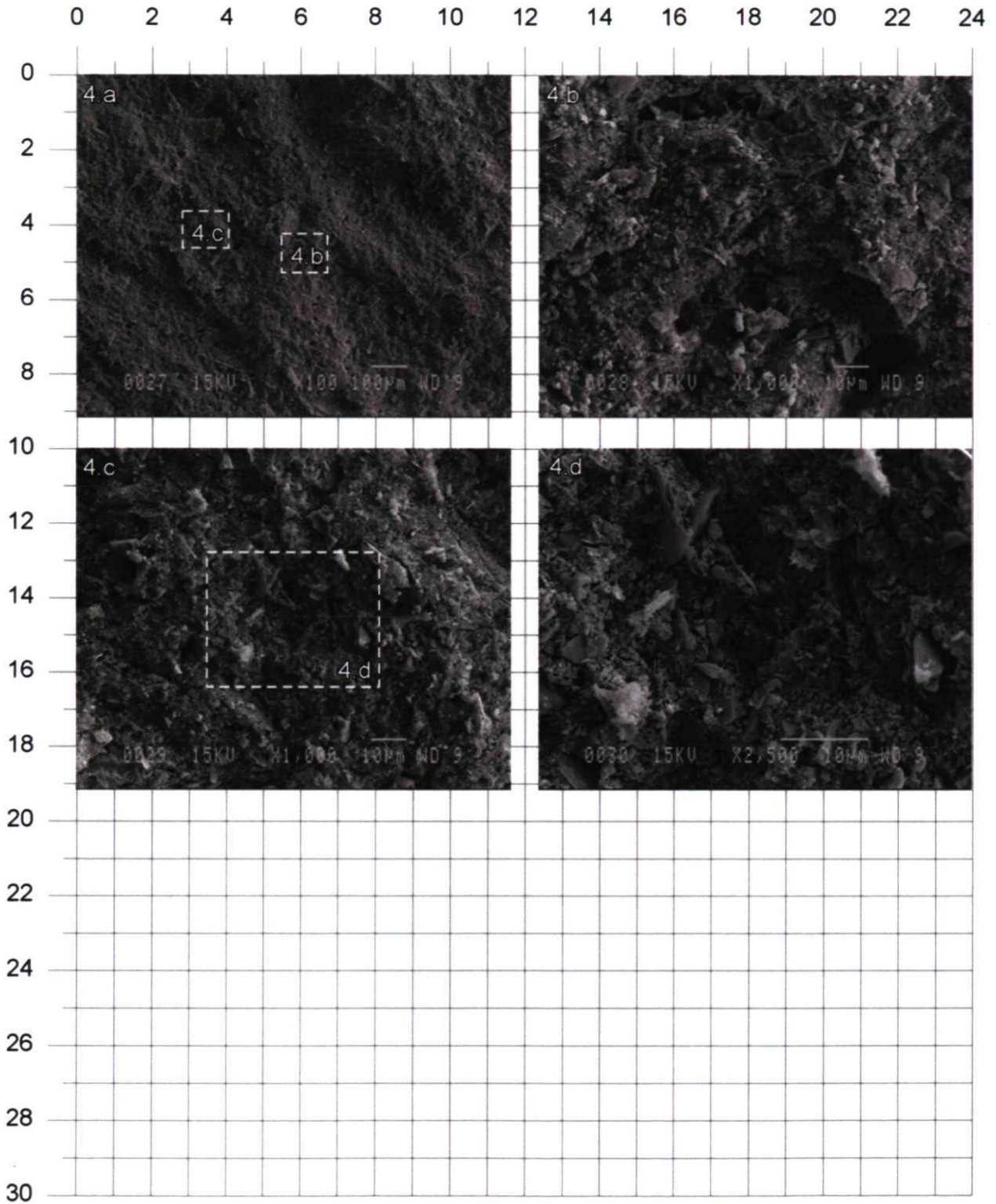
Échantillon : F46006-TM06 Série : 2
 Élévation moyenne : 19.55 m Images : a à f



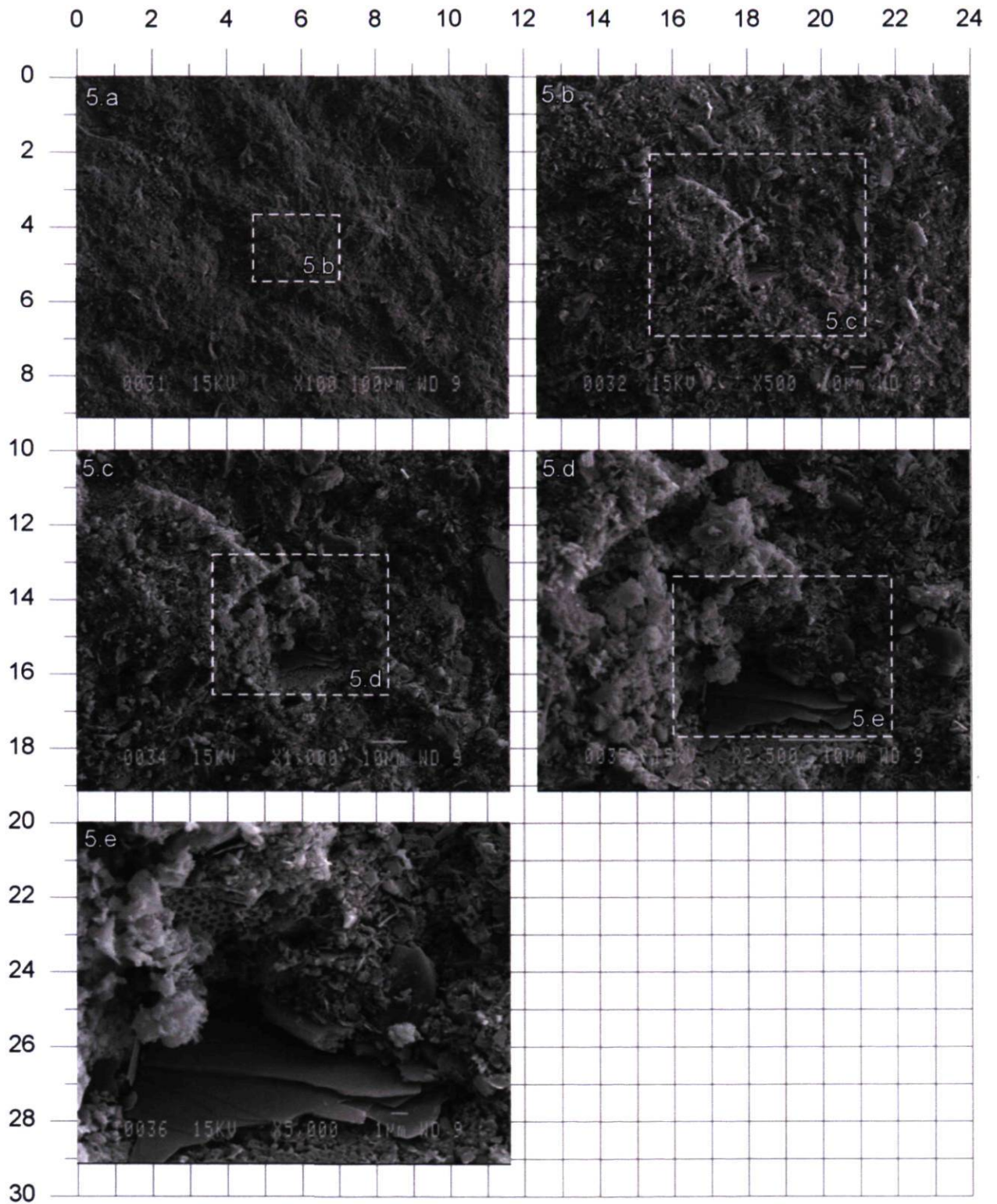
Échantillon : F46006-TM06 Série : 3
Élévation moyenne : 19.55 m Images : a à f



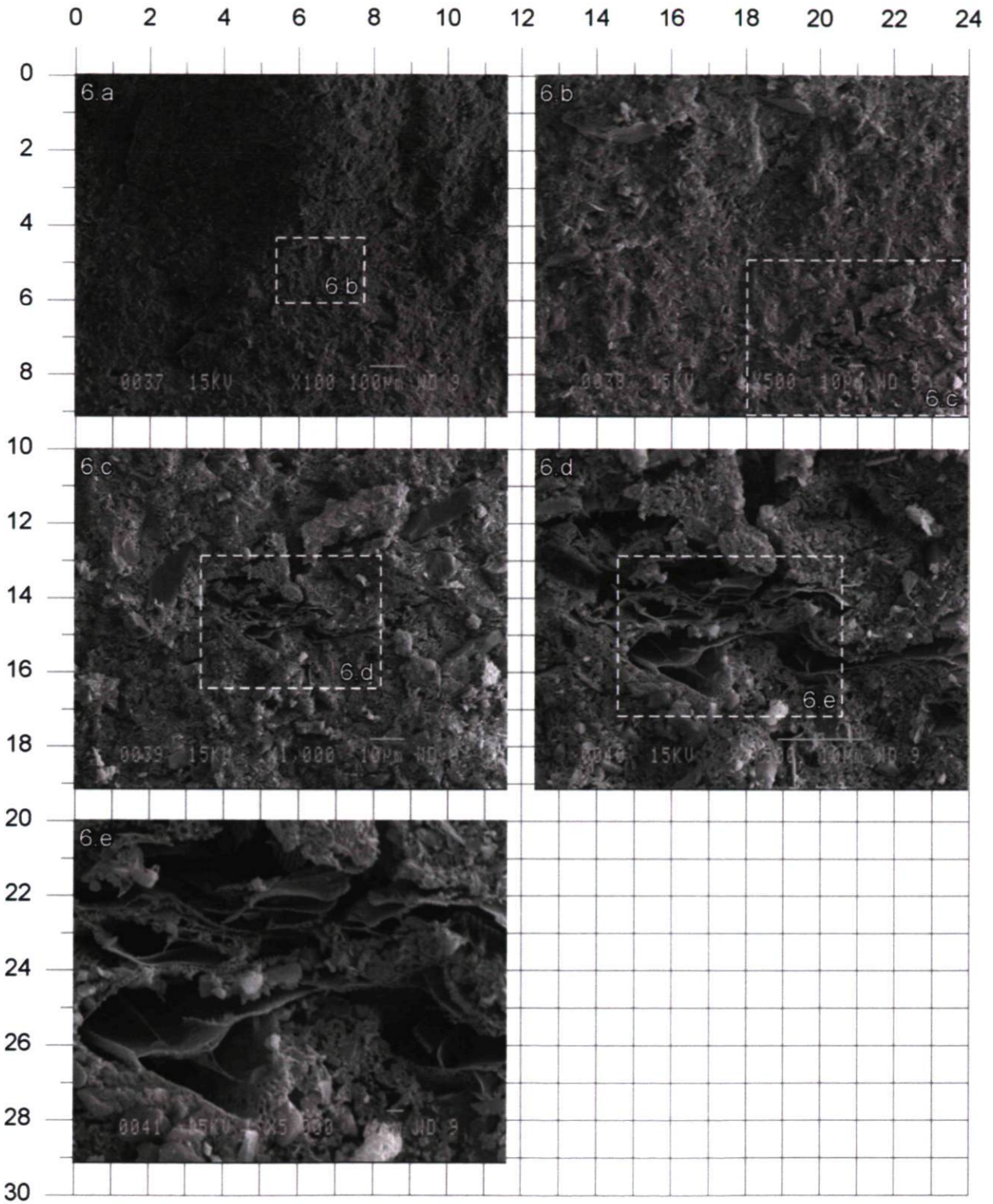
Échantillon : F46006-TM06 Série : 4
Élévation moyenne : 19.55 m Images : a à d



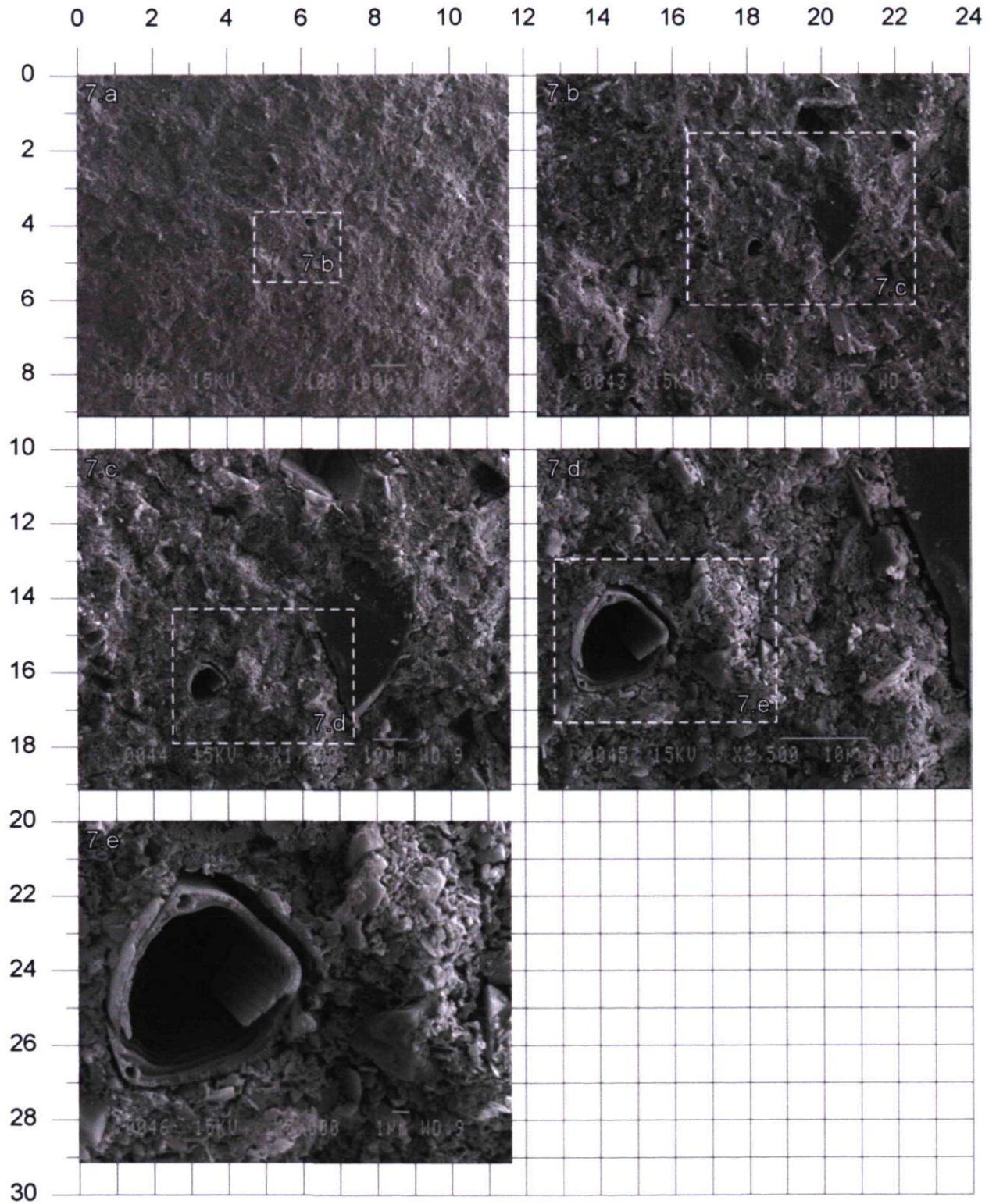
Échantillon : F46006-TM06 Série : 5
Élévation moyenne : 19.55 m
Images : a à e



Échantillon : F46006-TM06 Série : 6
 Élévation moyenne : 19.55 m Images : a à e



Échantillon : F46006-TM06 Série : 7
Élévation moyenne : 19.55 m



H.7.3 Grille d'analyses F46006-TM010

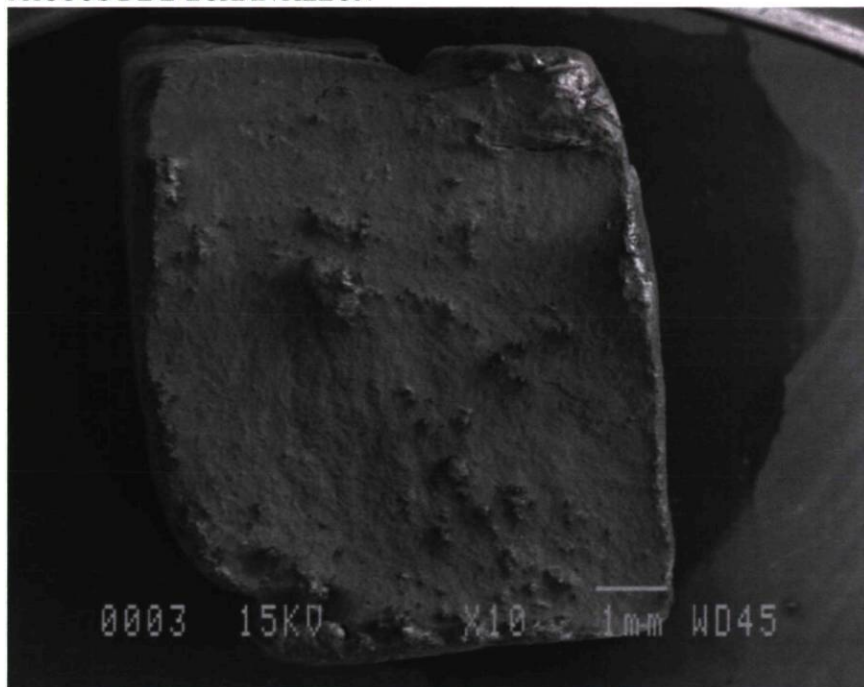
IDENTIFICATION

Site	Forage	Échantillon	Profondeur	Élévation moyenne
Colombier - escarpement	F46006	TM10	42.72 - 42.81 m	4.85 m

PROPRIÉTÉS

w _n	w _p	w _L	I _L	I _p	Fraction argile	Activité	Cu	Cur	St
38 %	29 %	46%	0.7	29	39 %	0.74	136 kPa	11 kPa	12

PHOTOS DE L'ÉCHANTILLON



Salinité	12.6
SS	39.89 m ² /g
CEC	7.9 equ/100 g
Calcite	0 %
Dolomite	2.31 %

QUALITE DE LA PREPARATION

COMMENTAIRES

Gel/Séchage	Bonne	
État de la surface :	Plane	
Coupe (H ou V)	Verticale	
Polarité	Conservée	
Remarque :	Petites fractures	

ÉCHANTILLON : F46006-TM10 ÉLÉVATION MOYENNE : 4.85 m

PARTICULES ELEMENTAIRES, TYPE ET FORME

		Sable 2mm – 63 um	Silt 63 – 2 um	Argile < 2 um	Matière organique	Diatomée	Foram.
	Quantité	Trace	Présence	Abonadanc e			
Particules	Arrondie						
	Angulaire	x	x				
	Plate			x			
	Flocon			x			
Micro-organismes	Centrique						
	Pennée						
	Tubulaire						
	Aiguille						
	Brisé						
	Taille (mm)						
	Remarque	Aucun micro-organisme trouvé					

MICROFABRIQUE DE L'ASSEMBLAGE

	Taille (um)	Rond	Angulaire	Orientation aléatoire	Orientation stratifiée
Agrégats	1-100	x	x	x	
Flocons	< 5			X	
Pellets					
Remarque	Plusieurs agrégats et beaucoup de particules en flocons				

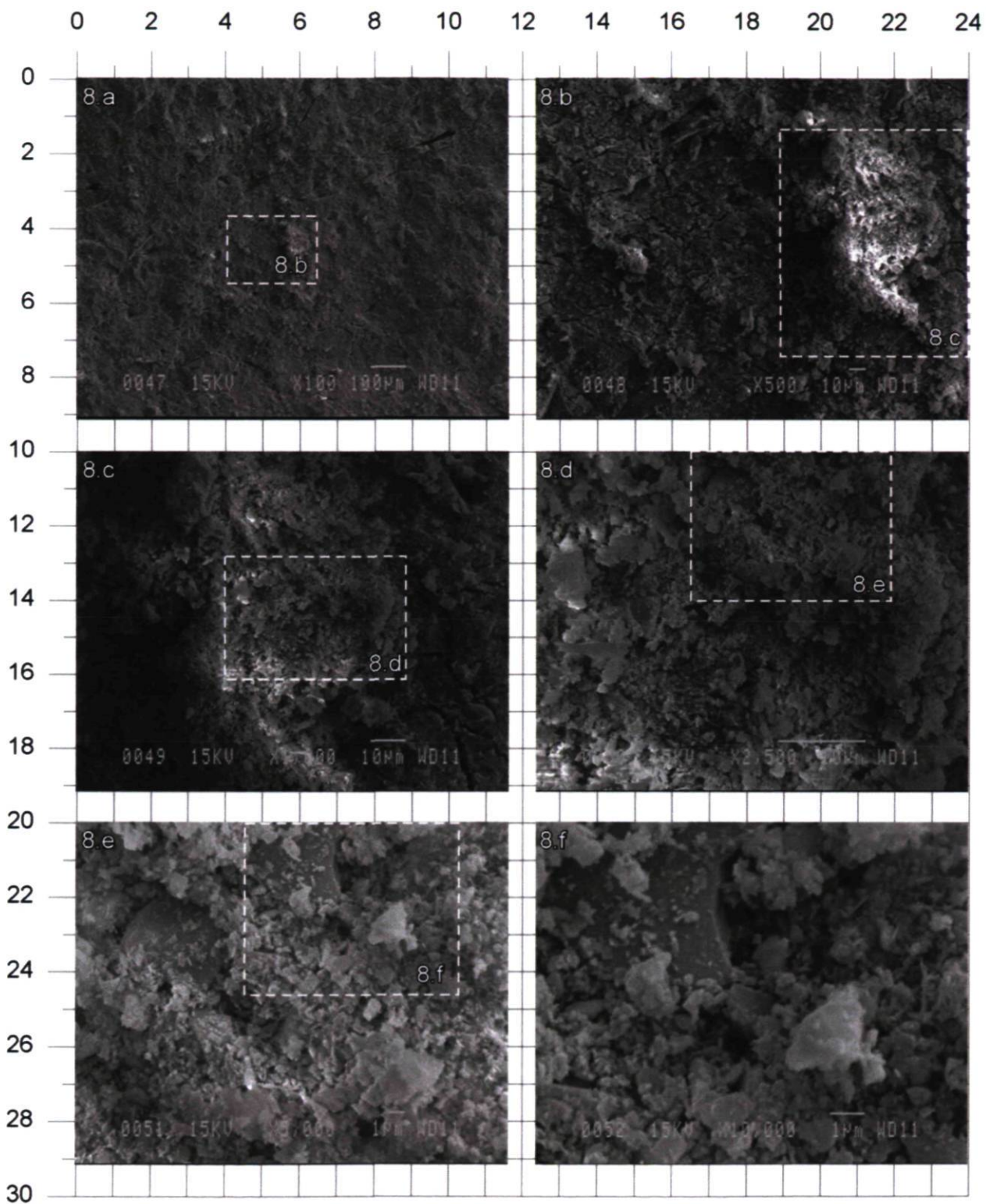
PORES

	Inter-agrégats	Intra- agrégats	Intra-squelettique	Squelettique
Diamètre				
Rond				
Irrégulier				
Remarque				

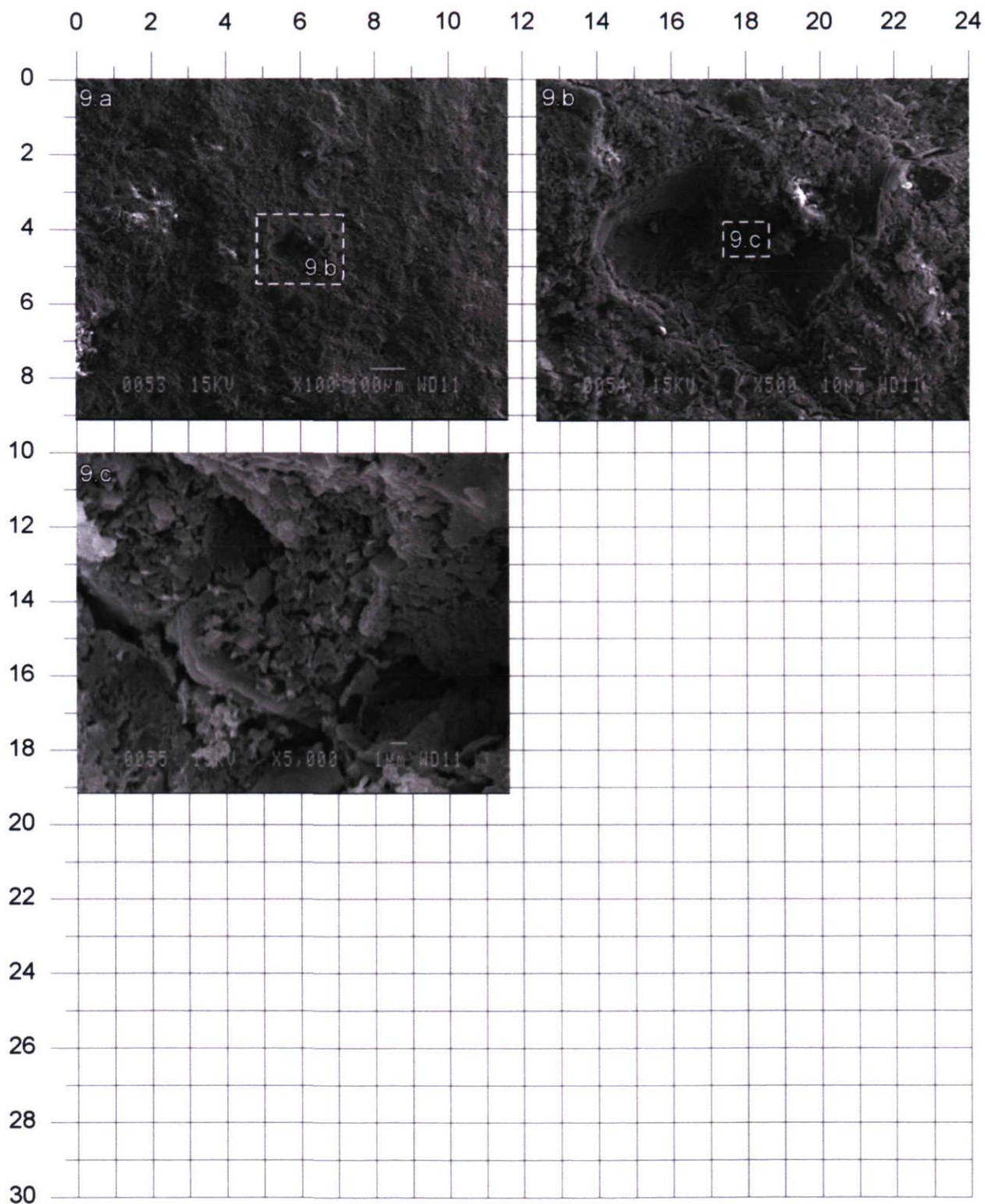
AUTRES ELEMENTS MICROSTRUCTURAUX

	Ouverture	Longueur	Épaisseur	Orientation aléatoire	Orienté
Fissures	2 um	2-30 um		x	
Ponts					
Vides					
Remarque	Beaucoup de petites fissures				

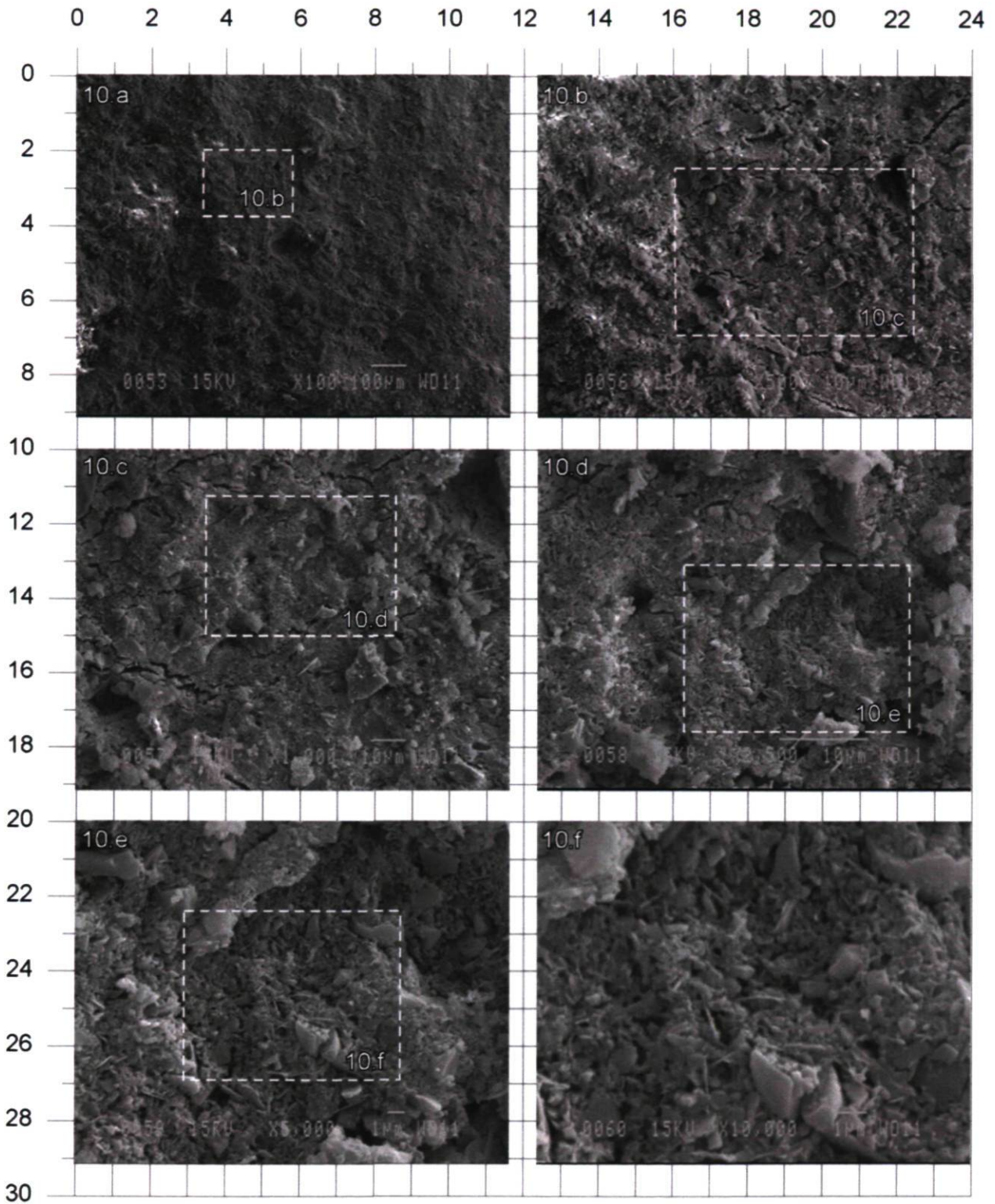
Échantillon : F46006-TM10 Série : 8
Élévation moyenne : 4.85 m Images : a à f



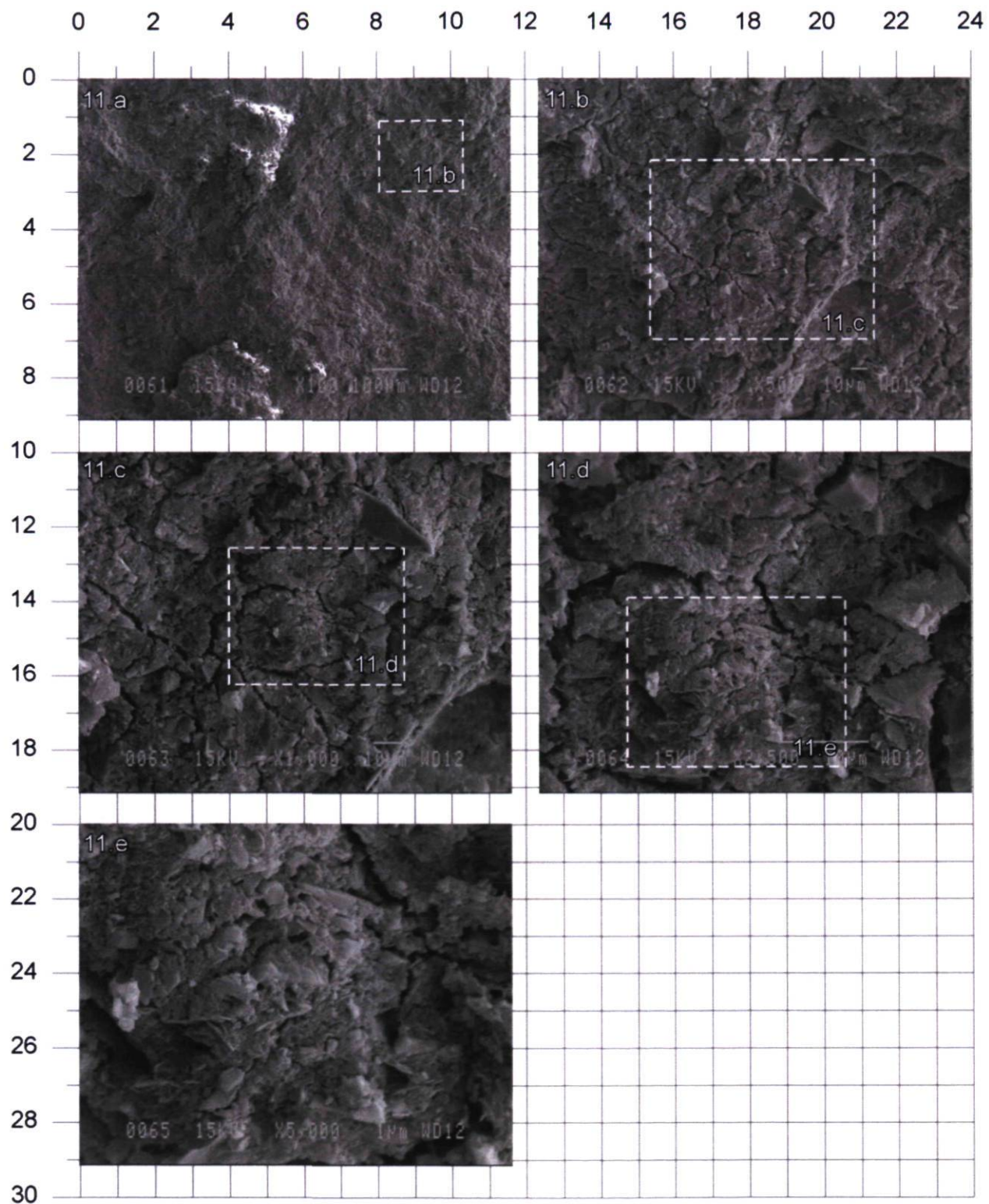
Échantillon : F46006-TM10 Série : 9
Élévation moyenne : 4.85 m Images : a à c



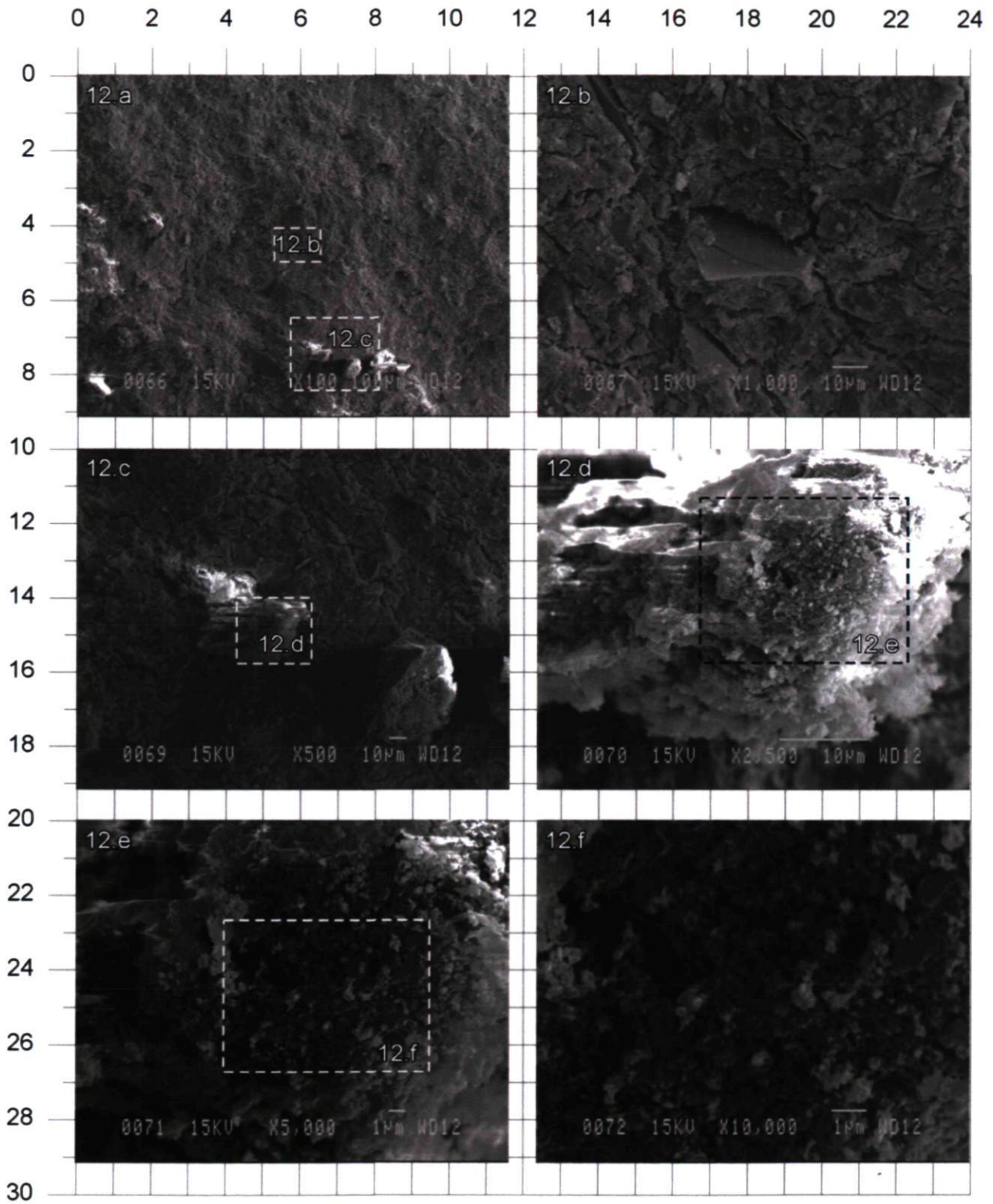
Échantillon : F46006-TM10 Série : 10
 Élévation moyenne : 4.85 m Images : a à f



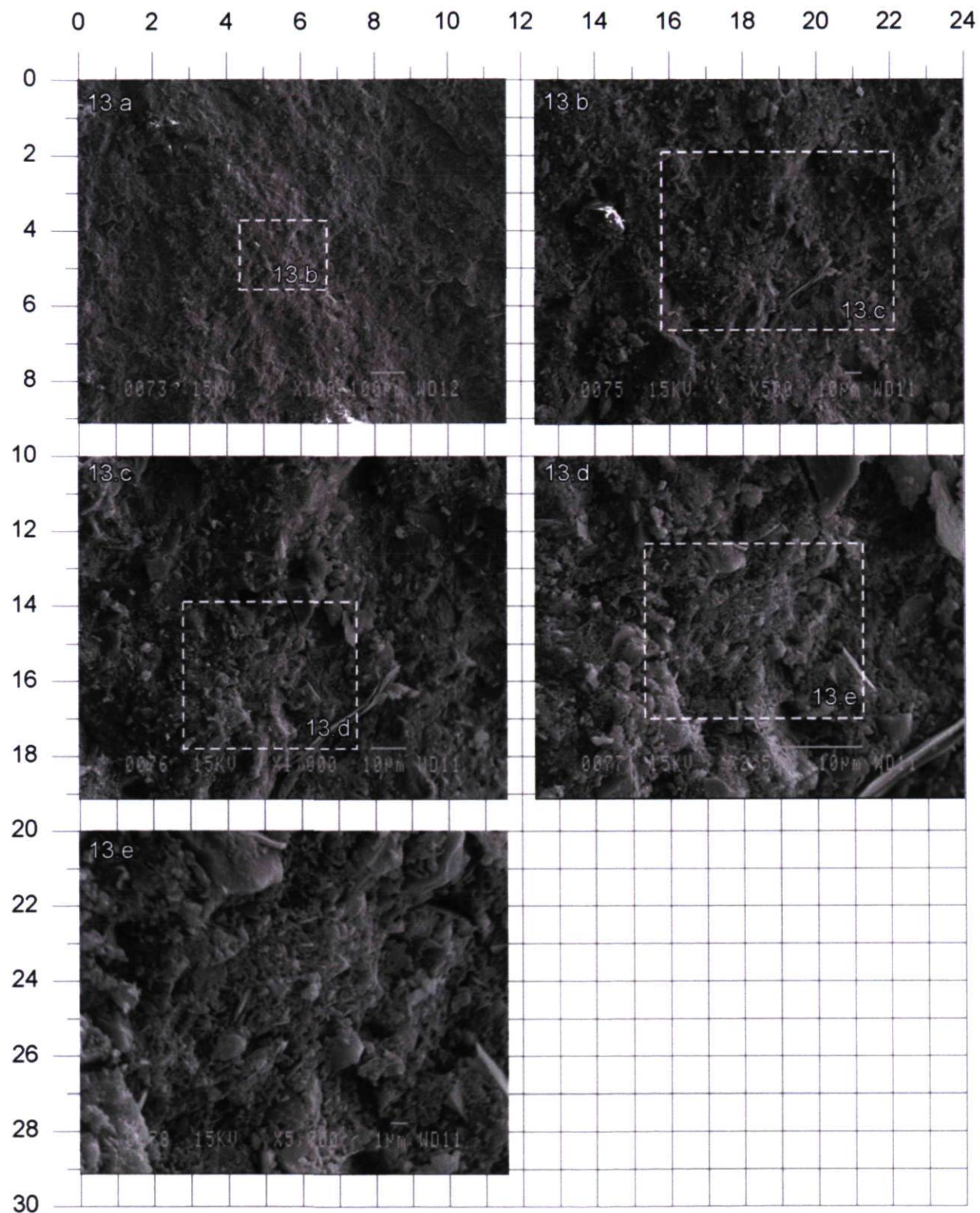
Échantillon : F46006-TM10 Série : 11
Élévation moyenne : 4.85 m Images : a à e



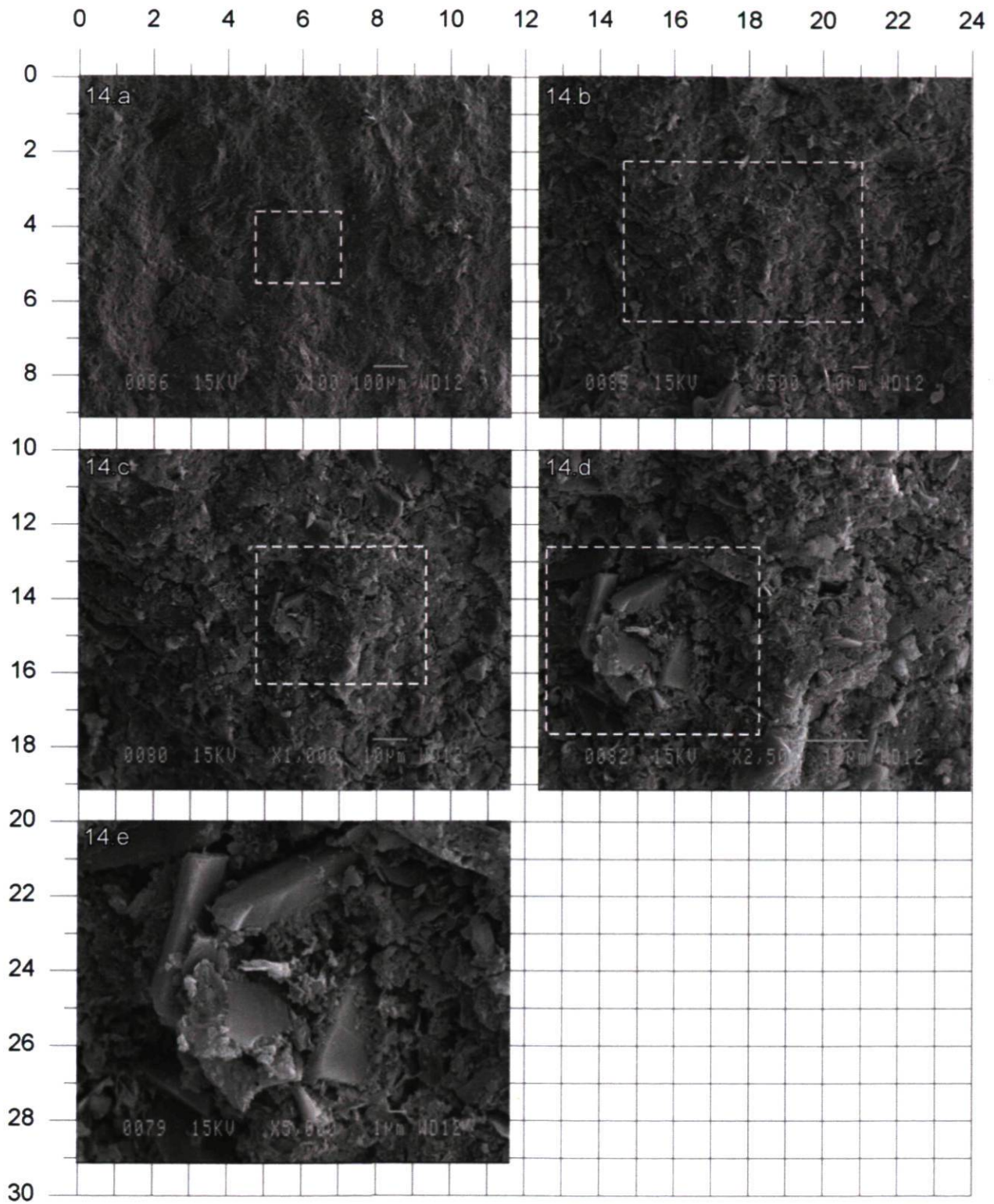
Échantillon : F46006-TM10 Série : 12
 Élévation moyenne : 4.85 m Images : a à f



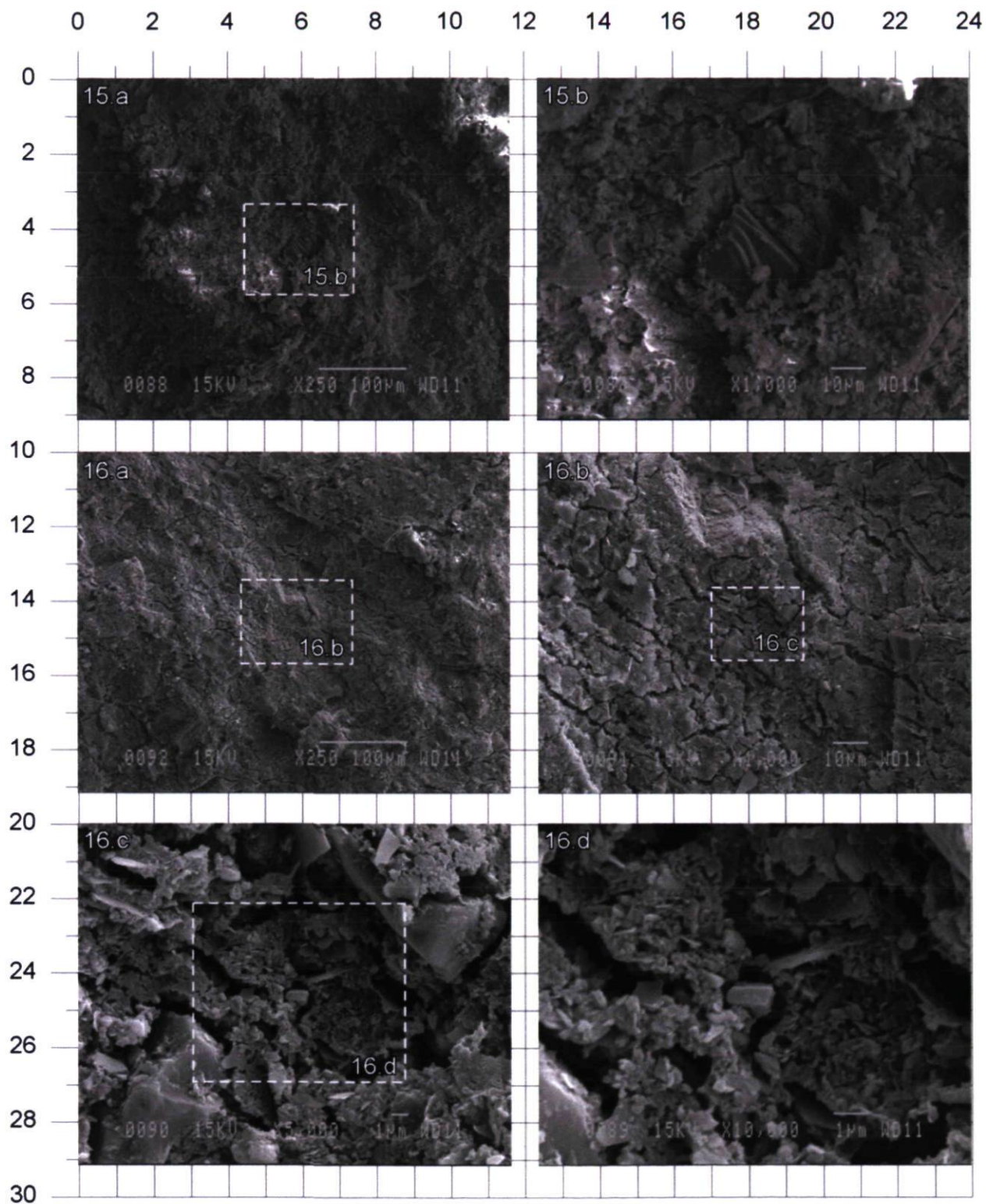
Échantillon : F46006-TM10 Série : 13
Élévation moyenne : 4.85 m Images : a à e



Échantillon : F46006-TM10 Série : 14
Élévation moyenne : 4.85 m Images : a à e



Échantillon : F46006-TM10 Séries : 15 et 16
Élévation moyenne : 4.85 m Images : a et b ; a à d



H.7.4 Grille d'analyses F46010-TM08

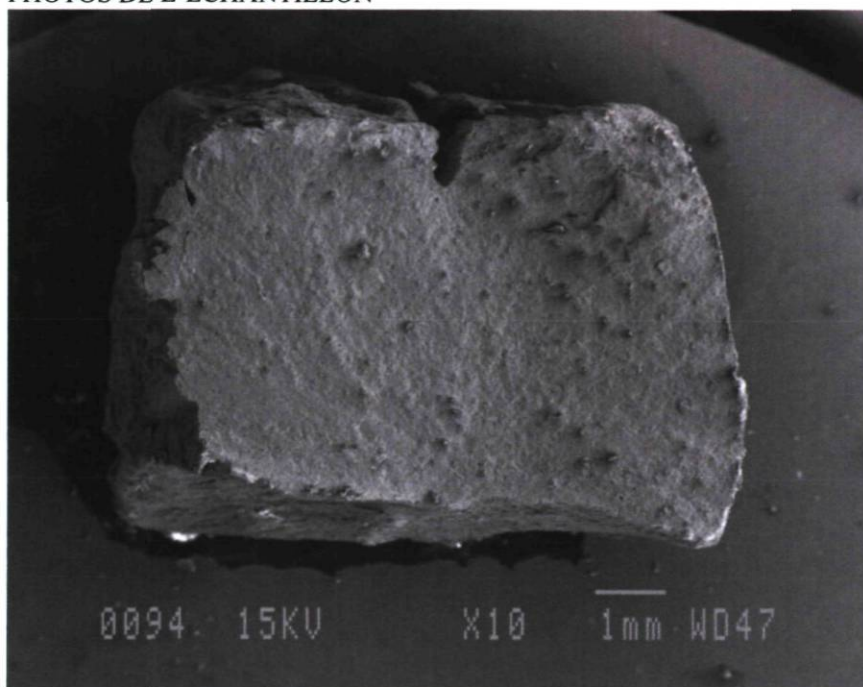
IDENTIFICATION

Site	Forage	Échantillon	Profondeur	Élévation moyenne
Colombier -plage	F46010	TM08	18.42-18.47 m	-10.61 m

PROPRIÉTÉS

w _n	w _p	w _L	I _L	I _p	Fraction argile	Activité	Cu	Cur	St
30 %	12 %	27 %	1.2	15 %	34 %	0.44	95 kPa	2.6 kPa	36

PHOTOS DE L'ÉCHANTILLON



Salinité	6.9 g/L
SS	20.82 m ² /g
CEC	1.2 equ/100 g
Calcite	0 %
Dolomite	1.36%

QUALITE DE LA PREPARATION

COMMENTAIRES

Gel/Séchage	Bonne	
État de la surface :	Plane	
Coupe (H ou V)	Verticale	
Polarité	Conservée	
Remarque :		

ÉCHANTILLON : F46010-TM08 ÉLÉVATION MOYENNE : -10.61 m

PARTICULES ELEMENTAIRES, TYPE ET FORME

		Sable 2mm – 63 um	Silt 63 – 2 um	Argile < 2 um	Matière organique	Diatomée	Foram.
	Quantité	Trace	Présence	Abondance		Présence	
Particules	Arrondie	x	x				
	Angulaire	x	x	x			
	Plate		x	x			
	Flocon			x			
Micro-organismes	Centrique					X	
	Pennée						
	Tubulaire						
	Aiguille						
	Brisé					x	
	Taille (mm)					30 um	
	Remarque	Beaucoup plus de diatomées					

MICROFABRIQUE DE L'ASSEMBLAGE

	Taille (um)	Rond	Angulaire	Orientation aléatoire	Orientation stratifiée
Agrégats	2-10	X		X	
Flocons			x		
Pellets					
Remarque					

PORES

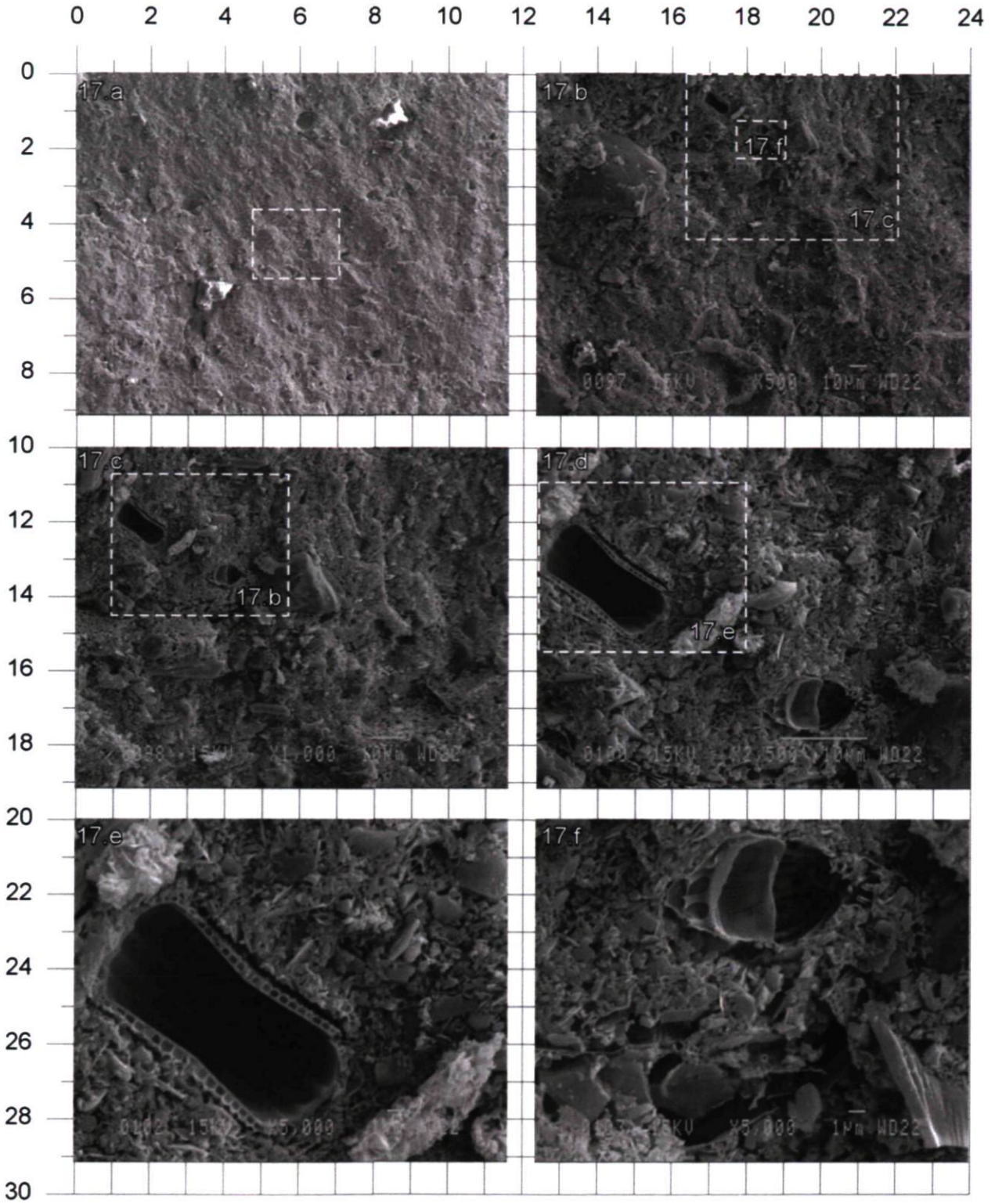
	Inter-agrégats	Intra- agrégats	Intra-squelettique	Squelettique
Diamètre	0.5 – 5 um	< 0.5 um	1-10 um	< 1 um
Rond				x
Irrégulier	x	x	x	
Remarque				

AUTRES ELEMENTS MICROSTRUCTURAUX

	Ouverture	Longueur	Épaisseur	Orientation aléatoire	Orienté
Fissures	1 um	> 10 um		x	
Ponts					
Vides					
Remarque	Peu de fissures				

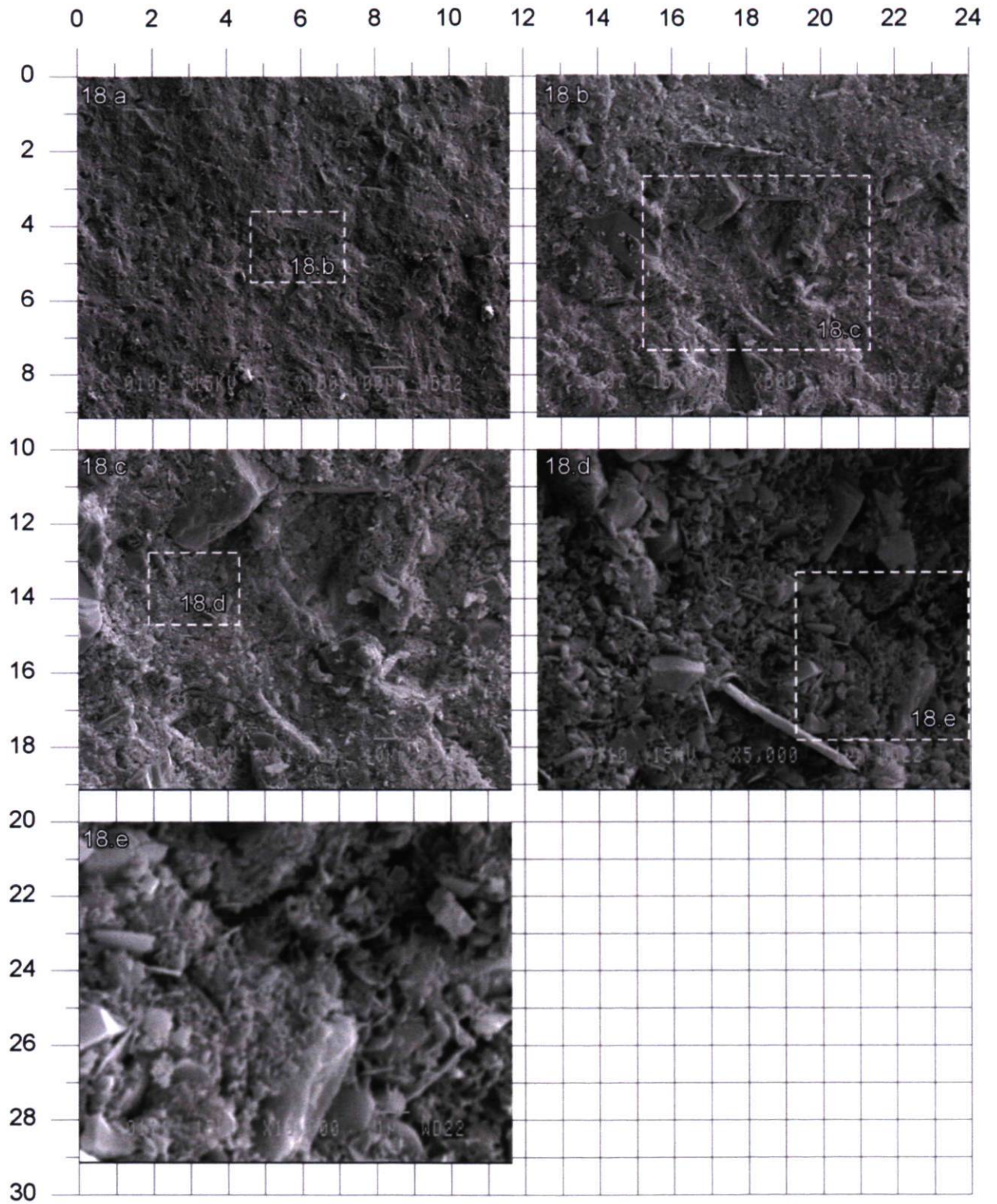
Échantillon : F46010-TM08
Élévation moyenne : -10.61 m

Série : 17
Images : a à f



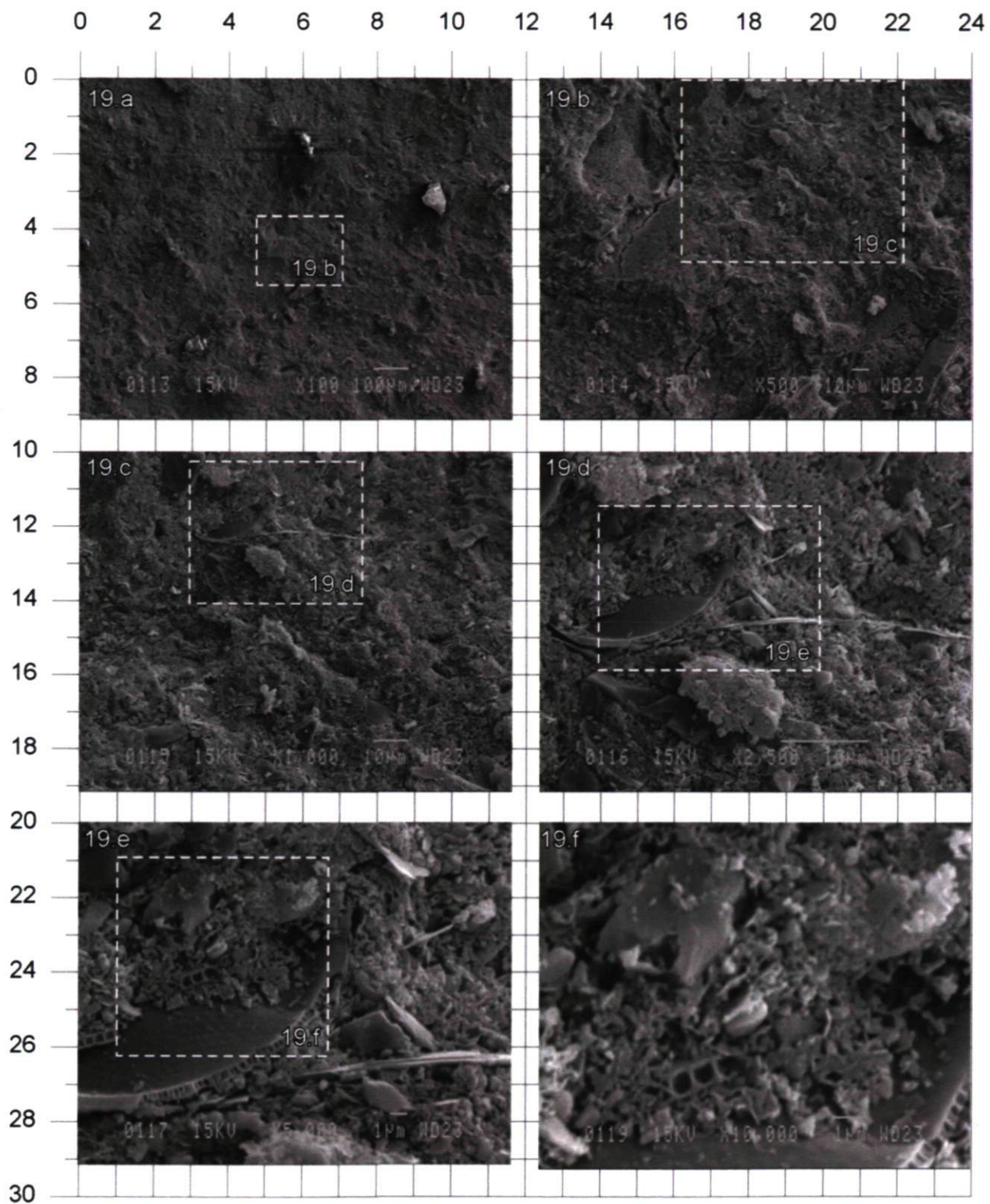
Échantillon : F46010-TM08
Élévation moyenne : -10.61 m

Série : 18
Images : a à e



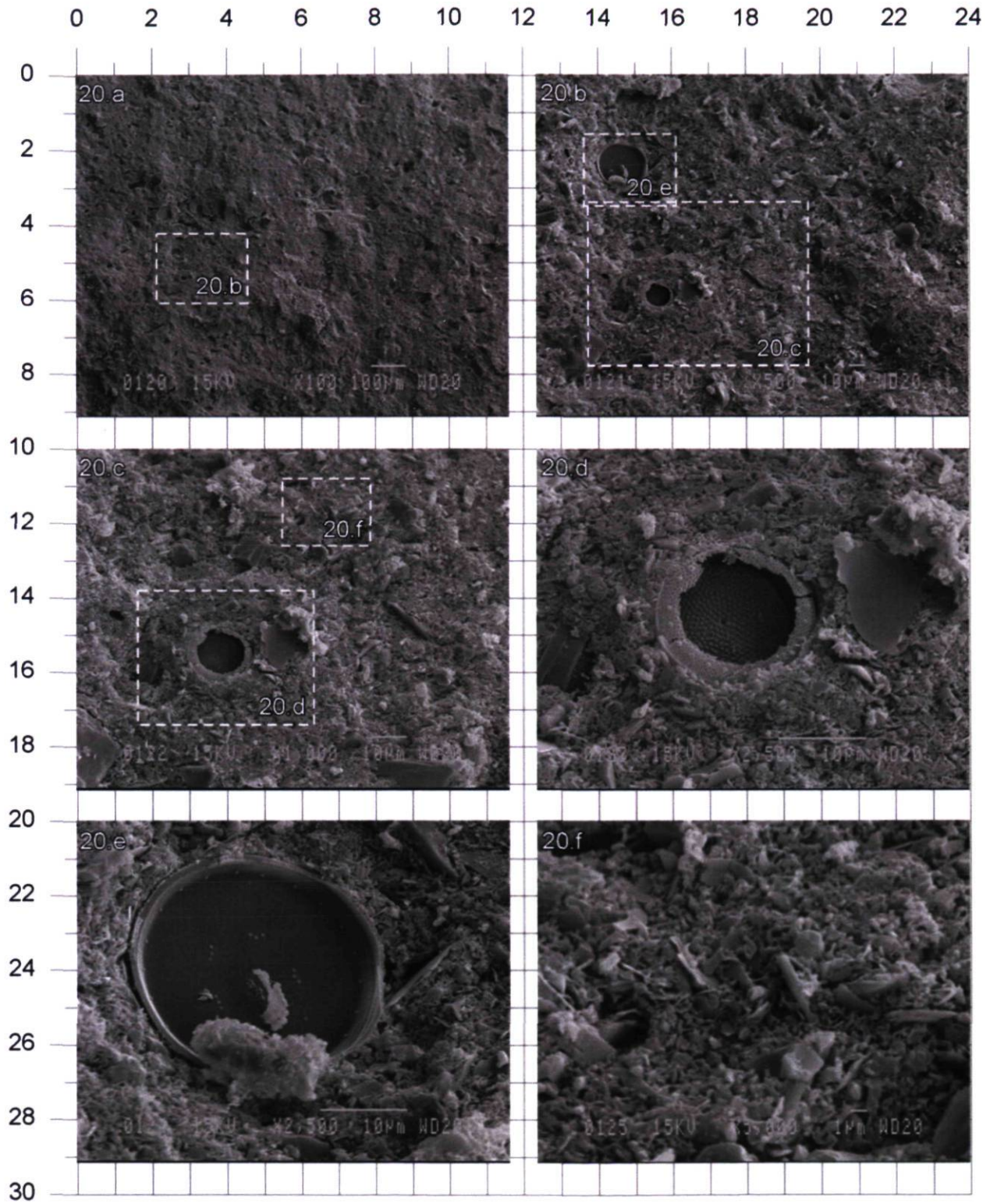
Échantillon : F46010-TM08
 Élévation moyenne : -10.61 m

Série : 19
 Images : a à f



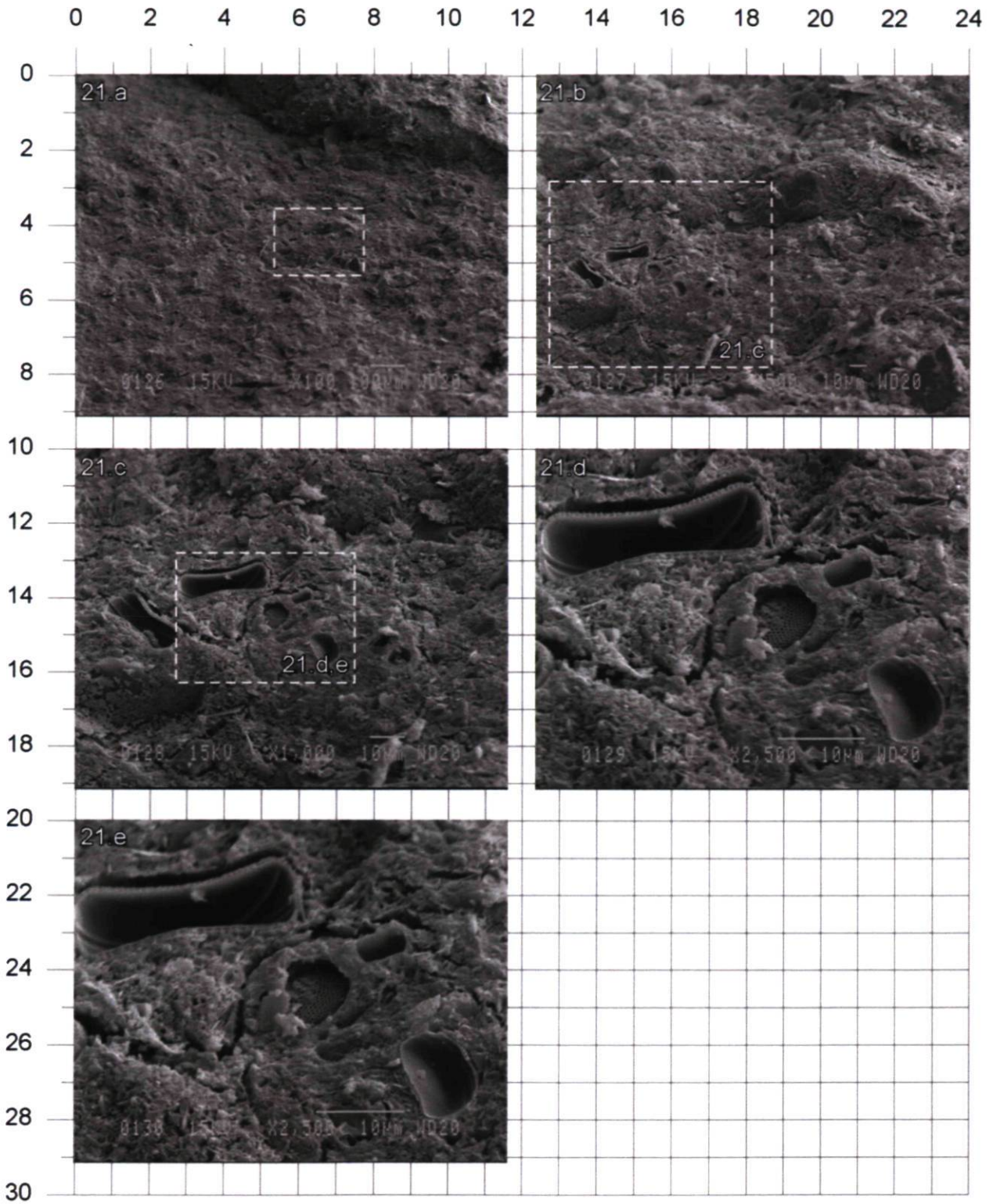
Échantillon : F46010-TM08
Élévation moyenne : -10.61 m

Série : 20
Images : a à f



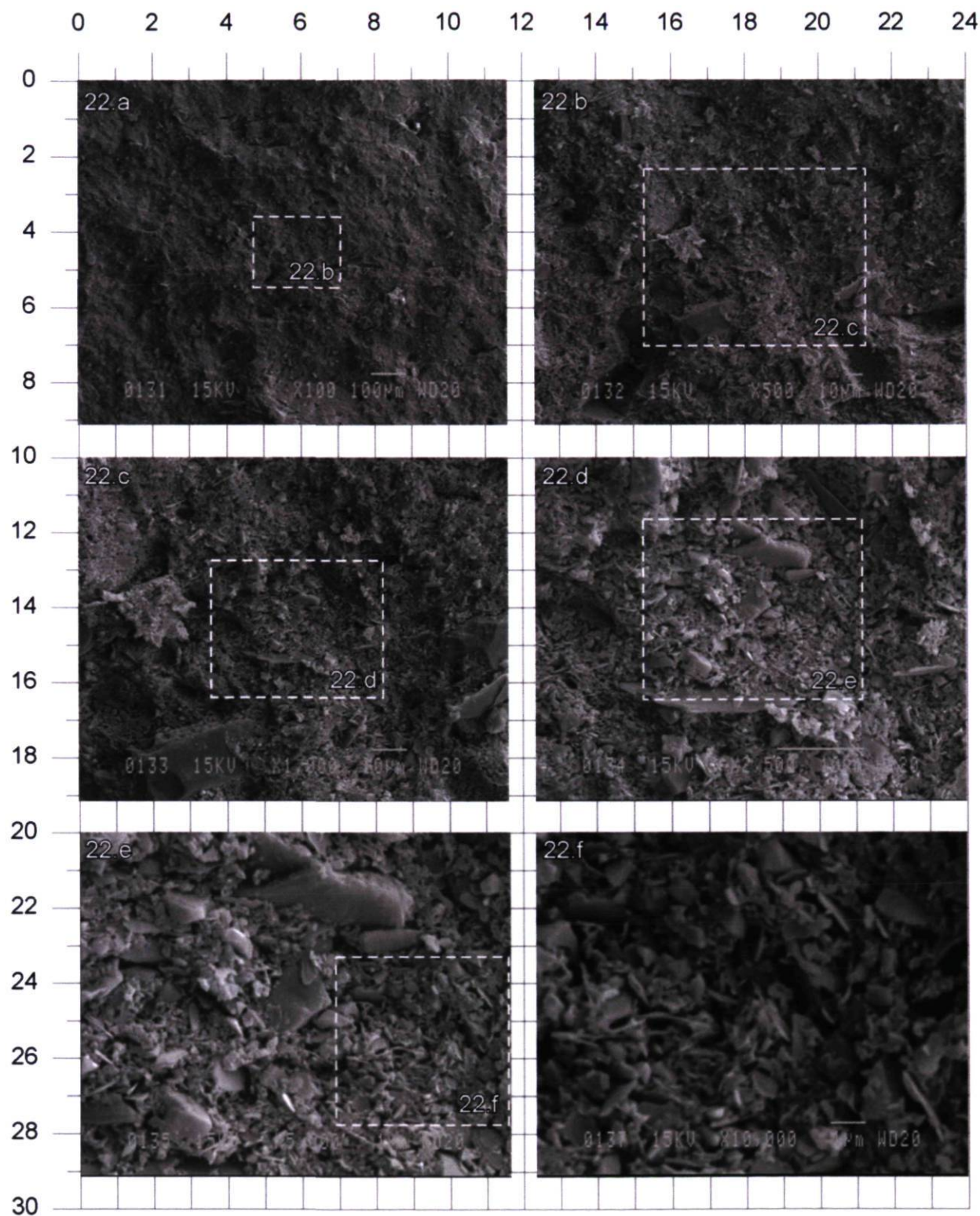
Échantillon : F46010-TM08
Élévation moyenne : -10.61 m

Série : 21
Images : a à e



Échantillon : F46010-TM08
Élévation moyenne : -10.61 m

Série : 22
Images : a à f



H.7.5 Grille d'analyses COR0307-BET2-42LEH

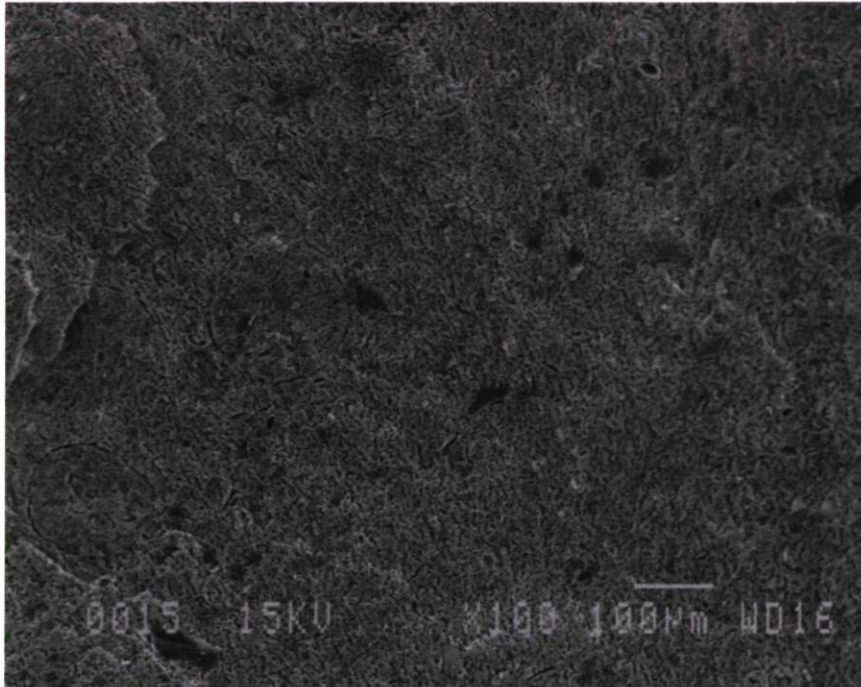
IDENTIFICATION

Site	Station	Échantillon	Profondeur	Élévation moyenne
Betsiamites - Chenal Laurentian	BET02	COR0307-42LEH	1.18-1.26 m	-345.8

PROPRIÉTÉS

w _n	w _p	w _L	I _L	I _p	Fraction argile	Activité	Cu	Cur	St
126 %	51 %	107 %	1.3 %	56 %	50 %	1.12	6.2 kPa	0.8 kPa	7.5

PHOTOS DE L'ÉCHANTILLON



Salinité	33 g/L
SS	88 m ² /g
CEC	-
Calcite	1.3 %
Dolomite	1.8 %

QUALITE DE LA
PREPARATION

COMMENTAIRES

Gel/Séchage	Bonne	
État de la surface :	Plane	
Coupe (H ou V)	Verticale	
Polarité	Conservée	
Remarque :		

ÉCHANTILLON : COR0307-42LEH ÉLÉVATION MOYENNE : -345.8 m

PARTICULES ELEMENTAIRES, TYPE ET FORME

		Sable 2mm – 63 um	Silt 63 – 2 um	Argile < 2 um	Matière organique	Diatomée	Foram.
	Quantité	Trace	Présence	Abondance		Abondance	
Particules	Arrondie	x	x				
	Angulaire	x	x	x			
	Plate		x	x			
	Flocon			x			
Micro-organismes	Centrique					X	
	Pennée						
	Tubulaire						
	Aiguille						
	Brisé					X beaucoup	
	Taille (mm)					30 um	
	Remarque	Quelques diatomées et présence de pyrite framboïdale de 10 um à 4, 28 sur image 24.a. Beaucoup de morceau de diatomées dans la matrice					

MICROFABRIQUE DE L'ASSEMBLAGE

	Taille (um)	Rond	Angulaire	Orientation aléatoire	Orientation stratifiée
Agrégats	2-10	X		X	
Flocons			x		
Pellets					
Remarque					

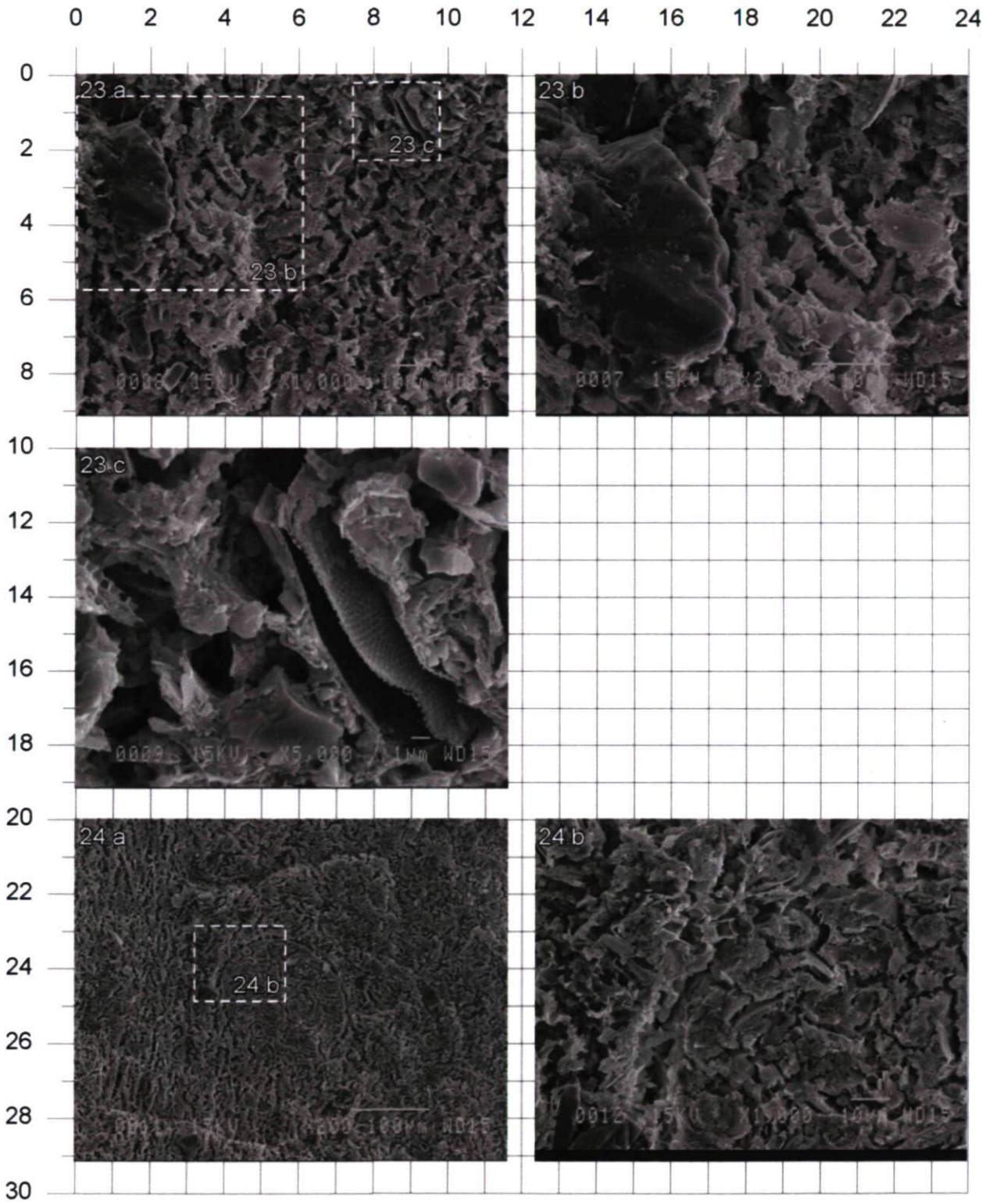
PORES

	Inter-agrégats	Intra- agrégats	Intra-squelettique	Squelettique
Diamètre	0.5 – 5 um	< 0.5 um	1-10 um	< 1 um
Rond				x
Irrégulier	x	x	x	
Remarque				

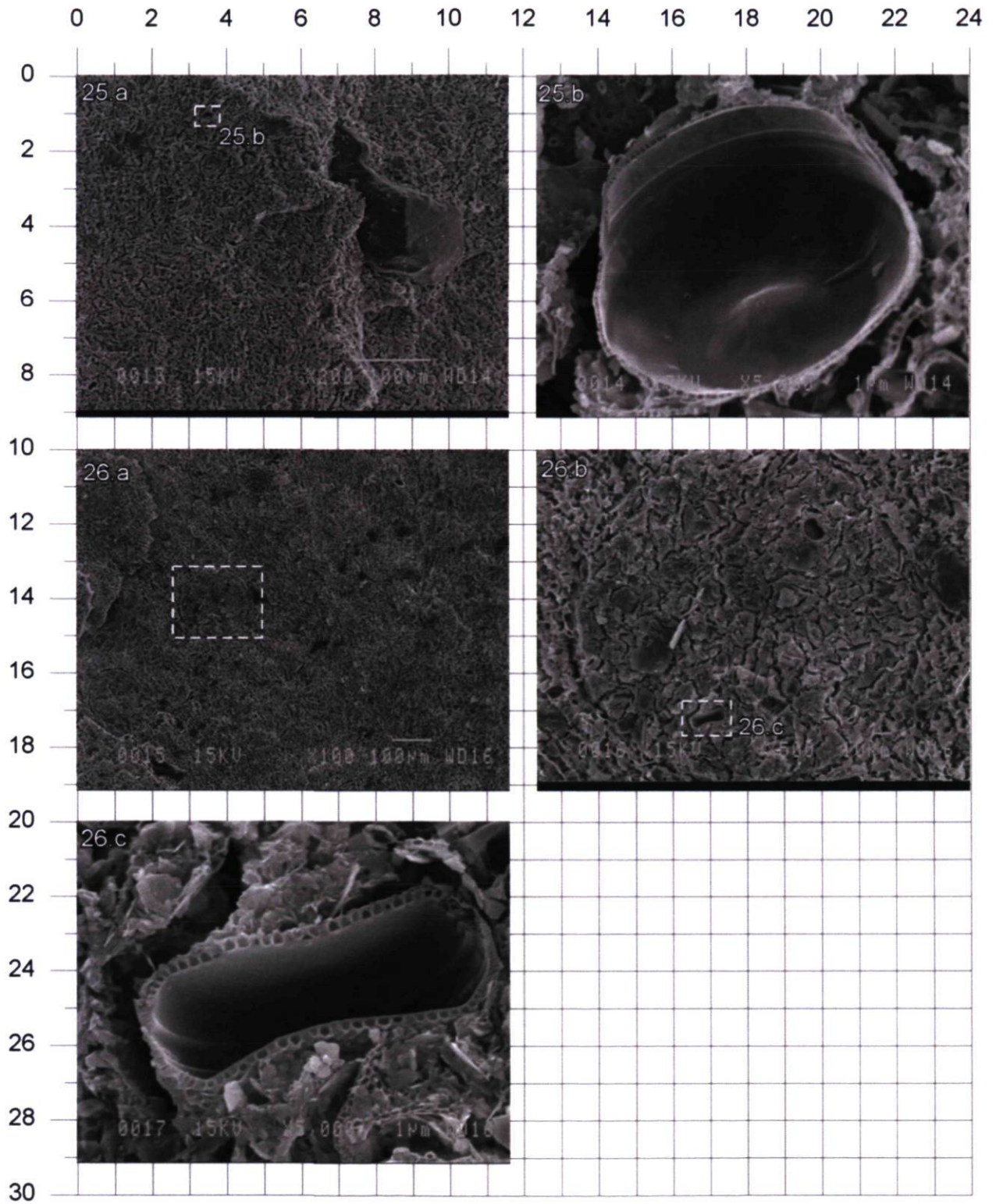
AUTRES ELEMENTS MICROSTRUCTURAUX

	Ouverture	Longueur	Épaisseur	Orientation aléatoire	Orienté
Fissures	1 um	> 10 um		x	
Ponts					
Vides					
Remarque	Peu de fissures				

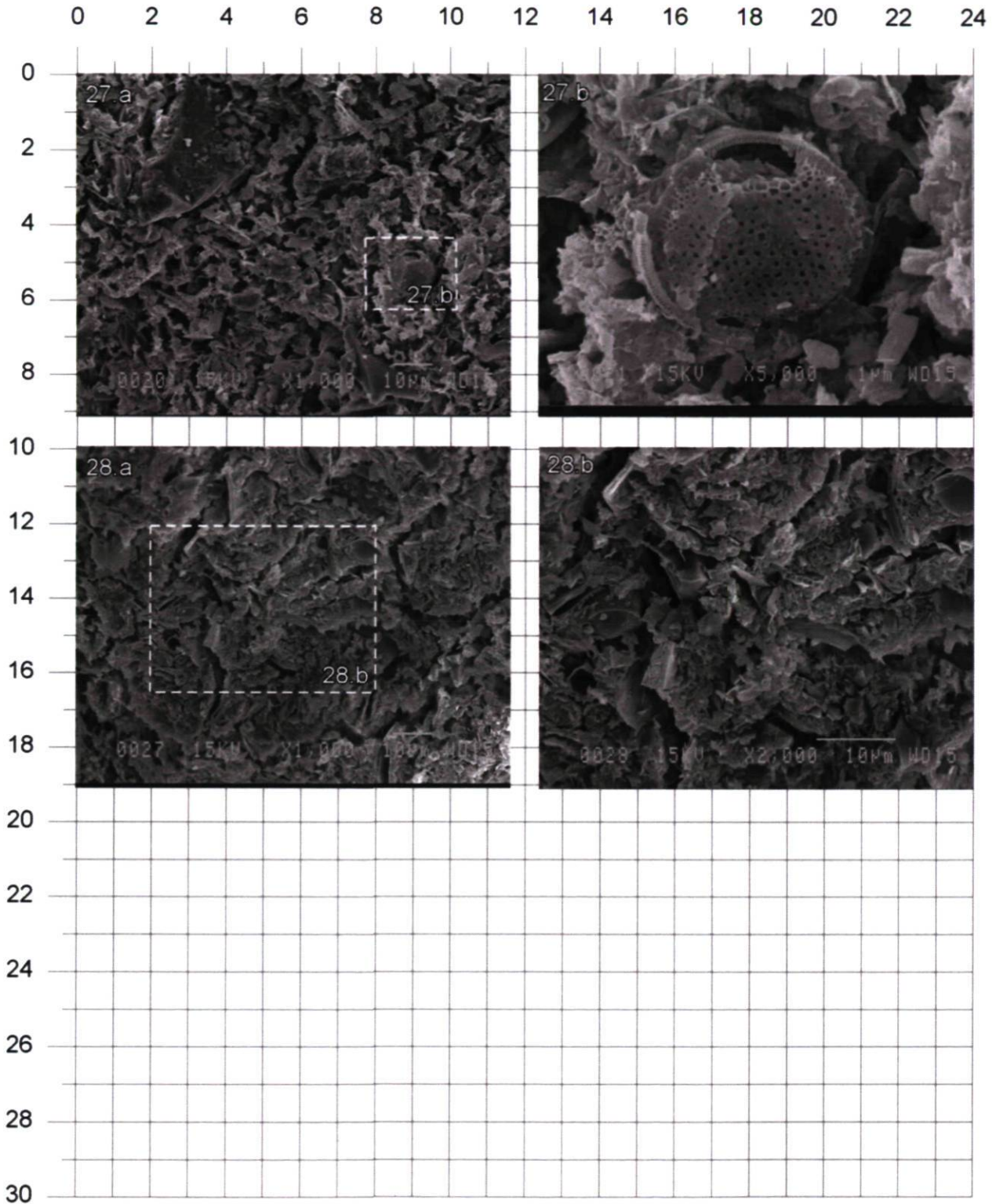
Échantillon : COR0307-BET02-LEH-42 Série : 23-24
Élévation moyenne : -345.8 m Images : a à c ; a et b



Échantillon : COR0307-BET02-LEH-42 Série : 25-26
Élévation moyenne : -345.8 m Images : a et b ; a à c




Échantillon : COR0307-BET02-LEH-42 Série : 27-28
Élévation moyenne : -345.8 m Images : a à b

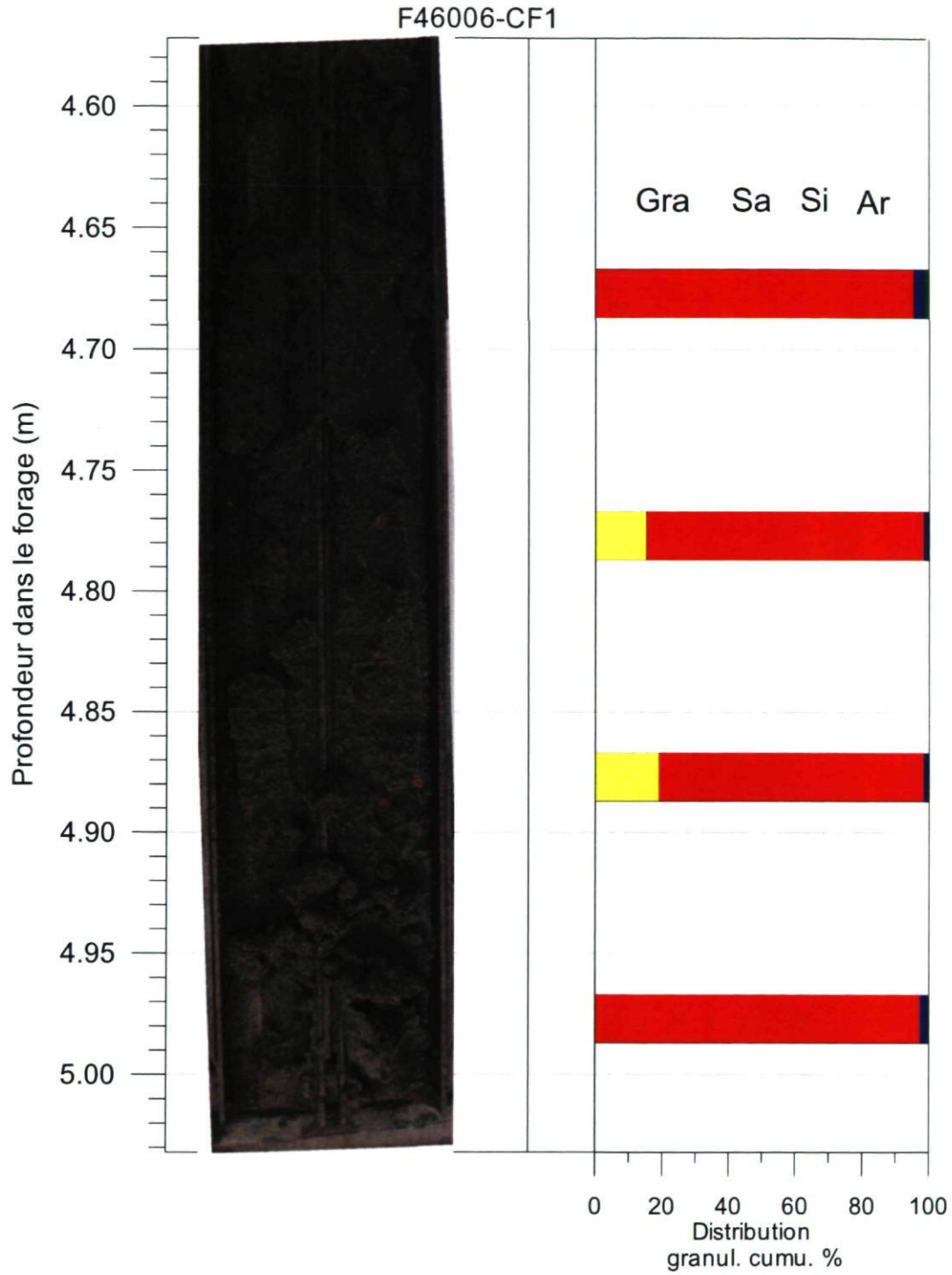


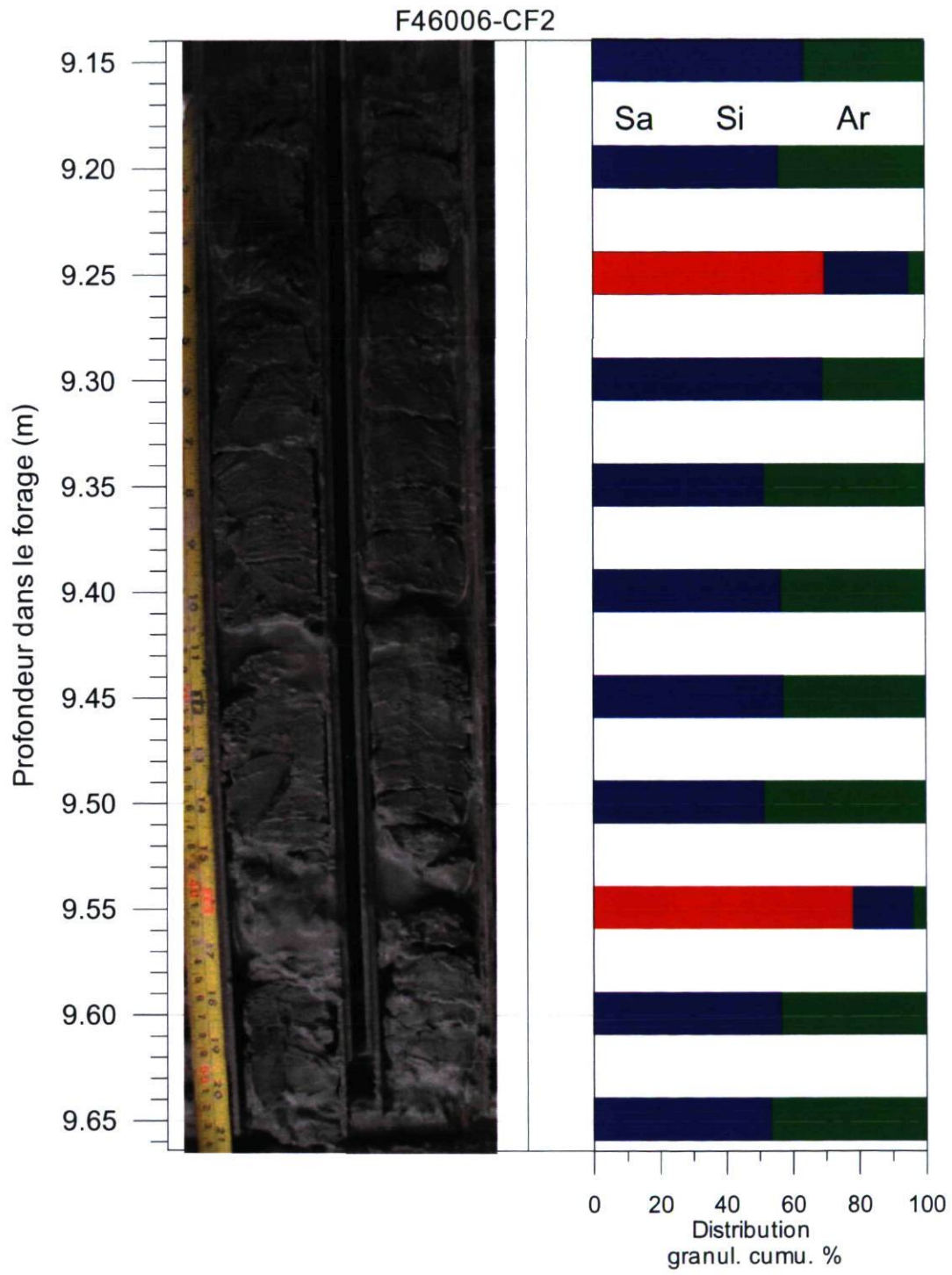
H.8 Données sédimentologiques obtenues lors de l'extraction des carottes

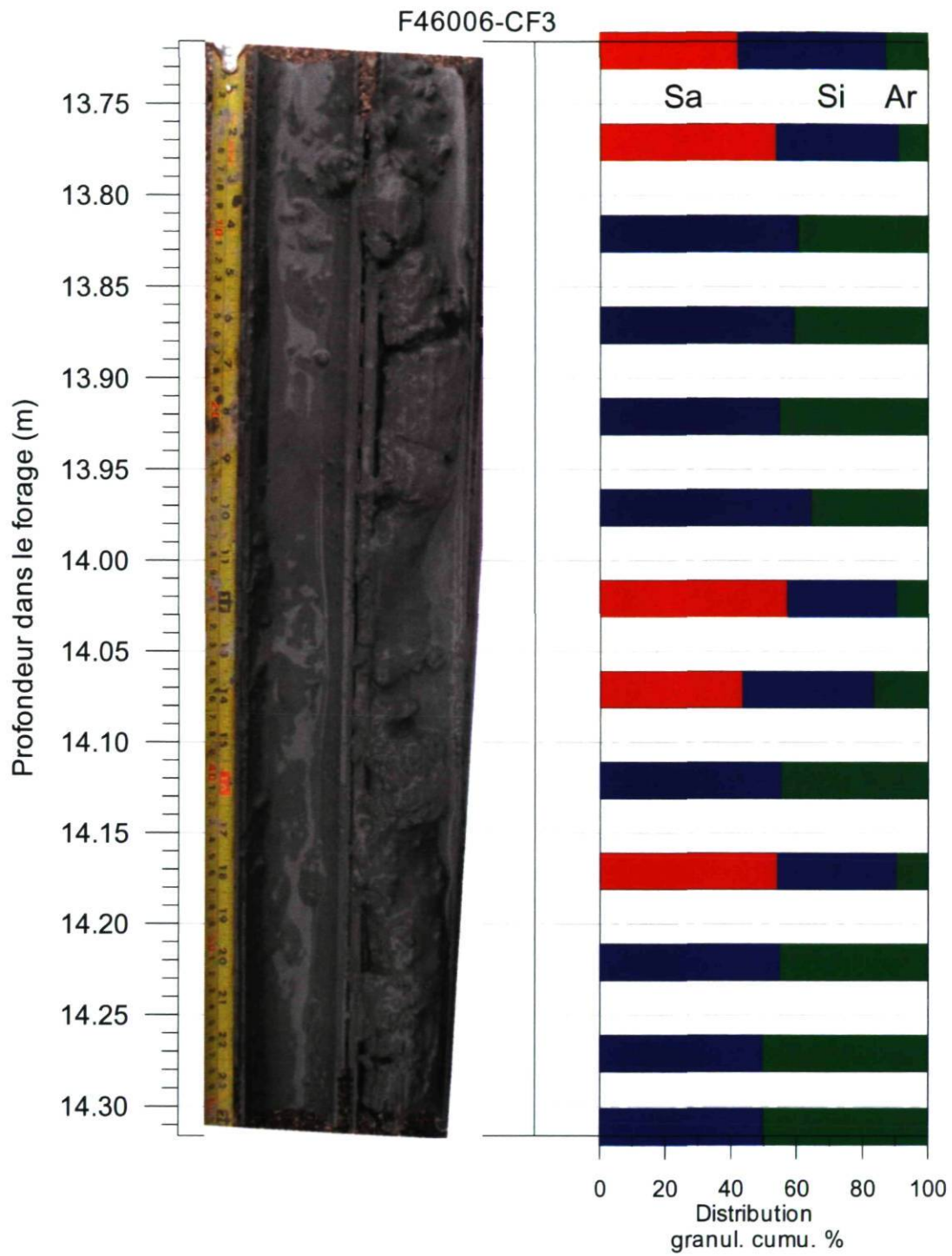
H.8.1 Tableau descriptif des analyses sédimentologiques effectuées

Résultats	Descriptions
Image Cat-Scan	Topogrammes des carottes sédimentaires (computerized axial tomography)
Profil de CT number	Les valeurs en échelle de gris des pixels des topogrammes peuvent être exprimées en nombre CT. Un nombre CT est une unité complexe qui relie la minéralogie, la teneur en matière organique, la taille granulométrique et la densité des grains (e.g., Boespflug et al. 1995; St-Onge et al. 2007)
Photo numérique	Au laboratoire, image obtenue avec l'appareil de photographie SmartCIS de SmartCube Pour les cuillères fendues, les images ont été obtenues sur le terrain et les proportions ne sont pas conservées. Les images sont donc seulement descriptives.
L*	Profil de réflectance obtenu par traitement d'image
Spectro	Profil de réflectance du sédiment obtenu avec le Spectrophotomètre X-Rite Digital Swatchbook DTP-22
Densité	Profil de densité obtenu à l'aide du GEOTEK MSCL
SI	Profil de susceptibilité magnétique obtenu à l'aide du GEOTEK MSCL
Distribution granul. Cumu. %	Distribution du pourcentage par volume d'argile, de silt et de sable, obtenue à l'aide du granulomètre laser Beckman Coulter LS-13320  <ul style="list-style-type: none"> Gra = Gravier Sa = Sable Si = Silt Ar = Argile

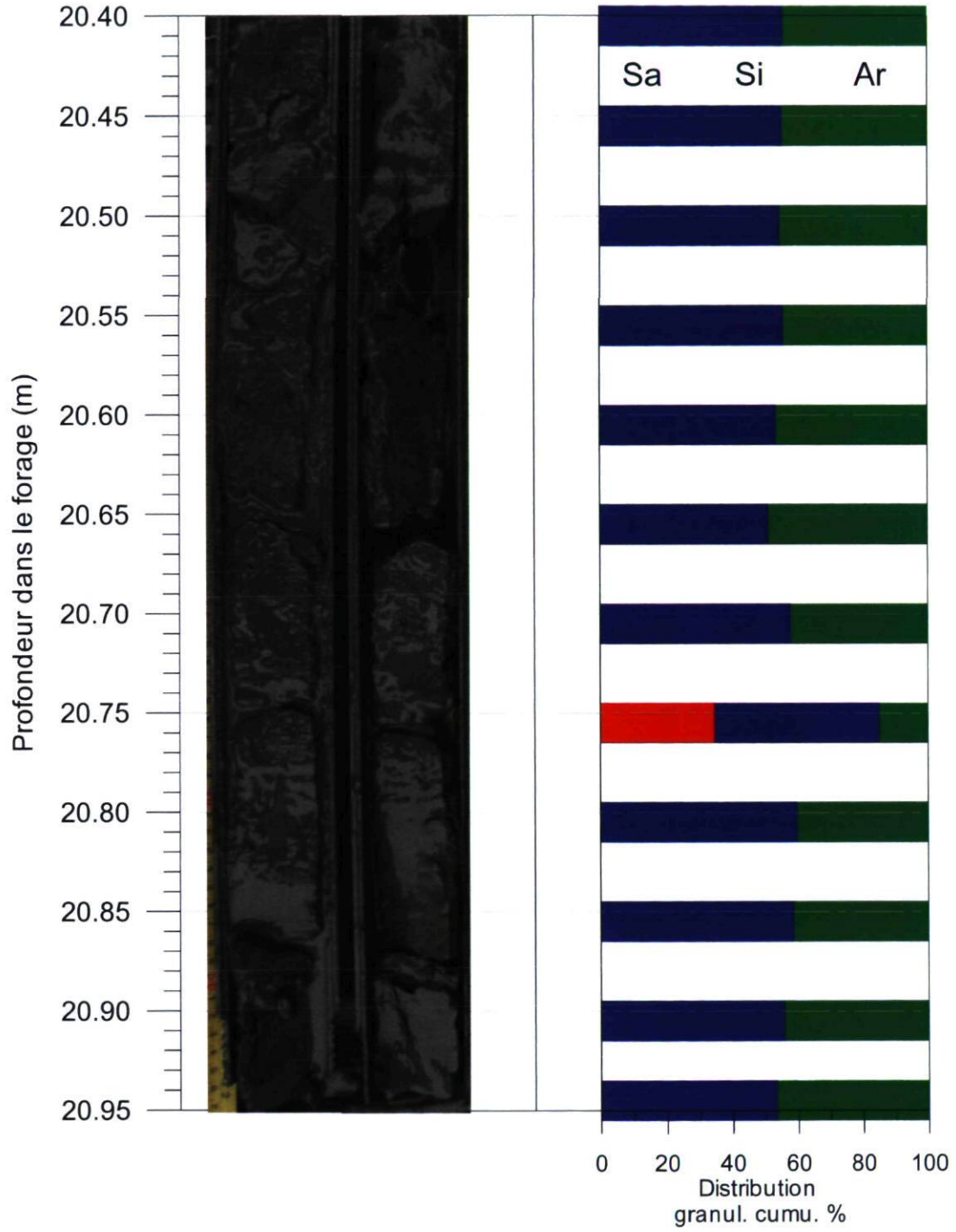
H.8.2 CAT-Scan et propriétés sédimentologiques - F46006

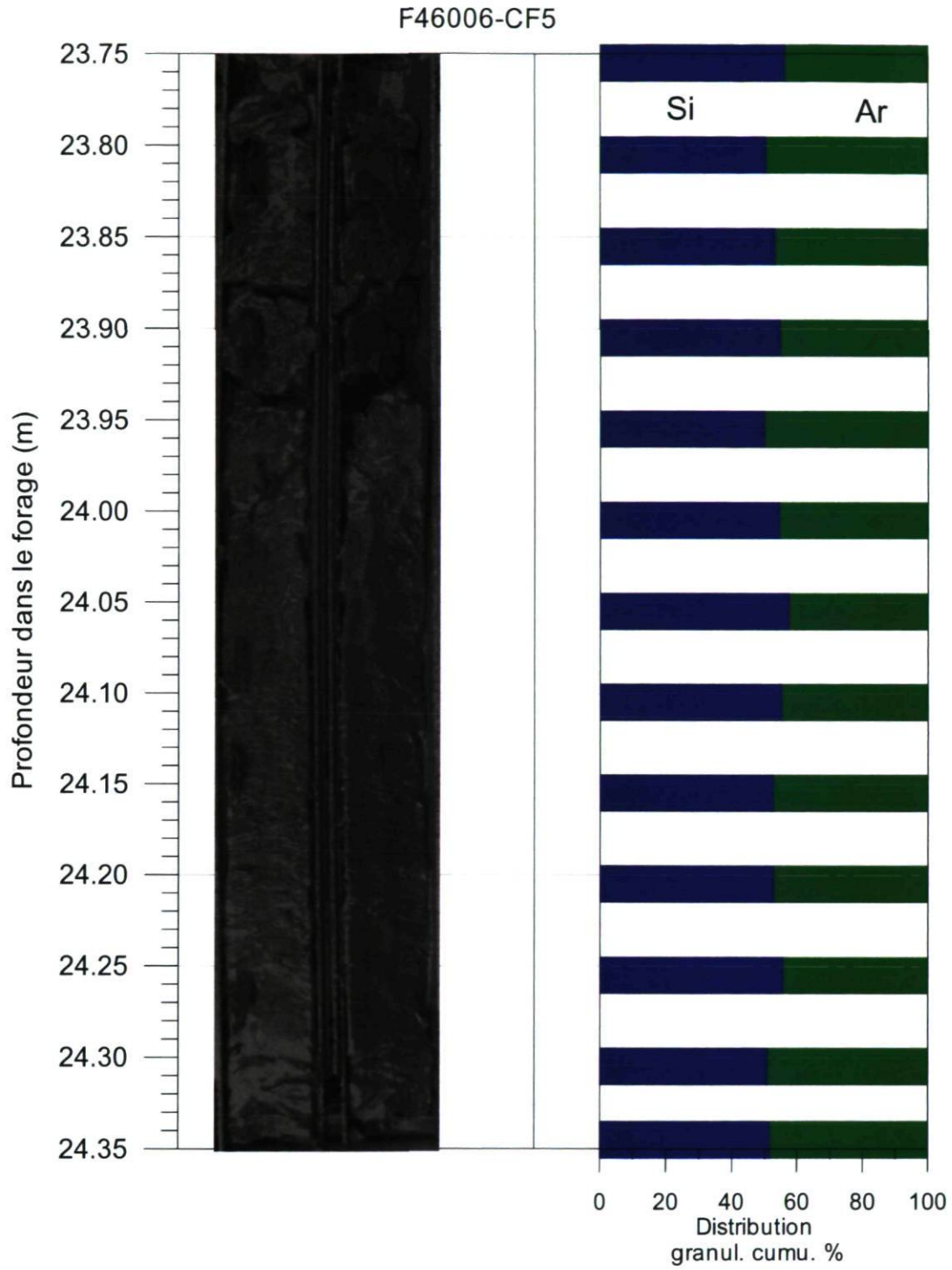


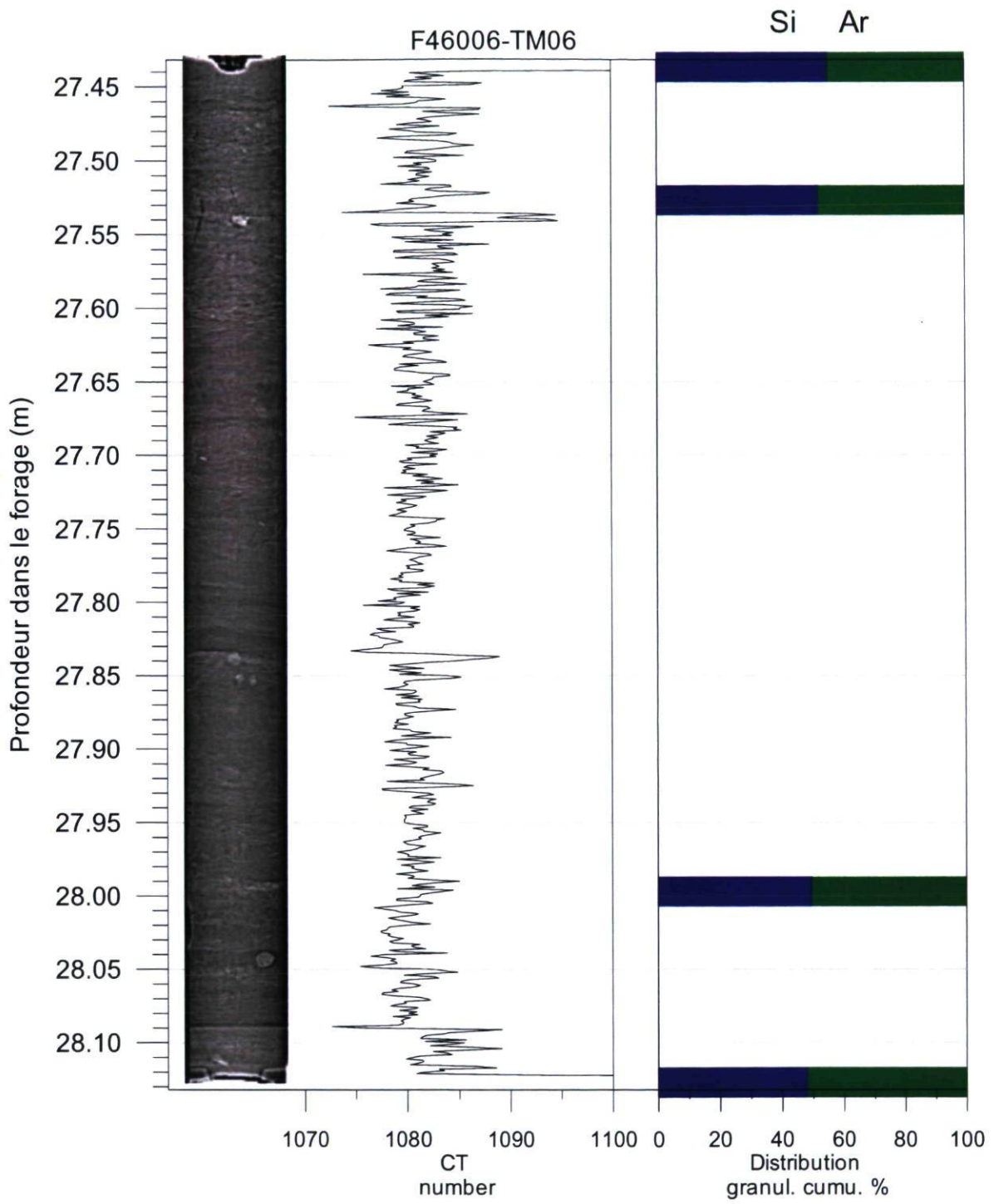


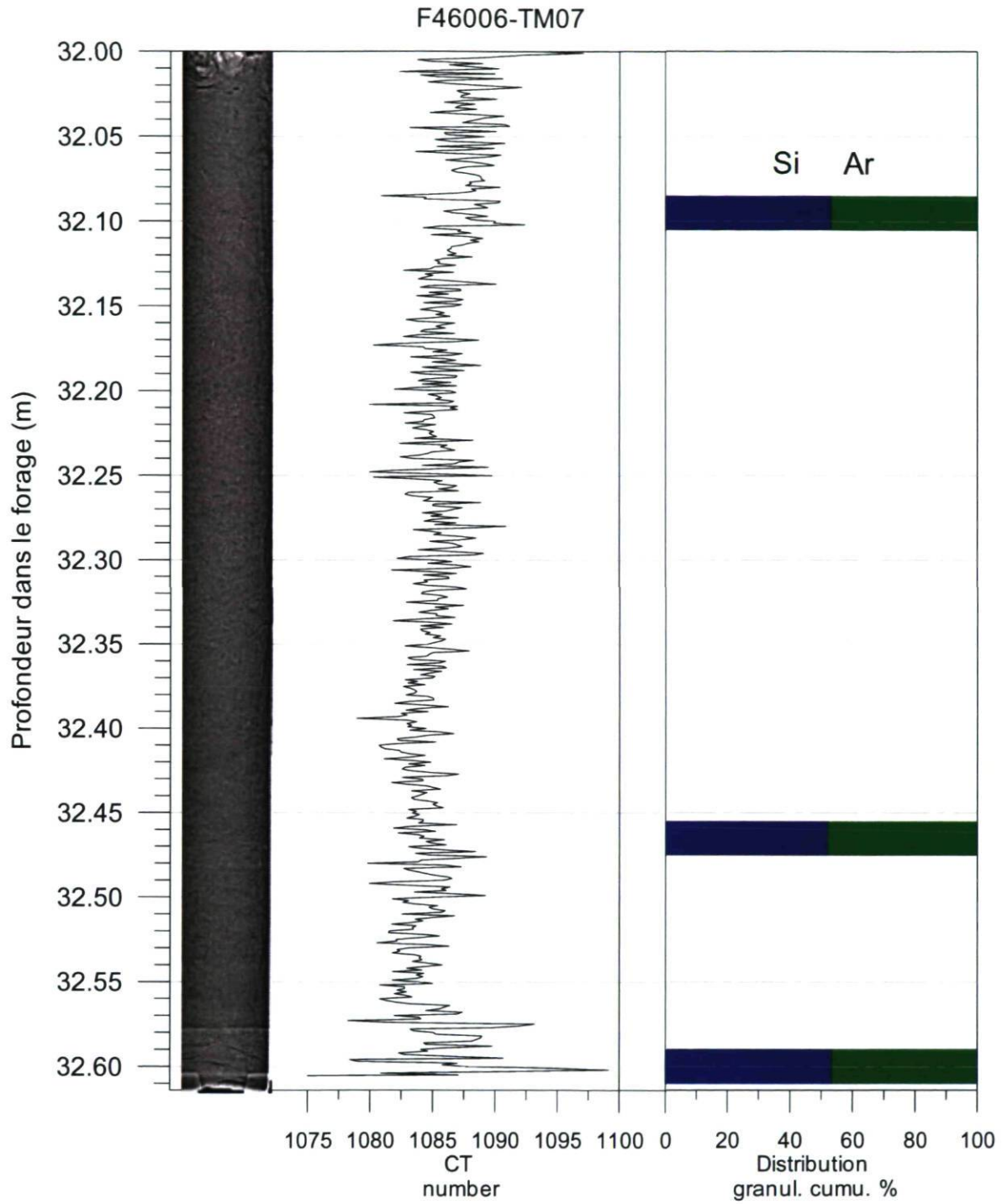


F46006-CF4

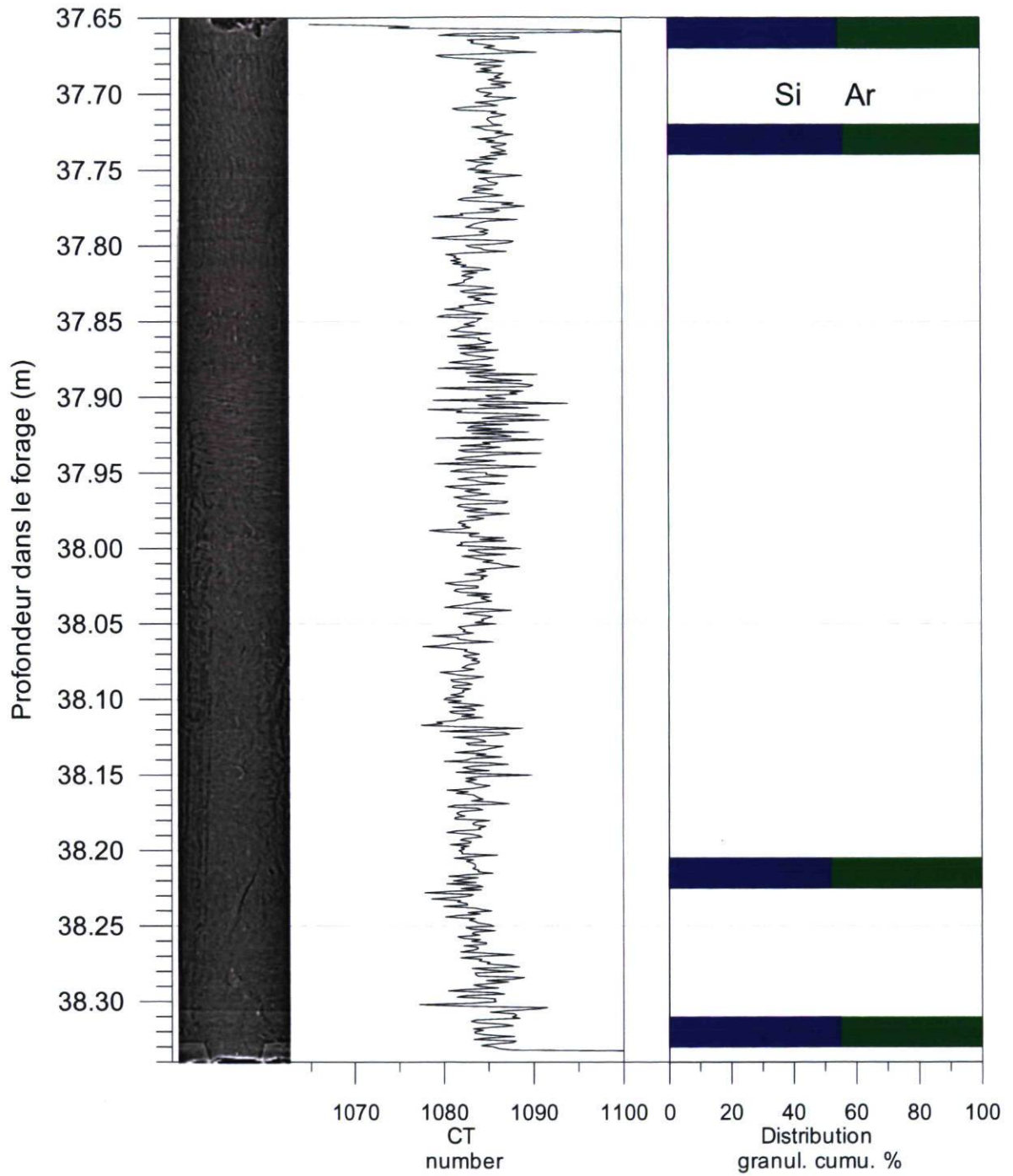


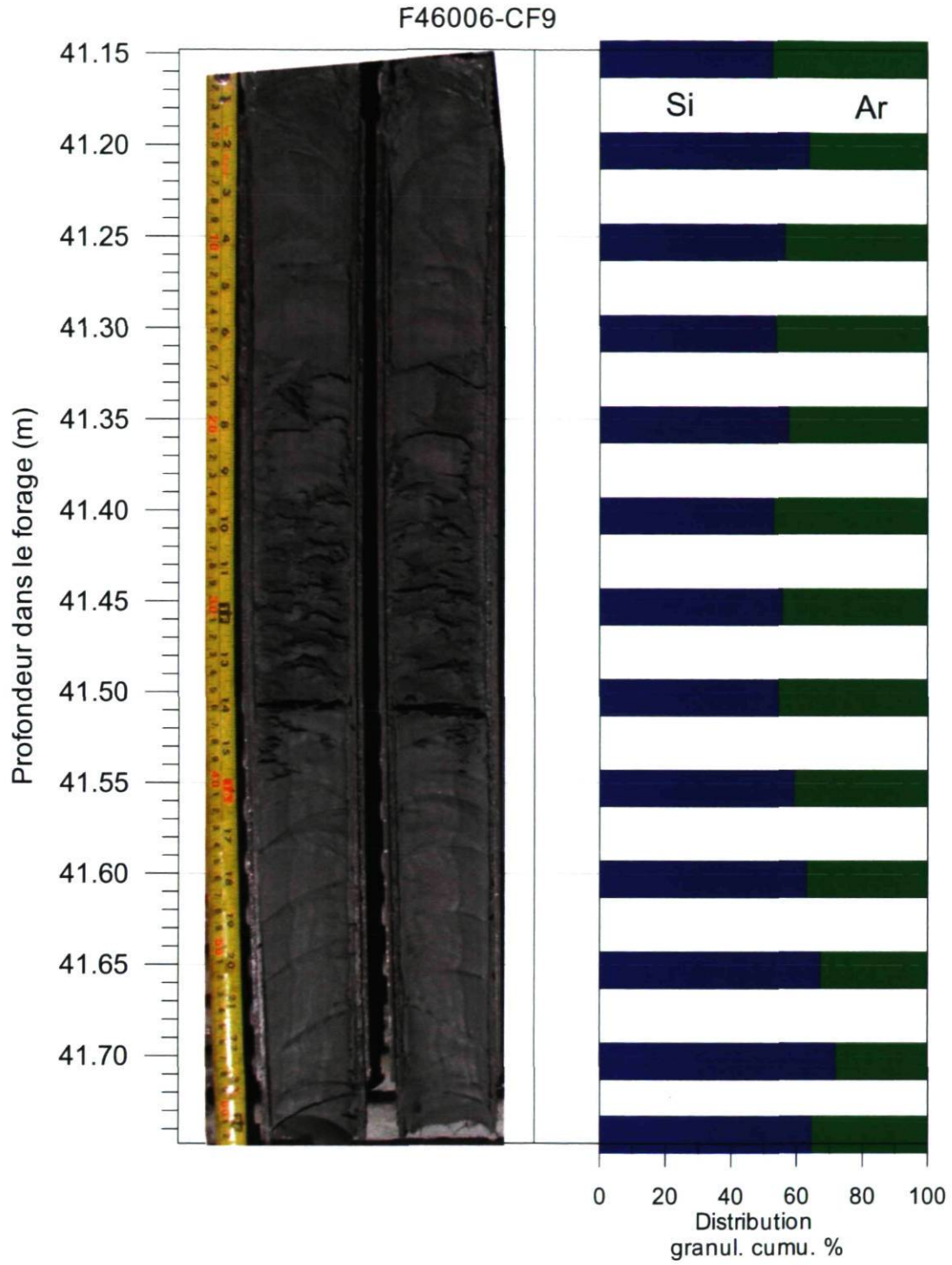


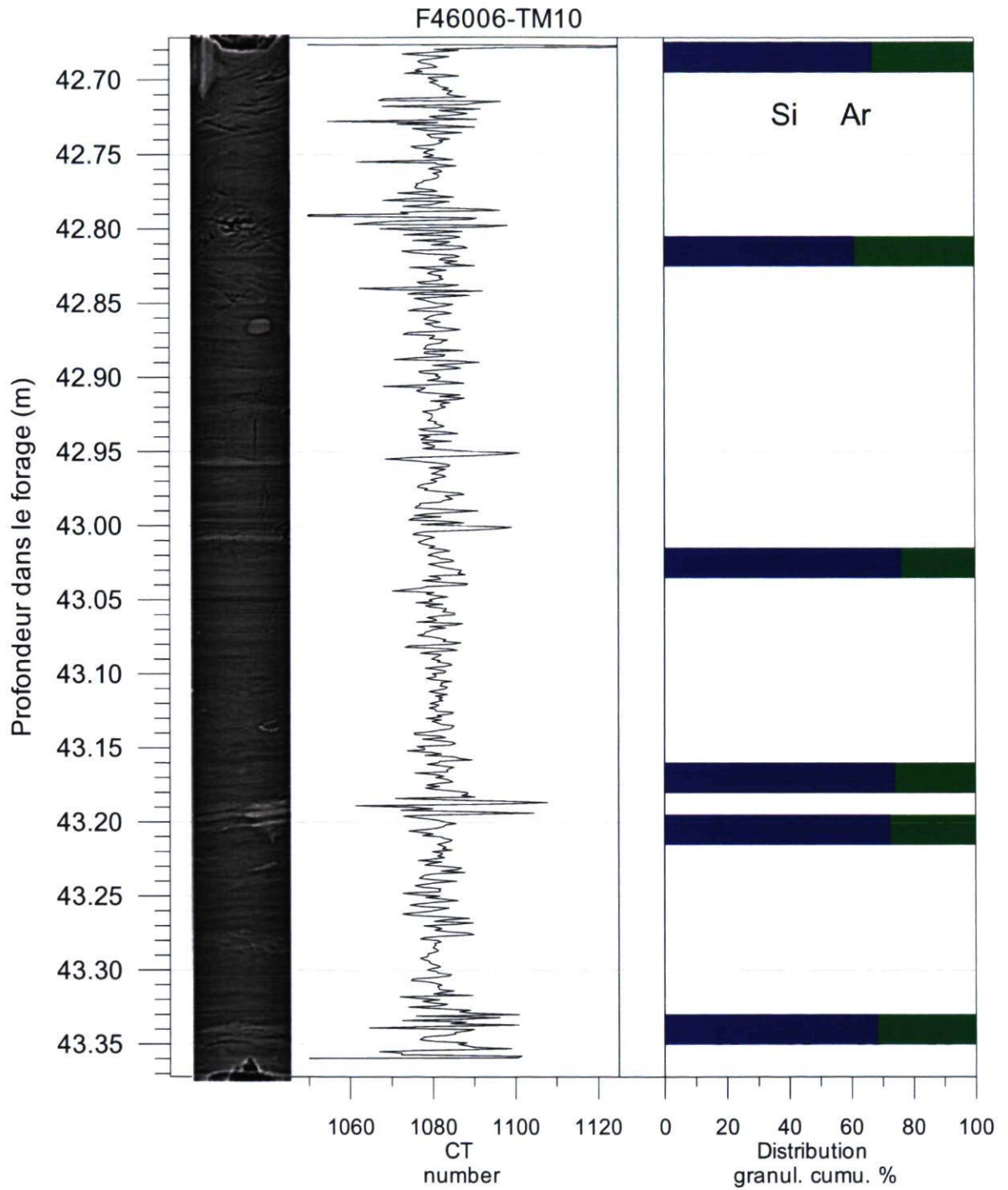


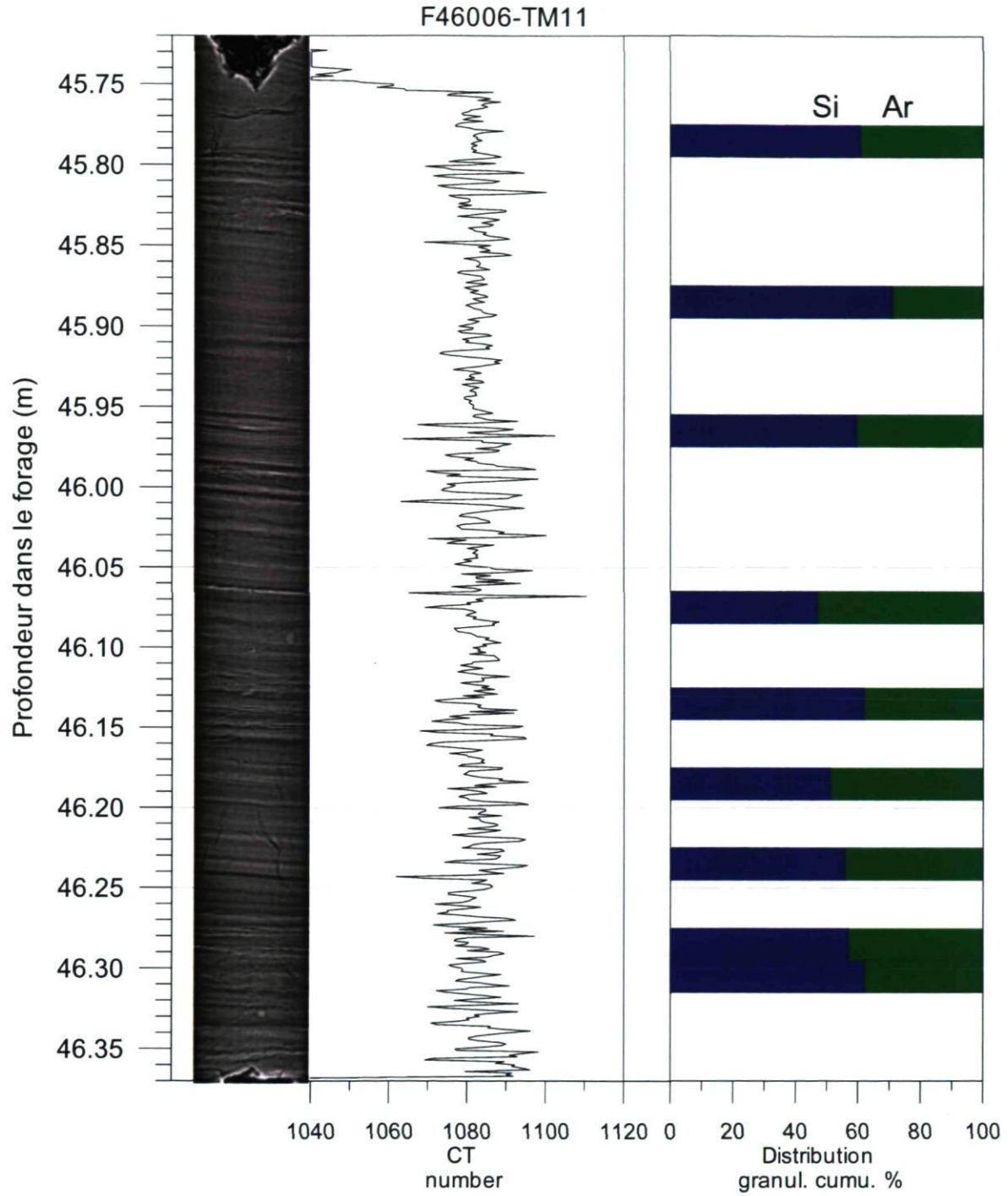


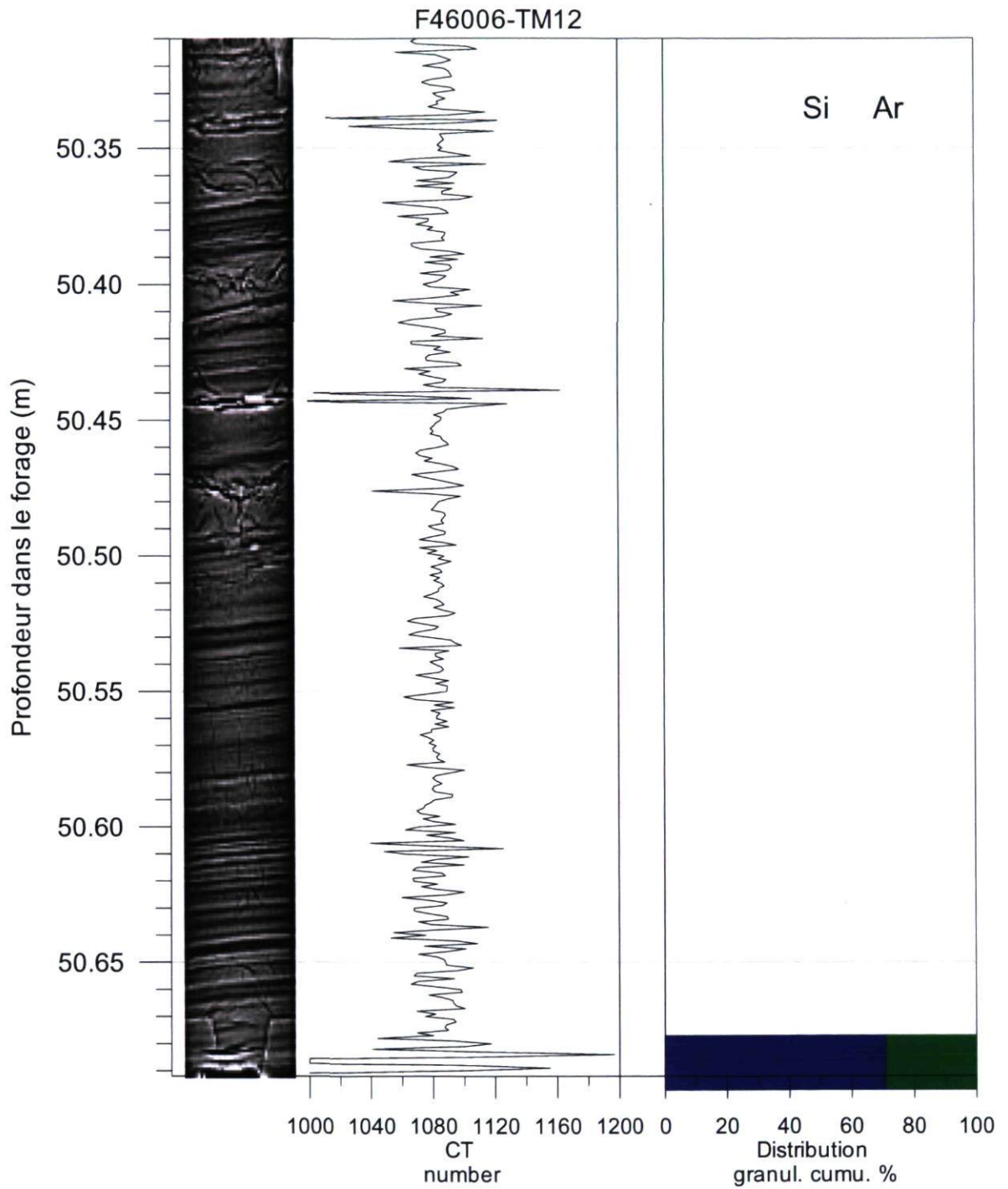
F46006-TM08

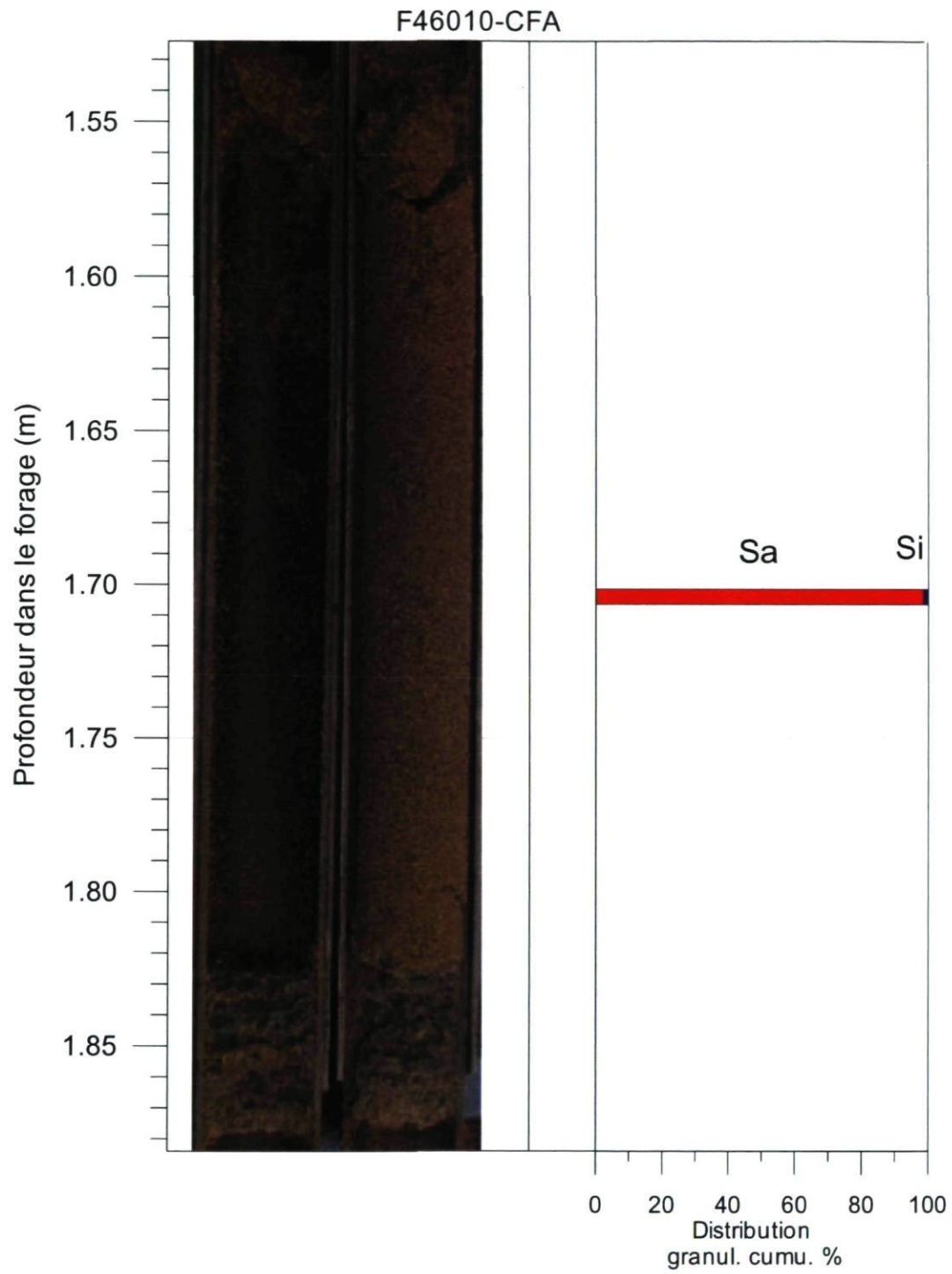


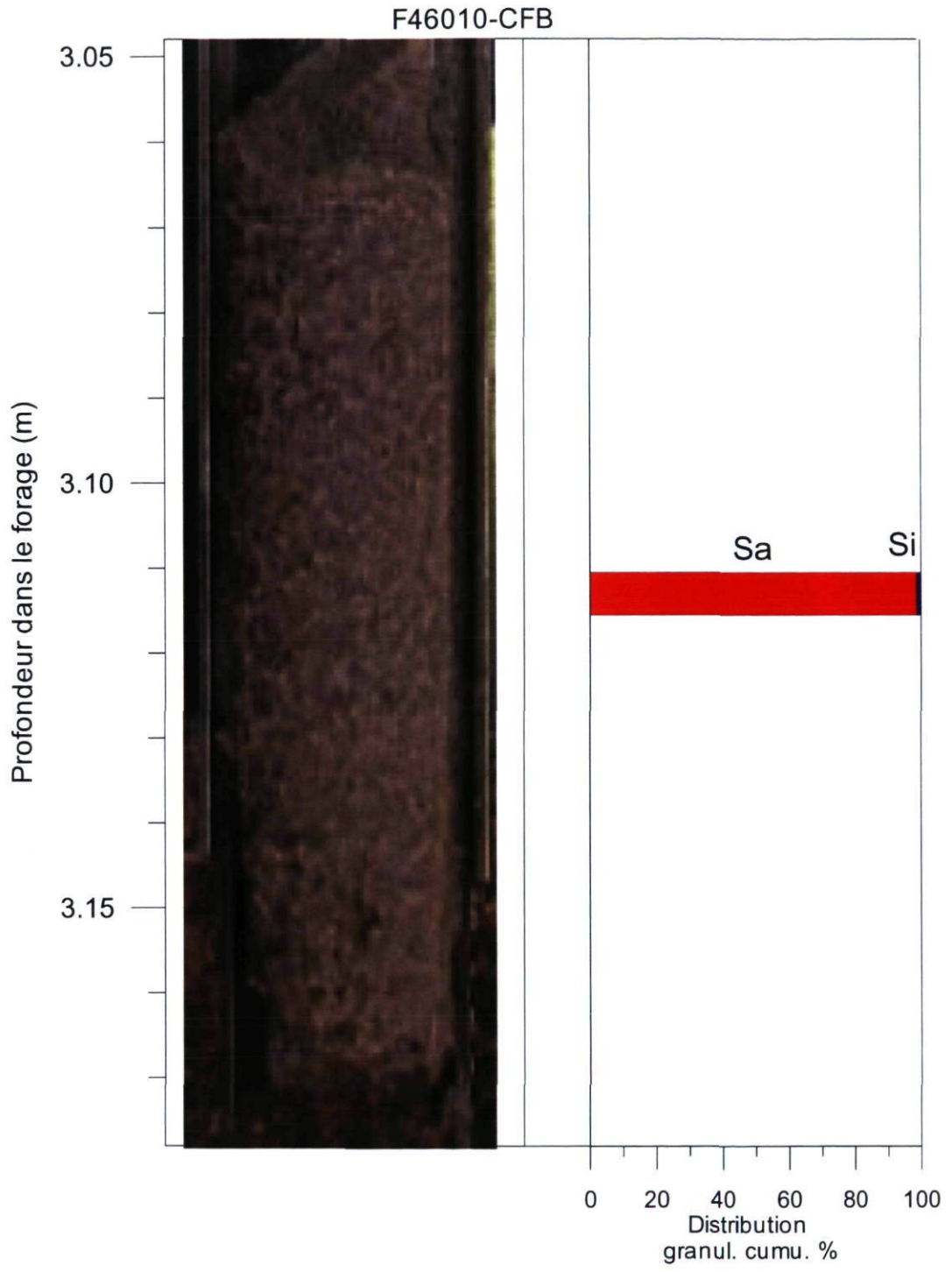




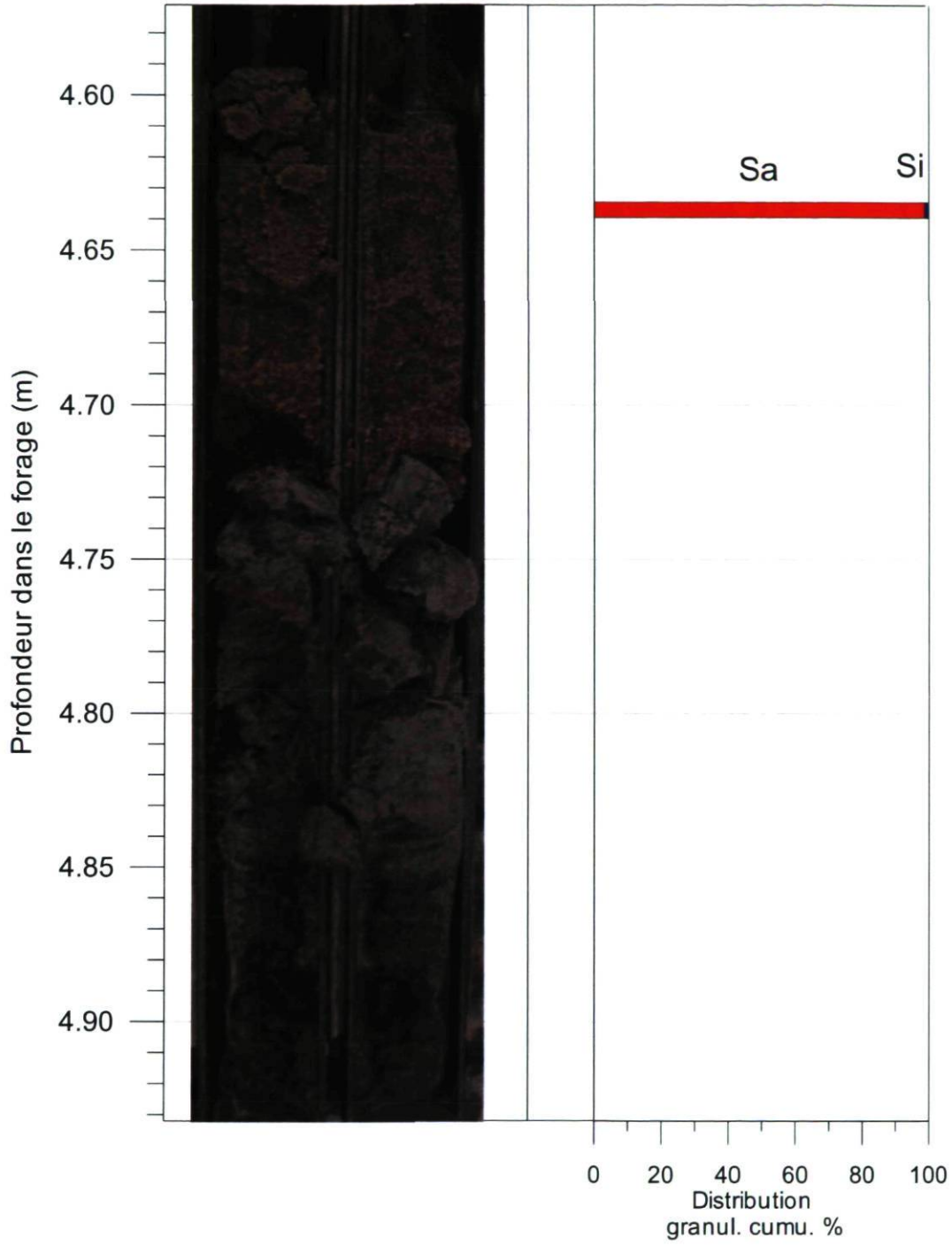




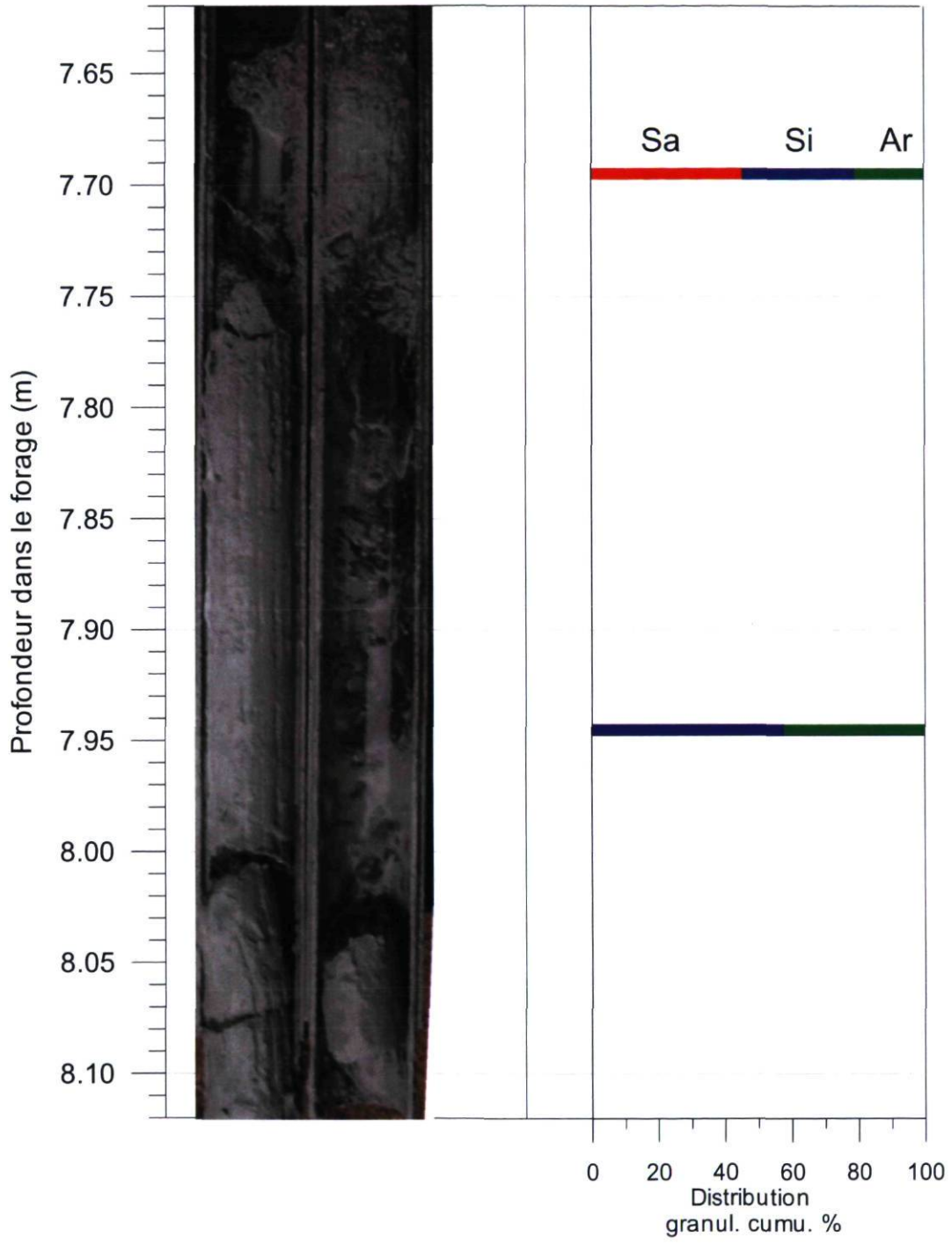
H.8.3 CAT-Scan, propriétés physiques et sédimentologiques - F46010

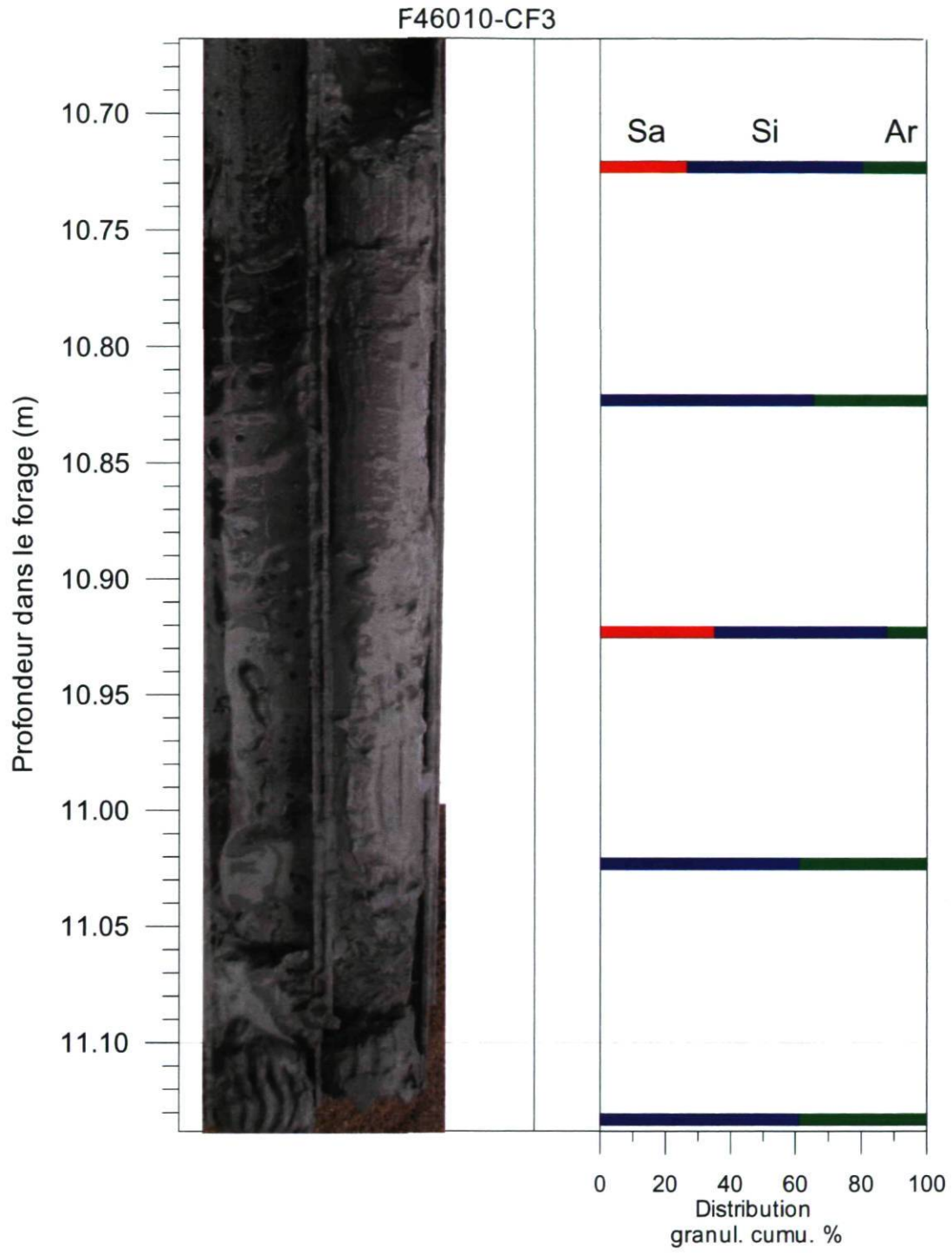


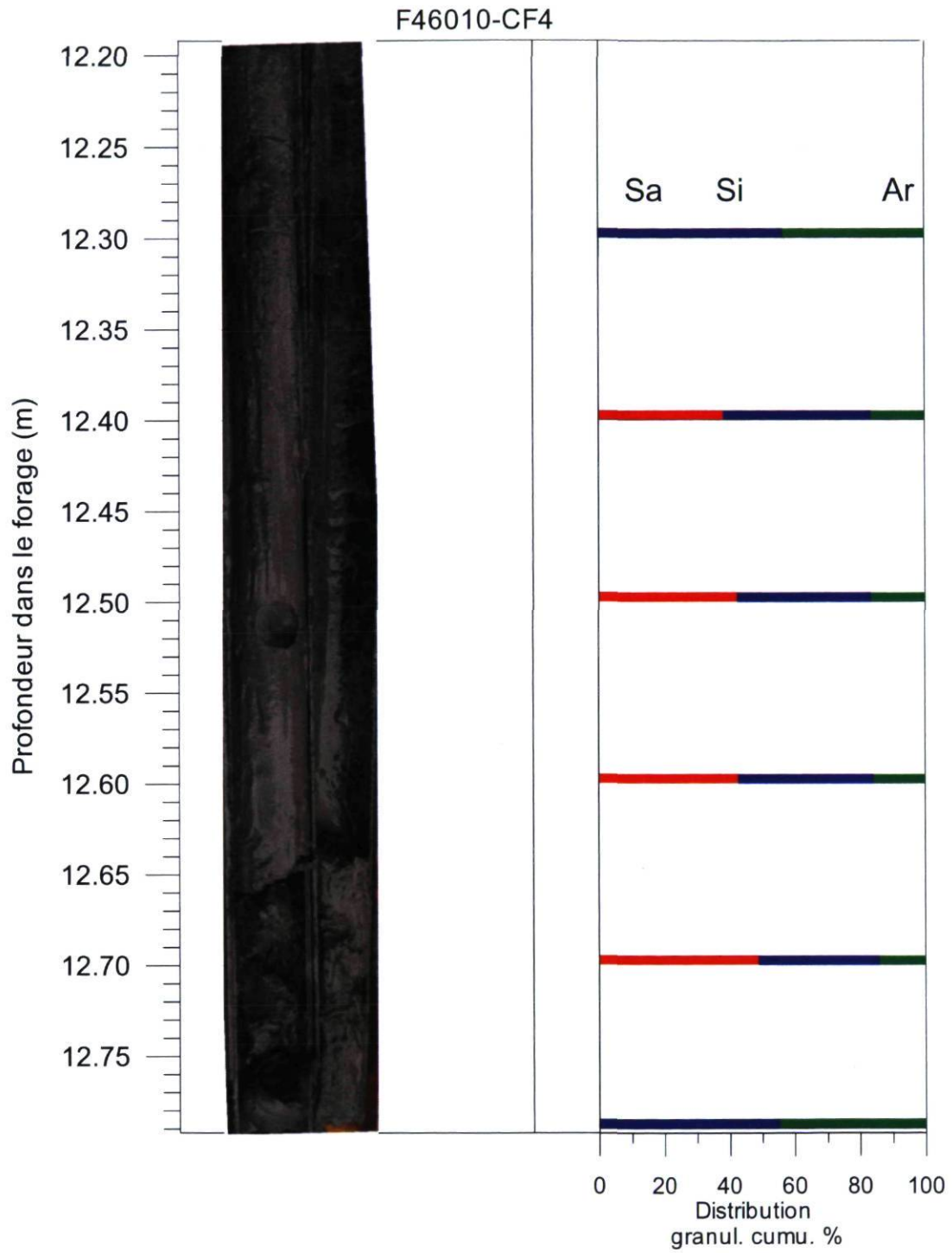
F46010-CF1

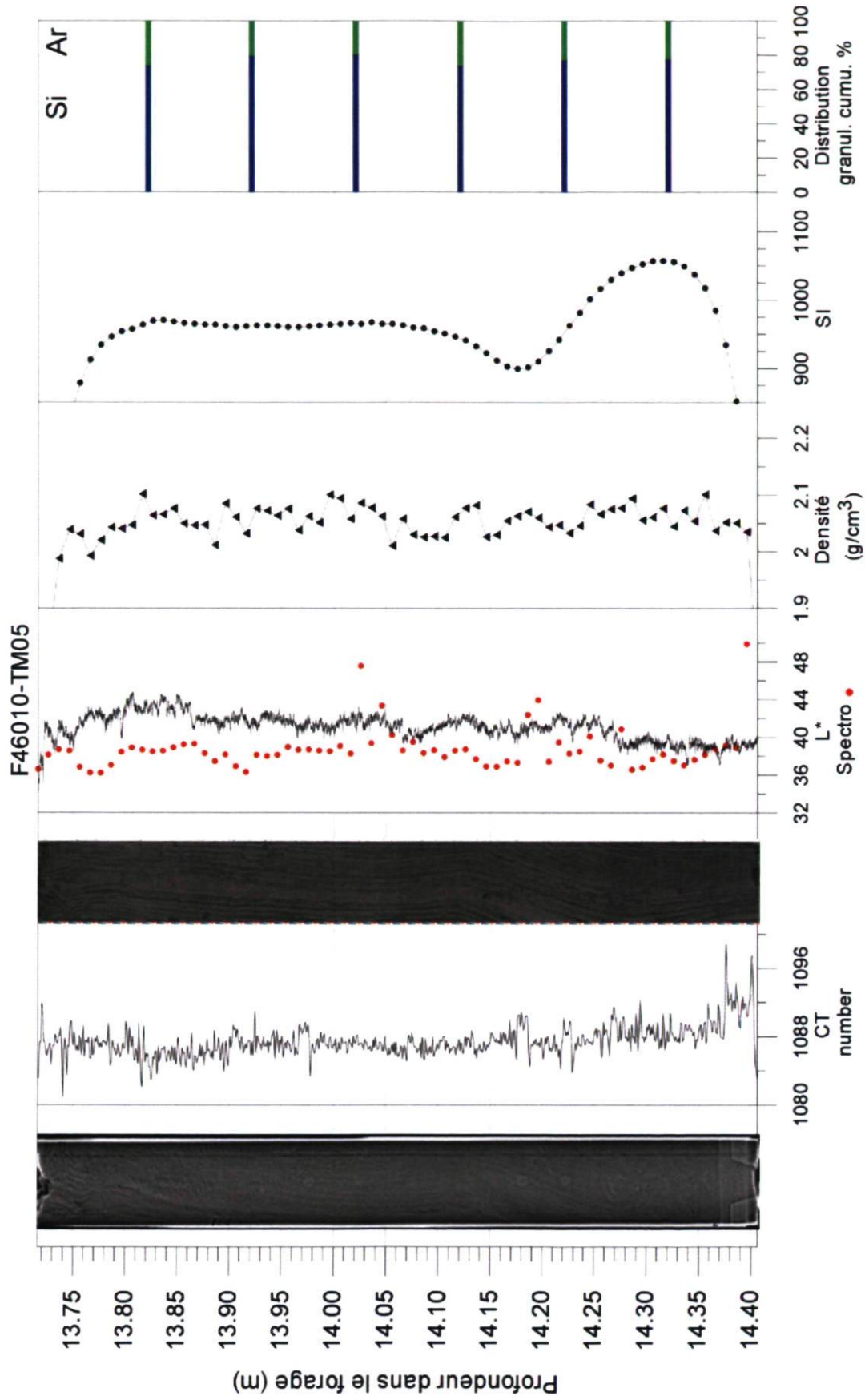


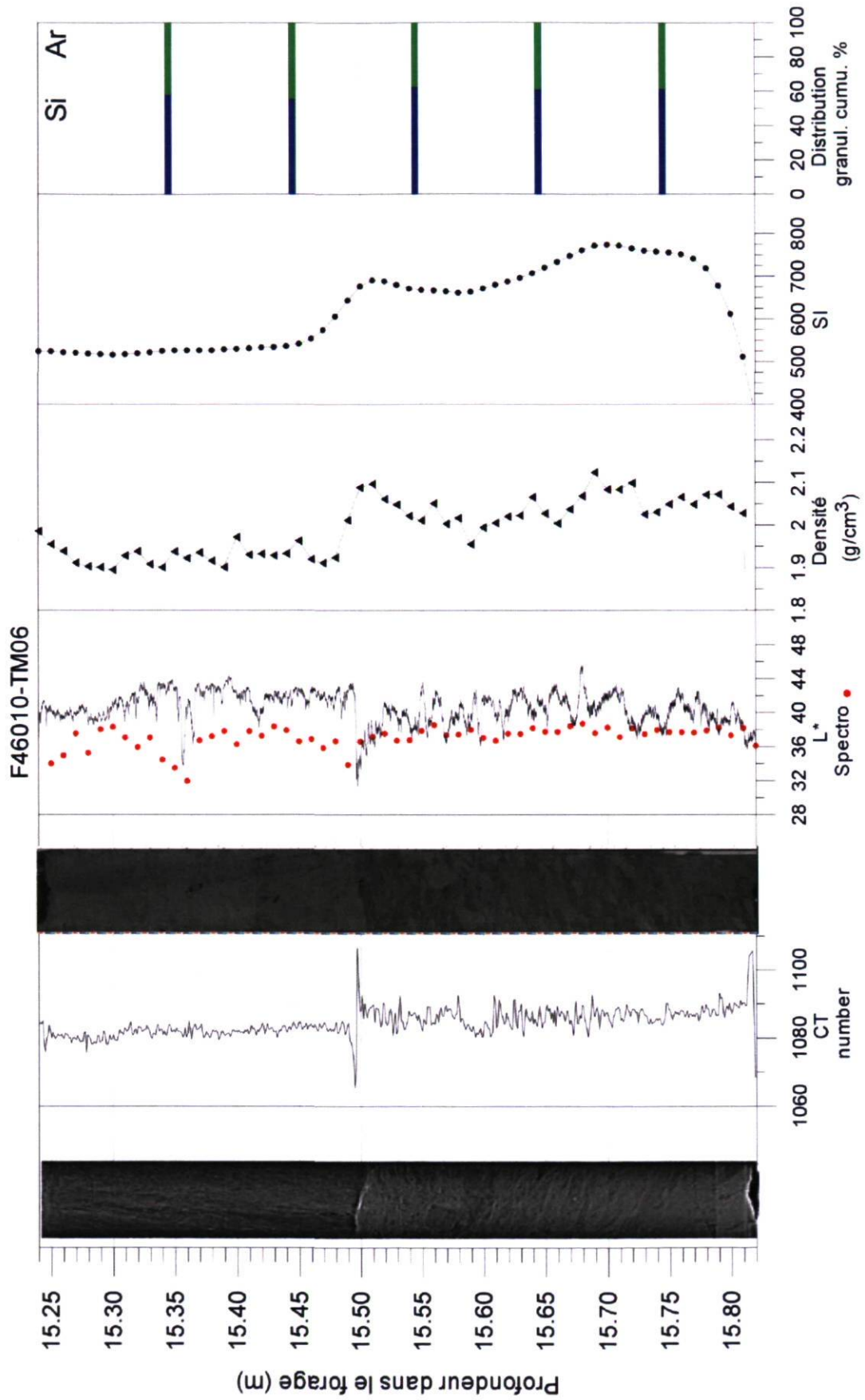
F46010-CF2

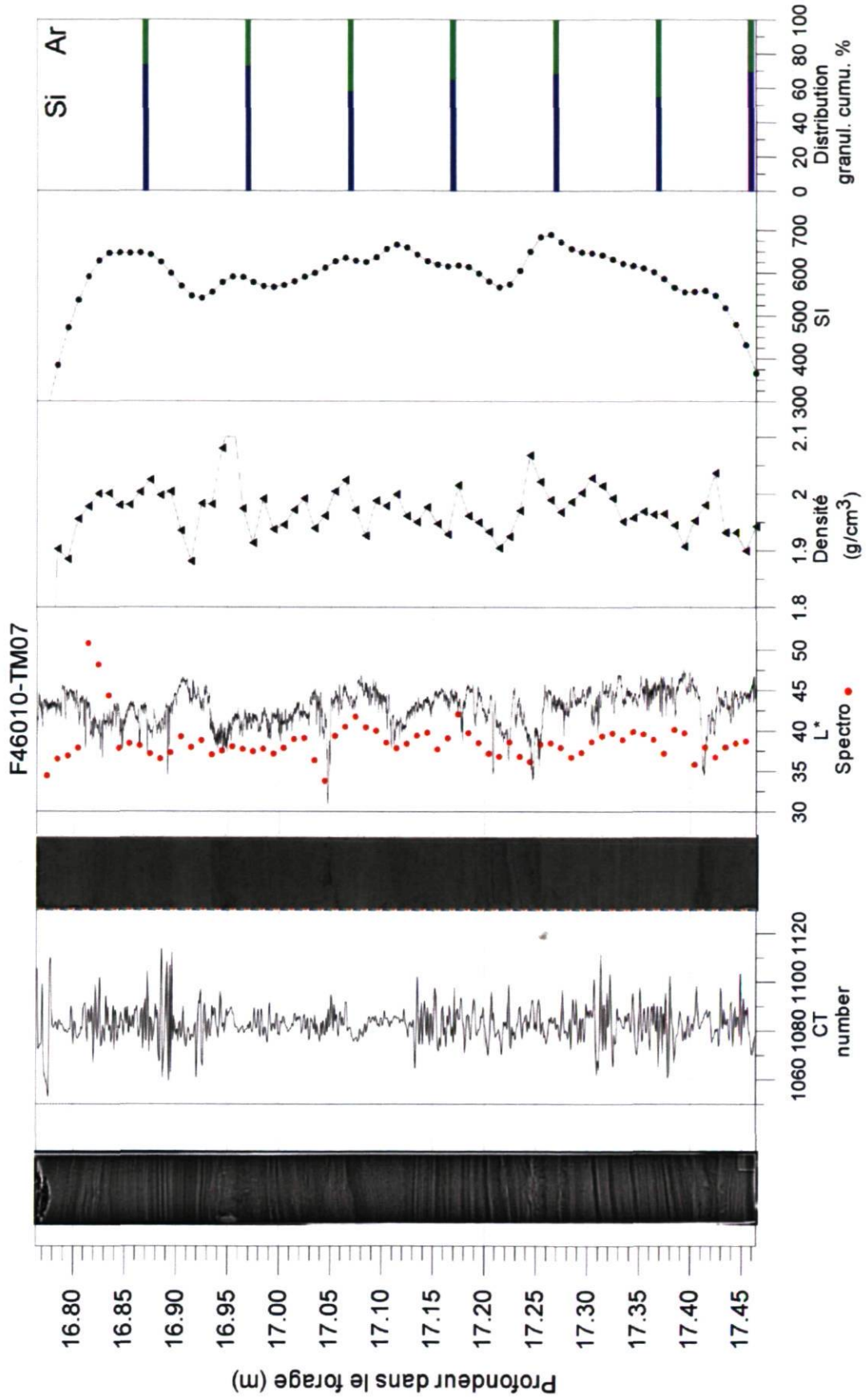


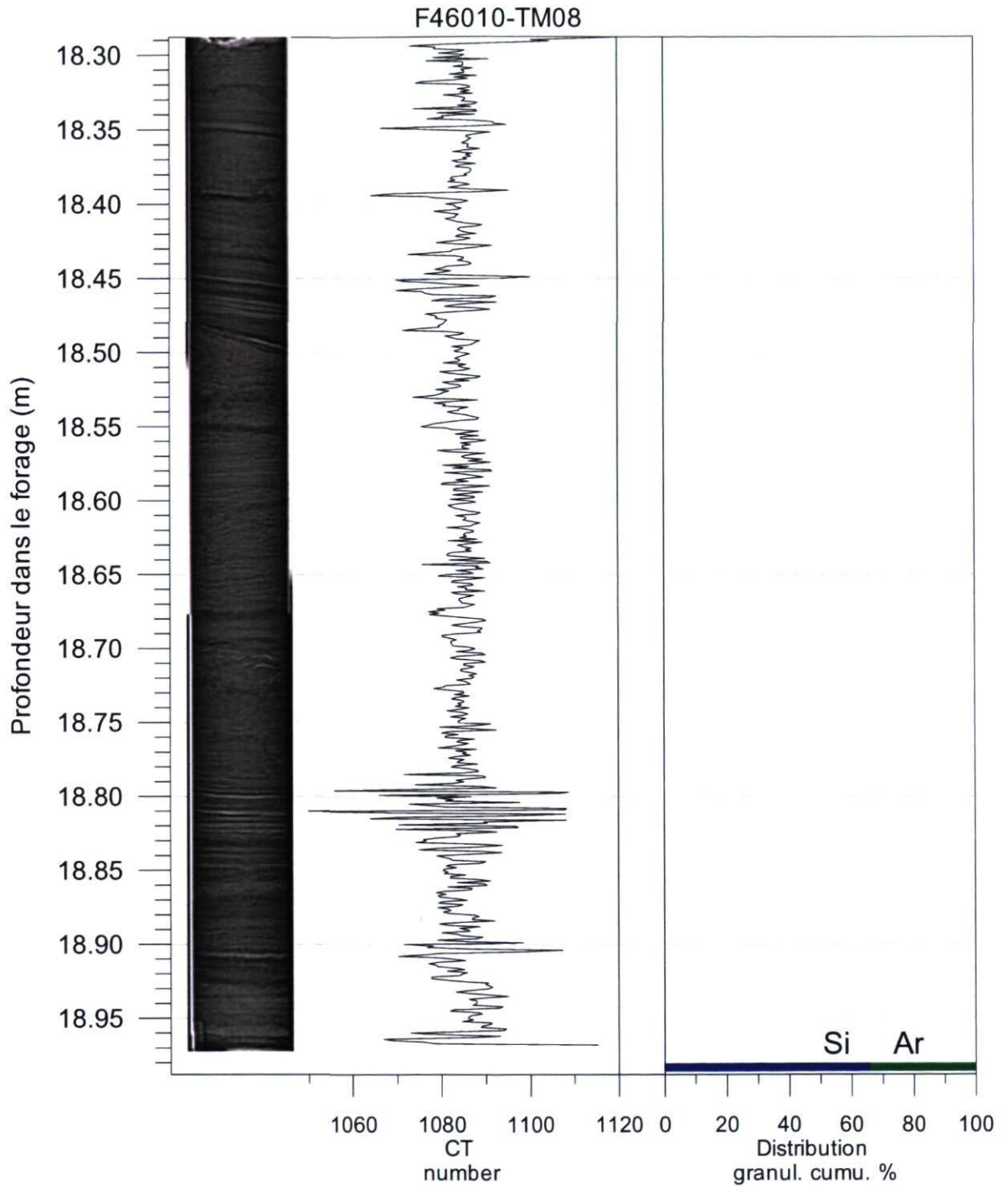


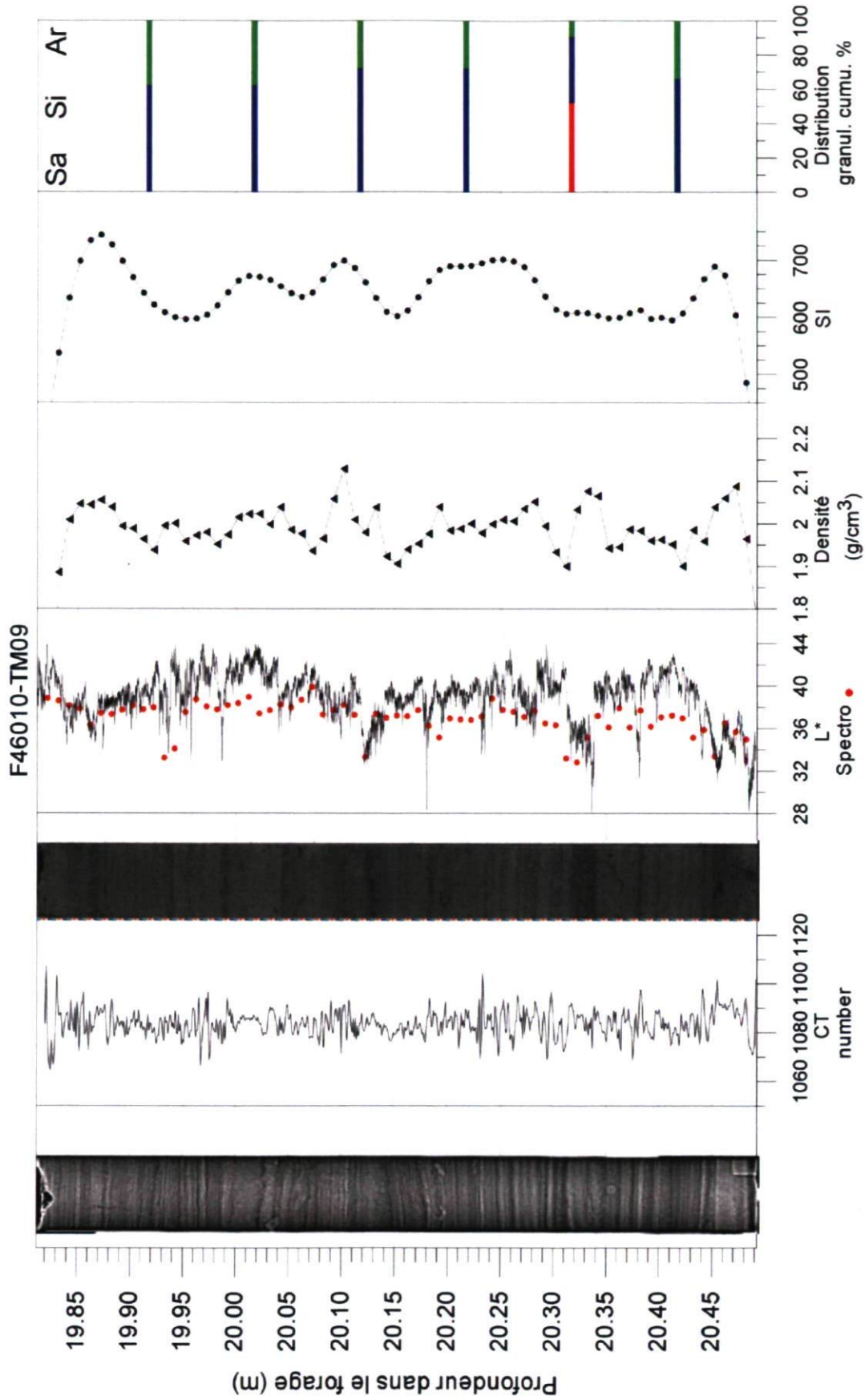


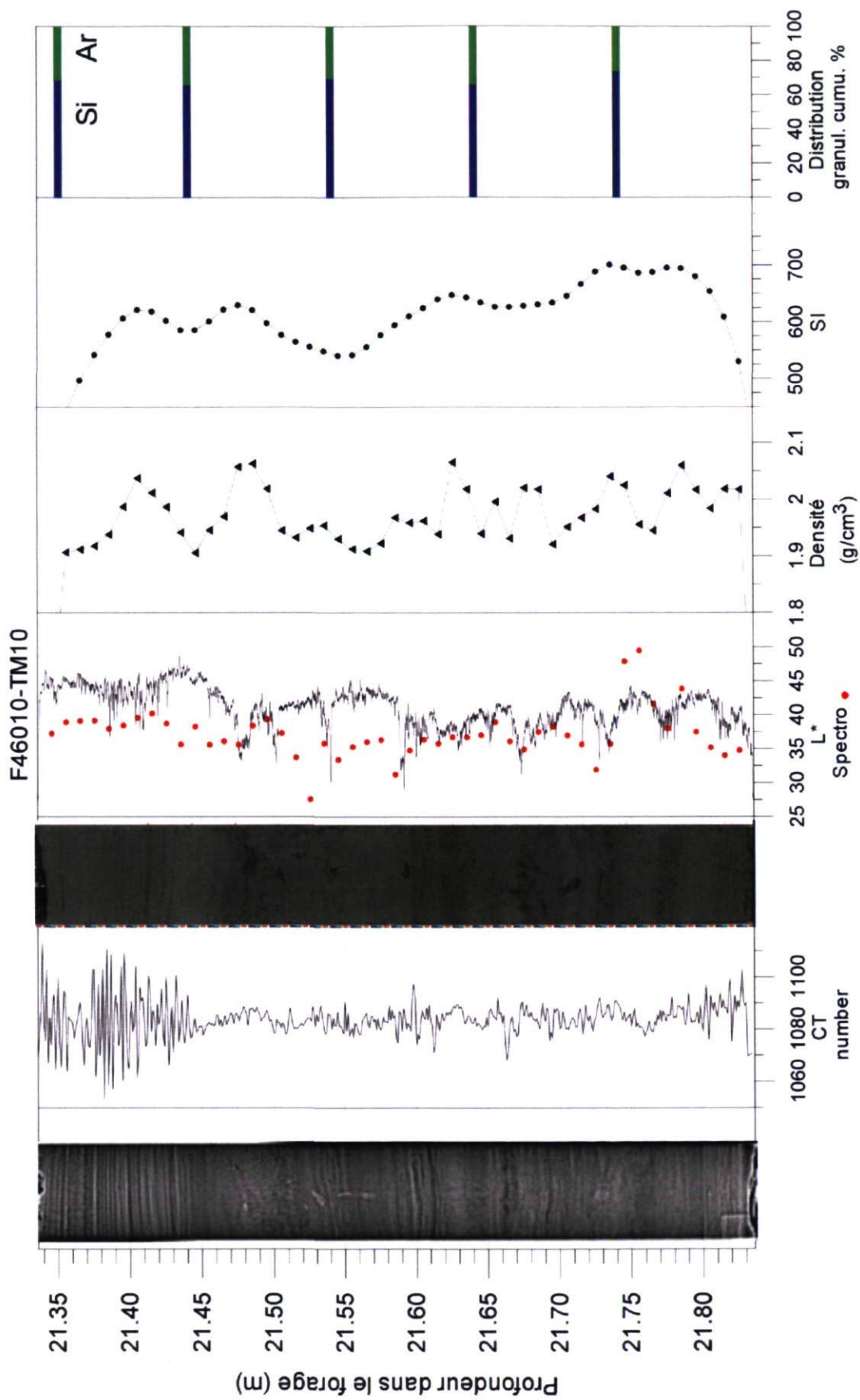


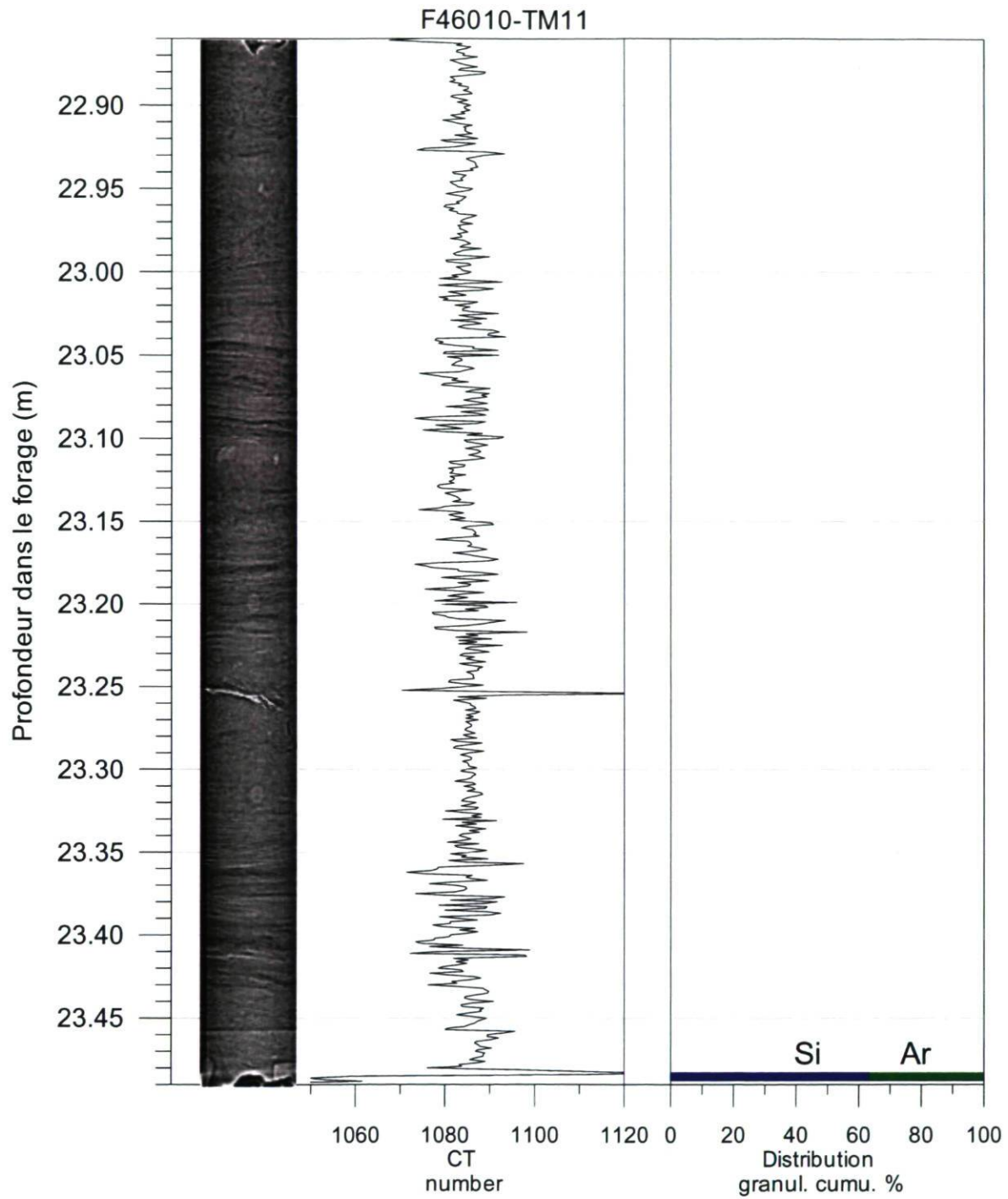


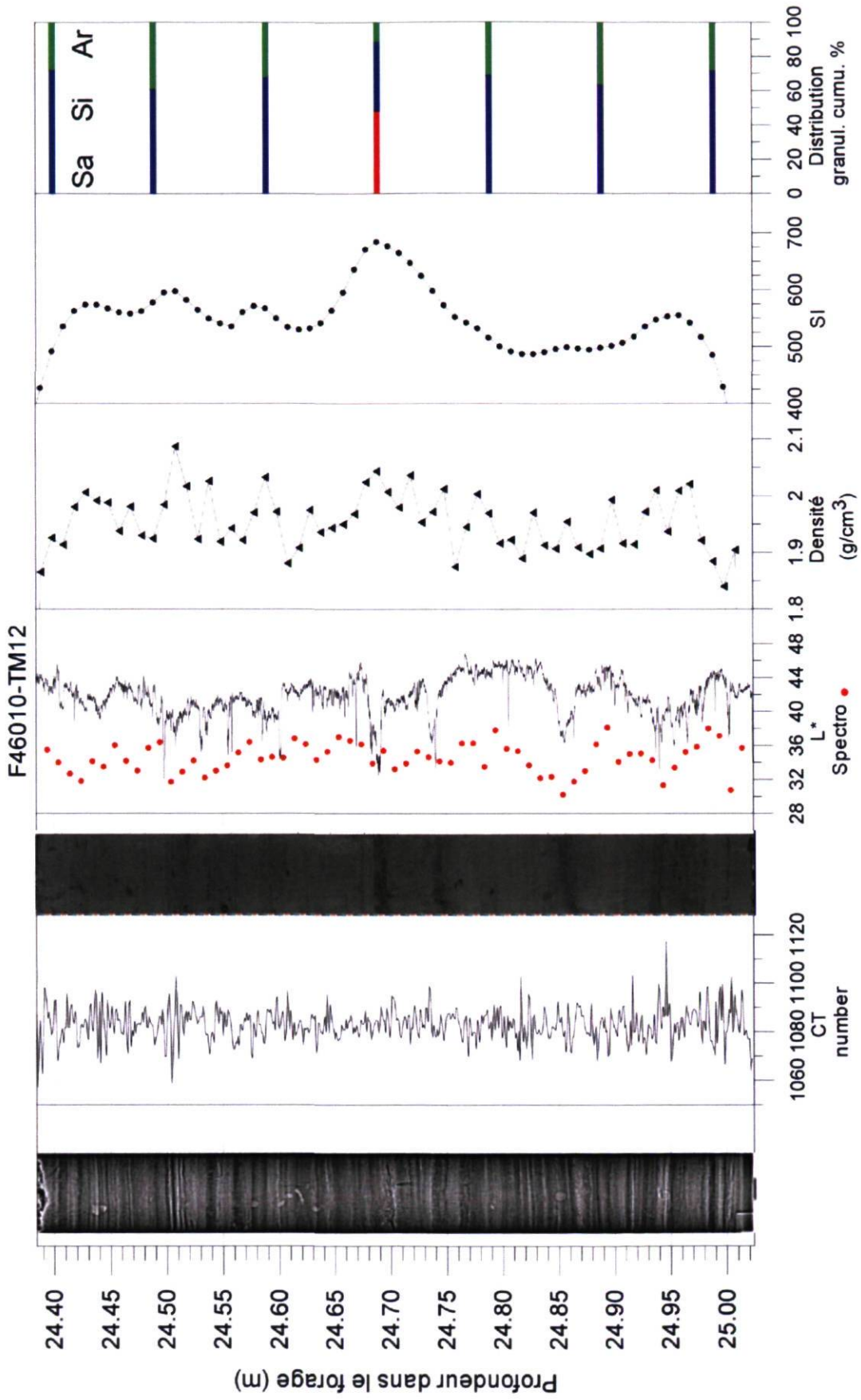


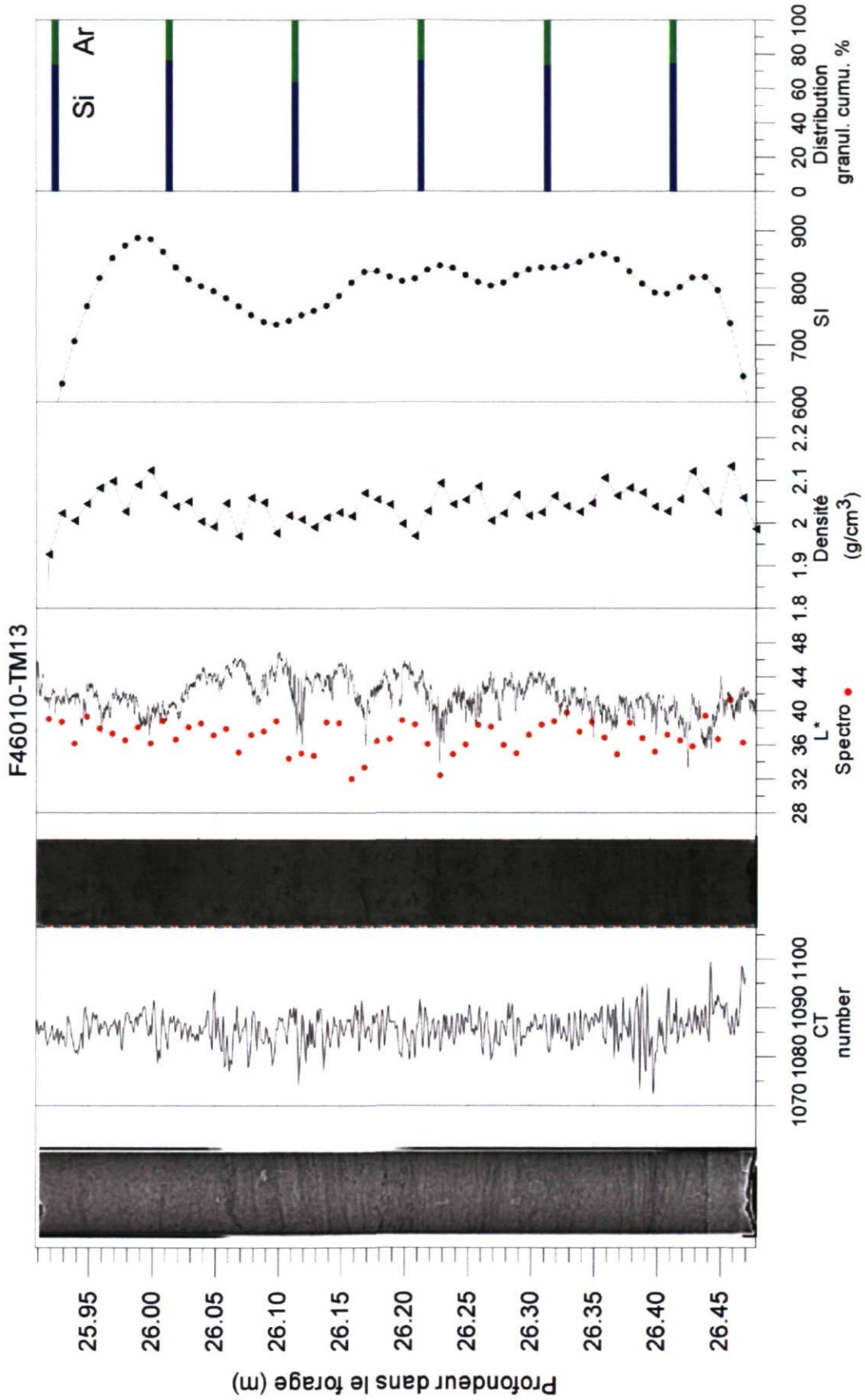


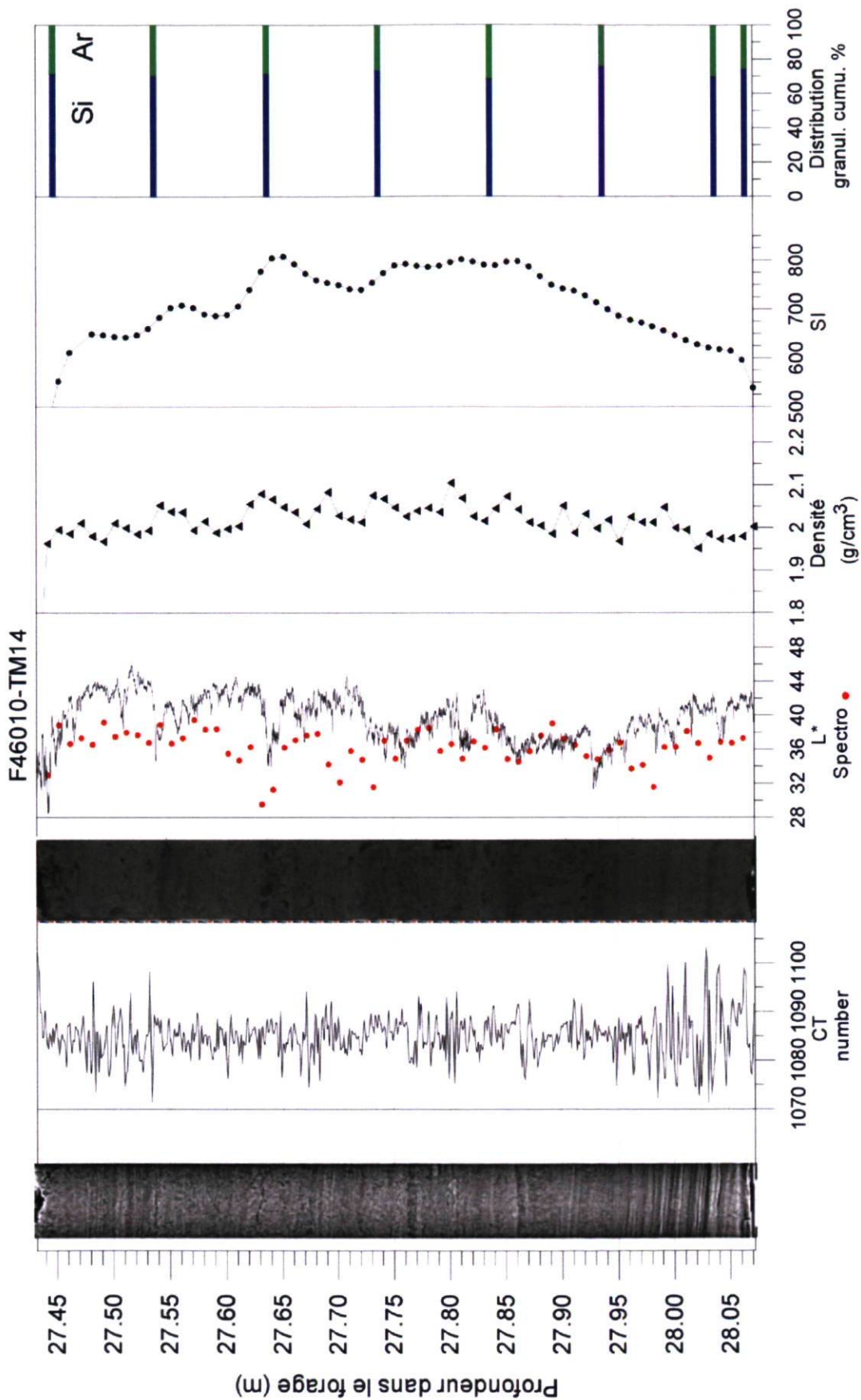


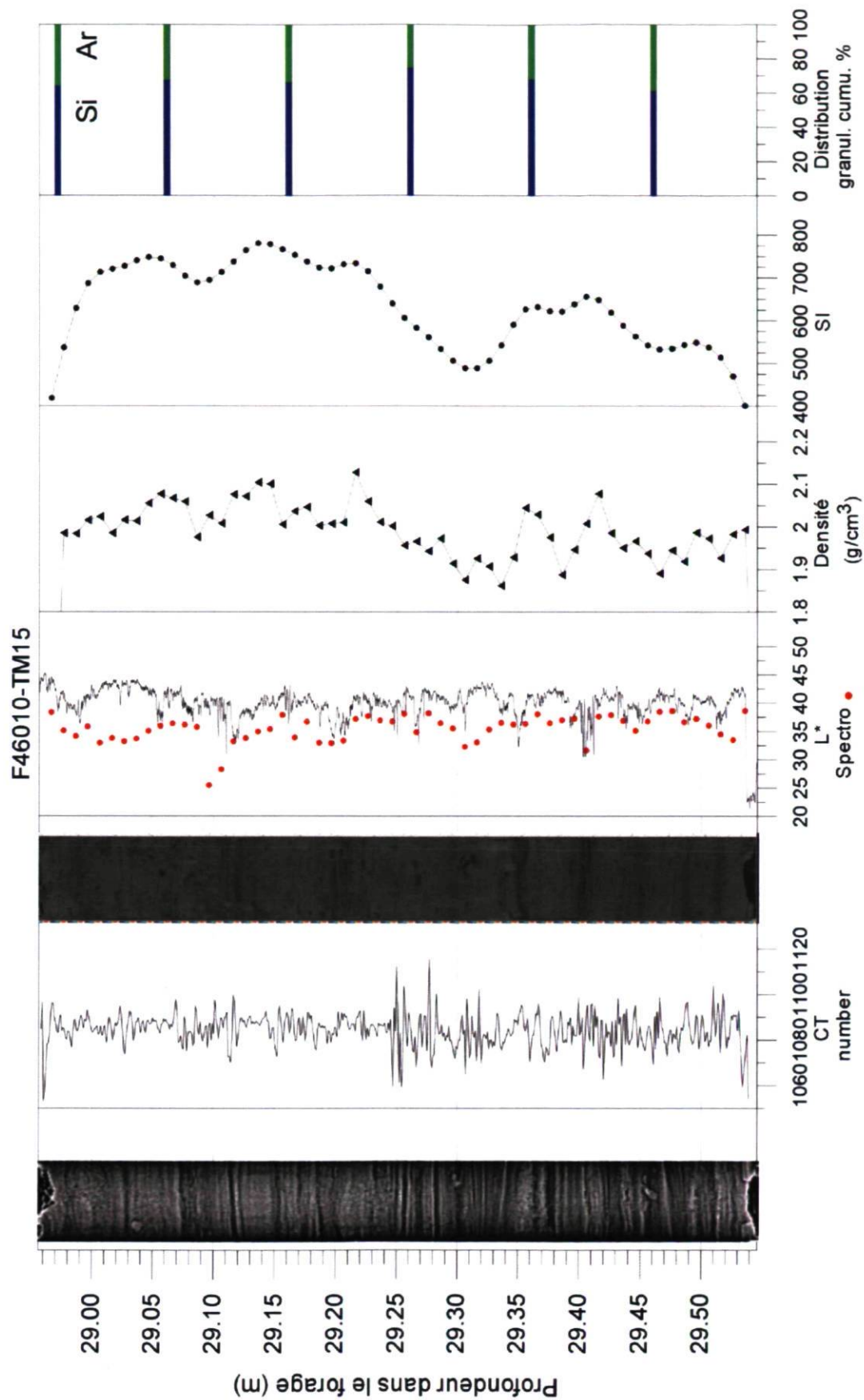


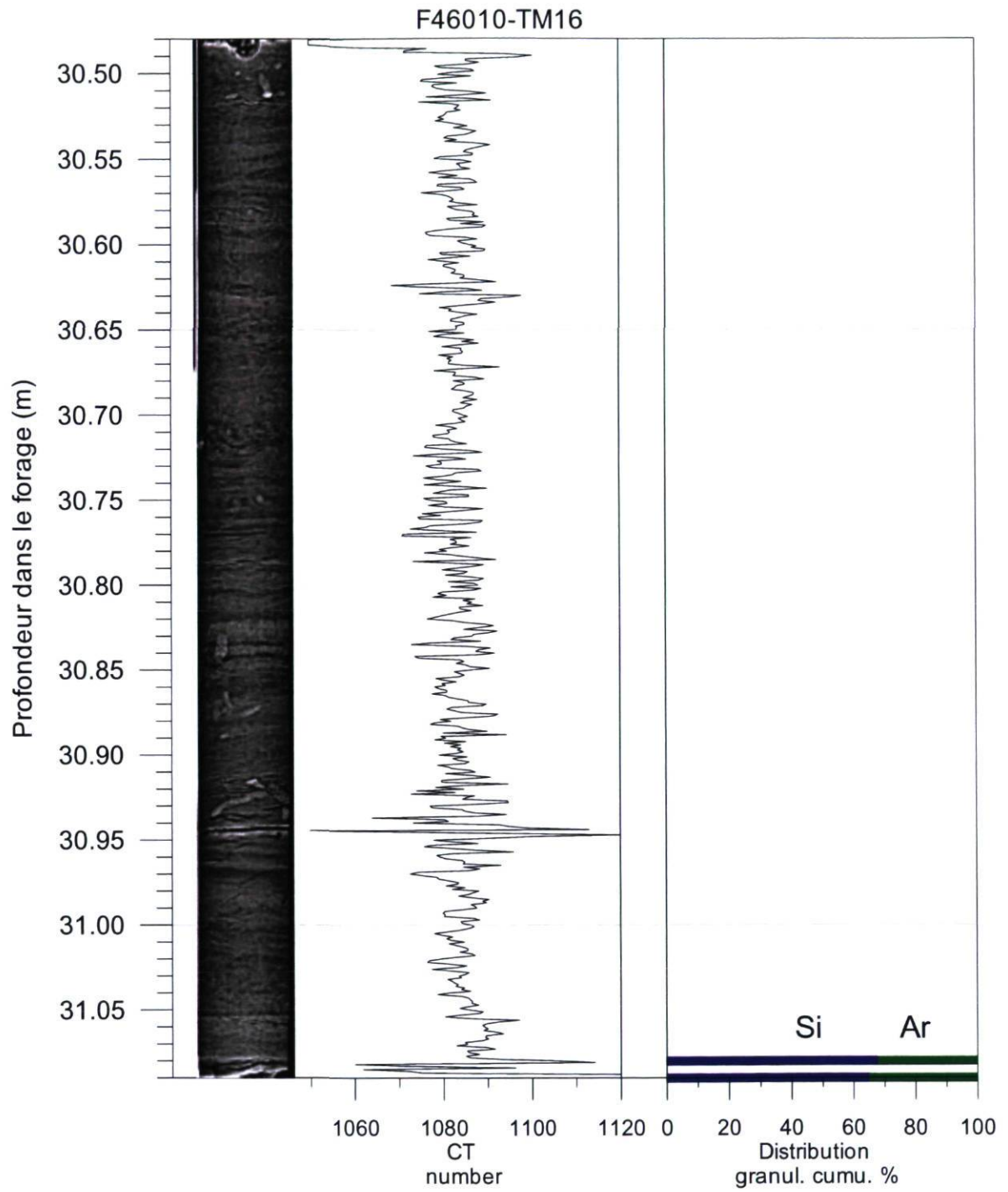


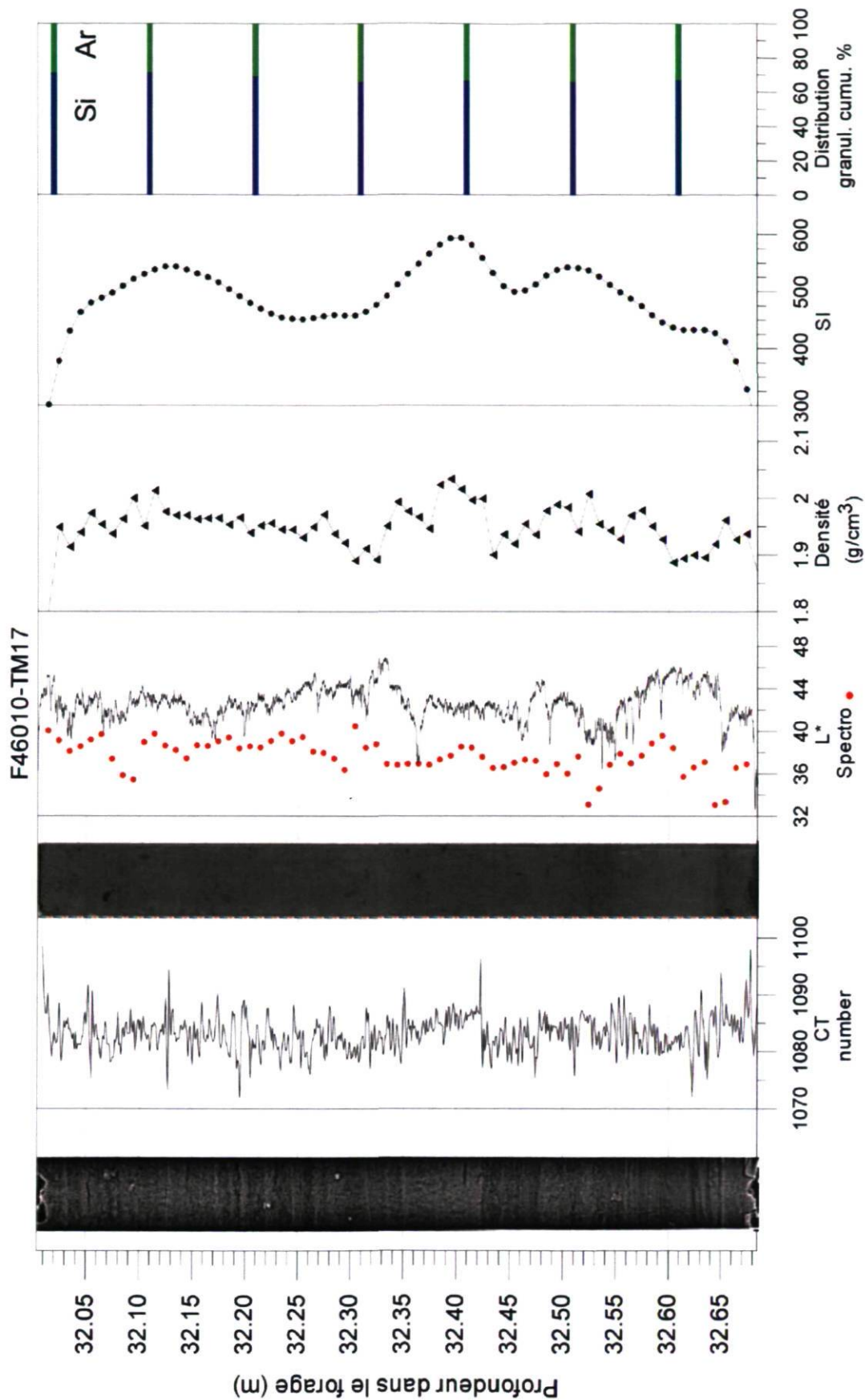


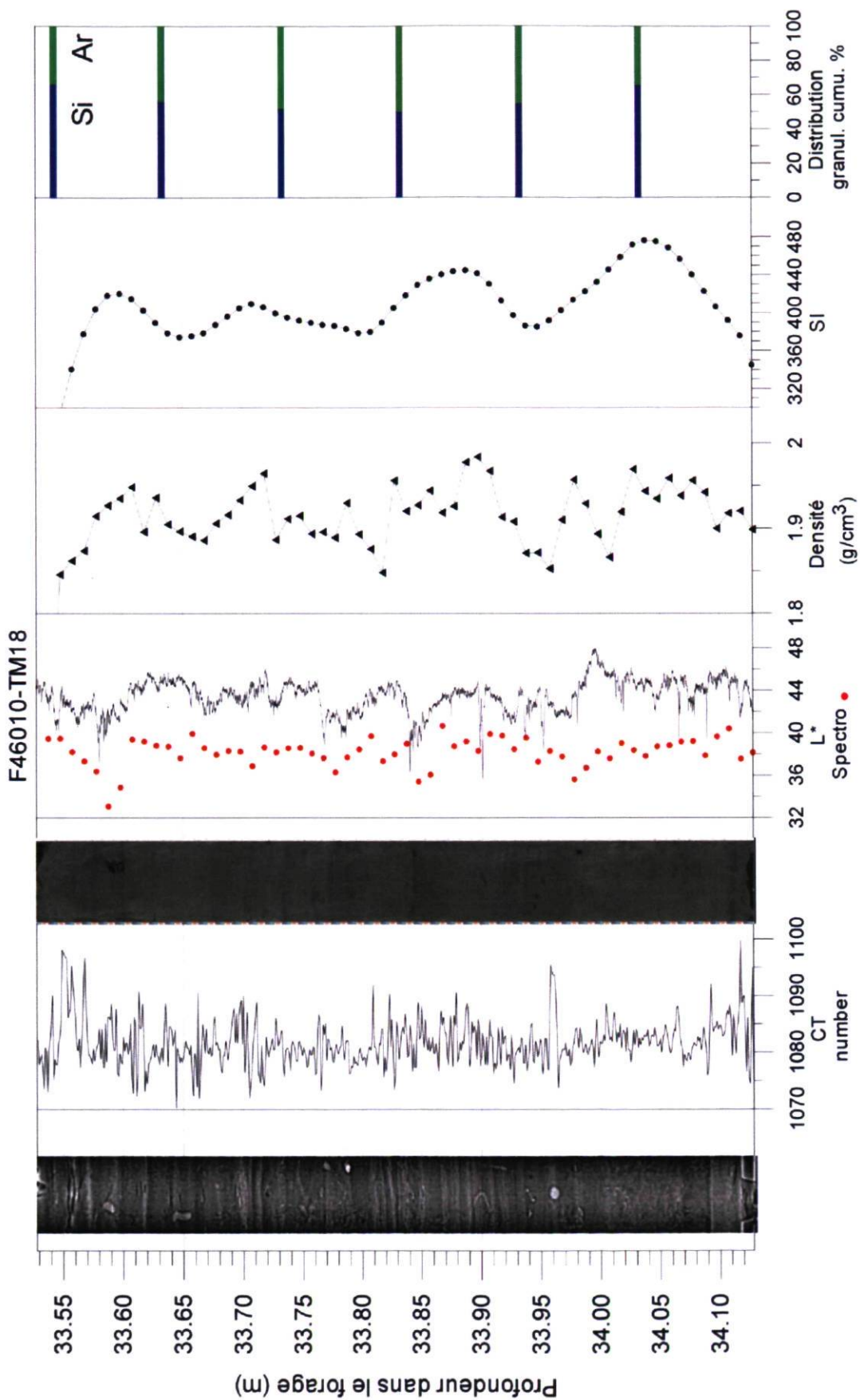


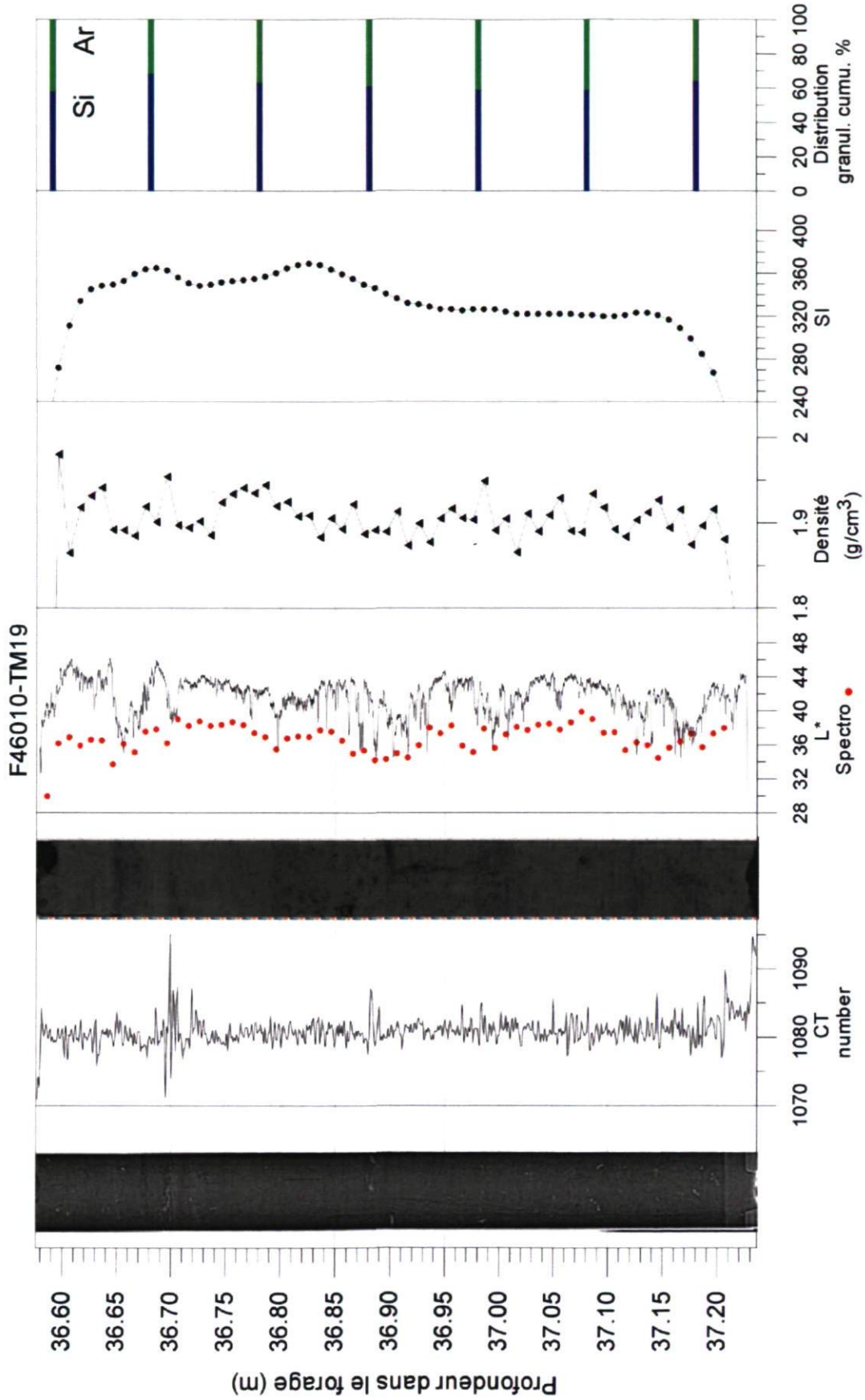


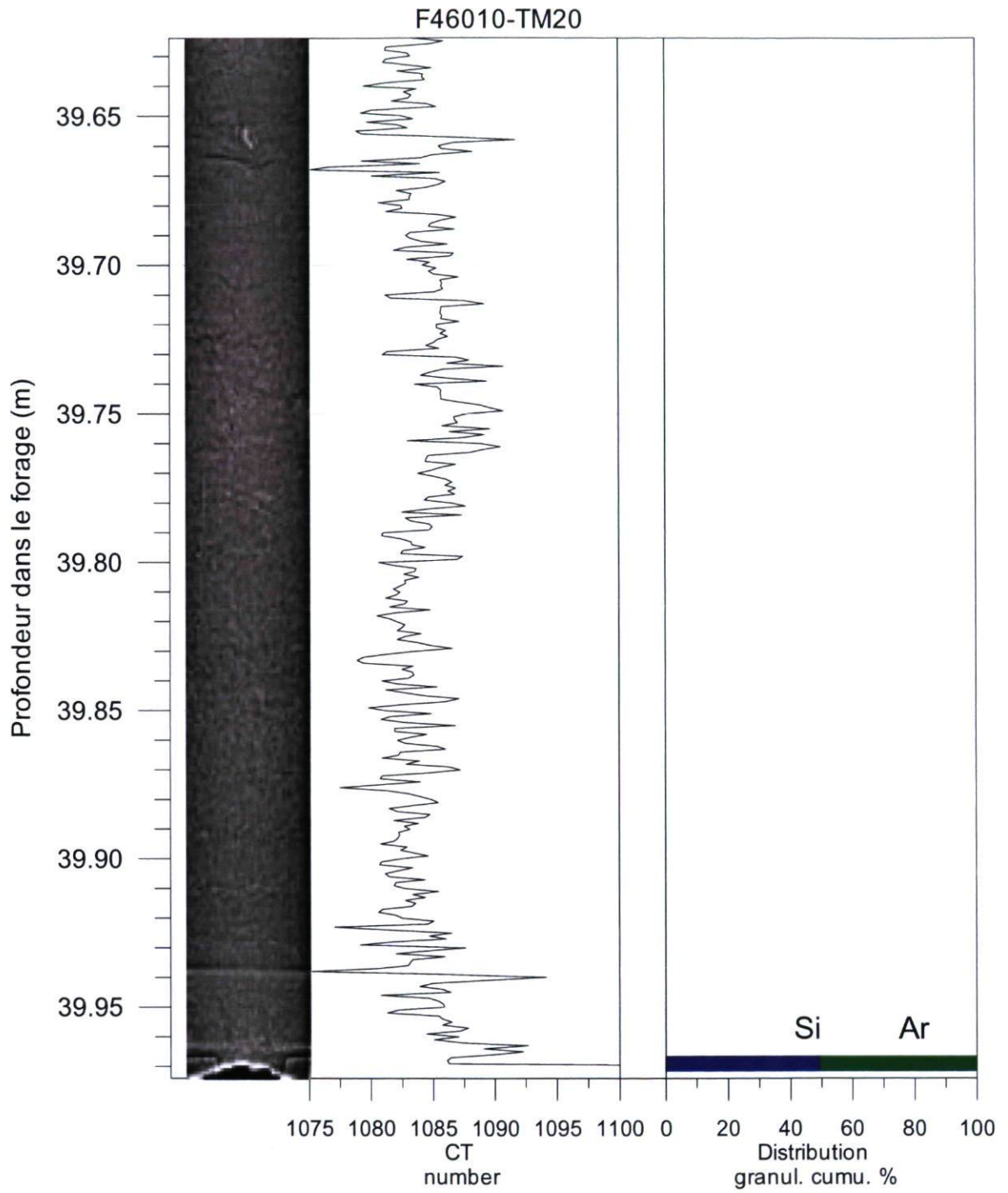


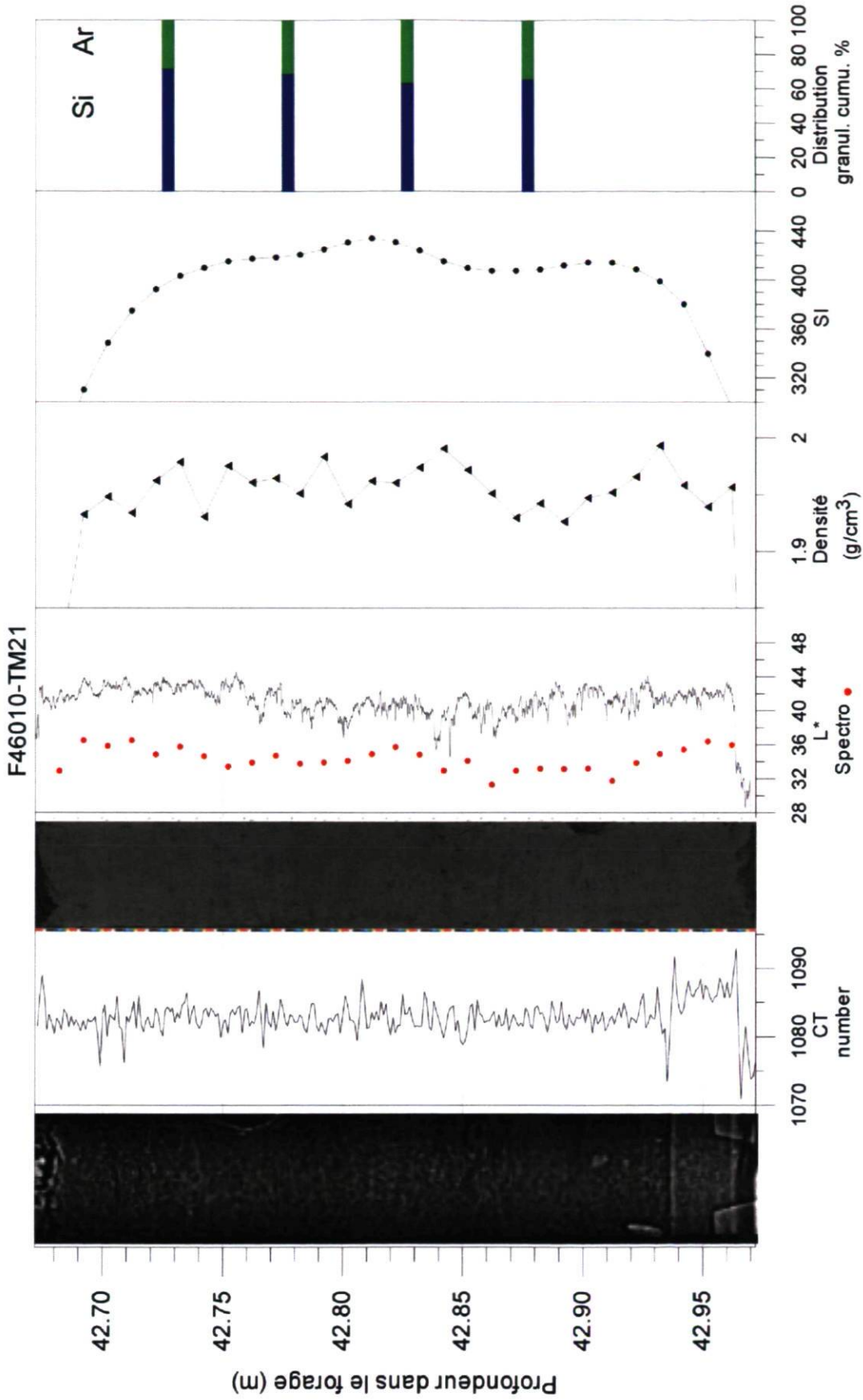




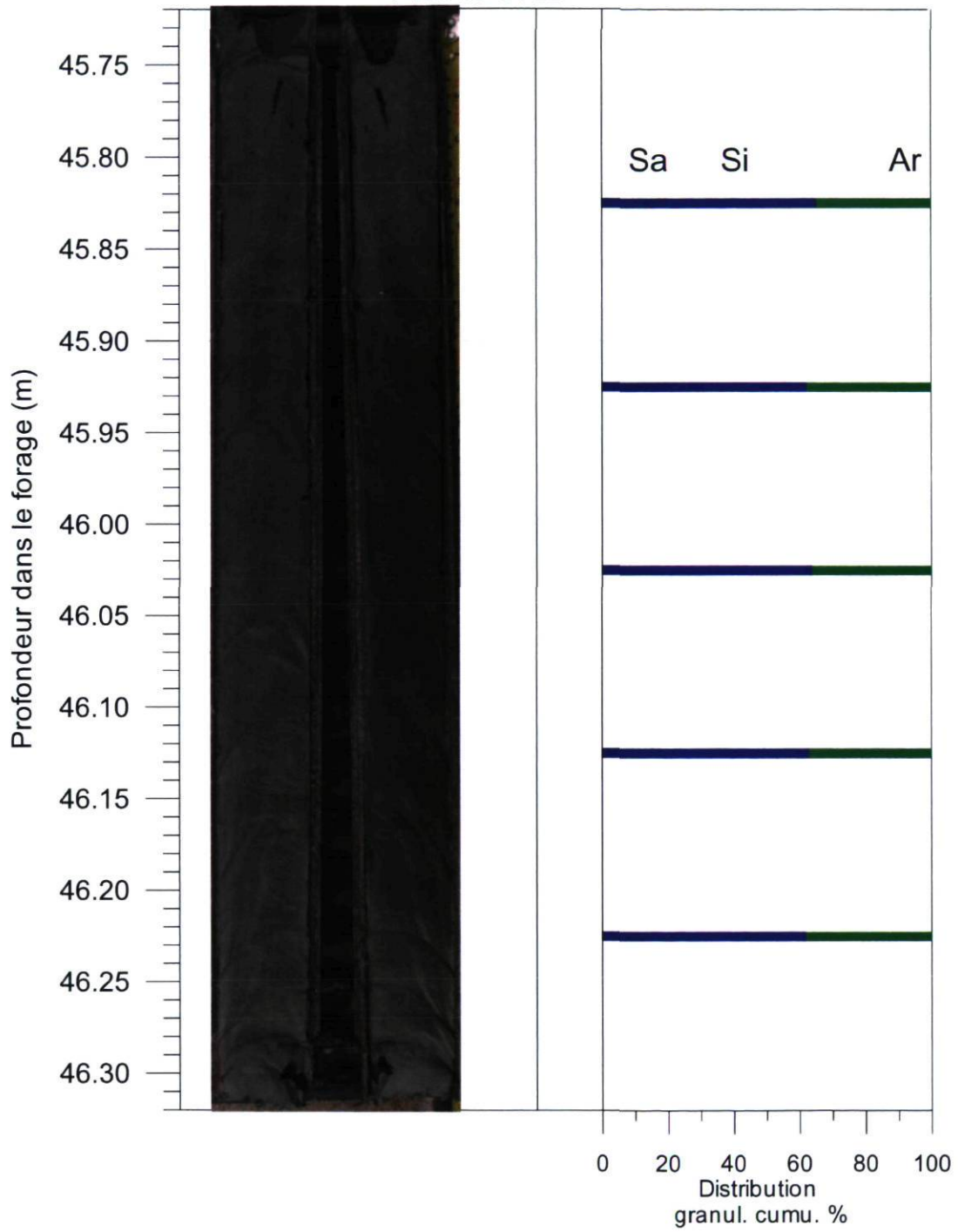


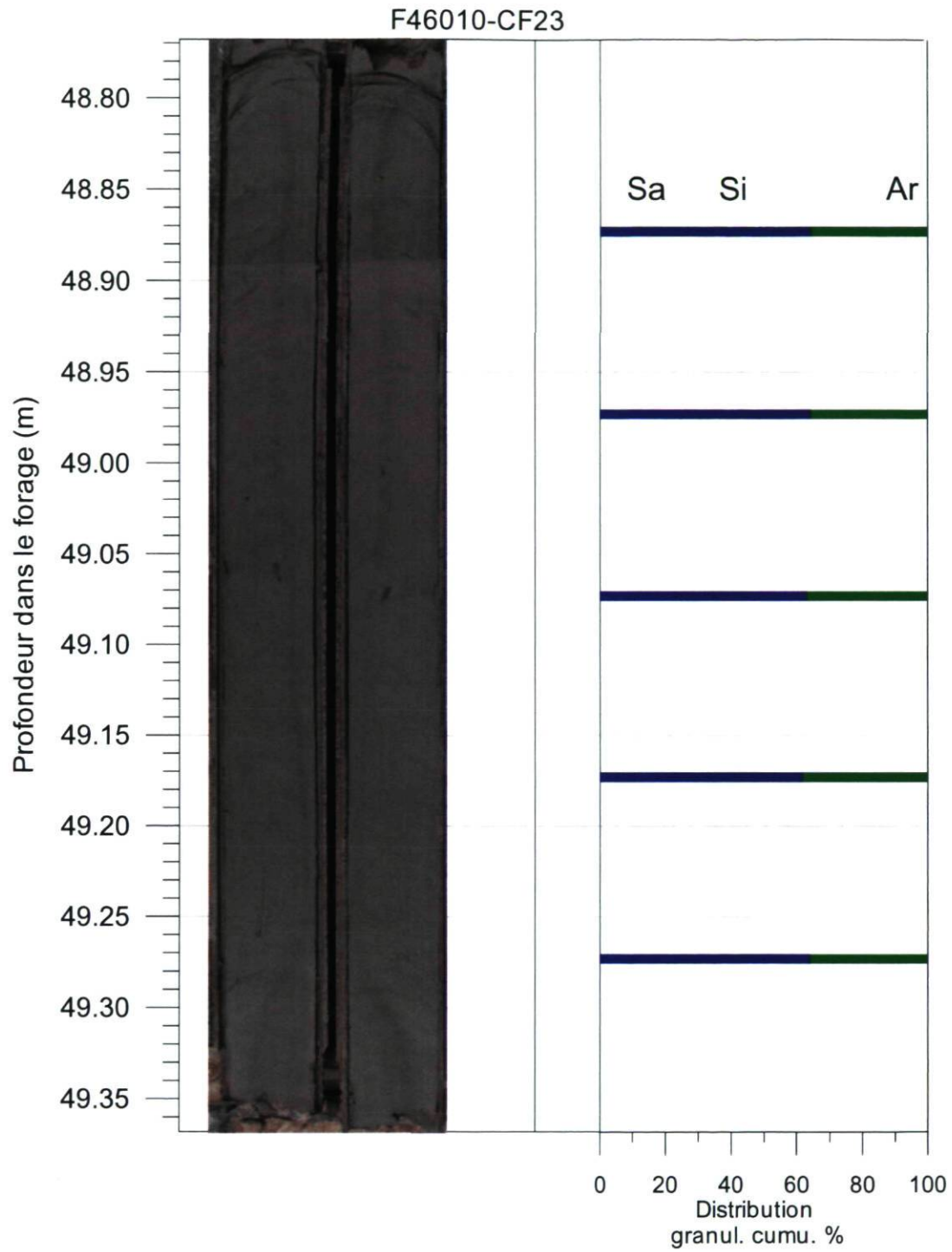


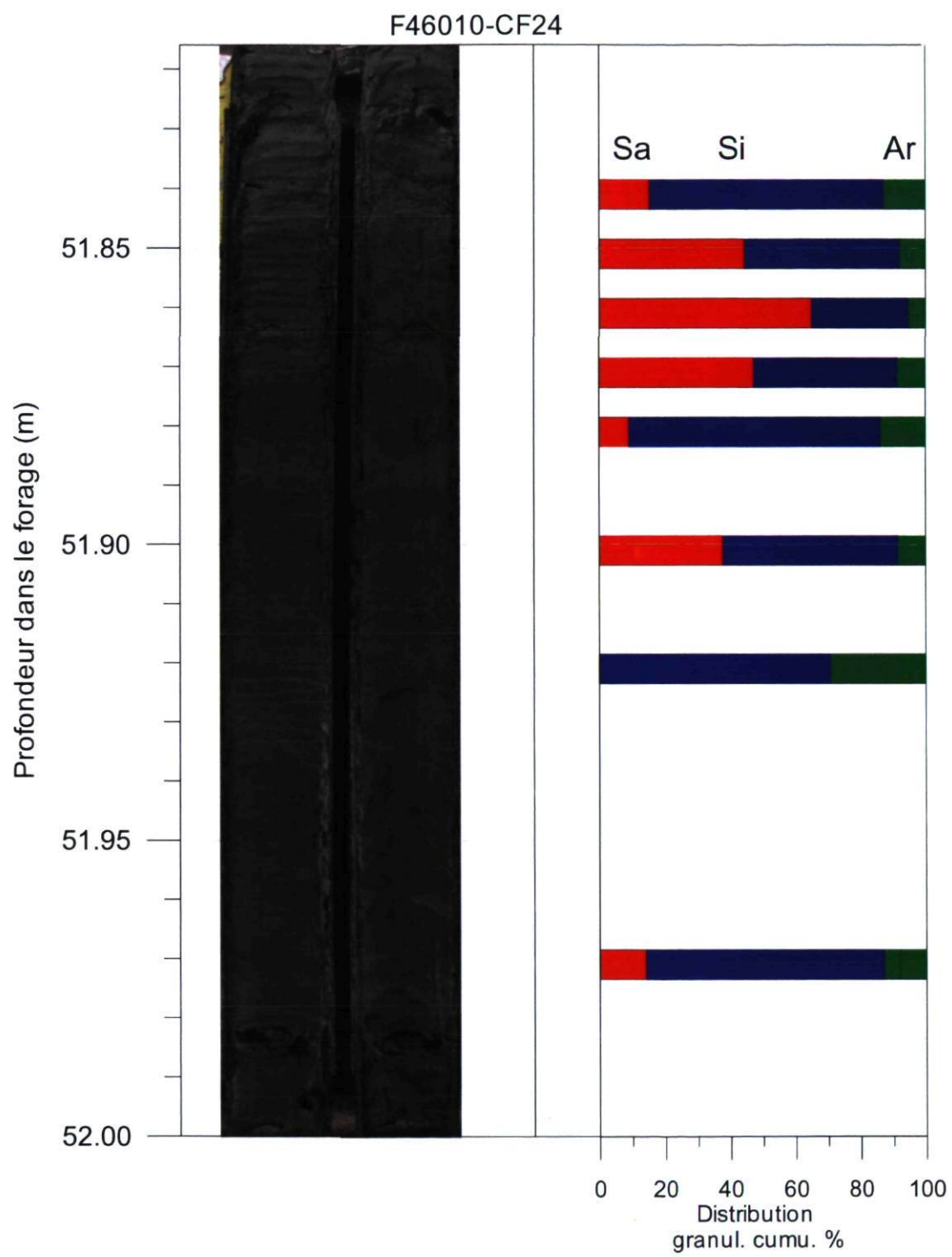


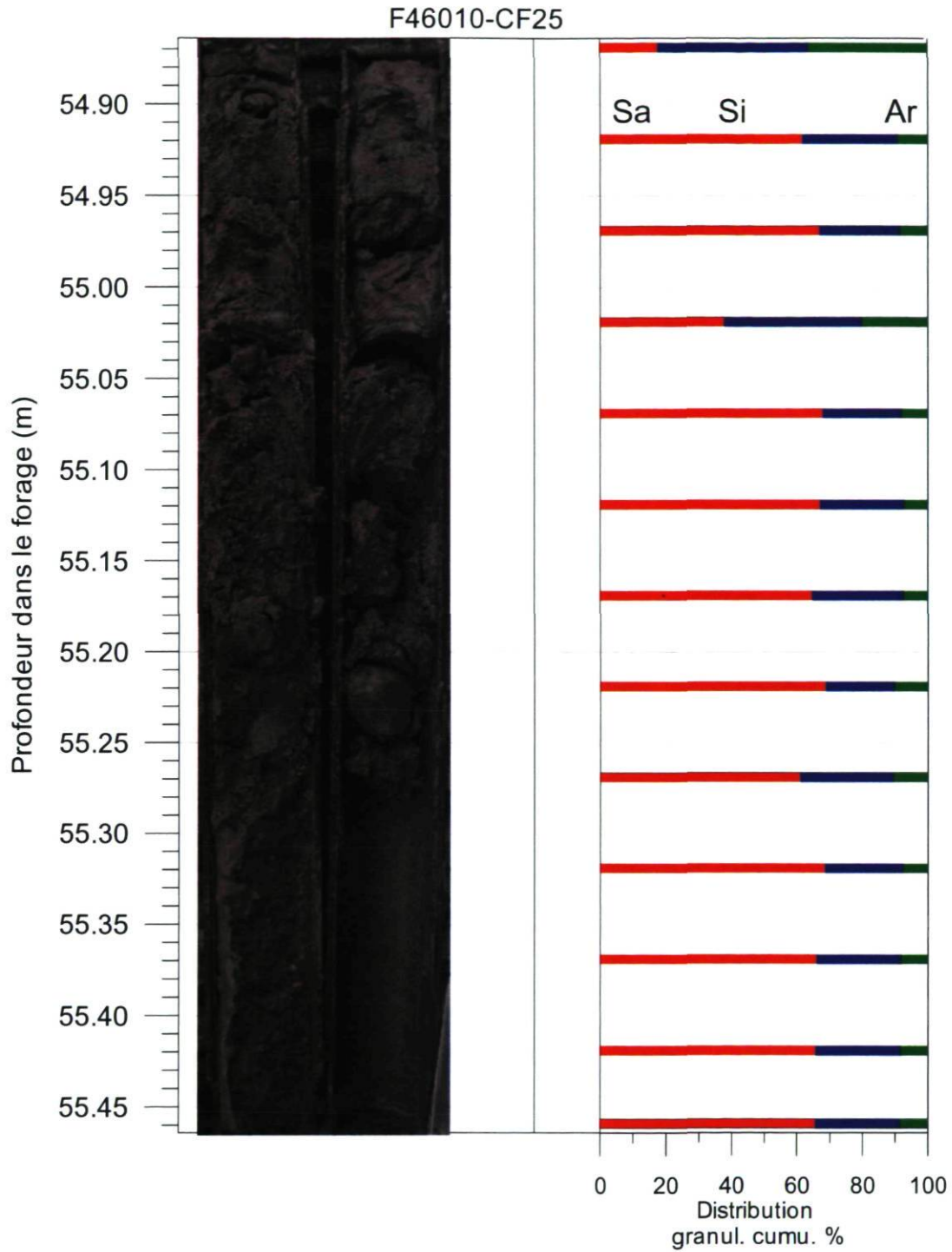


F46010-CF22









I Résultats des datations au ^{14}C

I.1 Tableaux des résultats des datations aux forages 46006 et 46010

Coordonnées des lieux de forages dans lesquels les coquilles ont été échantillonnées.

Forage	X (UTM 19N)	Y (UTM 19N)
F46006	516958	5416735
F46010	519128	5415969

University of California #	Université Laval #	Échantillon	Matériel	Prétraitement
UCIAMS-66258	ULA-1189	F46006-TM6	Fragment de coquille	Lessivage
UCIAMS-60876	ULA-972	F46006-TM7	Fragment de coquille	Lessivage
UCIAMS-60872	ULA-968	F46006-TM8	Fragment de coquille	Lessivage
UCIAMS-60874	ULA-970	F46006-TM8	Fragment de coquille	Lessivage
UCIAMS-66260	ULA-1191	F46010-TM11	Fragment de coquille	Lessivage
UCIAMS-60873	ULA-969	F46010-TM17	Fragment de coquille	Lessivage
UCIAMS-66259	ULA-1190	F46010-TM20	Fragment de coquille	Lessivage
UCIAMS-60875	ULA-971	F46010-TM21	Fragment de coquille	Lessivage
UCIAMS-66261	ULA-1192	F46010-CF22	Fragment de coquille	aucun

Échantillon	Fraction moderne	±	D^{14}C	±	Conv. age ^{14}C (ans BP)	±	Âge calibré (ans cal BP)	Élévation (m)
F46006-TM6	0.3155	0.0006	-685	0.6	9265	20	10136	19.57
F46006-TM7	0.3017	0.0008	-698	0.8	9625	25	10508	15.55
F46006-TM8	0.298	0.0008	-702	0.8	9725	25	10570	9.97
F46006-TM8	0.2973	0.0008	-703	0.8	9745	25	10585	9.41
F46010-TM11	0.3117	0.0006	-688	0.6	9365	20	10203	-15.27
F46010-TM17	0.3122	0.0008	-688	0.8	9350	25	10194	-24.17
F46010-TM20	0.2942	0.0006	-706	0.6	9830	20	10666	-32.07
F46010-TM21	0.2963	0.0009	-704	0.9	9770	25	10609	-34.97
F46010-CF22	0.2933	0.0009	-707	0.9	9850	25	10697	-38.05

Le ^{14}C des coquilles a été daté par spectrométrie de masse par accélérateur (AMS) au laboratoire du Keck-Carbon Cycle AMS de l'University de California à Irvine.





Les concentrations radiocarbone sont données comme fractions du standard moderne, D^{14}C , et l'âge radiocarbone conventionnel suit les conventions de Stuiver et Polach (Radiocarbon, v.19, p.355, 1977)

Des échantillons préparés (provenant de calcite sans ^{14}C) mesurant le bruit de fond de l'appareil, ont été soustraits.





Tous les résultats ont été corrigés en fonction du fractionnement isotopique selon les conventions de Stuiver et Polach (1977).


Pour tenir compte de l'âge apparent de réservoir de carbone inorganique dissous, une correction de 400 ans a été appliquée. Pour convertir les âges ^{14}C à des années calendriers, les dates ont été calibrées par CALIB 5.0.1 (Stuiver and Reimer 1993).

I.2 Photos des coquilles datées – 46006

Échantillon	Élévation (m)	Conv. age ¹⁴ C (ans BP)	±	Âge calibré (ans cal BP)	Commentaires	Photo
F46006-TM6	19.57	9265	20	10136	Bivalve complet 1x1 cm	
F46006-TM7	15.55	9625	25	10508	Fragment de bivalve blanc, 1 x 1 cm	
F46006-TM8	9.97	9725	25	10570	Gastéropode, 3 x 3 cm	
F46006-TM8	9.41	9745	25	10585	Coquille de 1 cm écrasée par remaniement	

I.3 Photos des coquilles datées - 46010

Échantillon	Élévation (m)	Conv. age ¹⁴ C (ans BP)	±	Âge calibré (ans cal BP)	Commentaires	Photo
F46010-TM11	-15.27	9365	20	10203	Fragment de coquille 1.5 cm	
F46010-TM17	-24.17	9350	25	10194	Fragment de coquille 1 mm x 1 mm	
F46010-TM20	-32.07	9830	20	10666	Petit fragment de coquille 5 x 8 mm	
F46010-TM21	-34.97	9770	25	10609	Fragment de coquille de bivalve 2x2cm	

Échantillon	Élévation (m)	Conv. age ¹⁴ C (ans BP)	±	Âge calibré (ans cal BP)	Commentaires	Photo
F46010-CF22	-38.05	9850	25	10697	Fragment coquille 0.25 mm x 0.25 mm	

I.4 Tableau des résultats des datations des troncs d'arbres

Coordonnées du site d'échantillonnage

X (UTM19)	Y (UTM 19)
516947	5415307

University of California #	Université Laval #	Échantillon	Matériel	Prétraitement
UCIAMS-80034	ULA-1768	COL-1 (bois)	Branche de conifère	HCl-NaOH-HCl
UCIAMS-80035	ULA-1769	COL-2 (bois)	Branche de conifère	HCl-NaOH-HCl
UCIAMS-80036	ULA-1770	COL-3 (bois)	Branche de conifère	HCl-NaOH-HCl

Échantillon	Fraction moderne	±	D ¹⁴ C	±	Conv. age ¹⁴ C (ans BP)	±	Âge calibré (ans cal BP) (2 sigma)		Distribution
UCIAMS-80034	0.9737	0.0018	-26.3	1.8	215	20	1647	1680	0.393
							1763	1801	0.494
UCIAMS-80035	0.9782	0.0018	-21.8	1.8	175	15	1667	1684	0.193
							1733	1783	0.525
UCIAMS-80036	0.9800	0.0018	-20.0	1.8	160	15	1668	1692	0.165
							1728	1781	0.528

Les trois branches datées ont été récupérées au niveau de la mer sur l'estran.

Les dates ont été calibrées avec le logiciel CALIB6.0 (Stuiver and Reimer 1993) et INTCAL09 (Reimer et al. 2009). Ce tableau présente la distribution probable à 95.4 % (2σ) de l'âge réel de l'échantillon. Seulement les deux plus importantes distributions sont présentées.

Image du site d'échantillonnage



J Rapport d'analyses des isotopes stables pour le ^{13}C et ^{18}O du CaCO_3

J.1 Tableau des résultats

Lieu des analyses : GEOTOP

No de d'identification du projet d'analyses: CA-5005

Pour: Guillaume St-Onge

Type d'analyse: ^{13}C et ^{18}O (CaCO_3)

$\delta^{13}\text{C}$ CaCO_3 exprimé en ‰ vs V-PDB ($\pm 0,05\%$ à 1σ)

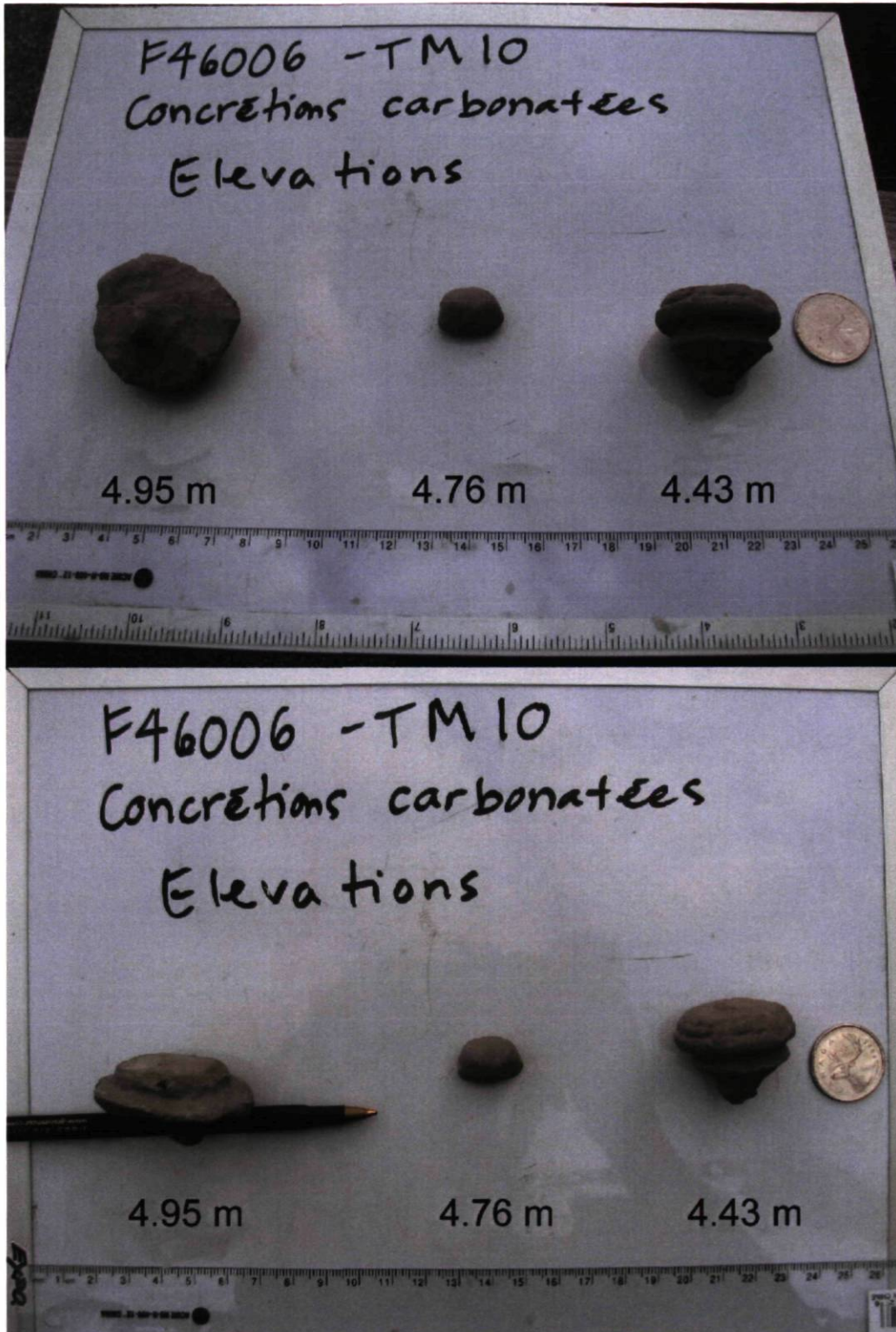
$\delta^{18}\text{O}$ CaCO_3 exprimé en ‰ vs V-PDB ($\pm 0,05\%$ à 1σ)

Les données brutes sont corrigées à l'aide du carbonate de référence UQ6 ($\delta^{13}\text{C}=+2,25\%$ vs V-PDB ; $\delta^{18}\text{O}=-1,4\%$ vs V-PDB).

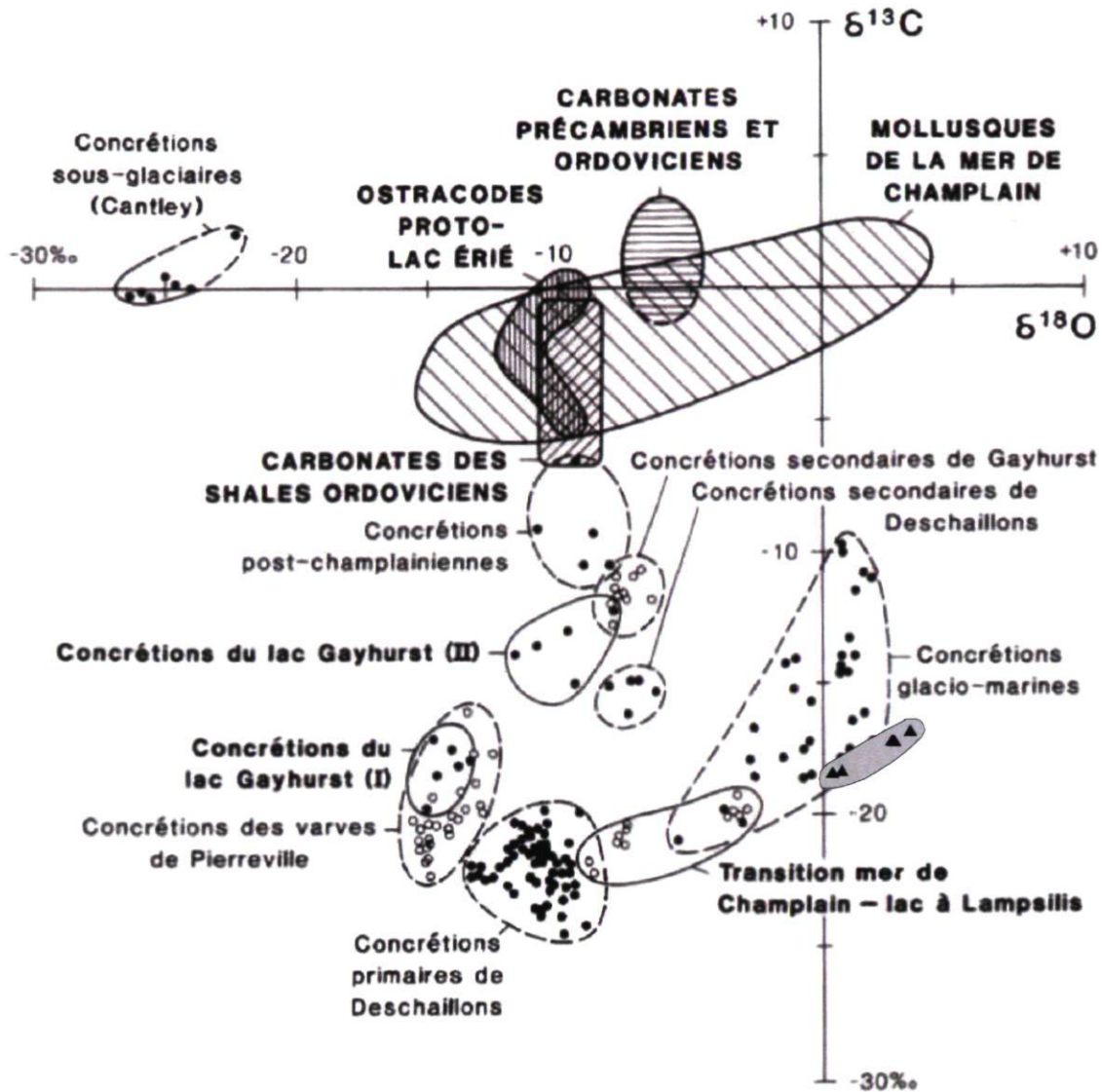
Forage	X (UTM19)	Y (UTM 19)
F46006	516958	5416735

Échantillon	ID labo	Profondeur dans le forage (m)	Élévation moyenne de la mesure (m)	Masse de l'échantillon (ug)	Date d'analyse	$\delta^{13}\text{C}$	$\delta^{18}\text{O}$
F46006-TM10-C1	CA5005 Concrétion 1 71ug	42.67	4.95	71	1/13/2009	-18.32	0.78
F46006-TM10-C1	CA5005 Concrétion 1 101ug	42.67	4.95	101	1/28/2009	-18.39	0.43
F46006-TM10-C2	CA5005 Concrétion 2 84ug	42.86	4.76	84	1/13/2009	-16.80	3.38
F46006-TM10-C3	CA5005 Concrétion 3 132ug	43.19	4.43	132	1/28/2009	-17.17	2.69
F46006-TM10-C4	CA5005 Concrétion 4 102ug	43.37	4.25	102	1/13/2009	-17.19	2.79
F46006-TM10-C4	CA5005 Concrétion 4 134ug	43.37	4.25	134	1/28/2009	-17.17	2.74

J.2 Photos des concrétions carbonatées



J.3 Corrélation régionales



Valeurs isotopiques en ^{18}O et ^{13}C des concrétions des basses-terres du St-Laurent, (Hillaire-Marcel et Causse, 1989). Les triangles dans la zone grise indiquent les valeurs obtenues pour les concrétions échantillonnées à Colombier dans le tube F46006-TM10.

Hillaire-Marcel, C., and Causse, C. 1989. Chronologie Th/U des concrétions calcaires des varves du lac glaciaire de Deschailions (Wisconsinien inférieur). *Canadian Journal of Earth Sciences*, 26(5): 1041-1052.

K Données de profilage de conductivité, température et de profondeur (CTD)

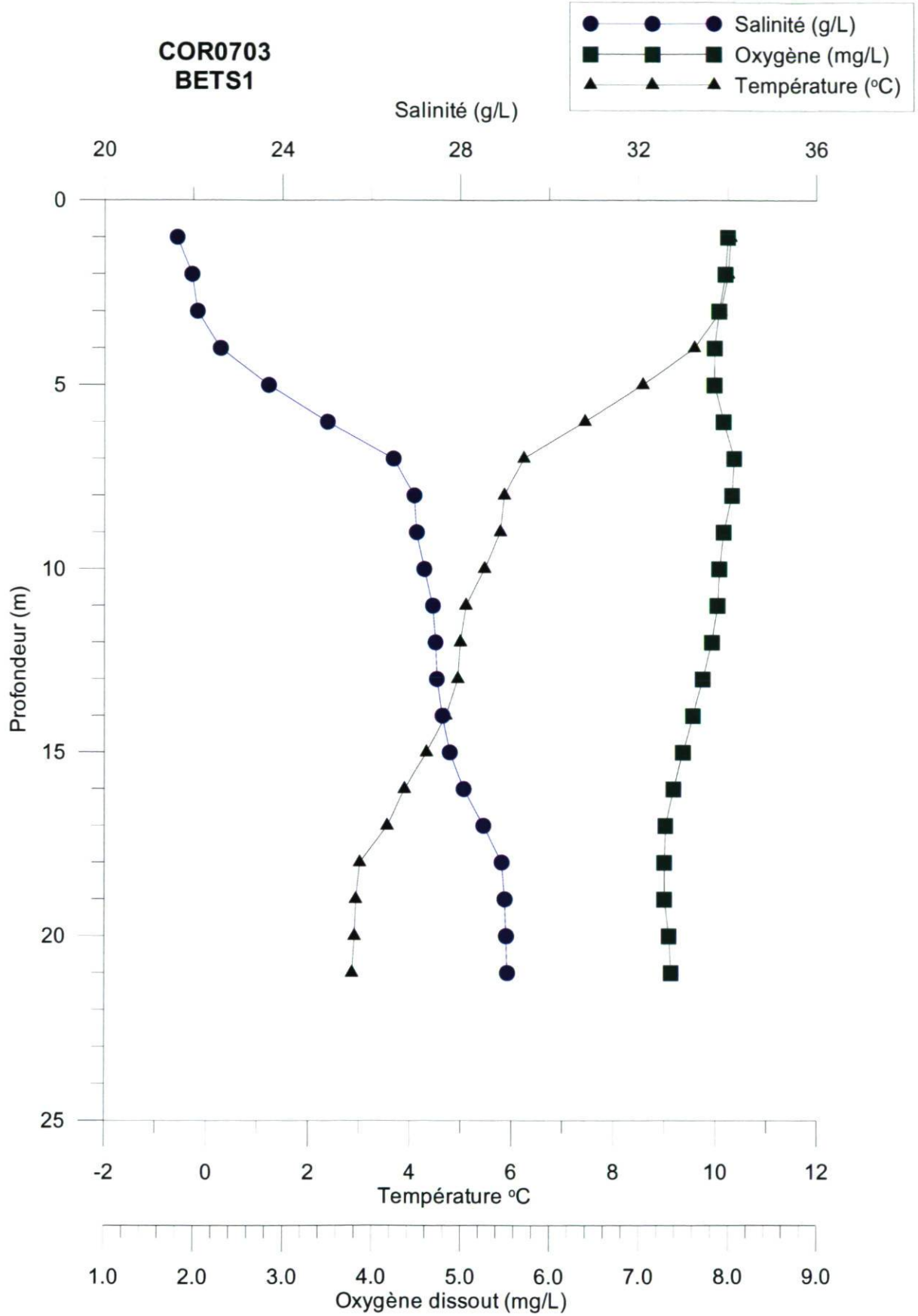
Nom de fichier	Station	Position	Latitude (N)	Longitude (W)	UTM X	UTM Y	Heure EDT	Prof totale (m)
CTD_2007002_001_1_DN.ODF	BETS1	Entrée	48°53,13	68°43,19	5414767	520528	17h25	26m
		Sortie	48°53,14	68°43,23	5414787	520480	17h30	
CTD_2007002_002_1_DN.ODF	BETS2	Entrée	48°51,13	68°41,09	5411087	523115	17h50	122m
		Sortie	48°51,10	68°41,22	5411021	522955	17h57	
CTD_2007002_003_1_DN.ODF	BETS3	Entrée	48°48,48	68°38,19	5406180	526682	18h23	326m
		Sortie	48°48,35	68°38,18	5405946	526697	18h38	

Date des trois mesures : 8 juin 2007

Mission : COR0703

Selon les conventions de Québec-Océan, les données traitées et validées de la mission COR0703 sont identifiées par le code 0702.

**COR0703
BETS1**



COR0703
BETS2

